Mitigating Interfacial Degradation in Sulfide-Based Solid-State Batteries using Polymer Coatings and Surface-Modified Solid Electrolytes

Dem Fachbereich Biologie und Chemie
der Justus-Liebig-Universität Gießen vor-
gelegte Dissertation zur Erlangung
des akademischen Grades
Doktor der Naturwissenschaften

Bing-Xuan Shi

April 2025

Dekan/Dean	Prof. Dr. Thomas Wilke
1. Gutachter / 1st Reviewer	Prof. Dr. Jürgen Janek (Justus-Liebig-Universität Gießen)
2. Gutachter / 2nd Reviewer	Prof. Dr. Helmut Ehrenberg (Karlsruher Institut für Technologie)
Eingereicht / Submitted	11.04.2025

Eigenständigkeitserklärung / Declaration of Originality

Die vorliegende Arbeit wurde im Zeitraum vom 01.03.2021 bis 11.04.2025 am Physikalisch-Chemischen Institut der Justus-Liebig Universität Gießen unter Betreuung von Prof. Dr. Dr. h. c. Jürgen Janek angefertigt.

Ich erkläre:

Ich habe die vorgelegte Dissertation selbstständig und ohne unerlaubte fremde Hilfe und nur mit den Hilfen angefertigt, die ich in der Dissertation angegeben habe. Alle Textstellen, die wörtlich oder sinngemäß aus veröffentlichten Schriften entnommen sind, und alle Angaben, die auf mündlichen Auskünften beruhen, sind als solche kenntlich gemacht. Ich stimme einer evtl. Überprüfung meiner Dissertation durch eine Antiplagiat-Software zu. Bei den von mir durchgeführten und in der Dissertation erwähnten Untersuchungen habe ich die Grundsätze guter wissenschaftlicher Praxis, wie sie in der „Satzung der Justus-Liebig-Universität Gießen zur Sicherung guter wissenschaftlicher Praxis“ niedergelegt sind, eingehalten.

This thesis was prepared in the period from 01.03.2021 to 11.04.2025 at the Physical-Chemical Institute of the Justus Liebig University Giessen under the supervision of

Prof. Dr. Dr. h. c. Jürgen Janek.

I declare that I have completed this dissertation single-handedly without the unauthorized help of a second party and only with the assistance acknowledged therein. I have appropriately acknowledged and cited all text passages that are derived verbatim from or are based on the content of published work of others, and all information relating to verbal communications. I consent to the use of an anti-plagiarism software to check my thesis. I have abided by the principles of good scientific conduct laid down in the charter of the Justus Liebig University Giessen „Satzung der Justus-Liebig-Universität Gießen zur Sicherung guter wissenschaftlicher Praxis“ in carrying out the investigations described in the dissertation.

Gießen, 11.04.2025

Bing-Xuan Shi

Abstract

The growing market for electric vehicles is driving demand for high-energy-density batteries. Conventional liquid electrolyte batteries (LEBs) are nearing their energy-density limits, while solid electrolyte batteries (SEBs) using high-nickel cathode active materials (CAMs), solid electrolytes (SEs), and the lithium metal anode promise much higher energy densities. Sulfide-based SEs, such as Li_6PS_5Cl, exhibit particularly high ionic conductivity, making them promising candidates for industrial applications. However, the interfacial degradation between sulfide-based SEs and electrodes limits their electrochemical performance. This dissertation explores innovative strategies to enhance the interfacial stability at both the cathode-electrolyte interphase (CEI) and the solid electrolyte interphase (SEI) in SEBs, focusing on polyelectrolyte coatings and modified sulfide-based SEs.

Polyelectrolytes are selected as electrode coating materials in this dissertation for their flexibility, ease of processing, and lower cost than inorganic coatings. Moreover, they provide intrinsic ionic conductivity compared to neutral polymers, which is essential in SEBs but less of a concern in LEBs. While polymers as coatings in LEBs are well-studied, there is limited insight into their use in SEBs. This gap motivates this dissertation, demonstrating how polyelectrolytes enhance interfacial stability and performance in SEBs. The journey begins with exploring a polycation coating on $LiNi_{0.83}Co_{0.11}Mn_{0.06}O_2$ using the spray-drying method, revealing their potential and limitations. The polycation coating uniformly covers CAM particles to enhance cycling stability, but improved lithium-ion conductivity is needed to prevent capacity loss. Building on these findings, a subsequent study introduces a polyanion/amide polymer blend as a coating on $LiNi_{0.9}Co_{0.05}Mn_{0.05}O_2$, with the polyanion providing a lithium source to mitigate capacity loss and the amide polymer serving as a coating inducer. However, the polyanion/amide polymer coating demonstrates stiffness that needs more flexibility. As a result, a polyelectrolyte complex (PEC) coating is developed for $LiNiO_2$ (LNO) cathode and a Si anode. This PEC employs a polycation to induce coating formation alongside a polyanion with a flowing nature that enhances both lithium-ion conductivity and flexibility.

On the other hand, compared with the use of polyelectrolyte coatings, the modification of sulfide-based SEs via solvent treatment provides another approach to reducing the interfacial degradation of SEBs. This method improves the interfacial stability between the LNO cathode and the sulfide-based SE while preventing dendrite formation from the lithium metal anode. Additionally, modified sulfide-based SEs reveal a mechanism for enhancing cathodic performance different from the polyelectrolyte coating layer. This suggests that the combination of polyelectrolyte coatings with modifications to sulfide-based SEs could further bolster interfacial stability.

This dissertation comprises four studies, including polyelectrolyte-coated electrodes and modified sulfide-based SEs in SEBs. Each study employs a distinct approach to mitigate interfacial degradation and shows promising potential for industrial application. Collectively, these investigations provide a comprehensive understanding of the strategies to improve interfacial stability while providing future strategies that can be further developed and studied.

Abbreviations

Abbreviation	Full form
A	Contact area
CAM	Cathode active material
CCD	Critical current density
CEI	Cathode-electrolyte interphase
CTTA	Coulometric titration time analysis
DMF	Dimethyl formamide
$E_{\mathrm{ele}}^{\mathrm{j}}$	Electrostatic energy
EIS	Electrochemical impedance spectroscopy
ESW	Electrochemical stability window
F	Faraday constant
FSI	Bis(fluorosulfonyl)imide
G/B	Pugh's ratio
HE	Hybrid electrolyte
HEB	Hybrid electrolyte battery
HOMO	Highest occupied molecular orbital energy
k	Kinetic constant of the $\Delta\xi$ growth
k'	Kinetic constant of the $\Delta R_{\mathrm{interphase}}$ growth
L_{diff}	Lithium-ion diffusion pathway length
LE	Liquid electrolyte
LEB	Liquid electrolyte battery (e.g. lithium-ion battery)
LiTFSI	Lithium bis(trifluoromethanesulfonyl)imide
LiSiPS	Tetra-Li_7SiPS_8
LNO	$LiNiO_2$
LUMO	Lowest occupied molecular orbital energy
m_{act}	Active mass
MCI	Mixed-ionic/electronic conducting interphase
NCM	$LiNi_xCo_yMn_zO_2$ ($x+y+z=1$)
NMP	*N*-Methyl-2-pyrrolidone
OCV	Open-circuit voltage
φ	Electric potential
PAA	Poly(acrylic acid)
PAH	Poly(allylamine)
PAMPS	Poly(acrylamido-2-methylpropanesulfonate)
PDADMA	Poly(diallyldimethylammonium)

PDDP	Poly(*N*,*N*-dimethyl-3,5-dimethylene piperidinium)
PE	Polymer electrolyte
PEB	Polymer electrolyte battery
PEC	Polyelectrolyte complex
PMMA	Polymethyl methacrylate
PSS	Poly(styrenesulfonate)
PVA	Poly(vinylamine)
PVBTA	Poly((4-vinylbenzyl)trimethylammonium
PVBTA-TFSI	Poly((4-vinylbenzyl)trimethylammonium bis(trifluo-romethanesulfonylimide))
PVP	Polyvinylpyrrolidone
PVS	Poly(vinylsulfonate)
q_{redox}	Redox capacity
$R_{\text{interphase}}$	Interphase resistance
RLC	Residual lithium compound
σ_{ele}	Electronic conductivity
σ_{ion}	Ionic conductivity
σ_{Li^+}	Ionic conductivity of the lithium ion
$\sigma_{\text{interphase}}$	Average conductivity of the interphase
SEI	Solid electrolyte interphase
SEM	Scanning electron microscopy
SEB	Solid electrolyte battery
SSB	Solid-state battery
SOC	State of charge
sPPSLi	Sulfonated polyphenylene sulfone
t	Time
TEM	transmission electron microscopy
T_{g}	Glass transition temperature
THF	Tetrahydrofuran
ToF-SIMS	Time-of-flight secondary ion mass spectrometry
$\tilde{\mu}_i^{\text{j}}$	Electrochemical potential
μ_i^{j}	Chemical potential
V_{m}	Average molar volume of the interphase
ξ	Euclidean distance
z_i	Charge number of the species "i"

Table of contents

1. Introduction

Rechargeable batteries have experienced significant evolution over the decades. The first commercial nickel–cadmium battery traces back to E. W. Jungner's 1899 patents in Sweden,[1] followed by nickel-metal hydride batteries.[2] In 1991, Sony Corporation introduced first commercialized lithium-ion batteries employing liquid electrolytes (LEs). In this dissertation, electrochemical cells using LEs are denoted as liquid electrolyte batteries (LEBs).[3] In 2001, Dahn's group further advanced ternary nickel-cobalt-manganese layered cathode materials (NCMs), $LiNi_xCo_yMn_zO_2$ ($x+y+z=1$), which have since become one of the most widely commercialized cathode active materials (CAMs).[4] Building on this progress, scientists continue to focus on enhancing battery energy density and power density. LEBs revolutionized energy storage and earned the 2019 Nobel Prize in chemistry, awarded to J.B. Goodenough, M.S. Whittingham, and A. Yoshino.

Batteries with an energy density of up to 200 $Wh \cdot kg^{-1}$ are suited only for simple energy storage purposes, whereas electric vehicles with a 600 km range require batteries with around 200~300 $Wh \cdot kg^{-1}$ energy density.[5] Since 2000, the energy density of LEBs has increased from 200 $Wh \cdot kg^{-1}$ to about 300 $Wh \cdot kg^{-1}$ by 2023.[6] For instance, a LEB based on $LiNi_{0.8}Co_{0.15}Al_{0.05}O_2$ versus graphite reaches an energy density of 265 $Wh \cdot kg^{-1}$ and 635 $Wh \cdot l^{-1}$.[6, 7] However, conventional LEBs are nearing their energy density limit (≈ 400 $Wh \cdot kg^{-1}$),[6] while vehicles with a 600~1200 km range require 300~600 $Wh \cdot kg^{-1}$.[5]

SSBs without any liquid components promise to pair with high energy density CAMs due to their potential for bipolar stacking, compatibility with lithium metal anodes, potentially lower cost (below 100 $\$ \cdot kWh^{-1}$), and improved safety. [5, 7, 8] Given their potential to surpass 500 $Wh \cdot kg^{-1}$,[9] SSBs are poised to become a key technology for future electric vehicles. For example, a SSB using a $LiNi_{0.8}Co_{0.15}Al_{0.05}O_2$ paired with a lithium metal anode may theoretically achieve an energy density of 393 $Wh \cdot kg^{-1}$ and 1143 $Wh \cdot L^{-1}$.[6, 7] Additionally, Lee et al. published an anode-free SSB that plates lithium metal from the CAM onto an Ag–C counter electrode, achieving an energy density over 900 $Wh \cdot L^{-1}$, surpassing LEBs (≈ 600 $Wh \cdot L^{-1}$).[10]

The field of SSBs encompasses solid electrolyte batteries (SEBs), polymer electrolyte batteries (PEBs), and hybrid electrolyte batteries (HEBs),[3] utilizing solid electrolytes (SEs), polymer electrolytes (PEs), and hybrid electrolytes (HEs), respectively.[3] High ionic conductivity (σ_{ion}) is required for these electrolytes, along with low electronic conductivity (σ_{ele}), excellent stability (thermal, electrochemical, and chemical), and ease of integration and processing. Among these electrolytes, SEs are gaining attention for commercialization due to their potential to replace LEs[6, 7] and their superior σ_{ion} compared to PEs.[11, 12] In addition, material costs account for over 75% of total production expenses in battery fabrication.[13] Sulfide-based SEs offer a cost advantage, with production costs estimated at 102 $\$ \cdot kWh^{-1}$, compared to 120 $\$ \cdot kWh^{-1}$ for conventional LEs.[13]

Recent developments from 2024 to the beginning of 2025 highlight the transformative potential of SEBs in driving industry growth. Honda, Nissan, and Toyota plan to begin SEB production in early 2025, while Idemitsu Kosan collaborates with Toyota on sulfide-based SEs. Mercedes-Benz and Factorial are

developing 'Solstice', which aims to achieve a SSB energy density of 450 Wh·kg^{-1}. ProLogium is investing €5.2 billion in a 48 GWh gigafactory to produce SEBs in Europe.

SEs can be classified into oxide-, halide-, and sulfide-based SEs.[11] Oxide SEs have better chemical and air stability than sulfide-based SEs but have significant grain boundary resistance.[12, 14, 15] Halide SEs are often used as a catholyte due to superior electrochemical stability against oxide CAM.[16] However, their stability is compromised when paired with lithium metal anodes.[12, 17] Notably, sulfide-based SEs show low grain boundary resistance[18] and have the highest σ_{ion} of around 2 to 10 mS·cm^{-1} at 25 °C among other SEs.[7, 19, 20] However, its (electro)chemical instability against cathode and anode electrodes hinders commercialization. As a result, this thesis focuses on improving the interfacial stability between electrodes and the sulfide-based SE.

On the other hand, PEs, including polyelectrolytes and/or nonconductive polymers combined with lithium salts, bring flexibility and easy processing.[6] Additionally, polymers have strong adhesive properties.[6] Hence, polymers are commonly used as binders in the CAM composite in SSBs and LEBs to enhance the composite layer thickness and increase the CAM content.[6] However, the σ_{ion} of PEs (below 10^{-1} mS·cm^{-1} at 25 °C) is not enough to be used as a catholyte,[7, 11, 12] as achieving σ_{ion} around 5 mS·cm^{-1} at 25 °C (by calculation of theoretical models) is essential for the catholyte in SSBs to ensure competitive performance.[21] On the other hand, sulfide-based SEs match the catholyte requirement that σ_{ion} is high enough. Therefore, integrating the benefits of polymers into SEBs requires further research.[6]

The role of polymers in sulfide-based SEBs is often limited to serving as binders or coatings on electrodes, yet they are essential.[6] It has several benefits over inorganic materials, such as mechanical properties (see **Section 2.9**) and better interfaces against SEs (see **Section 2.7.2**). However, limited literature explores the application of PE coatings on CAMs and the silicon anode in sulfide-based SEBs. Considering these factors, developing polymer coatings for electrodes is one of the focuses of this thesis.

The following paragraphs summarize four publications addressing interfacial degradation mitigation in the sulfide-based SEB. The CAMs for investigating the interfacial degradation include NCMs from MSE Supplies LLC and self-synthesized single-crystal $LiNiO_2$ (LNO). For full cells, the anodes consist of silicon or lithium metal, whereas half-cells use a LiIn alloy as the anode. **Publications A** and **B** have been consolidated into a patent, with application No. EP22199267.0 and PCT publication No. WO 2024/068975 A1. Additionally, **Publication C** corresponds to a patent, with application No. EP24199168.6. However, the patent for **Publication D** is currently being processed.

Publication A is titled “Mitigating Contact Loss in Li_6PS_5Cl-Based Solid-State Batteries Using a Thin Cationic Polymer Coating on NCM”. This study forms a 2~4 nm novel polycation coating on $LiNi_{0.83}Co_{0.11}Mn0.06O_2$ by a spray-drying method. The results show that the polycation-coated NCM has better cycling stability than the pristine NCM. Additionally, the spray-drying method is suitable for large-scale production for industrial applications. The polycation used as a coating material is poly((4-vinylbenzyl)trimethylammonium bis(trifluoromethanesulfonylimide)) (PVBTA-TFSI), as shown in **Figure 1a**.

Publication B is titled “Lithiated polymer coating for interface stabilization in Li_6PS_5Cl-based solid-state

batteries with high-nickel NCM". This study shows that using a polyanion as a lithium-ion source and polyvinylpyrrolidone (PVP) as a coating inducer creates a uniform 1~3 nm layer on $LiNi_{0.9}Co_{0.05}Mn_{0.05}O_2$ particles via spray-drying, improving electrochemical performance over the polycation coating. The polyanion used as a coating material is sulfonated polyphenylene sulfone (sPPSLi), as shown in **Figure 1b**.

Publication C is currently under review following its submission. It is titled "Surface Modification of Thiophosphate Solid Electrolyte for Performance Enhancement in Li|Li_6PS_5Cl|LNO Solid-State Batteries". This publication presents a novel modification method for sulfide-based SEs, Li_6PS_5Cl, providing an alternative approach to mitigate LNO/Li_6PS_5Cl interfacial degradation compared to directly applying coatings on LNOs. Moreover, modifying sulfide-based SEs enhances interfacial stability with the lithium metal anode.

Publication D is under preparation for submission. It is titled "Improving Sulfide-Based Solid-State Batteries Using a Novel Polyelectrolyte Complex Coating on High-nickel NCM and Silicon Anodes". This publication presents a polyelectrolyte complex (PEC) (**Figure 1c**) utilizing a polycation as a coating inducer and a polyanion with a flowing nature as a lithium-ion source to coat the $LiNi_{0.9}Co_{0.05}Mn_{0.05}O_2$ and LNO cathode, along with the silicon anode. The 1~3 nm PEC coating has a rubber-like mechanical property and uniformly covers electrode particles, effectively mitigating interfacial degradation at both the CAM and Si anode interfaces. Additionally, **Publications C** and **D** use the same batch of self-synthesized single-crystal LNO as a reference, thereby enabling a direct comparison of their interfacial degradation.

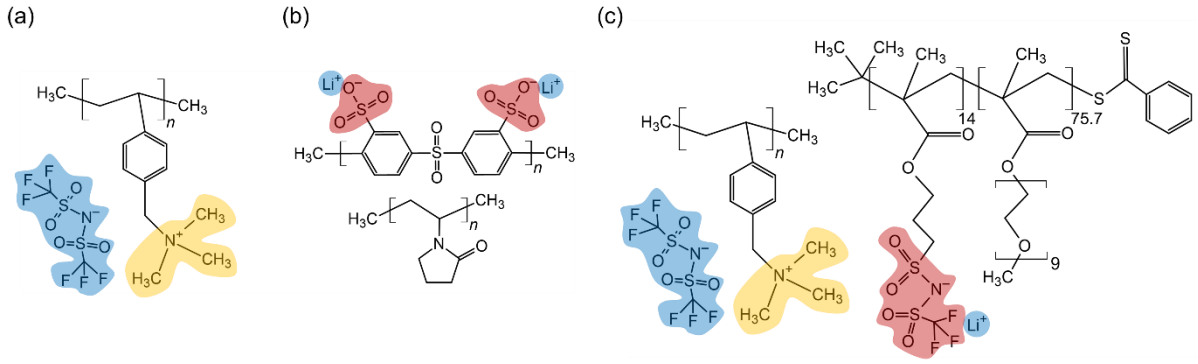

Figure 1. The polyelectrolyte structures tested in publications are illustrated. Counter ions are shown in blue, anionic species in red, and cationic species in yellow. (a) **Publication A:** PVBTA-TFSI (b) **Publication B:** sPPSLi blended with PVP. (c) **Publication D:** a PEC composed of PVBTA-TFSI and poly[(lithium 1-[3-(methacryloyloxy)propylsulfonyl]-1-(trifluoromethanesulfonyl)imide)-r-(poly(ethylene glycol) methyl ether methacrylate)].

2. Fundamentals

A SEB consists of three main components (see **Figure 2**): an anode (e.g., lithium metal or a silicon composite), a SE separator, and a composite cathode that incorporates a SE catholyte, conductive additives (e.g., vapor-grown graphitic carbon fiber, VGCF), and CAMs. During discharge, lithium ions move from the CAM to the anode through the SE; while charging, they reverse direction. However, degradation within the electrode bulk, combined with interfacial degradation such as unstable interphase formation and contact loss between the electrode materials and the SEs, leads to a decline in electrochemical performance. Precisely, the interphase formed at the anode is termed the solid electrolyte interphase (SEI), while at the cathode, it is known as the cathode-electrolyte interphase (CEI). This dissertation proposes using modified sulfide-based SEs and polymer coatings on CAMs and silicon anodes to mitigate interfacial degradation.

The following sections outline the fundamentals of various CAMs and their bulk degradation, particularly high-nickel NCM and LNO. Notably, as the nickel content in NCM increases, its electrochemistry increasingly resembles that of LNO. Consequently, the discussion primarily focuses on the electrochemistry of LNO, using it as a reference for understanding high-nickel NCM. Subsequently, sulfide-based SEs are introduced, followed by their interfacial degradation mechanisms, including CEI and SEI. Finally, the chapter introduces polyelectrolytes as coating materials for CAMs. The fundamental section provides background knowledge on electrode materials and their interfacial stability in sulfide-based SEBs.

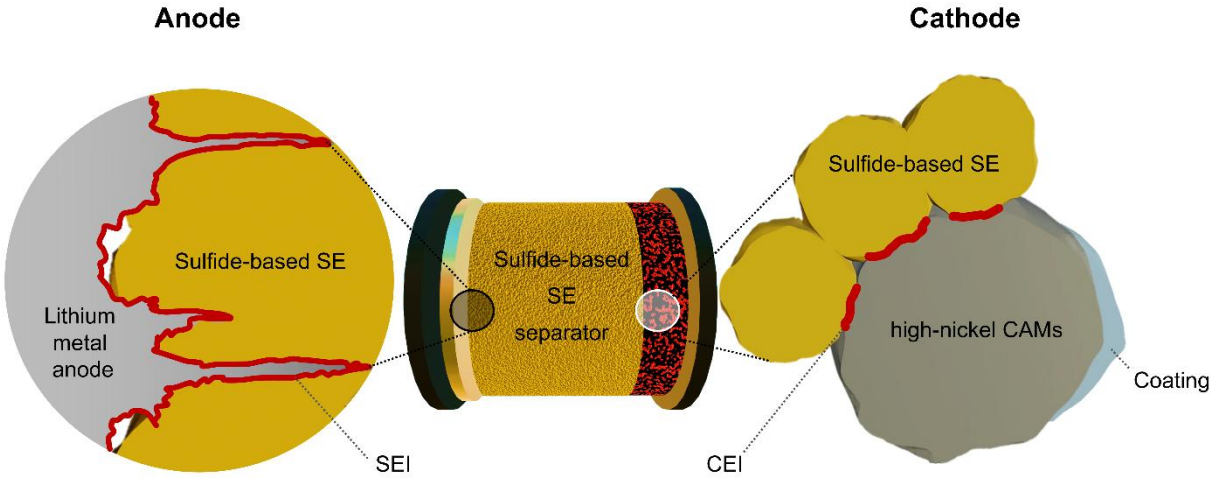

Figure 2. The schematic diagram of SEB illustrates the anode, separator, and cathode composite. The cathode (right) comprises CAMs, CEI, and a coating layer, with the sulfide-based SE as catholyte. The sulfide-based SE separator (middle) separates the cathode and anode (left), including the lithium metal anode, with the SEI.

2.1 The selection of CAMs

Ideally, CAMs should have high σ_{Li^+} and σ_{ele} and be (electro)chemically stable with SEs. Additionally, high safety, low cost, and low toxicity are essential for commercial applications. CAMs typically have a (1) $LiMPO_4$ olivine structure ($LiFePO_4$), (2) LiM_2O_4 spinel structure ($LiMn_2O_4$), or (3) $LiMO_2$ layered structure ($LiCoO_2$, $LiMnO_2$, LNO, lithium-rich CAMs, and NCM), where M represents transition metals.[22]

Olivine-structured $LiFePO_4$ is cost-effective, safe, and widely used in electric vehicles and energy storage systems. It provides a theoretical capacity of about 170 $mAh \cdot g^{-1}$ at a discharge voltage of around 3.4 V vs. Li^+/Li. However, $LiFePO_4$ has relatively low σ_{Li^+} and σ_{ele}. As a result, it requires modifications to enhance σ_{ele}, such as carbon coating.[23] Moreover, its energy density remains relatively low when paired with a graphite anode in LEBs (around 200 $Wh \cdot kg^{-1}$).[24] On the other hand, $LiMO_2$ features an α-$NaFeO_2$-type layered structure and crystallizes in the rhombohedral system (R-3m space group). In this structure, O_2^- ions form a cubic close-packed framework. Lithium ions and transition metals occupy the 3b and 3a sites, respectively.[25] As a result, $LiMO_2$ has superior lithium-ion diffusion in a two-dimensional structure and higher energy capacity than other CAMs.[22]

$LiCoO_2$, with a theoretical capacity of 274 $mAh \cdot g^{-1}$, introduced by Goodenough,[26] is the first commercialized layered CAM used in LEBs. It offers advantages in fast charging, but its practical capacity is half of its theoretical capacity. Additionally, it faces the stability issue at high voltages (> 4.2 V vs. Li^+/Li).[27] $LiMnO_2$ with a theoretical capacity of 285 $mAh \cdot g^{-1}$ is considered safer than the other layered $LiMO_2$, but repeated cycling converts it into spinel $LiMn_2O_4$.[28] While spinel structure improves lithium-ion transport due to a three-dimensional structure, it has lower theoretical capacity (≈ 148 $mAh \cdot g^{-1}$) and fades rapidly due to structural degradation.[28]

LNO offers a theoretical capacity comparable to LCO but benefits from lower costs than other layered $LiMO_2$. Additionally, it offers the highest practical capacity due to the highest lithium extraction ratio at the same cut-off voltage as $LiMnO_2$ and $LiCoO_2$.[29] However, despite decades of research, its commercialization remains limited due to the structural and CEI degradation. Moreover, precise composition control during synthesis is challenging because it is highly susceptible to lithium off-stoichiometry.[30]

Research on LNO has led to developing high-nickel NCMs, which involve the partial substitution of Ni with Co and Mn.[31-33] For example, $LiNi_{0.8}Co_{0.1}Mn_{0.1}O_2$ allows delithiation up to 0.8% at 4.3 V vs. Li^+/Li.[29, 32, 33] They have gained attention and are gradually replacing $LiFePO_4$ in the electric vehicle market.[34] The properties of NCM are influenced by the ratios of Ni, Co, and Mn (see **Figure 3a**).[32] Although higher nickel content enhances practical capacity, it also leads to more severe interfacial and structural instability. (see **Figure 3b**). Increased Co content improves rate capability, while increased Mn content improves thermal stability and safety.[31] Therefore, increasing the Ni content in NCM promise to boosting energy density if stability can be improved. Since LNO exhibits electrochemistry similar to high-nickel NCMs, though with more pronounced degradation, **Sections 2.2** to **2.4** use LNO as an example to illustrate these aspects.

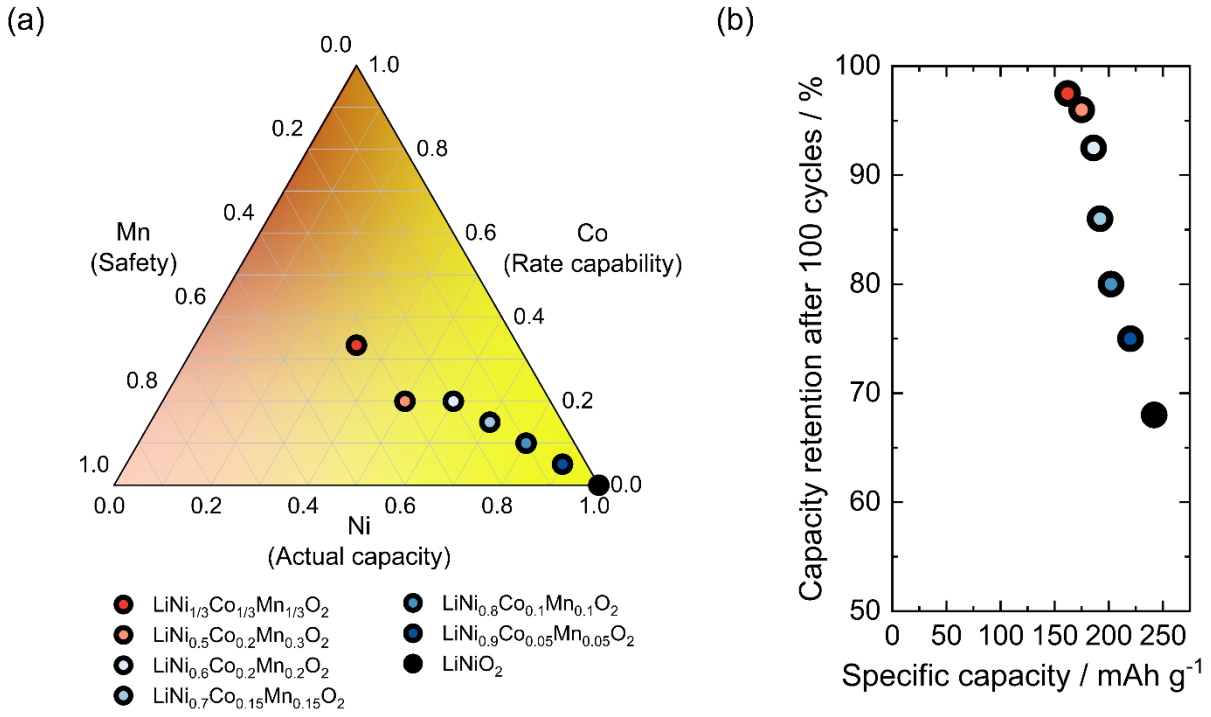

Figure 3. (a) Phase diagram of NCM composition showing several typical Ni-Co-Mn ratios. (b) Specific capacity ($mAh \cdot g^{-1}$) versus capacity retention (%) over 100 cycles for various NCM materials, correlated to (a), as analyzed in LEBs.[32] Figure (b) was modified based on the Ref. [32].

2.2 Synthesis challenges of LNO

Regardless of the synthesis method, LNO often exhibits lithium deficiency due to excess Ni^{2+} ions occupying lithium layers, referred to as 'off-stoichiometric' LNO. The off-stoichiometric LNO can be written as $Li_{1-z}Ni_{1+z}O_2$ or $[Li_{1-z}Ni^{2+}_z]_{3b}[Ni^{2+}_zNi^{3+}_{1-z}]_{3a}[O_2]_{6c}$ ($z > 0$,), where Ni^{2+} ions are present with half of them located in the Li layer and the other half in the Ni layer, causing cation disordering. This off-stoichiometry adversely affects its theoretical capacity, first-cycle Coulomb efficiency, and phase transition during charge and discharge, as discussed in **Section 2.4**.[30, 35]

Various synthesis methods have been developed, with solid-state reactions being the most common. The coprecipitation method, which involves mixing precursors in solution, is popular in industrial applications and relies on a calcination process similar to solid-state reactions.[30] Generally, Ni^{2+} precursors are oxidized to Ni^{3+} during synthesis with an O_2 flow. If Li_2O is used as a precursor, the reaction can be written as **Equation 1**.[30]

$$(1 - z')\,NiO + \frac{z'}{2}\,Li_2O + \frac{z'}{4}\,O_2 \rightarrow Li_{z'}Ni_{1-z'}O_2 \rightarrow \frac{1}{2}\,Li_{1-z}Ni_{1+z}O_2 \left(z' = \frac{1-z}{2}\right) \quad \textbf{(Eq. 1)}^{30}$$

The calcination temperature is critical because a high temperature above 800 °C produces a well-crystallized structure quickly but results in lower O_2 chemical potential, which hinders the complete oxidation of Ni^{2+} to Ni^{3+}. In addition, LNO can decompose above 800 °C (see **Equation 2**[30]). Both factors can cause the off-stoichiometric $Li_{1-z}Ni_{1+z}O_2$,[30, 35] which can be either a layered off-stoichiometric phase ($z <$

0.38) or a rock-salt type phase ($z > 0.38$), depending on the extent of the decomposition.

$$LiNiO_2 \rightarrow \frac{1}{1+z} Li_{1-z}Ni_{1+z}O_2 + \frac{z}{1+z} Li_2O + \frac{z}{2(1+z)} O_2 \quad \textbf{(Eq. 2)}^{30}$$

Calcination at lower temperatures around 700 °C is considered optimal. However, lower temperatures may cause impurity phases from unreacted precursors and poorly crystallized small particles. As a result, the decomposition temperature of lithium precursors must be optimized to react promptly with Ni while avoiding high temperatures causing LNO decomposition. Lithium precursors such as lithium hydroxides, oxides, nitrides, and peroxides are preferred due to their lower decomposition temperatures. Moreover, high Li/Ni ratios (more lithium precursors) reduce the off-stoichiometric $Li_{1-z}Ni_{1+z}O_2$ but necessitate a post-calcination washing process to remove unreacted precursors.[30] In this dissertation, LNO is synthesized using the procedure described by Rueß et al.[36] In this method, agglomerated LNO crystallites are exposed to a Li_2CO_3 melt. The Li_2CO_3 promotes primary particle growth and separation while maintaining a high Li_2O chemical potential that prevents lithium loss.[36]

2.3 Environmental influence on LNO

Several studies have reported the detrimental impact of atmospheric H_2O and CO_2 on the LNO through parasitic side reactions. Generally, LNO reacts with atmospheric H_2O and CO_2, reducing Ni^{3+} to Ni^{2+} and forming LiOH (Li and H are cation-exchanged) and Li_2CO_3 on the surface of LNO (see **Equation 3** to **5**). This reaction facilitates a near-surface transformation of layered structure into rock-salt phases.[37-39]

$$LiNiO_2 + x\,H_2O \rightarrow Li_{1-x}H_xNiO_2 + x\,LiOH \quad \textbf{(Eq. 3)}^{37}$$

$$2\,LiNiO_2 + x\,H_2O + xCO_2 \rightarrow 2\,Li_{1-x}H_xNiO_2 + x\,Li_2CO_3 \quad \textbf{(Eq. 4)}^{37}$$

$$2\,LiNiO_2 + CO_2 \rightarrow 2\,NiO + Li_2CO_3 + \frac{1}{2} O_2 \quad \textbf{(Eq. 5)}^{38}$$

Additionally, LiOH or Li_2CO_3 can come from the synthesis process. Moreover, the ambient air exposure/storage transforms residual Li_2O (from the synthesis) into LiOH and Li_2CO_3, with Li_2CO_3 being the predominant component.[38] As a result, residual lithium compounds (RLCs), e.g., LiOH and Li_2CO_3, are commonly present on the LNO surfaces.

In LEBs, RLCs increase slurry pH, leading to fluorinated polymer binder decomposition and gelation during cathode sheet preparation.[38, 40, 41] Additionally, RLCs decompose during electrochemical tests in LEBs, generating CO_2 and CO gaseous products[42] and reactive oxygen species[43]. In SEBs, avoiding fluorinated polymers in the slurry process or using a dry pressing method for cathode sheet preparation can prevent fluorinated binder gelation. However, RLCs impede ionic and electronic transport at the LNO/SE interface.[38, 44] Moreover, if RLCs get oxidized and form gaseous products,[45, 46] it is reasonable to expect increased contact resistance, as SE particles cannot fill cavities as do LEs.[38] Although in sulfide-based SEBs, an artificial Li_2CO_3 coating layer on the high-nickel NCM particle can reduce interfacial degradation, pure CO_2 or moisturized air reacting with high-nickel NCMs does not yield the same benefits.[38] Notably, the instability between LNO and H_2O highlights the importance of solvent selection for the wet coating process, requiring the avoidance of water and alcohol-based solvents.

2.4 Electrochemistry and degradation of LNO

During the charging step, an ideal LNO without off-stoichiometry undergoes oxidation from Ni^{3+} to Ni^{4+} through delithiation, achieving a high theoretical specific capacity of 275 $mAh \cdot g^{-1}$.[30] The strong electrostatic interactions from ionic bonds stabilize the structure and enable multiple phase transitions. The deintercalation of lithium ions from LNO (Li_xNiO_2, $0 < x < 1$) triggers phase transitions: hexagonal (H1, $x \approx 0.9$~0.78) → monoclinic (M, $x \approx 0.67$~0.4) → hexagonal (H2, $x \approx 0.34$~0.25) → hexagonal (H3, $x \approx 0.2$~0.11).[47, 48] These phase transitions are influenced by active mass (m_{act}) utilization. If LNO particles become completely isolated, m_{act} loss occurs, leading to irreversible capacity loss. On the other hand, if LNO is not isolated but encounters kinetic limitations in either electronic conduction or lithium-ion transport, the lithium-ion diffusion pathway length (L_{diff}) increases.

However, discrepancies in the lithium content (x value in Li_xNiO_2) corelated to different phases vary between literature sources and theoretical predictions.[47] One main reason is the inconsistent observations on the M phase caused by off-stoichiometry.[30, 47] The M phase is stabilized by the Ni in the lithium interslab. However, when cation disordered Ni^{2+} acts as a structural pillar, it reduces the structure flexibility and thus suppresses phase transitions. Consequently, the voltage curve becomes smoother, with less well-defined plateaus.[30, 47]

Capacity fading during cycling is most pronounced in the highly delithiated states of LNO, particularly the H2/H3 transition and the more lithiated H4 phase.[30, 49, 50] As both practical SEBs and LEBs rarely reach the H4 phase, the highly delithiated states in this dissertation focus solely on the H2/H3 transition and the H3 phase. The H2/H3 involves nearly all degradation processes discussed in this dissertation, including volume change, chemo-mechanical cracking, oxygen loss, rock-salt phase formation, and CEI degradation. On the other hand, H1/M reflects the cation disordering caused by off-stoichiometry and rock-salt phase degradation, leading to L_{diff} growth. Overall, H1/M and H2/H3 are influenced by the degradation process related to the m_{act} loss and L_{diff} growth.[51] In contrast, the M/H2 transition is majorly influenced by the m_{act} loss and less affected by kinetic constraints.[51]

Although CEI degradation between LNO and SEs can accelerate the deterioration of LNO bulk material, this section focuses solely on bulk degradation mechanisms for clarity. A detailed discussion on CEI degradation is provided in **Section 2.7**. Without considering CEI degradation, LNO encounters several challenges, which are explained in the following sections, including:[30]

(a) limited first-cycle Coulomb efficiency, typically 10~15% at room temperature;
(b) capacity fading during cycling mostly above 4.1 V vs. Li/Li^+, related to H2/H3 and H3;
(c) and safety concerns due to thermal instability, which is strongly related to O_2 gas evolution. However, this dissertation focuses solely on electrochemical performance and does not address safety-related experiments.

2.4.1 Limited first cycle Coulomb efficiency

The first-cycle Coulomb efficiency of LNO can be limited by cation disorder.[30, 52] During deintercalation of lithium ions from LNO, cation disordered Ni^{2+} ($r(Ni^{2+})$ = 0.69 Å) is oxidized to smaller Ni^{3+} ($r(Ni^{3+})$ = 0.56 Å) and occupying the lithium sites ($r(Li^{+})$: 0.076 nm)). This hinders lithium-ion diffusion at a high degree of lithiation during the discharge step by causing local shrinkage in six neighboring lithium-ion sites and thus hinders lithium ion reintercalation.[30, 53]

In addition, the optimal diffusion pathways via di-vacancies in the lithium lattice are only present below a lithium content of approximately $x \approx 0.8$ (H1 phase). Beyond this threshold, the reduced interlayer spacing and lower probability of encountering di-vacancies impede lithium-ion diffusion.[30, 53, 54] During charging, the H1/M has sufficient time for full conversion. However, during discharge, the H1/M takes place at the final stage, leaving insufficient time for full H1 phase recovery, ultimately leading to a loss of discharge capacity.[53]

Overall, in the first cycle, the insertion of lithium ions into the H1 phase at the end of the discharge is kinetically harder than the extraction of lithium ions.[53] The capacity lost in the first cycle can be recovered through a slow discharge at low voltage[55] and higher temperature[36]. However, CEI degradation in the first cycle can irreversibly reduce the first-cycle Coulomb efficiency, which is explained in **Section 2.7.3**. Additionally, CEI side reactions can induce cation disorder on the surface of LNO (**Section 2.4.4**), further reducing first-cycle Coulomb efficiency. Given that cation disorder is associated with Ni^{2+}, as Ni content in NCM increases toward LNO, the first-cycle Coulomb efficiency gradually decreases.

2.4.2 Volume changes and cracking

The H2/H3 of LNO involves significant unit cell shrinkage and anisotropic lattice volume decrease.[56, 57] Before the H2/H3, electrostatic forces dominate the interlayer spacing. Lithium ions extraction increases repulsion force between oxygen atoms, pushing the layers apart and causing a linear increase in the c-lattice parameter, which represents the interlayer spacing.[30, 49] During the H2/H3 transition, steric effects primarily govern interlayer spacing. This leads to the formation of a strongly covalent structure containing peroxide bonds, resulting in a sharp contraction of the c-lattice parameter.[30, 49] Afterward, the H3 phase retains the same overall structure as H1 and H2 but with a much smaller interlayer distance, hindering L_{diff}.[30, 58]

Moreover, the significant volume changes during the H2/H3 (≈ 4%) transition and H3 phase (≈ 2%) are much more intense than H1 to H2 (≈ 3%).[59] Such large volume changes induce significant strain at the CEI and along grain boundaries between primary particles, leading to contact loss, secondary particle cracking, and CEI fractures.[30] Regarding NCM,[56, 57, 60] below a lithium content of $x = 0.8$ ($LiNi_xCo_yMn_zO_2$), capacity fading is primarily due to interfacial degradation. Above x = 0.8, degradation is dominated by both volume changes and CEI degradation.[60]

Notably, the bulk expansion of high-nickel CAM particles often exceeds the cohesive strength of the coating material, making nano-meter coatings insufficient to suppress volumetric changes.[61]

Consequently, the coating layer cannot prevent volume change but must remain stable during it. Polymers are suitable coating materials due to their lower Young's modulus compared to inorganic coatings and their superior binding ability.[61] As a result, this instigates the exploration of polymers as a coating on high-nickel CAMs in this dissertation.

2.4.3 Oxygen loss from the lattice

Oxygen loss from the lattice causes damage to the structure of high-nickel CAMs and oxidizing the electrolytes.[49, 50, 59] Delithiation is one of the major factors driving oxygen loss.[49, 50] Ni cations oxidize from their valence state of 3^+ to 4^+, hence becoming more oxidative at higher state of charge (SOC), specifically near the H2/H3 phase transition.[62] This facilitates electron withdrawal from lattice O_2^- and release O_2 gas.[50] Moreover, elevated temperatures lead to accelerating oxygen loss.[50] Consequently, oxygen loss becomes more severe as the Ni content in CAMs increases. For instance, in NCMs, oxygen loss with its onset potential decreases as Ni content increases from ≈ 4.6 V vs. Li^+/Li for $Li(Ni_{0.33}Co_{0.33}Mn_{0.33})O_2$ to ≈ 4.2 V vs. Li^+/Li for $LiNi_{0.8}Co_{0.1}Mn_{0.1}O_2$.[49] Additionally, LNO experiences the most severe oxygen loss among high-nickel CAMs.

However, oxygen loss is more severe at the high-nickel CAM particle surface than in the bulk material. This is driven by the oxygenated reaction of SEs at CEI (**Section 2.7.3**).[50] Another reason is the kinetic hindrance of oxygen loss due to long diffusion pathways from the bulk to the surface.[49, 50] As a result, applying a surface coating to high-nickel CAMs to reduce oxygen loss has been demonstrated in the literature[50] and in publications within this dissertation.

2.4.4 Rock-salt phase formation

LNO degradation follows a pathway of layered (R3m, $LiNiO_2$, Ni^{3+}) → spinel (Fd3m, $LiNi_2O_4$) → rock-salt (Fm3m, NiO, Ni^{2+}).[50] The rock-salt phase is a consequence of cation disordering and oxygen evolution from the lattice,[49] and is equivalent to the thermal decomposition process of LNO (**Equation 2**).[49] The ideal rock-salt phase lacks lithium diffusion channels. Their accumulation results in the formation of a thick and highly resistive surface layer, which consequently degrades CEI.[49, 50]

For $0.5 < x < 1$ of Li_xNiO_2, the spinel structure is formed without oxygen loss due to cation disordering, as shown in **Equation 6**.[63] First, Ni^{2+} initially exists due to off-stoichiometry or through interfacial side reactions reducing Ni^{3+}/Ni^{4+}.[64, 65] Subsequently, Ni^{2+} migrates to lithium sites due to similar ionic radius. This cation disordering leads to the formation of spinel $LiNi_2O_4$, impairing lithium-ion transport, identical to its effect on first-cycle Coulomb efficiency (**Section 2.4.1**).

$$\mathrm{Li}_x\mathrm{NiO}_2\ (\text{layered}) \rightarrow (1-x)\ \mathrm{LiNi}_2\mathrm{O}_4\ (\text{spinel}) + (2x-1)\ \mathrm{LiNiO}_2\ (\text{layered}),\ 0.5 < x < 1 \quad \textbf{(Eq. 6)}[63]$$

For $x < 0.5$, more increased Ni^{4+} reduced to Ni^{2+}, resulting in increased cation disordering and forming more spinel $LiNi_2O_4$. If lithium sites become fully occupied, it results in the rock-salt NiO.[63, 65, 66] As a result, LNO degrades into spinel $LiNi_2O_4$, rock-salt NiO, and O_2 gas, as shown in **Equation 7**[63] and **Equation 8**[49]. Moreover, if the temperature increases, spinel $LiNi_2O_4$ becomes thermodynamically unstable and transforms into a rock-salt NiO with O_2 loss from the lattice, as shown in **Equation 9**.[63]

$$\mathrm{Li}_x\mathrm{NiO}_2\ (\text{layered}) \rightarrow x\,\mathrm{LiNi}_2\mathrm{O}_4\ (\text{spinel}) + (1-2x)\,\mathrm{NiO}\ (\text{rocksalt}) + \frac{1-2x}{2}\,\mathrm{O}_2,\ x < 0.5 \quad \textbf{(Eq. 7)}^{63}$$

$$\mathrm{Li}_x\mathrm{NiO}_2\ (\text{layered}) \rightarrow \mathrm{NiO}\ (\text{rocksalt}) + \frac{1}{2}\,\mathrm{Li}_2\mathrm{O} + \frac{2-x}{4}\,\mathrm{O}_2,\ x < 0.5 \quad \textbf{(Eq. 8)}^{49}$$

$$\mathrm{LiNi}_2\mathrm{O}_4\ (\text{spinel}) \rightarrow \mathrm{LiNiO}_2\ (\text{layered}) + \mathrm{NiO}\ (\text{rocksalt}) + \frac{1}{2}\,\mathrm{O}_2 \quad \textbf{(Eq. 9)}^{63}$$

In summary, Ni^{2+} off-stoichiometry and adverse side reactions at the LNO/SE interface result in O_2 gas evolution and cation disordering, such as spinel $LiNi_2O_4$ and rock-salt NiO. As a result, layered → spinel → rock-salt phase transformation worsens with increasing Ni content in CAMs, higher SOC, and higher temperature.[49, 50] Eventually, the H2/H3 phase transition disappears from the differential capacity plot.[49]

The rock-salt phase formation is more pronounced near particle surfaces due to interfacial side reactions and the slower oxygen evolution in the LNO bulk than at the interface. Additionally, the rock salt phase on LNO surface is more fragile than the bulk layered-LNO, leading to increased surface crack formation, also known as chemo-mechanical cracking.[49, 50] A coating or an artificial interface that mitigates interfacial side reactions can also suppress rock-salt phase transformation, hence reducing surface crack formation and particle cracking.

Overall, as Ni content in NCM increases, degradation intensifies—manifesting as rock-salt phase formation, oxygen evolution, volume changes, cracking, and reduced first-cycle coulomb efficiency. A similar Ni-dependent trend is observed in CEI degradation, as detailed in **Section 2.7.3**. Ultimately, LNO, with the highest Ni content, exhibits the most severe structural and CEI degradation. Consequently, **Publications C** and **D** employ LNO as a reference CAM to investigate degradation mitigation strategies achieved via the modified sulfide-based SE and the coating on the LNO, respectively.

2.5 Sufide-based SEs

Sulfide-based SEs have an ionic conductivity σ_{ion} around 2 to 10 mS·cm^{-1} and recently the highest σ_{ion} of 32 mS·cm^{-1} for $Li_{9.54}(Si_{0.6}Ge_{0.4})_{1.74}P_{1.44}S_{11.1}Br_{0.3}O_{0.6}$[19] at 25 °C has been reported,[19, 20, 67] surpassing other SEs[67]. Compared to oxide-based SEs, sulfide-based SEs exhibit higher σ_{ion} due to their highly polarizable sulfide framework and lower binding energy with lithium.[20, 68, 69] Additionally, the larger atomic radius of sulfur creates wider conduction channels and its softer nature further promotes lithium-ion transport.[20, 68, 69] Sulfide-based SEs includes Li_2S–P_2S_5 glass ceramics, $Li_{6-x}PS_{5-x}X_{1+x}$ (X = Cl, Br, or I) argyrodite, $Li_{4-x}Ge_{1-x}P_xS_{4-x}$ and $Li_{11-x}M_{2-x}P_{1+x}S_{12}$ (M = Ge, Sn, or Si) thio-LISICONs.[20]

2.5.1 Glass-Ceramic SEs

The development of sulfide-based SEs began with the glassy Li_2S–P_2S_5 ($(Li_2S)_x(P_2S_5)_{1-x}$) binary system, first reported in 1980[70], where substituting oxygen with sulfur in the phosphate structure significantly enhanced σ_{ion}.[71] Glassy $(Li_2S)_{75}(P_2S_5)_{25}$ composed solely of PS_4^{3-} units showed the highest σ_{ion} in Li_2S–P_2S_5 binary system, 2.8·10^{-1} mS·cm^{-1} at 25 °C.[71] In general, crystallization of glass in sulfide-based SEs reduces σ_{ion}. However, in 2005, Mizuno et al. showed that partial crystallization of $(Li_2S)_x(P_2S_5)_{1-x}$ ($x \geq 70$) glass ceramics enhances σ_{ion}.[72, 73] This is because high-temperature treatment forms metastable crystalline phases and hence boosts conductivity.[73] Different glass-ceramic compositions have since been extensively studied through controlled crystallization, including $LiPS_3$,[74] Li_2PS_3,[75-77] $Li_7P_3S_{11}$,[72, 73, 78-84] Li_3PS_4,[83, 85-88] and Li_7PS_6,[89] all of which are near or at the P_2S_5–Li_2S composition line in the Li–P–S phase diagram (see **Figure 4a**).[71] Based on the Li_2S–P_2S_5 binary system, argyrodite-type[90] and thio-LISICON[91] SEs have been developed.[91]

2.5.2 Argyrodite SEs

The argyrodite structure, initially identified in Ag_8GeS_6, is notable for its highly disordered cation arrangement, which facilitates significant Ag^+ mobility. Inspired by this, Deiseroth et al. proposed substituting one sulfur atom in Li_7PS_6 argyrodite with a halogen atom,[92] leading to a Li_2S–P_2S_5–LiX (X = F, Cl, Br, I) ternary system (see **Figure 4b**)[90] with an ionic formula of $(Li^+)_6(PS_4^{3-})S^{2-}X^-$.[92] The σ_{ion} for Li_6PS_5Cl, Li_6PS_5Br, Li_6PS_5I are 1.9 mS·cm^{-1}, 6.8·10^{-1} mS·cm^{-1}, and 4.6 · 10^{-4} mS·cm^{-1} at 25 °C, respectively.[71, 92] The σ_{ion} differences of these compounds reflect variations in anion disorder. In Li_6PS_5Cl, partial swapping occurs between S^{2-} and Cl^- sites, creating a disordered anion framework that facilitates higher σ_{ion}. However, in Li_6PS_5I, the larger I^- ion cannot interchange positions with S^{2-}, resulting in an ordered anion framework and significantly reduced σ_{ion}.[71, 93] The high σ_{ion} of Li_6PS_5Cl makes it suitable for electrochemical experiments and is used throughout this dissertation.

2.5.3 Thio-LISICON SEs

Thio-LISICON materials are derived from the Li_2S–P_2S_5–M_xS_y ternary system (M = Mg, Al, Si, Ge, etc.).[20, 91] Kanno and Murayama introduced $Li_{4-x}Ge_{1-x}P_xS_4$ through the substitution reaction, employing Ge as the M element.[69, 91] **Figure 4c** categorizes three compositional regions in the Li_4GeS_4–Li_3PS_4 ($Li_{4-x}Ge_{1-x}P_xS_4$) composition line: region Ⅰ ($0 < x \leq 0.6$), region Ⅱ ($0.6 < x < 0.8$), and region Ⅲ ($0.8 \leq$

x < 1.0).[91] The three monoclinic regions differ in cation ordering, with region Ⅱ exhibiting the highest σ_{ion} (> 10^{-3} S·cm^{-1} at 25 °C).[91] For instance, $Li_{10}GeP_2S_{12}$ (region Ⅱ) shows a σ_{ion} of 1.2 · 10^{-2} S·cm^{-1} at 25 °C,[91] making it ideal for SEBs. However, thio-LISICON SEs, with high-valence elements such as Ge or Si react with lithium metal to continuously form a mixed-ionic/electronic conducting interphase (MCI).[94] Continuous MCI formation causes thio-LISICON SEB capacity fade due to irreversible lithium consumption and increased interfacial resistance, limiting its practical application.[94, 95]

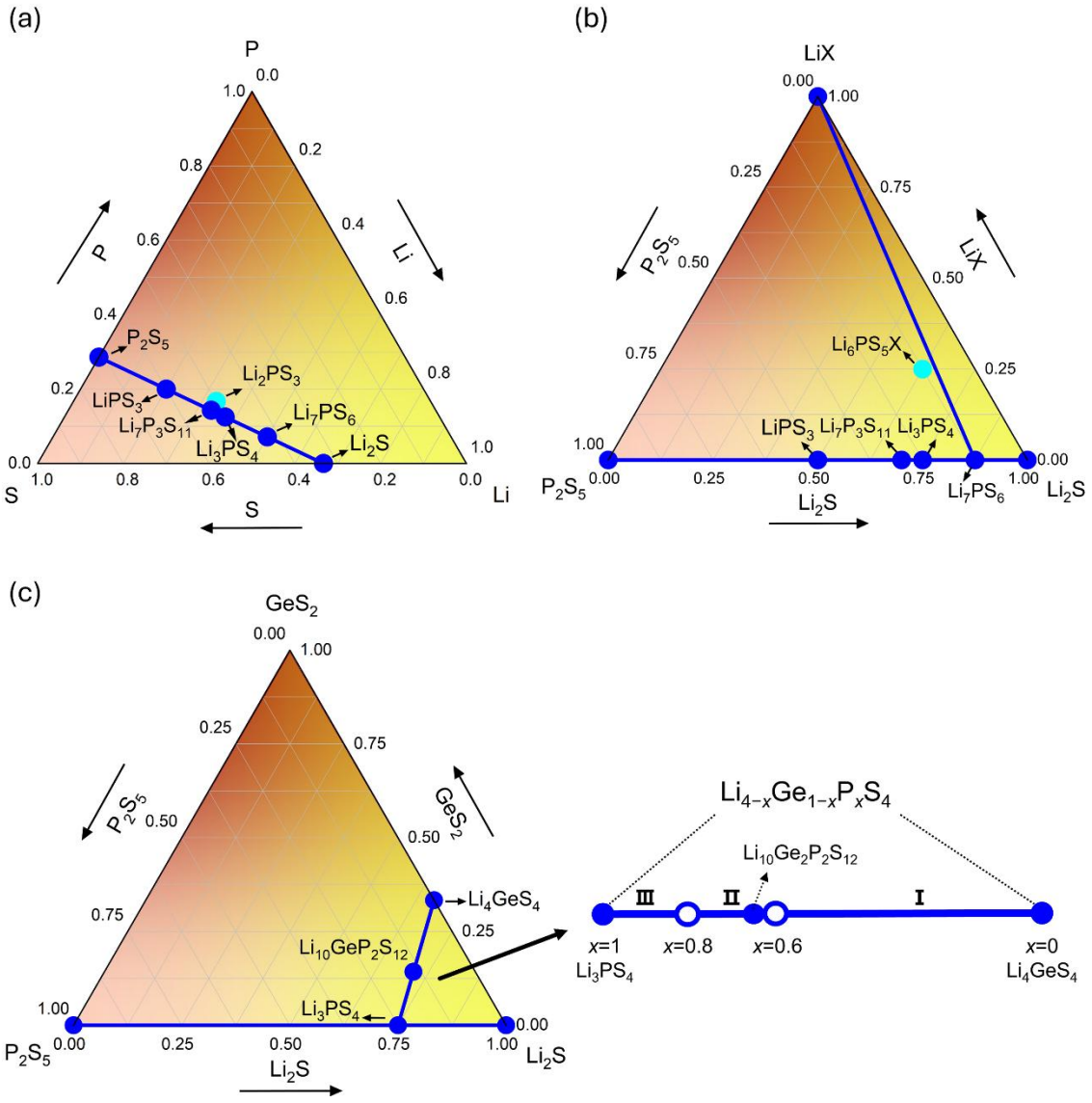

Figure 4. The ternary phase diagram of (a) Li−P−S,[71] (b) Li_2S–P_2S_5–LiX (X = F, Cl, Br, I),[90] and (c) Li_2S–P_2S_5–Ge_xS_y.[91] Each corner of the triangle represents a pure component, while any point within the triangle represents a specific compound composed of different ratio of the pure components. The composition line is expressed in blue. The light blue color indicates that this component is close to the composition line. On the right-hand side of the Figure (c), $Li_{4-x}Ge_{1-x}P_xS_4$ composition line is divided into three regions: region Ⅰ ($0 < x \leq 0.6$), region Ⅱ ($0.6 < x < 0.8$), and region Ⅲ ($0.8 \leq x < 1.0$). Figure (a), (b), and (c) were modified based on the Refs. [71], [90], and [91], respectively.

2.5.4 Electrochemical stability of sulfide-based SEs

The decomposition of sulfide-based SEs is partially redox reversible.[96-98] This partial redox reaction is observed in Li–S batteries using a sulfide-based SE as a catholyte, yielding the capacity that exceeds its theoretical limits of Li_2S and S.[96] The redox reactions of PS_4^{3-} are presented in **Equations 10** and **11**.[97] During oxidation of PS_4^{3-}, sulfur is redox-active ($S^{2-} \rightleftharpoons S + 2\ e^-$). During reduction of PS_4^{3-}, phosphorus shows redox activity ($P^{5+} + 5\ e^- \rightleftharpoons P$).[97, 98]

$$PS_4^{3-} + (5+x)\,e^- \rightleftharpoons 4\ S^{2-} + P^{x-} \quad \textbf{(Eq. 10)}[97]$$

$$2\ PS_4^{3-} \rightleftharpoons P_2S_7^{4-} + S + 2\,e^- \rightleftharpoons P_2S_6^{2-} + 2\ S + 4\ e^- \quad \textbf{(Eq. 11)}[97]$$

Using argyrodite Li_6PS_5X (X = Cl, Br, I) as an example, **Equation 10** and **11** can be rewritten to **Equation 12** and **13**, respectively.[96] S and P_2S_5 are the ideal oxidation products, and Li_3P is the ideal reduction product. However, LiX is electrochemically inactive after its formation and does not contribute to the reversible redox capacity (q_{redox}).[97]

$$Li_6PS_5X + 8\ Li^+ + 8\ e^- \rightleftharpoons LiX + Li_3P + 5\ Li_2S, \qquad q_{redox} = 499\ mAh{\cdot}g^{-1}\ \textbf{(Eq. 12)}[96]$$

$$Li_6PS_5X \rightleftharpoons LiX + \tfrac{1}{2}\ P_2S_5 + \tfrac{5}{2}\ S + 5\ Li^+ + 5\ e^-, \qquad q_{redox} = 798\ mAh{\cdot}g^{-1}\ \textbf{(Eq. 13)}[96]$$

The electrochemical stability window (ESW) of sulfide-based SEs is investigated using VGCF as a working electrode and LiIn as a counter electrode.[98, 99] If Li_6PS_5X is cycled reversibly to allow complete redox reactions, the ESW is limited to approximately 0.3 V.[96, 99] However, SEBs can be designed by controlling the cutoff voltage to prevent reversible redox reactions of SEs.[100] In a practical SEB, where oxidation and reduction are treated irreversibly for anodic and cathodic reactions, the ESW can extend to approximately 1.1 V.[97, 101]

Figure 5 shows the reduction of PS_4^{3-} starts at 1.1 V vs. Li^+/Li at the anode side of SEBs, producing S^{2-} and P, followed by the further reduction of P to P^{x-} ($0 < x \leq 3$) at 0.8 V vs. Li^+/Li.[97, 101] As a result, Li_6PS_5X decomposes into Li_2S, LiX, and P/Li_xP ($0 < x \leq 3$) at the anode side primarily during the first cycle.[94] Without further reactions at higher positive voltages that produce oxidation products,[99] these irreversible products form a SEI on the anode side in SEBs.

Regarding the cathode side of SEBs, the oxidation of S^{2-} to S is proposed to begin at 2.2 V vs. Li^+/Li.[97, 101] At around 2.9 V vs. Li^+/Li, P–S–S–P bonds form between PS_4^{3-} tetrahedral units, which then undergo a disproportionation reaction to produce $P_2S_7^{4-}$ (P–S–P) and S .[101, 102] At higher oxidative voltages, $P_2S_7^{4-}$ oxidizes to $P_2S_6^{2-}$, S, and possibly the ideal oxidation product, P_2S_5.[97, 102] Moreover, polysulfides, including Li-S_n-Li[103] and/or P-S_n-P[104] ($n \geq 2$), are observed.[87, 105] These polysulfides result from the polymerization or oligomerization of SE anions.[104] Overall, PS_4^{3-} in the SE are oxidized to various polyanions primarily during the first cycle, including $P_2S_7^{4-}$, $P_2S_6^{2-}$, P_2S_5, S, and S_x-like species (Li-S_n-Li and P-S_n-P),[103-105] without proceeding to more negative voltages that form reduction products.[99] Notably, these side reactions are non-conductive and occur between sulfide-based SEs and CAMs, leading to CAM isolation and a reduction in initial Coulomb efficiency.

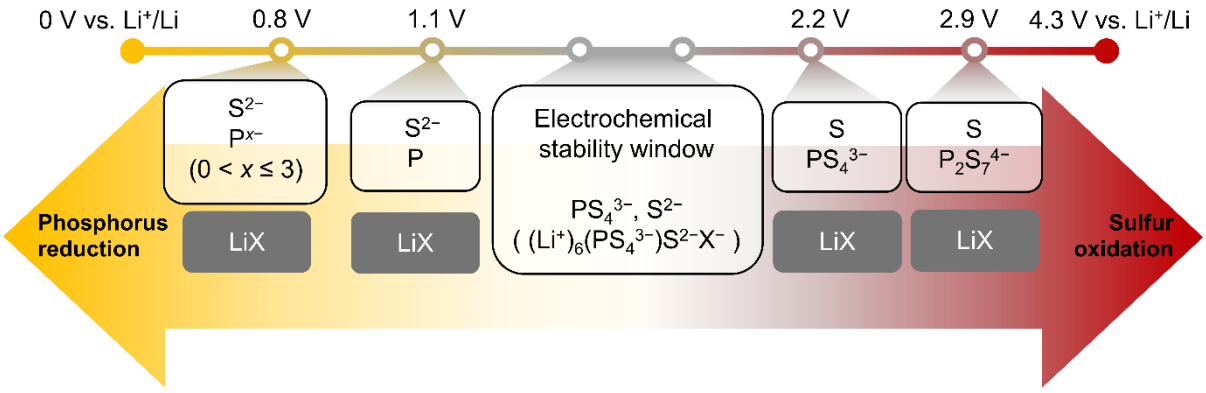

Figure 5. Sulfur oxidation and phosphorus reduction products based on different voltages (vs. Li^+/Li), collected from different literature,[96, 97, 101] are shown. The voltages for reactions are measured by cyclic voltammetry using VGCFs as the working electrode, stainless steels as the current collector, LiIn alloy as the counter electrode. The darker text color of LiX (X = Cl, Br, I) indicates that these species are inactive in the redox process.[97]

2.5.5 Liquid-phase synthesis and solvent stability

The ball-milling method is a standard dry approach for synthesizing sulfide-based SEs. Taking Li_6PS_5Cl as an example, the compounds Li_2S, P_2S_5, and LiCl, are mixed and ball milled in appropriate molar ratios, yielding low-crystallinity Li_6PS_5Cl. Calcination then produces high-crystallinity Li_6PS_5Cl.[106] Unlike ball-milling, liquid-phase synthesis is cost-effective and ideal for large-scale SE production.[20] As a result, understanding sulfide-based SE stability in solvents supports developing scalable synthesis methods.

Liu et al. first reported the liquid-phase synthesis of β-Li_3PS_4 using tetrahydrofuran (THF), demonstrating the reaction at room temperature, as shown in **Equation 14**.[87] The liquid-phase synthesis relies on polar or weakly protic solvents[107], which significantly influence the solubility and reactivity of PS_4^{3-} in sulfide-based SE.[108] During the synthesis, Li_3PS_4 complexed with the solvent precipitates (Li_3PS_4 · solvent). Other commonly used solvents[87] include acetonitrile,[109] diethylene glycol dimethyl ether,[110] dimethyl carbonate,[111] dimethoxyethane,[112] ethyl acetate,[113] ethylenediamine,[114] and *N*-methylformamide.[115-117] Additionally, argyrodite-type Li_6PS_5Cl is synthesized following a similar route as for β-Li_3PS_4 by mixing Li_2S, P_2S_5, and LiCl, using polar or weakly protic solvents,[108] e.g., ethylenediamine,[118] anisole,[119] and ethanol[106].

$$Li_2S + P_2S_5 \xrightarrow{THF} Li_3PS_4 \cdot 3\,THF \qquad \textbf{(Eq. 14)}^{87}$$

Thermal treatment is subsequently applied to remove the solvent and recrystallize β-Li_3PS_4 from the complexes. Notably, insoluble Li_3PS_4 · solvent complexes are stable at a moderate drying temperature of 120 °C. These complexes decompose upon heating to elevated temperatures more than 120 °C, yielding β-Li_3PS_4.[107] However, liquid-phase synthesis may generate impurities, such as Li_3PO_4. While ethanol with a high dielectric constant aids in precursor dissolution, it promotes Li_3PO_4 formation and accelerates PS_4^{3-} decomposition in the precursor solution.[108] Moreover, a combination of THF and

ethanol forms Li_3PO_4 due to a ring-opening reaction of THF.[108] The formation of side reaction products is highly complex and warrants further investigation.

Conversely, examining how polar solvent molecules interact with sulfide-based SEs can provide insights into the formation of side reaction products during synthesis. Polar solvents with Lewis-basic functional groups (e.g., water, *N*-methyl-2-pyrrolidinone (NMP), or alcohols) react with the electrophilic PS_4^{3-} group via the HSAB principle.[120] This reaction degrades the SE structure to generate polysulfide (P−S_n−P) and oxygenated products, lowering its σ_{ion} (see **Figure 6**).[121] Additionally, A higher donor number accelerates this degradation.

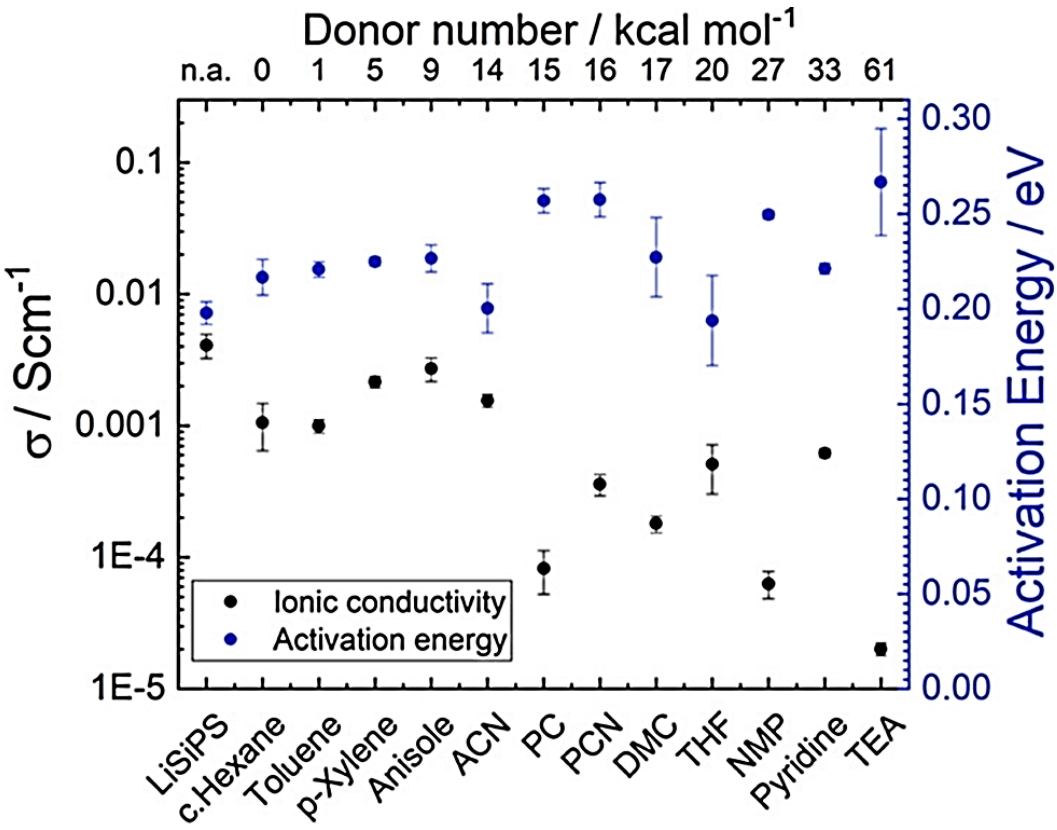

Figure 6. σ_{ion} of tetra-Li_7SiPS_8 (LiSiPS) after solvent treatment showing a decline with increasing the donor number. The desired high σ_{ion} above 1 mS·cm^{-1} is only persevered after treatment with a solvent donor number below 15 kcal·mol^{-1}. The activation energy of LiSiPS shows only minor changes after treatment with various solvents.[122] Reprinted without modification according to the creative commons license CC BY-NC 4.0 DEED (https://creativecommons.org/licenses/by/4.0/), from Anna-Katharina Hatz, Robert Calaminus, Julian Feijoo, Fiona Treber, Jakob Blahusch, Tobias Lenz, Marco Reichel, Konstantin Karaghiosoff, Nella M. Vargas-Barbosa,* and Bettina V. Lotsch*, Chemical Stability and Ionic Conductivity of LGPS-Type Solid Electrolyte Tetra-Li_7SiPS_8 after Solvent Treatment, ACS Applied Energy Materials, 2021, https://doi.org/10.1021/acsaem.1c01917, American Chemical Society.

Suspensions of sulfide-based SEs in polar solvents display various colors, indicating that different polysulfide chains are stabilized by solvent molecules. The deep blue color in the NMP suspension is due to the $[S_3]^{-\bullet}$ radical anion. THF suspension turns yellow from $[S_2]^{-\bullet}$ and $[S_4]^{2-}$ anions. Acetonitrile and propylene carbonate produce turquoise and dark green shades, respectively, likely due to $[S_3]^{-\bullet}$ and $[S_6]^{2-}$ anions. Green hues in propionitrile and pyridine are possibly from $[S_3]^{-\bullet}$ and $[S_4]^{2-}$ anions. Drying may lead to the formation of P−S_n−P precipitates, appearing as films or aggregates.[122] However, the P−S_n−P are generally undesirable due to low conductivity.[122, 123]

On the other hand, a proposed mechanism shows alcohols (particularly methanol) oxygenate PS_4^{3-} through a nucleophilic attack on the PS_4^{3-}, as shown in **Figure 7**.[122] However, this reaction might be sterically hindered. For instance, isopropyl alcohol does not dissolve *β*-Li_3PS_4.[107, 122] As oxygenated products from PS_4^{3-} may serve as a protective layer between sulfide-based SEs and both CAMs and lithium metal anode,[124] **Publication C** investigates modification on sulfide-based SEs using polar solvent.

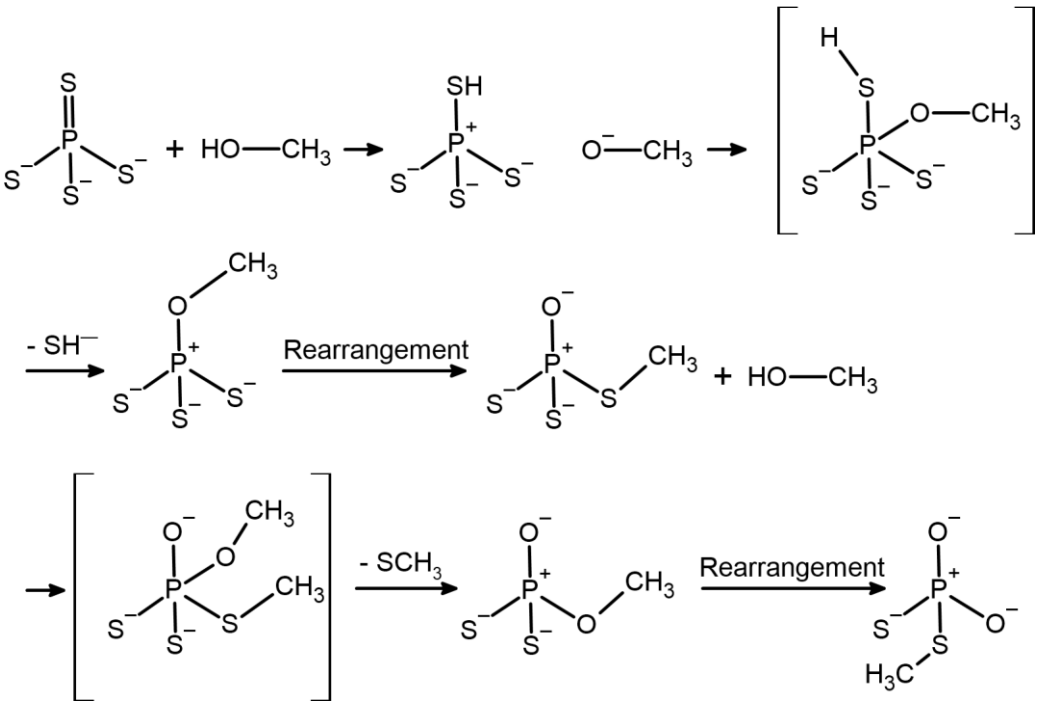

Figure 7. Proposed reaction mechanism for the decomposition of PS_4^{3-} in methanol, resulting in the formation of an oxygen-substituted thiophosphate.[122] The figure was redrawn and modified from Ref. [122].

2.6 Interphases in SEBs

The electrode/sulfide-based SE interphases form during cycling and even once contact forms. Without a stable interphase or protective coating layer at electrode/SE interfaces, the oxidation of sulfide-based SEs at the CEI and reduction at the SEI[94] may keep degrading the electrochemical performance.[61] As a result, this section focuses on the driving force of the interphase formation and the requirements for a stable interphase or coating layer.

Interphase formation is driven by the potential gradient across the interphases. **Table 1** provides definitions for the various potentials in electrochemistry that influence interphase formation.[125, 126] Generally, the electrochemical potential ($\tilde{\mu}_i$) represents the total Gibbs free energy change of a system when one mole of a species, i, is introduced from an infinite distance under the influence of an electric field. $\tilde{\mu}_i$ is the sum of the chemical potential (μ_i) and the electrostatic energy (E_{ele}). E_{ele} is the energy associated with the electric potential (φ). As a result, $\tilde{\mu}_i$ determines the flow of charge species in a system, including $\tilde{\mu}_{e^-}$ for electrons and $\tilde{\mu}_{Li}$ for ions.

Table 1. Potentials in electrochemistry.[125, 126] The component "i" can be Li, Li^+, or e^-, corresponds to neutral lithium, lithium ion, and electron, respectively. Additionally, phase "j" can be c, a, or SE, corresponds to cathode, anode, and SE, respectively.

Term	unit	Brief definition
Electrochemical potential ($\tilde{\mu}_i^j$)	J·mole^{-1}	Partial molar Gibbs free energy change by adding a mole of species i in phase j from infinite distance, considering electrostatic contributions. $\tilde{\mu}_{e^-}$ can be taken as the Fermi level.[125, 127] $\tilde{\mu}_i \equiv \mu_i + E_{ele} = \mu_i + z_i F \cdot \varphi$, where μ_i, E_{ele}, and $z_i F \cdot \varphi$ are detailed below.
Chemical potential (μ_i^j)	J·mole^{-1}	Partial molar Gibbs free energy change by adding a mole of species i in phase j from infinite distance, neglecting electrostatic contributions. $\mu_i \equiv \left(\partial G / \partial n_i\right)_{T,P}$
Electric potential (φ)	V	φ is also named Galvani or inner electric potential in some literatures. It is defined as the work needed to bring a unit point charge from infinity to a point inside a phase. Hence, $\Delta\varphi$ means the Electric potential difference between two points in the bulk of two phases. $\varphi \equiv x + \psi$, where x is the surface potential (caused by electric surface dipole) and ψ is the Volta potential (caused by net surface charge).
Electrostatic energy (E_{ele}^j)	J	E_{ele} is also named electric potential energy in some literatures. It describes the work required to bring the charged species from infinity into the system's interior. $E_{ele} \equiv z_i F \cdot \varphi$, where φ represents Electric potential and z_i represents the charge number (e.g., +1, −1, +2, −2) of the species "i". F is the Faraday constant.[125]

2.6.1 Interphases influenced by the (electro)chemical potential

A μ_{Li} profile helps to understand the electrodes/SEs interphase formation, as shown in **Figure 8a**.[61] ξ represents the distance. The anode exhibits the highest μ_{Li}^{a} compared to the SE (μ_{Li}^{SE}) and cathode (μ_{Li}^{c}), while the cathode exhibits the lowest μ_{Li}^{c}.[61, 99] Before reaching electrochemical equilibrium, lithium ions flow across the interphases, shifting μ_{Li} from high potential to lower potential until $\tilde{\mu}_{Li^+}$ becomes a constant.[127] The profile is simplified as straight lines, though actual distributions are nonlinear.[128]

A stable interphase which is not (or merely) electronic conductive leads to electrochemical equilibrium (stable OCV) when the interphase is thermodynamically or fully kinetically stabilized. Assuming highly mobile lithium ions, the $\tilde{\mu}_{Li^+}$ remains constant throughout the cell ($\Delta\tilde{\mu}_{Li^+} = 0$).[127] As a result, $\Delta\mu_{Li}$ across the interphases ($\mu_{Li}^{a} - \mu_{Li}^{SE}$ or $\mu_{Li}^{SE} - \mu_{Li}^{c}$) equals $\Delta\tilde{\mu}_{e^-}$ ($\tilde{\mu}_{e^-}^{a} - \tilde{\mu}_{e^-}^{SE}$ or $\tilde{\mu}_{e^-}^{SE} - \tilde{\mu}_{e^-}^{c}$) (see **Equation 15**), indicating that both μ_{Li} and $\tilde{\mu}_{e^-}$ decrease equally from the anode to the SE within SEI and from SE to the cathode within CEI.[61, 127]

$$\tilde{\mu}_{Li^+} = \mu_{Li} - \tilde{\mu}_{e^-};\ \Delta\tilde{\mu}_{Li^+} = 0 = \Delta\mu_{Li} - \Delta\tilde{\mu}_{e^-} \quad \textbf{(Eq. 15)}$$

Redox potentials between electrodes and SE, which define the ESW, are determined by the Gibbs free energy differences between the electrodes and SE[129] involving both $\Delta\mu_{Li}$ and $\Delta\tilde{\mu}_{e^-}$. Due to simplicity, $\tilde{\mu}_{e^-}$ is used to represent the redox reactions between electrodes and SE, as shown in **Figure 8b**. However, many reports incorrectly rely on the highest occupied molecular orbital (HOMO) and lowest unoccupied molecular orbital (LUMO) energies to determine electrochemical stability. HOMO–LUMO only reflects electron excitations in isolated molecules,[129, 130] considering only electron transfer and ignoring the necessary simultaneous lithium-ion transfer for charge neutrality.[130] During interphase formation, the electrochemical window expands until $\Delta\tilde{\mu}_{e^-}$ between electrodes and interphases becomes the same and hence no electron exchange between interphases and electrodes. However, electrochemical stability is influenced not only by thermodynamic factors but also by kinetics of decomposition and diffusion at the electrodes/SE interfaces.[130] As a result, electrochemical stability assessed through cyclic voltammetry is influenced by the scanning rate, making it not merely a thermodynamic property.

In SEBs where $\tilde{\mu}_{e^-}^{c} \neq \tilde{\mu}_{e^-}^{a}$ and $\Delta\tilde{\mu}_{Li^+} = 0$ at electrochemical equilibrium, the OCV measured by a voltmeter corresponds to $\Delta\tilde{\mu}_{e^-}$ between cathode and anode.[125] It is because that the $\Delta\tilde{\mu}_{e^-}$ is the driving force of the electronic charge flow. If $\mu_{e^-}^{a}$ equals $\mu_{e^-}^{c}$,[131] OCV expressed as **Equation 16**.[61, 125, 126, 131] However, the CEI and coating layers, which may cover the whole CAM particles, can block the σ_{ele} and lower $\tilde{\mu}_{e^-}^{c}$, resulting in higher OCV as measured by a voltmeter.

$$\text{OCV} = -\frac{\Delta\mu_{Li}}{F} = -\frac{\Delta\tilde{\mu}_{e^-}}{F} = -\frac{\tilde{\mu}_{e^-}^{a} - \tilde{\mu}_{e^-}^{c}}{F} = (\varphi^{a} - \varphi^{c}) = \Delta\varphi \quad \textbf{(Eq. 16)}^{[61, 125]}$$

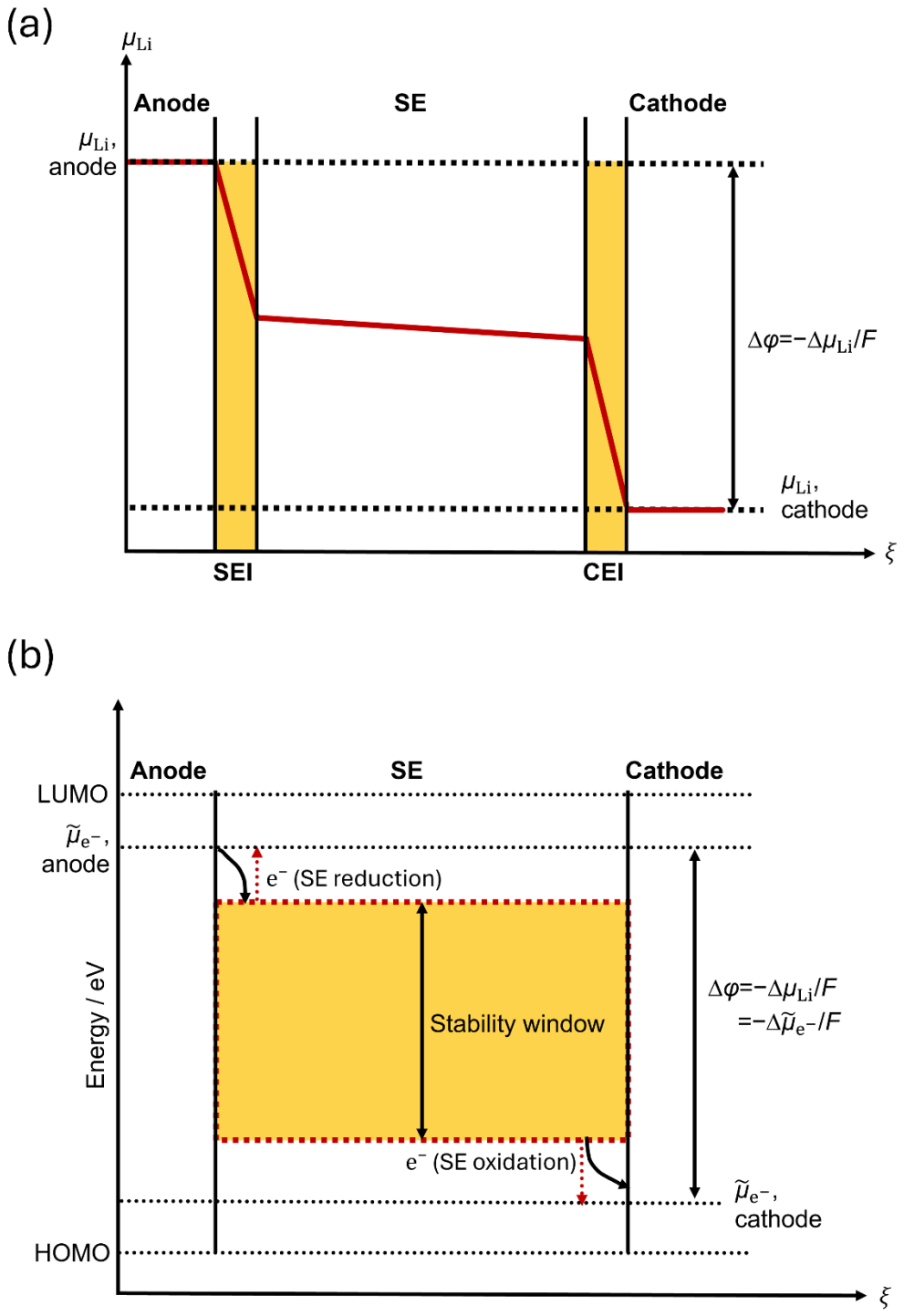

Figure 8. The schematic diagram of SEB, composed of anode, SEI, SE, CEI, and cathode, illustrates the distribution of (a) the μ_{Li}[61] and (b) $\tilde{\mu}_{e^-}$[129] across the cell components. In Figure (b,) a comparison is made between the ESW and the HOMO and LUMO levels. Redox reactions occur at the interfaces between electrodes and the SE. In both Figure a and b, The OCV ($\Delta\varphi$) can be determined by the difference in either the μ_{Li} or $\tilde{\mu}_{e^-}$. Figure (a) and (b) were redrawn and modified from Ref. [61] and [129], respectively.

2.6.2 The electronic conductivity of the SEI and CEI

Figure 9 illustrates the steady-state potential profiles at the SEI and CEI in an SEB.[128] To prevent SE reduction at the anode side, the μ_{Li} at the SEI/SE interface ($\mu_{\mathrm{Li}}^{\mathrm{SEI/SE}}$), must stay below the reduction limit of SE, $\mu_{\mathrm{Li}}^{\mathrm{SE,red}}$. This is achieved by a sufficient μ_{Li} and $\tilde{\mu}_{\mathrm{e}^-}$ drop in the SEI, which requires the SEI to have lower σ_{ele} than the SE (**Figure 9a)**. Similarly, the CEI must have lower σ_{ele} than the SE to prevent oxidation of the SE by maintaining a sufficient μ_{Li} and $\tilde{\mu}_{\mathrm{e}^-}$ drop in the CEI (**Figure 9b**). As a result, the μ_{Li} at the CEI/SE interface ($\mu_{\mathrm{Li}}^{\mathrm{CEI/SE}}$), must be higher than the oxidation limit of SE, $\mu_{\mathrm{Li}}^{\mathrm{SE,ox}}$.[128]

If σ_{ele} of the interphases or coatings is higher than that of SE, which correspond to MCI, the σ_{ele} within the MCI cannot decrease $\tilde{\mu}_{\mathrm{e}^-}$ from $\tilde{\mu}_{\mathrm{e}^-}^{\mathrm{a}}$ to $\tilde{\mu}_{\mathrm{e}^-}^{\mathrm{SE}}$ (**Figure 9c**) or $\tilde{\mu}_{\mathrm{e}^-}^{\mathrm{SE}}$ to $\tilde{\mu}_{\mathrm{e}^-}^{\mathrm{c}}$ (**Figure 9d**).[128] A minor decrease of $\tilde{\mu}_{\mathrm{e}^-}$ gives rise to a minor decrease of μ_{Li} from $\mu_{\mathrm{Li}}^{\mathrm{a}}$ to $\mu_{\mathrm{Li}}^{\mathrm{SE}}$ or $\mu_{\mathrm{Li}}^{\mathrm{SE}}$ to $\mu_{\mathrm{Li}}^{\mathrm{c}}$. As a result, $\mu_{\mathrm{Li}}^{\mathrm{SE,red}}$ is lower than the $\mu_{\mathrm{Li}}^{\mathrm{MCI/SE}}$ in the anode side, or $\mu_{\mathrm{Li}}^{\mathrm{SE,ox}}$ is higher than the $\mu_{\mathrm{Li}}^{\mathrm{MCI/SE}}$ in the cathode side. Consequently, $\Delta\tilde{\mu}_{\mathrm{Li}^+} = 0$ can never be reached and the interphase is continuously growing, leading to increased interfacial resistance.[127, 128] In conclusion, the polymer coating layer and the modification layer on the sulfide-based SE in this dissertation should exhibit lower a σ_{ele} than SE.

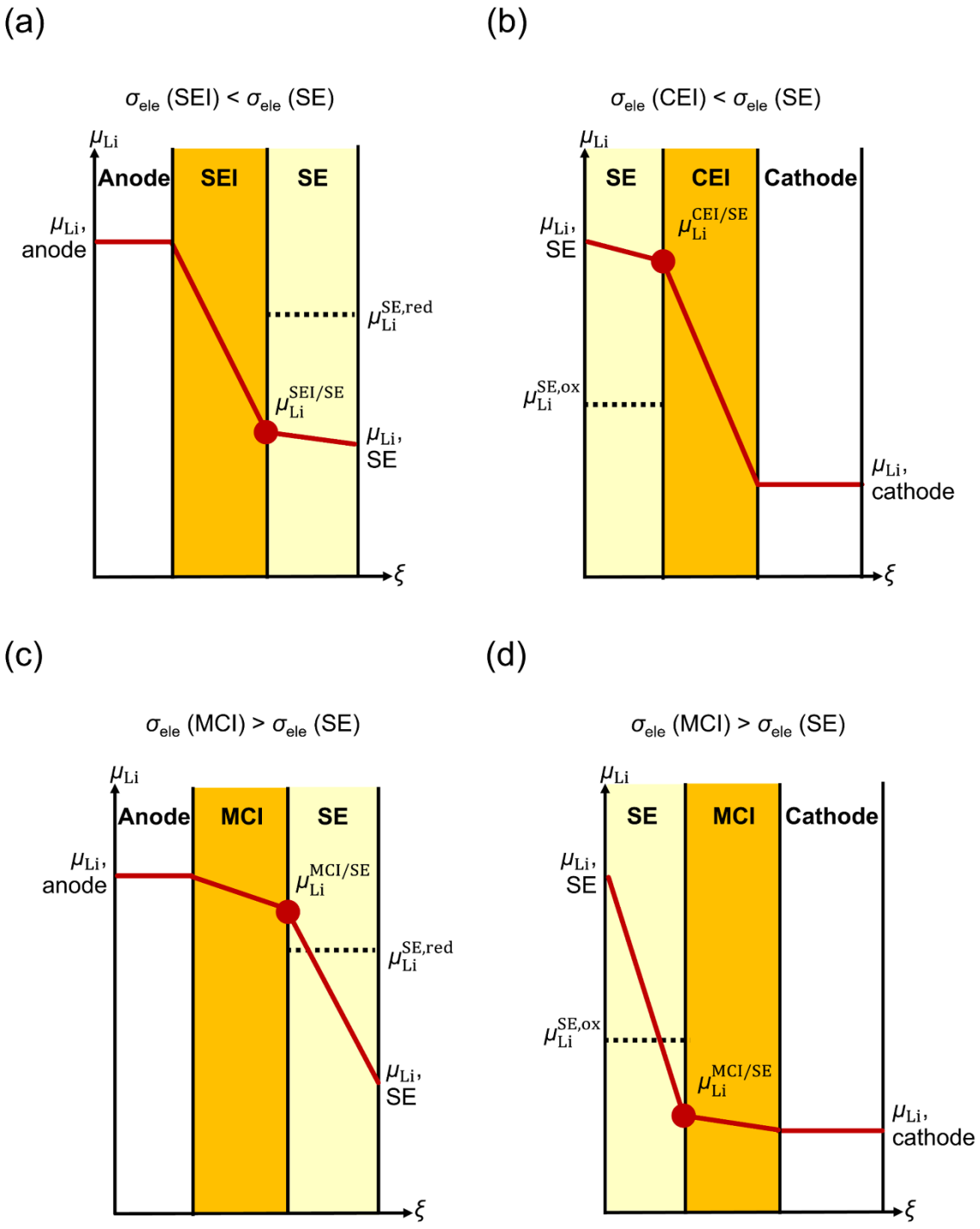

Figure 9. Schematic diagrams of the μ_{Li} profiles at the anode (a, c) and cathode (b, d) sides. In addition, Figures (a) and (b) refer to σ_{ele} of interphases lower than SE, while (c) and (d) refer to σ_{ele} of the interphases being higher than of the SE. The $\mu_{Li}^{SE,red}$ and $\mu_{Li}^{SE,ox}$ represent the reduction and oxidation chemical potentials of the SE. The $\mu_{Li}^{MCI/SE}$ denotes the μ_{Li} at the MCI/SE interface of the anode side and cathode side.[128] Figures (a)~(d) were redrawn and modified from Ref. [128].

2.6.3 Interphase growth kinetics

If σ_{ele} of interphases are lower than that of the SE, the kinetics of interphase growth are self-limited. The Wagner model describes the kinetics of diffusion-controlled solid-state reactions,[62, 132-134] suggesting that σ_{ele} limits the growth of interphases. However, the growth of interphases in the Wagner model never completely stops but continues at a minor rate.

The growing interphase thickness ($\Delta\xi$) is expressed in **Equation 17**.[62] V_{m} denotes the average molar volume of the interphase; z_i signifies the number of moles of lithium ion extracted from the solid electrolytes; *F* is Faraday's constant; and *t* indicates time of growing interphase. The lithium-ion conductivity at the interphase is σ_{Li^+}. $\Delta\mu_{\mathrm{Li}}$ is the chemical potential difference of lithium across the interphase. The kinetic constant *k* reflects the growth rate in terms of $\Delta\xi$. If resulting equation assumes $\sigma_{\mathrm{ele}} \ll \sigma_{\mathrm{Li}^+}$, *k* is influenced by σ_{ele} and $\Delta\mu_{\mathrm{Li}}$.[62]

$$\Delta\xi = \sqrt{\frac{V_{\mathrm{m}}}{z_i \cdot F^2} \cdot \frac{\sigma_{\mathrm{Li}^+} \cdot \sigma_{\mathrm{ele}}}{\sigma_{\mathrm{Li}^+} + \sigma_{\mathrm{ele}}} \cdot \Delta\mu_{\mathrm{Li}}} \cdot \sqrt{t} = k \cdot \sqrt{t};\ k = \sqrt{\frac{V_{\mathrm{m}}}{z_i \cdot F^2} \cdot \frac{\sigma_{\mathrm{Li}^+} \cdot \sigma_{\mathrm{ele}}}{\sigma_{\mathrm{Li}^+} + \sigma_{\mathrm{ele}}} \cdot \Delta\mu_{\mathrm{Li}}} \cong \sqrt{\frac{V_{\mathrm{m}}}{z_i \cdot F^2} \cdot \sigma_{\mathrm{ele}} \cdot \Delta\mu_{\mathrm{Li}}} \quad \textbf{(Eq. 17)}^{62}$$

The growing interphase resistance ($\Delta R_{\mathrm{interphase}}$) is shown in **Equation 18**.[132] The term "*A* " is the contact area and $\sigma_{\mathrm{interphase}}$ is the average conductivity of the interphase, which can be assumed that $\sigma_{\mathrm{interphase}} \cong \sigma_{\mathrm{Li}^+} \gg \sigma_{\mathrm{ele}}$.[132] The kinetic constant *k′* reflects the growth rate in terms of $\Delta R_{\mathrm{interphase}}$.

$$\Delta R_{\mathrm{interphase}} = \frac{\Delta\xi}{A \cdot \sigma_{\mathrm{interphase}}} = k' \cdot \sqrt{t} \quad \textbf{(Eq. 18)}^{132}$$

Overall, for a slow-growing interphase, its σ_{ele} should be low, and its σ_{Li^+} should be high.[134] Notably, $\Delta\xi$ and $\Delta R_{\mathrm{interphase}}$ increases in proportion to the square root of time. If *k* is known, the thickness of the interphase over time can be predicted.[132, 134] However, from the equations mentioned above, deviations occur when conductivities change during solid-state reactions, affecting the reaction kinetics.

Additionally, at a solid–solid interface, large gradients of chemical potential, lattice mismatch, or other defects can cause significant local free-energy changes that lead to deviations of the Wagner model. This is because the change in Gibbs free energy per atomic hop is assumed to be negligible compared to thermal energy, so the flux in a diffusion-controlled process is proportional to the driving force gradient (e.g., concentration or chemical potential gradient). This linear relationship is well described by Fick's laws that the transport coefficients are treated as constants or functions of state variables (pressure, temperature, etc.). As a result, the flux–gradient relationship in the Fick's laws are more likely to become nonlinear for interface-controlled processes, compared to diffusion-controlled processes.[135] This could explain the deviations from the linear relationship observed at the beginning of the measurements in electrochemical impedance spectroscopy (EIS),[133] and coulometric titration time analysis (CTTA)[94].

There are other factors that can change the boundary condition, leading to deviations of the Wagner model. For example, the interface often changes due to solid-state reactions, result in new product phases forming and growing.[135] On the other hand, crystals can experience elastic stress, which is usually unevenly distributed.[135, 136] Plastic deformation and dislocation formation occur when the stress

exceeds the yield strength, altering the crystal structure. While elastic deformations influence transport coefficients and driving force gradient, plastic deformations and dislocations primarily change transport coefficients.[135, 136] As a result, the Wagner model is assumed to be ideal for boundary conditions with homogeneous solid, dense, and fully covering interphases.[132]

2.7 CAM/SE interfacial degradation

The following sections introduce the interfacial degradation between the high-nickel CAM and sulfide-based SE, including (1) physical contact loss, (2) space charge layer (SCL), and (3) CEI degradation.[137, 138] In addition, particle cracking of high-nickel CAMs can be triggered by CEI degradation. **Figure 10** illustrates a schematic of the CEI degradation, showing that the polymer coatings promise to mitigate SCL degradation, CEI degradation, and cracking of high-nickel CAM particles except for physical contact loss. Without the coating protection, CAM particle cracking and the CEI degradation lead to a growth of L_{diff}.[51] If a CAM particle becomes completely isolated, possibly due to contact loss or the formation of an insulating CEI, it results in loss of m_{act}.[51]

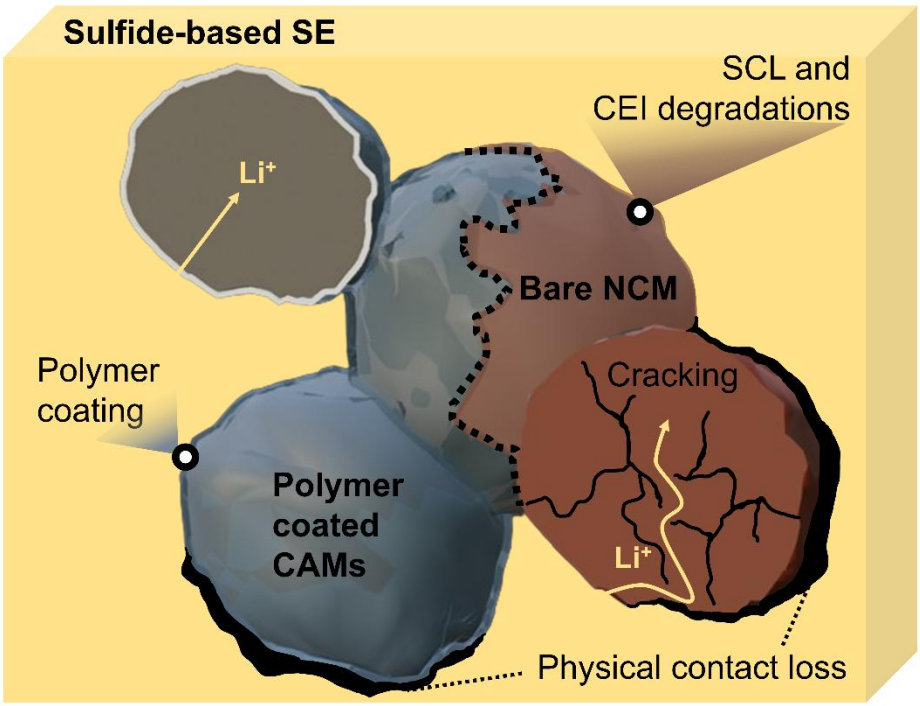

Figure 10. The schematic shows the CEI degradation mechanisms in the CAM composite, including interfacial degradation (physical contact loss, SCL, and CEI formation) and particle cracking.

2.7.1 Physical contact loss

The physical contact loss between CAMs and SEs is far more significant than in LEBs, as the LE can fill the gap caused by contact loss, hence increasing the active surface area. In contrast, the mechanical rigidity of SEs prevents these benefits, leading to degraded kinetics or m_{act} loss if CAMs become isolated.[51, 139, 140] Adjusting external pressure and Young's modulus of SEs can promote better CAM/SE contact due to improved elastic deformation of SEs.[141].[142] The Young's modulus, Shear modulus, hardness, and fracture toughness of different materials are summarized in **Figure 11**.[143]

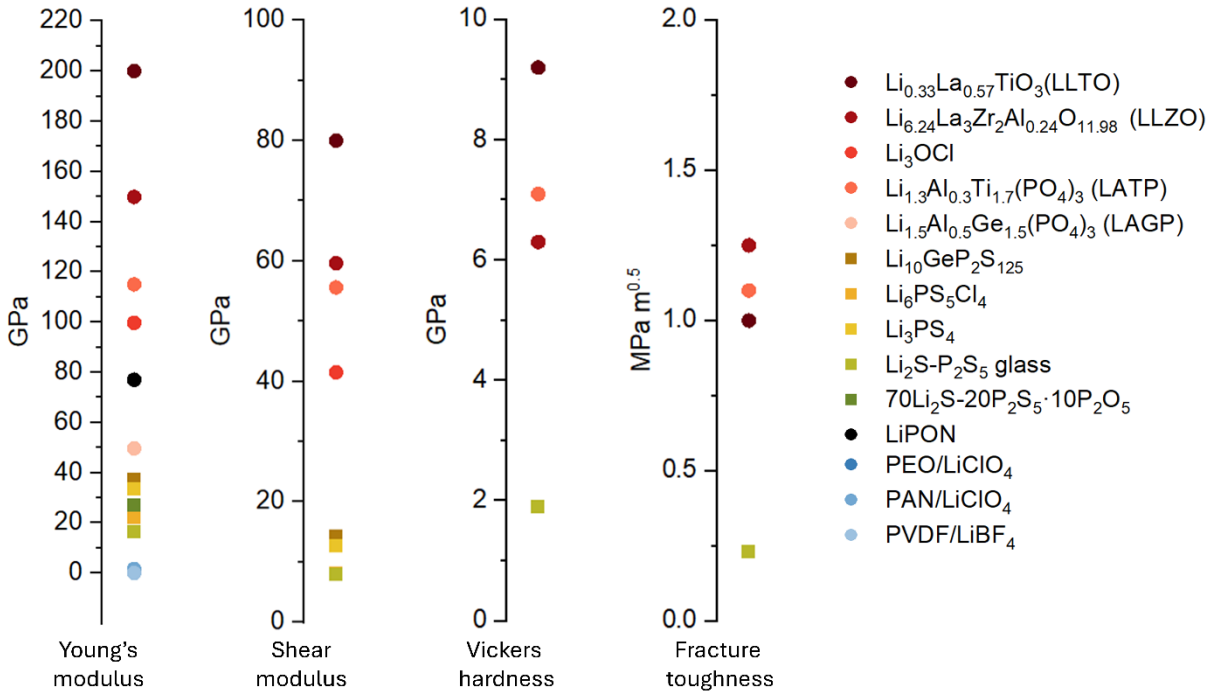

Figure 11. Overview of the mechanical properties of sulfide, oxide, polymer, and nitride electrolytes, including Young's modulus, shear modulus, hardness, and fracture toughness.[143] The figure was redrawn and modified from Ref. [143].

Oxide SEs exhibit a Young's modulus of 150~200 GPa and a hardness of 7~10 GPa, whereas sulfide-based SEs have lower values (a Young's modulus ≈ 20 GPa and a hardness ≈ 2 GPa). In comparison, CAMs possess a Young's modulus ranging from 80 to 200 GPa[144] and hardness between 3 and 30 GPa.[138, 141, 143, 144] Insufficient elastic deformation in both SEs and CAMs may impede the intimate interfacial contact. Furthermore, volume changes during cycling exacerbate contact loss.

However, when external pressure is applied, sulfide-based SE, such as Li_6PS_5Cl, exhibit much better compressibility than other SEs at room temperature, improving the CAM/SE contact.[141] This improvement is due to their lower Young's modulus or Pugh's ratio (*G/B*); for instance, Li_6PS_5Cl has a *G/B* value of 0.28, where *G* is the shear modulus, and *B* is the bulk modulus.[136, 145] Materials with a lower *G/B* ratio

(generally below about 0.5) can more easily accommodate stress through plastic deformation. In contrast, a higher *G/B* ratio indicates that the material is more prone to brittle fracture.[146]

2.7.2 Space charge layer

The formation of a SCL occurs at the interface between two phases when differences in chemical potential cause a redistribution of charge carriers in the boundary region to achieve thermodynamic equilibrium. Under electrochemical equilibrium, the $\tilde{\mu}_{\mathrm{Li}^+}$ remains constant throughout the cell components. At the sulfide-based SEs/CAMs interface, increased anodic polarization at the interface raises φ, leading to a sharp decrease in μ_{Li^+}. As a result, lithium-ions migrate from the SE to the cathode interface to maintain charge neutrality, resulting in separated regions of lithium-ion enrichment (CAM side)[147] and depletion (SE side)[147].[138, 147-149] [137]

The SCL may inhibit the charge transfer at the interface. In addition, considering that the charge carrier concentration in SE is usually in its optimal composition, lithium-ion depletion layer detrimentally decreases the σ_{ion} near the interface.[138] With increasing bias voltage, lithium-ions are extracted from the CAM to the anode side and then migrated to the interstitial vacancies of the SE. Due to the resistance from the lithium-ion depletion region, some of the extracted lithium-ions are trapped at the interface. These phenomena become more pronounced, causing increased interfacial resistance.[147] As a result, applying a suitable coating material as a buffer layer between CAMs and SEs can mitigate the detrimental effect from SCL.

The concept of the SCL explains the improved σ_{ion} observed at the polymer/SE interface.[138, 150] While the SCL between CAMs and SEs hinders interfacial ion transfer, the formation of local conjugated structures on the polymer side of the SCL in polymer/SE composites accelerates lithium-ion transfer.[150] Since the SCL thickness is typically on the nanometer scale, lithium ions can rapidly transfer between inorganic particles through the polymer phase when the polymer coating thickness is similar to SCL thickness. In contrast, with a thick polymer coating, the region far from the interface remains unaltered, weakening the charge compensation effect.[150] Consequently, the nano-meter polymer coating on CAMs is utilized in the publications.[138, 150]

2.7.3 Cathode degradation and CEI formation

The difference in μ_{Li} between sulfide-based SEs and high-nickel CAMs results in CEI formation. Before cycling at 0% SOC, high-nickel CAMs and sulfide-based SEs undergo chemical reactions at the interface. For example, NCMs react with SEs to generate transition metal sulfides (NiS, CoS, and MnS) and Li_2S as side products at the CEI. Such chemical degradation can lead to increased interfacial resistance due to thick CEI or crack formation on the surface of CAMs, which are detrimental to the first-cycle capacity.[151]

Additionally, the sulfide-based SE is oxidized into various polyanions during the first cycle, including $P_2S_7^{4-}$, $P_2S_6^{2-}$, P_2S_5, elemental S, and S_x-like species (Li-S_n-Li and P-S_n-P), as explained in **Section 2.5.4**.[104] However, the discharge process often reaches 2.6 V vs. Li^+/Li, which is not low enough for

triggering further reduction.[96, 98, 105] These side reaction products block the electronic and ionic transport, resulting in loss of m_{act} and low first-cycle Coulomb efficiency.[51]

Moreover, oxygen evolution from the surface region of the CAMs triggers oxygenated reactions with the SEs, leading to a gradual increase in the thickness of the CEI over cycling. The oxygenated side-reaction products include SO_x^{n-} (such as Li_2SO_4 and Li_2SO_3) and PO_x^{n-} (such as Li_3PO_4), which can be detected by time-of-flight secondary ion mass spectrometry (ToF-SIMS) [62, 104, 152, 153] and X-ray photoelectron spectroscopy (XPS)[104, 105, 152, 153]. In addition, differential electrochemical mass spectrometry can detect the evolution of O_2, CO_2, and SO_2 gas. The CO_2 is generated by the reaction of carbonated species with oxygen, whereas SO_2 results from the reaction of sulfide-based SE with oxygen.[45, 154] As O_2 loss primarily occurs at high SOC in the H2/H3 transition and subsequent delithiation states, the oxygenated side reaction products can act as an indicator for the degradation regarding H2/H3 transition.

Li_2SO_4 and Li_3PO_4 have a σ_{ion} at 25 °C around $1.4 \cdot 10^{-4}$ and $3.9 \cdot 10^{-6}$ mS·cm^{-1}, respectively. However, when the molar ratio of Li_2SO_4 to Li_3PO_4 is 1:3, σ_{ion} increases to around $1.6 \cdot 10^{-1}$ mS·cm^{-1}. Additionally, a 1:1 molar ratio results in a σ_{ion} around 9.9×10^{-2} mS·cm^{-1}.[155] As a result, the Li_2SO_4/Li_3PO_4 may not directly cause loss of m_{act} at the beginning of cycling but kinetically affect the electrochemical performance.[51] Moreover, an artificial CEI layer composed of Li_2SO_4/Li_3PO_4 may improve electrochemical performance.[156] This suggests that artificial oxygenated products on the surface of sulfide-based SEs could also serve as protective buffer layer, which becomes the motivation for **Publication C**.

2.8 Li/SE interfacial degradation

The Li/SE interface/interphase can be categorized into the thermodynamically stable (or fully kinetically stabilized) interface and thermodynamically unstable interphases, as shown in **Figure 12**. Thermodynamically unstable interphases include the MCI and SEI. MCI is an electronic and ionic conductive interphase, while SEI is kinetically self-limited due to low σ_{ele}.[130, 157] The SEI formation kinetics are influenced by σ_{ele} and $\Delta\mu_{Li}$ of the SEI, as explained in **Section 2.6.3**.

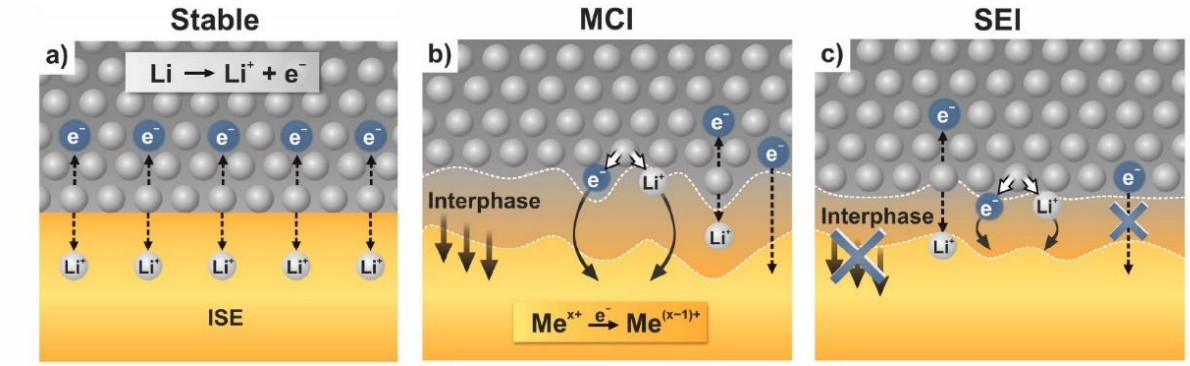

Figure 12. There are three types of interface/ interphases between lithium metal and an SE: (a) thermodynamically stable interface, (b) reactive MCI with high σ_{ele}, and (c) SEI with low σ_{ele}.[130, 157] (Reproduced with permission from Ref. [130], copyright 2015 Elsevier.)

Regarding the case of the thermodynamically stable interface (**Figure 12a**), SEs remain (electro)chemically stable in contact with lithium metal anode ($\mu_{\mathrm{Li}}^{\mathrm{a}} = \mu_{\mathrm{Li}}^{\mathrm{SE}}$), preventing any reduction of the SE upon contact with lithium metal anode.[130, 157] Although the binary lithium compounds like LiF, LiCl, or Li_3N are thermodynamical stable against the lithium metal anode, they typically form as decomposition products of LEs or SEs and function as a SEI.[99] Notably, **Publication C** demonstrates that the *in situ* formation of Li_3N as a component of the SEI may improve the SEI stability.

For the case of the thermodynamically unstable interphase, $\mu_{\mathrm{Li}}^{\mathrm{a}}$ is initially different from $\mu_{\mathrm{Li}}^{\mathrm{SE}}$, and the chemical reactions occur between the SE and lithium metal.[130, 157] This can result in an irreversible capacity loss in anode free cells.[94] MCI (**Figure 12b**) exhibits sufficient σ_{ele} and σ_{ion}, which can continuously grow into the SE and consume lithium metal, ultimately causing self-discharge of the battery. [130, 157] For instance, the high-valence metal ion in thio-LISICON $Li_{4-x}Ge_{1-x}P_xS_4$ and its reduction leads to the formation of an MCI against lithium metal anode rather than a dense and insulating SEI layer.[94] On the other hand, the SEI (**Figure 12c**) is a kinetically self-limiting interphase composed of solely ionically conducting products with low σ_{ele}.[130, 157] However, the SEI thickness varies across material systems due to differences in the σ_{ele} of SEI components.[94]

2.8.1 SEI degradation between Li_6PS_5Cl and lithium metal

The SEI formation between Li_6PS_5Cl and lithium metal is diffusion-controlled, which is proved by EIS,[133] and CTTA[94]. A Wagner model describes the diffusion-controlled reaction, as detailed in **Section 2.6.3**.[158] Experimental studies demonstrate that after one week, the SEI layer reaches a thickness of 235–305 nm as measured by ToF-SIMS and atomic force microscopy[159], and 315 nm according to CTTA calculations[94] and the Wagner model[158].

The diffusion-controlled phenomenon can be explained by the low σ_{ele} of the SEI around 10^{-10} S·cm^{-1} at 25 °C, as shown in **Figure 13**.[158, 160] The SEI comprises Li_2S, LiCl, and Li_3P (identical to **Eq. 12**[94]), resulting in a complex microstructure with multiple interfaces.[161] Among these components, Li_2S has a σ_{ele} around 10^{-11} mS·cm^{-1} at 25 °C, which is much lower than that of Li_3P around 1 mS·cm^{-1} at 25 °C.[158] The conductivity difference between the SEI and its intrinsic components arises from the formation of a mixed phase.[51] However, the SEI between Li_6PS_5Cl and lithium metal forms a porous microstructure, which can lead to dendrite growth due to non-uniform lithium-ion conduction (**Section 2.8.2**).[161]

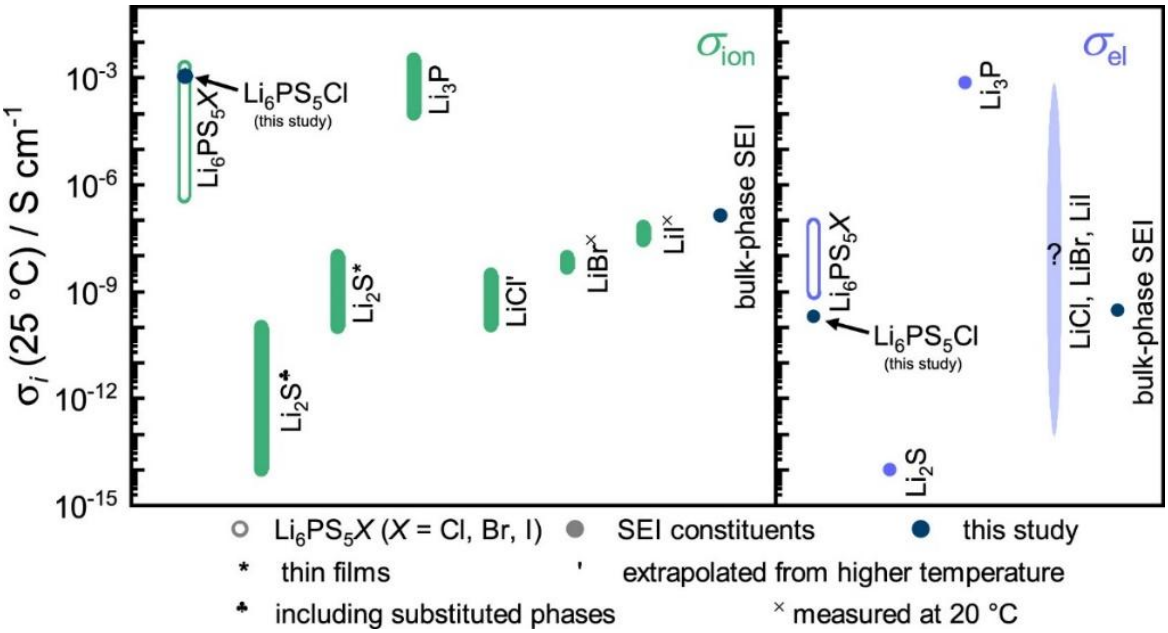

Figure 13. σ_{ion} and σ_{ele} at 25 °C for Li_6PS_5X (X = Cl, Br, I) and their typical SEI constituents. Note: substituted phases are excluded.[158] (Reproduced with permission from Ref. [158], copyright 2024 Joule.)

2.8.2 Lithium dendrite formation in SEBs

The tip-growth model of lithium is one of the earliest and most widely accepted mechanisms for lithium dendrite formation.[162] In this model, current constriction accumulates the charge at a tip, creating a strong localized electric field. Subsequently, lithium-ions deposit at the tip and lead to lithium nucleation and dendrite growth.[163-165] In general, non-uniform lithium-ion conduction leads to current constriction,[130] which can be due to: (1) poor contact, such as defects and pores, at the Li/SE interface,[136] (2) non-uniform side reaction product distribution and porous microstructure of SEI,[161] (3) grain boundaries and cracks within the SE, which jointly facilitate dendrite growth.[130, 136, 164, 165] **Publication C** forms an artificial SEI layer between lithium metal and Li_6PS_5Cl, primarily composed of Li_3N, which mitigates dendrite growth. This may be due to the strong wetting ability of Li_3N with the lithium metal anode, which reduces non-uniform Li-ion conduction and effectively prevents dendrite growth.[166]

A high shear modulus of a SE is often considered as necessary for inhibiting dendrite growth.[141] In contrast, dendrite growth can easily penetrate the soft polymer electrolytes because of their relatively low shear modulus.[167] According to the model from Monroe and Newman, dendrite growth is suppressed if the shear modulus of SEs are at least twice that of lithium (4.8 GPa at 298 K).[168] Most of the SEs exceed this threshold (see **Figure 11**). For example, the shear modulus of Li_6PS_5Cl is around 25 GPa.[143, 169] However, SEs typically exhibit a critical current density (CCD), defined as the maximum current density before shorting occurs, that is generally below 1 mA·cm^{-2}.[170] This is because the shear modulus criterion in the model is only suitable for a perfect Li/SE interface without poor contact and non-uniform SEI.[136, 171]

2.9 Polyelectrolytes as a coating material

For effective electronic percolation, CAM particles must maintain direct contact. A fully covered and electronic-insulated coating would hinder electronic transport between CAM particles. However, brittle coatings (such as $LiNbO_3$ with Young's modulus ≈ 195 GPa) can fracture at particle contact points due to mechanical mixing and electrode fabrication. Moreover, cycling-induced stress and volume change can lead to more coating fractures. Although coating fractures may create electronic transport pathways, the bare CAM surface is unprotected and vulnerable to CAM/SE interfacial degradation.[61]

In contrast, softer polymer-based coatings (Young's modulus ≈ 10 MPa or lower) exhibit elasticity comparable to thiophosphate solid electrolytes (Young's modulus ≈ 20 GPa). These coatings can deform and thin out under stress, facilitating particle contact while minimizing coating fractures.[61] On the other hand, polymers typically exhibit σ_{ele} below 10^{-16} S·cm^{-1},[172] much lower than the SEs (from 10^{-8} to 10^{-10} S·cm^{-1})[173]. The electronic conductivity of a coating or interphase is strongly related to the interfacial stability, as described in **Section 2.6**. As a result, the beneficial mechanical properties and low σ_{ele} of polymers serve as the key motivations for using them as coatings on CAMs in this dissertation.

On the other hand, the σ_{ion} of the 1 nm coating layer or interphase requires more than 0.1 μS·cm^{-1} to reach a resistance smaller than 1 Ω·cm^2.[61] Therefore, when the σ_{ion} of the coating layer is below 0.1 μS·cm^{-1}, common for polymers without plasticizers, a nanometer-scale thickness is essential to minimize resistance. Although incorporating plasticizers or lithium salts can enhance σ_{ion}, it may also reduce the quantity of the polymer-coating inducer and weaken electrostatic interactions between polymers and coated particles, potentially leading to coating failure. Compared to conventional PEs that require additional salts, polyelectrolytes offer the advantage of their intrinsic σ_{ion}, which is advantageous for applying a thin nanometer-scale coating without adding salt. Consequently, the polyelectrolytes are selected as a coating material in this dissertation.

2.9.1 Polycation and polyanion

Polyelectrolytes contain dissociating groups within their repeating units, leading to a charged polymer backbone balanced by counterions. **Figure 14** demonstrates three main parts in the structure of polyelectrolytes: the polymer backbone, ionic species, and the spacer. The backbone of polyelectrolytes can include functional groups, such as vinyl, peptide,[174] or sulfone,[175] with a possible intermediate functional group linking to the spacer.[176] The backbone affects the glass transition temperature (T_g) and mechanical properties.[177] The spacer within the polymer may consist of a short or long-chain structure, such as ethylene, ethylene oxide, and benzyl group. However, spacers have a complex influence, affecting both σ_{ion} and mechanical properties. A spacer facilitating the dissolution of counterions in the ionic species can enhance σ_{ion}, such as ethylene oxide. On the other hand, spacers can also increase T_g, reducing chain mobility and thereby lowering σ_{ion}.[176]

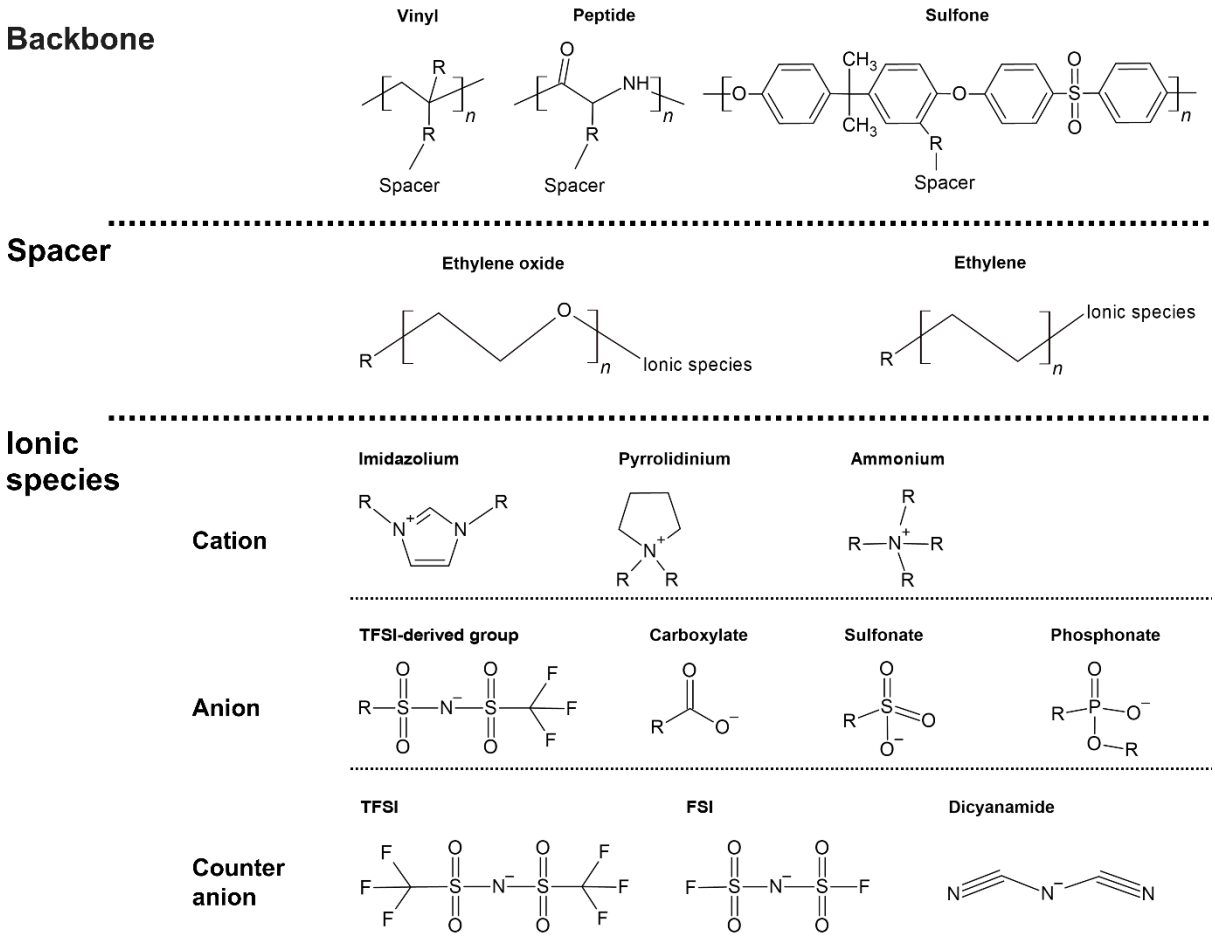

Figure 14. Examples of chemical structures of polyelectrolytes include backbones (top), spacers (middle), and ionic species (bottom). The ionic species of polycation and polyanion includes cation and anion functional groups, respectively. Counter anions for the polycations are shown in the bottom row of the ionic species, while the counter cation for the polyanions are considered as lithium ions.[176] The figure was redrawn and modified from Ref. [176].

Depending on the type of ionic species, the polyelectrolyte can be classified as either a polycation or a polyanion.[176] Polycations contain fixed cation functional groups, such as imidazolium, pyrrolidinium, or ammonium, paired with mobile counter anions, such as TFSI, FSI, or dicyanamide. As a result, polycations require extra lithium salt to function as lithium-ion conductors. In contrast, polyanions have fixed anion functional groups, such as a TFSI-derived group, carboxylate, sulfonate, and phosphonate, resulting in a high lithium ionic transfer number.[176] However, polycations can be used as coating inducers for CAMs and Si particles, which is studied in **Publications A** and **D**. Additionally, polycations are generally easier to synthesize and less costly compared to polyanions.[176]

Polyelectrolytes are normally amorphous due to counterions hindering crystallization.[178] If counterions in ionic species strongly coordinate with the polyelectrolytes, T_g may increase. To take an example from neutral polymers, the poly(ethylene oxide) exhibits strong lithium-ion coordination with lithium salts along

its entire polymer structure, which increases its T_g. In contrast, poly(ethylene carbonate) shows a decrease in T_g upon salt addition because its strong carbonate dipole effectively dissociates lithium ions.[176, 179]

Take an example of a polyanion, an increase in cationic counterion size ($Li^+ < Na^+ < Cs^+$) in the polyanion generally hinders the chain mobility, hence causing higher T_g. For polycation, T_g of poly(trimethylammonium-2-ethyl)X^- methacrylate varies with anionic counterions: 164 °C for Cl^-, 130 °C for BF_4^-, 164 °C for PF_6^-, 70 °C for $CF_3SO_3^-$, and 38 °C for TFSI.[178] Compared to PF_6^-, TFSI counter ions interact more weakly with the backbone and spacer of the polycation, resulting in a lower T_g of the polycation.[176] Moreover, anionic counterions significantly affect the thermal stability of polycation. For example, the thermal stability can be ranked as follows: $CF_3SO_3^-$ > TFSI > $C_{12}H_{25}C_6H_4SO_3^-$ > PF_6^- > Br^- > $C_{16}H_{34}PO_4^-$.[178] However, the underlying reason warrants further study. As higher T_g typically exhibit a higher Young's modulus, **Publications A** and **D** utilize a polycation with a TFSI counterion as the coating material to have lower T_g, resulting in a more deformable mechanical behavior.

Anionic counterions have a more pronounced effect on the solubility of polycations compared to the influence of cationic counterions on the solubility of polyanions. For instance, poly(1-vinyl-3-ethylimidazolium)X^- is water-soluble when X^- is a halide (e.g., Br^-). Replacing Br^- with BF_4^- or PF_6^- renders the polymer insoluble in water while allowing dissolution in methanol and polar aprotic solvents, including acetone, dimethyl sulfoxide, and dimethyl formamide (DMF). When replacing halide ions with TFSI or other hydrophobic anions, the polymer becomes soluble in less polar solvents like tetrahydrofuran and toluene.[178] On the other hand, cationic counterions in polyanions often restrict their solubility to water and other polar solvents with polarity similar to that of water. The solvent is crucial for the wet-coating process because the solvent should be stable against the coated materials. Moreover, the spray-drying process requires a low boiling point solvent. For instance, the boiling point of NMP exceeds 200 °C, making it unsuitable for the spray-drying process.

2.9.2 Polyelectrolyte complexes

PECs form spontaneously when oppositely charged polyelectrolytes mix in solution, driven by the entropy gain from counterion release.[180, 181] Therefore, the stoichiometric number of complex units in PEC is determined by the number of counter-charged groups. When the cation-to-anion ratio in PEC equals to one, the PEC is stoichiometric. Deviations from this ratio, known as overcompensation, are essential for processes like forming polyelectrolyte multilayers or quasi-stable nanoparticles in solution.[182] PECs are used in pharmaceutical applications, such as drug carrier systems and enzyme supports. Additionally, they are widely employed in dialysis and ultrafiltration membranes due to their high-water permeability. They also act as effective separators in primary and secondary LEBs and fuel cells.[180, 183]

In the initial stage of PEC formation, two opposing processes co-occur. First, ionic interactions cause oppositely charged polyelectrolytes to align and form an organized complex. Second, disordered aggregation causes oppositely charged polyelectrolytes to only partially neutralize each other, leaving some charged segments balanced by small counterions. Overall, the formation of the PEC is influenced by

the interaction between these two effects.[184, 185]

PEC formation occurs in three steps, ultimately resulting in a precipitate, as shown in **Figure 15**: (1) primary complex formation, where random ionic bonds form upon mixing cationic and anionic polymers; (2) secondary complex formation, after ionic bonds rearrange; and (3) inter-complex aggregation, in which the complexes coalesce into the entanglement, network, and fiber products.[185-187] Step (1) involves the rapid formation of secondary binding forces, such as Coulomb interactions.[185, 188] The step (2) involves forming new ionic bonds and rearranging the polymer chains into a stable conformation. In step (3), secondary complexes aggregate via hydrophobic interactions to form insoluble PEC aggregates.[185, 189] Notably, the entanglement product in step (3) can be formed directly from the step (1) because the precipitation occurs too rapidly, leaving no time for step (2) to take place.

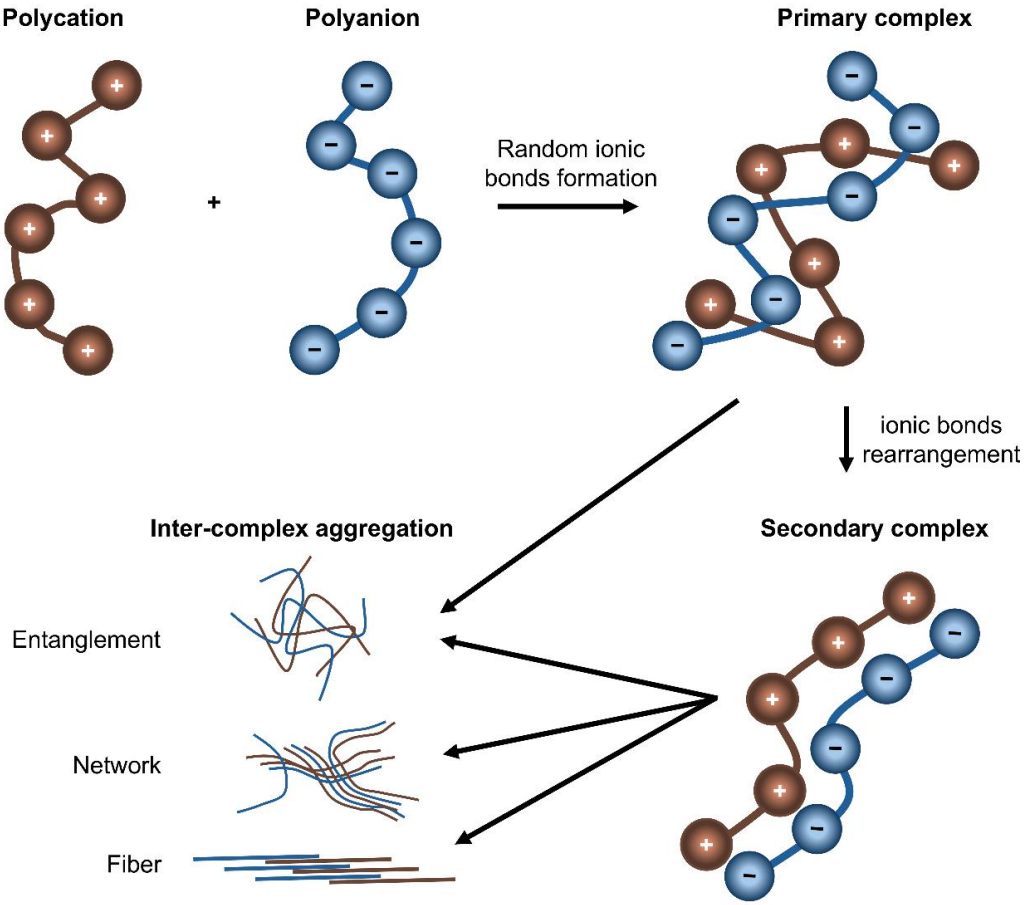

Figure 15. The schematic illustrates PEC aggregation in three steps: (1) primary complex formation (top right), (2) secondary complex formation (bottom right), and (3) inter-complex aggregation leading to precipitation (bottom left).[189] The figure was redrawn and modified from Ref. [189].

PEC properties are influenced by factors such as the molecular characteristics, including their degree of polymerization, charge density, steric hindrance of charges along the chain, polymer hydrophilicity or polarity, tacticity or chirality, and architecture.[190] Most PECs become brittle in the dry state due to strong ionic interaction strength within PECs, rendering them high T_g and insoluble in solvents.[191] The absence of the glass transition below the degradation temperature causes that these materials are not processable in the dry state.[180]

Environmental factors such as the ionic strength in the solution, dielectric constant, pH, and temperature can modulate the ionic interaction strength within PECs.[190] For instance, adding the solvent and salt can soften PECs by electrostatic screening,[180] enhancing chain mobility and increasing free volume for moving ions.[181] With enough solvent to disperse the PEC to form a coacervate, gradually reducing salt in a PEC/salt/solvent system promotes ion pairing, which increases viscosity until forming a rigid and glassy solid, while adding salt converts it back into a coacervate.[192-194] After softening by adding the solvent and salt, PECs exhibit ionic diffusion at least two orders of magnitude faster than polycations and polyanions, driven by rapid local rearrangements of ionic sites rather than full polymer chain mobility.[195] Therefore, ionic diffusion in PECs decreases as ionic interaction strength increases because stronger electrostatic forces restrict ion movement.[196]

Normally, PEC is unsuitable for wet coating methods due to its insolubility and brittle mechanical properties. Although adding salt can weaken the ionic interaction strength and form the coacervate,[192-194] a true solution in which the solute is completely dissolved at the molecular level is necessary.[192, 197] As a result, controlling ionic interaction strength without solvent and salt is necessary. As shown in **Figure 16**, without considering their counter ions, the interacting ionic species of polyelectrolytes influence the binding affinities in PECs.[196]

Notably, reducing ionic species and steric hindrance within the PEC can weaken the ionic interaction strength.[191] Polyelectrolytes with bulky side chains attached to the charged moiety can provide steric hindrance, thereby weakening the ionic interaction strength and lower the T_g.[191] This method yields thermoplastics with 100% charge density solely from ionic interaction between the polycation and polyanion.[191] However, this is insufficient to produce a true solution upon dissolution, which is necessary for wet coating processes. As a result, **Publication D** copolymerizes anionic polymer with the neutral repeated units (serving as internal plasticizers) to form a PEC with PVBTA-TFSI. This PEC exhibits rubber-like mechanical properties and is fully soluble in acetone without plasticizer and salt, making it suitable for wet coating applications.

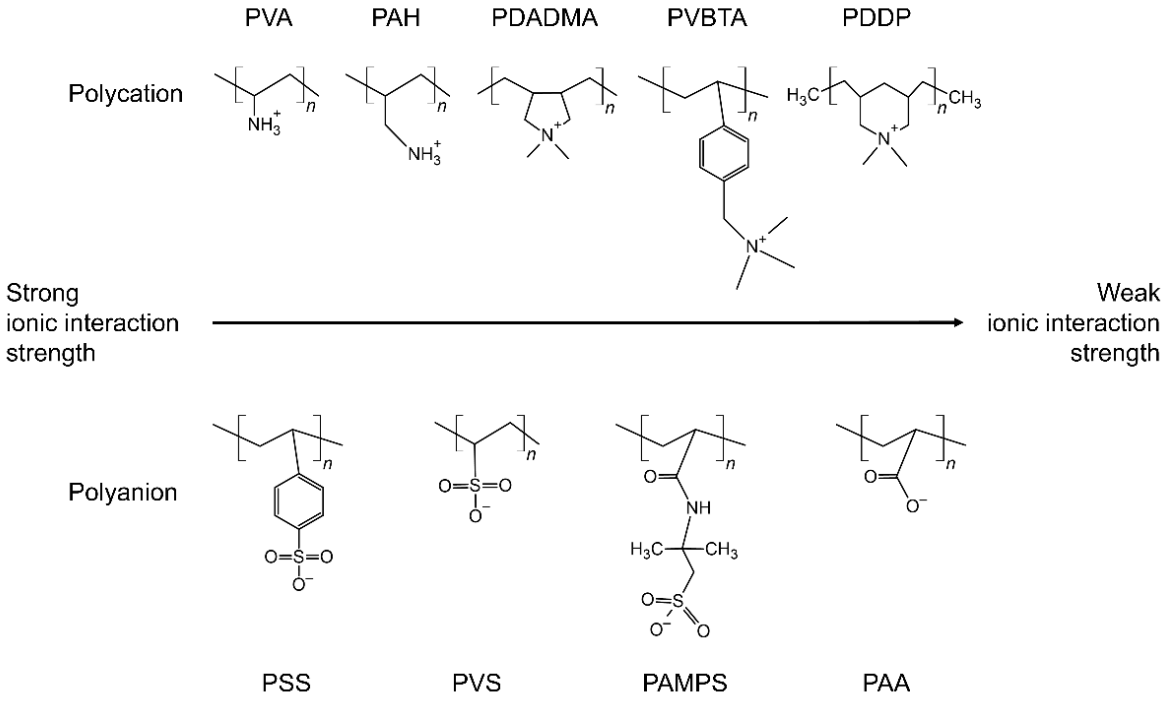

Figure 16. The schematic shows the ionic interaction strength between various polycations and polyanions, ranging from strong (left) to weak (right). Polycations include poly(vinylamine) (PVA), poly(allylamine) (PAH), poly(diallyldimethylammonium) (PDADMA), poly(vinylbenzyltrimethylammonium) (PVBTA), and poly(N,N-dimethyl-3,5-dimethylene piperidinium) (PDDP). Polyanions include poly(styrenesulfonate) (PSS), poly(vinylsulfonate) (PVS), poly(acrylamido-2-methylpropanesulfonate) (PAMPS), and poly(vinylamine) (PVA).[196] The figure was redrawn and modified from Ref. [196].

3. Results

3.1 Publication A

This part of the PhD project first aims to identify a polymer that can uniformly coat the entire NCM surface and to develop an effective coating technique for sulfide-based SEB. Moreover, this publication compares the performance of coated and pristine $LiNi_{0.83}Co_{0.11}Mn_{0.06}O_2$ as CAMs when in contact with a Li_6PS_5Cl catholyte. An In/InLi alloy serves as the counter electrode to evaluate the cathodic performance. In addition, Li_6PS_5Cl is used as both the separator and the catholyte.

Initially, PVP was chosen as the coating material to evaluate various methods, owing to its proven efficiency as a coating inducer.[198] A traditional wet-coating approach with vacuum filtration was initially tested. The coating precursor comprises the PVP and NCM suspension (0.6 g polymer, 200 ml NMP, and 2 g NCM)[198]. A vacuum is applied to remove the excess solvent from the coating precursor using a filtration setup. Subsequently, the product is dried in the vacuum oven under 100 °C for 24 hours. However, scanning electron microscopy (SEM) shows this method results in an uneven "island coating" and significant polymer aggregation separate from the NCM particles. This may be because the traditional wet-coating approach is insufficient for a uniform coating.

A rotary evaporation setup was tested as an alternative to traditional wet-coating methods for more efficient solvent removal and better control over the coating amount. In this method, a suspension of 0.1 g PVP, 100 mL acetone, and 2 g NCM is dried using a rotary evaporator, leveraging the low boiling point of acetone for rapid solvent removal. After rotary evaporation, the coated samples are dried in a vacuum oven at 100 °C for 24 hours. However, the PVP tends to adhere to the inner glass walls instead of coating the NCM particles, as confirmed by SEM. Additionally, electrochemical tests show no performance improvement compared to pristine NCM.

Ultimately, the spray-drying method overcame earlier challenges by providing a uniform polymer coating on the NCM surface. However, PVP degrades the cell performance due to its ionic insulation (see **Publication B**). Additionally, polymethyl methacrylate (PMMA) was tested using the spray-drying method, but its weak electrostatic interactions with NCM particles resulted in significant polymer aggregation separate from the NCM particles. Therefore, a self-synthesized cationic polymer (1 wt% relative to NCM), PVBTA-TFSI, is used in this dissertation, yielding a uniform 2~4 nm coating that enhances cycling stability compared to pristine NCM.

B.X.S. carried out the syntheses, electrochemical analyses and general materials characterization. Y.Y. performed the TOF-SIMS analysis and T.D. carried out the TEM experiments. S.S., R.R., K.V., A.H., and F.H.R. helped with the analysis and discussion of experimental data. B.X.S., S.S., and F.H.R. conceived the idea and prepared the manuscript. All authors participated in the analysis of the experimental results and contributed to the manuscript.

RESEARCH ARTICLE

ADVANCED ENERGY MATERIALS
www.advenergymat.de

Mitigating Contact Loss in Li_6PS_5Cl-Based Solid-State Batteries Using a Thin Cationic Polymer Coating on NCM

*Bing-Xuan Shi, Yuriy Yusim, Sudeshna Sen, Thomas Demuth, Raffael Ruess, Kerstin Volz, Anja Henss, and Felix H. Richter**

Thiophosphate-based solid-state batteries (SSBs) with high-nickel ternary cathode materials such as $LiNi_{0.83}Co_{0.11}Mn_{0.06}O_2$ (NCM) represent a promising next-generation energy storage technology due to their expected high specific discharge capacity and improved safety. However, rapid capacity fading caused by contact loss through interphase and crack formation during cell cycling is a significant problem hindering stable SSB cycling and high-energy-density applications. In this work, a uniform coating of poly((4-vinyl benzyl)trimethylammonium bis(trifluoromethanesulfonylimide)) (PVBTA-TFSI) on NCM is obtained via a spray-drying process. This exceptionally thin cationic polymer coating of only 2–4 nm thickness on NCM helps stabilize the interface between NCM and the Li_6PS_5Cl solid electrolyte (SE). Electrochemical tests confirm a significant improvement in long-term cycling performance and active mass utilization compared to uncoated NCM. In addition, the polymer coating effectively suppresses the degradation of the NCM/SE interface, particularly the formation of oxygenated species, and reduces the extent of particle cracking. Overall, these results highlight a new approach to mitigate SSB degradation using a thin cationic polymer coating on NCM for SSBs.

1. Introduction

Lithium solid-state batteries (SSBs) using solid electrolytes (SEs) to replace organic liquid electrolytes are expected to improve battery safety and performance. They promise to be excellent electrochemical energy storage devices for electric vehicles and large-scale applications.[1] In order to achieve higher energy density, intercalation-type cathode active materials and thiophosphate-based solid electrolytes have drawn much attention.[2] High-nickel ternary $LiNi_{1-x-y}Co_xMn_yO_2$ is a promising lithium SSB cathode active material due to its high energy density and low cost.[3] However, severe capacity fading caused by contact loss through interface degradation and particle cracking is observed when NCM and thiophosphate-based solid electrolytes are combined in a SSB composite cathode.

In general, interface degradation between NCM and solid electrolyte creates interfacial layers that interfere with lithium-ion and electron transport. Even at a state of charge (SOC) of 0%, chemical reactions at the NCM/SE interface cause capacity fading.[4] During the first charging process, electrochemical degradation occurs at the NCM/SE interface due to the limited electrochemical stability window of thiophosphate-based solid electrolytes. However, the discharge process is often terminated above 2.6 V (vs Li^+/Li), preventing reduction at the NCM/SE interface during discharge. Hence, oxidation of the solid electrolyte is much slower in subsequent cycles.[5–7]

Since the thiophosphate-based solid electrolyte is in direct contact with NCM, side reactions can occur that result in structural degradation of the surface of NCM and create a passivation layer at the NCM/SE interface. Therefore, oxygenated species such as SO_x^{n-} and PO_x^{n-} are detected by time-of-flight secondary ion mass spectrometry (ToF-SIMS) at the NCM/SE interface, and SO_2 gas is detected by differential electrochemical mass spectrometry during cycling. Oxygen loss causes mechanical cracking and plays an important role in interface degradation.[5,8–13] Additionally, lattice contraction and expansion of NCM during cycling contributes to capacity fading.[14–18] These degradation mechanisms have even stronger adverse effects in SSBs than in lithium-ion batteries due to contact loss between solid electrolyte and cathode active material.[19] Consequently, research efforts are devoted to improving the stability of the electrode-electrolyte interface.

In order to enhance the interfacial stability between NCM and thiophosphate-based solid electrolyte, surface modification

B.-X. Shi, Y. Yusim, S. Sen[+], R. Ruess, A. Henss, F. H. Richter
Institute of Physical Chemistry & Center for Materials Research (LaMa)
Justus Liebig University Giessen
Heinrich-Buff-Ring 17, 35392 Giessen, Germany
E-mail: felix.h.richter@phys.chemie.uni-giessen.de
T. Demuth, K. Volz
Department of Physics & Materials Sciences Center (WZMW)
Philipps-University Marburg
Hans-Meerwein Straße 6, 35032 Marburg, Germany

The ORCID identification number(s) for the author(s) of this article can be found under https://doi.org/10.1002/aenm.202300310

[+]Present address: WMG, University of Warwick, Coventry CV4 7AL, UK

DOI: 10.1002/aenm.202300310

ADVANCED SCIENCE NEWS
www.advancedsciencenews.com

ADVANCED ENERGY MATERIALS
www.advenergymat.de

by coating on NCM has been studied considerably. In general, wet and dry coating processes can hardly achieve a thin and uniform coating layer compared to atomic layer deposition.[20] As a result, atomic layer deposition is often used to prepare cathode active materials with inorganic coatings such as HfO_2.[21] However, scaling up the production of battery materials involving an ALD coating processes remains challenging.[22] Many research efforts focus on inorganic oxides as coating materials, such as $LiNbO_3$,[23–25] $Li_6ZnNb_4O_{14}$,[26] $LiAlO_2$,[27] Li_2ZrO_3,[25,28,29] $Li_4Ti_5O_{12}$,[30] Li_3BO_3,[31] and $Li_3B_{11}O_{18}$.[28,32] In addition, halide solid electrolyte coatings, such as Li_3YCl_6,[33] have been reported.

In addition, polymers can coat a substrate evenly if there is an attractive force between the functional groups of the polymer and the substrate.[34] For instance, polyvinylpyrrolidone can act as a surfactant, modifying the surface of metal oxides.[35] The mechanical properties of the coating material, along with its adhesion to the NCM, play a crucial role in the cathode performance during charge and discharge-induced volume changes. Polymers demonstrate great binding capability in composite cathodes. In contrast, inorganic materials, such as $LiNbO_3$ (Young's modulus ≈195 GPa), are inherently rigid and susceptible to fracture at the point contacts of NCM particles. Moreover, owing to its relatively weak binding capability, the coating material may delaminate from the NCM substrate due to contraction or cracking of NCM. On the other hand, the use of polymer-based coatings (Young's modulus ≈6 GPa) enables deformation and thinning, resulting in reduced cracking of coating layer and the preservation of contact between particles.[36,37] Notably, reduced cracking may stem from decreased side reaction at the NCM/SE interface.[10] However, a thin coating with few nanometers of thickness may not sufficiently restrict volume changes from NCM materials.[36]

Although poly(3,4-ethylenedioxythiophene) modification on NCM and carbon additives in SSBs via molecular layer deposition has been studied,[38] polymer coated NCMs are mostly adopted in lithium-ion batteries with liquid electrolytes.[35,39–48] Polyelectrolytes bear ionic groups and have affinity to inorganic surfaces through strong electrostatic interactions with metal-oxide surfaces. Moreover, a polyelectrolyte with bis(trifluoromethanesulfonyl)imide counter ion has previously been used as a cathode binder in batteries with liquid electrolyte,[49,50] implying the potential of polyelectrolytes as the promising coating material for inorganic substrates.[51,52]

Spray drying can be classified as a wet coating method applied in industry[53] and has successfully obtained uniform coatings on NCMs.[36] Depending on the particle size, the spray-drying method can usually obtain two coated products. First, if particles are smaller than the drops sprayed out, the particles can be enclosed in the droplets, forming a uniform coating.[54] Second, if the particles are more significant than the droplets, there will be many exposed parts on the surface of the particles after drying.[55] By using Mini Spray Dryer B-290 from BUCHI, a drop of the solution is ≈25 µm, much bigger than the NCM particles, which are ≈3–5 µm in diameter.

Herein, we present the first polyelectrolyte coated NCM for use in solid-state batteries. Spray drying is used to obtain a uniform and thin coating of polyelectrolyte on NCM as it can be easily coated on metal oxide due to electrostatic interactions.[51] Poly((4-vinylbenzyl)trimethylammonium bis(trifluoromethanesulfonylimide)) (PVBTA-TFSI) is adopted as a coating material for NCM in this study. The thin PVBTA-TFSI coating on NCM significantly decreases contact loss and improves the cycling performance. We also investigate interface degradation and lithium diffusion pathway length within the cathode composite in support of the electrochemical performance results.

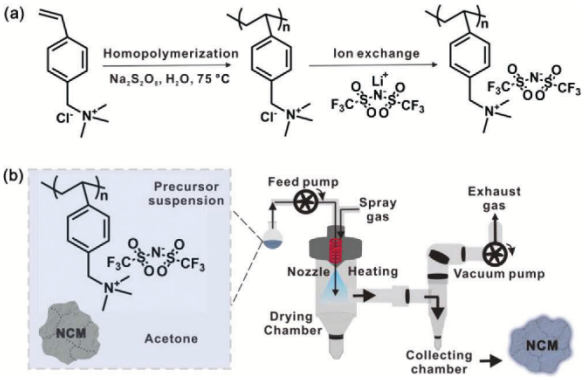

Figure 1. Schematic illustration of a) the PVBTA-TFSI synthesis and b) the process for spray coating of NCM particles, after which NCM is collected and further dried at 80 °C for 48 h in vacuum.

2. Results and Discussion

2.1. Characterization of PVBTA-TFSI Coated NCM

First, poly((4-vinylbenzyl)trimethylammonium chloride) (PVBTA-Cl) is dissolved in water solution to prepare PVBTA-TFSI through ion exchange with lithium bis(trifluoromethanesulfonyl)imide (LiTFSI). As water and alcohol solvents leach Li^+ out of NCM, these solvents must be avoided during the coating process.[56] After ion exchange with LiTFSI, PVBTA-TFSI is soluble in acetone, which is a suitable solvent for the coating process of NCM. Since the wet-coating method often gives a non-uniform and thick coating on the surface of particles,[20,36] the spray coating method is used here due to its possibility of obtaining a thin and uniform coating on NCM.[36]

Figure 1 shows a schematic illustration of polymer synthesis and the spray coating processes. The polymer is synthesized through free-radical polymerization followed by anion exchange with LiTFSI. A mixture of NCM/PVBTA-TFSI/acetone is used as the precursor suspension in the spray coating process. It is sprayed out of the nozzle and is dried at a temperature of 150 °C, which is much higher than the boiling point of acetone. The polyelectrolyte coating on NCM is obtained during the drying process in the drying chamber. Finally, the dried powder is collected in the collecting chamber.[53]

The structure of PVBTA-TFSI is confirmed by ^{1}H Nuclear Magnetic Resonance (^{1}H NMR) spectroscopy and matches the ^{1}H NMR spectra of the literature, as shown in Figure S1, Supporting Information.[57] After polymerization and ion exchange, the double bonds of the monomer (^{1}H NMR: δ = 6.71, 5.82, and 5.26 ppm in the ^{1}H NMR spectra) are no longer present

in the PVBTA-TFSI spectra.[58] Instead, a new ^{1}H-signal appears at 1.5 ppm, indicating that polymerization has been completed. Moreover, the aromatic protons (H3,4), benzylic protons (H5), and the protons of trimethylammonium cations (H6) still exist in the PVBTA-TFSI spectra, indicating that the polymer backbone structure is stable after ion exchange.

Figure S2, Supporting Information, shows the infrared spectra of PVBTA-Cl, and PVBTA-TFSI after anion exchange. Compared to PVBTA-Cl, PVBTA-TFSI shows new characteristic bands at 1346, 1176, 1132, and 1050 cm^{-1}, corresponding to SO_2 asymmetric stretching, CF_3 asymmetric stretching, SO_2 symmetric stretching, and S–N–S asymmetric stretching, respectively. These new peaks in the PVBTA-TFSI spectrum are attributed to TFSI anionic groups, demonstrating successful ion exchange.[57,58] X-ray diffraction (XRD) is utilized to measure if there is any crystalline phase from LiTFSI, as shown in Figure S3, Supporting Information. The XRD pattern of PVBTA-TFSI only shows a broad, amorphous peak at ≈20°, which indicates that the PVBTA-TFSI is an amorphous polymer without residual LiTFSI separated out.

The chemical stability between PVBTA-TFSI and the solid electrolyte Li_6PS_5Cl (LPSCl) is investigated by heating a mixture of LPSCl and PVBTA-TFSI at 80 °C in a vacuum chamber for 24 h. Then the samples are examined by XRD and Fourier-transform infrared spectroscopy (FT-IR) measurements, as shown in Figure S4a,b, Supporting Information. The results indicate that PVBTA-TFSI is chemically stable with LPSCl, as the spectra are identical before and after heating. Electrochemical stability between PVBTA-TFSI and LPSCl is assessed via cyclic voltammetry, scanning from 0 to 4 V (vs Li^+/Li-In) using a composite of vapor grown carbon fibers (VGCF) and LPSCl as the working electrode and a Li-In-alloy reference and counter electrode, as shown in Figure S5, Supporting Information. By comparing current densities between pristine and PVBTA-TFSI coated VGCF, the PVBTA-TFSI is found to have lower current density, confirming PVBTA-TFSI is electrochemical stable with LPSCl. Furthermore, the thermal stability of PVBTA-TFSI is measured by thermogravimetric analysis (TGA), as shown in Figure S6, Supporting Information. The PVBTA-TFSI decomposition temperature is ≈365 °C, and most of the decomposition happens ≈400 to 600 °C. This is much higher than the temperature applied for spray coating of NCM. The high glass transition temperature (T_g) of PVBTA-TFSI (74 °C) prevents softening of the polymer during cell operation, which may otherwise alter the coating layer morphology or cause deformation.[57] In addition, the TFSI counterion increases the solubility of the polymer in acetone, which is the solvent used for spray coating, and may also help with lithium ion conduction across the coating layer, the exact mechanism of which remains unclear so far.

The microstructure of the PVBTA-TFSI coated NCM is investigated using scanning electron microscopy (SEM), as shown in Figure S7, Supporting Information. The energy selective backscattered detector and energy dispersive X-ray (EDX) detector show that 5 wt% of PVBTA-TFSI coated on NCM (5P-NCM) has some polymer particles on the surface, which can be seen distinctly in Figure S7b,c , Supporting Information. However, the 1 wt% coated NCM (1P-NCM) shows almost no polymer particles, indicating that the content of polymer needs to be sufficiently low to avoid the formation and deposition of PVBTA-TFSI particles and ensure uniform deposition of PVBTA-TFSI on NCM. EDX analyses after focused ion beam (FIB)-cutting of coated and pristine NCM are shown in Figure S8, Supporting Information. As the fluorine signal overlaps with cobalt and the nitrogen signal is too weak to be seen even for 5P-NCM, carbon and sulfur are chosen to characterize the polymer coating. The EDX results show that the 1P-NCM has the most homogeneous coating.

The specific surface area of coated and pristine NCM is evaluated using the Brunauer–Emmett–Teller (BET) method. Pristine NCM, 1P-NCM, and 5P-NCM have a surface area of 0.593, 0.412, and 0.291 $m^2\ g^{-1}$, respectively. Although SEM can hardly tell the difference in particle aggregation between pristine and PVBTA-TFSI coated NCM, the BET measurement demonstrates that the surface area decreases with the polymer coating, which may be because the polymer decreases the surface roughness.

Transmission electron microscopy (TEM) is conducted in the bright field mode using an objective aperture to enhance the contrast between the coating layer and the NCM particles. The obtained TEM images confirm that a homogenous coating layer uniformly covers all observed particles, as shown in **Figure 2**a–c. The 1P-NCM has a uniform coating of ≈4–6 nm in total, while the 5P-NCM has a much thicker coating layer of ≈10 nm in total. Moreover, some places of 5P-NCM even show localized polymer aggregation with a thickness of 40–100 nm (Figure S9, Supporting Information), which matches with the SEM results in Figure S7b,c, Supporting Information. Unexpectedly, a 2–4 nm thick surface layer is also observed on the pristine NCM. However, this coating layer is thinner than the polymer coatings on the 1P-NCM and 5P-NCM. Therefore, 1P-NCM has the most uniform polymer coating of ≈2–4 nm thickness, and 5P-NCM has a polymer coating of ≈8 nm thickness with some polymer aggregation.

In order to characterize the coating composition and its distribution even more precisely, ToF-SIMS measurements are carried out as a technique with high surface sensitivity. To identify chemically the coating on the NCM particle structure, a pressed pellet of PVBTA-TFSI powder is measured as a reference material. Because of the collision cascade initiated by the highly energetic analysis, beam charged fragments such as CH_2OF^-, SNO^- and CF_3^- are formed during the ToF-SIMS measurement with a decent signal intensity (Figure 2d). As shown in Figure 2d, these fragments are also formed at the coated samples, confirming that the PVBTA-TFSI coating is present on the NCM particles. Interestingly, the intensities of the coating signals are higher for the 5P-NCM than for the 1P-NCM. This is in good agreement with the SEM and TEM results, which show that the 5P-NCM coating is thicker and more aggregated on the surface, resulting in higher signal intensity during ToF-SIMS measurements. In this context, it should be noted that due to the matrix effect[59] the intensities of the pristine PVBTA-TFSI polymer (reference material) cannot be compared with coated NCM samples.

In addition, the ToF-SIMS depth profiles in Figure S10, Supporting Information, show that the SNO^- signal decreases and the NiO_2^- signal increases faster for the 1P-NCM than for the 5P-NCM. This confirms that the 5 wt% coating is thicker than the 1 wt% coating. Moreover, ToF-SIMS images of the SNO^- signal (representing the polyelectrolyte coating) in Figure 2e validate that the coatings are distributed uniformly on the surface of the

ADVANCED SCIENCE NEWS
www.advancedsciencenews.com

ADVANCED ENERGY MATERIALS
www.advenergymat.de

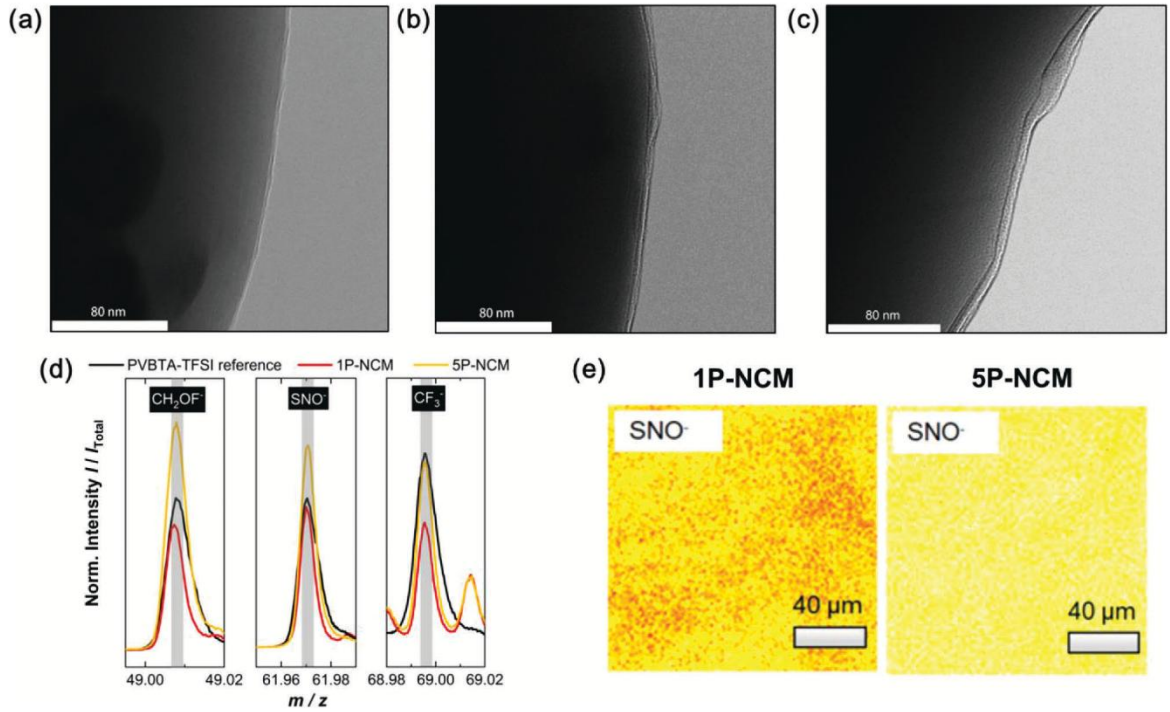

Figure 2. TEM images of a) pristine NCM, b) 1P-NCM, and c) 5P-NCM. These show that 1P-NCM has a 2–4 nm polymer coating layer covering the particles. However, 5P-NCM has a much thicker polymer coating layer of ≈8 nm. d) ToF-SIMS data of PVBTA-TFSI reference, 1P-NCM and 5P-NCM for CH_2OF^-, SNO^-, and CF_3^- fragments. e) ToF-SIMS mappings for the SNO^- fragment (representative of the polyelectrolyte coating) of 1P-NCM and 5P-NCM. ToF-SIMS evaluation confirms a homogenous PVBTA-TFSI coating on NCM.

NCM, which is consistent with the SEM and TEM results shown above.

In summary, taking the SEM, TEM, and ToF-SIMS results into account, the PVBTA-TFSI coating microstructure can be described as follows. The coating is distributed uniformly and covers the NCM particles. Furthermore, while the 1 wt% polymer coating is 2–4 nm thick, the 5 wt% polymer coating is thicker (8 nm) and has localized polymer aggregation with a thickness of 40–100 nm on the surface. Based on these analytical results, both coatings are expected to prevent direct physical contact between NCM and SE and stabilize the interface. The coating thickness of 1P-NCM matches with the best results of the poly(3,4-ethylenedioxythiophene) coating thickness (5 nm) on NCM published by Deng et al.[38]

2.2. Rate Capability Test

The performance of the coated NCMs is compared to that of the commercially obtained pristine NCM through rate capability and cycling stability tests in SSBs made of NCM, LPSCl and a lithium-indium alloy anode. Rate capability is investigated by running five cycles for each current density (0.1, 0.25, 0.5, and 1 C), as shown in **Figure 3**a. Initially, 1P-NCM and 5P-NCM do not perform better than pristine NCM. However, 5P-NCM and pristine NCM cells have similar performance at 0.5 and 1 C, but the capacity of 1P-NCM is 4% and 11.7% higher than pristine NCM at 0.5 and 1 C, respectively. The reasons that 1P-NCM exhibited better performance than the 5P-NCM and pristine NCM cells at 0.5 and 1 C might be due to the protection of polymer coating after several cycles or the effect of protection may be more pronounced at higher C-rates. Another possibility is that reduced crack formation of 1P-NCM, coupled with an optimal polymer content that does not cause insulation, leads to better performance at higher C-rates. However, the advantages conferred by the reduced crack formation are less pronounced at lower current density. Additionally, at the 25th cycle, the coated NCM shows better reversibility in the discharge process, as shown in Figure S11b, Supporting Information.

Figure 3b magnifies the galvanostatic charging profile from 2 to 3 V (vs Li^+/Li-In) in differential form for the first charge cycle. The area below 3 V in the dQ/dE diagram of pristine NCM is higher than that of 1P-NCM and 5P-NCM, respectively. This demonstrates that 5P-NCM and 1P-NCM have less electrochemical degradation at the NCM/SE interface than pristine NCM below 3 V, and this effect is the most significant in the first cycle.[60] However, the protective layer gives rise to a larger overpotential at ≈3 V (vs Li^+/Li-In) for the coated cells compared to the pristine cell in the first cycle, as shown in Figure S11a, Supporting Information. Overall, the 1P-NCM has the best performance compared to pristine NCM and 5P-NCM at 0.5 and 1 C. It is evident that the polymer coating reduces the electrochemical degradation below 3 V but increases the overpotential.

ADVANCED SCIENCE NEWS
www.advancedsciencenews.com

ADVANCED ENERGY MATERIALS
www.advenergymat.de

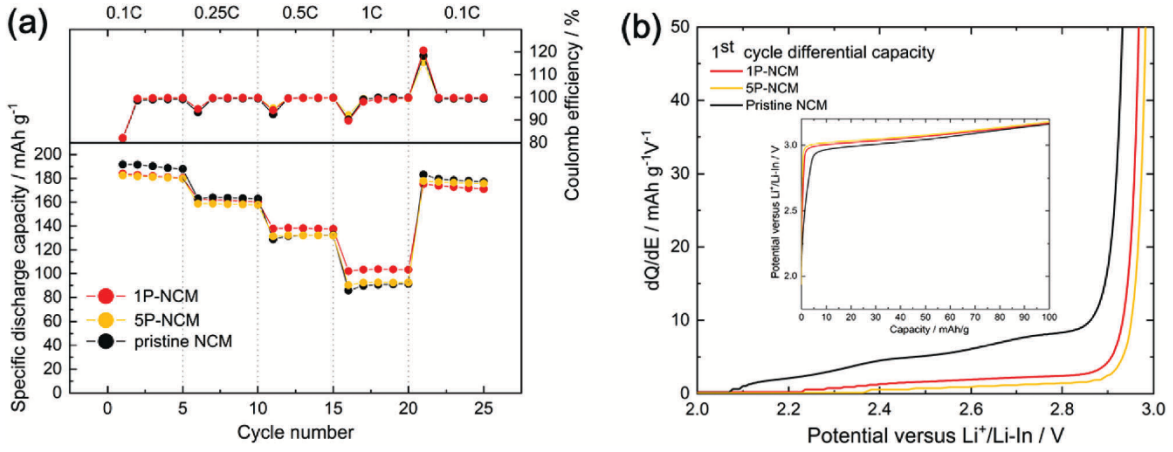

Figure 3. a) Rate capability tests of SSBs with lithium-indium alloy anode, LPSCl and pristine NCM, 1P-NCM, or 5P-NCM by testing different C-rates for 5 cycles each (0.1, 0.25, 0.5, 1, and then back to 0.1 C). The capacity under 0.5 and 1 C confirms the better rate capability for 1P-NCM. b) The differential capacity plot of the first cycle of the galvanostatic charging profile at 0.1 C is shown together with an enlargement from 2 to 3 V (vs Li^+/Li-In), and the inset shows the corresponding galvanostatic charging profiles. The lower differential capacity for 1P-NCM and 5P-NCM indicate less electrochemical degradation for coated NCM below 3 V (vs Li^+/Li-In).

2.3. Cycling Performance

In order to observe the influence of the PVBTA-TFSI coating layer on battery performance, 5P-NCM, 1P-NCM, and pristine NCM cells are galvanostatically cycled at 0.1 C (**Figure 4**a) and 0.25 C (Figure S12a, Supporting Information). At 0.1 C cycling (Figure 4a), the capacity retention of 1P-NCM is highest with 86% and that of 5P-NCM is about 75%. However, the capacity retention of pristine NCM is only ≈70%. This ranking is corroborated by the 0.25 C cycling performance (Figure S12a, Supporting Information). Therefore, 1P-NCM significantly improves the long-term cycling stability of NCM in SSBs with LPSCl.

The improved cycling performance of the SSBs with polyelectrolyte coated NCM can be caused by several reasons. For one, avoiding the electrochemically inactive interfacial layer between the active material and the electrolyte leads to higher active mass utilization of the cathode material.[8,61] Here, the active mass means the actual amount of active material utilized in the reaction. Interface decomposition between the active material and the electrolyte includes chemical,[4] electrochemical,[5–7] and chemo-mechanical degradation reactions.[5,8–13] This may form an electrochemically inactive interface, a high resistance interlayer and chemo-mechanical contraction,[62,63] all of which can cause a loss of contact between the NCM and the solid electrolyte, leading to increased cathode composite resistance ($R_{cathode}$).[64] For another, the improvement could be caused by preventing an increase of the lithium diffusion pathway.[8] Lithium diffusion pathway length may increase due to internal particle cracking,[14,15,17,19,65] contact loss, and interface decomposition as listed above.[8]

2.4. Contact Loss and Electrochemically Inactive Interfacial Layer

In this study, contact loss applies to both the formation of an electrochemically inactive interfacial layer and physical separation between the NCM and LPSCl electrodes. Both reduce the effective contact area of NCM/LPSCl during cycling, resulting in active mass loss and higher interface resistance. We summarize these two degradation mechanisms here using the term contact loss, as their influence on ion transport and cell performance is comparable and they are hard to distinguish experimentally. In order to quantify and analyze the extent of contact loss, the active mass and interfacial resistance in operating cells are measured during the cycling test. The impedance test is performed at 3.15 V (vs Li^+/Li-In) under the current of 0.1 C at specific cycles. The potential of 3.15 V (vs Li^+/Li-In) is chosen to ensure a sufficiently high lithium diffusion coefficient and lowest $R_{cathode}$ while avoiding significant degradation during the measurement. Moreover, the layered oxide cathode material impedance depends on the electrode's SOC, so it is necessary to measure the impedance at a fixed potential.[66]

Chronoamperometry is used right before electrochemical impedance spectroscopy (EIS) to ensure that the impedance can be measured at a sufficiently steady state. The cell voltage is stabilized at 3.15 V (vs Li^+/Li-In) until the current drops to less than 1%. This allows Li^+ diffusion within the NCM particles and dissipates the lithium concentration gradient within.[8,27,30] After crack formation in NCM particles, unlike liquid electrolytes, SEs cannot infiltrate these cracks. Therefore, while contact loss can change the interface resistance, the impact of particle crack formation is stronger on the lithium diffusion process within the NCM particles than on the charge transfer at the interface.[19]

Additionally, 2 h of relaxation time is used to record the open circuit potential (V_{OC}) after every charging and discharging process to calculate the active mass.[8] Briefly, a cell made of NCM cathode and lithium-indium alloy anode with a fixed potential has an equilibrium V_{OC} The V_{OC} follows a well-defined function versus SOC representing lithium content (x in $Li_xNi_{0.83}Mn_{0.06}Co_{0.11}O_2$) of NCM. Using the reference data of the V_{OC} function with x in $Li_xNi_{0.83}Mn_{0.06}Co_{0.11}O_2$ (Figure S13, Supporting Information), the actual specific capacity (Q_{act}) can be determined by the difference in SOC after the charging and

ADVANCED SCIENCE NEWS
www.advancedsciencenews.com

ADVANCED ENERGY MATERIALS
www.advenergymat.de

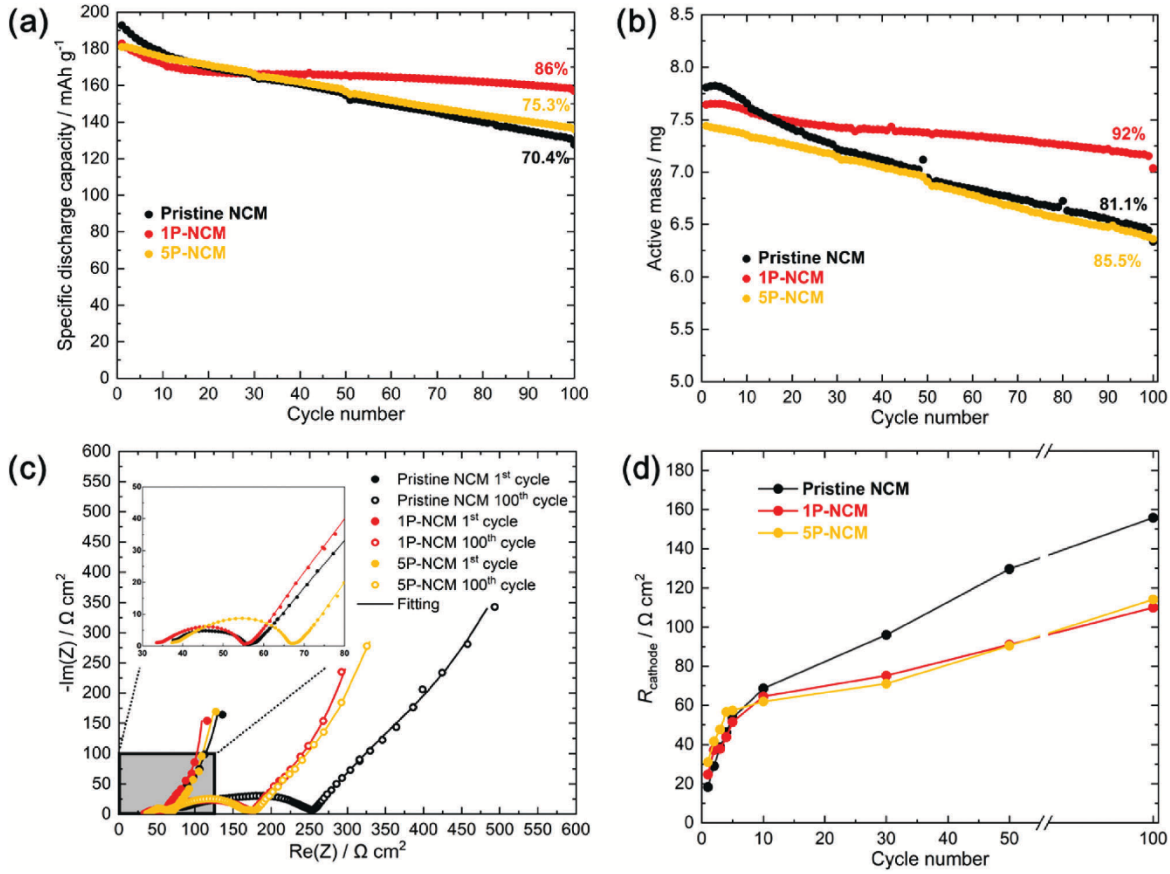

Figure 4. a) Long-term cycling capability of SSBs with lithium-indium alloy anode, LPSCl and pristine NCM, 1P-NCM, or 5P-NCM at 0.1 C, b) corresponding active mass evolution, c) Nyquist plot for first and 100th cycle, and d) $R_{cathode}$ versus cycles of polymer coated NCM and pristine NCM are compared. The impedance results and active mass calculations confirm that the polymer coating can effectively alleviate the contact loss and electrochemically inactive interfacial layer.

discharging process. Then the active mass (m_{act}) can be calculated by the measured discharge capacity (Q_{meas}) and Q_{act} in the following equation (Equation (1)).

$$m_{act} = \frac{Q_{meas}}{Q_{act}} \quad (1)$$

The m_{act} of PVBTA-TFSI coated NCM cells and pristine NCM cells of the 0.1 C cycling test are compared in Figure 4b. The actual mass of NCM in the electrodes is set to be 8.3 mg. Initially, 1P-NCM, 5P-NCM, and pristine NCM cells have a determined m_{act} of ≈7.6, 7.4, and 7.8 mg, respectively. This means that in the first cycle, the m_{act} for 1P-NCM and 5P-NCM is slightly less than for the pristine NCM due to polymer coating or polymer aggregation on NCM. However, after 100 cycles at 0.1 C, the retention of m_{act} of pristine, 1P-NCM, and 5P-NCM cells are ≈81%, 92%, and 86%, respectively. The better m_{act} retention for PVBTA-TFSI coated NCM cells during cycling is explained as the alleviation of contact loss caused by interface degradation. Nevertheless, 1P-NCM shows better m_{act} retention than 5P-NCM as the polymer coating layer of 5P-NCM is probably too thick, hindering charge transfer and electronic and ionic transport. Similar results can also be observed in the 0.25 C cycling test (Figure S12b, Supporting Information).

It is worth noting that the m_{act} of pristine and coated NCMs all show a close to linear decrease during cycling (Figure 4b). However, the capacity of pristine NCM and 1P-NCM has rapidly decayed in the beginning, and the capacity of 5P-NCM has a close to linear decay (Figure 4a). Therefore, it can be concluded that the rapid capacity decay for pristine NCM and 1P-NCM compared to 5P-NCM before the 30th cycle may be due to more severe mechanical degradation, such as particle cracking. In the early stages (≈30th cycles), 5P-NCM exhibits slower capacity degradation than pristine NCM and 1P-NCM. This improvement is attributed to the cohesive influence of the 5 wt% polymer coating, which effectively stabilizes the electrode. However, too much polymer content increases the lithium diffusion pathway length, reducing the capacity to less than 1P-NCM after 100 cycles. On the other hand, the m_{act} results are not as affected by the particle cracking within the NCM, but are more affected by the

ADVANCED SCIENCE NEWS
www.advancedsciencenews.com

ADVANCED ENERGY MATERIALS
www.advenergymat.de

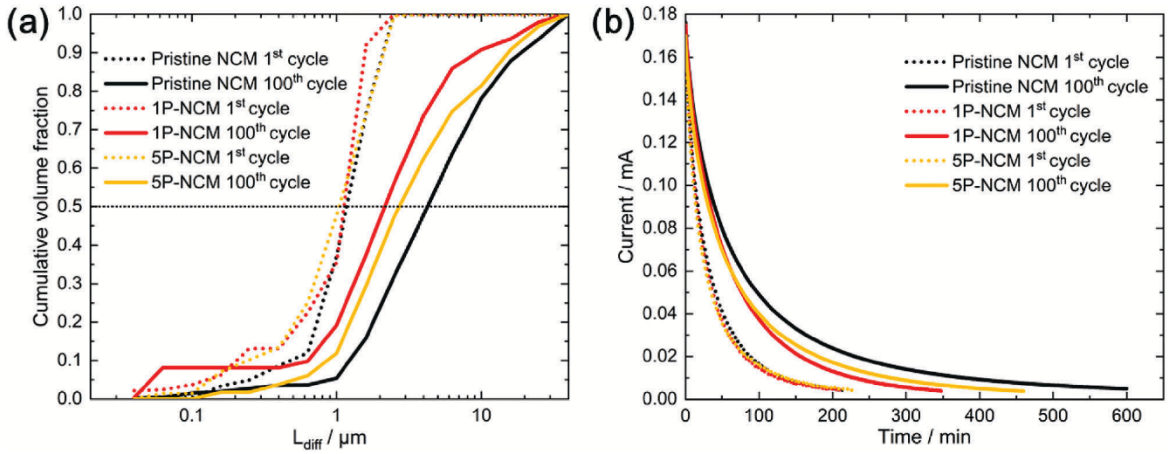

Figure 5. a) Evolution of the lithium diffusion pathway length (L_{diff}) estimated using the EIS-PSD model. The EIS-PSD model fits the Warburg impedance to obtain the cumulative volume fraction of particle sizes, representing lithium diffusion pathway length. b) The chronoamperometry measurement shows the time it takes for the current to drop to less than 1% of charging current, which is indicative of the lithium diffusion pathway length. The results of the EIS-PSD model and chronoamperometry measurement demonstrate that the polymer coating can lessen the length increase of the lithium diffusion pathways during cycling.

contact loss and interface degradation, giving rise to a constant linear decay.

EIS measurements of 0.1 C are carried out during cycling, as shown in Figure 4c,d. The transition line model is used for fitting. Additionally, the transition line model and fitting results are described in Figure S14 and Table S1, Supporting Information, respectively.[67] The interface between the cathode and the solid electrolyte is an essential factor affecting cathode resistance ($R_{cathode}$), providing information on contact loss and interface degradation. The cathode composite resistance $R_{cathode}$ is expressed as the geometric mean of the value charge transfer resistance (R_{ct}) multiplied by the sum of the electronic resistance (R_{ele}) and ionic resistance of electrolyte in the cathode composite (R_{ion}) (see Figure S14, Supporting Information).[67]

In the first cycle at 3.15 V (vs Li^+/Li-In), a thicker polymer coating layer gives rise to a higher $R_{cathode}$ (pristine NCM: 18.3 Ω cm^2, 1P-NCM: 24.8 Ω cm^2, 5P-NCM: 31.1 Ω cm^2), matching the first cycle m_{act} results mentioned above, as a thicker polymer coating layer gives rise to lower m_{act}. Nonetheless, the $R_{cathode}$ of the pristine NCM cell increases more significantly after 100 cycles than that of 1P-NCM and 5P-NCM cells (pristine NCM: 155.8 Ω cm^2, 1P-NCM: 110.4 Ω cm^2, 5P-NCM: 114.2 Ω cm^2). Although $R_{cathode}$of pristine NCM shows a 1.4 times higher value than that of 5P-NCM after 100 cycles, the retention of the 5P-NCM is 5% more than that of pristine NCM, and the capacity is also higher (the capacity of 5P-NCM is ≈10 mAh g^{-1} more than that of pristine NCM). The significant increase in the $R_{cathode}$ of the pristine NCM cell may be caused by severe interface degradation. Additionally, 1P-NCM and 5P-NCM cells have similar $R_{cathode}$ after 100 cycles, indicating that 1 wt% of the polymer coating layer is sufficient to act as a protective layer for NCM.

However, although the $R_{cathode}$ of 5P-NCM and 1P-NCM are similar, the observed difference in discharge capacity is attributed to the high polymer content in 5P-NCM. This excess polymer increases the lithium diffusion pathway length (see **Figure 5**), reducing the capacity below 1P-NCM after 100 cycles. The EIS measurements for 0.25 C cycling cells (Figure S12c, Supporting Information) also show the same conclusion as the 0.1 C results. Overall, EIS measurements and m_{act} calculations indicate that the polymer coating can act as a protective layer, alleviating contact loss at the NCM/LPSCl interface.

2.5. Lithium Diffusion Pathways within the Cathode Composite

The loss of m_{act} causes an irreversible capacity fading that increases with the number of charge–discharge cycles. In addition, the lithium diffusion pathway length also affects capacity fade. The lithium diffusion pathway length within the cathode composite is expected to increase during cycling due to contact loss, interface degradation, and NCM particle cracking. Warburg impedance in EIS is fitted using the particle size distribution (EIS-PSD) model reported in our previous study to determine the length of the lithium diffusion pathway within the cathode composite.[8]

In general, the ideal finite-space Warburg impedance describes the diffusion throughout the sample volume, including the ion-blocking boundary at the current collector and the innermost center of the NCM particles. If the frequency is low enough to access the blocking boundary, the impedance shows a continuous transition from 45° to 90° in the Nyquist plot.[68] Consequently, to measure the finite-space Warburg impedance in EIS, the lower cut-off frequency is set to 100 µHz. The finite-space Warburg impedance element of cylindrical particles ($Z_{fs}^{cylindrical}$) is used to describe the complex geometry of Li^+ diffusion in the NCM by fitting the finite space diffusion tail of EIS coupled with the transition line model, as shown in Figure S14, Supporting Information.

$$\tau_i = L_{diff}^2 / \tilde{D}_{Li} \quad (2)$$

ADVANCED SCIENCE NEWS
www.advancedsciencenews.com

ADVANCED ENERGY MATERIALS
www.advenergymat.de

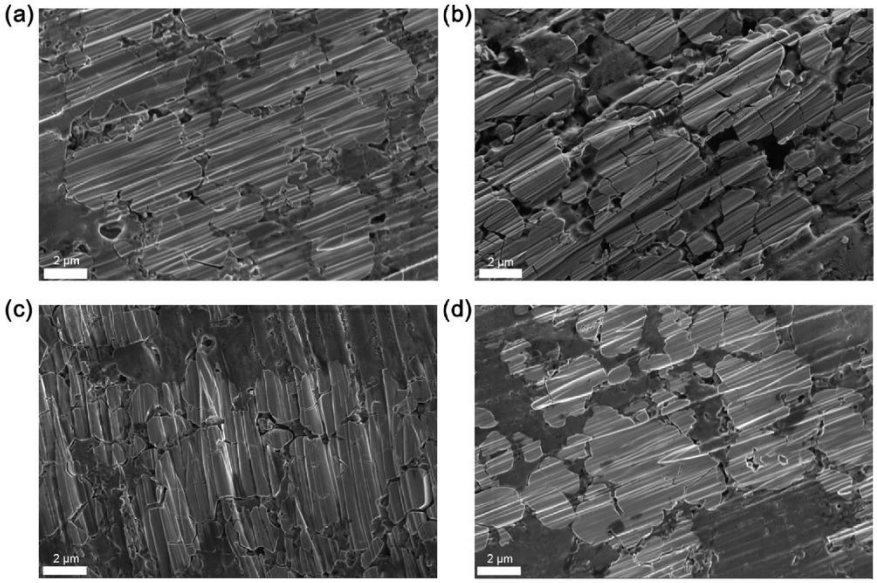

Figure 6. FIB-SEM images of cathode composites after 200 cycles at 0.25 C. Pristine NCM a) before and b) after cycling shows a big difference in NCM particle cracking. The cracking within the pristine NCM cathode happens severely after cycling. However, c) 1P-NCM and d) 5P-NCM cells after cycling show less cracking compared to pristine NCM after cycling.

and

$$Z_{\mathrm{fs}}^{\mathrm{cylindrical}} = \frac{1}{C_{\mathrm{diff}}} \left(\sum_i \frac{\Delta Q_i}{\tau_i} \frac{\sqrt{i\omega\tau_i}}{\coth \sqrt{i\omega\tau_i}} \right)$$

The $Z_{\mathrm{fs}}^{\mathrm{cylindrical}}$ is dependent on the characteristic time constant of lithium diffusion τ_i (Equation (2))[69] and the volume fraction of particle contribution ΔQ_i (Equation (3)).[8] C_{diff} is the total differential capacity of the entire electrode ($C_{\mathrm{diff}} = \partial Q/\partial E = 340\ \frac{mAh}{Vg}$), and calculated from the reference data at 3.15 V (vs Li^+/Li-In), which equals about 3.77 V (vs Li^+/Li), and $x = 0.6$ (Figure S13, Supporting Information). $\tilde{D}_{\mathrm{Li}}$ is the chemical diffusion coefficient of lithium and is assumed as 10^{-11} cm^2 S^{-1} at 25 °C, cited from our previous study and obtained by the fitting of the semi-finite part of the diffusion tail in EIS.[8] ω is the radial frequency. The thickness of the cylindrical particle (L_{diff}) in Equation (2) can be taken as the lithium diffusion pathway length. Therefore, if the lithium diffusion pathway length increases due to internal particle cracking, the finite-space Warburg impedance overestimates particle size.

Fitting of the impedance measurement yields L_{diff} values and the volume fractions (represented in a cumulative form) are shown in Figure 5a. It can be seen that L_{diff} of pristine NCM increases considerably (from ≈1.1 to 4.3 μm) compared to 1P-NCM (from ≈1.0 to 2.2 μm) and 5P-NCM (from ≈1.0 to 2.7 μm). This indicates that particle cracking is less severe for the PVBTA-TFSI coated NCM.

The results of chronoamperometry (Figure 5b) indicate the same conclusion. The time it takes for the current to drop to less than 1% of charging current is related to the lithium diffusion pathway length, that is, the longer the time, the longer the lithium diffusion pathway length.[70] Figure 5b shows that at the 100$^{\mathrm{th}}$ cycle of 0.1 C cycling, the pristine NCM cell needs 600 min. However, 5P-NCM and 1P-NCM cells need only 460 and 347 min, respectively. Additionally, chronoamperometry results for 0.25 C cycling give the same trends as for 0.1 C, as shown in Figure S15, Supporting Information.

Despite similar R_{cathode} values for 5P-NCM and 1P-NCM (refer to Figure 5), the discharge capacity difference after 100 cycles is due to the increased lithium diffusion pathway length, resulting in a reduced capacity for 5P-NCM compared to 1P-NCM. In addition, as the primary ion-conduction path occurs through interconnected LPSCl particles in the cathode composite, excess polymer may partially obstruct the lithium diffusion pathway.[71] Similar capacity degradation difference is also observed when increasing binder content to ≈4% in SSBs with NCM composite cathode and LPSCl electrolyte using ethyl cellulose as a binder.[72] Overall, the chronoamperometry and EIS-PSD calculation results indicate that after cycling the pristine NCM cell has a much longer lithium diffusion pathway length than the coated NCM cells.

2.6. Particle Cracking after Cycling

FIB-SEM is employed to observe the morphological change of the cross-section in the cathode composite after 200 cycles at 0.25 C, as shown in **Figure 6**. The pristine NCM cell shows more fracture lines within the particles than the 1P-NCM and 5P-NCM cells, and the 5P-NCM cells have the least cracking. One of the reasons for alleviating cracking may be due to the less lithium extracted from the NCM, especially for the second hexagonal phase to the third hexagonal phase (H2 + H3) transition during the charging

ADVANCED SCIENCE NEWS
www.advancedsciencenews.com

ADVANCED ENERGY MATERIALS
www.advenergymat.de

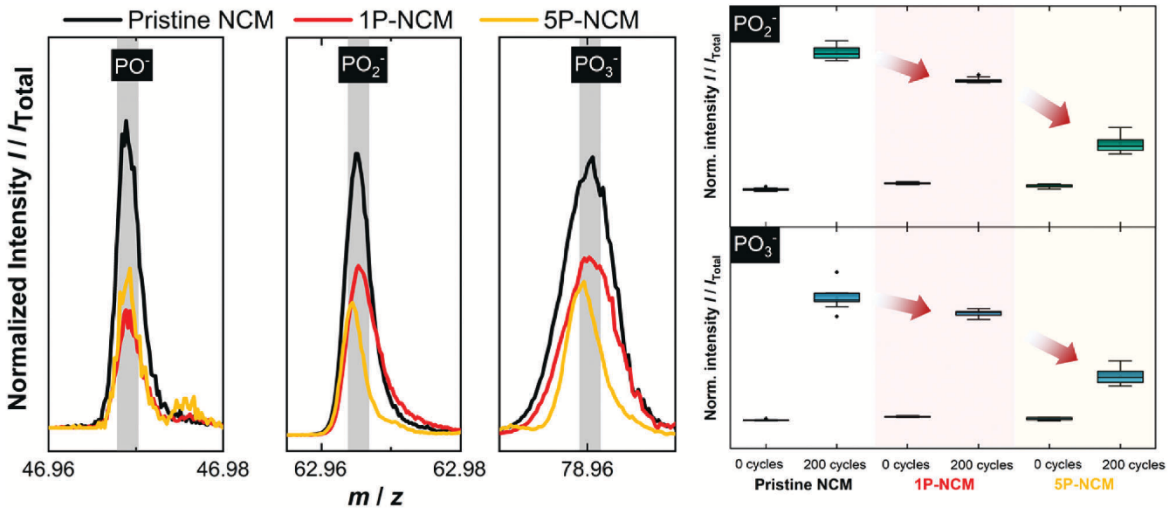

Figure 7. a) ToF-SIMS mass spectra for fragments that can be assigned to oxidative interfacial decomposition products such as PO^-, PO_2^-, and PO_3^- for pristine NCM, 1P-NCM, and 5P-NCM after 200 cycles. b) Corresponding boxplots of normalized intensities for PO_2^- and PO_3^- signals containing ten data points each. The 1P-NCM and 5P-NCM suppress the formation of oxidative decomposition products compared to the pristine NCM.

step, which has the most severe volume change.[73] However, the capacity (Figure S16, Supporting Information) and the area under the dQ/dE plot (Figure S11, Supporting Information) above 3.48 V (vs Li^+/Li-In), which is ≈4.1 V (vs Li^+/Li), is similar for both PVBTA-TFSI coated NCM cells and the pristine NCM cell in the first cycle charging step, indicating that all the NCM cells have similar H2+H3 phase transition processes. Moreover, as noted in section 2.5 (Figure 5), pristine NCM has the longest lithium diffusion pathway length, which is typically caused by particle cracking within the NCM, which matches with the low-angle FIB SEM results after cycling. It is likely that a thin coating with just a few nanometers is insufficient to inhibit fully the volume changes occurring in CAM materials. However, the NCM particle cracking may be alleviated because the polymer can reduce side reaction at the NCM/SE interface during cycling.[10]

2.7. Interfacial Stability after Cycling

ToF-SIMS analysis is carried out to identify decomposition products and to reveal the influence of the NCM coatings on degradation processes due to electrochemical cycling. In contrast to XPS, ToF-SIMS allows the detection of small amounts of interfacial decomposition products such as phosphates, which was demonstrated in detail by Walther et al.[11,23,74] In this work, we analyze composite cathodes with 1P-NCM and 5P-NCM and compare the results with data obtained for composite cathodes with pristine NCM.

In this context, the samples are analyzed before cycling and after 200 cycles, in line with the study by Walther et al.[23] As described by Walther et al., three different decomposition processes (current collector/solid electrolyte, carbon additive/solid electrolyte, NCM/solid electrolyte) must be considered. A good indication for oxidative decomposition processes of the solid electrolyte can be obtained by surface analysis of the composite cathode after removal of the stainless-steel current collector. Thereby, it should be mentioned that surface spectra lead to comparable results as depth profiling.

According to previous studies with ToF-SIMS, phosphate (PO_x^-) and sulfate/sulfite (SO_x^-) fragments are of particular interest to evaluate decomposition processes in thiophosphate-based composite cathodes due to electrochemical cycling.[11,23,74] However, since the PVBTA-TFSI coating in this work contains SO_2-groups, the analysis of sulfate/sulfite fragments may lead to misinterpretations. Thus, only phosphates are considered in the following analysis. In addition, a quantification of the degradation products is not possible with ToF-SIMS, since it is a semi-quantitative method (signal intensity is not only proportional to the concentration of the species). Thus, no y-axis values are shown in the images.[75]

A direct comparison of the mass spectra normalized to the total intensity after 0.25 C cycling (200 cycles) is exemplarily shown in **Figure 7**a. It can be seen that the amount of PO_x^- fragments, in particular PO^-, PO_2^-, and PO_3^-, is significantly higher for the uncoated sample than for the coated samples, which indicates that the 1 wt% and 5 wt% PVBTA-TFSI coatings suppress the formation of phosphates. Accordingly, the decomposition of the thiophosphate-based solid electrolyte is inhibited by the protective function of the PVBTA-TFSI coating since the direct physical contact between NCM and solid electrolyte is reduced. Furthermore, it can be seen that the amount of PO_2^- and PO_3^- fragments is higher for the 1P-NCM than for 5P-NCM. This indicates that the thicker 5 wt% coating is more effective in suppressing the decomposition of the solid electrolyte than the thinner 1 wt% coating. However, it can be seen that this trend is not valid for the PO^- signal, which could be due to mass interferences with the CCl^- signal that is already present in the composite cathode before cycling.

To ensure sufficient statistical sampling and reliability of the results, 10 mass spectra per sample were measured before and

ADVANCED SCIENCE NEWS
www.advancedsciencenews.com

ADVANCED ENERGY MATERIALS
www.advenergymat.de

after cycling. These are plotted in boxplots to semi-quantitatively compare normalized fragment intensities for the PO_2^- and PO_3^- fragments (see Figure 7b). It can be seen that the trend of having less decomposition products in the composite cathodes with coated NCM is confirmed. However, oxidative decomposition products can still be detected, which may form at the unprotected interface between the carbon additives and the solid electrolyte.

Overall, the comparison of oxidative decomposition products by ToF-SIMS confirms that PVBTA-TFSI coating significantly improves the interfacial stability at the NCM/SE interface in comparison to pristine, uncoated NCM. This supports the electrochemical data shown above. The present study demonstrates that polymers can act as suitable coating on NCM for use in solid-state batteries. Nevertheless, further investigation into the property-performance relationship is required, particularly regarding the significance of the polymer functional groups, charge and chemical nature of the counterion. Such dedicated investigations are expected to provide deeper insight into the structure-property relationship of polymer coatings in the near future.

3. Conclusion

This study presents a new approach to improve the cycling stability in SSB cathodes using an exceptionally thin cationic polymer coating on NCM. The PVBTA-TFSI polymer is synthesized by free-radical polymerization and ion exchange. It is applied as a coating on NCM by spray drying. TEM and ToF-SIMS measurements show that the spray drying method affords a uniform and thin polymer coating of only 2 nm to 4 nm thickness around the NCM particles by adding ≈1 wt% of polymer. The PVBTA-TFSI coated NCM exhibits better capacity retention and better active mass retention than the corresponding SSB cells with pristine NCM. In addition, the increase of the lithium diffusion pathway length during cycling is mitigated by the polymer coating, which is confirmed by chronoamperometry and EIS-PSD fitting. FIB-SEM after cycling shows that the polymer coating reduces the extent of particle cracking within NCM. Thus, the presented polymer coating mitigates several typical degradation mechanisms in Li_6PS_5Cl-based SSB cathodes.

4. Experimental Section

Reagents and Materials: (Vinylbenzyl)trimethylammonium chloride (VBTA-Cl) monomer, reagent grade sodium persulfate ($Na_2S_2O_8$) initiator, lithium bis(trifluoromethanesulfonyl)imide (LiTFSI), and vapor-grown carbon fibers (VGCF) were purchased from Sigma-Aldrich. Single crystal high-nickel $LiNi_{0.83}Co_{0.11}Mn_{0.06}O_2$ (NCM) was purchased from MSE Supplies (particle size ≈3–5 µm, and BET specific surface area ≈0.5–0.9 $m^2\ g^{-1}$). Li_6PS_5Cl (LPSCl) was purchased from NEI Corporation. Indium foil was purchased from chemPUR GmbH with 100 µm thickness and punched into a circular electrode of 9 mm in diameter. Lithium foil was purchased from Albemarle Rockwood Lithium GmbH with 125 µm thickness and punched into a circular electrode of 6 mm in diameter.

Synthesis of PVBTA-TFSI: Poly((4-vinylbenzyl)trimethylammonium bis(trifluoromethanesulfonylimide)) was synthesized through the route shown in Figure 1. First, free radical polymerization was conducted by mixing 5 g VBTA-Cl and 0.3 mL of saturated $Na_2S_2O_8$ solution in 20 mL of deionized water and then heated up and purged with N_2 flow at 75 °C for 48 h (molar ratio of VBTA-Cl:$Na_2S_2O_8$ = 1:0.3). After polymerization, PVBTA-Cl was purified by dialysis with a considerable amount of deionized water and further condensed by a rotary evaporator.

The condensed polymer solution was then added dropwise to the LiTFSI solution (7.5 g of LiTFSI dissolved in 20 g of deionized water) and stirred overnight for ion exchange. Once the PVBTA-Cl drops into the LiTFSI solution, the PVBTA-TFSI precipitates immediately. After ion exchange, PVBTA-TFSI was washed with deionized water by centrifuge three times to remove residual salts. Thereafter, PVBTA-TFSI was dried in a vacuum oven at 80 °C for 72 h and stored in the glove box.

^{1}H NMR (400 MHz, deuterated acetone): δ 1.36–1.99 (H1, H2), δ 2.05 (acetone-d6), δ 3.14 (H6), δ 4.4–4.9 (H5), and δ 6.5–7.4 (H3, H4). FT-IR of PVBTA-TFSI (cm^{-1}): 973 (C–N stretching), 1346, 1326, 1176, 1132, 1050 ($TFSI^-$), 1612, 1480, 1422 (aromatic C=C stretching), and 3043, 2922, 2852 (alkyl C–H stretching), 3400 (H_2O). FT-IR of PVBTA-Cl (cm^{-1}): 973 (C–N stretching), 1612, 1480, 1422 (aromatic C=C stretching), and 3015, 2922, 2852 (alkyl C–H stretching), 3400 (H_2O). FT-IR of LiTFSI (cm^{-1}): 1327 (SO_2 asymmetric stretching), 1245 (CF_3 symmetric stretching), 1204 (CF_3 asymmetric stretching), 1147 (SO_2 symmetric stretching), and 1065 (asymmetric S_2N stretching).

PVBTA-TFSI Coated NCM and PVBTA-TFSI Coated Vapor Grown Carbon Fibers: For PVBTA-TFSI coated NCM, Mini Spray Dryer B-290 from BUCHI was used to coat PVBTA-TFSI on NCM, as shown in Figure 1. 0.1 g (5 wt% with respect to NCM) or 0.02 g (1 wt% with respect to NCM) of polymer was mixed with 2 g of NCM and 30 g of acetone as the precursor suspension. The mixing step was conducted by vigorous stirring and takes 1 h to make sure the particle aggregation was broken into a smaller size. The inlet temperature was 150 °C, the volume flow (i.e., suction of vacuum pump) was 37 $m^3\ h^{-1}$, the feed rate of polymer solution was 8 mL min^{-1}, and the N_2 flow was 40 L min^{-1}. The spray drying condition was optimized to get the highest productivity of ≈50–70 wt%. Additionally, the 5 wt% PVBTA-TFSI coated NCM and 1 wt% PVBTA-TFSI coated NCM were noted as 5P-NCM and 1P-NCM, respectively, based on the NCM-polymer ratio of the precursor suspension. Finally, coated NCM was dried in vacuum at 80 °C for 48 h.

For PVBTA-TFSI coated VGCF, a precursor was prepared by dissolving 20 mg of PVBTA-TFSI polymer in 40 mL acetone. To create a carbon composite, 100 mg of VGCF was sonicated in 20 mL of acetone and then added dropwise to the PVBTA-TFSI polymer solution. The resulting dispersion was then ultrasonicated for 30 min and stirred overnight at room temperature to achieve a homogeneous solution. Next, the coated VGCF was vacuum filtered, washed with 20 mL of acetone, and dried in a vacuum oven at 80 °C.

X-Ray Diffraction: XRD was used to characterize PVBTA-TFSI and check the chemical stability between PVBTA-TFSI or LiTFSI and LPSCl by using Panalytical Empyrean XRD with Cu Kα radiation. Diffraction patterns were collected in a 2θ angular range from 10° to 85° with a step size of 0.026°, 0.04 rad. soller slits, and 1/2° anti-scatter slit. To check the chemical stability between PVBTA-TFSI or LiTFSI with LPSCl, PVBTA-TFSI or LiTFSI were mixed with LPSCl in a weight ratio of 1:1 (≈500 mg in total) by grinding in an agate mortar and then pressed into pellets (8 mm in diameter). After that, the pellets were heated and maintained at 80 °C for 24 h, followed by a grinding process in the agate mortar to turn pellets into powder. Finally, the powder after heating was characterized by XRD.

Thermogravimetric Analysis: TGA measurements were conducted with ≈20 mg of samples by STA 409 PC (Netzsch-Gerätebau GmbH) at the temperature ranging from 25 to 1000 °C, under air with a heating rate of 10 °C min^{-1}.

^{1}H Nuclear Magnetic Resonance: Bruker Avance II recorded the ^{1}H NMR spectra of PVBTA-TFSI at 400 MHz in deuterated acetone. The chemical shifts were recorded by parts per million (ppm). Tetramethylsilane was used as the internal reference for analysis.

Fourier-Transform Infrared Spectroscopy: FT-IR spectra of PVBTA-TFSI, PVBTA-Cl, and LiTFSI were recorded with a total number of 96 scans on an ATR-FTIR Thermo Fischer Scientific iD5 ATR spectrometer (550–4000 cm^{-1}). To check the chemical stability between PVBTA-TFSI or LiTFSI with LPSCl, PVBTA-TFSI or LiTFSI was mixed with LPSCl in the agate mortar and then pressed to pellets. Subsequently, the pellets were heated and

ADVANCED SCIENCE NEWS
www.advancedsciencenews.com

ADVANCED ENERGY MATERIALS
www.advenergymat.de

maintained at 80 °C for 24 h. FT-IR spectra were measured in pellet form before and after the heating process.

Brunauer–Emmett–Teller Analysis: Specific surface area calculations of PVBTA-TFSI coated and pristine NCMs were measured by the BET method. Before measurements, the samples were evacuated at 120 °C for 12 h in standard glass tubes. BET measurements were performed at an automated gas adsorption station (Autosorb-1-MP, Quantachrome Instruments) at 77 K maintained by liquid nitrogen in standard cryostats.

Scanning Electron Microscopy: SEM (Merlin, Zeiss) at an accelerating voltage of 3 kV and accelerating current of 200 pA was adopted to characterize the morphology of NCMs. Back-scattered electron images and secondary electron images were recorded. For sample preparation, polymer coatings and pristine NCMs were measured in powder form, sticking tightly on the conductive carbon tape.

Focused-Ion Beam Scanning Electron Microscopy: The cross-section of coated and pristine NCM powders and cathode composite pellets were analyzed using a XEIA Xe-plasma FIB (TESCAN). For sample preparation, FIB craters were milled in a low-angle condition with a 1 nA Xe-ion beam without any polished step under −135 °C maintained by liquid nitrogen. After that, back-scattered electron images and secondary electron images were recorded at an acceleration voltage of 3 kV and acceleration current of 200 pA.

Energy-Dispersive X-Ray Spectroscopy: After SEM or FIB-SEM measurements, energy-dispersive X-ray spectroscopy (X-Max-Extreme detector, Oxford Instruments) was adopted to characterize the coating layer on NCM. However, to get signals that are more precise from EDX, the accelerating voltage and current were raised to 5 kV and 2 nA, respectively. Additionally, the working distance was controlled at 5.5–5.6 mm. Elements for EDX analysis: C, N, O, F, S, Mn, Co, Ni.

Transmission Electron Microscopy: As the polymer is mainly made of the light element carbon, whereas NCM consisted of heavier transition metals, the materials exhibited a different contrast in TEM bright field images. These images were recorded with a TVIPS TEMCam XF416FS camera on a JEOL JEM-3010 microscope at 300 kV acceleration voltage. For this purpose, powder of uncoated or coated NCM particles was sprinkled on a holey carbon copper TEM grid. Loose powder was removed by evacuating the TEM holder in a pumping stand before transferring it to the TEM to preserve the TEM vacuum.

Time-Of-Flight Secondary Ion Mass Spectrometry: ToF-SIMS was performed using a M6 Hybrid SIMS (IONTOF GmbH) equipped with a 30 kV Bi-cluster primary ion gun for analysis and a 20 kV argon gas cluster source (GCIB) for depth profiling. The GCIB was highly suitable for organic-inorganic composite materials.[76,77] Charged fragments were obtained as a result of a collision cascade caused by the impact of the high-energy primary ion beam during ToF-SIMS measurements. All samples were prepared in a glovebox, attached to the sample holder using non-conductive adhesive tape and transferred to the SIMS instrument using the LEICA EM VCT500 shuttle (Leica Microsystems). Pristine and coated NCM materials were investigated. Furthermore, pristine (before cycling) and cycled (after cycling) composite cathodes were compared with uncoated and coated NCM after removal of the stainless-steel current collector. To ensure comparability, all samples were prepared in the same way and under the same conditions. For analysis, the instrument is operated in the spectrometry mode using Bi_3^+ as primary ions (0.60 pA) in the negative mode, which provides high mass resolution (full width at half maximum $m/\Delta m$ > 15 000 @ m/z = 62.97 (PO_2^-)). The analysis area was set to 100 × 100 µm^2, which was rasterized with 128 × 128 pixels and a primary ion dose of 1.0×10^{12} ions cm^{-2}. To ensure sufficient statistical sampling and reliability of the results, 10 mass spectra were measured per sample. For sputtering, Ar_{1500}^+ clusters were used (5 kV, 5 nA, 300 × 300 µm^2). The interlaced sputter mode was done with 3 s sputtering followed by scanning the 150 × 150 µm^2 field with 128 × 128 pixels. The evaluation of the ToF-SIMS data was performed with the software SurfaceLab 7.2 (IONTOF GmbH).

Electrode Composite and Cell Assembly: All of the cell tests were performed with a pellet-type cell casing inside an argon-filled glovebox (LabMaster, MBraun, Garching, Germany, <0.1 ppm of O_2, <0.1 ppm of H_2O). Asymmetric cells for electrochemical analysis except cyclic voltammetry were prepared: InLi | LPSCl | LPSCl, VGCF, NCM. First, 80 mg of LPSCl as a separator were pressed into a pellet within the peek cylinder insulator. Next, the cathode composite was made by mixing 70 wt% of pristine or coated NCM, 30 wt% of LPSCl, and an additional 1 wt% of VGCF in an agate mortar for ≈20 min. Then 12 mg of cathode composite was pressed on one side of the electrolyte. Finally, indium (100 µm thickness and 9 mm in diameter) and lithium foils (125 µm thickness and 6 mm in diameter) were pressed on the other side as the anode. After cell assembly, the whole stack of the cell was pressed under 30 kN for 3 min, resulting in ≈400 µm solid electrolyte with ≈30 µm cathode composite. Before electrochemical analysis, the whole cell was placed in an external aluminum framework (≈50 MPa). Details of the cell assembly were also depicted as a cross-section figure shown in Figure S17, Supporting Information.

For cyclic voltammetry, asymmetric cells of the following setup were prepared: InLi | LPSCl | LPSCl, carbon fibers. To prepare 100 mg of cathode composite, 9.09 mg of VGCF is added to 90.90 mg LPSCl, and mortared for 15 min. To prepare the cell for analysis, 80 mg of LPSCl were pressed into a pellet as a separator within the PEEK cylinder insulator. 30 mg of LPSCl-carbon fiber composite was pressed on one side of the electrolyte. Finally, indium (100 µm thickness and 9 mm in diameter) and lithium foils (125 µm thickness and 6 mm in diameter) were pressed on the other side as the anode. After cell assembly, the whole stack of the cell was pressed under 30 kN for 3 min. Before electrochemical analysis, the whole cell was placed in an external aluminum framework (≈50 MPa).

Electrochemical Analysis: Batteries were charged and discharged within the voltage window between 2.0 and 3.7 V (vs Li^+/Li-In) at 25 °C for cycling stability, chronoamperometry, and EIS. The cycling stability was performed at MACCOR electrochemical workstation. Additionally, EIS and chronoamperometry were conducted by VMP-300 (BioLogic) electrochemical workstation. The whole procedure was also shown in Figure S18, Supporting Information. The cycling test adopts two different currents, 0.1 and 0.25 C, however, the EIS measurements were conducted at 0.1 C. Initially, batteries were charged to 3.15 V (vs Li^+/Li-In), and then chronoamperometry was maintained at 3.15 V (vs Li^+/Li-In) until the current drops to less than 1% of charging current. After that, EIS was measured right after chronoamperometry at 3.15 V (vs Li^+/Li-In) from 1 MHz to 100 µHz. The sinusoidal amplitudes of EIS were applied as 10 mV for 1 MHz to 10 mHz; 5 mV for 10 mHz to 1 mHz; and 3 mV for 1 mHz to 100 µHz. The 0.25 C cycle stability runs 200 cycles, and the impedance was measured at the first, second, 53rd, 104th, 155th, and 206th cycles under 0.1 C at 3.15 V, as shown in Figure S12, Supporting Information. The 0.1 C cycle stability runs for 100 cycles, and the impedance is measured at first to fifth, 10th, 30th, 50th, and 100th cycles under 0.1 C at 3.15 V, as shown in Figure 4. The fitting of the impedance data follows the previous study by using the model as shown in Figure S14, Supporting Information. The low-frequency part was fitted by the finite-space Warburg impedance (Z_{fs}).[8]

Cyclic voltammetry experiments were conducted with a VMP-300 Biologic potentiostat at 25 °C. Before the measurement, the cells were maintained at open circuit voltage for 3 h. The cyclic voltammetry measurements used a two-electrode configuration with the anode acting as the reference electrode. First, the voltage sweep was initiated from open circuit voltage to 4 V versus the reference electrode at a scan rate of 1 mV s^{-1} for the oxidative sweep, and then the sweep was reversed until 0 V before returning to the starting potential.

Supporting Information

Supporting Information is available from the Wiley Online Library or from the author.

Acknowledgements

B.X.S., S.S., and F.H.R. acknowledge financial support from the German Federal Ministry of Education and Research (BMBF) for funding via the project FLiPS (03XP0261). Y.Y., T.D., R.R., K.V., and A.H. thank the funding from the BMBF in the framework of the FestBatt cluster of competence

(03XP0433C, 03XP0433D). A.H. is very grateful for funding from the BMBF Professorinnenprogramm III. In addition, the authors are very grateful to Dr. Rafael Meinusch and Prof. Bernd Smarsly for their help with nitrogen physisorption and TGA measurements.

Open access funding enabled and organized by Projekt DEAL.

Conflict of Interest

The authors declare no conflict of interest.

Author Contributions

B.X.S. carried out the syntheses, electrochemical analyses and general materials characterization. Y.Y. performed the TOF-SIMS analysis and T.D. carried out the TEM experiments. S.S., R.R., K.V., A.H., and F.H.R. helped with the analysis and discussion of experimental data. B.X.S., S.S., and F.H.R. conceived the idea and prepared the manuscript. All authors participated in the analysis of the experimental results and contributed to the manuscript.

Data Availability Statement

The data that support the findings of this study are available from the corresponding author upon reasonable request.

Keywords

high-nickel ternary cathode materials, interface degradation, polyelectrolyte, polymer coating, solid electrolytes, solid-state batteries

Received: January 31, 2023
Revised: March 21, 2023
Published online: May 10, 2023

[1] J. Schnell, T. Günther, T. Knoche, C. Vieider, L. Köhler, A. Just, M. Keller, S. Passerini, G. Reinhart, *J. Power Sources* **2018**, *382*, 160.
[2] S. Randau, D. A. Weber, O. Kötz, R. Koerver, P. Braun, A. Weber, E. Ivers-Tiffée, T. Adermann, J. Kulisch, W. G. Zeier, F. H. Richter, J. Janek, *Nat. Energy* **2020**, *5*, 259.
[3] S. Dühnen, J. Betz, M. Kolek, R. Schmuch, M. Winter, T. Placke, *Small Methods* **2020**, *4*, 2000039.
[4] S.-K. Jung, H. Gwon, S.-S. Lee, H. Kim, J. C. Lee, J. G. Chung, S. Y. Park, Y. Aihara, D. Im, *J. Mater. Chem. A* **2019**, *7*, 22967.
[5] J. Auvergniot, A. Cassel, J.-B. Ledeuil, V. Viallet, V. Seznec, R. Dedryvère, *Chem. Mater.* **2017**, *29*, 3883.
[6] D. H. S. Tan, E. A. Wu, H. Nguyen, Z. Chen, M. A. T. Marple, J.-M. Doux, X. Wang, H. Yang, A. Banerjee, Y. S. Meng, *ACS Energy Lett.* **2019**, *4*, 2418.
[7] G. F. Dewald, S. Ohno, M. A. Kraft, R. Koerver, P. Till, N. M. Vargas-Barbosa, J. Janek, W. G. Zeier, *Chem. Mater.* **2019**, *31*, 8328.
[8] G. Conforto, R. Ruess, D. Schröder, E. Trevisanello, R. Fantin, F. H. Richter, J. Janek, *J. Electrochem. Soc.* **2021**, *168*, 070546.
[9] N. Y. Kim, T. Yim, J. H. Song, J.-S. Yu, Z. Lee, *J. Power Sources* **2016**, *307*, 641.
[10] H. Zhang, H. Liu, L. F. J. Piper, M. S. Whittingham, G. Zhou, *Chem. Rev.* **2022**, *122*, 5641.
[11] F. Walther, R. Koerver, T. Fuchs, S. Ohno, J. Sann, M. Rohnke, W. G. Zeier, J. Janek, *Chem. Mater.* **2019**, *31*, 3745.
[12] T.-T. Zuo, R. Rueß, R. Pan, F. Walther, M. Rohnke, S. Hori, R. Kanno, D. Schröder, J. Janek, *Nat. Commun.* **2021**, *12*, 6669.
[13] T. Bartsch, F. Strauss, T. Hatsukade, A. Schiele, A. Y. Kim, P. Hartmann, J. Janek, T. Brezesinski, *ACS Energy Lett.* **2018**, *3*, 2539.
[14] S. H. Jung, U.-H. Kim, J.-H. Kim, S. Jun, C. S. Yoon, Y. S. Jung, Y.-K. Sun, *Adv. Energy Mater.* **2020**, *10*, 1903360.
[15] J.-M. Lim, T. Hwang, D. Kim, M.-S. Park, K. Cho, M. Cho, *Sci. Rep.* **2017**, *7*, 39669.
[16] E. Trevisanello, R. Ruess, G. Conforto, F. H. Richter, J. Janek, *Adv. Energy Mater.* **2021**, *11*, 2003400.
[17] Y. Han, S. H. Jung, H. Kwak, S. Jun, H. H. Kwak, J. H. Lee, S.-T. Hong, Y. S. Jung, *Adv. Energy Mater.* **2021**, *11*, 2100126.
[18] H.-H. Ryu, B. Namkoong, J.-H. Kim, I. Belharouak, C. S. Yoon, Y.-K. Sun, *ACS Energy Lett.* **2021**, *6*, 2726.
[19] R. Ruess, S. Schweidler, H. Hemmelmann, G. Conforto, A. Bielefeld, D. A. Weber, J. Sann, M. T. Elm, J. Janek, *J. Electrochem. Soc.* **2020**, *167*, 100532.
[20] U. Nisar, N. Muralidharan, R. Essehli, R. Amin, I. Belharouak, *Energy Storage Mater.* **2021**, *38*, 309.
[21] D. Kitsche, Y. Tang, Y. Ma, D. Goonetilleke, J. Sann, F. Walther, M. Bianchini, J. Janek, T. Brezesinski, *ACS Appl. Energy Mater.* **2021**, *4*, 7338.
[22] Y. Lei, J. Ni, Z. Hu, Z. Wang, F. Gui, B. Li, P. Ming, C. Zhang, Y. Elias, D. Aurbach, Q. Xiao, *Adv. Energy Mater.* **2020**, *10*, 2002506.
[23] F. Walther, F. Strauss, X. Wu, B. Mogwitz, J. Hertle, J. Sann, M. Rohnke, T. Brezesinski, J. Janek, *Chem. Mater.* **2021**, *33*, 2110.
[24] A. Y. Kim, F. Strauss, T. Bartsch, J. H. Teo, T. Hatsukade, A. Mazilkin, J. Janek, P. Hartmann, T. Brezesinski, *Chem. Mater.* **2019**, *31*, 9664.
[25] Y.-J. Kim, R. Rajagopal, S. Kang, K.-S. Ryu, *Chem. Eng. J.* **2020**, *386*, 123975.
[26] D. Kitsche, F. Strauss, Y. Tang, N. Bartnick, A.-Y. Kim, Y. Ma, C. Kübel, J. Janek, T. Brezesinski, *Batteries Supercaps* **2022**, *5*, 202100397.
[27] R. S. Negi, Y. Yusim, R. Pan, S. Ahmed, K. Volz, R. Takata, F. Schmidt, A. Henss, M. T. Elm, *Adv. Mater. Interfaces* **2022**, *9*, 2101428.
[28] Y.-Q. Zhang, Y. Tian, Y. Xiao, L. J. Miara, Y. Aihara, T. Tsujimura, T. Shi, M. C. Scott, G. Ceder, *Adv. Energy Mater.* **2020**, *10*, 1903778.
[29] F. Strauss, J. H. Teo, J. Maibach, A. Y. Kim, A. Mazilkin, J. Janek, T. Brezesinski, *ACS Appl. Mater. Interfaces* **2020**, *12*, 57146.
[30] R. S. Negi, P. Minnmann, R. Pan, S. Ahmed, M. J. Herzog, K. Volz, R. Takata, F. Schmidt, J. Janek, M. T. Elm, *Chem. Mater.* **2021**, *33*, 6713.
[31] S. H. Jung, K. Oh, Y. J. Nam, D. Y. Oh, P. Brüner, K. Kang, Y. S. Jung, *Chem. Mater.* **2018**, *30*, 8190.
[32] E. A. Wu, C. Jo, D. H. S. Tan, M. Zhang, J.-M. Doux, Y.-T. Chen, G. Deysher, Y. S. Meng, *J. Electrochem. Soc.* **2020**, *167*, 130516.
[33] J. S. Kim, S. Jung, H. Kwak, Y. Han, S. Kim, J. Lim, Y. M. Lee, Y. S. Jung, *Energy Storage Mater.* **2023**, *55*, 193.
[34] S. Sen, E. Trevisanello, E. Niemöller, B.-X. Shi, F. J. Simon, F. H. Richter, *J. Mater. Chem. A* **2021**, *9*, 18701.
[35] Q. Gan, N. Qin, Y. Zhu, Z. Huang, F. Zhang, S. Gu, J. Xie, K. Zhang, L. Lu, Z. Lu, *ACS Appl. Mater. Interfaces* **2019**, *11*, 12594.
[36] S. P. Culver, R. Koerver, W. G. Zeier, J. Janek, *Adv. Energy Mater.* **2019**, *9*, 1900626.
[37] A. Sakuda, A. Hayashi, M. Tatsumisago, *Curr. Opin. Electrochem.* **2017**, *6*, 108.
[38] S. Deng, Y. Sun, X. Li, Z. Ren, J. Liang, K. Doyle-Davis, J. Liang, W. Li, M. N. Banis, Q. Sun, R. Li, Y. Hu, H. Huang, L. Zhang, S. Lu, J. Luo, X. Sun, *ACS Energy Lett.* **2020**, *5*, 1243.
[39] G.-L. Xu, Q. Liu, K. K. S. Lau, Y. Liu, X. Liu, H. Gao, X. Zhou, M. Zhuang, Y. Ren, J. Li, M. Shao, M. Ouyang, F. Pan, Z. Chen, K. Amine, G. Chen, *Nat. Energy* **2019**, *4*, 484.
[40] Y. Huang, J. Xia, G. Hu, Y. Cao, Z. Peng, J. Fan, Y. Tao, T. Li, Z. Zhang, Z. Xue, K. Du, *Electrochim. Acta* **2020**, *332*, 135505.
[41] Y. Cao, X. Qi, K. Hu, Y. Wang, Z. Gan, Y. Li, G. Hu, Z. Peng, K. Du, *ACS Appl. Mater. Interfaces* **2018**, *10*, 18270.
[42] E.-H. Lee, J.-H. Park, J.-H. Cho, S.-J. Cho, D. W. Kim, H. Dan, Y. Kang, S.-Y. Lee, *J. Power Sources* **2013**, *244*, 389.

[43] H. Wang, J. Lin, X. Zhang, L. Wang, J. Yang, E. Fan, F. Wu, R. Chen, L. Li, *ACS Appl. Energy Mater.* **2021**, *4*, 6205.
[44] Y.-S. Lee, W.-K. Shin, A. G. Kannan, S. M. Koo, D.-W. Kim, *ACS Appl. Mater. Interfaces* **2015**, *7*, 13944.
[45] S. H. Ju, I.-S. Kang, Y.-S. Lee, W.-K. Shin, S. Kim, K. Shin, D.-W. Kim, *ACS Appl. Mater. Interfaces* **2014**, *6*, 2546.
[46] A. Yiğitalp, A. Taşdemir, S. Alkan Gürsel, A. Yürüm, *Energy Storage* **2020**, *2*, e154.
[47] D. Becker, M. Börner, A. Friesen, S. Klein, U. Rodehorst, M. Diehl, M. Winter, T. Placke, R. Schmuch, *J. Electrochem. Soc.* **2020**, *167*, 060524.
[48] B. Li, G. Li, D. Zhang, J. Fan, D. Chen, Y. Ge, F. Lin, C. Zheng, L. Li, *ChemistrySelect* **2019**, *4*, 6354.
[49] S. Vauthier, M. Alvarez-Tirado, G. Guzmán-González, L. C. Tomé, S. Cotte, L. Castro, A. Guéguen, D. Mecerreyes, N. Casado, *Mater. Today Chem.* **2023**, *27*, 101293.
[50] T. A. Ha, H. Li, X. Wang, L. A. O'Dell, M. Forsyth, C. Pozo-Gonzalo, P. C. Howlett, *ACS Appl. Energy Mater.* **2021**, *4*, 434.
[51] N. G. Hoogeveen, C. W. Hoogendam, R. Tuinier, M. A. Cohen Stuart, *Int. J. Polym. Anal. Charact.* **1995**, *1*, 315.
[52] C. Willa, J. Yuan, M. Niederberger, D. Koziej, *Adv. Funct. Mater.* **2015**, *25*, 2537.
[53] B. B. Patel, J. K. Patel, S. Chakraborty, *Recent Pat. Drug Delivery Formulation* **2014**, *8*, 63.
[54] L. S. C. Wan, P. W. S. Heng, C. G. H. Chia, *Int. J. Pharm.* **1991**, *77*, 183.
[55] W. I. J. Kariuki, B. Freireich, R. M. Smith, M. Rhodes, K. P. Hapgood, *Chem. Eng. Sci.* **2013**, *92*, 134.
[56] Y. Zhou, Z. Hu, Y. Huang, Y. Wu, Z. Hong, *J. Alloys Compd.* **2021**, *888*, 161584.
[57] D. Nikolaeva, I. Azcune, E. Sheridan, M. Sandru, A. Genua, M. Tanczyk, M. Jaschik, K. Warmuzinski, J. C. Jansen, I. F. J. Vankelecom, *J. Mater. Chem. A* **2017**, *5*, 19808.
[58] M. Li, L. Wang, B. Yang, T. Du, Y. Zhang, *Electrochim. Acta* **2014**, *123*, 296.
[59] A. Priebe, T. Xie, G. Bürki, L. Pethö, J. Michler, *J. Anal. At. Spectrom.* **2020**, *35*, 1156.
[60] S. Randau, F. Walther, A. Neumann, Y. Schneider, R. S. Negi, B. Mogwitz, J. Sann, K. Becker-Steinberger, T. Danner, S. Hein, A. Latz, F. H. Richter, J. Janek, *Chem. Mater.* **2021**, *33*, 1380.
[61] K. J. Kim, M. Balaish, M. Wadaguchi, L. Kong, J. L. M. Rupp, *Adv. Energy Mater.* **2021**, *11*, 2002689.
[62] K. Ishidzu, Y. Oka, T. Nakamura, *Solid State Ionics* **2016**, *288*, 176.
[63] R. Koerver, W. Zhang, L. de Biasi, S. Schweidler, A. O. Kondrakov, S. Kolling, T. Brezesinski, P. Hartmann, W. G. Zeier, J. Janek, *Energy Environ. Sci.* **2018**, *11*, 2142.
[64] R. Koerver, I. Aygün, T. Leichtweiß, C. Dietrich, W. Zhang, J. O. Binder, P. Hartmann, W. G. Zeier, J. Janek, *Chem. Mater.* **2017**, *29*, 5574.
[65] P. Li, Y. Zhao, Y. Shen, S.-H. Bo, *J. Phys. Condens. Matter* **2020**, *2*, 022002.
[66] J. Zhang, C. Zheng, L. Li, Y. Xia, H. Huang, Y. Gan, C. Liang, X. He, X. Tao, W. Zhang, *Adv. Energy Mater.* **2020**, *10*, 1903311.
[67] I. Kochetkov, T.-T. Zuo, R. Ruess, B. Singh, L. Zhou, K. Kaup, J. Janek, L. Nazar, *Energy Environ. Sci.* **2022**, *15*, 3933.
[68] J. Song, M. Z. Bazant, *J. Electrochem. Soc.* **2012**, *160*, A15.
[69] M. Doyle, J. Newman, *J. Appl. Electrochem.* **1997**, *27*, 846.
[70] C. J. Wen, B. A. Boukamp, R. A. Huggins, W. Weppner, *J. Electrochem. Soc.* **1979**, *126*, 2258.
[71] S. Wang, X. Zhang, S. Liu, C. Xin, C. Xue, F. Richter, L. Li, L. Fan, Y. Lin, Y. Shen, J. Janek, C.-W. Nan, *J. Materiomics* **2020**, *6*, 70.
[72] J. Zhang, H. Zhong, C. Zheng, Y. Xia, C. Liang, H. Huang, Y. Gan, X. Tao, W. Zhang, *J. Power Sources* **2018**, *391*, 73.
[73] H. Li, A. Liu, N. Zhang, Y. Wang, S. Yin, H. Wu, J. R. Dahn, *Chem. Mater.* **2019**, *31*, 7574.
[74] F. Walther, S. Randau, Y. Schneider, J. Sann, M. Rohnke, F. H. Richter, W. G. Zeier, J. Janek, *Chem. Mater.* **2020**, *32*, 6123.
[75] J. C. Vickerman, *Molecular Surface Mass Spectrometry by SIMS*, Wiley, New Jersey, USA **2009**.
[76] D. Rading, R. Moellers, H.-G. Cramer, E. Niehuis, *Surf. Interface Anal.* **2013**, *45*, 171.
[77] S. Rabbani, A. M. Barber, J. S. Fletcher, N. P. Lockyer, J. C. Vickerman, *Anal. Chem.* **2011**, *83*, 3793.

ADVANCED ENERGY MATERIALS

Supporting Information

for *Adv. Energy Mater.*, DOI 10.1002/aenm.202300310

Mitigating Contact Loss in Li_6PS_5Cl-Based Solid-State Batteries Using a Thin Cationic Polymer Coating on NCM

*Bing-Xuan Shi, Yuriy Yusim, Sudeshna Sen, Thomas Demuth, Raffael Ruess, Kerstin Volz, Anja Henss and Felix H. Richter**

Supporting information

Mitigating contact loss in Li_6PS_5Cl-based solid-state batteries using a thin cationic polymer coating on NCM

Bing-Xuan Shi,[a] Yuriy Yusim,[a] Sudeshna Sen,[a,b] Thomas Demuth,[c] Raffael Ruess,[a] Kerstin Volz,[c] Anja Henss,[a] Felix H. Richter*[a]

[a] Institute of Physical Chemistry & Center for Materials Research (LaMa), Justus Liebig University Giessen, Heinrich-Buff-Ring 17, 35392 Giessen, Germany

[b] Present address: WMG, University of Warwick, Coventry, CV4 7AL, United Kingdom

[c] Department of Physics & Materials Sciences Center (WZMW), Philipps-University Marburg, Hans-Meerwein Straße 6, 35032 Marburg, Germany.

* Corresponding author, Felix.H.Richter@pc.jlug.de

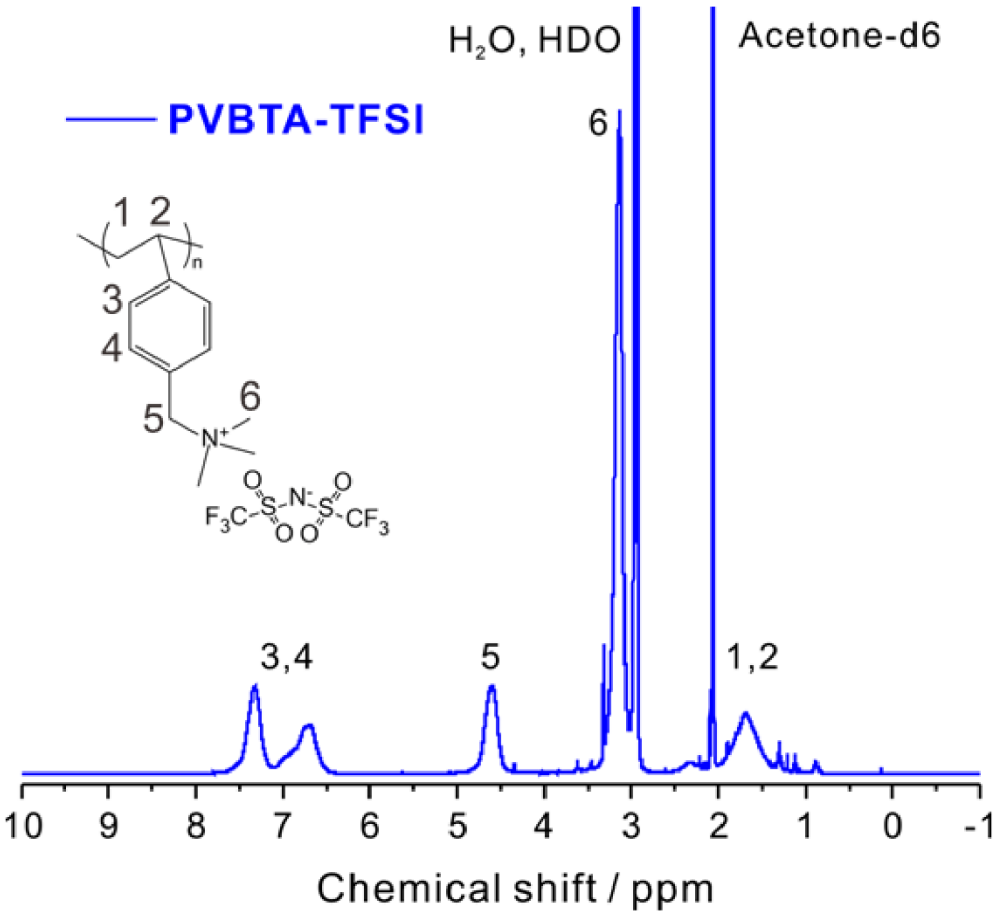

Figure S1 ^{1}H NMR spectra (400 MHz) of PVBTA-TFSI in deuterated acetone: δ 1.36-1.99 (H1, H2), δ 2.05 (acetone-d6), δ 3.14 (H6), δ 4.4-4.9 (H5), δ 6.5-7.4 (H3, H4).

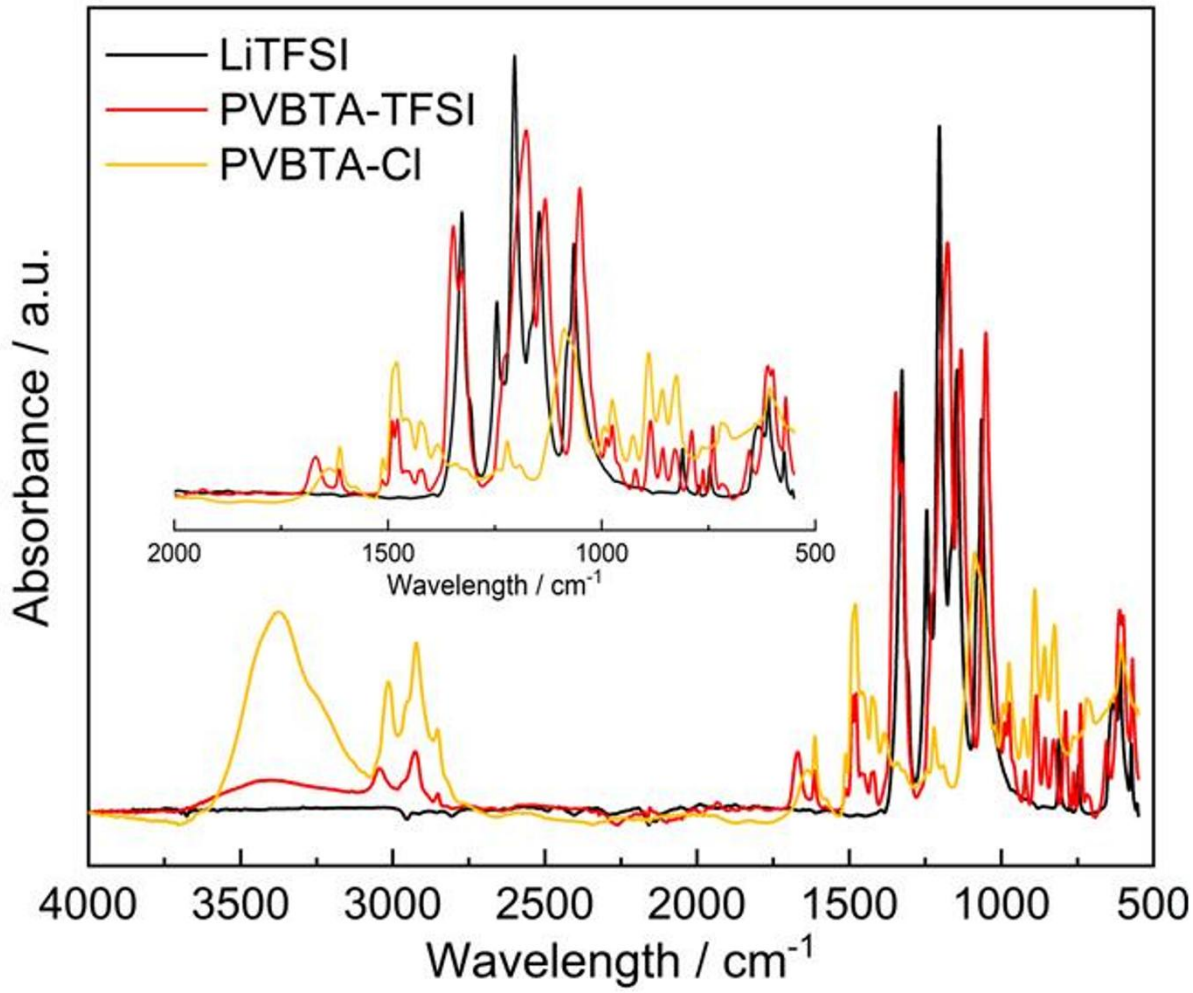

Figure S2 FT-IR spectra of PVBTA-TFSI, PVBTA-Cl, and LiTFSI. The inset shows the enlargement of FT-IR spectra ranging from 500 cm^{-1} to 2000 cm^{-1}. FT-IR of PVBTA-TFSI (in cm^{-1}): 973 (C-N stretching), 1346, 1326, 1176, 1132, 1050 (TFSI-), 1612, 1480, 1422 (aromatic C=C stretching), 3043, 2922, 2852 (alkyl C-H stretching), 3400 (H_2O). FT-IR of PVBTA-Cl (in cm^{-1}): 973 (C-N stretching), 1612, 1480, 1422 (aromatic C=C stretching), 3015, 2922, 2852 (alkyl C-H stretching), 3400 (H_2O). FT-IR of LiTFSI (in cm^{-1}): 1327 (SO_2 asymmetric stretching), 1245 (CF_3 symmetric stretching), 1204 (CF_3 asymmetric stretching), 1147 (SO_2 symmetric stretching), 1065 (S_2N asymmetric stretching).

2

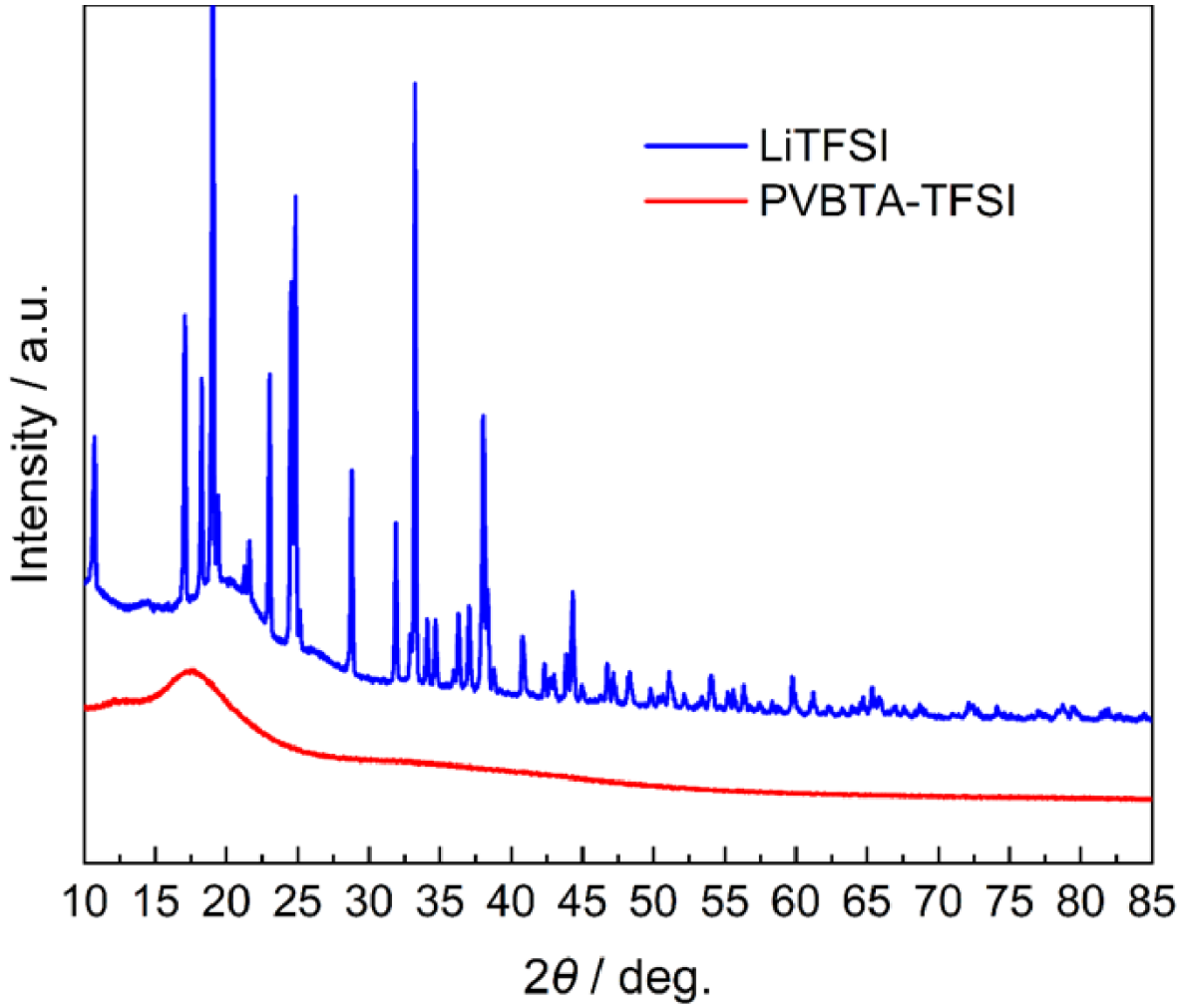

Figure S3 XRD patterns of LiTFSI and PVBTA-TFSI show that PVBTA-TFSI is an amorphous polymer that only has a broad amorphous peak around 20°. The result indicates the ion-exchange process is successful for PVBTA-TFSI and there is no residual LiTFSI.

(a)

3

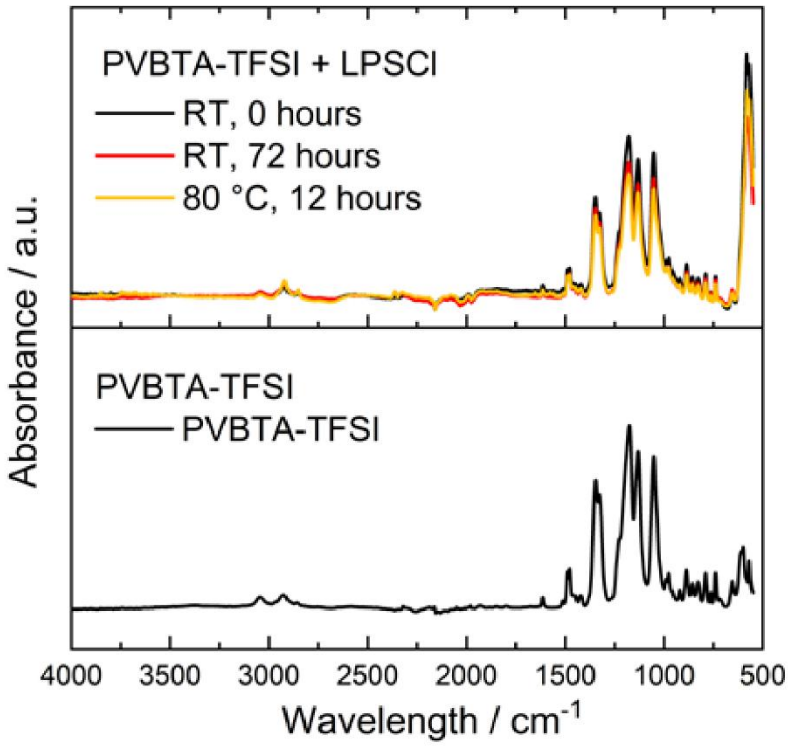

(b)

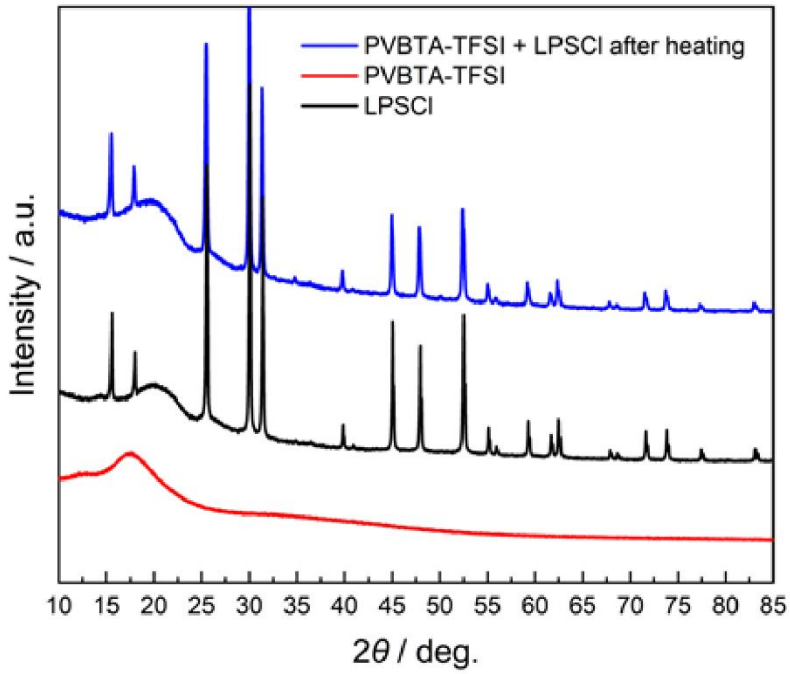

Figure S4 (a) FT-IR of PVBTA-TFSI and PVBTA-TFSI mixed with LPSCl shows no difference before and after heating. (b) XRD patterns of PVBTA-TFSI mixed with LPSCl after heating also match the reflections before heating.

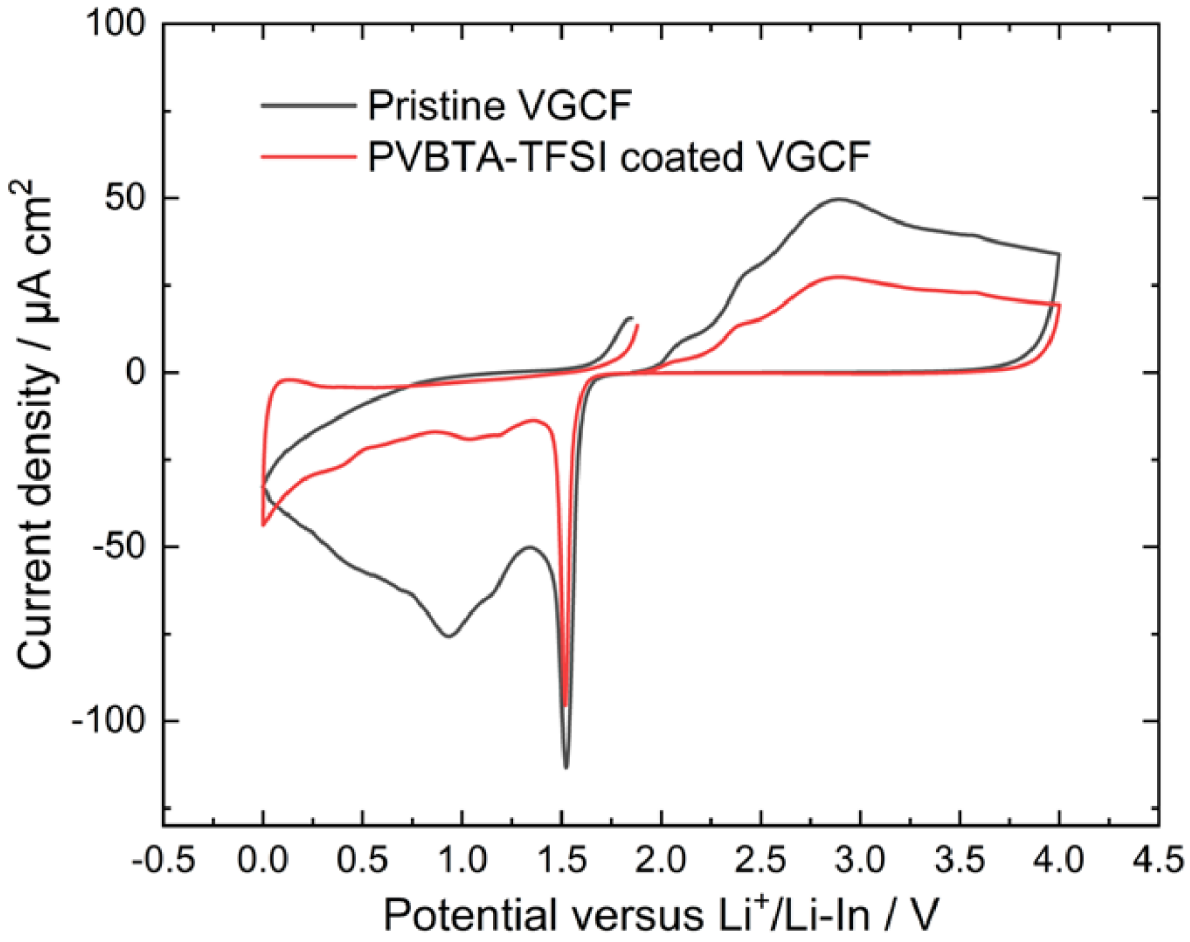

Figure S5 Cyclic voltammetry scan ranging from 0 V to 4 V (vs. Li^+/Li-In) at a scan rate of 1 $mV \cdot s^{-1}$ and starting from open circuit potential to assess the electrochemical stability of PVBTA-TFSI and LPSCl using a PVBTA-TFSI coating on vapor grown carbon fibers (VGCF). The electrochemical cell is assembled using VGCF/LPSCl as the working electrode, LPSCl as a separator, and an indium-lithium alloy reference and counter electrode. The results show that the PVBTA-TFSI coated VGCF exhibits lower current density compared to pristine VGCF, demonstrating that PVBTA-TFSI has a suitable electrochemical stability also in contact with LPSCl.

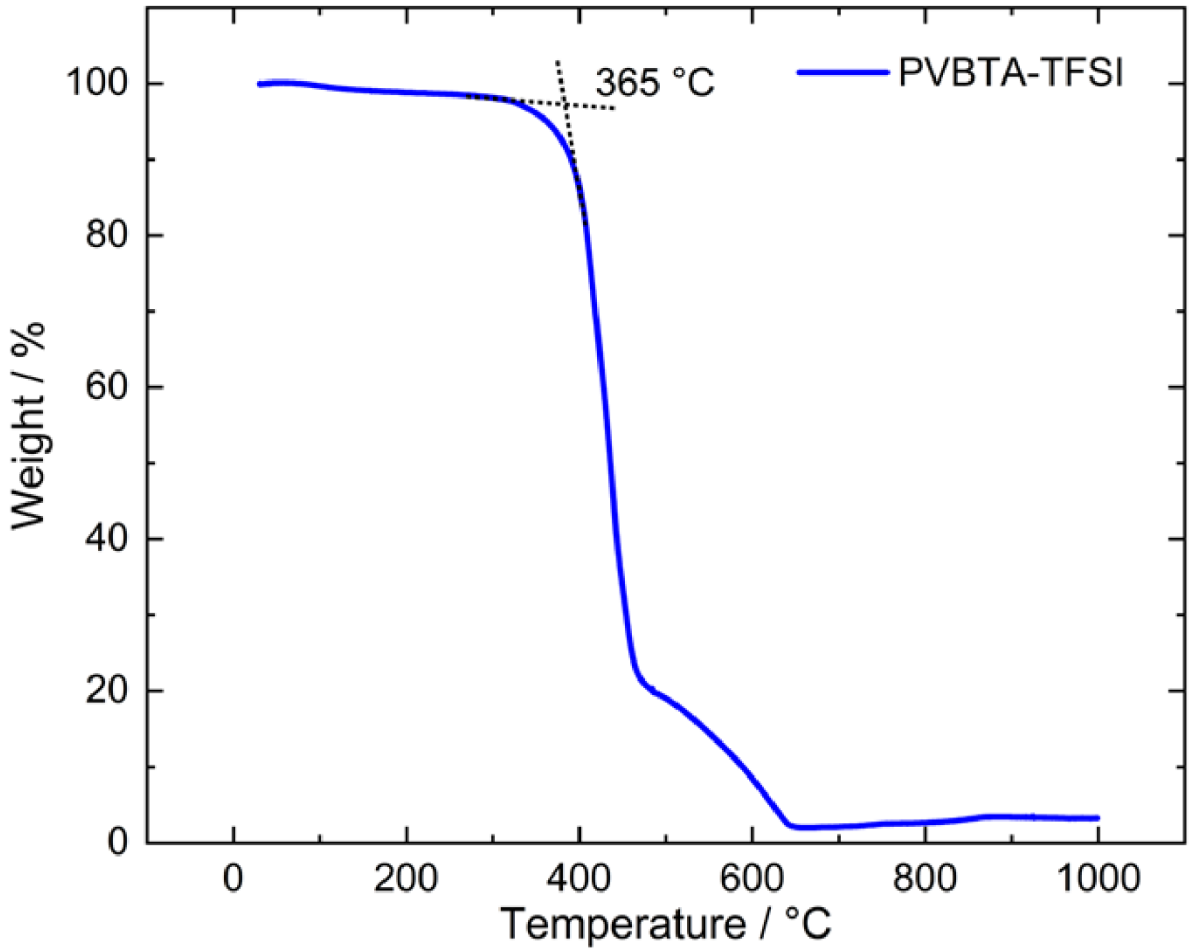

Figure S6 TGA of PVBTA-TFSI demonstrates that the decomposition temperature of PVBTA-TFSI in air is around 365 °C, which is higher than the inlet temperature applied for spray drying.

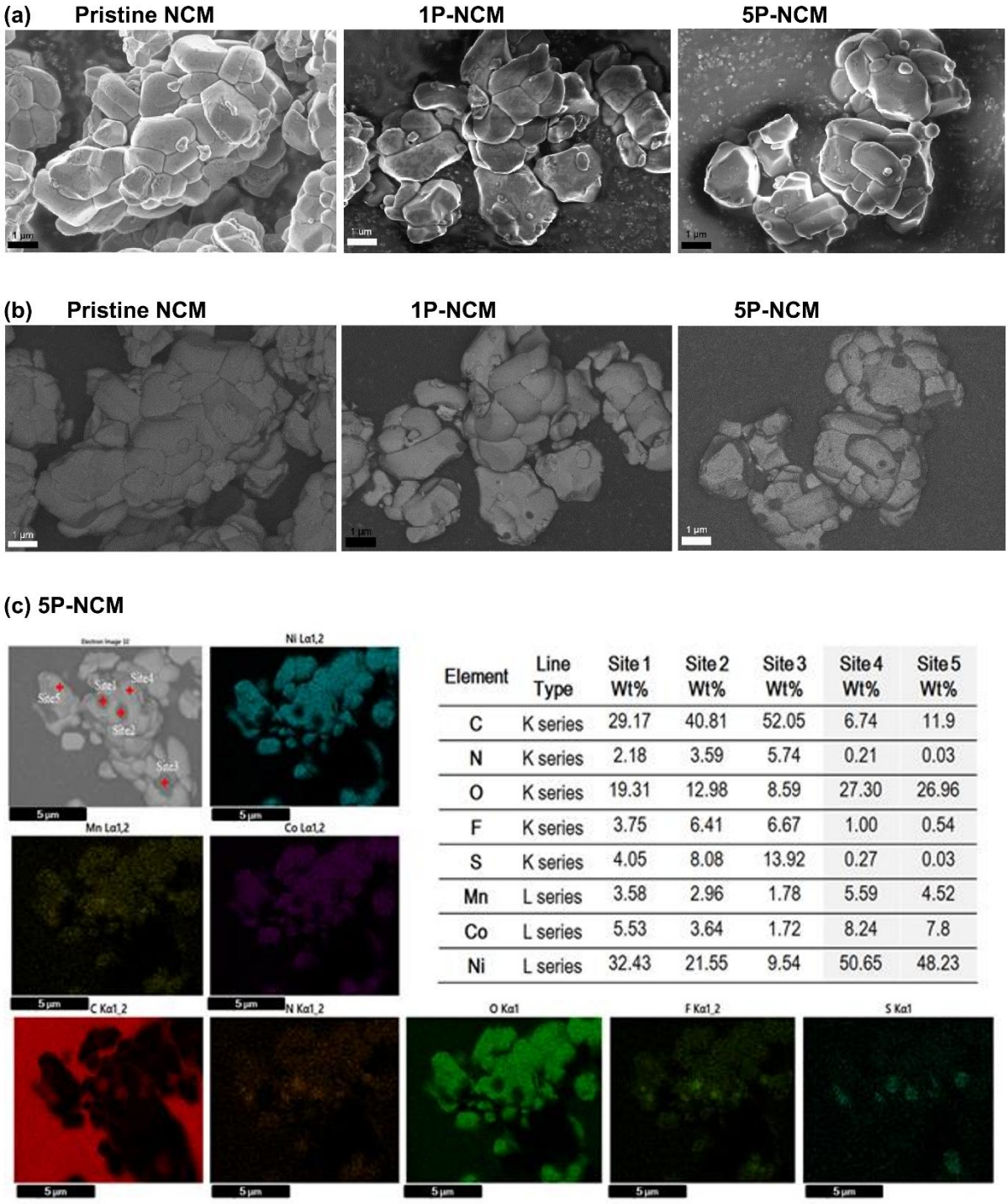

Element	Line Type	Site 1 Wt%	Site 2 Wt%	Site 3 Wt%	Site 4 Wt%	Site 5 Wt%
C	K series	29.17	40.81	52.05	6.74	11.9
N	K series	2.18	3.59	5.74	0.21	0.03
O	K series	19.31	12.98	8.59	27.30	26.96
F	K series	3.75	6.41	6.67	1.00	0.54
S	K series	4.05	8.08	13.92	0.27	0.03
Mn	L series	3.58	2.96	1.78	5.59	4.52
Co	L series	5.53	3.64	1.72	8.24	7.8
Ni	L series	32.43	21.55	9.54	50.65	48.23

Figure S7 (a) Secondary-electron SEM images and (b) energy selective backscattered (ESB) electron images (taken under 3 kV and 200 pA) shows that 5P-NCM has polymer aggregation spots on the surface. (c) The polymer aggregation spots on 5P-NCM are confirmed by EDX analysis under 5 kV and 2 nA.

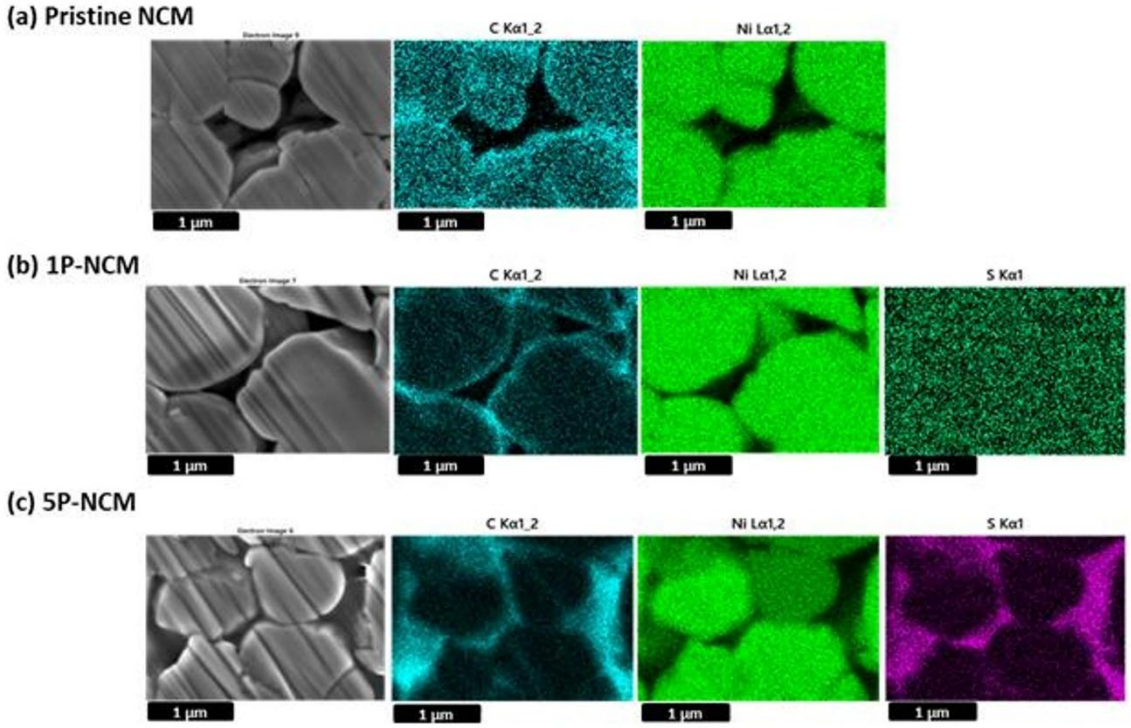

Figure S8 SEM images and EDX mappings after FIB-cutting for (a) pristine NCM, (b) 1P-NCM, (c) 5P-NCM were conducted under 5 kV and 2 nA. The results shows that 1P-NCM has the most homogeneous coating. However, 5P-NCM has some polymer aggregation spots and has a thicker polymer coating layer than 1P-NCM.

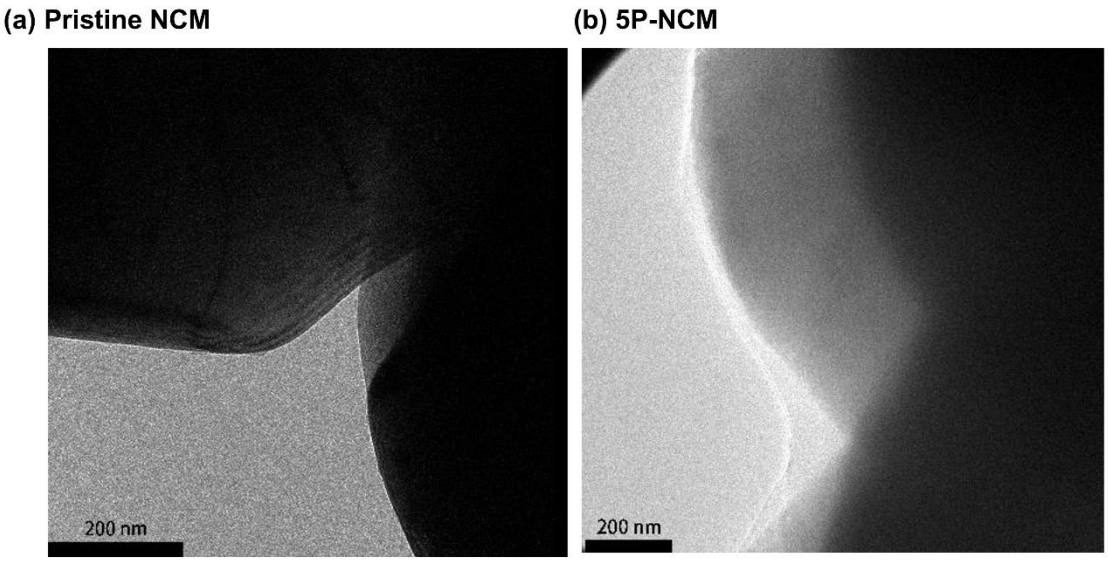

Figure S9 TEM images of (a) pristine NCM and (b) 5P-NCM. Some places of 5P-NCM have polymer aggregation around 100 nm.

(a)

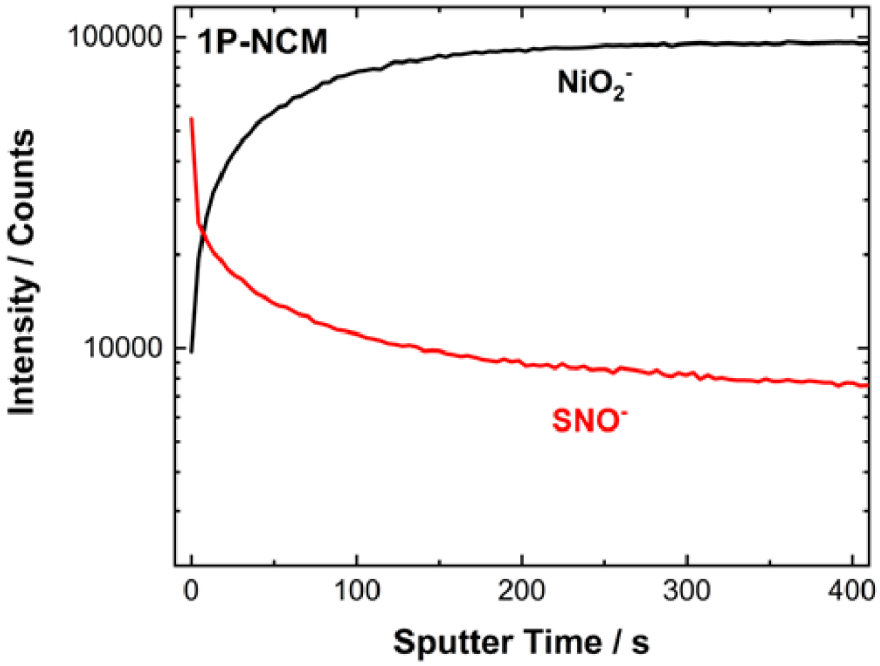

(b)

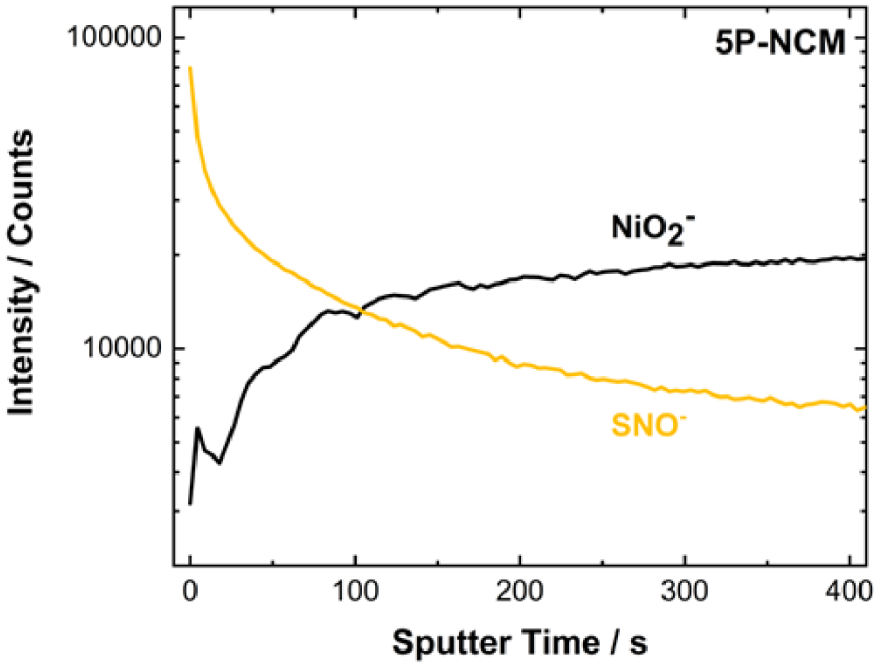

Figure S10 Comparison of ToF-SIMS depth profiles between SNO^- and NiO_2 of (a) 1P-NCM (red line) and (b) 5P-NCM (yellow line). SNO^- signal decreases and the NiO_2^- signal increases more rapidly for 1P-NCM than for 5P-NCM.

(a)

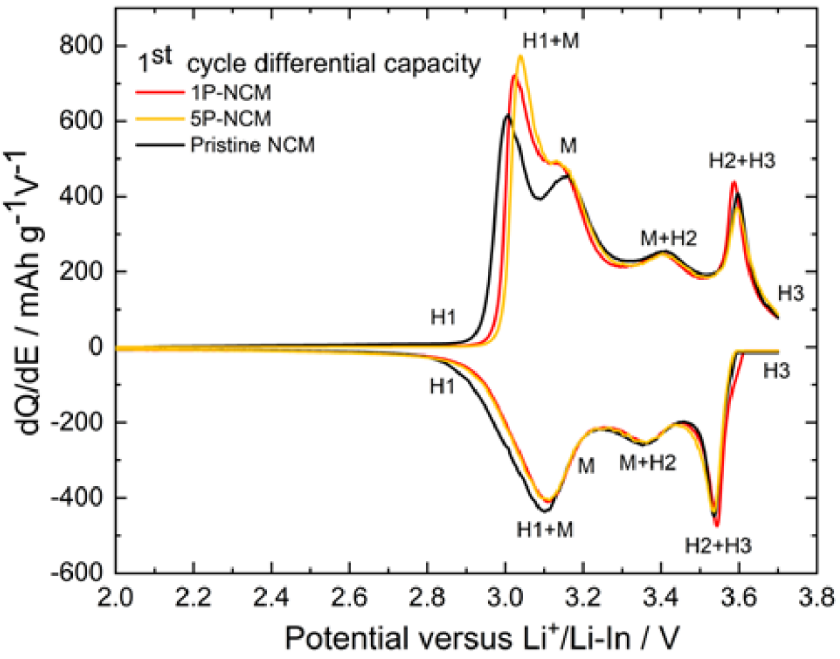

(b)

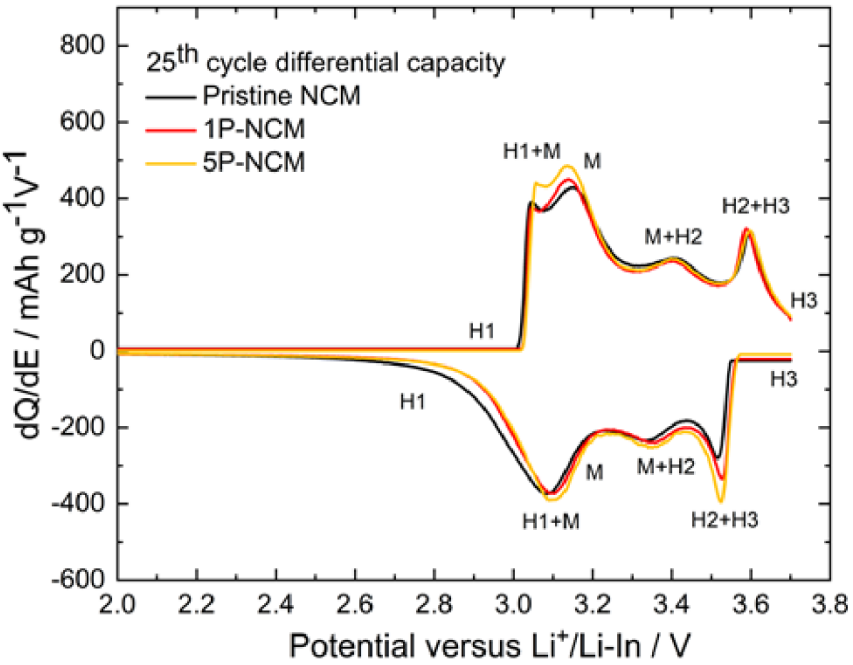

Figure S11 Comparison of differential capacity plots of (a) 0.1C 1st cycle and (b) 0.1C 25th cycle of PVBTA-TFSI coated and pristine NCM cells with LPSCl and lithium-indium alloy anode. In the first cycle, the coating layer gives rise to a larger overpotential at around 3 V (vs. Li^+/Li-In) for the coated cells compared to the pristine cell. At the 25th cycle, the coated NCM shows better reversibility in the discharge process.

(a)

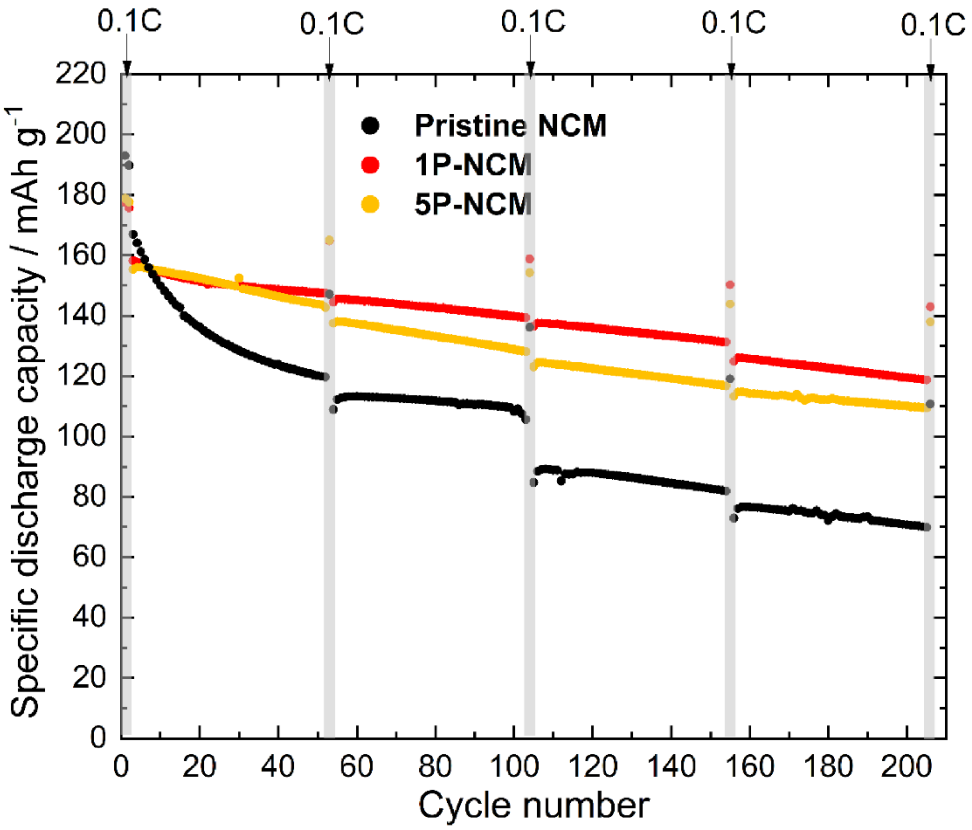
0.1C
0.1C
0.1C
0.1C
0.1C
Pristine NCM
1P-NCM
5P-NCM
Specific discharge capacity / mAh g-1
Cycle number
0
20
40
60
80
100
120
140
160
180
200
220

(b)

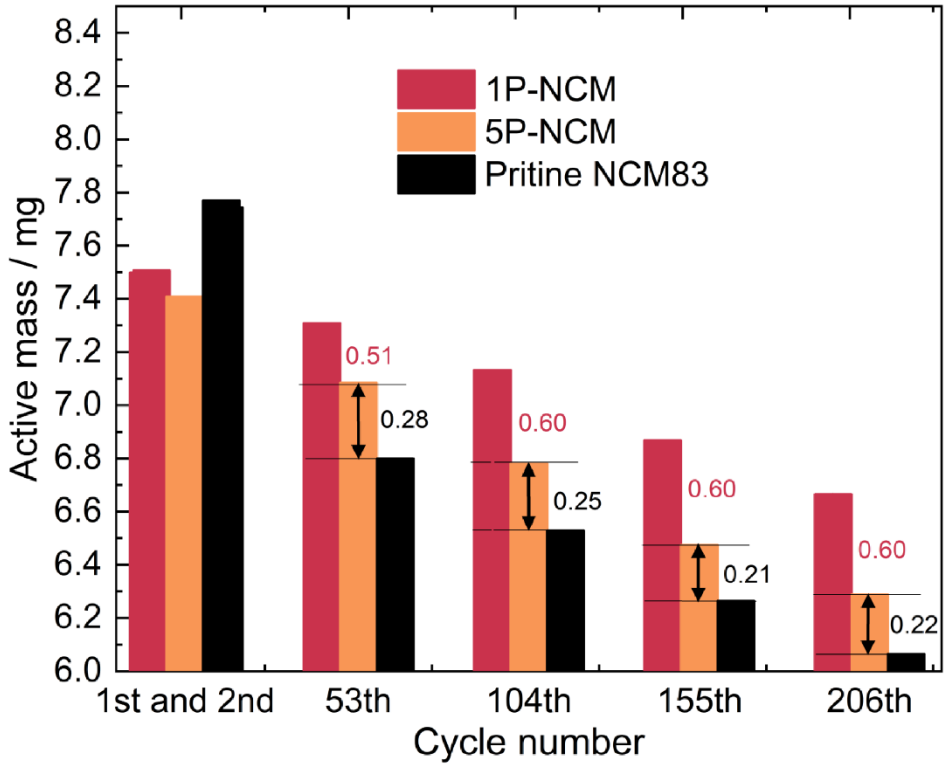
1P-NCM
5P-NCM
Pritine NCM83
Active mass / mg
Cycle number
1st and 2nd
53th
104th
155th
206th
0.51
0.28
0.60
0.25
0.60
0.21
0.60
0.22
6.0
6.2
6.4
6.6
6.8
7.0
7.2
7.4
7.6
7.8
8.0
8.2
8.4

11

(c)

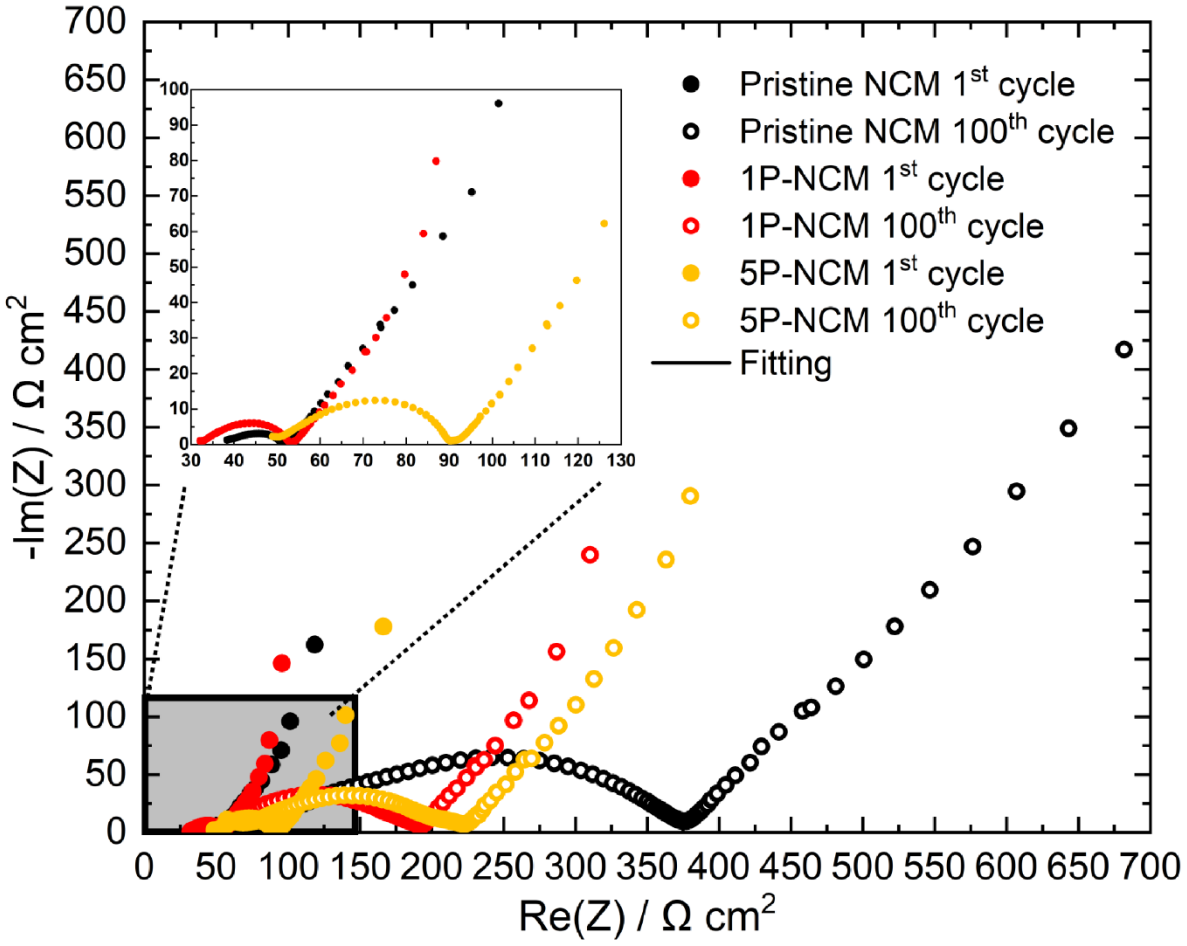

Figure S12 (a) Long-term cycling capability at 0.25C and (b) corresponding active mass evolution are compared. (c) During the 0.25C cycling test, EIS of 1P-NCM, 5P-NCM, and pristine NCM cells are measured right after 0.1C charging up to 3.15 V (vs. Li^+/Li-In) and chronoamperometry. The 1P-NCM shows the best 0.25C cycling performance and active mass retention. 5P-NCM takes second place, and pristine NCM presents the lowest capacity and active mass retention. Besides, 1P-NCM and 5P-NCM have similar total impedance after cycling. However, the pristine NCM has a much larger total impedance than the coated NCM after cycling. Overall, the 0.25C cycling results match well with the 0.1C cycling results.

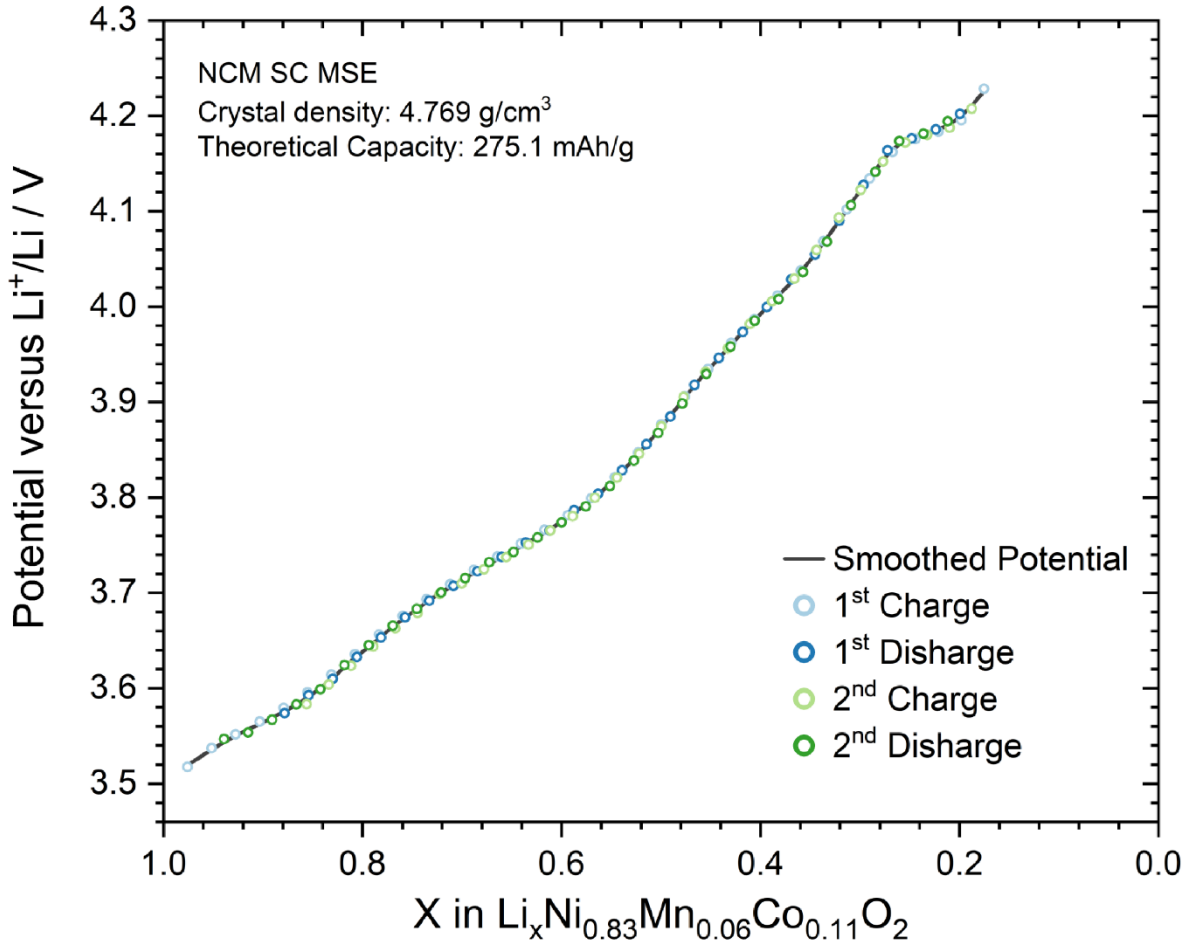

Figure S13 The V_{OC} (y-axis) follows a well-defined function vs. state of charge, which represents lithium content x in $Li_xNi_{0.83}Mn_{0.06}Co_{0.11}O_2$ (x-axis). The relationship between lithium content x in $Li_xNi_{0.83}Mn_{0.06}Co_{0.11}O_2$ and V_{OC} is obtained by galvanostatically charging and discharging a liquid lithium-ion battery at 0.02C. After every 20 minutes of charging or discharging, it relaxes for two hours to obtain V_{OC}. Besides, x in $Li_xNi_{0.83}Mn_{0.06}Co_{0.11}O_2$ can be calculated by the current and time.

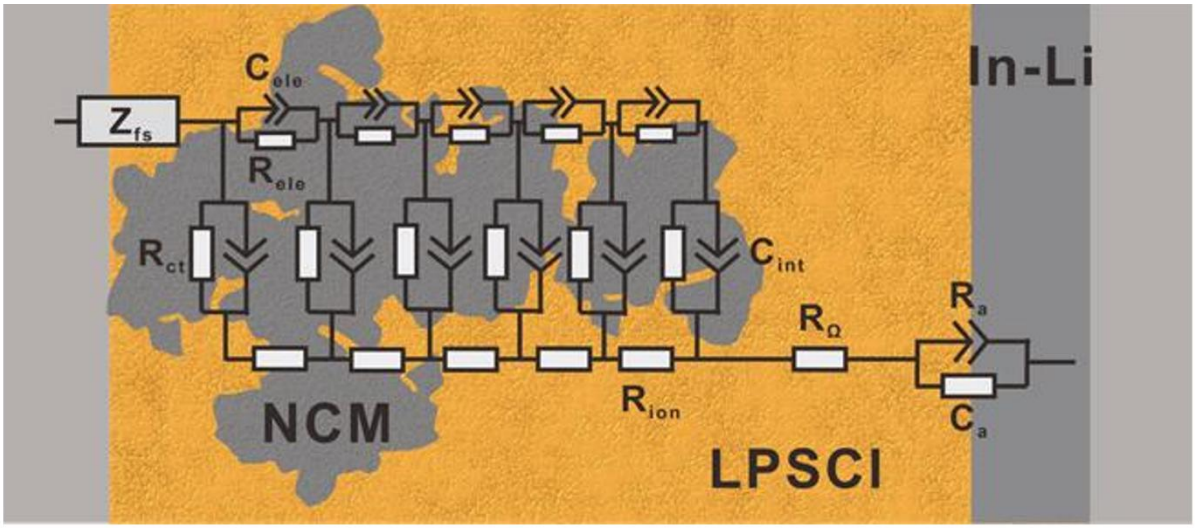

Figure S14 The transition line model equivalent circuit was used for the EIS-PSD model to estimate the lithium diffusion pathway length. $Z_{\mathrm{fs}}^{\mathrm{cylindrical}}$ describes the finite space diffusion behavior. R_{ct} and C_{int} represent charge transfer resistance and NCM/SE interface capacitance within the cathode composite, respectively. R_{ele} and C_{ele} represent electronic resistance and capacitance within the cathode composite, respectively. R_{ion} represents ionic resistance within the cathode composite. R_{Ω} represents the bulk resistance of the solid electrolyte separator. R_a and C_a represent interface resistance and capacitance between anode and electrolyte, respectively. Besides, the cathode composite resistance $R_{cathode}$ is expressed as the geometric mean of the value R_{ct} multiplied by the sum of the R_{ele} and R_{ion} ($R_{cathode} = \sqrt{R_{ct} \times (R_{ele} + R_{ion})}$).[1]

Table S1 Fitting parameters and results of impedance spectra of the 0.1C cycling test after 1st, 2nd, 3rd, 4th, 5th, 10th, 30th, 50th, and 100th cycle.

5P-NCM	Parameter	1st cycle	2nd cycle	3rd cycle	4th cycle	5th cycle	10th cycle	30th cycle	50th cycle	100th cycle
Electrolyte	R_{Ω} / Ω	29.66303	28.76932	30.3089	30.03593	30.33327	28.90384	32.48128	31.55207	31.55207
Anode	R_a / Ω	4.975571	1.944134	5	5.734171	9.547901	4.706753	11.69673	7.474538	22.03523
Cathode	$R_{cathode}$ / Ω	31.08665	41.58766	47.62101	56.62038	57.32069	61.93654	71.02633	90.52815	114.2053
1P-NCM	Parameter	1st cycle	2nd cycle	3rd cycle	4th cycle	5th cycle	10th cycle	30th cycle	50th cycle	100th cycle
Electrolyte	R_{Ω} / Ω	26.50942	26.98185	30.0736	29.69225	29.52685	33.20478	30.55595	30.83985	26.24353
Anode	R_a / Ω	4.834044	4.699702	9.702336	9.888491	9.722268	8.01015	29.68394	10.8649	20.55684
Cathode	$R_{cathode}$ / Ω	24.78915	37.24038	37.866	43.83942	51.49124	64.5251	75.17648	91.08244	110.0461
Pristine NCM	Parameter	1st cycle	2nd cycle	3rd cycle	4th cycle	5th cycle	10th cycle	30th cycle	50th cycle	100th cycle
Electrolyte	R_{Ω} / Ω	36.71254	37.63909	37.66642	39.68655	40.72608	40.9861	40.9861	47.94843	52.35665
Anode	R_a / Ω	1.479214	4.526362	4.493133	6.834455	8.01015	19.95528	25.7272	26.34742	30.91555
Cathode	$R_{cathode}$ / Ω	18.31281	29.06279	38.61496	46.24732	53.52506	68.60484	96.08689	129.6937	155.8007

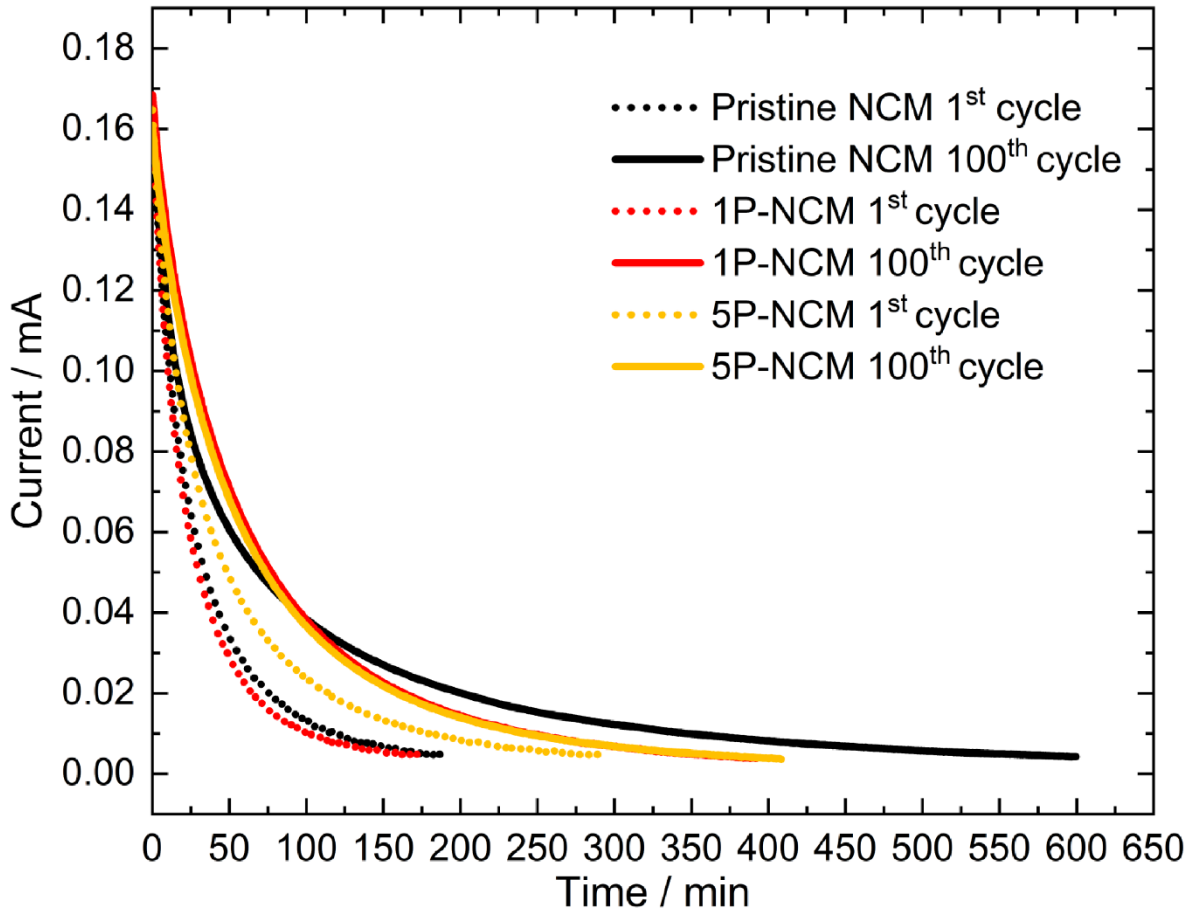

Figure S15 Evolution of the lithium diffusion pathway length of 0.25C cycling performance by chronoamperometry measurement at 3.15 V (vs. Li^+/Li-In). The pristine NCM cell has a much longer lithium diffusion path length than the coated NCM cells after cycling. The results draw the same conclusion of the chronoamperometry measurement at 3.15 V (vs. Li^+/Li-In) during 0.1C cycling performance.

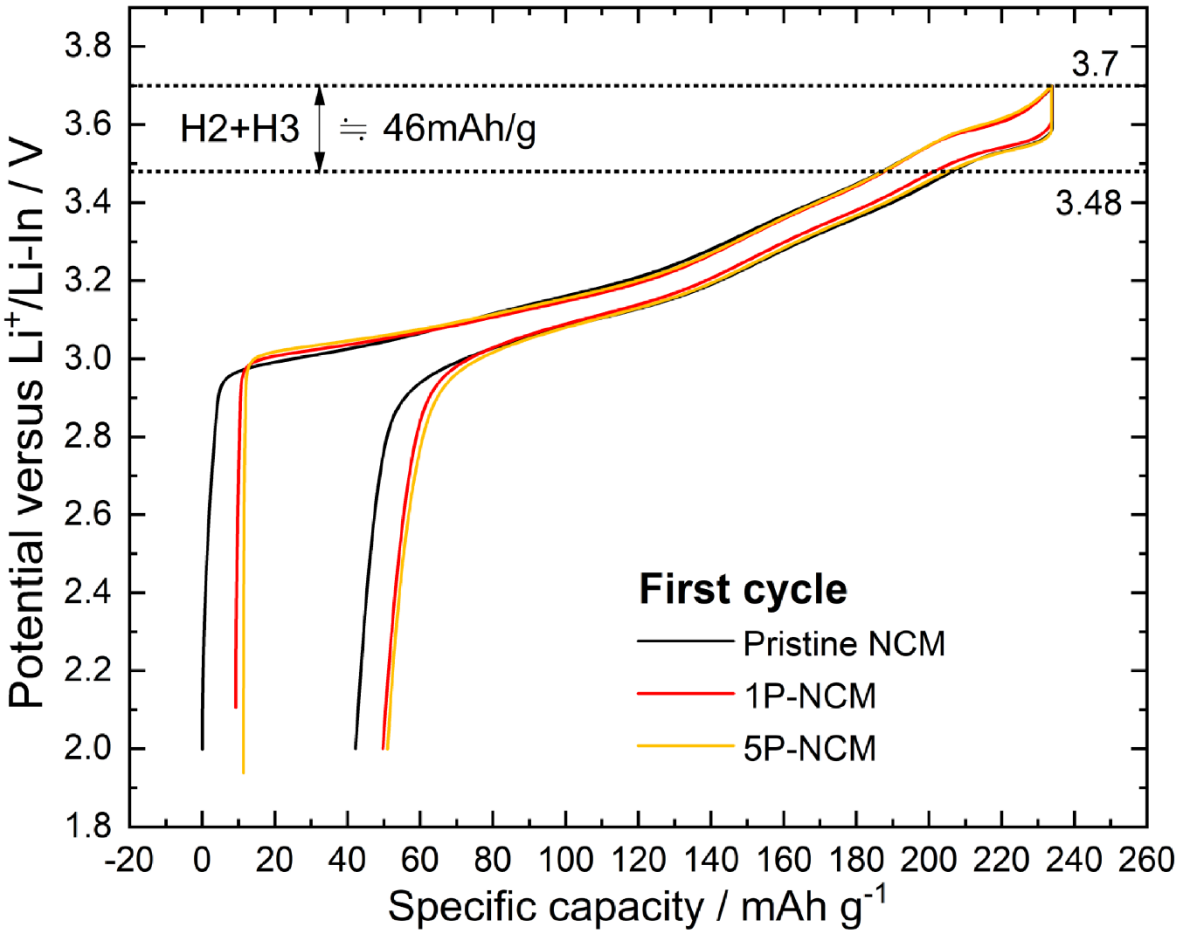

Figure S16 Charge/discharge curves of the first cycle at 0.1C. The first cycle capacity is the same for three cells in the H2+H3 range, which means that the capacity improvement for the coated NCM is not due to less lithium extraction from H2+H3 range. To evaluate performance and capacity specifically within the H2+H3 range, we aligned the charge-discharge data of pristine NCM, 1P-NCM, and 5P-NCM with the H2+H3 range overlap. The charge/discharge curves of 1P-NCM and 5P-NCM are shifted to the right by 9.3 mAh·g^{-1} and 11.3·mAh g^{-1}, respectively.

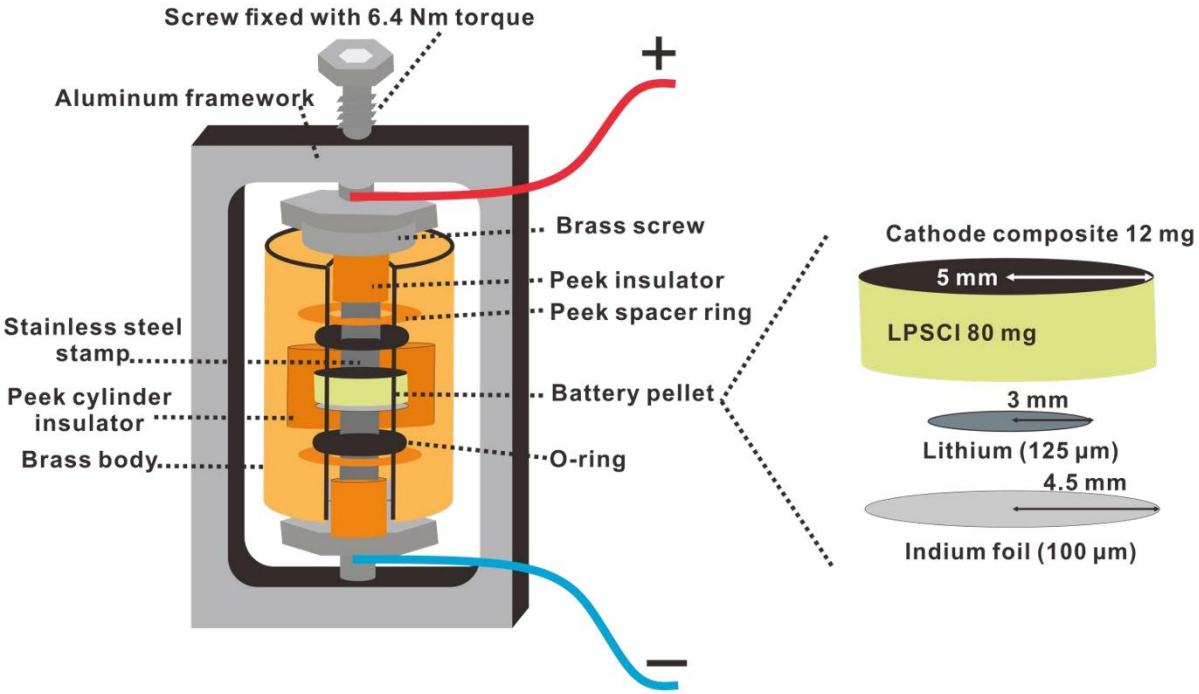

Figure S17 Schematic of the cell casing and the structure of the SSB pellet. The SSB pellet contains cathode composite, LPSCl solid electrolyte separator, lithium foil, and indium foil, which are pressed inside a peek cylinder. Stainless steel stamps are used as current collectors. O-rings isolate the SSB pellet from air.

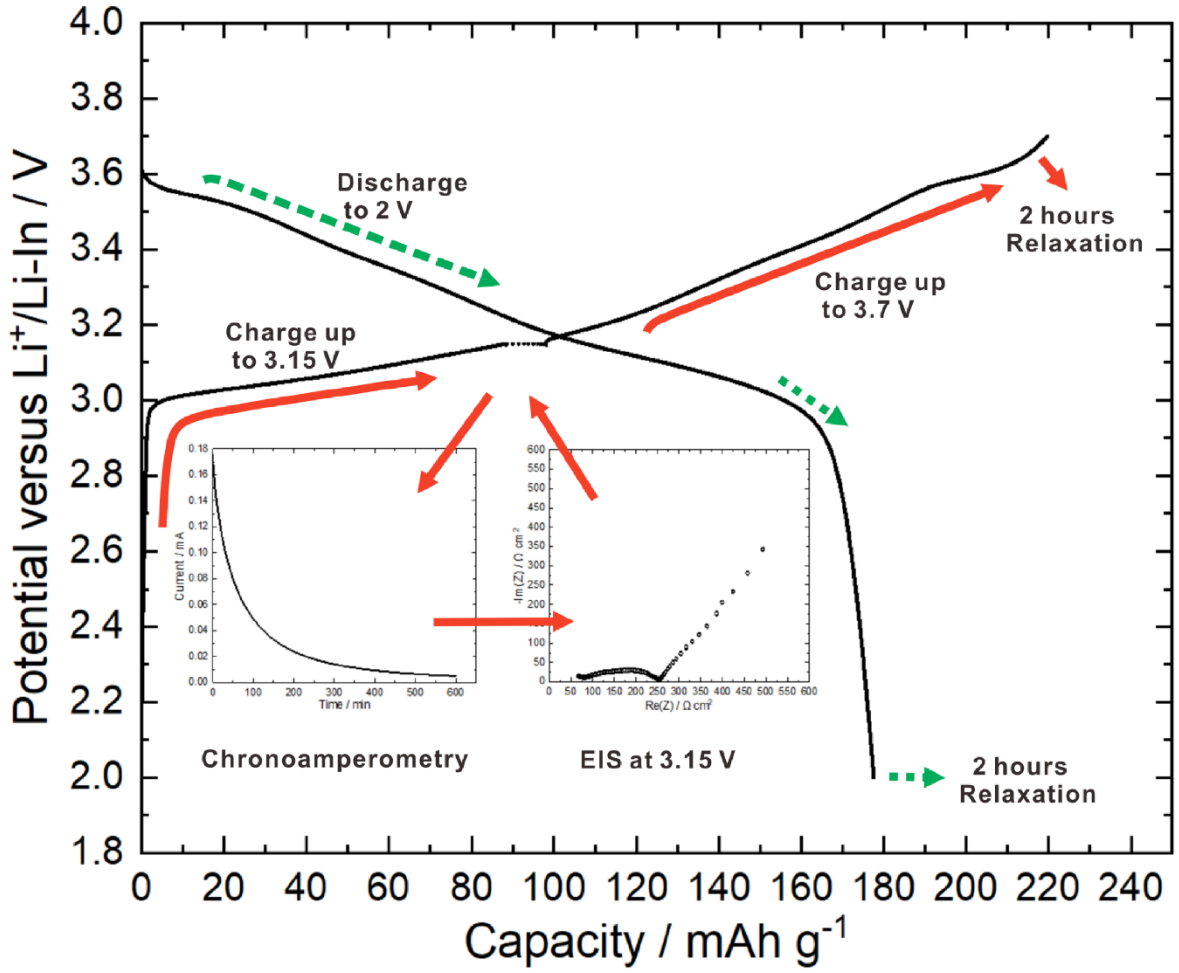

Figure S18 Schematic of electrochemical analysis. SSBs were galvanostatically charged to 3.15 V (vs. Li^+/Li-In) and then maintained at the potential at 3.15 V (vs. Li^+/Li-In) until the current drops to less than 1%. After that, EIS was measured from 1 MHz to 100 μHz. Subsequently, The SSBs were galvanostatically charged to 3.7 V (vs. Li^+/Li-In), followed by a 2 hour relaxation process. Finally, the SSBs were discharged to 2.0 V (vs. Li^+/Li-In), followed by a 2 hour relaxation process.

[1] I. Kochetkov, T.-T. Zuo, R. Ruess, B. Singh, L. Zhou, K. Kaup, J. Janek and L. Nazar, *Energy & Environmental Science*, 2022, **15**, 3933-3944.

3.2 Publication B

From the results of **Publication A**, using a cationic polymer as a coating material for NCM resulted in a capacity loss in SEBs due to the absence of σ_{Li^+} in the polymer. Consequently, **Publication B** aims to identify a coating material for NCM that offers σ_{Li^+}. The coating process is conducted using the spray-drying method. To evaluate the electrochemical performance of different coated NCM in SEB, pristine and coated $LiNi_{0.9}Co_{0.05}Mn_{0.05}O_2$ is used as a CAM. Li_6PS_5Cl is used as a separator and catholyte. An In/InLi alloy is used as a counter electrode.

Initially, experiments used a spray-drying method to create a coating on NCM from a mixture of LiTFSI, an ionic liquid (1-methyl-1-butylpyrrolidiniumbis(trifluoromethanesulfonyl)imide), and the PVBTA-TFSI (0.01 g LiTFSI, 0.02 g ionic liquid, 0.03 g PVBTA-TFSI, 200 ml acetone, and 6 g NCM). The LiTFSI/ionic liquid/PVBTA-TFSI mixture was prepared using the ratio reported in the literature.[199] Notably, using LiTFSI alone with PVBTA-TFSI is impractical because the ion-exchange synthesis saturates the polymer with TFSI counterions, preventing a homogeneous film and leading to phase separation. However, SEM reveals that the LiTFSI/ionic liquid/polycation mixture as a coating material forms distinct aggregated particles, probably due to insufficient coating inducer PVBTA-TFSI, resulting in coating failure.

Directly coating NCM with an anionic polymer appears more effective. However, the first challenge is finding an anionic polymer that dissolves in polar aprotic solvents or non-polar solvents that are stable with NCM (see **Section 2.3**). Additionally, the electrostatic interaction between the anionic polymer and NCM is insufficient, resulting in separated polymer aggregation particles instead of a uniform coating layer on NCM.

To overcome these challenges, PVP is used as a coating inducer and is combined with lithiated sulfonated polyphenylene sulfone (sPPSLi), which provides σ_{Li^+}. The spray-drying method using DMF as a solvent to achieve a uniform 1~3 nm coating on NCM. Notably, the boiling point of DMF appears to constrain the choice of solvent; solvents with higher boiling points, such as NMP, cannot be effectively dried during the coating process. Additionally, nano-IR confirms the complete and pinhole-free coverage of the coating on NCM. The PVP/sPPSLi coated NCM exhibited a first-cycle discharge capacity of 186 $mAh \cdot g^{-1}$, which is comparable to the 183 $mAh \cdot g^{-1}$ of pristine NCM. Additionally, the PVP/sPPSLi coated NCM shows improved cycling stability compared to pristine NCM, retaining 78.3% of its capacity after 100 cycles versus 69% for pristine NCM. This improvement is because the PVP/sPPSLi coating can mitigate CEI degradation between NCM and the Li_6PS_5Cl catholyte, thereby reducing m_{act} loss and limiting the growth of L_{diff}.

B.X.S. was responsible for the electrochemical analyses, and general characterization of materials. Y.Y. conducted the TOF-SIMS analysis, while T.D. performed the TEM experiments. F.W. and R.B. conducted the nano-IR analysis. K.V., A.H., and F.H.R. contributed to the analysis and interpretation of the experimental data. A.M. and G.T. provided the anionic polymer. The research concept was conceived by B.X.S. and F.H.R., who also prepared the manuscript. All authors contributed to the manuscript and the analysis of experimental results.

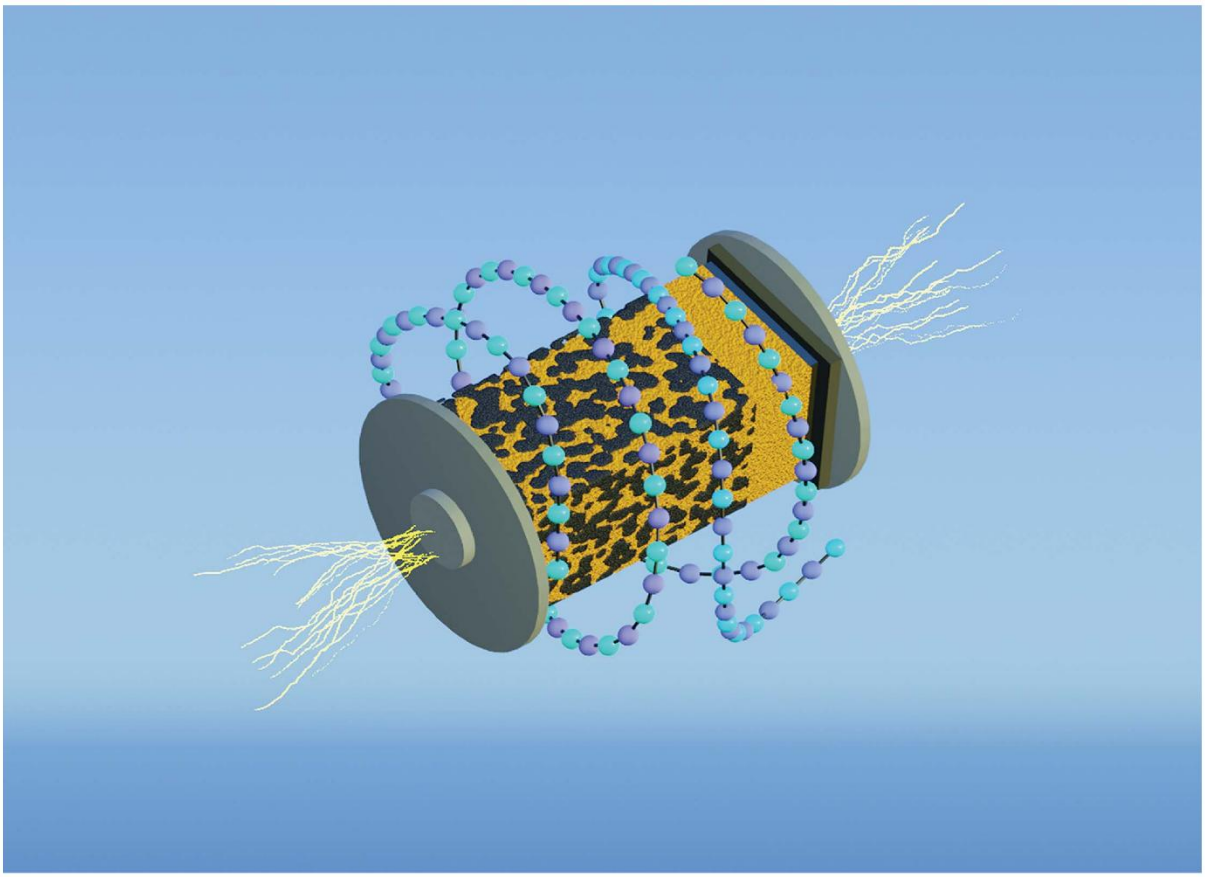

Highlighting a study of polymer coating on NCM cathode active material particles from the group of Dr Felix H. Richter, Center for Materials Research, Institute of Physical Chemistry, Justus-Liebig-University Giessen, Germany.

Lithiated polymer coating for interface stabilization in Li_6PS_5Cl-based solid-state batteries with high-nickel NCM

This study demonstrates a scalable spray-coating method to apply a 1–3 nm sulfonated polyphenylene sulfone/polyvinylpyrrolidone coating on NCM, enhancing interface stability and mitigating degradation in sulfide-based solid-state batteries.

As featured in:

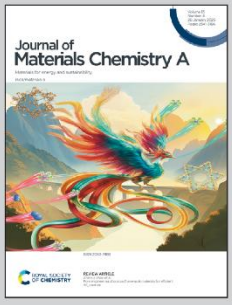

See Felix H. Richter *et al.*, *J. Mater. Chem. A*, 2025, **13**, 2600.

ROYAL SOCIETY OF CHEMISTRY

rsc.li/materials-a

Registered charity number: 207890

Journal of Materials Chemistry A

ROYAL SOCIETY OF CHEMISTRY

PAPER

View Article Online
View Journal | View Issue

Cite this: J. Mater. Chem. A, 2025, 13, 2600

Lithiated polymer coating for interface stabilization in Li_6PS_5Cl-based solid-state batteries with high-nickel NCM†

Bing-Xuan Shi,[a] Franjo Weber,[b] Yuriy Yusim,[a] Thomas Demuth,[c] Kilian Vettori,[a] Andreas Münchinger,[d] Giorgi Titvinidze,[de] Kerstin Volz,[c] Anja Henss,[a] Rüdiger Berger[b] and Felix H. Richter[*a]

Received 11th October 2024
Accepted 20th November 2024

DOI: 10.1039/d4ta07265k

rsc.li/materials-a

Li_6PS_5Cl-based solid-state batteries with high-nickel $LiNi_{0.9}Mn_{0.05}Co_{0.05}O_2$ (NCM) promise higher energy density and safety than lithium-ion batteries with liquid electrolyte. However, their cycling performance is often limited by interface degradation between NCM and solid electrolyte. Here, a sulfonated polyphenylene sulfone/polyvinylpyrrolidone (sPPSLi/PVP) coating on NCM particles is presented that mitigates this issue. This uniform coating impedes direct contact between NCM and solid electrolyte, which lessens interface degradation and improves cycling performance. Electrochemical impedance spectroscopy and chronoamperometry show a reduced interface resistance and Li^+-ion transport length during cycling for sPPSLi/PVP-coated NCM in Li_6PS_5Cl-based solid-state batteries. Additionally, the coating effectively suppresses side reactions, particularly the formation of oxygenated species, at the NCM/SE interface. Overall, sPPSLi/PVP-coated NCM shows remarkable improvements in cycling stability and rate capability, emphasizing the significance of applying polymer coatings.

1. Introduction

An important sub-group of solid-state batteries is solid electrolyte batteries (SEBs) in which ion transport occurs through ion hopping in inorganic solid electrolytes (SEs), as classified by Sen and Richter.[1] They are promising alternatives to lithium-ion batteries, also called liquid electrolyte batteries (LEBs), as they promise to reach higher energy density[2,3] and enhanced safety.[4] The sulfide-based SE Li_6PS_5Cl exhibits sufficient ionic conductivity of around 2 mS cm^{-1} (ref. 5 and 6) for investigating the fundamental working principles of SEBs. Developing SEBs faces technical challenges,[7] particularly high interfacial resistance and instability between electrode materials and SEs.[8,9] Additionally, moisture sensitivity, densification, and the preparation of thin SE membranes complicate the fabrication of SEBs.[2,10]

In the SEB cathode, high-nickel $LiNi_{0.9}Mn_{0.05}Co_{0.05}O_2$ (NCM) as the cathode active material is advantageous in providing high energy density and low cost.[11,12] However, NCM suffers from poor cycling stability and surface instability when in contact with SEs.[13,14] Even at 0% state of charge (SOC), NCM and Li_6PS_5Cl chemically react at the interface, leading to capacity fading.[15] The cathodic instability of Li_6PS_5Cl leads to electrochemical degradation at the electrode–electrolyte interface, which decreases Coulomb efficiency.[16–19] In addition, oxidation reactions at the NCM/SE interface coupled with NCM oxygen loss occur at high SOC (around 3.5 *vs.* In/LiIn), forming a passivation layer with oxygenated species.[20–22] Chemo-mechanical fracture of NCM particles is also significantly driven by oxygen loss at the NCM/SE interface.[8,23,24]

Surface coatings on NCM are applied to alleviate the interface stability between NCM and Li_6PS_5Cl. Hence, they should be made of a material that is electronically insulating and electrochemically stable.[25] However, such a coating may restrict electronic conduction within the cathode, which needs to be taken into account. Regarding ionic conductivity of the coating, it is to be noted that to keep Li^+ transport resistance below 1 Ω cm^2 with a 1 nm thick coating, an ionic conductivity of only 10^{-4} mS cm^{-1} is sufficient.[26] Overall, this necessitates optimization of the coating thickness and coverage to avoid impeding electron and Li^+ transport between particles.

Many inorganic materials have been developed as surface coatings for NCM,[27] such as metal oxides, including $LiNbO_3$,[28–30] $Li_6ZnNb_4O_{14}$,[31] $LiAlO_2$,[32] Li_2ZrO_3,[29,33] $Li_4Ti_5O_{12}$,[34] Li_3BO_3,[35]

[a]Institute of Physical Chemistry & Center for Materials Research (LaMa), Justus-Liebig-University Giessen, Heinrich-Buff-Ring 17, 35392 Giessen, Germany. E-mail: Felix.H.Richter@phys.chemie.uni-giessen.de
[b]Max Planck Institute for Polymer Research, Ackermannweg 10, 55128, Mainz, Germany
[c]Department of Physics & Materials Sciences Center (WZMW), Philipps-University Marburg, Hans-Meerwein Straße 6, 35032 Marburg, Germany
[d]Hahn-Schickard, Georges-Köhler-Allee 103, 79110 Freiburg, Germany
[e]Agricultural University of Georgia, 240 David Aghmashenebeli Alley, 0131 Tbilisi, Georgia

† Electronic supplementary information (ESI) available. See DOI: https://doi.org/10.1039/d4ta07265k

$Li_2B_4O_7$,[36] and $Li_3B_{11}O_{18}$;[37] and halide electrolytes including Li_3YCl_6.[38] However, inorganic coatings can crack or detach during volume change of NCM.[26] Compared to the elastic modulus of ceramics like $LiNbO_3$ (~195 GPa), polymers have a lower elastic modulus (~6 GPa), which is close to that of thiophosphate-based SEs (~20 GPa).[26,39] Polymers are also expected to bind more readily to NCM, reducing fractures at particle contact points.[26] However, it needs to be considered that the mechanical properties of nanometer-thick coatings may differ from bulk properties due to polymer chain rearrangement at the surface or interfacial interactions with NCM.[40,41]

Deng *et al.* explored modifying NCM and carbon additives with poly(3,4-ethylenedioxythiophene) (PEDOT) *via* molecular layer deposition in a $^{In}SEB^{NCM}$.[42] In addition, NCMs coated with polymers such as polyvinylpyrrolidone (PVP),[43] PEDOT,[44] poly(3,4-ethylene dioxythiophene)-*co*-poly(ethylene glycol) (PEDOT-*co*-PEG),[45,46] polyacrylonitrile,[47] polyaniline,[48] poly(tris(2-(acryloyloxy)ethyl) phosphate),[49] polysiloxane,[50] Nafion,[51] bis(carboxyethylgermanium)-based polymer,[52] and polypyrrole[53] have been tested in a variety of LEBs. Our previous work introduced a polycation coating of poly((4-vinyl benzyl) trimethylammonium bis(trifluoromethanesulfonylimide)) (PVBTATFSI), applied through a scalable spray drying method to improve the NCM/SE interface durability and $^{LiIn}SEB^{NCM}$ cycling performance.[54]

However, the lack of Li^+ in the PVBTATFSI coating may not be ideal, which is why we test sulfonated poly(phenylene sulfone) in its lithiated form (sPPSLi, Fig. S1†) in the study presented here. Sulfonated polyphenylene sulfone is a material known for its superior proton conductivity and low water transport rates, which is excellent for use as an electrolyte in polymer electrolyte membrane fuel cells.[55] It has a high glass transition temperature exceeding 300 °C at which polymer decomposition starts. Additionally, the aromatic backbone offers superior thermal and oxidative stability compared to other sulfonated poly(arylene) polymers, enhancing its suitability for environments that demand high durability and resistance to degradation.[55,56] Therefore, sPPSLi is expected to be an excellent candidate for polymer coatings in SEBs. This is because maintaining a high glass transition temperature ensures that sPPSLi retains its mechanical strength and stability both during the coating process and throughout the operation of the device.

Here, we present polymer coatings that reduce NCM surface degradation and enhance the electrochemical performance of SEBs. A blend of sPPSLi and PVP is coated on $LiNi_{0.9}Mn_{0.05}Co_{0.05}O_2$ particles by spray drying, which reduces capacity loss at the NCM/SE interface. The addition of PVP is required to create a strong bond between NCM and sPPSLi, which enhances interface stability.[43] Analysis of interfacial degradation and Li^+ pathways demonstrate improved electrochemical cycling of a Li_6PS_5Cl-based $^{LiIn}SEB^{NCM}$ with sPPSLi/PVP-coated NCM.

2. Results and discussion

2.1 Characterization of sPPSLi/PVP-coated NCM

We first attempted to apply a 1 wt% anionic sPPSLi coating on NCM (without PVP) using a spray drying apparatus. During spray-drying, the precursor solution is atomized into fine ≈25 μm droplets and quickly dried to coat the NCM surface, ensuring the final composition matches the precursor solution. For reasons of consistency and comparability, the nominal content of 1 wt% of polymer is based on our previous findings that produced a 2 nm coating thickness with cationic PVBTATFSI of the same nominal content.[54] If required, the weight ratio can be further optimized in future work. Unfortunately, water and alcohols that are often good solvents for anionic polymers can leach Li^+ from NCM when exposed to protic solvents during the coating process. To avoid this issue, sPPSLi is dissolved in dimethylformamide (DMF) for the coating of NCM by spray drying.[57] Scanning electron microscopy (SEM) images of the produced sPPSLi-NCM samples show localized deposition of particulate sPPSLi polymer on the sPPSLi-NCM surface (Fig. S2†). The results indicate that the electrostatic attraction between sPPSLi and NCM is insufficient to form a uniform coating on its own. This may be due to layered oxides displaying a negative zeta potential, favoring electrostatic attraction to polycations rather than polyanions in neutral to basic conditions.[58]

Consequently, we use PVP as a coating mediator for sPPSLi, which facilitates a uniform coating of both polymers on NCM.[43] A 1 : 1 weight ratio of PVP to sPPSLi (1 wt% of coating in total compared to NCM) is chosen here to demonstrate its feasibility. SEM images of the produced sPPSLi/PVP-NCM coated powder demonstrate a marked reduction in isolated polymer particles, as shown in Fig. S2.† It is worth noting that a stable and transparent polymer true solution (solute particle size less than 1 nm) is necessary for the spray drying process to form a uniform coating. sPPSLi and PVP create a transparent and stable solution in DMF, which is different to some other polymers that precipitate when mixing with PVP.[59] Using infrared spectroscopy, we find that PVP manifests a robust electrostatic attraction with sPPSLi, indicated by the red-shift in C=O stretching mode from 1669 cm^{-1} to 1656 cm^{-1}, as shown in Fig. S3.† Together, these results suggest a uniform and homogeneous sPPSLi/PVP coating is present on sPPSLi/PVP-NCM as there is no apparent difference in SEM images between pristine NCM (pNCM) and sPPSLi/PVP-NCM.

We use transmission electron microscopy (TEM) to compare pNCM and sPPSLi/PVP-NCM samples. The TEM images in Fig. 1 show that pNCM does not have a surface coating and that sPPSLi/PVP-NCM has an amorphous coating of around 1–3 nm thickness, as is evident from the amorphous surface layer that lies on top of the lattice planes of NCM. Although every investigated particle exhibits a uniform coating layer, TEM alone cannot confirm the chemical composition of the coating. Therefore, we use scanning force microscopy based infrared microscopy (nano-IR) in photo-induced force microscopy mode to verify the composition and distribution of the sPPSLi/PVP coating on the NCM substrate.

In nano-IR (Fig. S4†), an IR laser is focused on the tip of a scanning force microscope. For samples that interact with IR light of a specific wavenumber, photo-induced forces are generated. The photo-induced forces excite oscillation of the cantilever, which can be detected by the photodiode *via* the

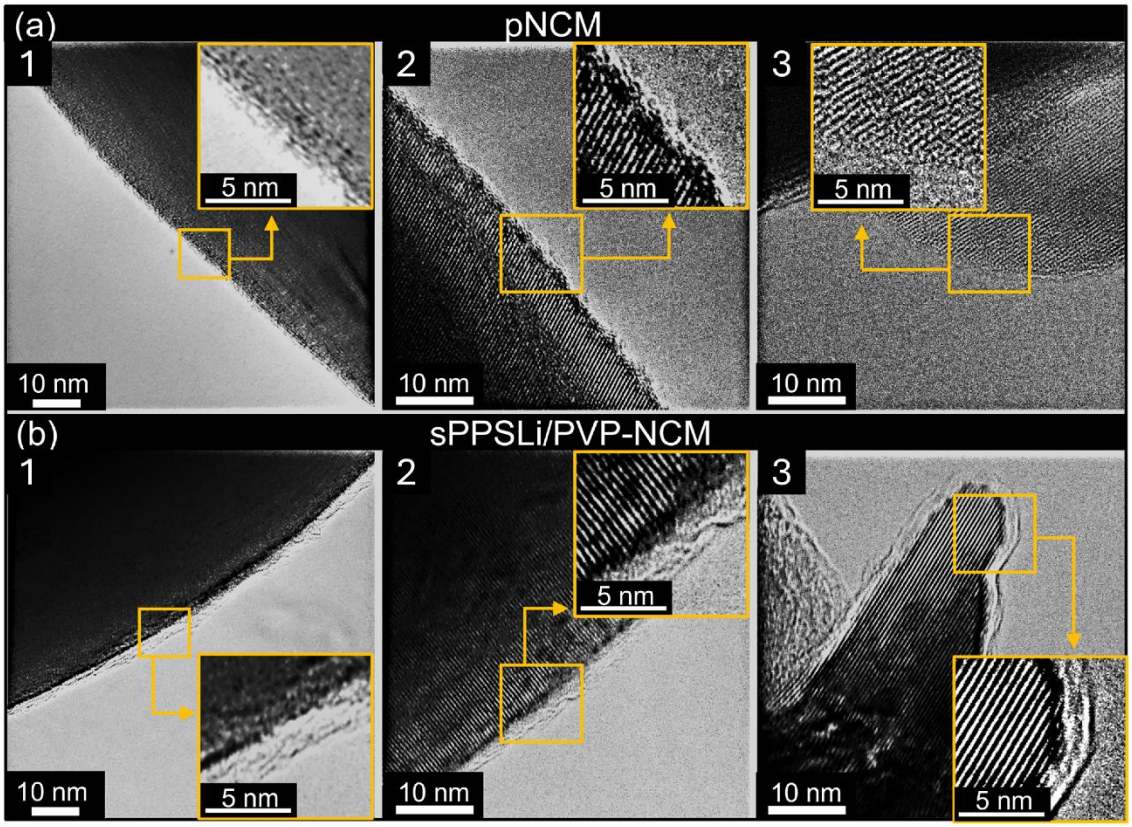

Fig. 1 TEM images of (a) pNCM and (b) sPPSLi/PVP-NCM. The insets show a magnification of the coating layer, providing a clearer presentation of its thickness of around 1 to 3 nm. Each panel is labeled from 1 to 3, showing different particles.

deflected laser beam.[60] The amplitude of oscillation is directly correlated to the absorption of the sample at the used IR wavenumber.[61] For polymer samples, this method has proven useful for determining their lateral distribution.[62]

To verify the polymer on top of the NCM particles, we record nano-IR spectra at several locations on a coated NCM particle (Fig. 2a) and on a reference sample of the polymer (Fig. S5†). Both spectra show the same carbonyl stretching mode and fingerprint between 1500 cm^{-1} and 1000 cm^{-1} (Fig. 2b). The carbonyl stretching shift in the sPPSLi/PVP-NCM nano-IR spectrum, compared to sPPSLi/PVP, likely arises from the unique mechanical properties of nanometer-thick coatings, influenced by polymer chain rearrangement and interactions with NCM.[40,41]

The nano-IR spectra are also identical to the far field Fourier transform infrared spectroscopy (FTIR) absorption spectrum of the polymer. The equivalence of the spectra confirms that the NCM particles are coated with a blend of sPPSLi and PVP. To find potential pinholes in the polymer coating, we scan the surfaces while detecting the nano-IR response at 1677 cm^{-1}, which corresponds to the stretching mode of the carbonyl double bond (Fig. 2c). The nano-IR signal never vanishes in this measurement. We conclude that the sPPSLi/PVP coating is present at every tip position and that the NCM particles are practically fully covered with a layer of sPPSLi/PVP.

To chemically identify the sPPSLi/PVP coating on NCM, time of flight secondary ion mass spectrometry (ToF-SIMS) is used as surface sensitive technique. Therefore, mass spectra of the reference materials such as sPPSLi, PVP and NCM are compared to mass spectra of sPPSLi/PVP-NCM. As illustrated in Fig. 2d, the reference signals for SO^-, C_2SO^- (representing sPPSLi) and $C_3H_6NO^-$ (representing PVP) can be identified on the surface of sPPSLi/PVP-NCM, which confirms the presence of the coating. The NiO_2^- fragment (representing NCM) is also detected, which is probably due to the partial removal of the polymer coating under Bi^{3+} primary ions in the imaging mode.[63] When analyzing the surface in the imaging mode with Bi^{3+} as primary ions (0.1 pA), it can be seen that the intensity of the coating fragments decreases and the intensity of the NCM fragments increases with increasing ion dose (Fig. S6†). This indicates that the polymer coating is gradually removed during the measurement, confirming its very thin nature.

Based on the SEM, TEM, nano-IR, and ToF-SIMS analyses, the sPPSLi/PVP-NCM particles exhibit a uniform 1–3 nm thick coating layer of sPPSLi/PVP. This indicates that the sPPSLi/PVP coating may prevent direct physical contact between NCM and

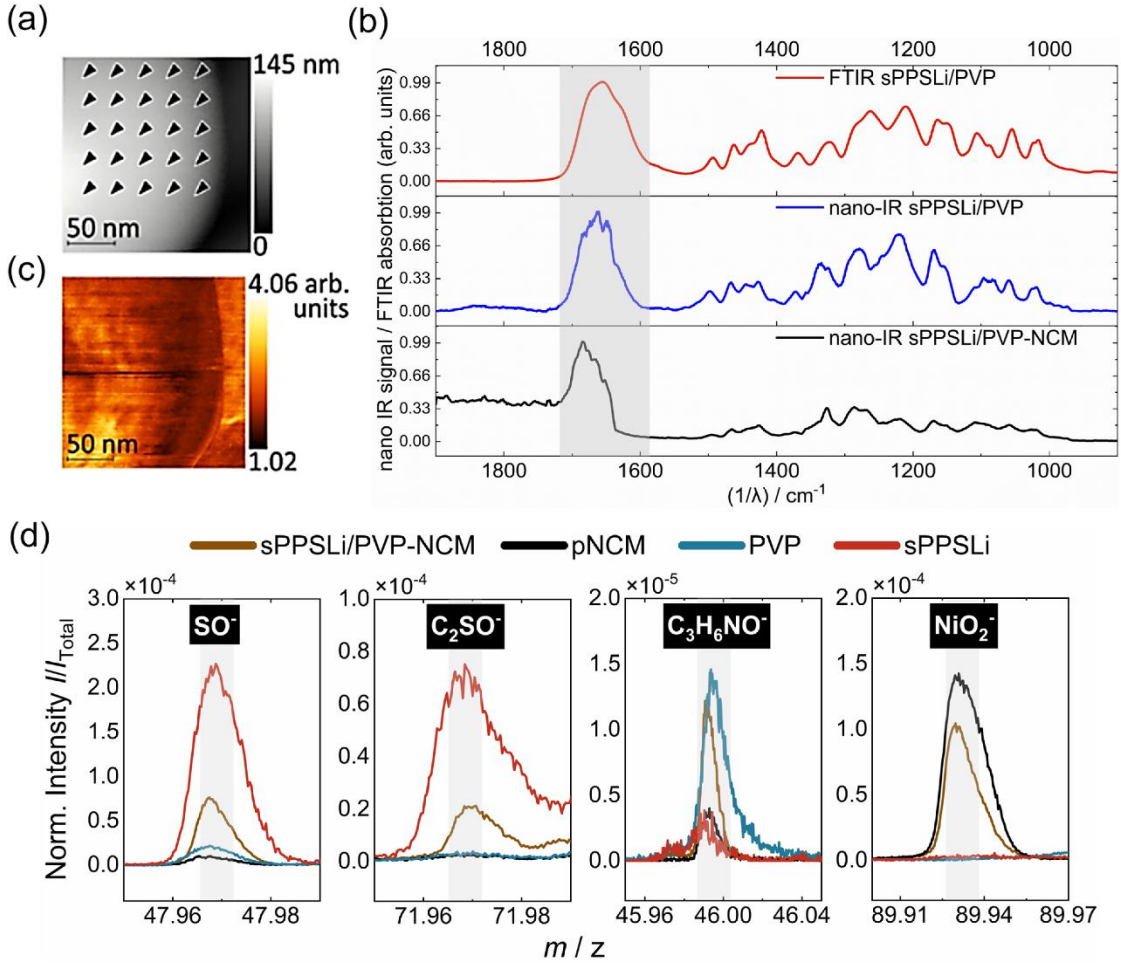

Fig. 2 (a) The topography of a sPPSLi/PVP-NCM particle with positions indicated as triangles where nano-IR spectroscopy is performed. (b) Fourier-transform infrared (FTIR) spectrum of sPPSLi/PVP polymer reference, nano-IR spectrum of sPPSLi/PVP polymer reference, and nano-IR spectrum of sPPSLi/PVP-NCM particles. (c) The stretching mode of the carbonyl double bond (1677 cm^{-1}) is adopted for nano-IR mapping at the same particle as shown in (a). (d) ToF-SIMS analysis of sPPSLi/PVP-NCM, pNCM, PVP and sPPSLi.

SE. The thickness of the sPPSLi/PVP coating of 1–3 nm matches the coating thickness observed to be suitable for coatings of poly(3,4-ethylene dioxythiophene)[42] and cationic polymer PVBTATFSI as well.[54]

2.2 Chemical and electrochemical stability between sPPSLi/PVP and Li_6PS_5Cl

The chemical stability of sPPSLi/PVP and Li_6PS_5Cl is investigated by X-ray diffraction (XRD) and FTIR analyses. Prior to XRD and FTIR analysis, a mixture of sPPSLi/PVP polymer and Li_6PS_5Cl is heated in a vacuum chamber at 80 °C for 24 hours to test whether there is a chemical reaction between the two compounds. The FTIR spectra of the mixed composite before and after heating are identical (Fig. S7a†). This suggests that the molecular structure of the polymer remains unchanged during the heating process. Moreover, the XRD result shows that the mixed composite of the sPPSLi/PVP polymer and Li_6PS_5Cl after 80 °C heating is identical to pristine Li_6PS_5Cl without any heat treatment, which indicates that the bulk structure of Li_6PS_5Cl of the mixed composite is not altered (see Fig. S7b†). Overall, the FTIR and XRD measurements indicate that sPPSLi/PVP polymer is chemically stable to Li_6PS_5Cl.

To assess the electrochemical stability of the sPPSLi/PVP polymer with Li_6PS_5Cl, vapor-grown carbon fibers (VGCFs) are coated with the sPPSLi/PVP polymer utilizing the same spray drying method. Polymer-coated or pristine VGCF is used as the working electrode in combination with a LiIn alloy counter electrode to compare potential side reactions. 80 mg of Li_6PS_5Cl is adopted as the separator. Subsequently, the electrochemical stability of the sPPSLi/PVP polymer with Li_6PS_5Cl is evaluated through cyclic voltammetry, with scanning range from 0 V to 4.5 V (*vs.* In/LiIn). As evident in Fig. S8,† the sPPSLi/PVP-coated

VGCF exhibits a diminished current density and has no additional side reaction peaks compared to pristine VGCF, indicating that the sPPSLi/PVP polymer coating is electrochemically stable to Li_6PS_5Cl.

2.3 Impact of coatings on rate capability

To assess how the presented coatings affect the rate capability of SEBs, pellet-type cells are prepared with Li_6PS_5Cl and cycled under C-rates of 0.1C, 0.25C, 0.5C, 1C (1C corresponds to 2.1 mA cm^{-2}). The general configuration of the $^{LiIn}SEB^{NCM}$ is LiIn|Li_6PS_5Cl|Li_6PS_5Cl/VGCF/NCM, as shown in Fig. S9a.† The rate capability results with pNCM and sPPSLi/PVP-NCM are shown in Fig. 3. Additionally, 1 wt% PVP-coated NCM (PVP-NCM), and 1 wt% PVBTATFSI-coated NCM (PVBTATFSI-NCM) are prepared and tested here to investigate two polymer coatings that do not contain lithium. In comparison, the lithium-containing polymer coating sPPSLi/PVP-NCM demonstrates a considerable improvement in specific capacity (q), particularly at high C-rates.

In the first cycle, pNCM has 183 mA h g^{-1} discharge capacity and 77% Coulomb efficiency; PVBTATFSI-NCM has 170 mA h g^{-1} discharge capacity and 79% Coulomb efficiency; and sPPSLi/PVP-NCM has 188 mA h g^{-1} discharge capacity and 80% Coulomb efficiency. The first cycle Coulomb efficiency is affected by the limited reversibility of Li^+-insertion in the H1 phase of the NCM bulk material.[64] Another contributing factor may be fewer side reactions at the NCM/SE interface.[65] As the coating mainly alters surface rather than bulk properties, the improved discharge capacity and Coulomb efficiency for sPPSLi/PVP-NCM should be due to reduced side reactions and improved interfacial kinetics at the electrode–electrolyte interface.

In contrast, PVP-NCM only achieves 138 mA h g^{-1} discharge capacity and 70% Coulomb efficiency in the first cycle. Among the compared SEBs, the PVP-NCM displayed the lowest capacity across all C-rates. This may be attributed to the insulation of NCM particles through the PVP coating that might obstruct Li^+ and/or electron transport. As some capacity remains, not all NCM surfaces appear to be fully blocked, indicating partial coverage of the NCM with PVP. Partial PVP coverage can be explained by the cell preparation causing damage to the PVP layer and exposing NCM to the electrolyte. This example shows that not any polymer can simply be coated to automatically improve cycling performance, but that careful further analysis into the properties required of a suitable polymer coating must be done.

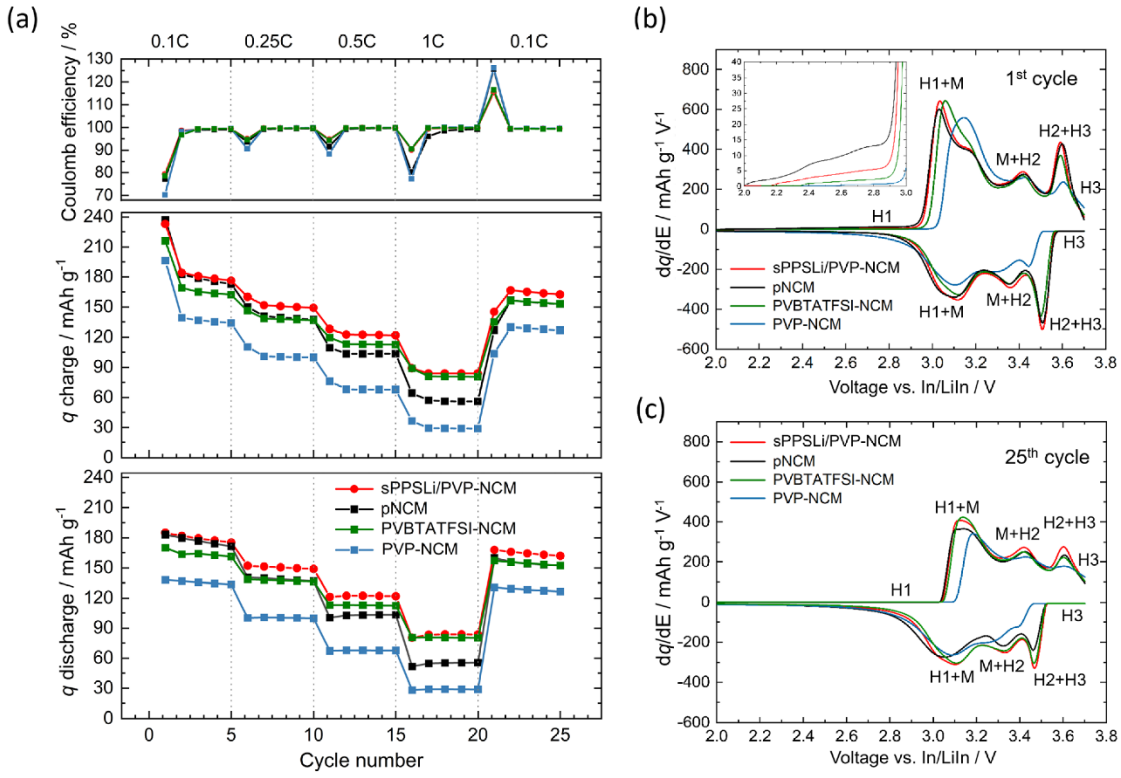

Fig. 3 (a) Specific capacity q and Coulomb efficiency at different C-rates of $^{LiIn}SEB^{NCM}$ using pNCM, sPPSLi/PVP-NCM, PVP-NCM, or PVBTATFSI-NCM, tested at C-rates of 0.1C to 1C in a pellet-type cell (LiIn|Li_6PS_5Cl|Li_6PS_5Cl/VGCF/NCM) with 2.1 mA h cm^{-2} nominal area capacity. Differential capacity dq/dE at 0.1C (b) in the 1st cycle and (c) in the 25th cycle. The inset in (b) shows an enlargement from 2–3 V (*vs.* In/LiIn) of the 1st cycle.

Fig. 3b and c depict the Differential capacity dq/dE of the first and 25th cycle, respectively. Fig. S10† depicts the charge/discharge curves for the first and 25th cycle at a rate of 0.1C. In the first cycle, the differential capacity plots show similar areas above 3.48 V (*vs.* In/LiIn) for sPPSLi/PVP-NCM and pNCM during initial charging, suggesting that the sPPSLi/PVP coating does not affect the H2 + H3 phase transition.[23] Subsequently, sPPSLi/PVP-NCM shows clearer H2 + H3 phase transition than pNCM in the first discharge cycle. Additionally, the inset within Fig. 3b shows that all coated NCM have lower differential capacity than pNCM below 3 V (*vs.* In/LiIn) during initial charging, indicating less electrochemical degradation of Li_6PS_5Cl for all coated NCM compared to pNCM.[66] The electrochemical degradation is indicative of the oxidation of Li_6PS_5Cl forming sulfur and P_2S_5 starting from about 2 V *vs.* In/LiIn.[17,19] H1/M (3 V *vs.* In/LiIn) and H2/H3 (3.6 V *vs.* In/LiIn) transitions are primarily influenced by active mass utilization and kinetic limitations at the NCM|Li_6PS_5Cl interface.[23] The first cycle dq/dE result reflects the improvement of the first cycle Coulomb efficiency.

At the 25th cycle, sPPSLi/PVP-NCM demonstrates improved reversibility and higher differential capacity compared to pNCM and other coated NCM above 3.48 V *vs.* In/LiIn. This process is associated with the H2 + H3 phase transition, as illustrated in Fig. 3c. The improved H2 + H3 phase transition indicates that the sPPSLi/PVP coating mitigates electrochemical degradation caused by oxidative reactions and chemo-mechanical degradation in this voltage range.[22,23,67] In conclusion, sPPSLi/PVP-NCM shows the best performance of all tested materials, which is mainly due to minimized side reactions without hindering the H2 + H3 phase transitions.

2.4 Evaluation of cycling performance and active mass

To assess the cycling performance, $^{LiIn}SEB^{sPPSLi/PVP\text{-}NCM}$ and $^{LiIn}SEB^{pNCM}$ are investigated using the method as shown in Fig. S9b.†[54] First, the SEBs undergo 0.1C galvanostatic charging to 3.15 V (*vs.* In/LiIn). Then chronoamperometry is performed holding the potential at 3.15 V (*vs.* In/LiIn) until the current decreases to 2%. Chronoamperometry ensures that the impedance can be measured at a fixed SOC at 3.15 V (*vs.* In/LiIn). Following this, electrochemical impedance spectroscopy (EIS) is conducted at 3.15 V (*vs.* In/LiIn), ranging from 1 MHz to 100 μHz. As the charge transfer resistance (R_{ct}) varies with changes in the SOC, the chosen potential of 3.15 V (*vs.* In/LiIn) ensures high Li^+ diffusion coefficient and low R_{ct}.[68,69] Additionally, compared to 3.7 V (*vs.* In/LiIn) after the charging step, 3.15 V (*vs.* In/LiIn) prevents notable degradation during measurement. The SEBs are charged to 3.7 V (*vs.* In/LiIn) and then relaxed for 2 hours. They are then discharged to 2.0 V (*vs.* In/LiIn) with another 2 hours relaxation period. These relaxation periods determine the active mass, which refers to the quantity of NCM involved in the charging and discharging process.[23,54]

Fig. 4a compares the 0.1C cycling performance of sPPSLi/PVP-NCM and pNCM. Initially, the sPPSLi/PVP-NCM displays a discharge capacity of 186 mA h g^{-1}, higher than that of pNCM (181 mA h g^{-1}). After 100 cycles, sPPSLi/PVP-NCM retains 78.3% of its capacity, whereas pNCM retains approximately 69%. After increasing the number of cycles to 152 at the same 0.1C rate, the sPPSLi/PVP-NCM retains a capacity of 71.6%, whereas pNCM has decreased to 59.6%. The larger capacity retention for sPPSLi/PVP-NCM demonstrates that the sPPSLi/PVP polymer coating enhances the long-term cycling stability in SEBs.

Fig. 4b demonstrates a comprehensive comparison of the active mass (m_{act}) calculation results of the tested SEBs. A cell consisting of NCM and a lithium–indium alloy anode has an open-circuit voltage (OCV) with a well-defined correlation to the SOC. The SOC represents the lithium content (denoted as 'x' in $Li_xNi_{0.9}Mn_{0.05}Co_{0.05}O_2$) within NCM. A LEB consisting of NCM and a lithium anode is used to obtain the reference correlation function of OCV *vs.* SOC (Fig. S11†). By utilizing a LEB for the reference correlation function, the influence of contact loss between NCM and the liquid electrolyte on the measurement can be minimized.[70] Based on reference data of the OCV *vs.* SOC, we can ascertain the specific discharge capacity at a particular SOC (q_{SOC}). Consequently, the m_{act} can be acquired using the measured discharge capacity (Q_{meas}) and q_{SOC} *via* eqn (1):[23,54]

$$m_{act}(g) = \frac{Q_{meas}\ (mA\ h)}{q_{SOC}\left(\frac{mA\ h}{g}\right)} \quad (1)$$

sPPSLi/PVP-NCM displays an m_{act} retention of 83.7% after the 152nd cycle, which is higher than that of pNCM (78.8%). The loss of m_{act} is primarily attributed to contact loss, which isolates some NCM particles causing irreversible capacity decay. Contact loss is assumed to encompass two surface degradation mechanisms: firstly, the formation of an electrochemically inactive interfacial layer due to unwanted side reactions (including chemical, electrochemical, and chemo-mechanical degradations); and secondly, the physical separation between the NCM and Li_6PS_5Cl materials. These mechanisms reduce the effective contact area between NCM and Li_6PS_5Cl during cycling, resulting in active mass loss and elevated interface resistance. Therefore, both contact loss mechanisms have a comparable impact on battery performance, making their experimental differentiation difficult. Overall, the sPPSLi/PVP coating improves SEB performance by mitigating detrimental contact loss.

On the other hand, a passivation layer and particle cracking within NCM can extend the Li^+ diffusion pathway. Once cracks form within NCM particles, SEs cannot penetrate these cracks, which leads to an increase of the Li^+ diffusion pathway. The formation of cracks within NCM particles has a stronger influence on the Li^+ diffusion pathway than on the charge transfer at the interface.[23] This increased Li^+ diffusion pathway length causes the disparity between the measured specific discharge capacity (q_{meas}) and the specific capacity contributed by m_{act} (q_{act}) during cycling.[23] The q_{act} is obtained by m_{act} retention and the first cycle q_{meas} *via* eqn (2):[23]

$$\frac{n^{th}\text{cycle}\ m_{act}(g)}{1^{st}\text{cycle}\ m_{act}(g)} \times 1^{st}\text{cycle}\ q_{meas} = q_{act}\ \text{at}\ n^{th}\text{cycle} \quad (2)$$

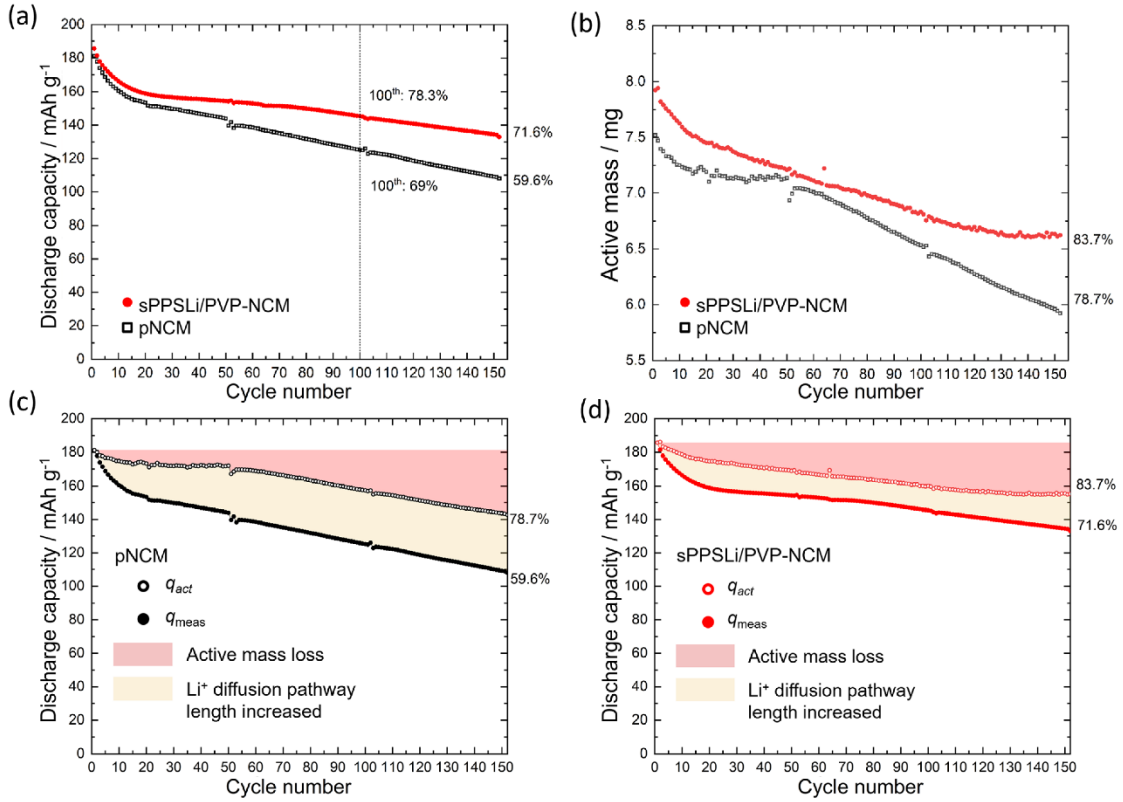

Fig. 4 (a) Cycling performance at 0.1C of $^{LiIn}SEB^{pNCM}$ and $^{LiIn}SEB^{sPPSLi/PVP\text{-}NCM}$ at 25 °C. (b) Corresponding evolution of m_{act}. For (c) pNCM and (d) sPPSLi/PVP-NCM, capacity loss is plotted, respectively, and split into the loss of m_{act} and the loss due to increased Li^+ diffusion pathway length. The pink area represents the loss of m_{act}. The yellow area illustrates the increasing Li^+ diffusion pathway length, determined as the difference between q_{meas} and q_{act}.

The q_{act} is compared with q_{meas}, as shown in Fig. 4c and d. The capacity decay caused by the increase of the Li^+ diffusion pathway length is assumed as the difference between q_{meas} and q_{act}. The $^{LiIn}SEB^{pNCM}$ exhibits a more pronounced increase in Li^+ diffusion pathway length and a more significant m_{act} loss (see Fig. 4c) than the $^{LiIn}SEB^{sPPSLi/PVP\text{-}NCM}$ (see Fig. 4d). In the following sections of this paper, we analyze how the sPPSLi/PVP coating mitigates both contact loss and increase of Li^+ diffusion pathway length.

2.5 Interfacial degradation analyzed by EIS and ToF-SIMS

To explore contact loss in-depth, the interfacial resistance in SEBs is measured at 3.15 V (*vs.* In/LiIn) under 0.1C by EIS, as mentioned in Section 2.4. The impedance data and fitting results using the transition line model[22,71] are shown in Fig. 5. The transition line model is used to characterize the resistance of the composite cathode, including electronic resistance (R_{ele}), ionic transport resistance (R_{ion}), and charge transfer resistance (R_{ct}), as shown in Fig. 5a. The finite-space Warburg element of cylindrical particles (Z_{fs}) describes the complex geometry of Li^+ diffusion in NCM by fitting the finite space diffusion tail in the Nyquist plot. C_{dc} stands for the differential capacitance of NCM. C_{int} and C_{ion} denote the constant phase element related to the interfacial capacitance and ionic transport capacitance within the cathode composite, respectively. The transition line model coupled with electrolyte resistance (R_Ω), resistance of anode (R_{anode}), and anode capacitance (C_{anode}) are used to model the whole SEB.[22]

R_{ct} is employed as a metric for contact loss and interface degradation. However, it is challenging to extract R_{ct} from the EIS data using a transition line model. This is because the impedance follows a typical Gerischer-type relationship.[67] Consequently, we determine the composite resistance of the cathode, denoted as $R_{cathode}$. This is defined as the geometric mean of R_{ct} and the sum of R_{ele} and R_{ion} *via* eqn (3):

$$R_{cathode} = \sqrt{R_{ct} \times (R_{ele} + R_{ion})} \quad (3)$$

The fitting results are shown in Fig. 5c and Table S1.† In the initial cycle at a voltage of 3.15 V (*vs.* In/LiIn), it is observed that $R_{cathode}$ of sPPSLi/PVP-NCM is 8 Ω cm^2 higher than that of pNCM (18 Ω cm^2 for pNCM and 26 Ω cm^2 for sPPSLi/PVP-NCM). The observed deviation may arise from the additional charge transfer and Li^+ transport resistances of the coating. It is worth noting that ionic conductivity of sPPSLi/PVP polymer is around 3.4×10^{-8} S cm^{-1} at 25 °C (Fig. S12†). This indicates that a ~1–

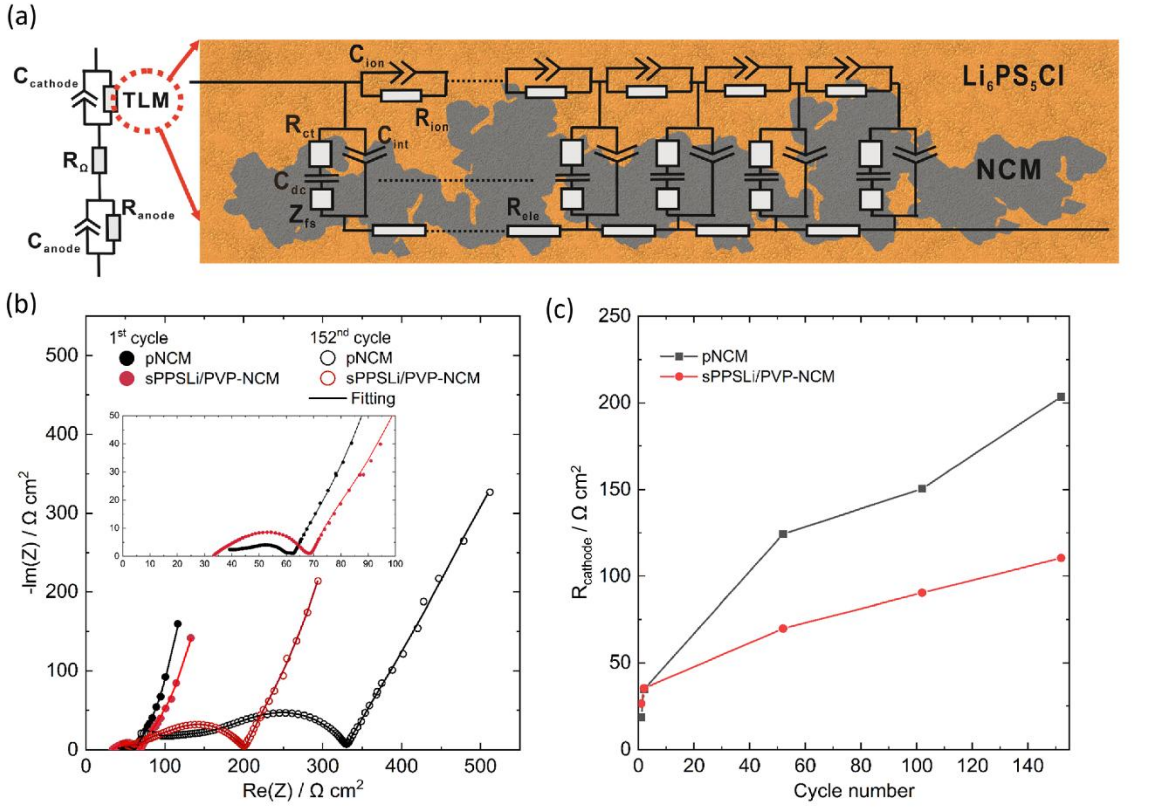

Fig. 5 (a) Equivalent circuit for impedance fitting in the form of the transition line model. R_{ct}, R_{ele}, and R_{ion} denote charge transfer, electronic, and ionic transport resistances in the cathode composite, respectively. Z_{fs} denotes the finite-space Warburg element of cylindrical particles. C_{dc} represents the differential capacitance of NCM, while C_{int} and C_{ion} signify interfacial and ionic transport capacitances. The full SEB model integrates the transition line model with R_{Ω}, R_{anode}, and C_{anode}. (b) Nyquist plots of $^{LiIn}SEB^{pNCM}$ and $^{LiIn}SEB^{sPPSLi/PVP\text{-}NCM}$ at 25 °C during the 1st and 152nd cycles. (c) The $R_{cathode}$ values of different cycles of $^{LiIn}SEB^{pNCM}$ and $^{LiIn}SEB^{sPPSLi/PVP\text{-}NCM}$ are compared.

3 nm coating might contribute around ~3–9 Ω cm^2 of Li^+ transport resistance.[26] These aspects necessitate further investigation of interface resistance (NCM/coating and coating/Li_6PS_5Cl) to elucidate the underlying mechanisms.

During cycling, $R_{cathode}$ for pNCM exhibits a more pronounced increase than that of sPPSLi/PVP-NCM: 151 Ω cm^2 for pNCM and 90 Ω cm^2 for sPPSLi/PVP-NCM after 102 cycles, and 203 Ω cm^2 for pNCM and 110 Ω cm^2 for sPPSLi/PVP-NCM after 152 cycles. This results in $R_{cathode}$ for pNCM being about 1.8 times that of the sPPSLi/PVP-NCM after 152 cycles (see Fig. 5b and c). The notable increase in $R_{cathode}$ for pNCM after cycling may be due to contact loss at the NCM/SE interface. This result is consistent with the lower m_{act} retention for pNCM compared to sPPSLi/PVP-NCM after cycling, as discussed above.

ToF-SIMS is performed to identify the decomposition products and to reveal the influence of the sPPSLi/PVP coating on the interfacial degradation due to electrochemical cycling. It allows the detection of interfacial decomposition products such as phosphates and sulfates in the composite cathode, which was comprehensively described by Walther *et al.*[30,72,73] Using this method, the surfaces of the composite cathodes with sPPSLi/PVP-NCM and pNCM were analyzed before cycling and after 152 cycles. Therefore, the current collector of cycled SEBs was removed to access the critical interfaces in the composite cathode. Since the sPPSLi/PVP coating in this work contains SO_2^- groups, the analysis of sulfate/sulfite fragments can lead to misinterpretations of ToF-SIMS data. Thus, only phosphates are considered in the following analysis. Since TOF-SIMS is a mass spectrometry technique that detects fragments generated by Bi^{3+} primary ions, PO_2^- and PO_3^- are sufficient to differentiate phosphorus oxide compounds, while PO^- does not directly represent stable phosphorus oxide compounds.[67,72] In this context, it should be noted that ToF-SIMS is a semi-quantitative method, as signal intensity depends not only on the concentration of the species but also on the chemical surrounding of the analyte (matrix effects).

In Fig. 6a, the mass spectra of PO_2^- and PO_3^- before cycling and after 152 cycles are exemplarily shown. The amount of PO_x^- fragments, in particular PO_2^- and PO_3^-, is lower for the coated than for the uncoated sample, which indicates that the coating reduces the formation of phosphates during cycling. Consequently, decomposition of the solid electrolyte is reduced by the protective function of the sPPSLi/PVP coating. Still, some decomposition products can be detected. This may be caused by

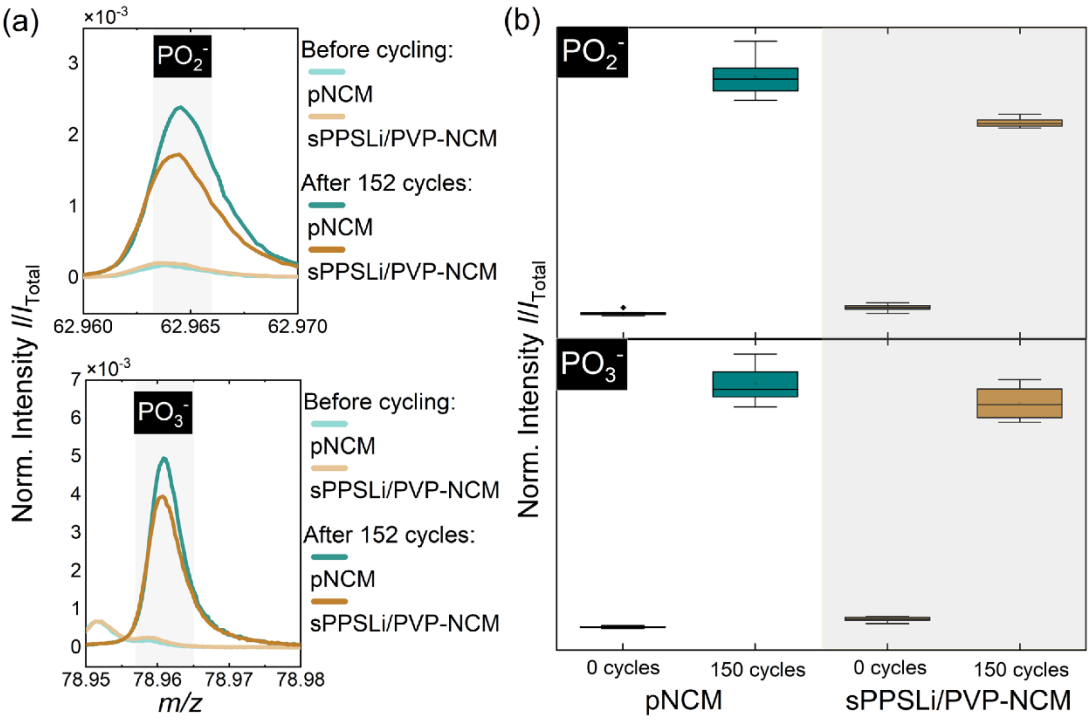

Fig. 6 (a) ToF-SIMS mass spectra for fragments that can be attributed to oxidative interfacial degradation products, such as PO_2^- and PO_3^- for pNCM and sPPSLi/PVP-NCM before cycling and after 152 cycles. (b) Corresponding boxplots of normalized intensities for degradation signals containing eight data points each.

partial detachment of the coating during preparation of the cathode composite, which was ground in an agate mortar. To ensure sufficient statistics and reliability of the data, eight mass spectra at different positions on the same sample were measured before and after cycling. The resulting data is summarized in box plots for semiquantitative comparison in Fig. 6b. The data confirms that the sPPSLi/PVP coating results in less decomposition products in the composite cathodes after electrochemical cycling. In summary, ToF-SIMS analysis of oxidative decomposition products indicates that using a sPPSLi/PVP coating enhances the interfacial stability at the NCM/SE interface, compared to pNCM. This evidence aligns with the results of electrochemical impedance spectroscopy.

2.6 Analysis of Li^+ diffusion pathway length

The growth of the Li^+ diffusion pathway length (L_{diff}) gives rise to capacity decay during battery cycling. Factors such as particle cracking within the NCM and the passivation layer obstructing Li^+ and electron transport can extend L_{diff}. The value of L_{diff} within the cathode composite is determined by fitting the Warburg impedance. The fitting is obtained from the EIS results using the finite-space Warburg element of cylindrical particles (Z_{fs}), with the particle size distribution model (EIS-PSD) (Fig. 5a).[23,54] In addition, chronoamperometry also provides valuable insights into L_{diff}.[54]

The finite-space Warburg impedance is generally used to model the diffusion process across the entire volume of a sample, accounting for the ion-blocking boundary at the current collector as well as the inner core of the NCM particles. When the frequency is sufficiently low to reach the ion-blocking border, a continuous transition is observed in the Nyquist plot, ranging from 45° and gradually approaching 90°.[74,75] As a result, to accurately determine the finite-space Warburg impedance through EIS, the lower frequency limit is set at 100 μHz. The finite-space Warburg element of cylindrical particles ($Z_{fs}^{cylindrical}$) delineates the intricate geometry of Li^+ diffusion within the NCM. The thickness of the cylindrical particle can be taken as L_{diff}, acquired by fitting the EIS finite space diffusion tail using eqn (4) and (5) with the transition line model.

$$\tau_i = L_{diff}^2/\tilde{D}_{Li} \quad (4)$$

and

$$Z_{fs}^{cylindrical} = \frac{1}{C_{diff}}\left(\sum_i \frac{\Delta\phi_i}{\tau_i}\frac{\sqrt{i\omega\tau_i}}{\coth\sqrt{i\omega\tau_i}}\right) \quad (5)$$

In eqn (4), τ_i is the characteristic time constant of Li^+ diffusion. The diffusion coefficient of Li^+ in NCM ($\tilde{D}_{Li}$) is assumed to be around 10^{-11} cm^2 s^{-1} at 25 °C.[23,54] In eqn (5), the volume fraction of the particle contribution is denoted as $\Delta\phi_i$, indicating the amount of the NCM particle which has L_{diff} of τ_i to reach the finite condition. $C_{diff} = dq/dE$ equating to 392 mA h V^{-1} g^{-1} is the total differential capacity at 3.15 V (*vs.* In/LiIn) calculated

from cycling results of a $^{Li}LEB^{NCM}$ (see Fig. S11†). ω is the radial frequency. Fitting of the impedance data leads to L_{diff} and $\Delta\phi_i$, presented cumulatively in Fig. 7a.

At the initial cycle at 3.15 V (*vs.* In/LiIn), pNCM and sPPSLi/PVP-NCM show comparable L_{diff}, around 1.3 μm, matching the NCM particle radius. By the 152nd cycle, the L_{diff} for pNCM is twice as large as that for sPPSLi/PVP-NCM (5.2 μm for pNCM and 2.5 μm for sPPSLi/PVP-NCM). In conclusion, EIS-PSD fitting results show that a 1 wt% sPPSLi/PVP polymer coating layer mitigates the growth of L_{diff}. Fig. 7b shows that the chronoamperometry results confirm the conclusion of EIS-PSD.[23] The time it takes for the current to decrease below 2% is directly proportional to L_{diff}.[54,76] Initially, pNCM and sPPSLi/PVP-NCM exhibit an identical current reduction time, indicating that they possess the same L_{diff}. However, pNCM takes around 800 minutes at the 152nd cycle, whereas sPPSLi/PVP-NCM takes only about 400 minutes at the 152nd cycle. Overall, both EIS-PSD analysis and chronoamperometry results show that the L_{diff} for sPPSLi/PVP-NCM is about half that of pNCM after 152 cycles. This result aligns with the higher capacity loss in pNCM than sPPSLi/PVP-NCM due to higher L_{diff}, as shown in Fig. 4c and d.

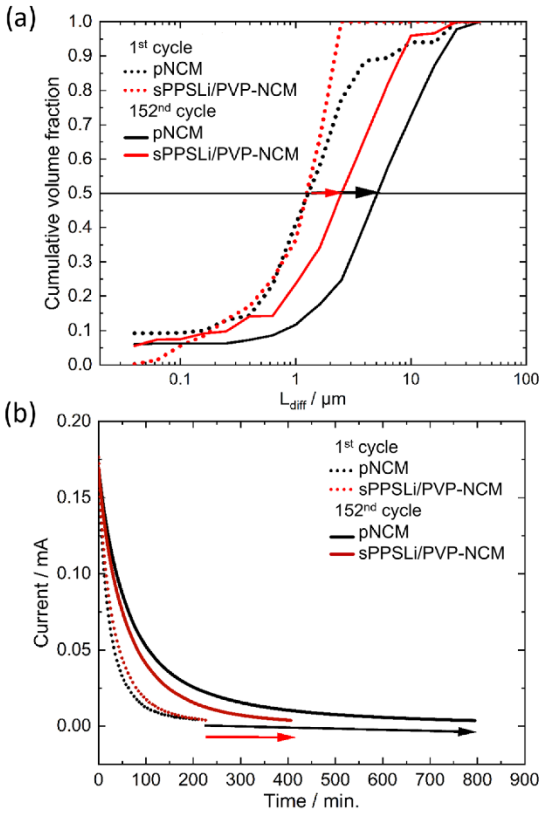

Fig. 7 (a) L_{diff} obtained using the EIS-PSD model for $^{LiIn}SEB^{pNCM}$ and $^{LiIn}SEB^{sPPSLi/PVP\text{-}NCM}$ in the 1st and 152nd cycles. The Warburg impedance is fitted through the EIS-PSD model to yield the cumulative volume fraction of particle size of different L_{diff}. (b) The chronoamperometry measurement shows the duration required for the current to drop below 2% of the initial charging current, which is proportional to L_{diff}.

2.7 SEM cross-sections of NCM cathode before and after cycling

Using ion beam milling with SEM, we examine the morphology changes within cross-sections of composite cathodes of $^{LiIn}SEB^{pNCM}$ and $^{LiIn}SEB^{sPPSLi/PVP\text{-}NCM}$ after 152 cycles under 0.1C. The NCM particles appear as brighter areas in the SEM images, whereas Li_6PS_5Cl is represented by the darker regions. Before cycling, the coated NCM cathode composite shows no noticeable differences compared to the pristine one. The cracking that

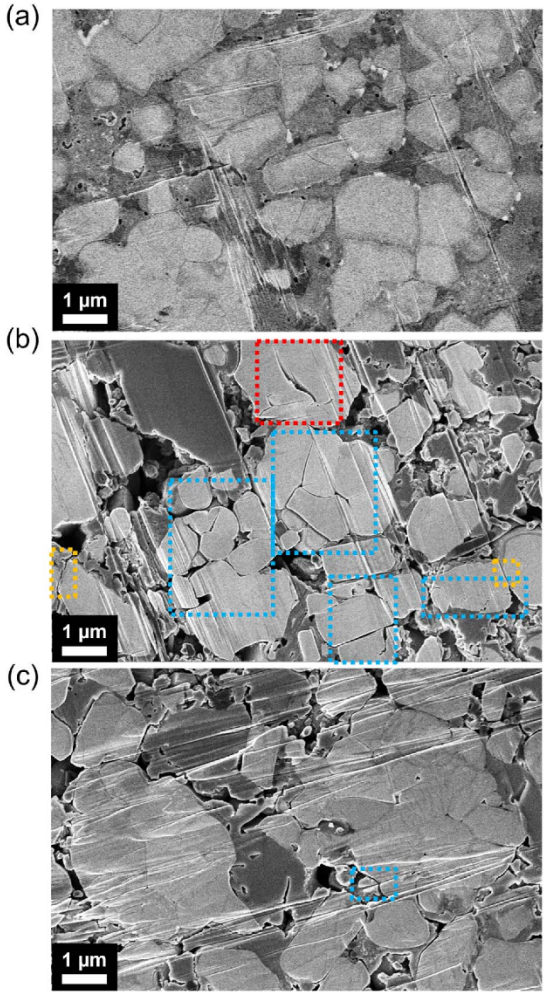

Fig. 8 SEM images of composite cathodes cross-sectioned by ion beam milling. (a) Li_6PS_5Cl/VGCF/pNCM cathode composite before cycling, (b) Li_6PS_5Cl/VGCF/pNCM cathode composite after 152 cycles at a rate of 0.1C, and (c) Li_6PS_5Cl/VGCF/sPPSLi/PVP-NCM cathode composite after 152 cycles at a rate of 0.1C. The red box indicates primary particle cracking, the orange box marks intergranular particle cracking, and the blue box highlights cracking that may be due to either of these causes.

separates whole particles is likely due to intergranular particle cracking. On the other hand, cracking occurring within a particle but not entirely separating the two particles is referred to as primary particle cracking. After 152 cycles, sPPSLi/PVP-NCM has fewer fractures within its particles than pNCM, as shown in Fig. 8. However, both SEBs show physical separation between NCM and Li_6PS_5Cl after cycling.

The reduced number of fractures may be due to less interfacial side reactions during cycling and less extraction of Li^+ from sPPSLi/PVP-NCM.[24] If the Li^+ extraction from NCM is relatively small, especially during the H2 + H3 phase transition, the particles are less likely to fracture.[77] However, the area under the differential capacity plots at around 3.48 V (*vs.* In/LiIn) of the first cycle is similar for pNCM and sPPSLi/PVP-NCM (Fig. 3). This indicates that both SEBs undergo comparable H2 + H3 phase transition processes. Therefore, we can rule out reduced Li^+ extraction from sPPSLi/PVP-NCM as the cause of the reduced cracking. On the other hand, a thin coating of only a few nanometers likely does not suppress the volumetric changes that occur in NCM during cycling. As a result, the cracking within sPPSLi/PVP-NCM particles may be mitigated by minimizing side reactions at the NCM/SE interface during cycling. Overall, sPPSLi/PVP-NCM has lower L_{diff} than pNCM due to less cracking within the particles.

3. Conclusion

To improve capacity retention of NCM in solid-state batteries, we present a sPPSLi/PVP polymer coating applied on NCM particles through spray drying. Nano-IR imaging, TEM images, and SIMS analysis show uniform coverage of NCM by a 1–3 nm thick sPPSLi/PVP layer. Electrochemical tests highlight enhanced cycling stability and rate performance of sPPSLi/PVP-NCM over the uncoated pNCM. The sPPSLi/PVP coating improves battery performance by stabilizing the NCM/Li_6PS_5Cl interface and shortening the Li^+ diffusion pathway compared to pNCM. In the rate capability test, sPPSLi/PVP-NCM consistently outperforms pNCM and other polymer-coated NCMs for all tested C-rates (0.1–1C). Results from the ToF-SIMS analysis of oxidative decomposition products and electrochemical impedance spectroscopy confirm the improvement of interfacial stability at the NCM/Li_6PS_5Cl interface during cycling. Moreover, the $^{LiIn}SEB^{sPPSLi/PVP\text{-}NCM}$ exhibits a shorter L_{diff} compared to the $^{LiIn}SEB^{pNCM}$ after cycling, as evidenced by EIS-PSD analysis and chronoamperometry. SEM images of composite cathode cross-sections show that a 1–3 nm thick sPPSLi/PVP coating can mitigate particle cracking, leading to enhanced solid-state battery performance. It is evident that polymer coatings can be used to improve cycling performance, which demonstrates the significance of applying polymer coatings in developing high-performance batteries.

4. Experimental methods

4.1 Reagents and materials

VGCF and DMF are purchased from Sigma-Aldrich. $LiNi_{0.9}Mn_{0.05}Co_{0.05}O_2$ is purchased from MSE Supplies, with a particle size between 2.0 μm and 6.0 μm and a Brunauer–Emmett–Teller (BET) specific surface area of approximately 0.90 ± 0.25 m^2 g^{-1}. Li_6PS_5Cl is purchased from NEI Corporation. Indium foil with a thickness of 100 μm is sourced from chemPUR GmbH and punched into a 9 mm diameter circular disc. Lithium foil with a thickness of 125 μm is purchased from Albemarle Rockwood Lithium GmbH and punched into a 6 mm diameter circular disc. PVBTATFSI[54] and sPPSLi[56] are synthesized following the respective literature procedures.[55,56] The molecular weight of the sPPSLi polymer is 102 kDa (weight average, determined by gel permeation chromatography) with a polydispersity index of 1.76. PVP (K30) with a molecular weight around 40 kDa is purchased from Sigma-Aldrich.

4.2 Polymer-coated NCM and VGCF

A mini-Spray Dryer B-290 from BUCHI is used to coat various polymers on NCM and VGCF, including PVBTATFSI, sPPSLi, PVP, and sPPSLi/PVP (1 : 1 ratio of weight). Firstly, 20 mg of polymer (1 wt% compared to NCM) is mixed with 2 g of NCM and 30 g of DMF as the NCM precursor suspension. For VGCF precursor suspension, 50 mg of polymer (10 wt% compared to VGCF) is mixed with 500 mg of VGCF and 30 g of DMF. This mixture is stirred vigorously for 1 hour before spray drying. However, the VGCF precursor is first sonicated by ultrasonic cleaner (VWR®) for 1 hour and then stirred vigorously for 1 hour before spray drying. The inlet temperature for spray drying is set to 200 °C, which is much higher than the DMF boiling point (153 °C). The suction of the vacuum pump is set to 37 m^3 h^{-1}. The feed rate of precursor solution is 4 mL min^{-1} if using DMF as the solvent. The N_2 flow is set to 40 L min^{-1}. The spray drying conditions are optimized to get the highest productivity around 75%. After spray drying, sPPSLi/PVP polymer coated VGCF, sPPSLi/PVP-NCM, PVP-NCM, and PVBTATFSI-NCM are dried in vacuum oven at 80 °C for 72 hours.

4.3 X-ray diffraction (XRD)

XRD is used to check the chemical stability between the sPPSLi/PVP polymer and Li_6PS_5Cl by using a Panalytical Empyrean XRD with Cu Kα radiation. Diffraction patterns are collected in a 2θ angular range from 10° to 85° with a step size of 0.026°, 0.04 rad. soller slits, and 1/2° anti-scatter slit. To check the chemical stability between the sPPSLi/PVP polymer with Li_6PS_5Cl, the sPPSLi/PVP polymer is mixed with Li_6PS_5Cl in a weight ratio of 1 : 1 (around 500 mg in total) by grinding in an agate mortar and then pressed into pellets (8 mm in diameter). After that, the pellets are heated and maintained at 80 °C for 24 hours, followed by a grinding process in the agate mortar to turn pellets into powder. Finally, the sPPSLi/PVP polymer powder after heating is characterized by XRD and compared with pristine Li_6PS_5Cl.

4.4 Fourier-transform infrared spectroscopy (FTIR)

FTIR spectra are recorded with a total number of 96 scans on an ATR-FTIR Thermo Fischer Scientific iD5 ATR spectrometer (550–4000 cm^{-1}). To check the chemical stability between sPPSLi/PVP with Li_6PS_5Cl, the sPPSLi/PVP polymer is mixed

with Li_6PS_5Cl in a weight ratio of 1 : 1 (around 500 mg in total) by grinding in an agate mortar and then pressed into pellets (8 mm in diameter). Subsequently, the pellets are heated and maintained at 80 °C for 24 hours. FTIR spectra are measured in pellet form before and after the heating process.

4.5 Scanning electron microscopy (SEM)

SEM (Merlin, Zeiss) at an acceleration voltage of 3 kV and acceleration current of 200 pA is adopted to characterize the morphology of NCM and particle cracking in the cathode composite after cycling. Back-scattered electron images and secondary electron images are recorded. For characterization of pNCM and sPPSLi/PVP-NCM, samples are measured in powder form, sticking tightly on the conductive copper tape. The particle cracking in the cathode composite after cycling is examined using SEM images taken following ion beam milling (Leica EM TIC 3X). Ion beam milling is conducted at 6 kV and 2 mA for 6 hours, at a temperature of −80 °C.

4.6 Transmission electron microscopy (TEM)

As the polymer is mainly made of the light element carbon, whereas NCM consists of heavier transition metals, the materials exhibit a different contrast in TEM bright field images. These images are recorded with a TVIPS TEMCam XF416FS camera on a JEOL JEM-3010 microscope at 300 kV acceleration voltage. For this purpose, powder of uncoated or coated NCM particles is sprinkled on a holey carbon copper TEM grid. Loose powder is removed by evacuating the TEM holder in a pumping stand before transferring it to the TEM to preserve the TEM vacuum.

4.7 Time-of-flight secondary ion mass spectrometry (ToF-SIMS)

Time-of-flight secondary ion mass spectrometry (ToF-SIMS) is carried out using a M6 Hybrid SIMS (IONTOF GmbH) equipped with a 30 kV Bi-cluster primary ion gun for analysis. During ToF-SIMS measurements, charged fragments are obtained through a collision cascade caused by the impact of the high-energy primary ion beam. All samples are prepared in a glovebox, attached to the sample holder using non-conductive adhesive tape and transferred to the SIMS instrument using the LEICA EM VCT500 shuttle (Leica Microsystems). In this work, sPPSLi and PVP polymers are first investigated in pure form and then compared with pristine and coated NCM. In addition, pristine (before cycling) and cycled (after cycling) composite cathodes are analyzed with uncoated and coated NCM. Therefore, the stainless-steel current collector was removed after cycling. All samples were prepared in the same way and under the same conditions. If not specified otherwise, the instrument was operated in the spectrometry mode using Bi_3^+ as primary ion species (0.19 pA) in the negative mode, which provides high mass resolution (full width at half maximum (FWHM) $m/\Delta m >$ 16 000 @ $m/z = 62.97$ (PO_2^-)). The analysis area is set to 75 × 75 μm^2, which is scanned with 64 × 64 pixels and a primary ion dose of 10^{12} ions cm^{-2} to keep the static limit. The spectra are calibrated on the following species: C^-, C_2^-, C_3^-, C_4^-, PO^-, PO_2^- and PO_3^-. To ensure reliability of our data, 8 mass spectra were measured per sample. For imaging, Bi_3^+ as primary ion species in imaging mode was used (0.11 pA). The area for imaging is set to 20 × 20 μm^2, which is scanned with 256 × 256 pixels. The evaluation of the ToF-SIMS data was performed with the software SurfaceLab 7.3 (IONTOF GmbH).

4.8 Scanning force microscopy based infrared spectroscopy (nano-IR)

We perform nano-IR using the photo-induced force microscopy mode in the Visa Scope by Molecular Vista. We measure surface topography and photo-induced force microscopy amplitude simultaneously. For the topography measurement, we mechanically excite the cantilever at its second resonance frequency. The topography is recorded by an electronic feedback loop that kept the amplitude of the oscillation constant by varying the tip-sample distance. The photo-induced force microscopy amplitude is recorded at the first resonance frequency of the cantilever. This is achieved by modulating the incoming IR light at a frequency equal to the difference between the first and second eigenmodes. In this way, the modulated IR light generates a sideband of the excitation at the second resonant frequency, which is located at the first resonance frequency. Spectra of the photo-induced force microscopy amplitude are recorded by sweeping the wavenumber of the IR light. During the recording of the spectra, the incoming laser power is kept constant using a polariser. The spectral data was exported and then imported into OriginPro 2022 (version 9.9.0.225). Each individual spectrum is normalized based on its maximum photo-induced force microscopy amplitude. The data was then smoothed using the adjacent averaging filter with an averaging window of 10 pixels. Data visualization for the topography and nano-IR signal mapping was performed by Surface Works 3.0 by Molecular Vista and Inkscape 1.3.

4.9 Electrode composite and cell assembly

Cell tests are conducted using pellet-type cells inside an argon-filled glovebox (LabMaster, MBraun, Garching, Germany) with less than 0.1 ppm each of O_2 and H_2O. For most electrochemical analysis except cyclic voltammetry and ionic conductivity tests, asymmetric cells for rate capability and cycling performance are assembled as InLi|Li_6PS_5Cl|Li_6PS_5Cl, VGCF, and NCM. First, 80 mg of Li_6PS_5Cl is pressed into a 10 mm diameter pellet inside a cylindrical PEEK insulator. The cathode composite is formed by mixing the weight ratio of 69.3% NCM (either pristine or coated), 29.7% Li_6PS_5Cl, and 1% VGCF. This mixture is ground in an agate mortar for about 20 minutes. 12 mg of this cathode mixture is then pressed onto one side of the electrolyte, resulting in an area mass loading of 10.6 mg cm^{-2}. On the opposite side, indium (100 μm thick, 9 mm diameter) and lithium foils (125 μm thick, 6 mm diameter) serve as the anode. Post-assembly, the cell is compressed under 30 kN for 3 minutes using automatic press Atlas Autotouch automatic press, yielding a 400 μm solid electrolyte alongside a 30 μm composite cathode. During the analysis, the assembled cell is placed in an external aluminum frame exerting approximately 50 MPa of

stack pressure. A cross-sectional representation of this assembly is shown in Fig. S9a.†

For cyclic voltammetry, the cell setup is LiIn|Li_6PS_5Cl|Li_6PS_5Cl/VGCF in which the VGCF is either polymer-coated or pristine VGCF. To make a 100 mg cathode composite, 9.1 mg of VGCF is combined with 90.9 mg Li_6PS_5Cl and ground for 20 minutes. 80 mg of Li_6PS_5Cl is then pressed into a 10 mm diameter pellet inside the PEEK insulator as a separator. This is followed by pressing 30 mg of the Li_6PS_5Cl-VGCF-composite onto one side of the electrolyte. Like the previous assembly, indium and lithium foils are pressed on the opposite side of the anode. The cell stack is compressed under 30 kN for 3 minutes using automatic press Atlas Autotouch automatic press. During the analysis, the cell is positioned inside an external aluminum frame exerting around 50 MPa.

For the ionic conductivity measurement of the polymer, the cell setup is assembled as follows. Firstly, 0.16 g of dried polymer powder is compressed into a 10 mm diameter pellet in the PEEK at 30 kN for 3 minutes using automatic press Atlas Autotouch automatic press. To make sure that there is no moisture influencing the ionic conductivity, the pellet is further dried under vacuum ($\sim 10^{-2}$ mbar) and 120 °C for 72 hours. Subsequently, both sides are coated with platinum using the sputtering method (Leica Sputter Coater ACE600). Finally, stainless steel stamps are attached on both sides to complete the cell assembly.

4.10 Liquid electrolyte batteries (LEBs)

To create an OCV *vs.* capacity reference curve without the influence of contact loss between CAM and SE, a $^{Li}LEB^{NCM}$ is prepared. The cathode slurry is prepared by dispersing NCM, PVDF binder (Solef 5130, Solvay) and super-P carbon additives (Sigma-Aldrich) in a weight ratio of 94 : 3 : 3 in NMP (Sigma-Aldrich). Then the cathode sheet is prepared by tape casting procedure using the cathode slurry (solid content of 56% and doctor blade thickness of 60 μm). For cell assembly, a cathode with 12 mm diameter is punched from the dried sheet (120 °C for 12 h in vacuum) and pressed at 200 MPa. The electrolyte is 1 M $LiPF_6$ in EC : DEC (1 : 1 vol%) with a glass fiber separator and a Celgard separator (in contact with the cathode side). A 14 mm diameter lithium metal disc is used as the anode. CR2032 coin cell casings with aluminum coating on the cathode cases are used to avoid parasitic currents that appear especially in the first cycles. First two formation cycles to 4.17 V (*vs.* Li^+/Li) includes chronoamperometry at 3 V for 36 hours to ensure stable SEI formation. Then 0.1C pulses for 10 minutes with 2 h subsequent relaxation are applied 80 times with an upper cutoff voltage of 4.3 V (*vs.* Li^+/Li). This is repeated for the discharge. After this pulse-relaxation-procedure similar to GITT experiments, a final checkup cycle similar to the second formation cycle is applied to ensure that no drastic changes to the cell occurred during the experiment.

4.11 Electrochemical analysis

For the cycling stability test, $^{LiIn}SEB^{NCM}$ are charged and discharged under 0.1C (calculated based on the practical capacity of NCM, which is around 200 mA h g^{-1} and 2.1 mA h cm^{-2}) within a voltage window ranging from 2.0 V to 3.7 V (*vs.* In/LiIn) at a constant temperature of 25 °C in a VMP-300 (BioLogic) electrochemical workstation to assess chronoamperometry and EIS. Batteries are first charged under 0.1C to a voltage of 3.15 V (*vs.* In/LiIn). Chronoamperometry is then performed continuously at this voltage until the observed current diminishes below 2% of the charging current. Subsequently, EIS measurements between 1 MHz and 100 μHz are carried out immediately after the chronoamperometry. EIS sinusoidal amplitudes are set at 10 mV (from 1 MHz to 10 mHz), 5 mV (from 10 mHz to 1 mHz), and finally, 3 mV (from 1 mHz to 100 μHz). Amplitudes are adjusted per frequency to approximate a linear current response and reduce errors. Smaller AC amplitudes enhance linearity. After that, the batteries are continuously charged and discharged at a rate of 0.1C. The MACCOR electrochemical workstation is used for continuous cycling stability testing with a constant current of 0.1C. The whole testing process is schematically shown in Fig. S9b.† The impedance fitting model is depicted in Fig. 5a, where the low-frequency segment is fitted with the finite-space Warburg impedance (Z_{fs}). For rate capability tests, SEBs are charged and discharged under C-rates of 0.1C, 0.25C, 0.5C, 1C. within a voltage window ranging from 2.0 V to 3.7 V (*vs.* In/LiIn) at a constant temperature of 25 °C in MACCOR electrochemical workstation.

Cyclic voltammetry experiments are conducted by a VMP-300 Biologic potentiostat at 25 °C to determine the electrochemical stability. The measurement protocol involves a two-electrode setup, with the LiIn anode as the reference and counter electrode. The initial voltage sweeps from the OCV to 4 V relative to the reference electrode at a 1 mV s^{-1} scan rate for the oxidative phase. Subsequently, this sweep direction is inverted until it reaches 0 V before returning to the original potential.

Additionally, the ionic conductivity of sPPSLi/PVP is measured by EIS using VMP-300 Biologic potentiostat with the climate chamber (Weiss Technik) controlling the temperature from 10 °C to 80 °C. EIS sinusoidal amplitude is set at 100 mV from 1 MHz to 100 mHz to enhance the AC current response, compensating for the low ionic conductivity of the polymer film.

Data availability

Supporting data for this article are provided in the ESI.† Additional raw data can be obtained from the corresponding authors upon request.

Author contributions

B. X. S. was responsible for the electrochemical analyses, and general characterization of materials. Y. Y. conducted the TOF-SIMS analysis, while T. D. performed the TEM experiments. F. W. and R. B. conducted the nano-IR analysis. K. V., A. H., and F. H. R. contributed to the analysis and interpretation of the experimental data. A. M. and G. T. provided the anionic polymer. The research concept was conceived by B. X. S. and F. H. R., who also prepared the manuscript. All authors contributed to the manuscript and the analysis of experimental results.

Conflicts of interest

The authors declare no conflict of interest.

Acknowledgements

B. X. S. and F. H. R. acknowledge German Federal Ministry of Education and Research (BMBF) for their financial support through the project FLiPS (03XP0261). Similarly, Y. Y., T. D., K. V., and A. H. appreciate the funding received from the BMBF as part of the FestBatt competence cluster (03XP0433C, 03XP0433D). Additionally, A. H. extends special thanks for the support provided under the BMBF Professorinnenprogramm III. F. W. acknowledges support from theMax Planck Graduate Center with the Johannes Gutenberg University (MPGC). A. M. and G. T. acknowledge funding from the German Federal Ministry of Education and Research project "Fluorfreie MEA" (Grant 03HY106C). The authors also thank Dr Klaus-Dieter Kreuer for guidance and valuable discussions.

References

1 S. Sen and F. H. Richter, *Adv. Sci.*, 2023, **10**, 2303985.
2 J. Schnell, T. Günther, T. Knoche, C. Vieider, L. Köhler, A. Just, M. Keller, S. Passerini and G. Reinhart, *J. Power Sources*, 2018, **382**, 160–175.
3 D. H. S. Tan, Y. S. Meng and J. Jang, *Joule*, 2022, **6**, 1755–1769.
4 X. Yu, R. Chen, L. Gan, H. Li and L. Chen, *Engineering*, 2023, **21**, 9–14.
5 S. Sen, E. Trevisanello, E. Niemöller, B.-X. Shi, F. J. Simon and F. H. Richter, *J. Mater. Chem. A*, 2021, **9**, 18701–18732.
6 Q. Zhang, D. Cao, Y. Ma, A. Natan, P. Aurora and H. Zhu, *Adv. Mater.*, 2019, **31**, 1901131.
7 Y. Guo, S. Wu, Y.-B. He, F. Kang, L. Chen, H. Li and Q.-H. Yang, *eScience*, 2022, **2**, 138–163.
8 A. Banerjee, X. Wang, C. Fang, E. A. Wu and Y. S. Meng, *Chem. Rev.*, 2020, **120**, 6878–6933.
9 Y. Yusim, E. Trevisanello, R. Ruess, F. H. Richter, A. Mayer, D. Bresser, S. Passerini, J. Janek and A. Henss, *Angew. Chem., Int. Ed.*, 2023, **62**, e202218316.
10 R. Chen, Q. Li, X. Yu, L. Chen and H. Li, *Chem. Rev.*, 2020, **120**, 6820–6877.
11 S. Dühnen, J. Betz, M. Kolek, R. Schmuch, M. Winter and T. Placke, *Small Methods*, 2020, **4**, 2000039.
12 Y. Wang, Z. Wang, D. Wu, Q. Niu, P. Lu, T. Ma, Y. Su, L. Chen, H. Li and F. Wu, *eScience*, 2022, **2**, 537–545.
13 T. Demuth, T. Fuchs, F. Walther, A. Pokle, S. Ahmed, M. Malaki, A. Beyer, J. Janek and K. Volz, *Matter*, 2023, **6**, 2324–2339.
14 C. Yu, F. Zhao, J. Luo, L. Zhang and X. Sun, *Nano Energy*, 2021, **83**, 105858.
15 S.-K. Jung, H. Gwon, S.-S. Lee, H. Kim, J. C. Lee, J. G. Chung, S. Y. Park, Y. Aihara and D. Im, *J. Mater. Chem. A*, 2019, **7**, 22967–22976.
16 G. F. Dewald, S. Ohno, M. A. Kraft, R. Koerver, P. Till, N. M. Vargas-Barbosa, J. Janek and W. G. Zeier, *Chem. Mater.*, 2019, **31**, 8328–8337.
17 D. H. S. Tan, E. A. Wu, H. Nguyen, Z. Chen, M. A. T. Marple, J.-M. Doux, X. Wang, H. Yang, A. Banerjee and Y. S. Meng, *ACS Energy Lett.*, 2019, **4**, 2418–2427.
18 Y. Zhu, X. He and Y. Mo, *ACS Appl. Mater. Interfaces*, 2015, **7**, 23685–23693.
19 S. Wang, M. Tang, Q. Zhang, B. Li, S. Ohno, F. Walther, R. Pan, X. Xu, C. Xin, W. Zhang, L. Li, Y. Shen, F. H. Richter, J. Janek and C.-W. Nan, *Adv. Energy Mater.*, 2021, **11**, 2101370.
20 J. Auvergniot, A. Cassel, J.-B. Ledeuil, V. Viallet, V. Seznec and R. Dedryvère, *Chem. Mater.*, 2017, **29**, 3883–3890.
21 T. Bartsch, F. Strauss, T. Hatsukade, A. Schiele, A. Y. Kim, P. Hartmann, J. Janek and T. Brezesinski, *ACS Energy Lett.*, 2018, **3**, 2539–2543.
22 T.-T. Zuo, R. Rueß, R. Pan, F. Walther, M. Rohnke, S. Hori, R. Kanno, D. Schröder and J. Janek, *Nat. Commun.*, 2021, **12**, 6669.
23 G. Conforto, R. Ruess, D. Schröder, E. Trevisanello, R. Fantin, F. H. Richter and J. Janek, *J. Electrochem. Soc.*, 2021, **168**, 070546.
24 H. Zhang, H. Liu, L. F. J. Piper, M. S. Whittingham and G. Zhou, *Chem. Rev.*, 2022, **122**, 5641–5681.
25 T. Nakamura, K. Amezawa, J. Kulisch, W. G. Zeier and J. Janek, *ACS Appl. Mater. Interfaces*, 2019, **11**, 19968–19976.
26 S. P. Culver, R. Koerver, W. G. Zeier and J. Janek, *Adv. Energy Mater.*, 2019, **9**, 1900626.
27 J. Hertle, F. Walther, T. Lombardo, C. Kern, B. Pavlovic, B. Mogwitz, X. Wu, H. Schneider, M. Rohnke and J. Janek, *ACS Appl. Mater. Interfaces*, 2024, **16**, 9400–9413.
28 A. Y. Kim, F. Strauss, T. Bartsch, J. H. Teo, T. Hatsukade, A. Mazilkin, J. Janek, P. Hartmann and T. Brezesinski, *Chem. Mater.*, 2019, **31**, 9664–9672.
29 Y.-J. Kim, R. Rajagopal, S. Kang and K.-S. Ryu, *Chem. Eng. J.*, 2020, **386**, 123975.
30 F. Walther, F. Strauss, X. Wu, B. Mogwitz, J. Hertle, J. Sann, M. Rohnke, T. Brezesinski and J. Janek, *Chem. Mater.*, 2021, **33**, 2110–2125.
31 D. Kitsche, F. Strauss, Y. Tang, N. Bartnick, A.-Y. Kim, Y. Ma, C. Kübel, J. Janek and T. Brezesinski, *Batteries Supercaps*, 2022, **5**, e202100397.
32 R. S. Negi, Y. Yusim, R. Pan, S. Ahmed, K. Volz, R. Takata, F. Schmidt, A. Henss and M. T. Elm, *Adv. Mater. Interfaces*, 2022, **9**, 2101428.
33 F. Strauss, J. H. Teo, J. Maibach, A. Y. Kim, A. Mazilkin, J. Janek and T. Brezesinski, *ACS Appl. Mater. Interfaces*, 2020, **12**, 57146–57154.
34 R. S. Negi, P. Minnmann, R. Pan, S. Ahmed, M. J. Herzog, K. Volz, R. Takata, F. Schmidt, J. Janek and M. T. Elm, *Chem. Mater.*, 2021, **33**, 6713–6723.
35 S. H. Jung, K. Oh, Y. J. Nam, D. Y. Oh, P. Brüner, K. Kang and Y. S. Jung, *Chem. Mater.*, 2018, **30**, 8190–8200.
36 E. A. Wu, C. Jo, D. H. S. Tan, M. Zhang, J.-M. Doux, Y.-T. Chen, G. Deysher and Y. S. Meng, *J. Electrochem. Soc.*, 2020, **167**, 130516.
37 Y.-Q. Zhang, Y. Tian, Y. Xiao, L. J. Miara, Y. Aihara, T. Tsujimura, T. Shi, M. C. Scott and G. Ceder, *Adv. Energy Mater.*, 2020, **10**, 1903778.

38 J. S. Kim, S. Jung, H. Kwak, Y. Han, S. Kim, J. Lim, Y. M. Lee and Y. S. Jung, *Energy Storage Mater.*, 2023, **55**, 193–204.
39 A. Sakuda, A. Hayashi and M. Tatsumisago, *Curr. Opin. Electrochem.*, 2017, **6**, 108–114.
40 J. Chang, K. B. Toga, J. D. Paulsen, N. Menon and T. P. Russell, *Macromolecules*, 2018, **51**, 6764–6770.
41 J. Y. Chung, A. J. Nolte and C. M. Stafford, *Adv. Mater.*, 2011, **23**, 349–368.
42 S. Deng, Y. Sun, X. Li, Z. Ren, J. Liang, K. Doyle-Davis, J. Liang, W. Li, M. Norouzi Banis, Q. Sun, R. Li, Y. Hu, H. Huang, L. Zhang, S. Lu, J. Luo and X. Sun, *ACS Energy Lett.*, 2020, **5**, 1243–1251.
43 Q. Gan, N. Qin, Y. Zhu, Z. Huang, F. Zhang, S. Gu, J. Xie, K. Zhang, L. Lu and Z. Lu, *ACS Appl. Mater. Interfaces*, 2019, **11**, 12594–12604.
44 G.-L. Xu, Q. Liu, K. K. S. Lau, Y. Liu, X. Liu, H. Gao, X. Zhou, M. Zhuang, Y. Ren, J. Li, M. Shao, M. Ouyang, F. Pan, Z. Chen, K. Amine and G. Chen, *Nat. Energy*, 2019, **4**, 484–494.
45 S. H. Ju, I.-S. Kang, Y.-S. Lee, W.-K. Shin, S. Kim, K. Shin and D.-W. Kim, *ACS Appl. Mater. Interfaces*, 2014, **6**, 2546–2552.
46 Y.-S. Lee, W.-K. Shin, A. G. Kannan, S. M. Koo and D.-W. Kim, *ACS Appl. Mater. Interfaces*, 2015, **7**, 13944–13951.
47 Y. Huang, J. Xia, G. Hu, Y. Cao, Z. Peng, J. Fan, Y. Tao, T. Li, Z. Zhang, Z. Xue and K. Du, *Electrochim. Acta*, 2020, **332**, 135505.
48 Y. Cao, X. Qi, K. Hu, Y. Wang, Z. Gan, Y. Li, G. Hu, Z. Peng and K. Du, *ACS Appl. Mater. Interfaces*, 2018, **10**, 18270–18280.
49 E.-H. Lee, J.-H. Park, J.-H. Cho, S.-J. Cho, D. W. Kim, H. Dan, Y. Kang and S.-Y. Lee, *J. Power Sources*, 2013, **244**, 389–394.
50 H. Wang, J. Lin, X. Zhang, L. Wang, J. Yang, E. Fan, F. Wu, R. Chen and L. Li, *ACS Appl. Energy Mater.*, 2021, **4**, 6205–6213.
51 A. Yiğitalp, A. Taşdemir, S. Alkan Gürsel and A. Yürüm, *Energy Storage*, 2020, **2**, e154.
52 D. Becker, M. Börner, A. Friesen, S. Klein, U. Rodehorst, M. Diehl, M. Winter, T. Placke and R. Schmuch, *J. Electrochem. Soc.*, 2020, **167**, 060524.
53 B. Li, G. Li, D. Zhang, J. Fan, D. Chen, Y. Ge, F. Lin, C. Zheng and L. Li, *ChemistrySelect*, 2019, **4**, 6354–6360.
54 B.-X. Shi, Y. Yusim, S. Sen, T. Demuth, R. Ruess, K. Volz, A. Henss and F. H. Richter, *Adv. Energy Mater.*, 2023, **13**, 2300310.
55 C. C. de Araujo, K. D. Kreuer, M. Schuster, G. Portale, H. Mendil-Jakani, G. Gebel and J. Maier, *Phys. Chem. Chem. Phys.*, 2009, **11**, 3305–3312.
56 M. Schuster, K.-D. Kreuer, H. T. Andersen and J. Maier, *Macromolecules*, 2007, **40**, 598–607.
57 Y. Zhou, Z. Hu, Y. Huang, Y. Wu and Z. Hong, *J. Alloys Compd.*, 2021, **888**, 161584.
58 M. H. Pyun and Y. J. Park, *Nanoscale Res. Lett.*, 2016, **11**, 272.
59 C. Lau and Y. Mi, *Polymer*, 2002, **43**, 823–829.
60 A. A. Sifat, J. Jahng and E. O. Potma, *Chem. Soc. Rev.*, 2022, **51**, 4208–4222.
61 R. A. Murdick, W. Morrison, D. Nowak, T. R. Albrecht, J. Jahng and S. Park, *Jpn. J. Appl. Phys.*, 2017, **56**, 8S1.
62 C. Sprau, J. Kattenbusch, Y. Li, E. Müller, D. Gerthsen, R. Berger, J. J. Michels and A. Colsmann, *Sol. RRL*, 2021, **5**, 2100238.
63 T. Sui, B. Song, J. Dluhos, L. Lu and A. M. Korsunsky, *Nano Energy*, 2015, **17**, 254–260.
64 C. Hong, Q. Leng, J. Zhu, S. Zheng, H. He, Y. Li, R. Liu, J. Wan and Y. Yang, *J. Mater. Chem. A*, 2020, **8**, 8540–8547.
65 R. Koerver, I. Aygün, T. Leichtweiß, C. Dietrich, W. Zhang, J. O. Binder, P. Hartmann, W. G. Zeier and J. Janek, *Chem. Mater.*, 2017, **29**, 5574–5582.
66 S. Randau, F. Walther, A. Neumann, Y. Schneider, R. S. Negi, B. Mogwitz, J. Sann, K. Becker-Steinberger, T. Danner, S. Hein, A. Latz, F. H. Richter and J. Janek, *Chem. Mater.*, 2021, **33**, 1380–1393.
67 T.-T. Zuo, F. Walther, J. H. Teo, R. Rueß, Y. Wang, M. Rohnke, D. Schröder, L. F. Nazar and J. Janek, *Angew. Chem., Int. Ed.*, 2023, **62**, e202213228.
68 E. Trevisanello, R. Ruess, G. Conforto, F. H. Richter and J. Janek, *Adv. Energy Mater.*, 2021, **11**, 2003400.
69 W. Waag, S. Käbitz and D. U. Sauer, *Appl. Energy*, 2013, **102**, 885–897.
70 R. Ruess, S. Schweidler, H. Hemmelmann, G. Conforto, A. Bielefeld, D. A. Weber, J. Sann, M. T. Elm and J. Janek, *J. Electrochem. Soc.*, 2020, **167**, 100532.
71 J. Moškon and M. Gaberščcek, *J. Power Sources Adv.*, 2021, **7**, 100047.
72 F. Walther, S. Randau, Y. Schneider, J. Sann, M. Rohnke, F. H. Richter, W. G. Zeier and J. Janek, *Chem. Mater.*, 2020, **32**, 6123–6136.
73 F. Walther, R. Koerver, T. Fuchs, S. Ohno, J. Sann, M. Rohnke, W. G. Zeier and J. Janek, *Chem. Mater.*, 2019, **31**, 3745–3755.
74 J. Song and M. Z. Bazant, *J. Electrochem. Soc.*, 2013, **160**, A15.
75 J. Song and M. Z. Bazant, *Electrochim. Acta*, 2014, **131**, 214–227.
76 M. D. Levi and D. Aurbach, *Charact. Mater.*, 2012, **3**, 913–932.
77 H. Li, A. Liu, N. Zhang, Y. Wang, S. Yin, H. Wu and J. R. Dahn, *Chem. Mater.*, 2019, **31**, 7574–7583.

Supporting Information

Lithiated Polymer Coating for Interface Stabilization in Li_6PS_5Cl-Based Solid-State Batteries with High-Nickel NCM

Bing-Xuan Shi,[a] Franjo Weber,[b] Yuriy Yusim,[a] Thomas Demuth,[c] Kilian Vettori,[a] Andreas Münchinger,[d] Giorgi Titvinidze,[d,e] Kerstin Volz,[c] Anja Henss,[a] Rüdiger Berger, [b] Felix H. Richter*[a]

[a] Institute of Physical Chemistry & Center for Materials Research (LaMa), Justus-Liebig-University Giessen, Heinrich-Buff-Ring 17, 35392 Giessen, Germany

[b] Max Planck Institute for Polymer Research, Ackermannweg 10, 55128, Mainz, Germany.

[c] Department of Physics & Materials Sciences Center (WZMW), Philipps-University Marburg, Hans-Meerwein Straße 6, 35032 Marburg, Germany.

[d] Hahn-Schickard, Georges-Köhler-Allee 103, 79110 Freiburg, Germany

[e] Agricultural University of Georgia, 240 David Aghmashenebeli Alley, 0131 Tbilisi, Georgia

[*] Corresponding author, Felix.H.Richter@phys.chemie.uni-giessen.de

Keywords: Solid-state batteries, polymer coating, cathode, solid electrolyte, interface degradation, polyanion

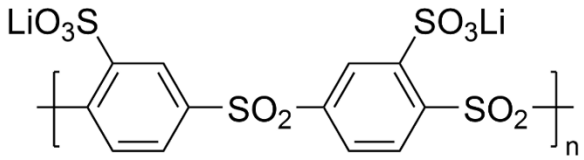

Figure S1. Chemical structure of sulfonated poly(phenylene sulfone) in its lithiated form (sPPSLi).

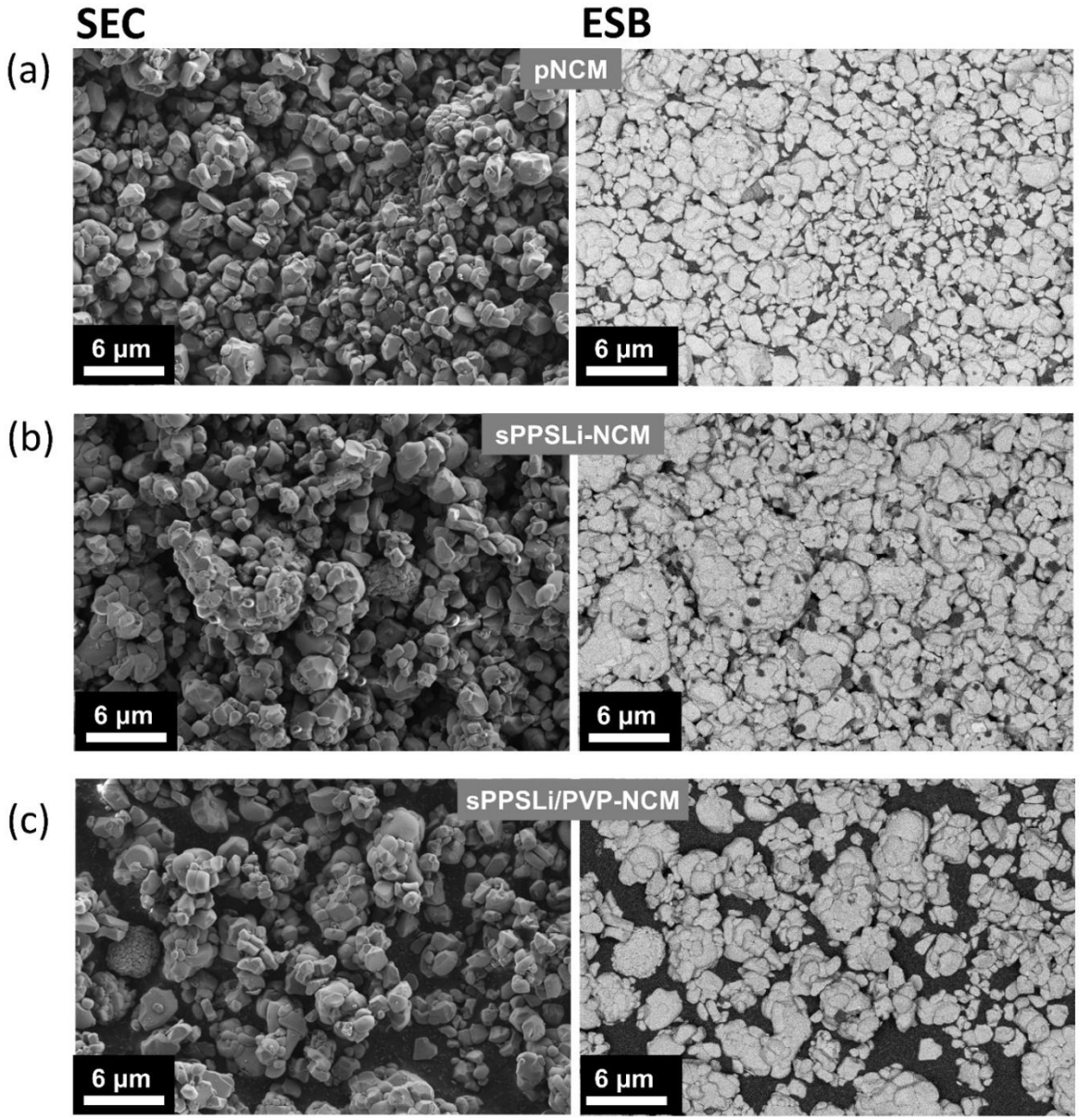

Figure S2. SEM analysis of (a) pNCM, (b) sPPSLi-NCM, and (c) sPPSLi/PVP-NCM with secondary electron images (SEC) shown on the left and energy-selective backscattered electron images (ESB) shown on the right. (Interpretation: sPPSLi-NCM shows some polymer particle aggregation on the surface of NCM, which is evident as dark spots visible in the ESB image of sPPSLi-NCM; in contrast, sPPSLi/PVP-NCM and pNCM show no polymer particles, suggesting that the sPPSLi/PVP-NCM is coated uniformly.)

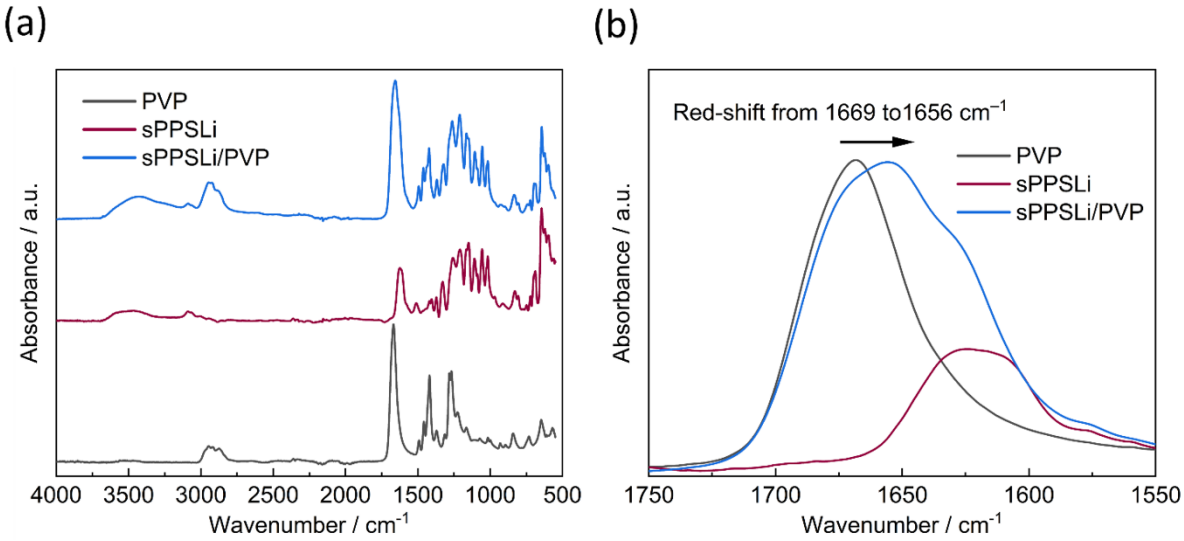

Figure S3. (a) FT-IR spectra of PVP, sPPSLi, and sPPSLi/PVP mixture with 1:1 weight ratio (96 scans each). (b) Magnification of the image in (a) to focus on the region with 1550 cm^{-1} to 1750 cm^{-1} wavenumber. (Interpretation: this region corresponds to the C=O bond. The electrostatic interaction between PVP and sPPSLi is evident from the red-shift observed in the C=O stretching frequency, moving from 1669 cm^{-1} to 1656 cm^{-1}.)

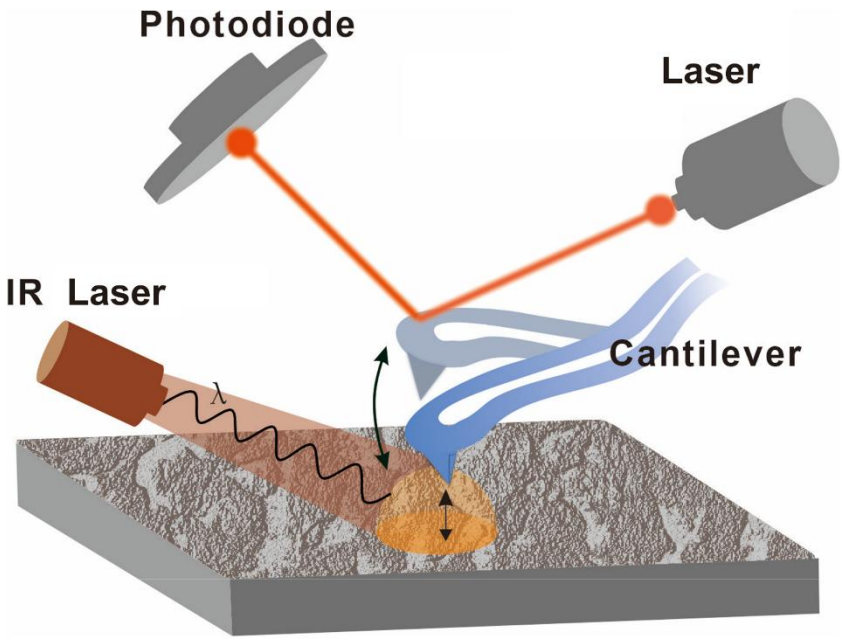

Figure S4. Schematic of the working principle of nano-infrared microscopy (nano-IR).

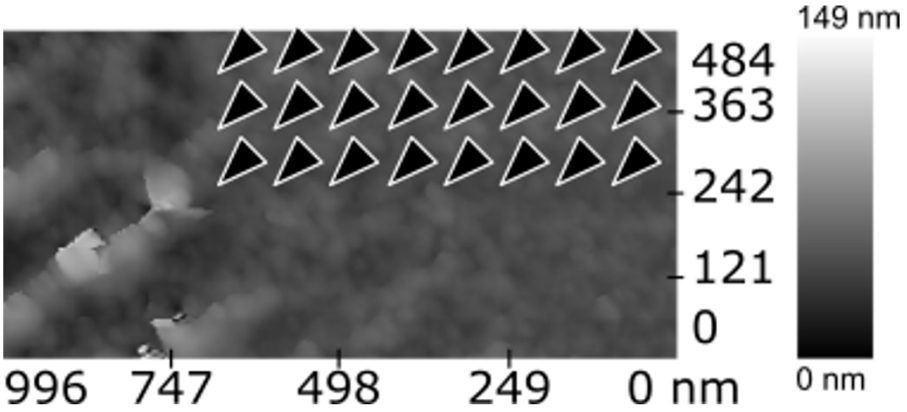

Figure S5. Topography of the sPPSLi/PVP polymer film with positions where photo-induced force microscopy was performed (black triangles). The sPPSLi/PVP polymer film is prepared by pressing sPPSLi/PVP powder into a pellet.

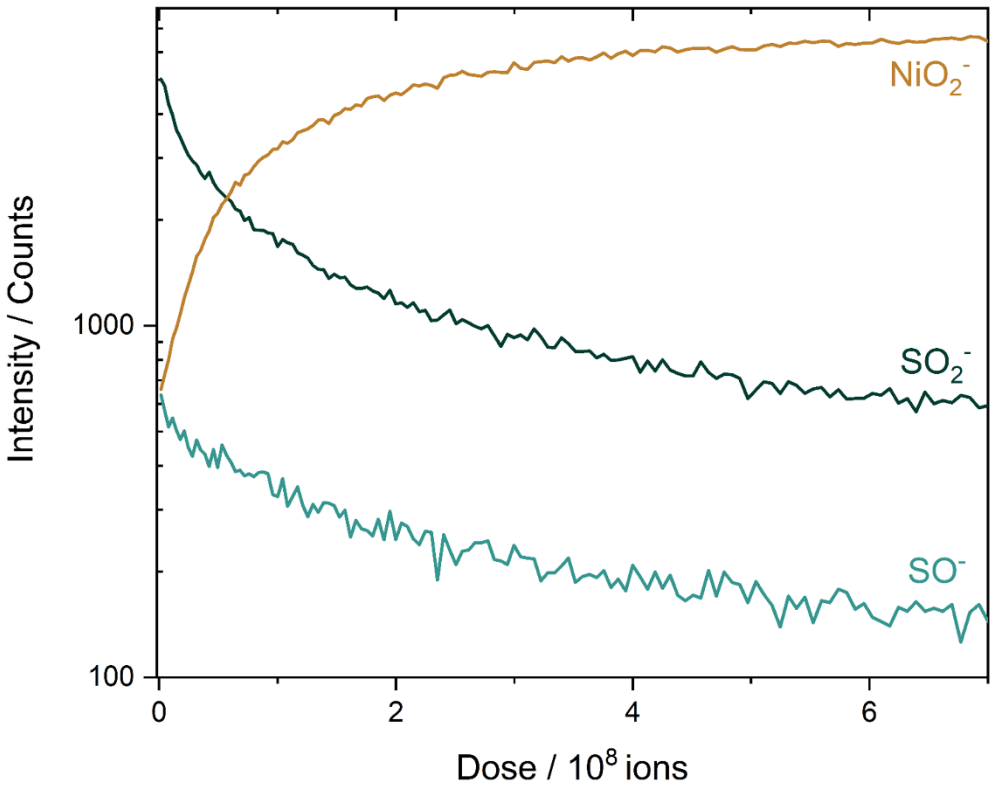

Figure S6. ToF-SIMS depth profiles of sPPSLi/PVP-NCM following the SO_2^-, SO^-, and NiO_2^- fragments. (Interpretation: the SO_2^- and SO^- signals decrease, and the NiO_2^- signal increases when analyzing the surface in the imaging mode with Bi^{3+} as primary ions (0.1 pA). This indicates that the polymer is gradually removed from the surface of the sPPSLi/PVP-NCM particles during the measurement.)

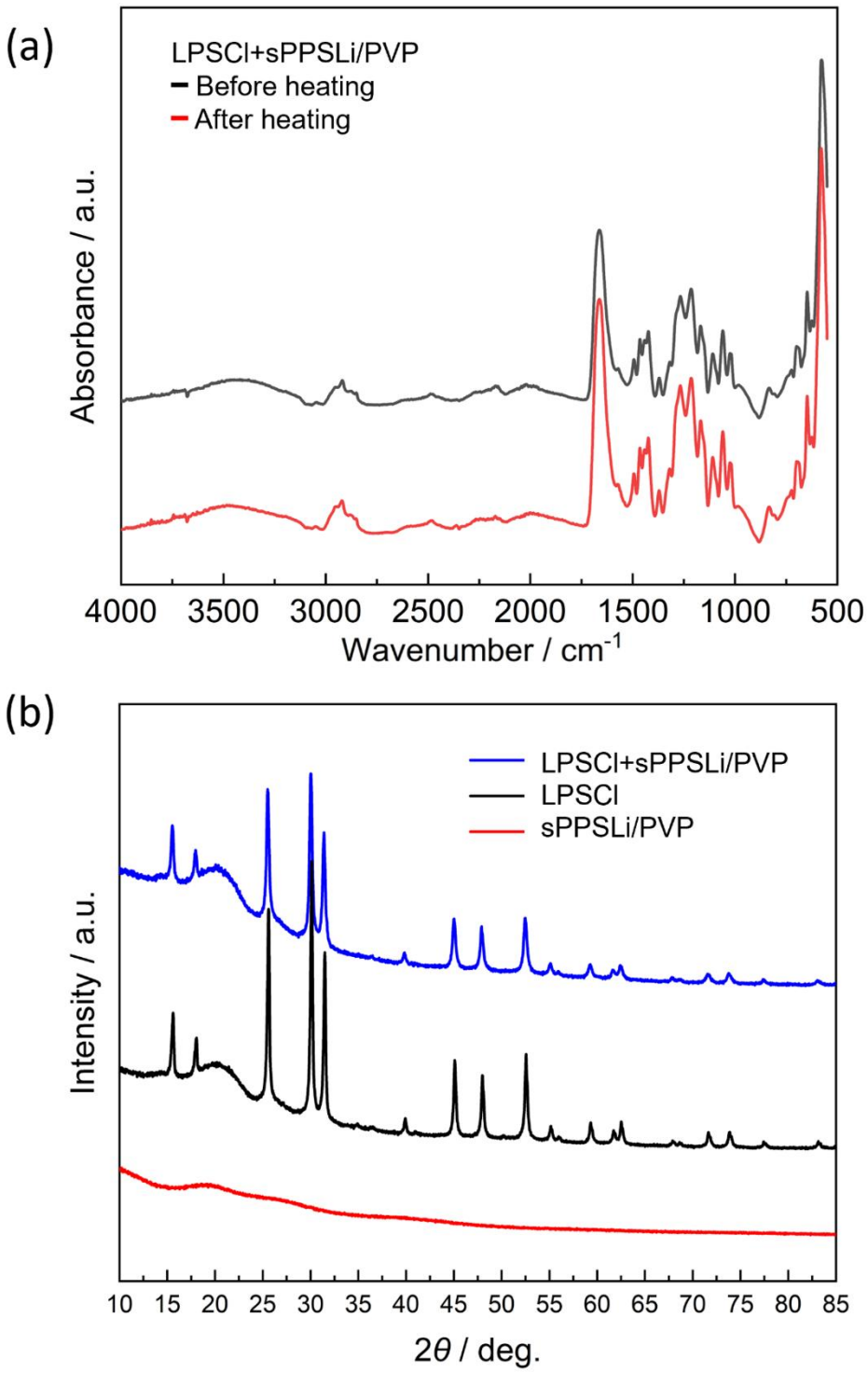

Figure S7. (a) FT-IR of Li_6PS_5Cl mixed with sPPSLi/PVP polymer complex shows no difference before and after heating in a vacuum chamber at 80 °C for 24 hours. (b) XRD patterns of sPPSLi/PVP mixed with Li_6PS_5Cl after heating at 80 °C for 24 hours also match the reflections of Li_6PS_5Cl before heating. In addition, sPPSLi/PVP is shown to be amorphous.

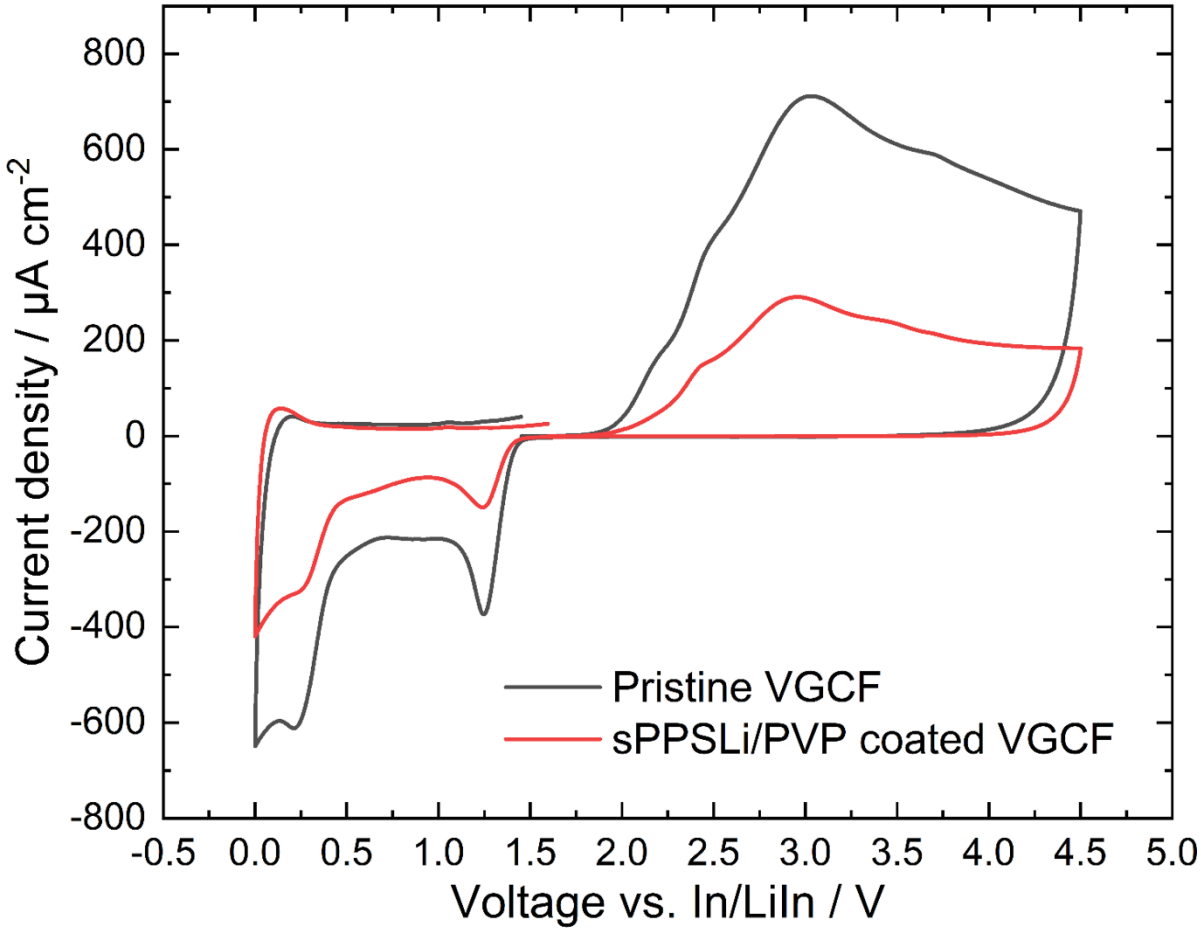

Figure S8. The electrochemical stability window is measured by cyclic voltammetry for the range of 0 V to 4.5 V (vs. In/LiIn) with a scan rate of 1 mV s^{-1}, initiating from the open circuit potential. The electrochemical cell was constructed using VGCF/Li_6PS_5Cl composite as the working electrode, Li_6PS_5Cl as the separator, and an indium-lithium alloy as the counter electrode.

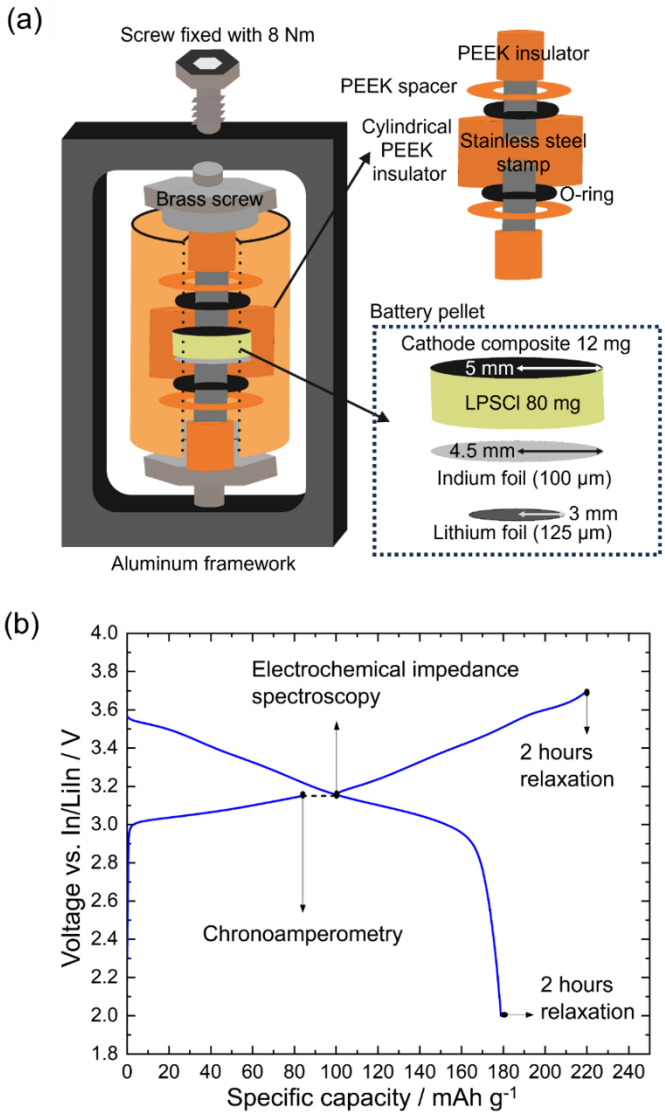

Figure S9. (a) Schematic illustrating the cell casing and the architecture of the SEB pellet. The SEB pellet comprises 12 mg of cathode composite, 80 mg of Li_6PS_5Cl solid electrolyte separator, 9 mm in diameter of indium foil, and 6 mm in diameter of lithium foil, all compacted within a PEEK cylinder. Stainless steel terminals serve as current collectors, while O-rings ensure the SEB pellet remains airtight and protected from external air. (b) Schematic of performed electrochemical analysis. SEBs are initially galvanostatically charged to 3.15 V (vs. In/LiIn). They are held at this potential until the current decreases to below 2% (chronoamperometry). Following this, EIS measurements are taken from 1 MHz to 100 µHz. EIS sinusoidal amplitudes are set at 10 mV (from 1 MHz to 10 mHz), 5 mV (from 10 mHz to 1 mHz), and finally 3 mV (from 1 mHz to 100 µHz). The SEBs are then galvanostatically charged to 3.7 V (vs. In/LiIn), followed by a 2-hour relaxation period. Finally, they are discharged to 2.0 V (vs. In/LiIn) and then undergo another 2-hour relaxation period. The relaxation periods are required for the active mass calculation.

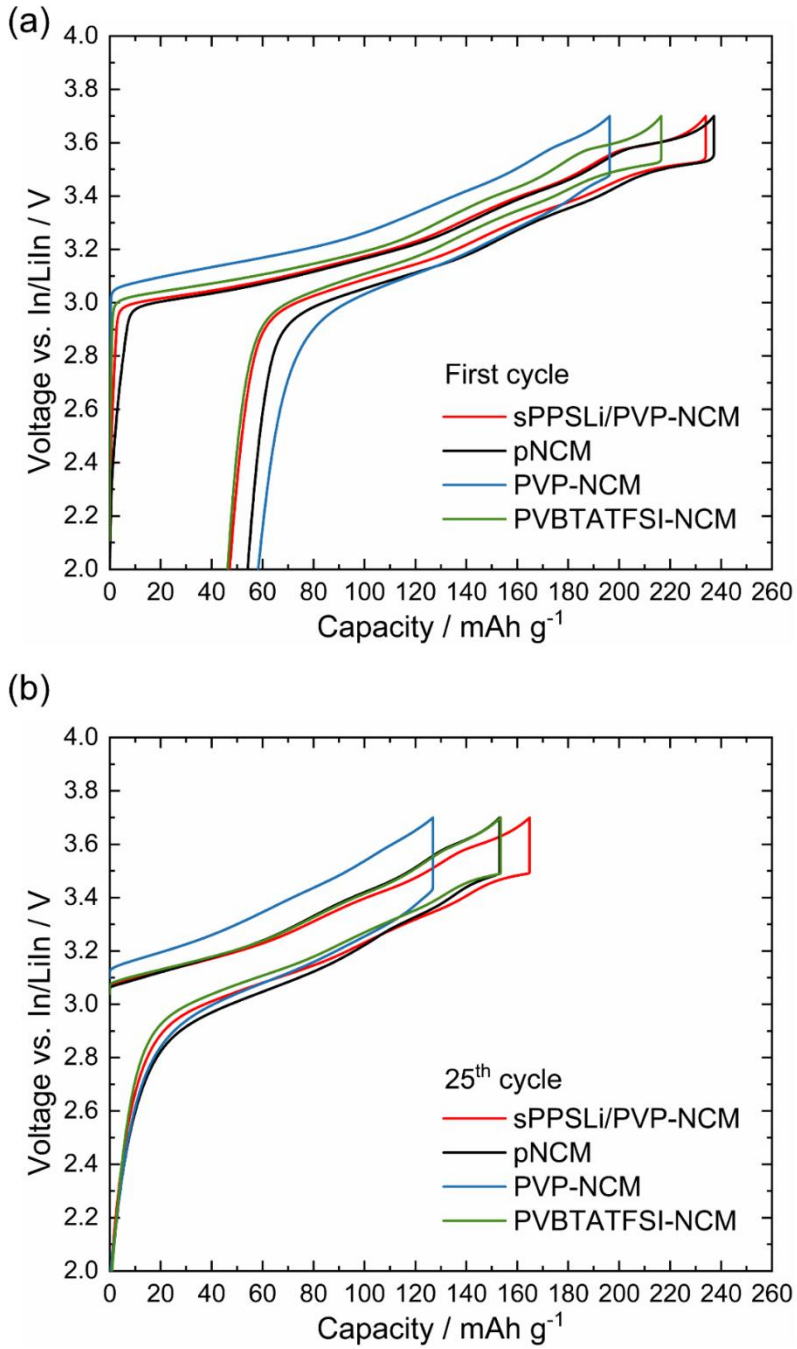

Figure S10. Charge/discharge curves of the (a) first and (b) 25th cycle at 0.1C.

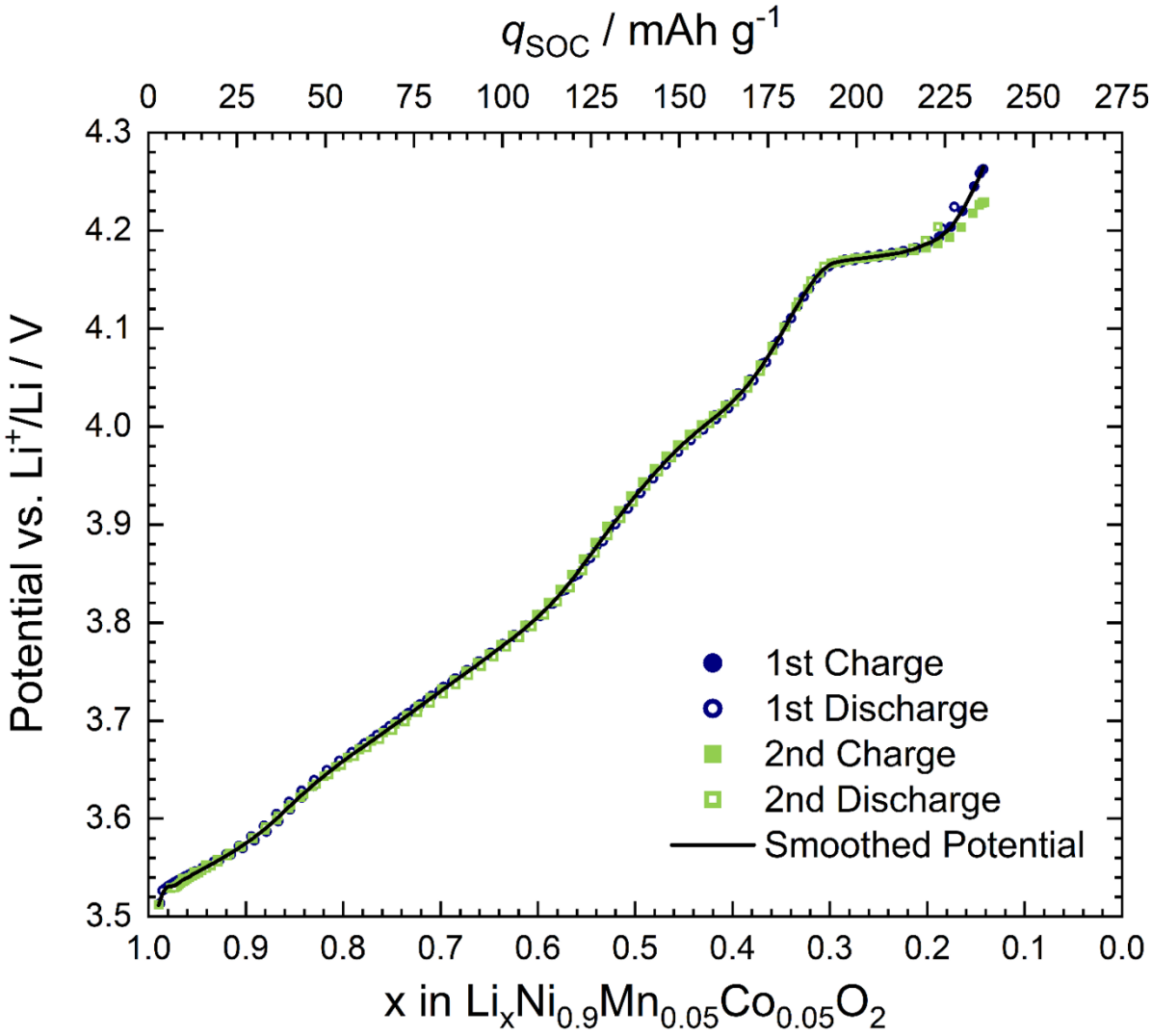

Figure S11. Illustration of the relationship between the open circuit voltage (OCV) (vertical axis) and the state of charge (SOC), represented by the Li^+ content x in $Li_xNi_{0.9}Mn_{0.05}Co_{0.05}O_2$ (horizontal axis). This relationship is derived from galvanostatic charge-discharge cycles of a $^{Li}LEB^{NCM}$ at a rate of 0.1C. Every 10-minute interval of charging or discharging is followed by a two-hour relaxation period to measure the OCV. Using the known time and current to obtain the amount of charge per GITT pulse step, we can calculate x in $Li_xNi_{0.9}Mn_{0.05}Co_{0.05}O_2$.

Table S1. Fitting of impedance data of $^{LiIn}SEB^{pNCM}$ and $^{LiIn}SEB^{sPPSLi/PVP-NCM}$ at 25 °C using the transition line model.

$^{LiIn}SEB^{pNCM}$

Cycle number	**1**	**2**	**52**	**102**	**152**
$R_{cathode}$ / Ω cm^2	18.5	34.7	124.2	150.5	203.4
R_{Ω} / Ω cm^2	33.8	37.1	41.0	44.1	54.6
R_{anode} / Ω cm^2	6.8	1.5	15.7	27.3	37.7

$^{LiIn}SEB^{sPPSLi/PVP-NCM}$

Cycle number	**1**	**2**	**52**	**102**	**152**
$R_{cathode}$ / Ω cm^2	26.4	35.2	69.7	90.3	110.4
R_{Ω} / Ω cm^2	33.0	33.0	46.3	46.3	39.3
R_{anode} / Ω cm^2	2.9	1.8	26.6	25.7	31.4

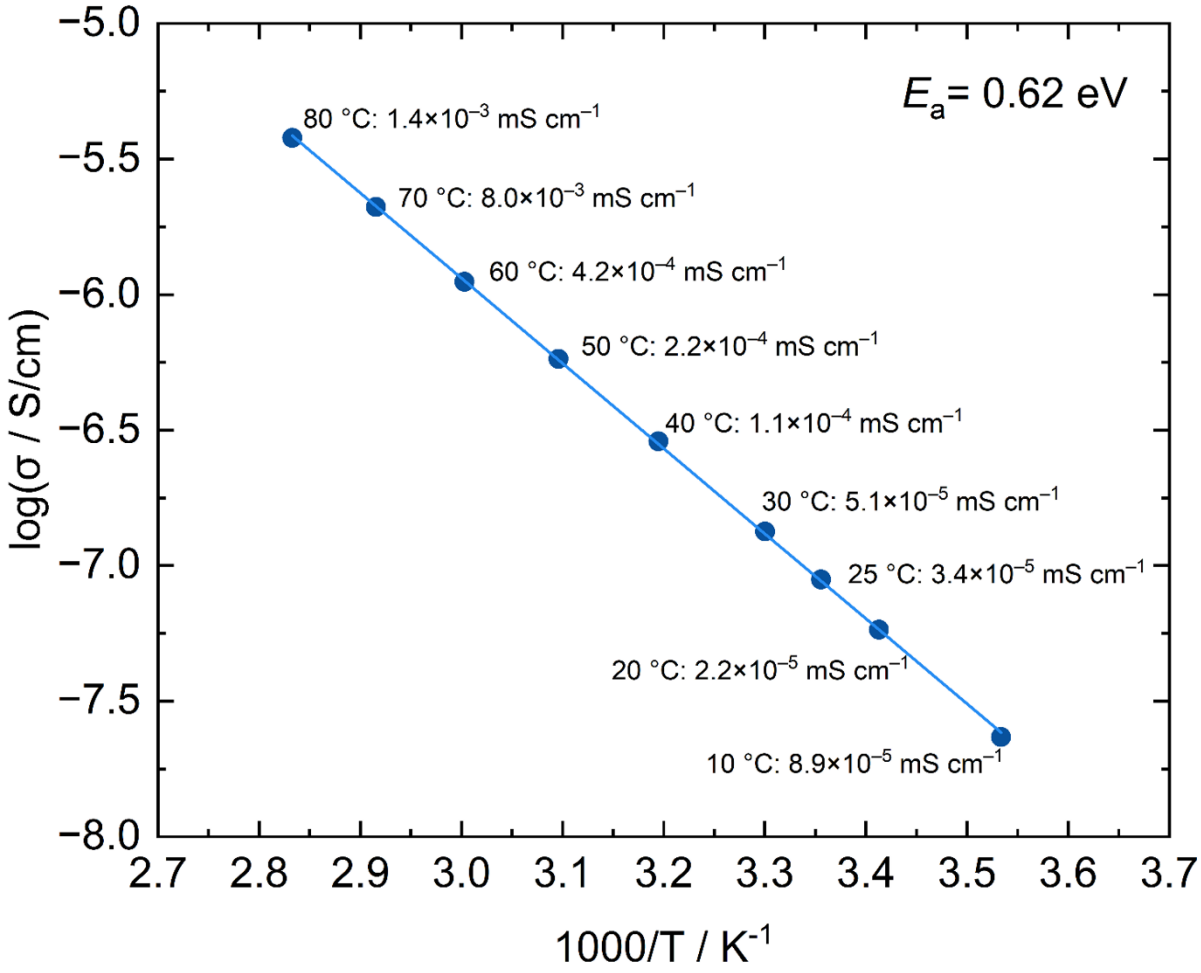

Figure S12. Arrhenius plot of conductivity of the sPPSLi/PVP polymer complex obtained by compressing sPPSLi/PVP into a pellet and applying a platinum sputter coating on both sides. The activation energy (E_a = 0.62 eV) is calculated by the slope of the log(σ / S/cm) vs 1000/T / K^{-1}, following the Arrhenius equation: $\sigma = \sigma_0 \cdot e^{-E_a/kT}$. σ is the conductivity measured by EIS. σ_0 is the pre-exponential factor. E_a is the activation energy. k is the Boltzmann constant 8.617 · 10^{-5} eV/K. T is the temperature.

3.3 Publication C

Publication C is currently under review following its submission. The primary objective of this publication is to introduce a new modification method for sulfide-based SEs. In this study, Li_6PS_5Cl is employed as a catholyte and separator. Self-synthesized single crystalline LNO is used as a CAM to test pristine and modified Li_6PS_5Cl. Choosing the self-synthesized LNO as a CAM is important because the commercially available NCM may already be coated or doped, which could mask the effects of CEI degradation. In contrast, LNO provokes the most severe side reactions among high-nickel CAMs. This characteristic makes it an ideal candidate for studying CEI degradation. The single-crystal structure of LNO mitigates its particle cracking during cycling and 60 MPa of external pressure mitigates the contact loss, allowing a more focused CEI degradation study.

Sulfide-based SEs may react with or dissolve in polar solvents, leading to the formation of polysulfides (see **Section 2.5.5**). Because the polar solvent is used during synthesis, side reaction products such as Li_3PO_4 can occur in the production of sulfide-based SEs. However, oxygenated products have been recognized as a beneficial artificial CEI in the study of Zuo et al.[124] This insight has led to deliberately passivating the sulfide-based SE to form an artificial CEI and SEI.

This publication presents an entirely new modification method for sulfide-based SEs, improving cycling stability and rate capability by mitigating CEI degradation. Furthermore, utilizing modified LPSCl as a separator can effectively suppress dendrite growth from the lithium metal anode. A key advantage of this approach lies in its industrial scalability, as it seamlessly integrates with established processes such as cathode sheet casting and wet milling.

B.X.S. was responsible for the electrochemical analyses, and general characterization of materials. T.W., Y.Y., and B.X.S. conducted the TOF-SIMS analysis, while T.D. performed the TEM experiments. S.L.B. and Y.Y. conducted the XPS analysis. B.X.S. and B.A. conducted the CTTA measurement. K.V. contributed to the LEB measurement. S.S. and B.J. contributed with DFT calculations. K.V., A.H., K.A., and F.H.R. contributed to the analysis and interpretation of the experimental data. The research concept was conceived by B.X.S. and F.H.R., who also prepared the manuscript. All authors contributed to the manuscript and the analysis of experimental results.

Surface Modification of Thiophosphate Solid Electrolyte for Performance Boost in Li|LPSCl|LNO Solid-State Batteries

Bing-Xuan Shi,[a] Timo Weintraut,[b] Thomas Demuth,[c] Sabrina Sicolo,[d] Boburmirzo Juraev,[d] Sebastian Leonard Benz,[a] Burak Aktekin,[a] Kilian Vettori,[b] Yuriy Yusim,[a] Karsten Albe,[d] Kerstin Volz,[c] Anja Henss,[b] Felix H. Richter*[,a]

[a] Institute of Physical Chemistry & Center for Materials Research (LaMa), Justus-Liebig-University Giessen, Heinrich-Buff-Ring 17, 35392 Giessen, Germany

[b] Institute of Experimental Physics, Heinrich-Buff- Ring 16 and Center for Materials Research, 35392 Giessen, Germany

[c] Department of Physics & Materials Sciences Center (WZMW), Philipps-University Marburg, Hans-Meerwein Straße 6, 35032 Marburg, Germany.

[d] Fachgebiet Materialmodellierung, Institut für Materialwissenschaft, Technische Universität Darmstadt, Otto-Berndt-Str. 3, D-64287 Darmstadt, Germany

*Corresponding author, Felix.H.Richter@phys.chemie.uni-giessen.de

Keywords: Solid-state batteries, solid electrolyte, surface modification, interface degradation, cathode active material, dendrite formation

Abstract

Thiophosphate solid electrolytes (SEs) may enable the energy storage transformation to solid-state batteries, but interface instability and lithium dendrite formation significantly limit their practical application. To address these challenges, we present a scalable N-methyl-2-pyrrolidone (NMP) surface modification to boost the performance of Li_6PS_5Cl (LPSCl) SE. This NMP surface modification improves electrochemical stability, catholyte performance, and suppresses lithium dendrite growth when used as a separator with a lithium metal anode. As a catholyte, the modified LPSCl (mLPSCl) increases the first cycle discharge capacity by ~17 $mAh \cdot g^{-1}$ and improves capacity retention by 10% over pristine LPSCl (pLPSCl) after 100 cycles. As a separator, higher critical current density can be reached with mLPSCl (1.6 $mA \cdot cm^{-2}$) than with pLPSCl (1 $mA \cdot cm^{-2}$) before shorting of the cell. Paired with single crystal $LiNiO_2$ (LNO) and lithium metal anode, mLPSCl achieves over 100 stable cycles, significantly outperforming the cell with pLPSCl, which shorts after 25 cycles. Overall, this study introduces a scalable method for modifying LPSCl by solvent treatment that improves cathode performance and mitigates dendrite formation against lithium metal anode.

1. Introduction

The field of solid-state batteries encompasses solid electrolyte batteries (SEBs), polymer electrolyte batteries (PEBs), and hybrid electrolyte batteries (HEBs), [1] utilizing solid electrolytes (SEs), polymer electrolytes (PEs), and hybrid electrolytes (HEs), respectively. [1] They promise enhanced safety[2] and higher energy density[3] than liquid electrolyte batteries (LEBs), which are more generally known as lithium-ion batteries and use flammable organic liquid electrolytes. [1, 4] Choice of the electrolyte type defines the cell chemistry and properties. An ideal electrolyte should demonstrate high ionic conductivity, negligible electronic conductivity, and a suitable electrochemical window. [1, 4] Thiophosphate-based SEs show low grain boundary resistance[5] and have high ionic conductivity up to 32 $mS \cdot cm^{-1}$ for $Li_{9.54}(Si_{0.6}Ge_{0.4})_{1.74}P_{1.44}S_{11.1}Br_{0.3}O_{0.6}$, [6] 10 $mS \cdot cm^{-1}$ for $Li_{10}GeP_2S_{12}$, and 2 $mS \cdot cm^{-1}$ for Li_6PS_5Cl (LPSCl). [7]

However, the best-conducting thiophosphate SEs contain high-valence elements such as germanium or silicon and form a mixed conducting interphase (MCI) when reduced by lithium metal. [8] Continuous MCI formation causes capacity fade due to irreversible lithium consumption and increased interface resistance. [8] In contrast, LPSCl decomposes into LiCl, Li_2S, and Li_3P below 1.7 V vs. Li^+/Li, forming a solid electrolyte interphase (SEI) against lithium metal anode. [8, 9] This SEI with low electronic conductivity[10] slows down diffusion-controlled solid-state reactions. [8, 11] Therefore, we use LPSCl in this study due to its better compatibility with lithium metal. However, LPSCl can still suffer from dendrite formation due to uneven current distribution arising from structural imperfections such as voids and cracks. [12, 13]

In the composite cathode, use of $LiNiO_2$ (LNO) is preferred to maximize the practical capacity, [14, 15]. However, LNO experiences similar yet more severe interface stability issues with LPSCl compared to high-nickel $LiNi_xMn_yCo_{1-x-y}O_2$ (NCM). [16] Use of LNO typically suffers from degradation at the cathode-electrolyte interface (CEI) at 0% state of charge (SOC), causing capacity fading. [17] The oxidation of LPSCl above 2.3 V vs. Li^+/Li results in the formation of elemental sulfur, $Li-[S]_n-Li$ and $P-[S]_n-P$ (including polysulfide and n=2 related to $P_2S_7^{4-}$, $P_2S_6^{2-}$ and P_2S_5) in contact with the cathode active material, carbon additive, and current collector. [9, 18] These reactions lower the Coulomb efficiency of the initial cycle by obstructing ion transport and charge transfer at the CEI. [19] Moreover, at a high SOC at around 4.2 V vs. Li^+/Li, oxidation reactions at the CEI lead to the formation of a decomposition layer and the rock salt phase on LNO, impeding the lithium ion transport at the CEI. [20-22] Rock salt phase [22] coupled with volume change[23-26] during cycling also causes chemomechanical stress and fracture. [22, 27-29]

Surface modification of LPSCl is gaining attention for its ability to protect both cathode and anode. For example, ball milling is used to incorporate additives into LPSCl, such as poly(ethylene glycol) dimethyl ether[30, 31] and lithium difluoro(oxalate)borate. [32] Similarly, vapor-

phase[33] and atomic layer[34] deposition are used to coat polydimethylsiloxane and Al_2O_3 on LPSC, respectively. Moreover, gas-solid reactions are used to form coatings on LPSCl, such as Li_2CO_3[35, 36] and LiF. [37] However, solvent treatment methods have not yet demonstrated similar improvements[38] as the electrophilic P^{5+} group of thiophosphate SEs is unstable in polar solvents such as water, N-methyl-2-pyrrolidone (NMP), and alcohols, which act as Lewis base. [39, 40] As a result, using non-polar solvents like xylene or toluene is essential for slurry preparation[40] and reducing SE particle size via wet ball-milling. [41-43]

Suspensions of thiophosphate SEs in polar solvents display various colors, indicating that different polysulfide chains are stabilized by each solvent. Hatz et al. reported that the deep blue color in NMP suspensions is due to the $[S_3]^{-}\bullet$ radical anion. [39] Drying can lead to the formation of $P-[S]_n-P$, appearing as a passivation coating or aggregates. [39] The $P-[S]_n-P$ bonds in thiophosphates are generally undesirable, as they lower ionic conductivity and compromise battery performance. [39] Moreover, Wissel et al. observed that thiophosphate SEs and polar solvents form stable complexes below 120 °C with vacuum. [44] These complexes decompose or are evaporated only at higher temperatures. [39, 44]

Here, we present a method for the deliberate solvent modification of LPSCl, using NMP diluted in o-xylene, which enhances the electrochemical performance of thiophosphate-based SEBs. Single crystal LNO cathode active material is chosen for stronger CEI degradation than NCM and reduced particle cracking, [14-16] which is beneficial for studying interfacial degradation. [45] Solvent exposure forms a protective layer on LPSCl, which demonstrates superior cycling stability and rate capability when paired with LNO. It also effectively inhibits dendrite growth when lithium metal is used as an anode, contributing to longer battery operation. Our findings offer a scalable strategy for modifying thiophosphate SEs, leading to the demonstration of a $^{Li}SEB^{LNO}$.

Results and discussion

2.1 Preparation and characterization of m^{x}LPSCl

As polar solvents destabilize the electrophilic P^{5+} in LPSCl, leading to P−[S]$_n$−P precipitates, [39] we anticipate that exposing LPSCl to a small amount of polar solvent may create a surface-modified LPSCl with a controlled passivation layer as coating. To achieve this, 1 g of wet ball-milled LPSCl and 40 mL of o-xylene are mixed with different amounts of NMP and then vacuum-dried at 120 °C for 48 hours. **Figure 1** lists the experimental conditions used to create surface modified LPSCl (m^{x}LPSCl; x represents the NMP content in µL) named m$^{0.4}$LPSCl, m^{5}LPSCl, m^{20}LPSCl, m^{200}LPSCl, m^{2k}LPSCl, to m^{10k}LPSCl, respectively. Additionally, LPSCl treated solely with NMP is termed m^{NMP}LPSCl, which is further processed to ht-m^{NMP}LPSCl through an additional 48-hour vacuum-drying step at 150 °C. Electrochemical impedance spectroscopy (EIS) results (**Figure S1**) show that among the m^{x}LPSCl samples, m$^{0.4}$LPSCl has the highest ionic conductivity (1.5 mS·cm^{-1}, 68% of pLPSCl). In contrast, m^{10k}LPSCl has the lowest conductivity (0.12 mS·cm^{-1}, 6% of pLPSCl), which indicates that excessive modification overly hinders ionic transport.

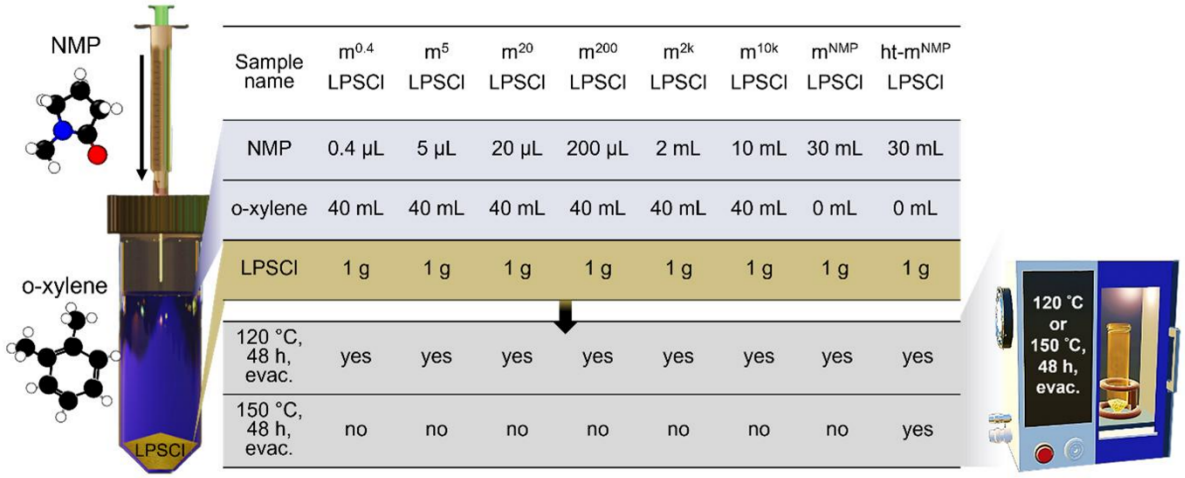

Sample name	m$^{0.4}$ LPSCl	m^{5} LPSCl	m^{20} LPSCl	m^{200} LPSCl	m^{2k} LPSCl	m^{10k} LPSCl	m^{NMP} LPSCl	ht-m^{NMP} LPSCl
NMP	0.4 µL	5 µL	20 µL	200 µL	2 mL	10 mL	30 mL	30 mL
o-xylene	40 mL	40 mL	40 mL	40 mL	40 mL	40 mL	0 mL	0 mL
LPSCl	1 g	1 g	1 g	1 g	1 g	1 g	1 g	1 g
120 °C, 48 h, evac.	yes	yes	yes	yes	yes	yes	yes	yes
150 °C, 48 h, evac.	no	no	no	no	no	no	no	yes

Figure 1. The schematic and table depict LPSCl mixed with varying NMP amounts in o-xylene, vacuum-dried at 120 °C for 48 hours to produce m^{x}LPSCl (x represents the NMP content in µL). LPSCl treated with NMP alone and vacuum-dried at 120 °C is termed m^{NMP}LPSCl, with further drying at 150 °C for 48 hours yielding ht-m^{NMP}LPSCl.

Fourier-transform infrared spectroscopy (FTIR) identifies organic groups on m^{x}LPSCl (**Figure S2a)** with features like pure NMP (**Figure S2b**), suggesting that NMP complexes with LPSCl. The C=O stretching frequency shifts from 1675 cm^{-1} in pure NMP to about 1630 cm^{-1} in

m^{x}LPSCl. This suggests an electrostatic interaction between the C=O group and P^{5+} in LPSCl, aligning with Oh et al.'s findings that Lewis-basic solvents interact with P^{5+} in SEs. [40] In addition, FTIR of ht-m^{NMP}LPSCl shows a marked decrease in NMP intensity after heating (**Figure S2c**), indicating LPSCl·NMP complex decomposition or evaporation above 120 °C. [44]

The degradation products between NMP and LPSCl are analyzed using X-ray photoelectron spectroscopy (XPS) by comparing pLPSCl, m^{NMP}LPSCl (**Figure 2a**), and ht-m^{NMP}LPSCl (**Figure S3**). m^{NMP}LPSCl and ht-m^{NMP}LPSCl contain the most degradation products, aiding XPS analysis in revealing their chemical composition. The relative mol% of different byproducts according to each specific element in XPS are compared in **Figure S4**. The N 1s XPS spectrum of both m^{NMP}LPSCl and ht-m^{NMP}LPSCl exhibits a C–N–C signal at 400.2 eV, which indicates the presence of an amide group (N-(C=O)-), [46] and is absent in pLPSCl. This result confirms the complexation of NMP and LPSCl, consistent with the FTIR results. [44]

The S 2p XP-spectrum of pLPSCl reveals three signals, representing different sulfur species on the surface. The signals represent Li_2S at 160.4 eV, PS_4^{3-} at 161.5 eV and a shoulder at 162.1 eV indicates P−[S]$_n$−P. [47] m^{NMP}LPSCl exhibits stronger P−[S]$_n$−P (22 mol%) than pLPSCl (8 mol%). Additionally, sulfide species (S_x) appear at 163.2 eV in m^{NMP}LPSCl, accounting for 11 mol%.[9] These results confirm the precipitation of S_x and P−[S]$_n$−P on the surface of LPSCl or as separated particles upon drying after solvent treatment, as reported by Hatz et al. [39] However, Li_2S is removed from m^{NMP}LPSCl during sample preparation, as Li_2S is dissolved in NMP and discarded with the supernatant. For ht-m^{NMP}LPSCl, SO_x species appear at 166.9 eV (12 mol%) and the Li_2S signal increases to 6 mol%, while the P−[S]$_n$−P and S_x related signals respectively decrease to 12 mol% and 4 mol%. This suggests that P−[S]$_n$−P and S_x might be reduced to Li_2S. [9] Additionally, NMP may oxidize P−[S]$_n$−P and S_x at 150 °C to form SO_x.

The P 2p spectra each have two signals: the main signal at 131.9 eV from PS_4^{3-} and the signal at 132.9 eV indicating oxidized phosphorus species (P_{ox}) such as, P−[S]$_n$−P and PO_x. [47] m^{NMP}LPSCl and ht-m^{NMP}LPSCl both exhibit a more intense signal at 132.9 eV (74 mol%) than pLPSCl (2 mol%). These results confirm that NMP may oxidize LPSCl, supporting the S 2p spectrum results.

Time-of-flight secondary ion mass spectrometry (TOF-SIMS), more surface-sensitive than XPS, [47] analyzes m^{200}LPSCl to confirm the presence of a modification layer, supporting XPS results. The scan is conducted over a 200×200 μm^2 area with a resolution of 128×128 pixel and an ion dose of 10^{12} ions cm^{-2}. We focus on detecting specific ion fragments based on the observation of the m^{NMP}LPSCl XPS results discussed above: CN^-, S_x (S_2^-, S_3^-, S_4^-), P−[S]$_n$−P (PS_2^-), PO_x^- (PO_2^-), SO_x^- (SO^- and SO_2^-), PSO^-, PSO_2^-, and Cl^- (**Figure 2b**). PO^-, PO_4^-, SO_3^-, and SO_4^- are excluded here due to negligible intensity contributions. Additionally, PO_3^- excluded due to its intensity interfered by the intense $Li^{37}Cl^{35}Cl^-$ signal.

For CN^-, S_x, $P-[S]_n-P$, PO_x^-, SO_x^-, PSO^-, and PSO_2^-, m^{200}LPSCl demonstrates increased normalized intensities compared to pLPSCl, aligning with the XPS results. Additionally, PSO^- and PSO_2^- fragments may represent oxidative PS_4^{3-} compounds, such as $(PS_{4-x}O_x)^{3-}$. Additionally, Cl^- intensity is lower in m^{200}LPSCl compared to pLPSCl. This may be attributed to the surface being covered by a modification layer, or to the removal of Cl^- during solvent treatment[49]. Overall, FTIR, XPS, and ToF-SIMS results reveal that the modification layer comprises NMP, S_x, $P-[S]_n-P$, PO_x^-, SO_x^-, and oxidative PS_4^{3-}.

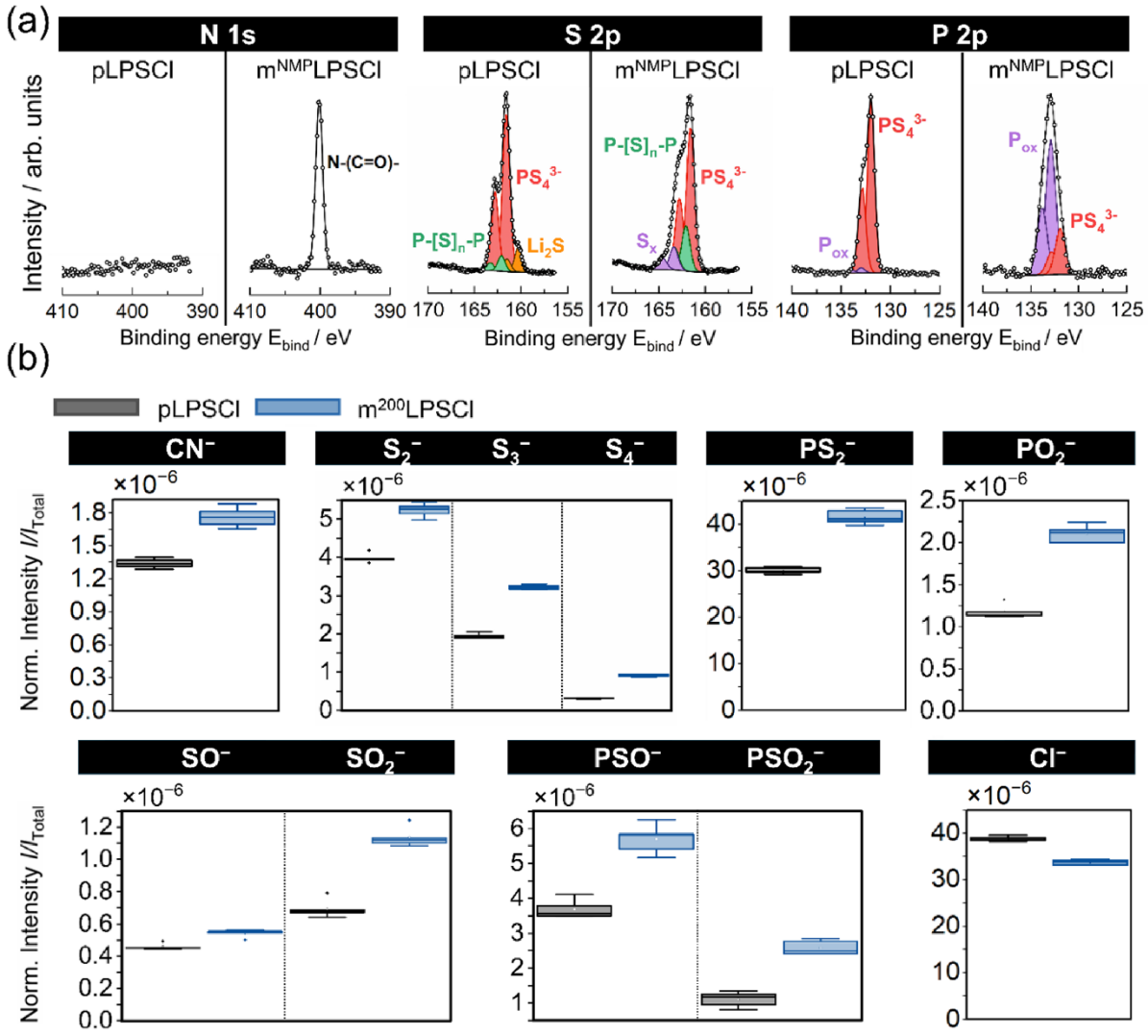

Figure 2. (a) N 1s, S 2p, and P 2p XPS spectra of pLPSCl and m^{NMP}LPSCl. (b) ToF-SIMS box plots compare the ion intensities of CN^-, S_x (S_2^-, S_3^-, S_4^-), $P-[S]_n-P$ (PS_2^-), PO_x^- (PO_2^-), SO_x^- (SO^- and SO_2^-), oxidative PS_4^{3-} compounds (PSO^- and PSO_2^-), and Cl^- between pLPSCl and m^{200}LPSCl samples.

Transmission electron microscopy (TEM) in combination with energy dispersive X-ray spectroscopy (EDX) can reveal structural as well as chemical information about the samples. The EDX mapping (**Figure 3a**) and spectra (**Figure 3b**) show that there is no nitrogen present for pLPSCl, but a distinct N signal can be detected for both m^{200}LPSCl and m^{NMP}LPSCl. While weak carbon and oxygen signals stemming from contaminations exist for pLPSCl, the intensity of both peaks is increased in the modified samples. The elemental maps of N, C, and O, indicative of the polymer, confirms that the modification layer uniformly coats the entire mLPSCl particle. However, m^{NMP}LPSCl has only little traces of chlorine (**Figure 3c**). Referring to the report by Indrawan et al., we hypothesize that excess NMP might extract chlorine from LPSCl. [49] Further studies are needed to explore the underlying mechanisms. **Figure S5** presents an HR-TEM image of an m^{200}LPSCl particle with an amorphous surface layer and crystalline lattice planes, indicating that solvent treatment with a small amount of NMP preserves the internal crystallinity. This is corroborated by X-ray diffraction (XRD) results (**Figure S6**).

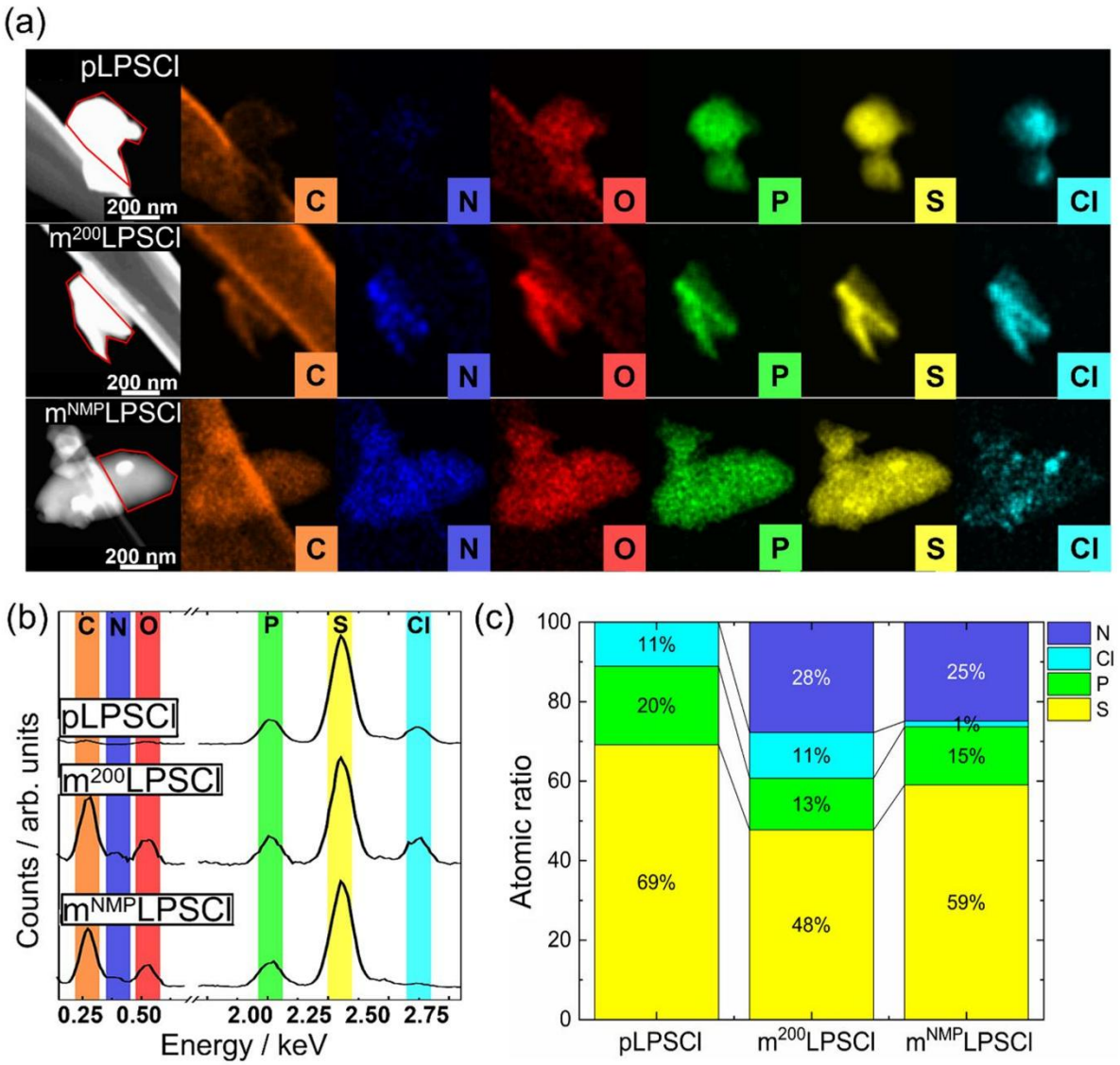

Figure 3. (a) EDX elemental maps of pLPSCl, m^{200}LPSCl, and m^{NMP}LPSCl. (b) EDX spectra of pLPSCl, m^{200}LPSCl, and m^{NMP}LPSCl from the red-marked areas in (a). (c) The average atomic ratios of N, P, S, and Cl obtained from EDX spectra of pLPSCl, m^{200}LPSCl, and m^{NMP}LPSCl are summarized. Each sample is measured across three particles to ensure quantification reliability, and the corresponding values are listed in **Table S1**.

2.2 DFT investigation of NMP adsorption and reactivity on mLPSCl surface

Density functional theory (DFT) calculations are employed to understand the atomic scale interactions and energetics of NMP adsorption on the LPSCl surface, offering critical insights into its surface stability and reactivity. After obtaining the relaxed slab structure (section 4.14), a single NMP molecule is brought close to the surface of the argyrodite slab. A strong interaction occurs between the lithium ions on the surface and the oxygen atom of the NMP molecule. There are numerous degrees of freedom for adsorption, and NMP can bind to the surface in various configurations (**Figure S7**). A common feature across these configurations is the interaction of NMP-oxygen with lithium ions from the surface. The most stable configuration exhibits an adsorption energy of 1.03 eV (**Figure 4(II)**). Neglecting the influence of surface coverage, which should be accounted for in a rigorous analysis, [50] we can estimate the desorption temperature, T_d, using the Arrhenius equation for the desorption rate:

$$\nu = \nu_0 \cdot \exp\left(\frac{-E_a}{k_B \cdot T}\right) \qquad [1]$$

where ν is the rate of desorption, ν_0 is the pre-exponential factor, E_a is the adsorption energy (1.03 eV in this case), k_B is the Boltzmann constant, and T is the temperature. Assuming typical values of 1 s^{-1} for ν and 10^{13} s^{-1} for ν_0, we estimate a desorption temperature of approximately 399 K = 126 °C, which aligns with the experimental observation.

To further investigate this interaction, phonon calculations are performed for both the NMP molecule in vacuum and the combined NMP-argyrodite slab system using the finite differences method. [51] The analysis reveals a noticeable red shift in the C=O bond frequency, which aligns with the experimental FTIR measurement (**Figure S2**). Specifically, the C=O bond frequency measures 1710 cm^{-1} in a vacuum and decreases to 1674 cm^{-1} after interaction with the argyrodite surface. Visual analysis of the bond length indicates a concurrent elongation of the C=O bond, from 1.23 Å in vacuum to 1.25 Å after adsorption (**Figure S8**). This change in both bond frequency and bond length further confirms the significant interaction between NMP and lithium on the argyrodite surface.

When an additional NMP molecule adsorbs onto the argyrodite surface, the C=O bond frequencies shift further to the range of 1655–1662 cm^{-1}. This further red shift in frequency at double NMP coverage mirrors the experimental trend, where increasing the amount of NMP in solution led to lower C=O frequencies when mixed with argyrodite (**Figure S2a**). From an energetic standpoint, the addition of the second molecule reduced the average adsorption energy of the system to −0.82 eV.

The hard and soft acids and bases theory and experimental results suggest the oxidation of PS_4^{3-} units, which results from the substitution of a sulfur atom in the PS_4^{3-} unit with oxygen

from NMP. Multiple attempts at using ab initio molecular dynamics simulations at varying temperatures failed to produce any reaction. To further explore the thermodynamics of this reaction, we conducted static energy calculations where the reactant is the NMP molecule adsorbed on LPSCl, and the product is an NMP molecule (with the oxygen replaced by sulfur) adsorbed on LPSCl, forming a PS_3O unit. The slightly negative reaction enthalpy (−0.07 eV) suggests that the oxidation of LPSCl by NMP could be thermodynamically feasible **(Figure 4(III)**) despite NMP's well-known chemical stability under neutral conditions.[52-54] The lack of observed reactions in multiple investigations, combined with the failure of nudged elastic band (NEB) calculations[55, 56] to identify a saddle point, suggests that the reaction barrier may be substantial or the mechanism might be highly complex. The adsorption energy of N-methyl-2-thiopyrrolidone is 0.69 eV (**Figure 4(IV)**), which, according to equation [1], suggests that desorption occurs almost instantaneously at the operating temperature of 290 K.

One key observation is that the limited availability of surface PS_4^{3-} tetrahedra prone to O-S exchange would still imply the presence of adsorbed, unreacted NMP. This suggests that after some initial reactivity, the remaining NMP molecules are likely to stay attached to the surface, possibly requiring further energy input or structural changes to detach.

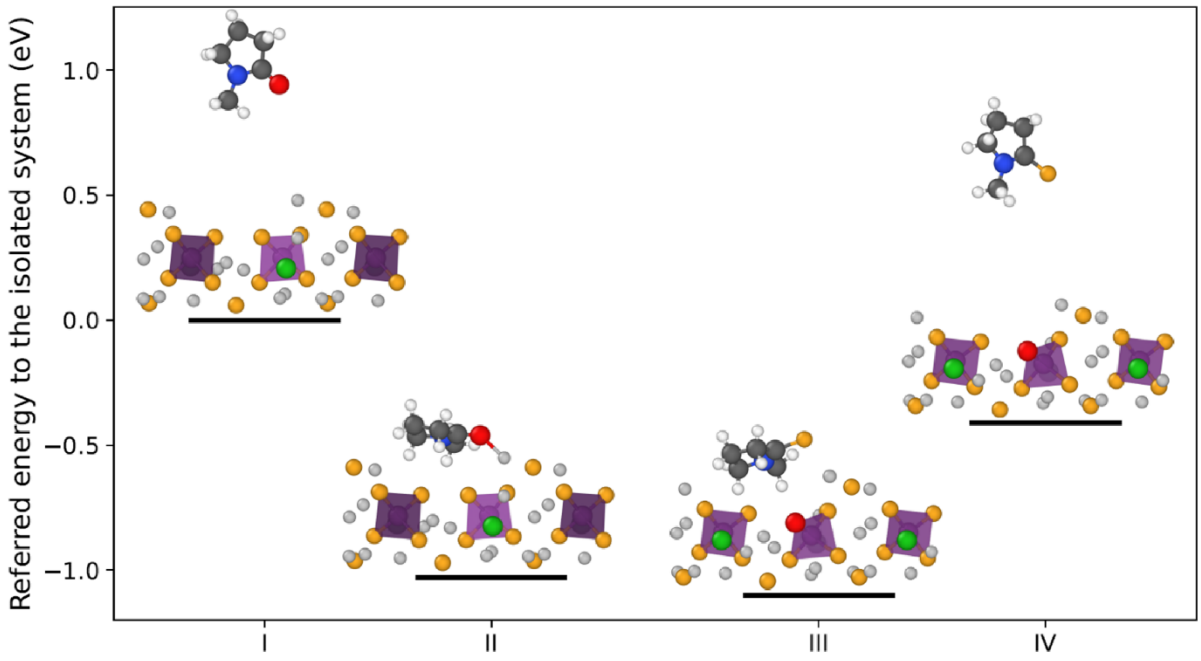

Figure 4. Illustration of the four stages of the NMP-argyrodite interaction: (I) The total energies of the isolated argyrodite and NMP molecule serve as the reference for the energy scale; (II) Adsorption: NMP adsorbs onto the argyrodite surface with a binding energy of −1.03 eV; (III) Exchange: Sulfur-oxygen exchange occurs between NMP and a surface PS_4^{3-} tetrahedron, with an energy gain of −0.07 eV relative to the previous step; (IV) Desorption: The newly formed N-methyl-2-thiopyrrolidone (NMP-S) has an adsorption energy of 0.69 eV and can readily desorb under operating conditions. In the NMP molecule, hydrogen, oxygen, nitrogen, and carbon atoms are represented by white, red, blue, and gray colors, respectively. In the LPSCl structure, lithium, phosphorus, sulfur, and chlorine atoms are depicted as light gray, purple, orange, and green, respectively.

2.3 Rate capability and cycling stability of ^{LiIn}SEB^{LNO} with m^{x}LPSCl

To compare the electrochemical performance of single crystal LNO in combination with pLPSCl or m^{x}LPSCl, pellet-type cells are tested in a LiIn|LPSCl|LPSCl/VGCF/LNO configuration (^{LiIn}SEB^{LNO}, practical capacity: 2.1 mAh·cm^{-2} at 200 mAh·g^{-1}; 1C corresponds to 2.1 mA·cm^{-2}). LiIn alloy is used as an anode counter electrode due to its thermodynamic and kinetic stability with LPSCl. [18, 57] Vapor-grown carbon fiber (VGCF) is included in the composite cathode for electronic conductivity enhancement. To mitigate contact loss, 60 MPa of stack pressure is applied during cycling of ^{LiIn}SEB^{LNO}. Three cell types (**Figure 5a**) are compared in rate capability and cycling stability tests: 1) cells with pLPSCl for both catholyte and separator are named pp-^{LiIn}SEB^{LNO}; 2) cells with pLPSCl for the separator and m$^{0.4}$LPSCl for the catholyte are named pm^{x}-^{LiIn}SEB^{LNO}; 3) cells using m^{x}LPSCl for both catholyte and separator are named

mm^{x}-^{LiIn}SEB^{LNO}.

The results of the rate capability tests shown in **Figure 5b** demonstrate that both pm$^{0.4}$-^{LiIn}SEB^{LNO} and mm$^{0.4}$-^{LiIn}SEB^{LNO} outperform pp-^{LiIn}SEB^{LNO} across all C-rates. In the first cycle at 0.1C, pm$^{0.4}$-^{LiIn}SEB^{LNO} achieves higher specific discharge capacity (154 mAh·g^{-1}) and Coulomb efficiency (72%) than mm$^{0.4}$-^{LiIn}SEB^{LNO} (151 mAh·g^{-1} and 70%) and pp-^{LiIn}SEB^{LNO} (140 mAh·g^{-1} and 67%). The first cycle Coulomb efficiency can be influenced by lithium ion reversibility of bulk LNO[58] and reduced side reactions at the LNO|LPSCl CEI[19]. As m$^{0.4}$LPSCl does not change the bulk properties of LNO, the improved Coulomb efficiency of pm$^{0.4}$-^{LiIn}SEB^{LNO} and mm$^{0.4}$-^{LiIn}SEB^{LNO} are probably enabled by reduced side reactions or an improved interface. At 1C, pm$^{0.4}$-^{LiIn}SEB^{LNO} reaches 63 mAh·g^{-1}, outperforming both mm$^{0.4}$-^{LiIn}SEB^{LNO} and pp-^{LiIn}SEB^{LNO} (around 55 mAh·g^{-1}). The difference between pm$^{0.4}$-^{LiIn}SEB^{LNO} and mm$^{0.4}$-^{LiIn}SEB^{LNO} may be because using m$^{0.4}$LPSCl as a separator compromises ionic conductivity. Notably, increasing modification intensity leads to declining rate capability and rising polarization (**Figure S9**), which shows that there is a sweet spot between a slight modification that protects the interface and an excessive modification that compromises the conductivity to a level detrimental to cell performance.

Figure 5c presents the 1st and 25th cycle differential capacity (dq/dE) of pp-^{LiIn}SEB^{LNO}, pm$^{0.4}$-^{LiIn}SEB^{LNO}, and mm$^{0.4}$-^{LiIn}SEB^{LNO}. The M/H2 transition (3.4 V vs. In/LiIn) [59] is particularly sensitive to changes in active mass utilization. [27] Here, active mass refers to the utilization of lithium ions in LNO, which may decrease mainly due to contact loss or insulating CEI. [27] For the first cycle, similar integral areas of M/H2 transition for pm$^{0.4}$-^{LiIn}SEB^{LNO}, mm$^{0.4}$-^{LiIn}SEB^{LNO}, and pp-^{LiIn}SEB^{LNO} indicate equal active mass utilization. By the 25th cycle, the improved M/H2 transition for pm$^{0.4}$-^{LiIn}SEB^{LNO} and mm$^{0.4}$-^{LiIn}SEB^{LNO} compared to pp-^{LiIn}SEB^{LNO} indicates active mass utilization can be improved by using m$^{0.4}$LPSCl as a catholyte.

Differential capacity peaks at H1/M transition (3 V vs. In/LiIn) [59] are influenced by the kinetic limitation in the H1 phase[27, 60] and active mass utilization[27]. A thick but partially conductive CEI can contribute to kinetic limitations. [27] pm$^{0.4}$-^{LiIn}SEB^{LNO} and mm$^{0.4}$-^{LiIn}SEB^{LNO} show improved differential capacity of H1/M over pp-^{LiIn}SEB^{LNO} in the 1st and 25th cycles. This suggests that m$^{0.4}$LPSCl enhances interfacial kinetics of the CEI in the first cycle, while the improvement in the 25th cycle reflects a combined effect of better active mass utilization and interfacial kinetics.

At H2/H3 transition, LNO undergoes oxygen loss[22] and c-axis shrinkage[23, 24, 26]. In the 25th cycle, the differential capacity of H2/H3 is improved for pm$^{0.4}$-^{LiIn}SEB^{LNO}, mm$^{0.4}$-^{LiIn}SEB^{LNO} compared to pp-^{LiIn}SEB^{LNO}. This suggests modification may reduce CEI degradation at H2/H3, such as oxygenated reactions. [20, 21, 27] Overall, mm$^{0.4}$-^{LiIn}SEB^{LNO} and pm$^{0.4}$-^{LiIn}SEB^{LNO} show improved rate capability over pp-^{LiIn}SEB^{LNO} due to better CEI stability.

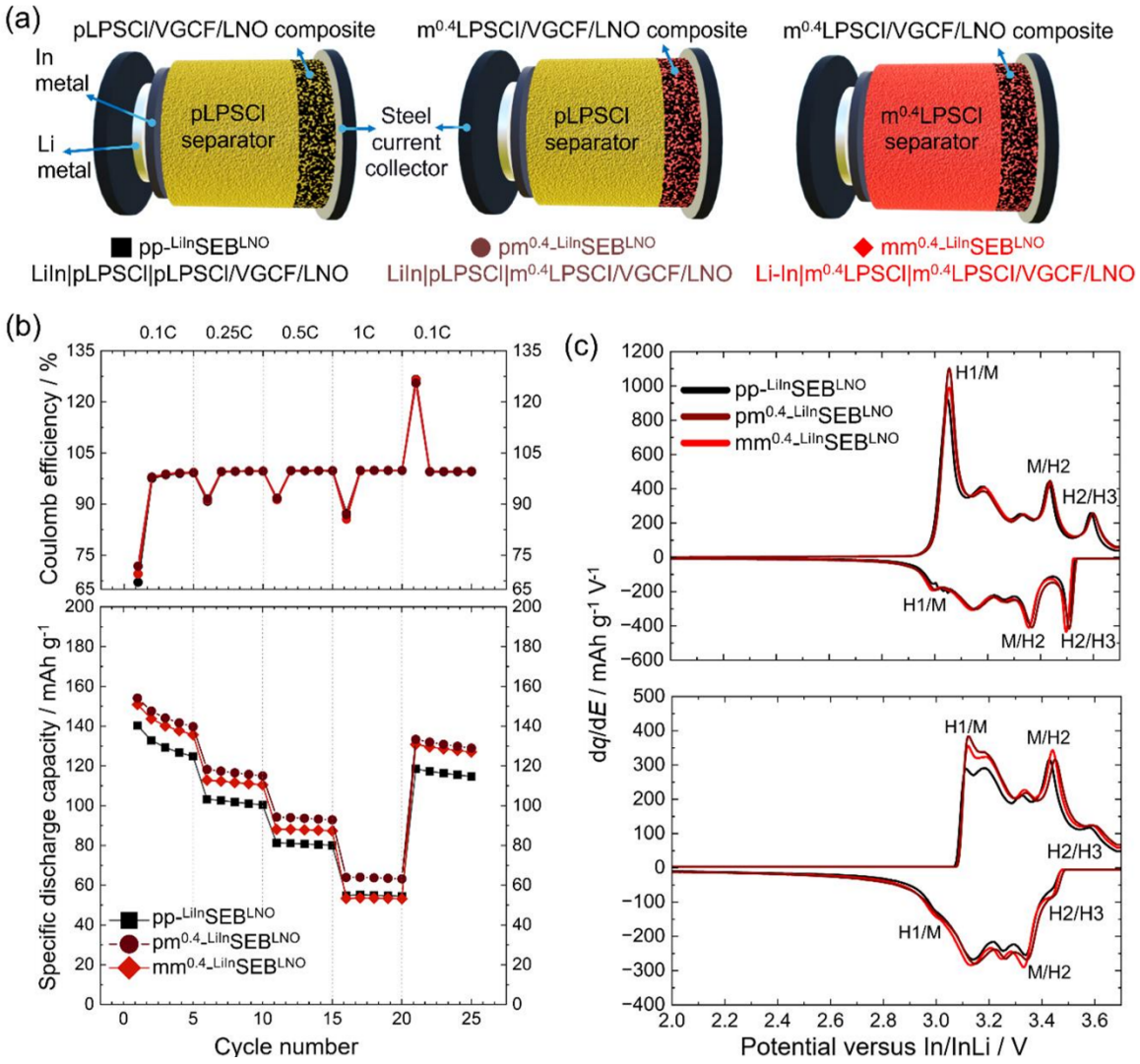

Figure 5. The rate capability of pp-^{LiIn}SEB^{LNO}, pm$^{0.4}$-^{LiIn}SEB^{LNO}, and mm$^{0.4}$-^{LiIn}SEB^{LNO} are analyzed by pellet-type cells. (a) Schematics of the different cell configurations. (b) Coulomb efficiency (top) and specific discharge capacity (bottom) for several C-rates. (c) Differential capacity of the 1st (top) and 25th (bottom) cycles at a 0.1C rate, with LNO phase transitions (H1↔M↔H2↔H3) indicated.

Next, only pp-^{LiIn}SEB^{LNO} and mm$^{0.4}$-^{LiIn}SEB^{LNO} are used to evaluate the cathode cycling performance at 0.1C at 25 °C. pm$^{0.4}$-^{LiIn}SEB^{LNO} is excluded from the cycling stability test to ensure consistent electrolyte use for both the catholyte and separator, to prevent LNO from contacting different electrolytes. EIS is measured during cycling at 1st, 2nd, 50th, and 100th cycles with the procedure shown in **Figure S10**. For each EIS measurement, SEBs are first charged to 3.15 V vs. In/LiIn followed by the chronoamperometry (CA) at 3.15 V vs. In/LiIn until the current decreases to 2%. CA ensures a consistent SOC at this voltage and gives information regarding the lithium diffusion pathway length (L_{diff}).[57, 61] EIS with a frequency range

from 1 MHz to 100 μHz is then performed at 3.15 V vs. In/LiIn to evaluate cathode resistance ($R_{cathode}$). This potential is chosen for its high lithium diffusion and minimal charge transfer resistance (R_{ct}), which varies with SOC. [25, 62] This also prevents measuring impedance at higher voltages with severe degradation. Subsequently, SEBs are recharged to 3.7 V vs. In/LiIn followed by a 2 h relaxation step, then discharged to 2.0 V vs. In/LiIn followed by another 2 h relaxation step. The relaxation steps are used to determine the active mass (m_{act}). [27, 57]

Figure 6a shows that mm$^{0.4}$-^{LiIn}SEB^{LNO} has a higher discharge capacity than pp-^{LiIn}SEB^{LNO} throughout cycling. After 100 cycles, mm$^{0.4}$-^{LiIn}SEB^{LNO} retains 68% of its capacity, 10% more than pp-^{LiIn}SEB^{LNO}, indicating improved cycling stability with surface modification. The cycling performance is affected by m_{act} loss and L_{diff} increase. [27, 57] L_{diff} may increase during cycling due to internal particle cracking. [27, 57] However, If contact loss and CEI degradation do not isolate LNO particles, they may increase L_{diff} rather than causing m_{act} loss. [27, 57]

The second and final cycles of CA are analyzed for L_{diff}, excluding first cycle effects from InLi alloy formation (**Figure S11**). In the second cycle, CA at 3.15 V vs. In/LiIn shows that the mm$^{0.4}$-^{LiIn}SEB^{LNO} has slightly longer charge time (191 minutes) than pp-^{LiIn}SEB^{LNO} (161 minutes). This may be attributed to the lower ionic conductivity of m$^{0.4}$LPSCl compared to pLPSCl. After 100 cycles, mm$^{0.4}$-^{LiIn}SEB^{LNO} and pp-^{LiIn}SEB^{LNO} have similar increased charge times of 480 and 550 minutes, respectively. This suggests comparable L_{diff} due to similar degree of cracking in both SEBs after cycling. [57, 61] To check for contact loss and particle cracking, we examine the SEB cathode cross-section after 100 cycles at 0.1C using ion beam milling and scanning electron microscopy (SEM). Both SEBs show no obvious contact loss between LNO and LPSCl, nor obvious LNO particle cracking (**Figure S12**). This aligns with the expected crack resistance of single crystal LNO. [15, 27] As a result, the improvement of cycling stability in mm$^{0.4}$-^{LiIn}SEB^{LNO} over pp-^{LiIn}SEB^{LNO} is primarily due to reduced CEI side reactions, independent of particle cracking and contact loss.

Figure 6b demonstrates m_{act} results obtained by analyzing the open circuit voltage (OCV). The calculation is published in our previous research. [62] In general, the SOC represents the lithium content in LNO, which reflects in OCV. A ^{Li}LEB^{LNO} with minimal contact loss can provide the OCV vs. SOC as a reference for ^{LiIn}SEB^{LNO} (**Figure S13**). [62] However, the voltage measured against LiIn (V vs. In/LiIn) in ^{LiIn}SEB^{LNO} needs to be converted to the Li^+/Li reference scale (V vs. Li^+/Li) by adding 0.62 V, enabling direct comparison with the ^{Li}LEB^{LNO} reference. From this reference data, the specific discharge capacity at a particular state of charge (q_{soc}) can be calculated. m_{act} of ^{LiIn}SEB^{LNO} is then obtained through dividing the measured discharge capacity (Q_{meas}) by q_{soc}: [27, 57]

$$m_{\mathrm{act}}(\mathrm{g}) = \frac{Q_{\mathrm{meas}}(mAh)}{q_{soc}(\frac{mAh}{g})} \qquad [2]$$

Ideally, the cells should have m_{act} of 8.3 mg. Both mm$^{0.4}$-^{LiIn}SEB^{LNO} and pp-^{LiIn}SEB^{LNO} start with similar m_{act} utilization of around 7.8 mg in the first cycle. The difference between the ideal and actual m_{act} in the first cycle arises from cathode distribution inefficiencies and internal resistance. After 100 cycles, mm$^{0.4}$-^{LiIn}SEB^{LNO} has better m_{act} retention of 84%, outperforming pp-^{LiIn}SEB^{LNO} (73%). Consequently, the improved cycling performance of mm$^{0.4}$-^{LiIn}SEB^{LNO} over pp-^{LiIn}SEB^{LNO} appears to be due to better m_{act} utilization, enabled by reduced side reactions at the LNO|m$^{0.4}$LPSCl interface. This result aligns with the differential capacity findings from the rate capability test.

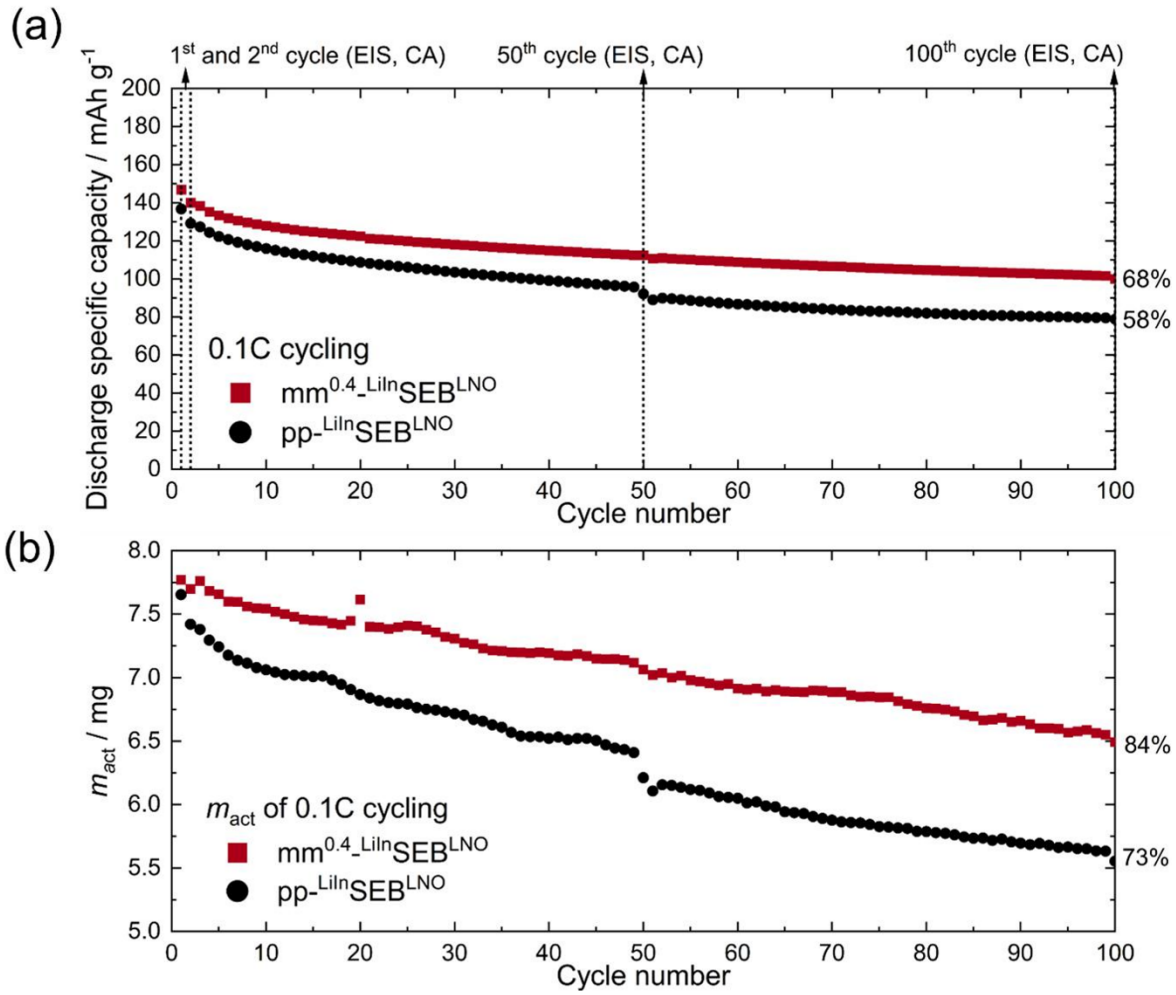

Figure 6. 0.1C cycling performance of pellet-type pp-^{LiIn}SEB^{LNO} and mm$^{0.4}$-^{LiIn}SEB^{LNO} cells. EIS and CA are measured at the 1st, 2nd, 50th, and 100th cycles. The (a) specific capacity of discharge and (b) m_{act} are plotted against cycle numbers.

2.4 Cathode interface degradation analyzed by EIS and CV

EIS measurements can corroborate the results of m_{act} utilization, as it depends heavily on the contact area between LNO and LPSCl, where a smaller area leads to increased interfacial resistance. EIS of ^{LiIn}SEB^{LNO} during cycling are taken at 3.15 V vs. In/LiIn after CA across the 1st, 2nd, 50th, and 100th cycles. **Figure 7a** displays the transition line model (TLM) [63, 64] for fitting of impedance data. Charge transfer resistance (R_{ct}) is used to assess CEI degradation over cycling. However, the Gerischer-type impedance makes it difficult to accurately separate R_{ct} from electronic (R_{ele}) and ionic (R_{ion}) transport resistances in the composite cathode. [64] Therefore, the cathode resistance ($R_{cathode}$) is calculated via equation [3] [64]:

$$R_{\text{cathode}} = \sqrt{R_{\text{ct}} \cdot (R_{\text{ele}} + R_{\text{ion}})} \qquad [3]$$

The fitting results and corresponding Nyquist plots are shown in **Table S2** and **Figure 7b**. The similar apex frequency in both SEBs, marked in blue on each Nyquist plot, suggests that impedance growth during cycling is due to the same interfacial contribution from $R_{cathode}$. Initially, $R_{cathode}$ of mm$^{0.4}$-^{LiIn}SEB^{LNO} is 22 Ω cm^2, which is higher than that of pp-^{LiIn}SEB^{LNO} at 18 Ω cm^2. In addition, the electrolyte resistance (R_Ω) of mm$^{0.4}$-^{LiIn}SEB^{LNO} (44 Ω·cm^2) is higher than that of pp-^{LiIn}SEB^{LNO} (30 Ω·cm^2). The higher initial resistance of mm$^{0.4}$-^{LiIn}SEB^{LNO} compared to pp-^{LiIn}SEB^{LNO} likely stems from the modification hindering ionic transport. After 50 and 100 cycles, $R_{cathode}$ has increased more for pp-^{LiIn}SEB^{LNO} (50th: 427 Ω·cm^2, 100th: 939 Ω·cm²) than for mm$^{0.4}$-^{LiIn}SEB^{LNO} (50th: 233 Ω·cm^2, 100th: 579 Ω·cm^2). Since the modification should not prevent contact loss, which is rather mitigated by applying 60 MPa of pressure during cycling, the larger increase of $R_{cathode}$ for pp-^{LiIn}SEB^{LNO} than for mm$^{0.4}$-^{LiIn}SEB^{LNO} may result from stronger CEI degradation. This leads to poorer active mass utilization of pp-^{LiIn}SEB^{LNO} (**Figure 6b**).

Electrochemical stability between VGCF and LPSCl should also be considered, as LPSCl may be oxidized to elemental sulfur and P_2S_5. [9, 18] Cyclic voltammetry (CV) is employed to assess electrochemical stability with VGCF serving as the working electrode to enhance interfacial contact area. [18, 57] The LiIn alloy is known to provide thermodynamic and kinetic stability with pLPSCl, making it a suitable counter electrode. [18, 57] However, the stability of LiIn|m$^{0.4}$LPSCl needs to be verified. LiIn|pLPSCl|m$^{0.4}$LPSCl/VGCF and LiIn|m$^{0.4}$LPSCl|m$^{0.4}$LPSCl/VGCF show overlapping CV results from OCV to 4 V and back to 0 V vs. In/LiIn (1 mV·s^{-1}), confirming that both LiIn|pLPSCl and LiIn|m$^{0.4}$LPSCl contribute equally to the CV results (**Figure S14a**).

Building on this verification, further CV analysis of LiIn|pLPSCl|pLPSCl/VGCF is compared with the two configurations mentioned above to check the electrochemical stability between m$^{0.4}$LPSCl and pLPSCl with VGCF (**Figure S14b**). The results show that LiIn|pLPSCl|pLPSCl/VGCF exhibits a higher current density than both LiIn|pLPSCl|m0.4LPSCl/VGCF and LiIn|m$^{0.4}$LPSCl|m$^{0.4}$LPSCl/VGCF. This confirms that m$^{0.4}$LPSCl improves electrochemical stability against VGCF compared to pLPSCl.

To separately analyze oxidative and reductive processes, two CV scans from OCV to 4 V and from OCV to 0 V vs. In/LiIn are recorded, respectively. The results show that LiIn|$m^{0.4}$LPSCl|$m^{0.4}$LPSCl/VGCF exhibits a lower current density and a wider stability window (1.15 V) compared to LiIn|pLPSCl|pLPSCl/VGCF (1 V) (**Figure S14c**). Further modifications from m^{5}LPSCl to m^{10k}LPSCl progressively reduced current density, confirming enhanced electrochemical stability (**Figure S14d**). Overall, m^{x}LPSCl demonstrates improved electrochemical stability with VGCF.

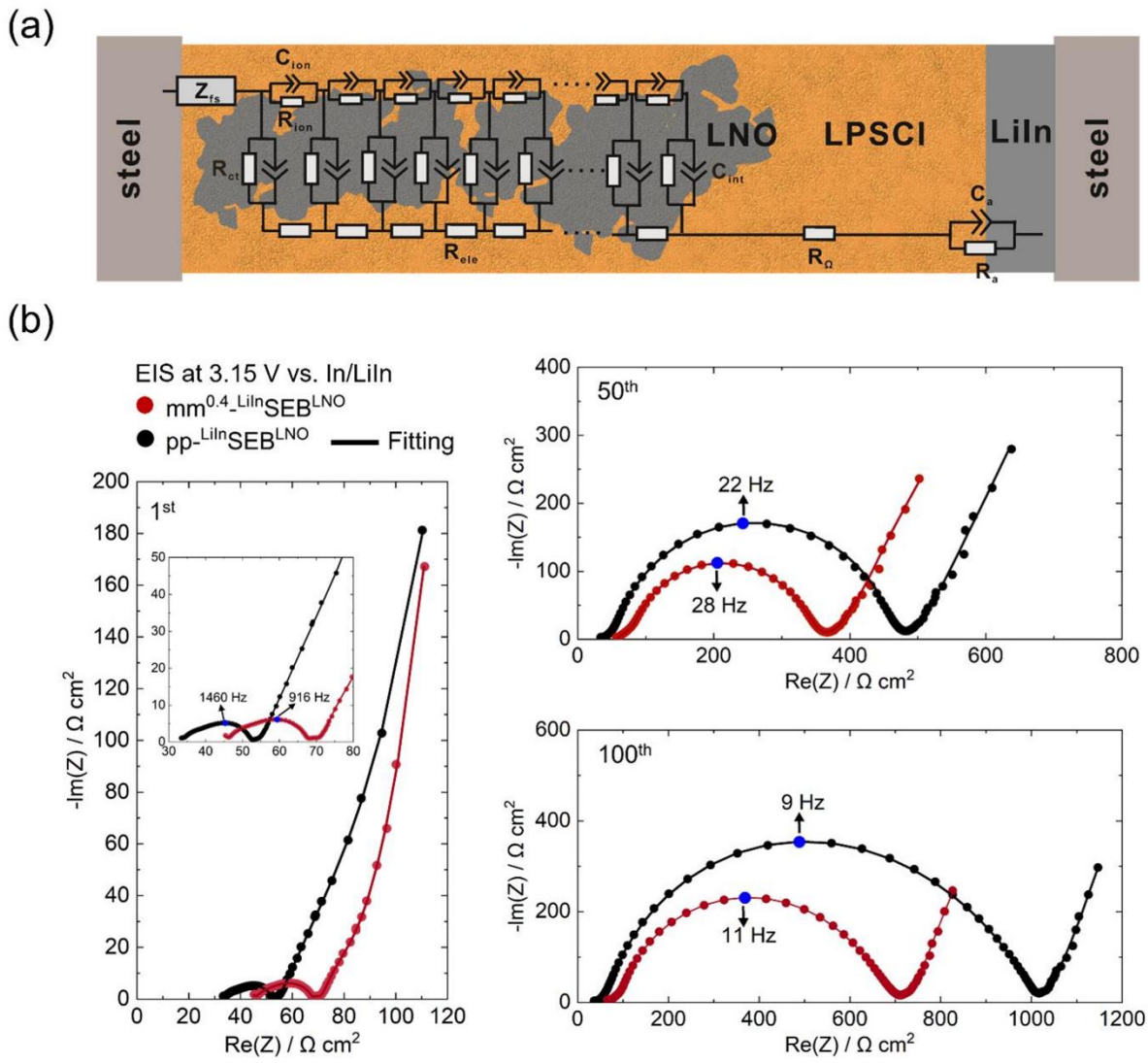

Figure 7. (a) Schematic illustration of the TLM for impedance fitting includes resistances for charge transfer (R_{ct}), electronic transport (R_{ele}), and ionic transport (R_{ion}) in the cathode composite, complemented by interfacial capacitances (C_{int}) and ionic transport capacitances (C_{ion}). The finite space Warburg element (Z_{fs}) represents the influence of current constriction. [27] The complete SEB model incorporates electrolyte resistance (R_Ω), anode resistance (R_a), and capacitance (C_a). (b) Nyquist plots show the impedance for 1st (left), 50th (upper right), and 100th (bottom right) cycles for pp-^{LiIn}SEB^{LNO} and mm$^{0.4}$-^{LiIn}SEB^{LNO}. An inset in the figure (left) highlights the spectrum from the 1st cycle. The apex frequency is marked in blue on each Nyquist plot.

2.5 Cathode interface degradation analyzed by ToF-SIMS

TOF-SIMS semi-quantitatively[65] detects decomposition products between LNO and LPSCl, such as phosphates (PO_x^-, including PO_2^- and PO_3^-) and sulfates (SO_x^-, including SO_2^- and SO_3^-),[47, 66-68] before and after cycling of pp-^{LiIn}SEB^{LNO} and mm$^{0.4}$-^{LiIn}SEB^{LNO}. Initially, surface analyses are conducted on the cathode composite surface that had been in contact with the steel current collector.[67] **Figure 8a** presents boxplots comparing PO_x^- and SO_x^- fragment intensities before and after cycling. The results show that pp-^{LiIn}SEB^{LNO} exhibits higher intensity of PO_x^- compared to mm$^{0.4}$-^{LiIn}SEB^{LNO}. This suggests that the modification layer effectively reduces the formation of PO_x^-. However, SO_x^- intensity decreases significantly for both pLPSCl and m$^{0.4}$LPSCl after cycling. This result aligns with findings from Walther et al. when VGCF is used as a conductive agent.[66]

Subsequently, wedge-shaped sputter craters are formed by increasing the sputter dose density across a rectangular area from left to right, thereby allowing depth-dependent analysis from shallow to deep, respectively. A schematic of such a wedge-shaped sputter crater is shown in **Figure 8b**. This allows visualization of the depth distribution of side reaction products from the shallow end of the crater to the deep end of the crater. As a result, **Figure 8c** shows the normalized surface spectra as the line distribution of PO_x^- and SO_x^- for pp-^{LiIn}SEB^{LNO} and mm$^{0.4}$-^{LiIn}SEB^{LNO} before and after cycling. NiO_2^- signals start to occur at the same sputtering depth for all samples (**Figure S15**). For simplification, the average NiO_2^- value across all samples is plotted in **Figure 8c** to mark the point at which sputtering begins to reach the LNO particles.

Before cycling, the cathode composites of pp-^{LiIn}SEB^{LNO} and mm$^{0.4}$-^{LiIn}SEB^{LNO} show consistent overlap for PO_x^- and SO_x^- as the contact between LNO (fully lithiated) and LPSCl during sample preparation leads to the formation of PO_x^- and SO_x^-.[67] Therefore, any differences between the samples detected after cycling can be attributed to variations in degradation between the tested cells, as semi-quantitative analysis is feasible for samples under the same testing conditions.

After cycling, the PO_x^- signal intensity of pp-^{LiIn}SEB^{LNO} is more intense than that of mm$^{0.4}$-^{LiIn}SEB^{LNO} in the shallow region of the sputter crater, whereas the SO_x^- shows consistent overlap. This aligns with the surface spectral analyses conducted prior to crater formation, as discussed in **Figure 8a**. However, the SO_x^- signal intensity of pp-^{LiIn}SEB^{LNO} begins to surpass that of mm$^{0.4}$-^{LiIn}SEB^{LNO} when the sputtering depth increases. Overall, the PO_x^- signal intensity spans the entire depth from the steel to the LNO surface, whereas the SO_x^- signal is weaker near the surface of the pellet that had been in contact with the steel current collector.[66] However, the underlying mechanisms that cause the variations in PO_x^- and SO_x^- distribution remain unclear and warrant further research. In summary, ToF-SIMS analysis reveals that the

mm$^{0.4}$-^{LiIn}SEB^{LNO} demonstrates improved CEI stability over pp-^{LiIn}SEB^{LNO}, as indicated by its lower PO_x^- and SO_x^- intensities after cycling.

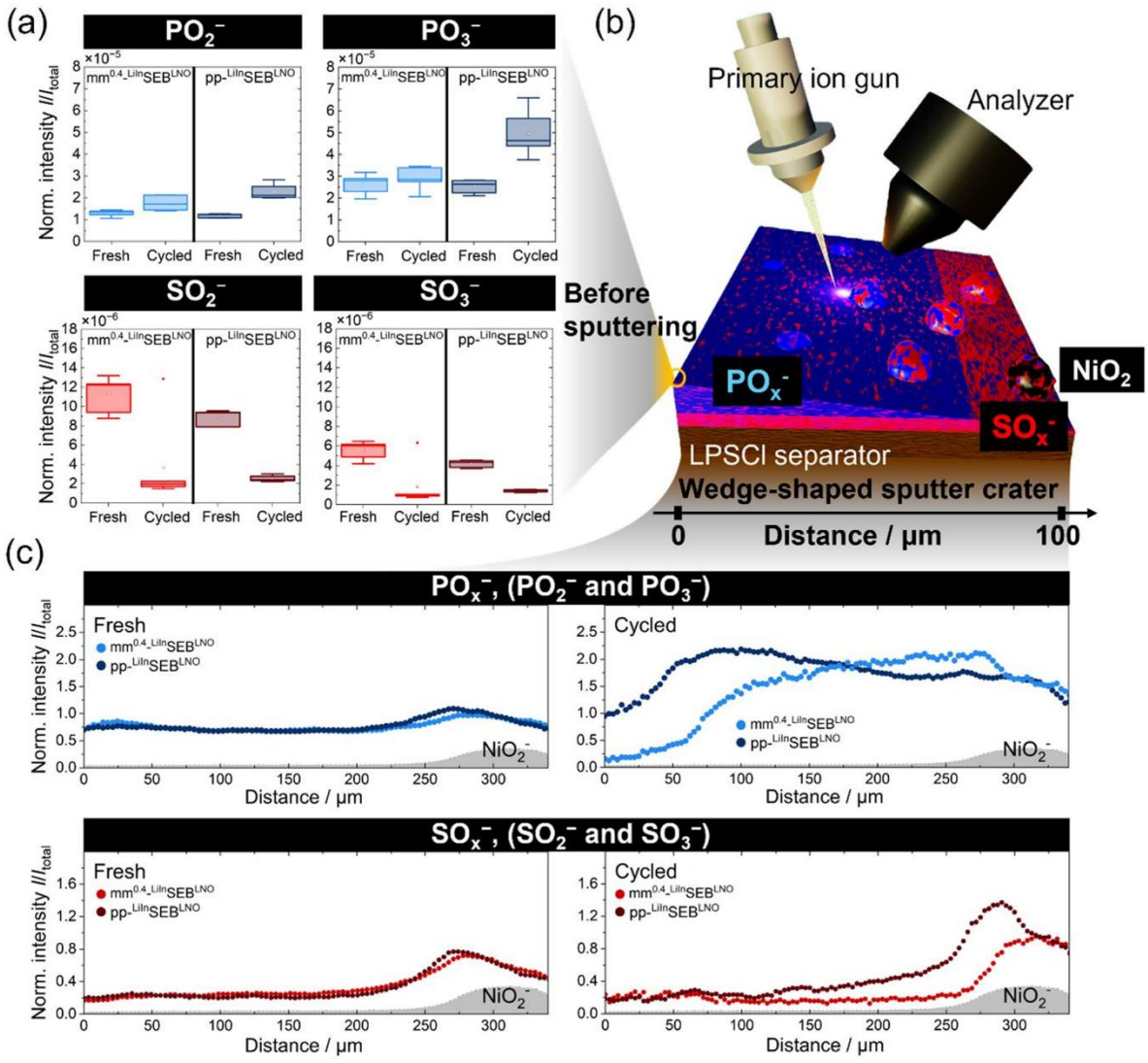

Figure 8. ToF-SIMS detects PO_x^- (PO_2^- and PO_3^-) and SO_x^- (SO_2^- and SO_3^-) decomposition products in the cathode composite of pp-^{LiIn}SEB^{LNO} and mm$^{0.4}$-^{LiIn}SEB^{LNO} before and after cycling. (a) PO_x^- and SO_x^- are presented as boxplots with normalized intensities based on six data points. (b) A schematic illustrates wedge-shaped crater formation by increasing sputter dose density from left to right. Subsequently, ToF-SIMS is used to detect side reaction products. The blue layers and dots represent PO_x^-, while the red layers and dots represent SO_x^-. The round shapes indicate the LNO particle which gives NiO_2^- intensity. (c) Normalized ToF-SIMS surface spectra display PO_x^- and SO_x^- distributions, with the gray area indicating average NiO_2^- values where sputtering reaches LNO particles.

2.6 Cycling stability of $^{Li}SEB^{LNO}$ using a $m^{0.4}LPSCl$ separator

To evaluate the cell performance with lithium metal and LNO, cycling tests are performed with the cell configuration Li|LPSCl|LPSCl/VGCF/LNO, denoted as $^{Li}SEB^{LNO}$. The $m^{0.4}LPSCl$, shown to enhance cathode performance in $^{LiIn}SEB^{LNO}$, is used as a catholyte with the LNO cathode in this section. Consequently, we compare lithium metal anode interfacial stability using either pLPSCl or $m^{0.4}LPSCl$ as separator, thus forming two cells named $pm^{0.4}$-$^{Li}SEB^{LNO}$ and $mm^{0.4}$-$^{Li}SEB^{LNO}$, respectively. Both cell configurations are schematically shown in **Figure 9a**. Cycling tests are conducted at a rate of 0.1C (2.1 $mA \cdot cm^{-2}$, derived from a LNO practical capacity of 200 $mAh \cdot g^{-1}$) and at a temperature of 25 °C.

Figure 9b shows that both $pm^{0.4}$-$^{Li}SEB^{LNO}$ and $mm^{0.4}$-$^{Li}SEB^{LNO}$ exhibit similar performances from the 1st cycle (around 140 $mAh \cdot g^{-1}$) to the 25th cycle (around 111 $mAh \cdot g^{-1}$). This suggests that the Li|$m^{0.4}LPSCl$ and Li|pLPSCl SEI exhibits a similar capacity degradation. The slightly lower capacity of $^{Li}SEB^{LNO}$ (**Figure 9b**) than $^{LiIn}SEB^{LNO}$ (**Figure 6a**) may be due to the different pressure applied during cycling—20 MPa for $^{Li}SEB^{LNO}$ versus 60 MPa for $^{LiIn}SEB^{LNO}$. The reduced pressure for $^{Li}SEB^{LNO}$ is for preventing lithium metal from being pressed through the separator, causing a short circuit. After 25 cycles, the $pm^{0.4}$-$^{Li}SEB^{LNO}$ experiences a short circuit. In contrast, the $mm^{0.4}$-$^{Li}SEB^{LNO}$ maintains 71.5% capacity retention after 100 cycles (around 97 $mAh \cdot g^{-1}$), similar to the retention of $mm^{0.4}$-$^{LiIn}SEB^{LNO}$. This demonstrates that $m^{0.4}LPSCl$ separator effectively impedes dendrite growth in $mm^{0.4}$-$^{Li}SEB^{LNO}$. To further explore this, we examine the SEI stability between $m^{0.4}LPSCl$ and lithium metal in the following sections.

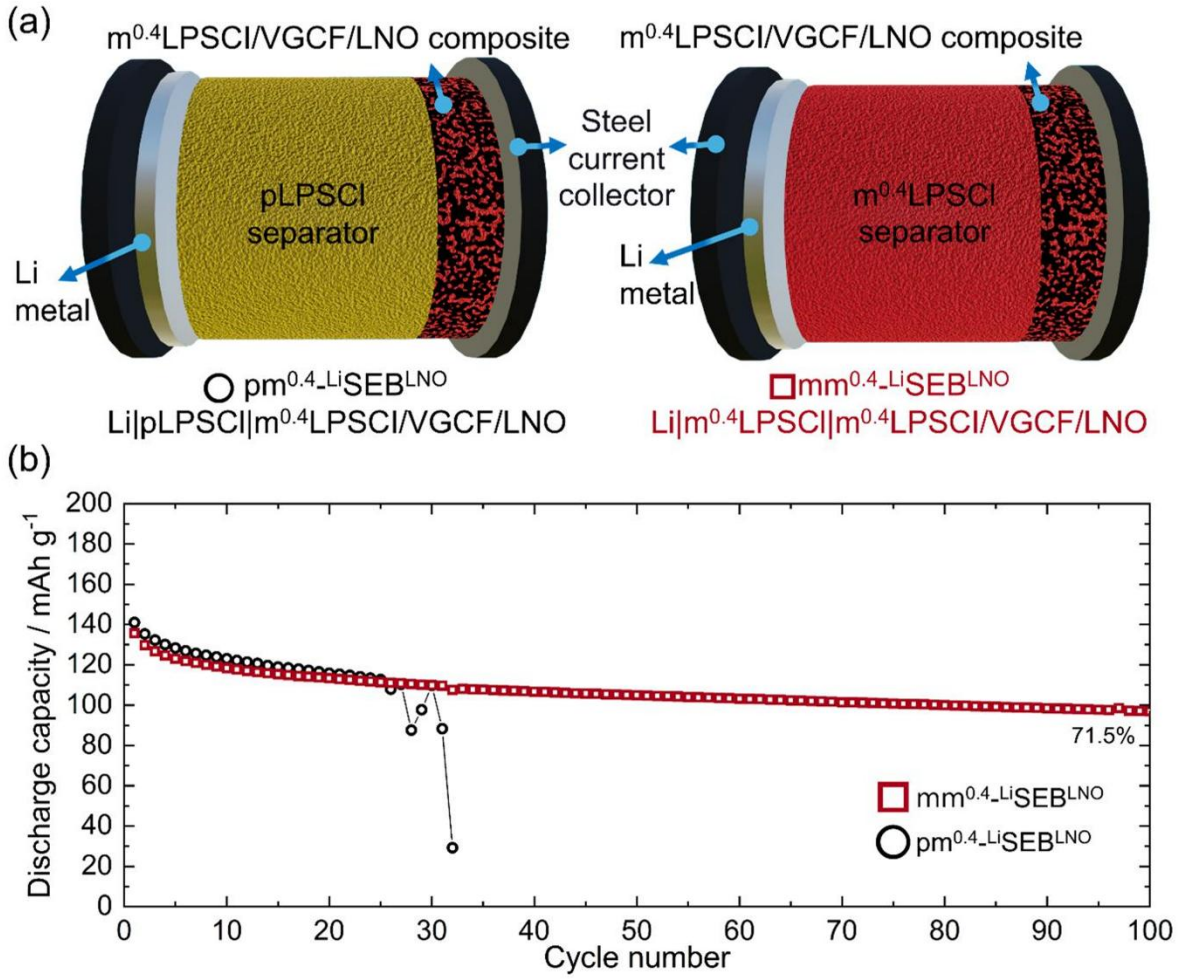

Figure 9. (a) The schematic depicts the cell configurations of $pm^{0.4}$-$^{Li}SEB^{LNO}$ (Li|pLPSCl|$m^{0.4}$LPSCl/VGCF/LNO) and $mm^{0.4}$-$^{Li}SEB^{LNO}$ (Li|$m^{0.4}$LPSCl|$m^{0.4}$LPSCl/VGCF/LNO). Both SEBs consist of a lithium metal anode and an $m^{0.4}$LPSCl/VGCF/LNO cathode composite, differing only in their separators: pLPSCl for $pm^{0.4}$-$^{Li}SEB^{LNO}$ and $m^{0.4}$LPSCl for $mm^{0.4}$-$^{Li}SEB^{LNO}$. (b) Cycling performance of pellet-type $mm^{0.4}$-$^{Li}SEB^{LNO}$ and $pm^{0.4}$-$^{Li}SEB^{LNO}$.

2.7 Stability between lithium metal anode and LPSCl

Critical current density (CCD) tests assess the risk of short-circuits from dendrite growth in symmetric Li|LPSCl|Li cells. The CCD characterizes two key failure modes: (1) pore formation at the Li|LPSCl interface, causing current localization leading to dendrite growth, and (2) lithium dendrite formation and fracture within the separator. [69] Since surface modification does not prevent contact loss, we focus on dendrite formation within the separator. To mitigate pore formation, we apply 20 MPa of pressure during cycling and increase the current density by 0.1 $mA \cdot cm^{-2}$ per CCD test step. [69] Additionally, the charge per step is fixed at 1 $mAh \cdot cm^{-2}$.

Figure 10a shows the CCD results. pLPSCl and $m^{0.4}$LPSCl short-circuit at 1 $mA \cdot cm^{-2}$ and 1.6 $mA \cdot cm^{-2}$, respectively. For $m^{0.4}$LPSCl, the increased voltage due to pore formation is observed as of a current density of 1.3 $mA \cdot cm^{-2}$, which accelerates dendrite growth. [12, 69, 70] The coupled EIS measurements after every current step are shown in **Figure S16**. Impedance drops sharply at 1 $mA \cdot cm^2$ for pLPSCl and 1.6 $mA \cdot cm^2$ for $m^{0.4}$LPSCl, indicating a short circuit, consistent with CCD results. In addition, EIS shows higher R_Ω for $m^{0.4}$LPSCl (49 $\Omega \cdot cm^2$) than pLPSCl (27 $\Omega \cdot cm^2$), but both have similar Li|LPSCl resistance (8 $\Omega \cdot cm^2$) after the first 0.1 $mA \cdot cm^{-2}$ cycle. It confirms that the $m^{0.4}$LPSCl does not contribute additional interfacial resistance against lithium metal and can improve CCD.

Fuchs et al. report that unidirectional current density (UCD) tests with one-way stripping can support CCD to distinguish pore formation at a Li|LPSCl interface and dendrite formation within separators. [69] **Figure 10b** shows UCD results using the same configuration and pressure as in the CCD test. The result reveals that pLPSCl and $m^{0.4}$LPSCl short-circuit at approximately 0.7 $mA \cdot cm^{-2}$ and 1.2 $mA \cdot cm^{-2}$, respectively, aligning with the results of CCD.

To distinguish pore formation and dendrite growth in UCD, EIS after each stripping step (**Figure S17a**) reveals impedance increases from pore formation, which are not evident in CCD tests. **Figure S17b** shows similar impedance increases (5 $\Omega \cdot cm^2$) from 0.1 to 0.6 $mA \cdot cm^2$ for both pLPSCl and $m^{0.4}$LPSCl samples, indicating comparable pore formation. [69] In addition, the absence of a rapid voltage rise before pLPSCl short circuit suggests that pore formation is not its primary cause. [69] As a result, $m^{0.4}$LPSCl can better mitigate dendrite formation within the separator than pLPSCl under similar extent of pore formation. On the other hand, the $m^{0.4}$LPSCl shows a sudden voltage rise before short-circuiting at 1.2 $mA \cdot cm^{-2}$, suggesting pore formation at the Li|$m^{0.4}$LPSCl interface as a key cause for short-circuiting at high current density. [69]

Reduced dendrite formation within the separator could stem from inhibiting lithium infiltration due to lower electronic conductivity of the separator[30] or a stable artificial SEI forming between lithium metal and $m^{0.4}$LPSCl. Direct current (DC) polarization method tests show that the electronic conductivity of $m^{0.4}$LPSCl ($1.5 \cdot 10^{-10}$ $S \cdot cm^{-1}$) is slightly lower than of pLPSCl

($2.9 \cdot 10^{-10}$ $S \cdot cm^{-1}$) (**Figure S18**). Consequently, we further investigate the SEI formation between $m^{0.4}$LPSCl and lithium metal in the following sections. Overall, the higher CCD and UCD for $m^{0.4}$LPSCl than pLPSCl confirms its ability to delay dendrite formation within the separator.

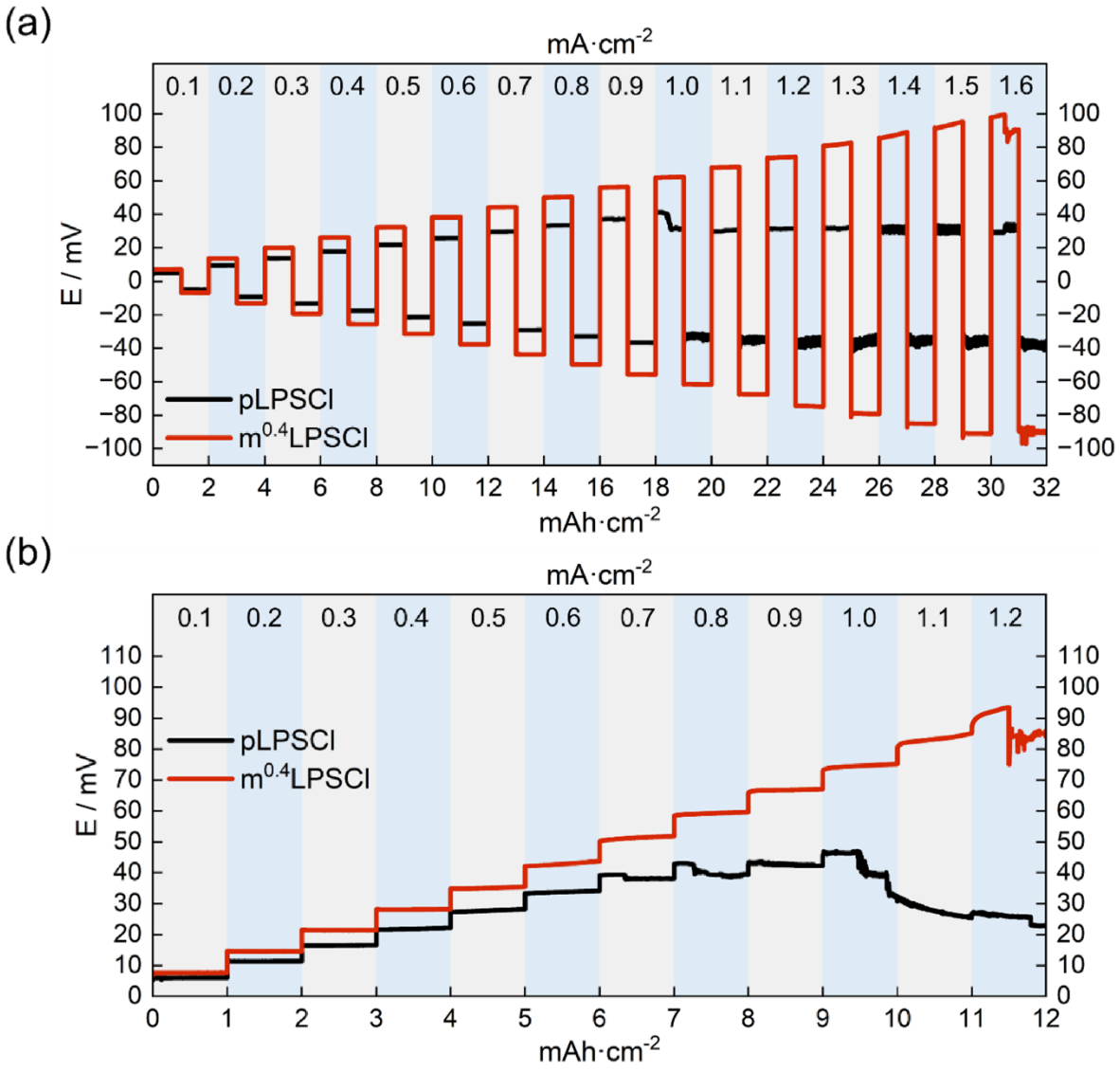

Figure 10. (a) CCD tests of symmetric Li|LPSCl|Li cells cycled under the pressure of 20 MPa. The current density is gradually increased by 0.1 $mA \cdot cm^{-2}$ per step. Additionally, the charge per step is fixed at 1 $mAh \cdot cm^{-2}$. (b) UCD tests of symmetric Li|LPSCl|Li cells cycled under the pressure of 20 MPa. The current density is gradually increased by 0.1 $mA \cdot cm^{-2}$ per step. Additionally, the charge per step is fixed at 1 $mAh \cdot cm^{-2}$.

2.8 CTTA assesses SEI growth at the Li|LPSCl interface

To quantify SEI growth over time at the Li|LPSCl SEI, we apply the method of coulometric titration time analysis (CTTA) [8] to the cell configuration LiIn|LPSCl|steel. After applying 15.6 μA·cm^{-2} for 0.1 hours to plate lithium metal at the steel current collector, the cell voltage is −0.62 V as lithium metal deposits at the steel working electrode. Ideally, with a stable SE without side reactions in contact with lithium metal, the cell potential would remain constant. In contrast, side reactions that consume lithium metal cause the potential to rise over time once lithium depletes or loses contact with the working electrode. As soon as the cell voltage reaches −0.57 V, we apply more cycles of CTTA with fixed charge (Q). The time required to consume the same amount of lithium metal increases with number of titration steps (τ_i), which indicates the formation of a SEI due to accumulation of side reaction products. [8] The cumulative charge (Q_Σ) consumed in these side reactions can be expressed as equation [4]: [8]

$$Q_\Sigma = \sum Q \cdot (\tau_i) \qquad [4]$$

Figure 11a shows a gradual decrease in the lithium metal consumption rate as the experiment progresses. This suggests that the SEI growing at the interface has passivation characteristics. [8] However, pLPSCl needs 384 hours to reach 30 μAh of cumulative charge, which is longer than that of m$^{0.4}$LPSCl at 230 hours. This suggests that m$^{0.4}$LPSCl undergoes additional side reactions with the lithium metal anode, forming an artificial SEI layer that may improve CCD and UCD performance.

Figure 11b shows that SEI growth for both m$^{0.4}$LPSCl and pLPSCl follows a linear relationship with the square root of time. This suggests that SEI growth follows diffusion-controlled kinetics, meaning SEI formation continue indefinitely. [8, 11] Notably, while SEI formation and loss of active lithium metal may seem minor in short-term studies, they pose an issue for the "anode-free" cell concept. [8] As a result, lithium metal consumption for pLPSCl and m$^{0.4}$LPSCl is calculated using the square root of time after 1 year (8760 hours). The accumulated charge of SEI formation reaches about 0.14 mAh·cm^{-2} (SEI thickness 1.3 μm) for pLPSCl and 0.18 mAh·cm^{-2} (SEI thickness 1.6 μm) for m$^{0.4}$LPSCl at 25 °C. The thickness calculation assumes that a charge of 1 μAh·cm^{-2} (≈ 3.7 × 10^{-8} mol·cm^{-2}) of Li metal corresponds to an SEI thickness of approximately 9 nm, based on a compact mixture of Li_2S, LiCl, and Li_3P, without considering any gaseous products. [8] This suggests a minimal difference in lithium metal consumption between m$^{0.4}$LPSCl and pLPSCl.

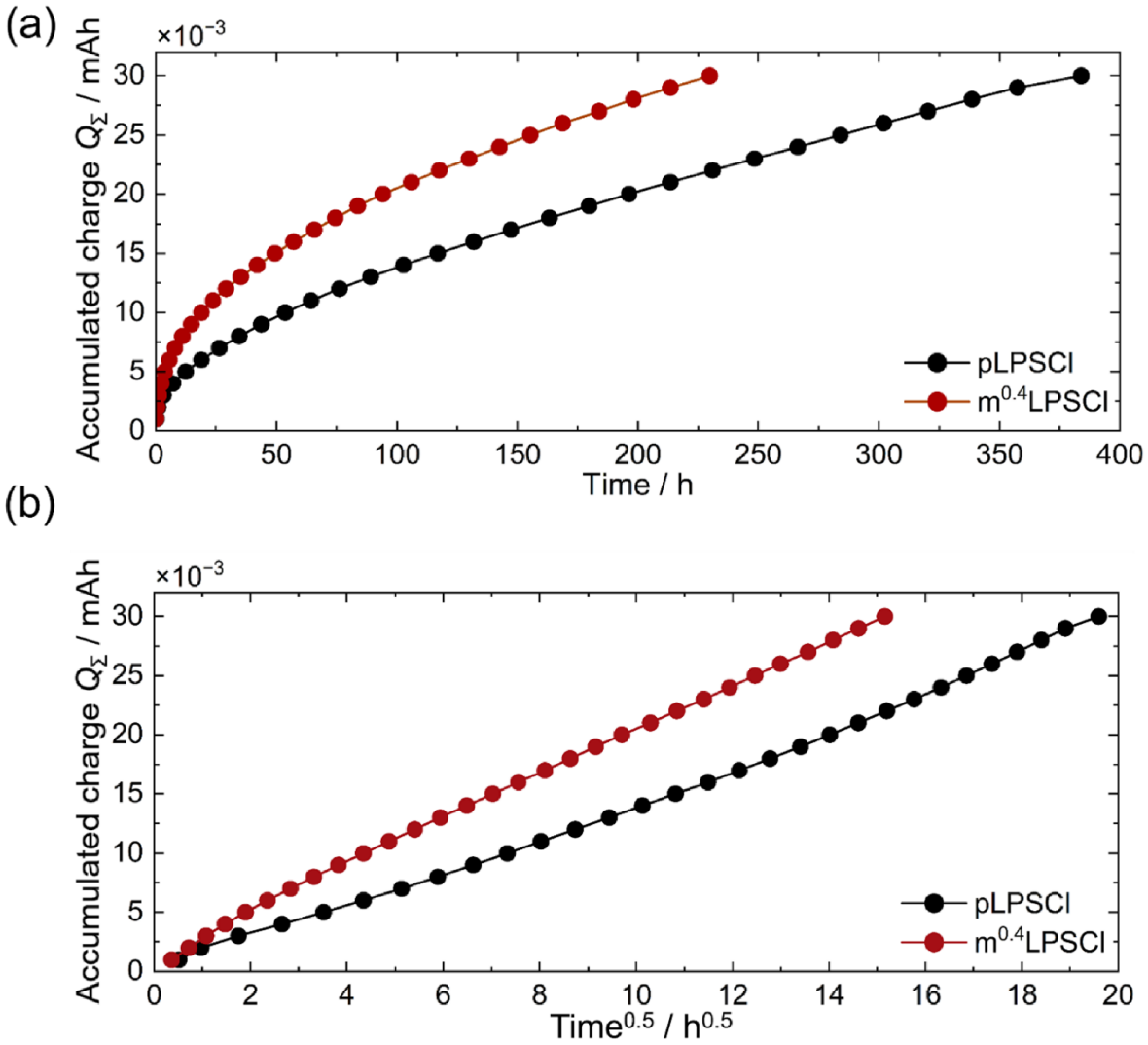

Figure 11. CTTA test results comparing LiIn|pLPSCl|steel and LiIn|m$^{0.4}$LPSCl|steel cells by repeated application of 15.6 µA·cm^{-2} for 0.1 hours per step until an accumulated charge of 30 µAh is reached. The accumulated charge from lithium metal consumption during CTTA is plotted (a) as a function of time and (b) against the square root of time.

2.9 *In situ* XPS analysis assesses the chemical structure of the SEI

In situ XPS can be used to examine degradation products of the reaction between lithium metal and LPSCl. [71] **Figure 12a** illustrates how this analysis is carried out: lithium metal is deposited onto the sample using a sputter gun, while XPS monitors SEI formation after each lithium deposition step. [71] To investigate the influence of modification, the extensively modified m^{NMP}LPSCl is selected and compared with pLPSCl. The degradation products between pLPSCl and lithium metal include Li_2S, Li_3P, and LiCl. [8, 71] Given the presence of NMP molecules on the m^{NMP}LPSCl surface, the analysis herein focuses on O 1s, Li 1s, N 1s, S 2p, and P 2p spectra, associated with SEI formation on m^{NMP}LPSCl (**Figure 12b**) and pLPSCl (**Figure 12c**) respectively. The Cl 2p spectrum is excluded as LiCl remains stable against lithium, [9] with minimal binding energy differences between Cl^- in argyrodite. [71]

The SEI for both pLPSCl and m^{NMP}LPSCl contains Li_2O (528.9 eV), Li_2S (160.4 eV), reduced phosphorous species (P_{red}) [9] (130.1 eV), and Li_3P (126.4 eV). [71] Li_2O formation is commonly observed during operando scanning prior to lithium plating, likely due to trace oxygen impurities, and therefore observed in both samples. [76] A unique feature of m^{NMP}LPSCl is highlighted in the N 1s spectrum, where the N-(C=O) peak is observed reduced to Li_3N after lithium deposition. [72] This artificial SEI containing Li_3N is particularly significant, as Li_3N is known to exhibit high ionic conductivity (~10^{-3} $S \cdot cm^{-1}$) and enhances interfacial stability at the Li|$m^{0.4}$LPSCl interface. [73 74] Additionally, Park et al. reported that Li_3N has strong wetting interaction with lithium metal anode, effectively preventing dendrite growth. [75] Notably, as lithium deposition increases, the S 2p and P 2p spectra indicate a deceleration of side reactions (Li_2S, P_{red}, and Li_3P) in both m^{NMP}LPSCl and pLPSCl, suggesting a stabilization of SEI formation (**Figure S19**). [8, 71] These properties of SEI composition may contribute to the improved CCD and UCD performance of $m^{0.4}$LPSCl.

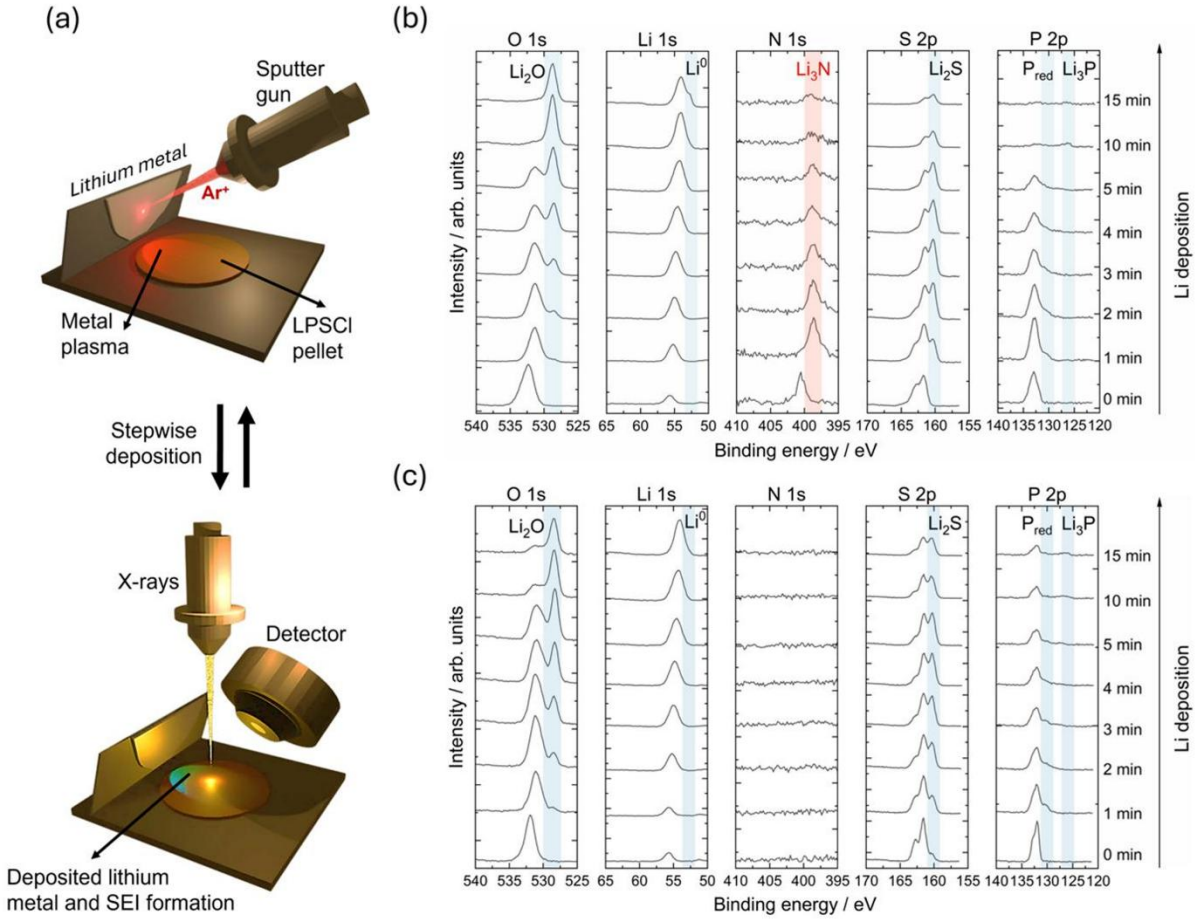

Figure 12. (a) Schematic illustration of *in situ* XPS. Lithium metal is sequentially deposited onto the samples using a sputter gun (top), with XPS (bottom) continuously monitoring binding energy changes during the lithium metal deposition. The O 1s, N 1s, S 2p, P 2p, and Li 1s XPS spectra of (b) m^{NMP}LPSCl and (c) pLPSCl pellets with increasing lithium deposition (bottom to top) highlight the formation of side reaction products: Li_2O (528.9 eV), Li^0 (53.9 eV), Li_3N (398.5 eV), Li_2S (160.4 eV), P_{red} (130.1 eV), and Li_3P (126.4 eV).

3. Conclusion

In this study, we present a method to modify LPSCl by diluting NMP in o-xylene, followed by vacuum drying at 120 °C for two days. This process results in a surface modification layer of m^xLPSCl, consisting of NMP complexed with LPSCl, along with the formation of polysulfides, sulfate, and phosphate. This paper employs LNO as the cathode active material due to its high practical capacity despite its instability with LPSCl, making it valuable for studying interfacial degradation. Our results demonstrate that using $m^{0.4}$LPSCl as a catholyte improves cycling performance due to better active mass utilization. ToF-SIMS analysis confirms that m^xLPSCl effectively mitigates LNO|LPSCl interface degradation and, particularly the formation of oxygenated species. When $m^{0.4}$LPSCl is used as a separator against the lithium metal anode, it exhibits improved cycling stability beyond 100 cycles without short-circuiting, whereas pLPSCl short-circuits after 25 cycles. This improvement may stem from Li_3N formation at the interface, creating an artificial SEI layer that inhibits dendrite formation, as confirmed by CTTA and *in situ* XPS. These findings highlight a new approach to mitigate solid-state battery degradation.

. Experimental methods

4.1. Reagents and materials

Lithium hydroxide monohydrate ($LiOH \cdot H_2O$), nickel oxide (NiO), lithium carbonate (Li_2CO_3), vapor grown carbon fibers (VGCF), ortho-xylene (o-xylene), and anhydrous N-methyl-2-pyrrolidone, 99.5% (NMP) were purchased from Sigma-Aldrich. The water content of NMP was measured using Karl Fischer titration, revealing that the obtained NMP solvent contained only 0.2 ppm of water. Indium foil (thickness 100 µm) was obtained from chemPUR GmbH. Lithium metal foil (thickness 100 µm) was bought from Albemarle Rockwood Lithium GmbH. $LiNiO_2$ (LNO) was self-synthesized by the steps described in section 4.2. Li_6PS_5Cl was bought from NEI Corporation. The LPSCl was then wet milled to reduce the particle size by the steps described in section 4.3. All LPSCl samples in this study were pre-treated by wet milling[41-43] to reduce particle size, essential for use as a catholyte[41, 77] and separator[12].

4.2. Synthesis of single crystal LNO

To obtain single crystal LNO, 10 g of $LiOH \cdot H_2O$ is manually ground in an agate mortar for 30 minutes. Then, 16.18 g of NiO is added and again ground for 30 minutes. The mixture is loaded into alumina crucibles and annealed under an oxygen flow at 780 °C for 6 hours. After that, the samples are annealed at 680 °C for another 6 hours. Both heating and cooling ramps are set to 100 $K \cdot h^{-1}$. The resulting black brick-like LNO precursor is manually ground in an agate mortar for 20 minutes. To ensure sufficient lithiation, 6.39 g of Li_2CO_3 is added to LNO precursor and the mixture is manually ground in an agate mortar for 20 minutes again. The mixture is loaded into alumina crucibles and annealed under an oxygen flow at 750 °C for 40 hours and after that at 680 °C for another 20 hours. Both heating and cooling ramps are set to 100 $K \cdot h^{-1}$. To remove excess Li_2CO_3, the LNO precursor is washed by ice-cooled deionized water (1 g LNO precursor, per 30 mL water) by vigorously agitated for 1 min. The mixture is immediately centrifuged at 4000 rpm for 2 minutes, and the supernatant is discarded. The ishing process is repeated three times, with a total water contact time of less than 12 minutes for the LNO precursor. To remove water, a final washing step with ethanol is performed. The resulting LNO precursor is dried in a vacuum oven at 60 °C overnight. Afterward, LNO precursor is loaded into alumina crucibles and annealed at 680 °C for 3 h under oxygen flow (100 $cm^3 \cdot min^{-1}$). Finally, the obtained LNO is manually ground in an agate mortar for 20 minutes and sieved (45 µm mesh size) inside a glovebox. The LNO powder is then sieved again with 20 µm mesh size. 13.34 g of LNO was obtained. The synthesized LNO was analyzed with SEM (**Figure S20**) and XRD (**Figure S21**). [15]

4.3. Wet ball milling process for LPSCl

The Fritsch premium line Pulverisette 7 ball milling instrument was located outside the glovebox, but sample transfers are protected from air exposure. The rest of the procedure was conducted entirely inside the glovebox.15 g of LPSCl is mixed with 50 mL of o-xylene and 80 g of 1 mm ZrO_2 balls in an 80 mL ZrO_2 lined pot. The mixture is ball milled at 500 rpm for 10 minutes, followed by a resting period of 10 minutes. This cycle is repeated six times. Thereafter, the mixture is sieved (mesh size 100 µm) to remove the ZrO_2 balls and centrifuged to get the pLPSCl powder. The ZrO_2 balls are washed three times with o-xylene using a Hielscher UP100H Ultrasonic Processor to remove any residues of pLPSCl adhering to the ZrO_2 balls. The collected pLPSCl is dried by Buchi B-585 at 120 °C with $2 \cdot 10^{-2}$ mbar for 2 days. Finally, the LPSCl is ground for 10 minutes to break up aggregates, then sieved (mesh size 20 µm).

4.4. Synthesis of m^{x}LPSCl

Sample preparation was carried out either under vacuum or inside a glovebox (oxygen and water vapor concentrations below 0.1 ppm) to prevent air exposure. 1 g of LPSCl, 40 mL of *o*-xylene, and different amounts of NMP are added to a centrifuge tube and mixed by shaking for one minute. After shaking, the mixture is centrifuged at 4000 rpm for 2 minutes and the supernatant is discarded. The resulting powder is dried by Buchi B-585 at 120 °C with $2 \cdot 10^{-2}$ mbar for 48 hours. **Figure 1** lists the varying amounts of NMP used to create modified m^{x}LPSCl. Additionally, LPSCl treated solely with NMP without o-xylene, is termed m^{NMP}LPSCl. To further investigate if temperature increases affect the modification, m^{NMP}LPSCl undergoes additional drying at 150 °C by Buchi B-585 with $2 \cdot 10^{-2}$ mbar for 48 hours, which is termed ht-m^{NMP}LPSCl.

4.5. X-ray diffraction

XRD is used to check the crystalline structure of pLPSCl and m^{x}LPSCl by using a Panalytical Empyrean XRD with Cu Kα radiation. Diffraction patterns are collected in a 2θ angular range from 10° to 85° with a step size of 0.026°, 0.04 rad. soller slits, and 1/2° anti-scatter slit. For checking the LNO crystalline structure, XRD is performed on LNO powders filled into glass capillaries with 0.5 mm inner diameter. The samples are mounted in an Empyrean 3 diffractometer (Malvern PANalytical) with Mo Kα source and measured in Debye–Scherrer geometry. The angular 2Θ range is 5°–40° with a step size of 0.007° and a scan speed of 1° min^{-1}.

4.6. Fourier-transform infrared spectroscopy

FTIR spectra are recorded with a total number of 96 scans on an ATR-FTIR Thermo Fischer Scientific iD5 ATR spectrometer (550-4000 cm^{-1}). To check the chemical structure of m^{x}LPSCl

samples, 80 mg of samples are pressed into pellets (10 mm in diameter). The pressure applied for making pellets is 3 kN for 3 minutes using automatic press Atlas Autotouch automatic press.

4.7. Scanning electron microscopy

SEM (GeminiSEM 560) at an acceleration voltage of 2 kV with Aperture Size of 20 µm is adopted to characterize the morphology of LNO and the cathode composite after cycling. Back-scattered electron images and secondary electron images are recorded. The samples are measured in powder form, sticking tightly on the conductive copper tape. The examination of particle cracking in the cathode composite after cycling is performed using SEM images obtained after ion beam milling with a Leica EM TIC 3X with three Ar^+-ion guns at 6 kV and 2.2 mA for a duration of 6 hours, at a temperature of −80 °C.

4.8. Transmission electron microscopy

Powder of pLPSCl, m^{200}LPSCl, and m^{NMP}LPSCl is dispersed on lacey carbon copper TEM mesh grids inside an argon-filled glovebox and loaded into a Mel-Build TEM holder with inert gas and vacuum transfer as well as liquid nitrogen cooling capability. The sample is transferred in an argon atmosphere to an external pumping stand and evacuated. After evacuation, the holder is transferred in vacuum to a double Cs-corrected JEOL JEM 2200FS TEM with in-column omega filter and 200 kV acceleration voltage. All measurements are performed at cryogenic temperatures of –100 °C to reduce beam damage to the highly electron beam sensitive LPSCl. High-resolution (HR)-TEM images are recorded with a TVIPS TemCam XF416FS camera. The EDX data is recorded in scanning mode with a semi-convergence angle of 15.07 mrad using a Bruker Nano XFlash Detector 5060 and evaluated using the Software Bruker Esprit 2.3.

4.9. Time-of-flight secondary ion mass spectrometry

All ToF-SIMS measurements are conducted on an M6 Plus instrument (IONTOF GmbH, Münster, Germany) in negative ion mode. All surface spectra are acquired using the Nanoprobe 50 LMIG in bunched mode with 30 keV Bi_3^+ clusters as primary ion species. Surface spectra for statistical comparison of fragment ion intensities are acquired in an area of 200x200 μm^2 with 128x128 pixels and a dose density of $1 \cdot 10^{12}$ ions·cm^{-2}. To ensure reliability of our data, 5 mass spectra were measured per sample. For wedge preparation the DSC/S sputter gun with 2 kV Cs^+ is used in a 300x100 μm^2 area with 200 ms maximum dwell time. Subsequent surface spectra of the wedges are acquired at 400x400 μm^2 and 256x256 pixels with a dose density of $5 \cdot 10^{11}$ ions·cm^{-2}. For data evaluation, 20 line scans of the wedges in x-direction are summed up using the SurfaceLab 7.4 Software (IONTOF GmbH, Münster, Germany) to generate the graphs.

4.10. X-ray photoelectron spectroscopy

XPS is conducted using a PHI5000 Versa Probe IV from Physical Electronics GmbH equipped with an aluminum anode (Al Kα = 1486.6 eV). The settings include a beam power of 50 W, voltage of 15 kV, and a beam diameter of 200 μm. The analyzer pass energy is set to 224 eV for survey scans and 55 eV for detailed spectra. Samples are transported in an argon-filled transfer module. Regarding *in situ* XPS, lithium metal is sequentially deposited onto the samples at a rate of 0.25 nm·min^{-1}, reaching a total thickness of 33 nm. Throughout this process, changes in the binding states are continuously monitored. Data evaluation utilizes CasaXPS software. The XPS spectra of the samples are initially calibrated using the adventitious carbon signal at 284.8 eV to identify the main S 2p component (PS_4^{3-}). The XPS spectra can then be calibrated based on the PS_4^{3-} signal at 161.6 eV. [66]

4.11. Cell assembly

The ^{LiIn}SEB^{LNO} are assembled in the configuration of LiIn|LPSCl|LPSCl/VGCF/LNO. ^{LiIn}SEB^{LNO} are prepared in an argon-filled glovebox (LabMaster model, MBraun, Garching, Germany), which maintains oxygen and water vapor concentrations below 0.1 ppm each. Firstly, 80 mg of LPSCl is compressed into a 10 mm diameter pellet that functions as a separator within a PEEK casing. Subsequently, the cathode composite is prepared by mixing twenty ZrO_2 balls (3 mm diameter) with 201 mg of cathode composite, consisting of 69.3% LNO, 29.7% LPSCl, and 1% vapor-grown carbon fiber (VGCF). The mixing is conducted by using ball milling with 30 Hz and 1 hour (mini-mill PULVERISETTE 23). A 12 mg cathode composite mixture is then compressed onto one side of the separator. On the opposite side, indium (100 μm thick and 9 mm in diameter) and lithium metal foils (1.8 mg, 125 μm thick, and 6 mm in diameter) are positioned in such a way that indium should contact LPSCl, while lithium metal should not directly contact LPSCl. Following the assembly, the cell undergoes compression at 30 kN for 3 minutes using Atlas Autotouch automatic press, resulting in a separator with thickness of around 650 μm and a composite cathode thickness of around 40 μm. The assembled ^{LiIn}SEB^{LNO} is subsequently encased within an external steel frame that applies approximately 60 MPa of pressure.

When using lithium metal (3.2 mg, 125 μm thick, and 8 mm in diameter) instead of Li-in alloy, the ^{Li}SEB^{LNO} are assembled in the form of Li|LPSCl|LPSCl/VGCF/LNO. In ^{Li}SEB^{LNO}, the catholyte is m$^{0.4}$LPSCl. The separators either use 100 mg of pLPSCl, or 100 mg of m$^{0.4}$LPSCl, both pressed into 10 mm diameter pellets. The cathode composite weighing 12 mg is then pressed on one side of the separator. The ^{Li}SEB^{LNO} needs to be pressed at 30 kN for 3 minutes first before placing the lithium metal foils, because higher pressure causes lithium metal to form a short circuit. The assembled ^{Li}SEB^{LNO} is subsequently encased within an external aluminum frame applying 20 MPa of pressure (controlled by a pressure sensor) during cycling.

CV is used to test the electrochemical stability in the cell configuration LiIn|LPSCl|LPSCl/VGCF. To prepare a 99 mg LPSCl/VGCF composite, 9 mg of VGCF is mixed with 90 mg of LPSCl by using ball milling with 30 Hz and 1 hour (mini-mill PULVERISETTE 23). Subsequently, 80 mg of LPSCl is compressed into a 10 mm diameter pellet that functions as a separator within a PEEK insulator. An additional 30 mg of the LPSCl/VGCF composite is then pressed onto one side of this separator. Indium and lithium metal foils are positioned on the opposite side as the counter electrode, with indium metal in direct contact with the LPSCl. The entire cell stack is compressed under a force of 30 kN for 3 minutes using Atlas Autotouch automatic press. The cell is encased in an external aluminium frame that exerts approximately 50 MPa of pressure.

For the ionic and electronic conductivity measurements of the electrolytes, the cell setup is assembled symmetrically, as steel|LPSCl|steel. 80 mg of LPSCl is compressed into a 10 mm diameter pellet that functions as a separator within a PEEK insulator. The entire cell stack is compressed under a force of 30 kN for 3 minutes using Atlas Autotouch automatic press. The cell is encased in an external aluminium frame that exerts approximately 50 MPa of pressure.

For CTTA, the configuration of the cells is steel|LPSCl|LiIn. 80 mg of LPSCl is compressed into a 10 mm diameter pellet that functions as a separator within a PEEK insulator. The entire cell stack is then compressed under a force of 30 kN for 3 minutes. Indium (100 µm thick and 9 mm in diameter) and lithium metal foils (125 µm thick and 6 mm in diameter) are placed on one side of the separator but with indium contacting the LPSCl separator. A 9.5 mm round steel sheet is placed on the other side of the separator. The cell is encased in an external aluminum frame that exerts approximately 10 MPa of pressure during the measurement.

4.12. Electrochemical measurements

For the cycling stability test of cells using LiIn as anode, $^{LiIn}SEB^{LNO}$ are charged and discharged under 0.1C. The C-rate calculations in this study are based on the practical capacity of LNO, which is around 200 mAh·g^{-1}, so that the area loading is 10.6 mg·cm^{-2}, and the area capacity is 2.1 mAh·cm^{-2} in the cells. The voltage window ranges from 2.0 V to 3.7 V vs. In/LiIn at a consistent temperature of 25 °C. A VMP-300 Biologic potentiostat is used to assess CA and EIS. For EIS, the cells are measured during cycling at 1st, 2nd, 50th, and 100th cycles. The cells are first charged under 0.1C to a voltage of 3.15 V vs. In/LiIn. Following this, CA remains consistent at this voltage until the observed current diminishes below 2% of the charging current. Subsequently, EIS measurements between 1 MHz and 100 µHz are carried out immediately after chronoamperometry. EIS sinusoidal amplitudes are set at 10 mV (from 1 MHz to 10 mHz), 5 mV (from 10 mHz to 1 mHz), and finally, 3 mV (from 1 mHz to 100 µHz). Amplitudes are adjusted per frequency to approximate a linear current response and reduce errors, as smaller AC amplitudes improve linearity. After that, the cells continuously finish charging and discharging under 0.1C. **Figure S10** illustrates the testing process, including CA

and EIS measurements, taking the first cycle as an example. MACCOR electrochemical workstation manages the continuous cycling stability tests with a constant current of 0.1C from 2.0 V to 3.7 V vs. In/LiIn at a constant temperature of 25 °C without CA and EIS measurements. For rate capability tests, batteries are charged and discharged under 0.1C within a voltage window ranging from 2.0 V to 3.7 V vs. In/LiIn at a consistent temperature of 25 °C in MACCOR electrochemical workstation.

For the cycling stability test of cells using lithium as an anode, only MACCOR electrochemical workstation is used to manage the continuous cycling stability tests with a constant current of 0.1C from 2 V to 4.3 V vs. Li^+/Li at a temperature of 25 °C.

CV experiments are conducted using a VMP-300 Biologic potentiostat at 25 °C to determine electrochemical stability. The initial voltage sweeps from the OCV to 4 V and/or 0 V at a 1 $mV \cdot s^{-1}$ scan rate.

Additionally, the ionic conductivity is measured by EIS using VMP-300 Biologic potentiostat with the climate chamber (Weiss Technik) controlling the temperature from −40 °C to 80 °C. EIS sinusoidal amplitudes are set at 100 mV from 1 MHz to 100 mHz.

Electronic conductivity is measured by DC polarization using VMP-300 Biologic potentiostat at room temperature. We use CA to maintain a constant voltage for 5 h and observe the resulting current response.

CTTA is measured by applying a current of 10 µA (15.6 $\mu A \cdot cm^{-2}$) for 0.1 hours, delivering 1 µAh of charge (1.56 µAh cm^{-2}) from In/LiIn counter electrode to the steel collector. Following this, the cell voltage typically drops to −0.62 V, due to lithium metal deposition on the current collector. Later, the cell is maintained at OCV until the side reactions consume the plated lithium metal completely. The absence of lithium metal on current collector is detected by the cell voltage and a subsequent lithium plating step is performed when the cell voltage exceeds −0.57 V. These steps are then repeated until the accumulated charge reaches 30 µAh.

4.13. Acquisition of open circuit voltage vs. capacity reference

To create an open circuit voltage vs. capacity reference curve, a $^{Li}LEB^{LNO}$ is prepared. The cathode consists of a 94/3/3 ratio of LNO/Super P carbon/PVDF binder, respectively. This cathode is prepared in a tape casting procedure from a slurry with NMP as solvent with a solid content of 56 wt% and a doctor blade thickness of 60 µm. For the cell assembly, a cathode with 12 mm diameter is punched from the dried sheet (120 °C for 12 h in vacuum) and pressed at 2000 atm. The electrolyte is 1 M $LiPF_6$ in ethylene carbonate:diethyl carbonate (1:1 vol%) with a glass fiber separator and a Celgard separator (in contact with the cathode). 14 mm diameter lithium metal anode is used as the anode. CR2032 coin cell casings with aluminum coating on the cathode are used to avoid parasitic currents that appear especially in the first

cycles. First, two formation cycles to 4.17 V vs. Li^+/Li are applied at 3 V for 36 hours to ensure stable SEI formation. Then, the cell is charged to upper cutoff voltage of 4.3 V vs. Li^+/Li. Next, 0.1C pulses for 10 minutes with 2 h subsequent relaxation each are applied 80 times with an upper cutoff voltage of 4.3 V vs. Li^+/Li. This is repeated for the discharge curve. After this pulse-relaxation procedure (similar to GITT experiments), a final checkup cycle similar to the second formation cycle is applied to ensure that no drastic changes occurred during the experiment.

4.14. Density functional theory calculations

DFT calculations are conducted using the Vienna Ab-initio Simulation Package (VASP) [78-80] with projector-augmented wave (PAW) pseudopotentials. [81, 82] The Perdew-Burke-Ernzerhof (PBE) exchange-correlation functional within the generalized gradient approximation (GGA) is employed. [83] For the slab and adsorption calculations, the convergence criteria for self-consistent field calculations are set to 10^{-6} eV for energy and 10^{-2} eV $Å^{-1}$ for forces. A plane wave basis set cutoff energy of 700 eV is applied, and the Brillouin zone is sampled using a k-point spacing of 0.25 $Å^{-1}$. A single molecule of NMP in vacuum is relaxed at the Γ-point only using the same convergence criteria. Surface energies for different crystallographic planes are created using the pymatgen code, [84] and ultimately a 1 × 1 × 5 (001) non-polar, symmetric slab (260 atoms) is chosen as a representative LPSCl surface. It is important to note that this analysis neglects possible surface segregation or reconstruction, which may introduce additional factors that are not fully accounted for. Furthermore, interactions with solvents have not been explicitly treated in this study. However, this concern is mitigated by the fact that all measurements are conducted on dried samples rather than in solution, thereby minimizing the potential impact of solvent interactions on the results. The visualizations are done using the OVITO software. [85]

Acknowledgements

B.X.S. and F.H.R. acknowledge German Federal Ministry of Education and Research (BMBF) for their financial support through the project FLiPS (03XP0261). Similarly, T.W., S.L.B., Y.Y., B.A. T.D., K.V., and A.H. appreciate the funding received from the BMBF as part of the FestBatt competence cluster (03XP0433C, 03XP0433D). Additionally, A.H. extends special thanks for the support provided under the BMBF Professorinnenprogramm III. S.S. and B.J. gratefully acknowledge the computing time provided to them at the NHR Center NHR4CES at TU Darmstadt (project number p0022791) and at RWTH Aachen University.

Conflict of Interest

The authors declare no conflict of interest.

Author Contributions

B.X.S. was responsible for the electrochemical analyses, and general characterization of materials. T.W., Y.Y., and B.X.S. conducted the TOF-SIMS analysis, while T.D. performed the TEM experiments. S.L.B. and Y.Y. conducted the XPS analysis. B.X.S. and B.A. conducted the CTTA measurement. K.V. contributed to the LEB measurement. S.S. and B.J. contributed with DFT calculations. K.V., A.H., K.A., and F.H.R. contributed to the analysis and interpretation of the experimental data. The research concept was conceived by B.X.S. and F.H.R., who also prepared the manuscript. All authors contributed to the manuscript and the analysis of experimental results.

5. References

1. S. Sen and F. H. Richter, *Advanced Science*, 2023, **10**, 2303985.
2. X. Yu, R. Chen, L. Gan, H. Li and L. Chen, *Engineering*, 2023, **21**, 9-14.
3. D. H. S. Tan, Y. S. Meng and J. Jang, *Joule*, 2022, **6**, 1755-1769.
4. J. Janek and W. G. Zeier, *Nature Energy*, 2016, **1**, 16141.
5. S. Narayanan, U. Ulissi, J. S. Gibson, Y. A. Chart, R. S. Weatherup and M. Pasta, *Nature Communications*, 2022, **13**, 7237.
6. Y. Li, S. Song, H. Kim, K. Nomoto, H. Kim, X. Sun, S. Hori, K. Suzuki, N. Matsui, M. Hirayama, T. Mizoguchi, T. Saito, T. Kamiyama and R. Kanno, *Science*, 2023, **381**, 50-53.
7. Q. Zhang, D. Cao, Y. Ma, A. Natan, P. Aurora and H. Zhu, *Advanced Materials*, 2019, **31**, 1901131.
8. B. Aktekin, L. M. Riegger, S.-K. Otto, T. Fuchs, A. Henss and J. Janek, *Nature Communications*, 2023, **14**, 6946.
9. S. Wang, M. Tang, Q. Zhang, B. Li, S. Ohno, F. Walther, R. Pan, X. Xu, C. Xin, W. Zhang, L. Li, Y. Shen, F. H. Richter, J. Janek and C.-W. Nan, *Advanced Energy Materials*, 2021, **11**, 2101370.
10. C. D. Alt, N. U. C. B. Müller, L. M. Riegger, B. Aktekin, P. Minnmann, K. Peppler and J. Janek, *Joule*, 2024, DOI: https://doi.org/10.1016/j.joule.2024.07.006.
11. L. M. Riegger, S. Mittelsdorf, T. Fuchs, R. Rueß, F. H. Richter and J. Janek, *Chemistry of Materials*, 2023, **35**, 5091-5099.
12. D. K. Singh, A. Henss, B. Mogwitz, A. Gautam, J. Horn, T. Krauskopf, S. Burkhardt, J. Sann, F. H. Richter and J. Janek, *Cell Reports Physical Science*, 2022, **3**, 101043.

13. D. K. Singh, T. Fuchs, C. Krempaszky, B. Mogwitz and J. Janek, *Advanced Science*, 2023, **10**, 2302521.

14. A. Chakraborty, S. Kunnikuruvan, S. Kumar, B. Markovsky, D. Aurbach, M. Dixit and D. T. Major, *Chemistry of Materials*, 2020, **32**, 915-952.

15. R. Rueß, D. Gomboso, M. Ulherr, E. Trevisanello, Y. Ma, A. Kondrakov, T. Brezesinski and J. Janek, *Journal of The Electrochemical Society*, 2023, **170**, 020533.

16. H. Komatsu, S. Banerjee, M. L. Holekevi Chandrappa, J. Qi, B. Radhakrishnan, S. Kuwata, K. Sakamoto and S. P. Ong, *The Journal of Physical Chemistry C*, 2022, **126**, 17482-17489.

17. S.-K. Jung, H. Gwon, S.-S. Lee, H. Kim, J. C. Lee, J. G. Chung, S. Y. Park, Y. Aihara and D. Im, *Journal of Materials Chemistry A*, 2019, **7**, 22967-22976.

18. D. H. S. Tan, E. A. Wu, H. Nguyen, Z. Chen, M. A. T. Marple, J.-M. Doux, X. Wang, H. Yang, A. Banerjee and Y. S. Meng, *ACS Energy Letters*, 2019, **4**, 2418-2427.

19. R. Koerver, I. Aygün, T. Leichtweiß, C. Dietrich, W. Zhang, J. O. Binder, P. Hartmann, W. G. Zeier and J. Janek, *Chemistry of Materials*, 2017, **29**, 5574-5582.

20. J. Auvergniot, A. Cassel, J.-B. Ledeuil, V. Viallet, V. Seznec and R. Dedryvère, *Chemistry of Materials*, 2017, **29**, 3883-3890.

21. T.-T. Zuo, R. Rueß, R. Pan, F. Walther, M. Rohnke, S. Hori, R. Kanno, D. Schröder and J. Janek, *Nature Communications*, 2021, **12**, 6669.

22. H. Zhang, H. Liu, L. F. J. Piper, M. S. Whittingham and G. Zhou, *Chemical Reviews*, 2022, **122**, 5641-5681.

23. S. H. Jung, U.-H. Kim, J.-H. Kim, S. Jun, C. S. Yoon, Y. S. Jung and Y.-K. Sun, *Advanced Energy Materials*, 2020, **10**, 1903360.

24. J.-M. Lim, T. Hwang, D. Kim, M.-S. Park, K. Cho and M. Cho, *Scientific Reports*, 2017, **7**, 39669.

25. E. Trevisanello, R. Ruess, G. Conforto, F. H. Richter and J. Janek, *Advanced Energy Materials*, 2021, **11**, 2003400.

26. H.-H. Ryu, B. Namkoong, J.-H. Kim, I. Belharouak, C. S. Yoon and Y.-K. Sun, *ACS Energy Letters*, 2021, **6**, 2726-2734.

27. G. Conforto, R. Ruess, D. Schröder, E. Trevisanello, R. Fantin, F. H. Richter and J. Janek, *Journal of The Electrochemical Society*, 2021, **168**, 070546.

28. C. S. Yoon, D.-W. Jun, S.-T. Myung and Y.-K. Sun, *ACS Energy Letters*, 2017, **2**, 1150-1155.

29. A. Banerjee, X. Wang, C. Fang, E. A. Wu and Y. S. Meng, *Chemical Reviews*, 2020, **120**, 6878-6933.

30. X. Yang, X. Gao, M. Jiang, J. Luo, J. Yan, J. Fu, H. Duan, S. Zhao, Y. Tang, R. Yang, R. Li, J. Wang, H. Huang, C. Veer Singh and X. Sun, *Angewandte Chemie International Edition*, 2023, **62**, e202215680.

31. H. Huo, M. Jiang, B. Mogwitz, J. Sann, Y. Yusim, T.-T. Zuo, Y. Moryson, P. Minnmann, F. H. Richter, C. Veer Singh and J. Janek, *Angewandte Chemie International Edition*, 2023, **62**, e202218044.

32. K. Wang, Z. Liang, S. Weng, Y. Ding, Y. Su, Y. Wu, H. Zhong, A. Fu, Y. Sun, M. Luo, J. Yan, X. Wang and Y. Yang, *ACS Energy Letters*, 2023, **8**, 3450-3459.

33. K. T. Kim, J. Woo, Y.-S. Kim, S. Sung, C. Park, C. Lee, Y. J. Park, H.-W. Lee, K. Park and Y. S. Jung, *Advanced Energy Materials*, 2023, **13**, 2301600.

34. Z. D. Hood, A. U. Mane, A. Sundar, S. Tepavcevic, P. Zapol, U. D. Eze, S. P. Adhikari, E. Lee, G. E. Sterbinsky, J. W. Elam and J. G. Connell, *Advanced Materials*, 2023, **35**, 2300673.

35. X. Zhang, X. Li, S. Weng, S. Wu, Q. Liu, M. Cao, Y. Li, Z. Wang, L. Zhu, R. Xiao, D. Su, X. Yu, H. Li, L. Chen, Z. Wang and X. Wang, *Energy & Environmental Science*, 2023, **16**, 1091-1099.

36. S.-K. Jiang, S.-C. Yang, W.-H. Huang, H.-Y. Sung, R.-Y. Lin, J.-N. Li, B.-Y. Tsai, T. Agnihotri, Y. Nikodimos, C.-H. Wang, S. D. Lin, C.-C. Wang, S.-H. Wu, W.-N. Su and B. J. Hwang, *Journal of Materials Chemistry A*, 2023, **11**, 2910-2919.

37. Y. Jin, Q. He, G. Liu, Z. Gu, M. Wu, T. Sun, Z. Zhang, L. Huang and X. Yao, *Advanced Materials*, 2023, **35**, 2211047.

38. Y. Nikodimos, S.-K. Jiang, S.-J. Huang, B. W. Taklu, W.-H. Huang, G. B. Desta, T. M. Tekaligne, Z. B. Muche, K. Lakshmanan, C.-Y. Chang, T. M. Hagos, K. N. Shitaw, S.-C. Yang, S.-H. Wu, W.-N. Su and B. J. Hwang, *ACS Energy Letters*, 2024, **9**, 1844-1852.

39. A.-K. Hatz, R. Calaminus, J. Feijoo, F. Treber, J. Blahusch, T. Lenz, M. Reichel, K. Karaghiosoff, N. M. Vargas-Barbosa and B. V. Lotsch, *ACS Applied Energy Materials*, 2021, **4**, 9932-9943.

40. D. Y. Oh, Y. J. Nam, K. H. Park, S. H. Jung, K. T. Kim, A. R. Ha and Y. S. Jung, *Advanced Energy Materials*, 2019, **9**, 1802927.

41. P. Minnmann, L. Quillman, S. Burkhardt, F. H. Richter and J. Janek, *Journal of The*

Electrochemical Society, 2021, **168**, 040537.

42. J. M. Lee, Y. S. Park, J.-W. Moon and H. Hwang, *Frontiers in Chemistry*, 2021, **9**.

43. L. Karger, B. N. Nunes, Y. Yusim, A. Mazilkin, R. Zhang, W. Zhao, A. Henss, A. Kondrakov, J. Janek and T. Brezesinski, *Advanced Materials Interfaces*, 2024, **11**, 2301067.

44. K. Wissel, L. M. Riegger, C. Schneider, A. I. Waidha, T. Famprikis, Y. Ikeda, B. Grabowski, R. E. Dinnebier, B. V. Lotsch, J. Janek, W. Ensinger and O. Clemens, *ACS Applied Energy Materials*, 2023, **6**, 7790-7802.

45. Y. Kim, W. M. Seong and A. Manthiram, *Energy Storage Materials*, 2021, **34**, 250-259.

46. Y. Wu, P. Jiang, M. Jiang, T.-W. Wang, C.-F. Guo, S.-S. Xie and Z.-L. Wang, *Nanotechnology*, 2009, **20**, 305602.

47. F. Walther, R. Koerver, T. Fuchs, S. Ohno, J. Sann, M. Rohnke, W. G. Zeier and J. Janek, *Chemistry of Materials*, 2019, **31**, 3745-3755.

48. A. Priebe, T. Xie, G. Bürki, L. Pethö and J. Michler, *Journal of Analytical Atomic Spectrometry*, 2020, **35**, 1156-1166.

49. R. F. Indrawan, H. Gamo, A. Nagai and A. Matsuda, *Chemistry of Materials*, 2023, **35**, 2549-2558.

50. M. Polanyi, *Transactions of the Faraday Society*, 1932, **28**, 316-333.

51. Y. Le Page and P. Saxe, *Physical Review B*, 2002, **65**, 104104.

52. Y. J. Ou, X. M. Wang, C. L. Li, Y. L. Zhu and X. L. Li, *IOP Conference Series: Earth and Environmental Science*, 2017, **100**, 012036.

53. G. Lennon, S. Willox, R. Ramdas, S. J. Funston, M. Klun, R. Pieh, S. Fairlie, S. Dobbin and D. F. Cobice, *Journal of Analytical Methods in Chemistry*, 2020, **2020**, 8265054.

54. D. M. Sim, H. J. Han, S. Yim, M.-J. Choi, J. Jeon and Y. S. Jung, *ACS Omega*, 2017, **2**, 4678-4687.

55. G. Mills, H. Jónsson and G. K. Schenter, *Surface Science*, 1995, **324**, 305-337.

56. H. JÓNSSON, G. MILLS and K. W. JACOBSEN, in *Classical and Quantum Dynamics in Condensed Phase Simulations*, DOI: 10.1142/9789812839664_0016, pp. 385-404.

57. B.-X. Shi, Y. Yusim, S. Sen, T. Demuth, R. Ruess, K. Volz, A. Henss and F. H. Richter, *Advanced Energy Materials*, 2023, **13**, 2300310.

58. C. Hong, Q. Leng, J. Zhu, S. Zheng, H. He, Y. Li, R. Liu, J. Wan and Y. Yang, *Journal of*

Materials Chemistry A, 2020, **8**, 8540-8547.

59. M. Mock, M. Bianchini, F. Fauth, K. Albe and S. Sicolo, *Journal of Materials Chemistry A*, 2021, **9**, 14928-14940.

60. H. Li, N. Zhang, J. Li and J. R. Dahn, *Journal of The Electrochemical Society*, 2018, **165**, A2985.

61. M. D. Levi and D. Aurbach, in *Characterization of Materials*, DOI: https://doi.org/10.1002/0471266965.com125, pp. 1-21.

62. R. Ruess, S. Schweidler, H. Hemmelmann, G. Conforto, A. Bielefeld, D. A. Weber, J. Sann, M. T. Elm and J. Janek, *Journal of The Electrochemical Society*, 2020, **167**, 100532.

63. J. Moškon and M. Gaberšček, *Journal of Power Sources Advances*, 2021, **7**, 100047.

64. T.-T. Zuo, F. Walther, J. H. Teo, R. Rueß, Y. Wang, M. Rohnke, D. Schröder, L. F. Nazar and J. Janek, *Angewandte Chemie International Edition*, 2023, **62**, e202213228.

65. J. C. Vickerman, *Molecular Surface Mass Spectrometry by SIMS*, Wiley, 2009.

66. F. Walther, F. Strauss, X. Wu, B. Mogwitz, J. Hertle, J. Sann, M. Rohnke, T. Brezesinski and J. Janek, *Chemistry of Materials*, 2021, **33**, 2110-2125.

67. F. Walther, S. Randau, Y. Schneider, J. Sann, M. Rohnke, F. H. Richter, W. G. Zeier and J. Janek, *Chemistry of Materials*, 2020, **32**, 6123-6136.

68. T. Lombardo, F. Walther, C. Kern, Y. Moryson, T. Weintraut, A. Henss and M. Rohnke, *Journal of Vacuum Science & Technology A*, 2023, **41**.

69. T. Fuchs, C. G. Haslam, F. H. Richter, J. Sakamoto and J. Janek, *Advanced Energy Materials*, 2023, **13**, 2302383.

70. T. Krauskopf, H. Hartmann, W. G. Zeier and J. Janek, *ACS Applied Materials & Interfaces*, 2019, **11**, 14463-14477.

71. S. Wenzel, S. J. Sedlmaier, C. Dietrich, W. G. Zeier and J. Janek, *Solid State Ionics*, 2018, **318**, 102-112.

72. S. D. S. Fitch, G. E. Moehl, N. Meddings, S. Fop, S. Soulé, T.-L. Lee, M. Kazemian, N. Garcia-Araez and A. L. Hector, *ACS Applied Materials & Interfaces*, 2023, **15**, 39198-39210.

73. P. Ren, X. Wang, B. Huang, Z. Liu and R. Liu, *Journal of Energy Storage*, 2024, **82**, 110200.

74. Y. Liu, H. Su, M. Li, J. Xiang, X. Wu, Y. Zhong, X. Wang, X. Xia, C. Gu and J. Tu, *Journal of*

Materials Chemistry A, 2021, **9**, 13531-13539.

75. K. Park and J. B. Goodenough, *Advanced Energy Materials*, 2017, **7**, 1700732.

76. B. Aktekin, E. Kataev, L. M. Riegger, R. Garcia-Diez, Z. Chalkley, J. Becker, R. G. Wilks, A. Henss, M. Bär and J. Janek, *ACS Energy Letters*, 2024, **9**, 3492-3500.

77. E. Schlautmann, A. Weiß, O. Maus, L. Ketter, M. Rana, S. Puls, V. Nickel, C. Gabbey, C. Hartnig, A. Bielefeld and W. G. Zeier, *Advanced Energy Materials*, 2023, **13**, 2302309.

78. G. Kresse and J. Furthmüller, *Phys Rev B Condens Matter*, 1996, **54**, 11169-11186.

79. G. Kresse and J. Hafner, *Physical Review B*, 1994, **49**, 14251-14269.

80. G. Kresse and J. Hafner, *Physical Review B*, 1993, **47**, 558-561.

81. G. Kresse and D. Joubert, *Physical Review B*, 1999, **59**, 1758-1775.

82. P. E. Blöchl, *Phys Rev B Condens Matter*, 1994, **50**, 17953-17979.

83. J. P. Perdew, K. Burke and M. Ernzerhof, *Physical Review Letters*, 1996, **77**, 3865-3868.

84. R. Tran, Z. Xu, B. Radhakrishnan, D. Winston, W. Sun, K. A. Persson and S. P. Ong, *Scientific Data*, 2016, **3**, 160080.

85. A. Stukowski, *Modelling and Simulation in Materials Science and Engineering*, 2010, **18**, 015012.

Supporting Information

Surface Modification of Thiophosphate Solid Electrolyte for Performance Boost in Li|LPSCl|LNO Solid-State Batteries

Bing-Xuan Shi,[a] Timo Weintraut,[a] Thomas Demuth,[b] Sabrina Sicolo,[c] Boburmirzo Juraev,[c] Sebastian Leonard Benz,[a] Burak Aktekin,[a] Kilian Vettori,[a] Yuriy Yusim,[a] Karsten Albe,[c] Kerstin Volz,[b] Anja Henss,[a] Felix H. Richter*,[a]

[a] Institute of Physical Chemistry & Center for Materials Research (LaMa), Justus-Liebig-University Giessen, Heinrich-Buff-Ring 17, 35392 Giessen, Germany

[b] Department of Physics & Materials Sciences Center (WZMW), Philipps-University Marburg, Hans-Meerwein Straße 6, 35032 Marburg, Germany.

[C] Fachgebiet Materialmodellierung, Institut für Materialwissenschaft, Technische Universität Darmstadt, Otto-Berndt-Str. 3, D-64287 Darmstadt, Germany

[*] Corresponding author, Felix.H.Richter@phys.chemie.uni-giessen.de

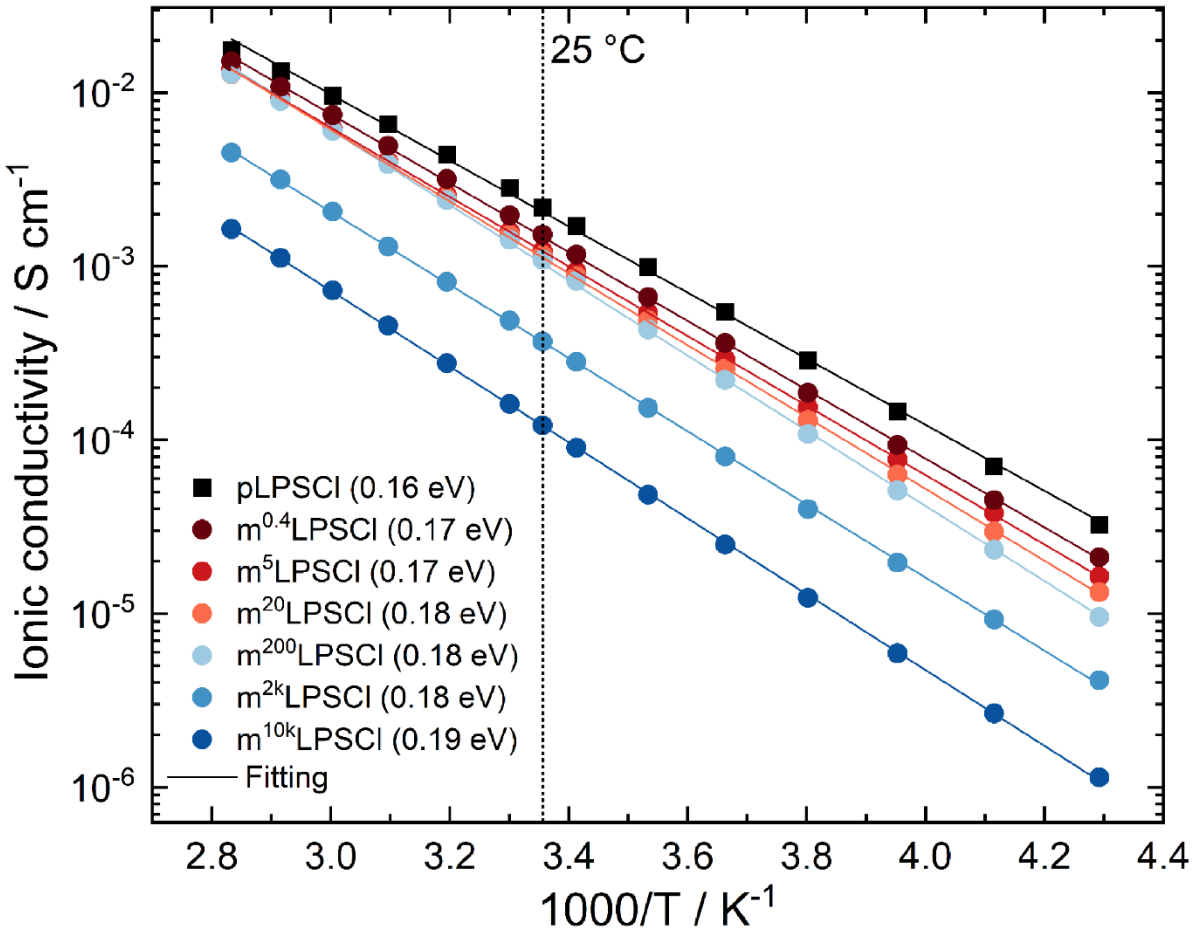

Figure S1. The Arrhenius plot measured by EIS compares the ionic conductivity of pLPSCl and mLPSCl samples in the symmetrical cell, steel|Li_6PS_5Cl|steel, at different temperatures ranging from -40 °C to 80 °C.

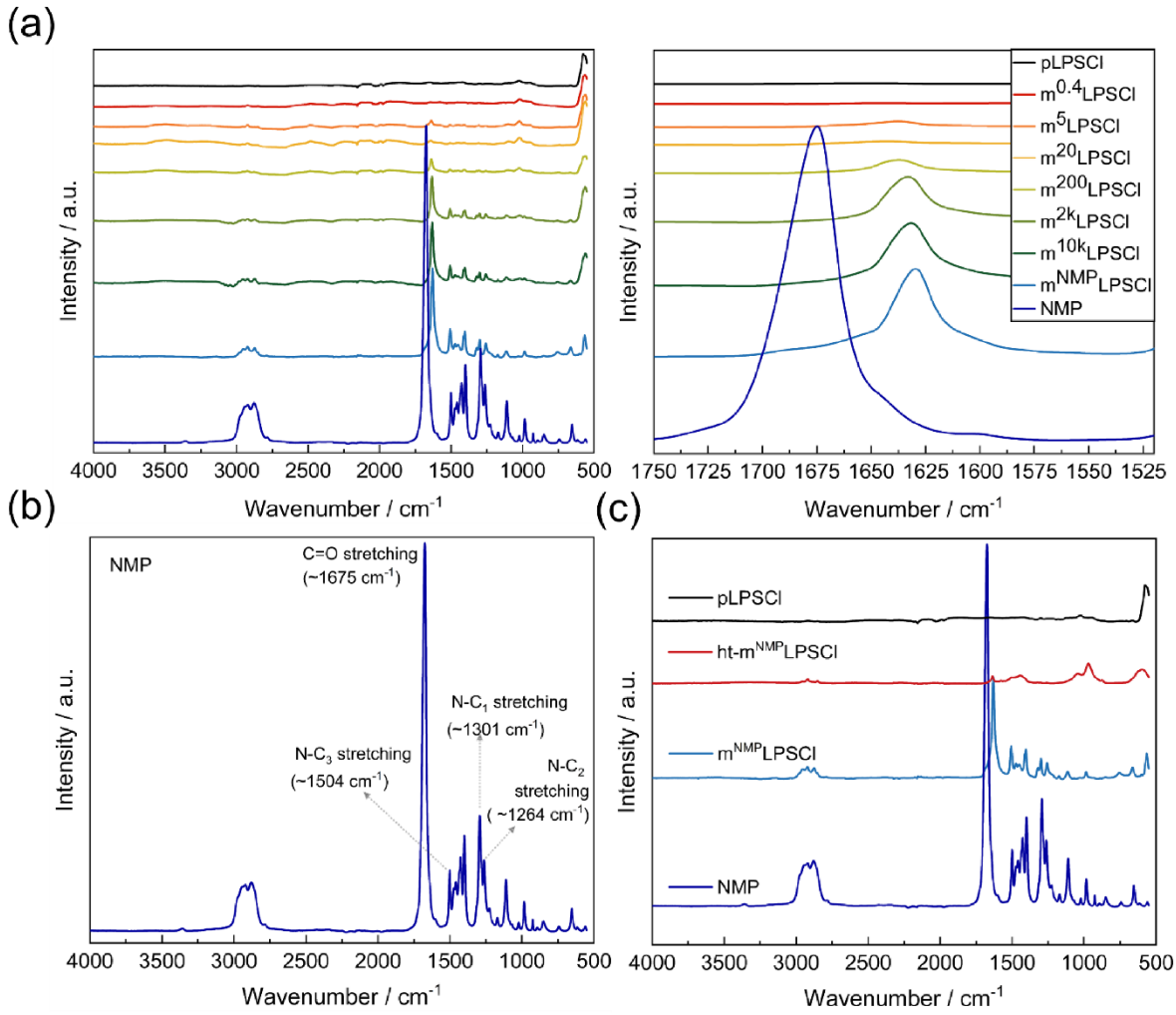

Figure S2. (a) FTIR spectra of pLPSCl and mLPSCl samples. The broad range spectra (left) highlight the overall molecular vibrational modes. Detailed spectra (right) focus on the C=O stretching frequency and indicate electrostatic interactions. (b) The wavenumbers of NMP solvent functional groups, including C=O stretching (~1675 cm^{-1}) and N-C stretching (~1504 cm^{-1}, ~1301 cm^{-1}, and ~1264 cm^{-1}). (c) The FT-IR spectra of ht-m^{NMP}LPSCl and m^{NMP}LPSCl are compared with those of NMP solvent and pLPSCl.

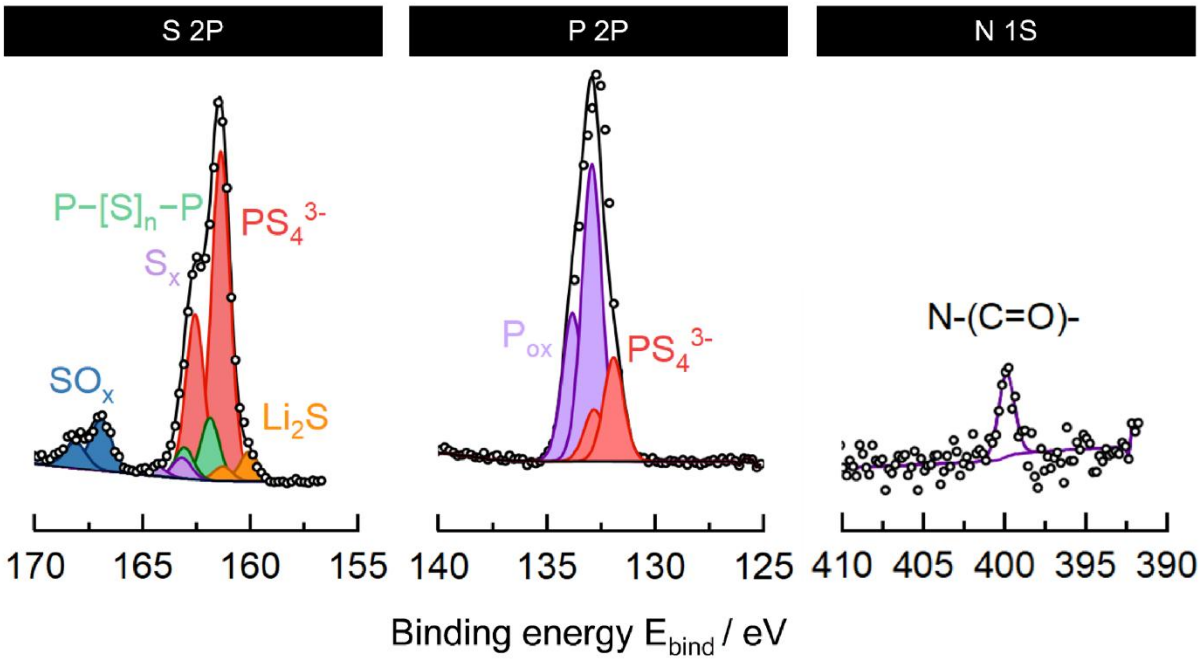

Figure S3. XPS results of S 2p, P 2p, and N 1S spectra for ht-m^{NMP}LPSCl.

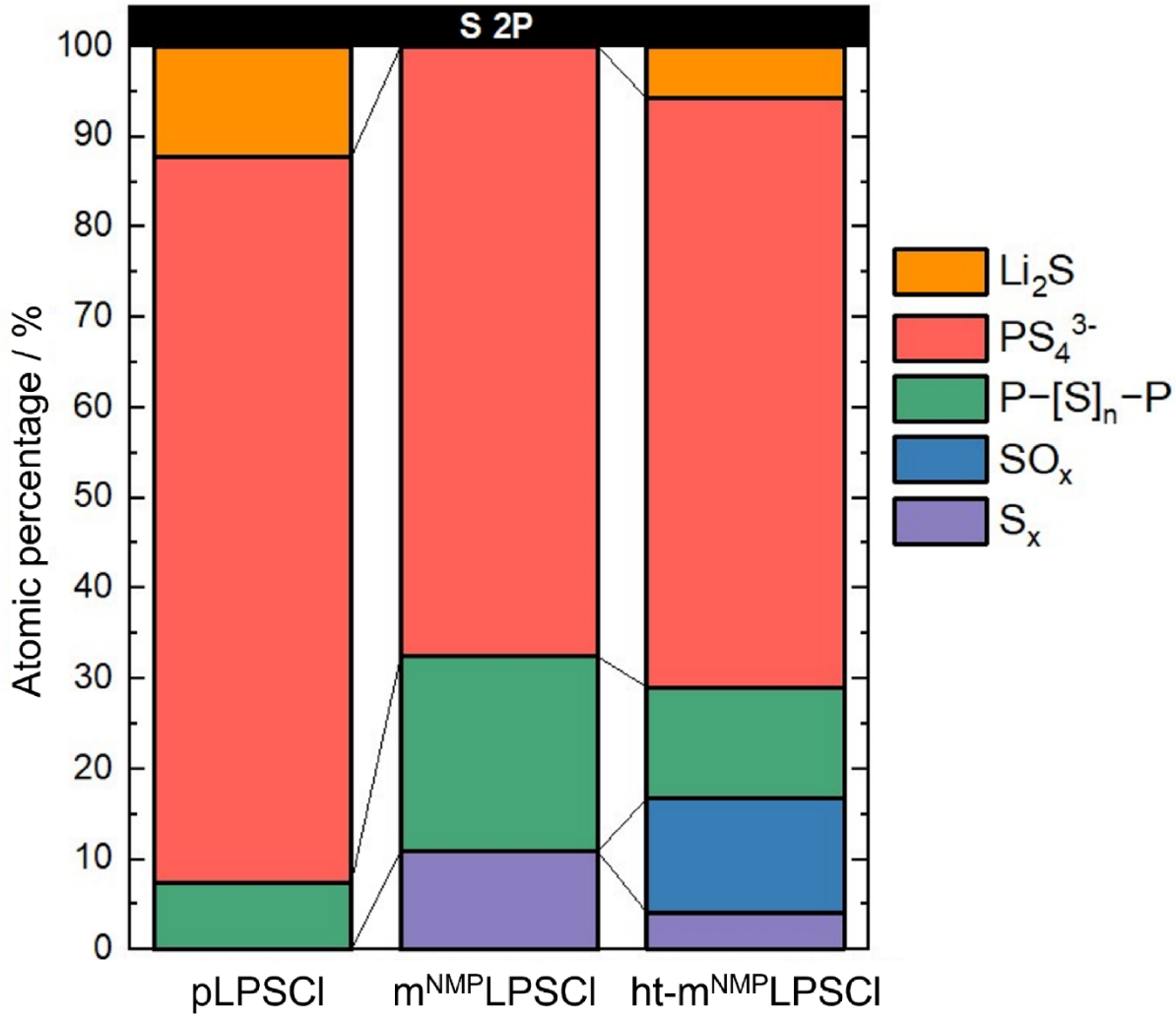

Figure S4. pLPSCl, m^{NMP}LPSCl, and ht-m^{NMP}LPSCl as measured by XPS. The relative ratios of S 2p, P 2p, and N 1s for the various byproducts as determined from the XPS analysis after fitting.

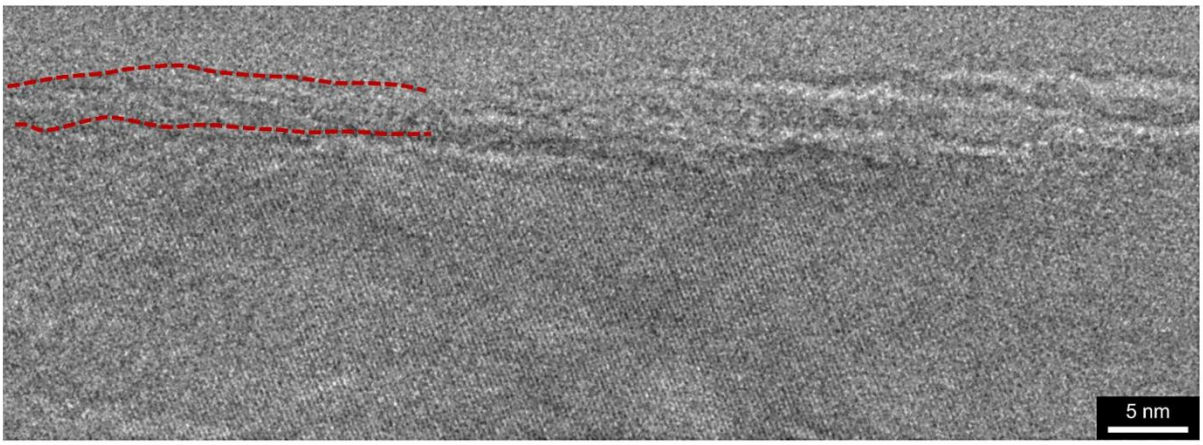

Figure S5. HR-TEM image of the crystalline lattice planes at a m^{200}LPSCl particle surface. (Note: As the particles degrade within seconds of electron beam exposure, the modification layer may be even more beam-sensitive and could degrade before image capture. Hence, we estimate the modification layer to have been at least ~5 nm thick.)

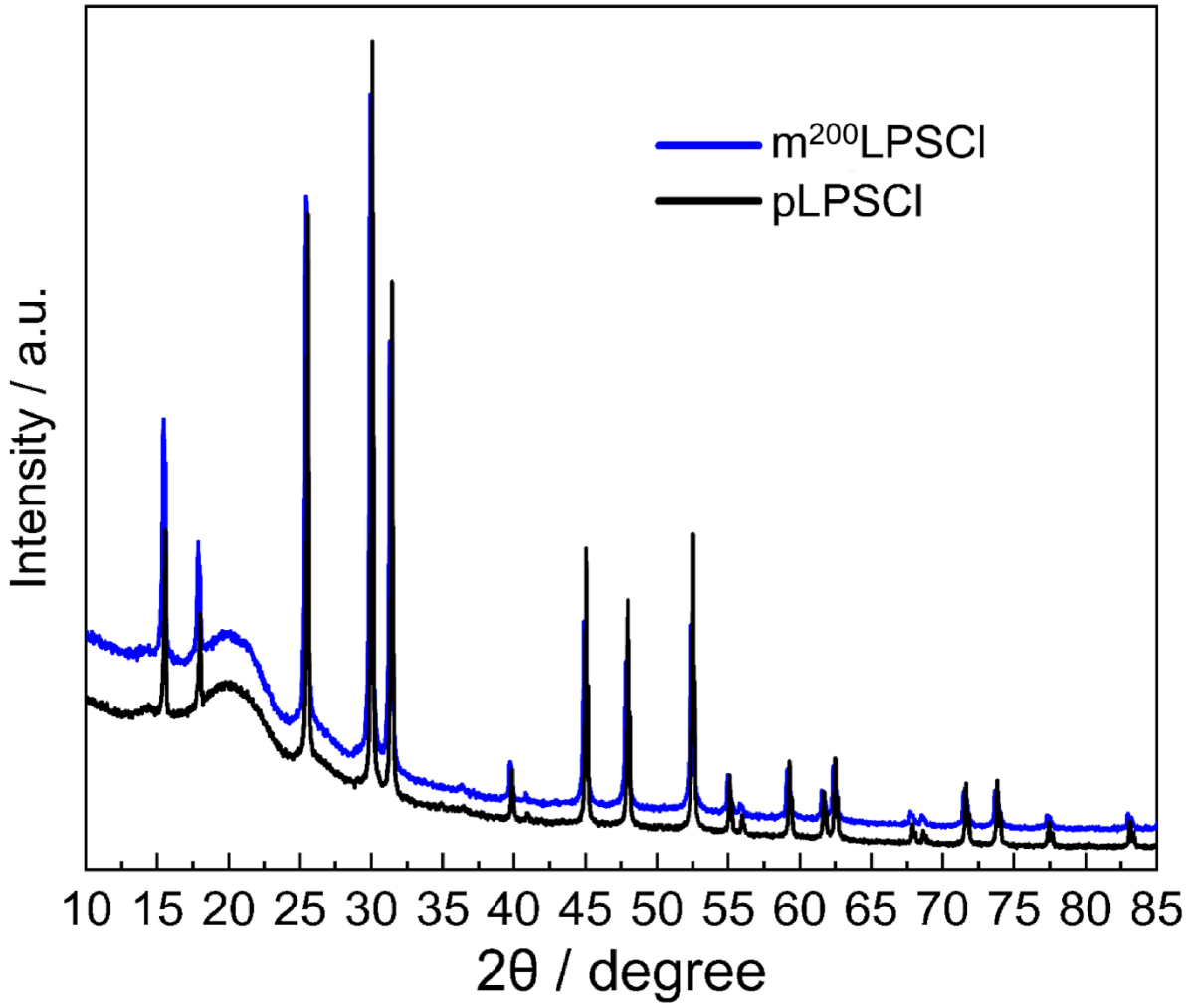

Figure S6. XRD patterns of m^{200}LPSCl and pLPSCl.

Table S1. pLPSCl, m^{200}LPSCl, and m^{NMP}LPSCl are measured by HR-TEM with EDX. The table shows the average molar ratios of N, P, S, and Cl for pLPSCl, m^{200}LPSCl, and m^{NMP}LPSCl, based on EDX data. Each sample includes measurements from three different particles.

pLPSCl

Atomic ratios (%)	**S**	**P**	**Cl**	**N**
Particle 1	65	22	13	0
Particle 2	71	20	9	0
Particle 3	71	17	12	0
Average	69	20	11	0

m^{200}LPSCl

Atomic ratios (%)	**S**	**P**	**Cl**	**N**
Particle 1	47	13	11	29
Particle 2	48	14	11	27
Particle 3	48	13	12	27
Average	48	13	11	28

m^{NMP}LPSCl

Atomic ratios (%)	**S**	**P**	**Cl**	**N**
Particle 1	56	14	2	28
Particle 2	61	16	2	22
Particle 3	60	14	1	25
Average	59	15	1	25

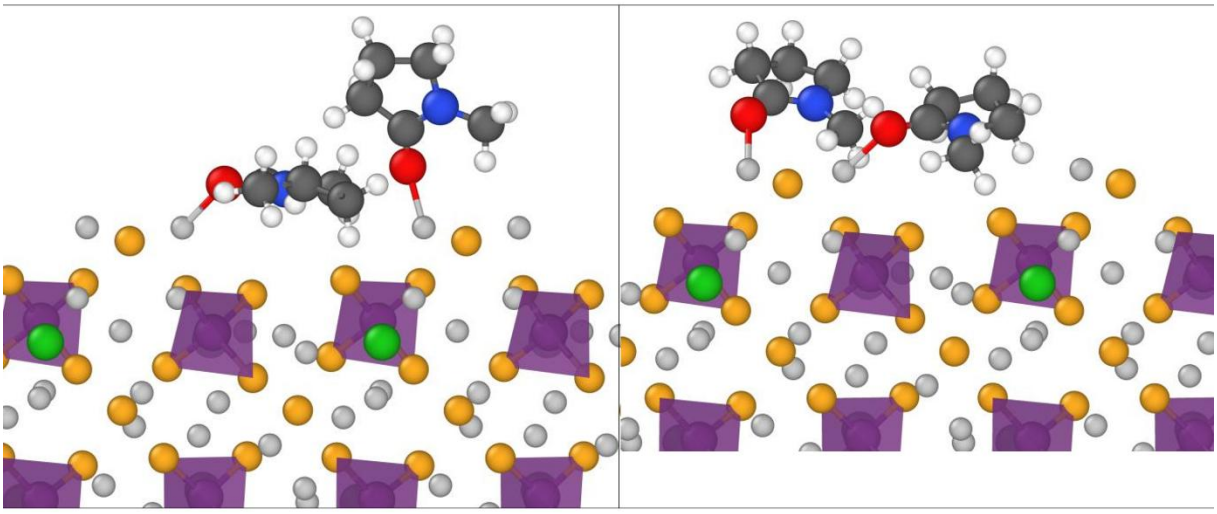

Figure S7. Different adsorption sites of NMP on LPSCl surface.

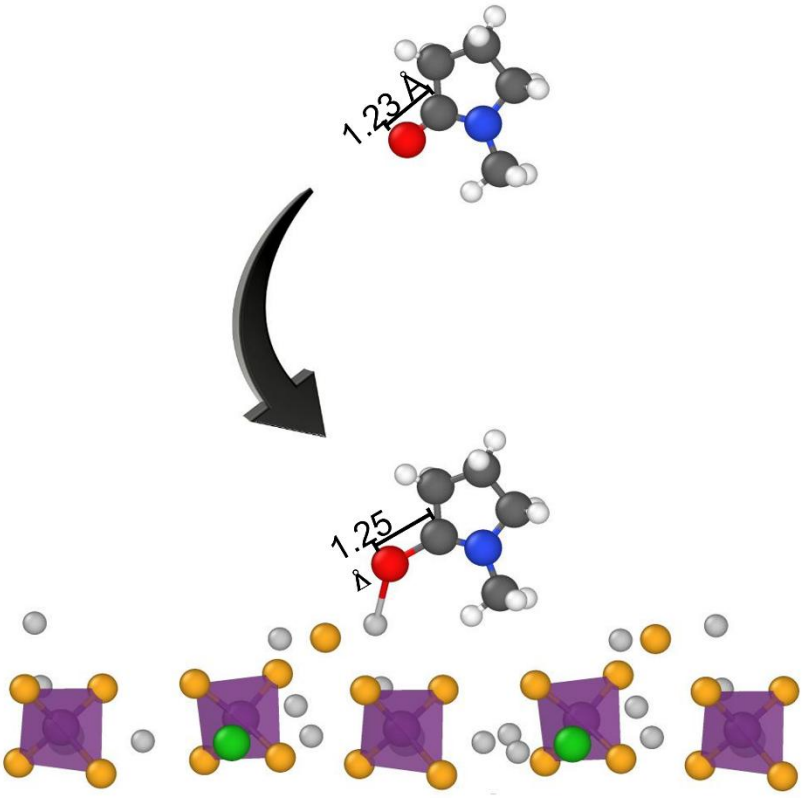

Figure S8. Graphical representation of NMP adsorption on LPSCl surface and C=O bond stretching.

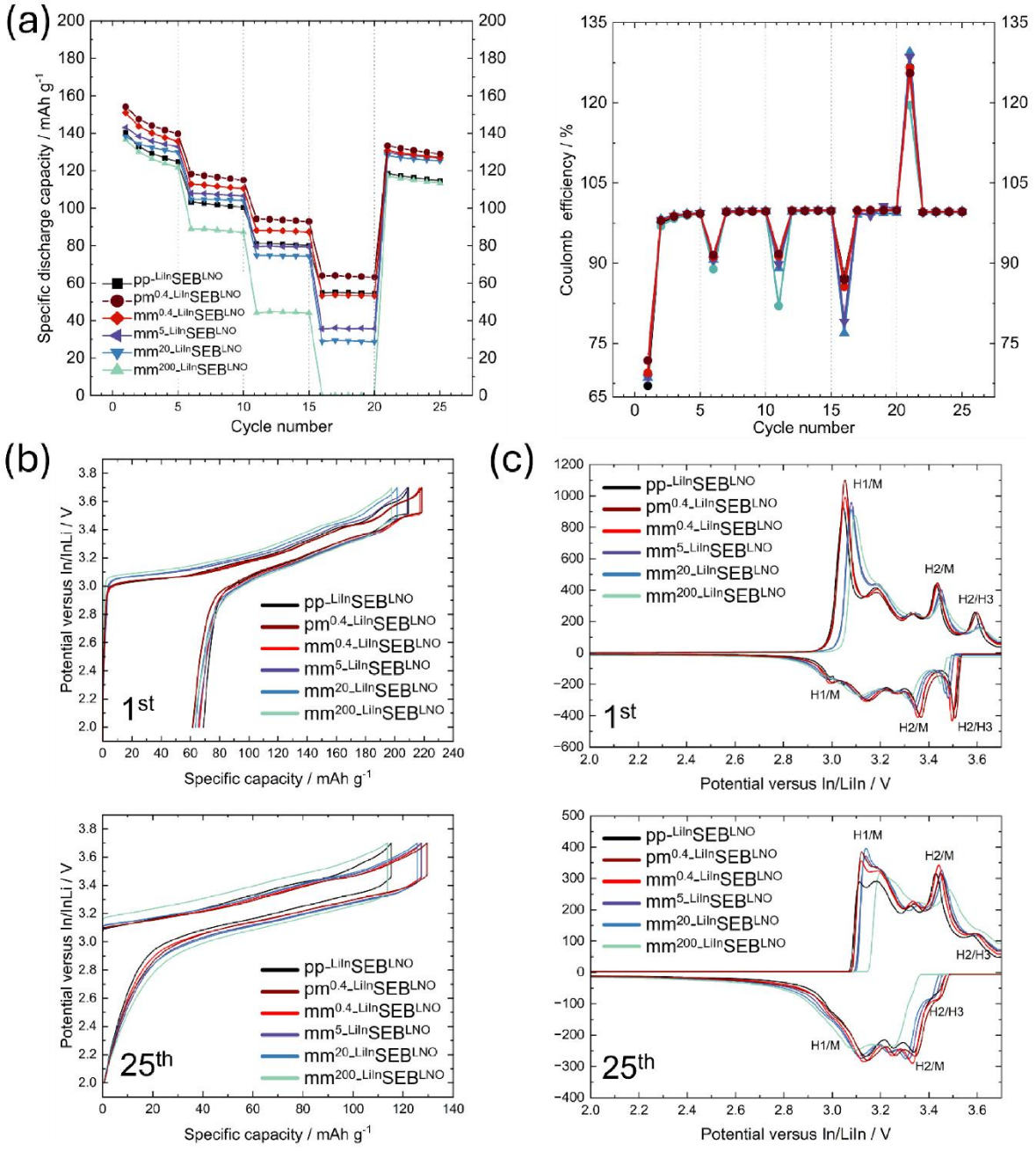

Figure S9. The rate capability of pp-^{LiIn}SEB^{LNO}, pm$^{0.4}$-^{LiIn}SEB^{LNO}, mm$^{0.4}$-^{LiIn}SEB^{LNO}, mm^{5}-^{LiIn}SEB^{LNO}, mm^{20}-^{LiIn}SEB^{LNO}, and mm^{200}-^{LiIn}SEB^{LNO} are analyzed by pellet-type cells. (a) The figure displays the specific discharge capacity (left) and Coulomb efficiency (right) across various C-rates (0.1C, 0.25C, 0.5C, 1C, and back to 0.1C). In addition, (b) the galvanic charge and discharge plots and (c) the differential capacity plots of 1st (above) and 25th (below) cycles at a 0.1C rate are shown.

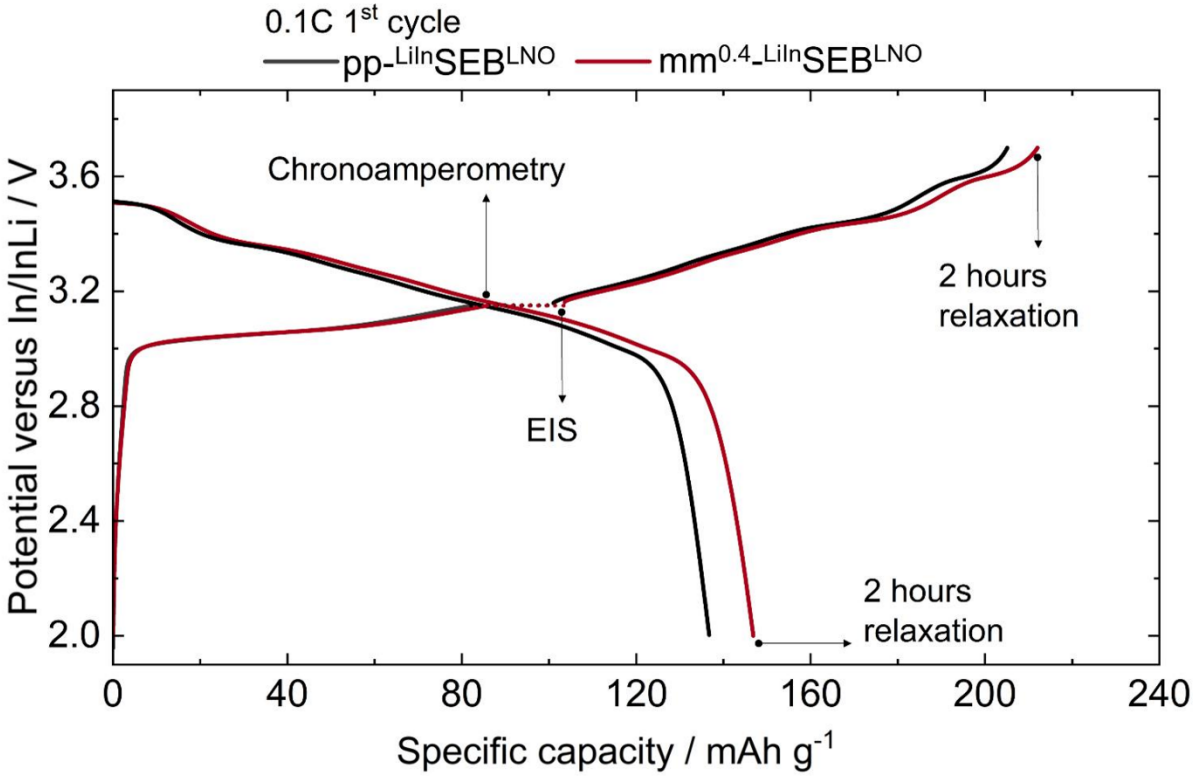

Figure S10. The figure shows mm$^{0.4}$-^{LiIn}SEB^{LNO} and pp-^{LiIn}SEB^{LNO} charge and discharge processes in the first cycle coupled with EIS and chronoamperometric measurements. First, the SEBs are galvanostatically charged at 0.1C to a voltage of 3.15 V vs. In/LiIn. This is followed by a chronoamperometric step, wherein the potential is maintained at 3.15 V vs. In/LiIn until the current diminishes to 2% of its initial value. This approach ensures that the EIS are conducted at a consistent SOC. EIS is then performed at the same potential, ranging from 1 MHz to 100 μHz. Subsequently, the SEBs are galvanostatically charged to 3.7 V vs. In/LiIn, followed by a 2 h relaxation period. Finally, the SEBs are discharged to 2.0 V vs. In/LiIn, accompanied by another 2 h relaxation period.

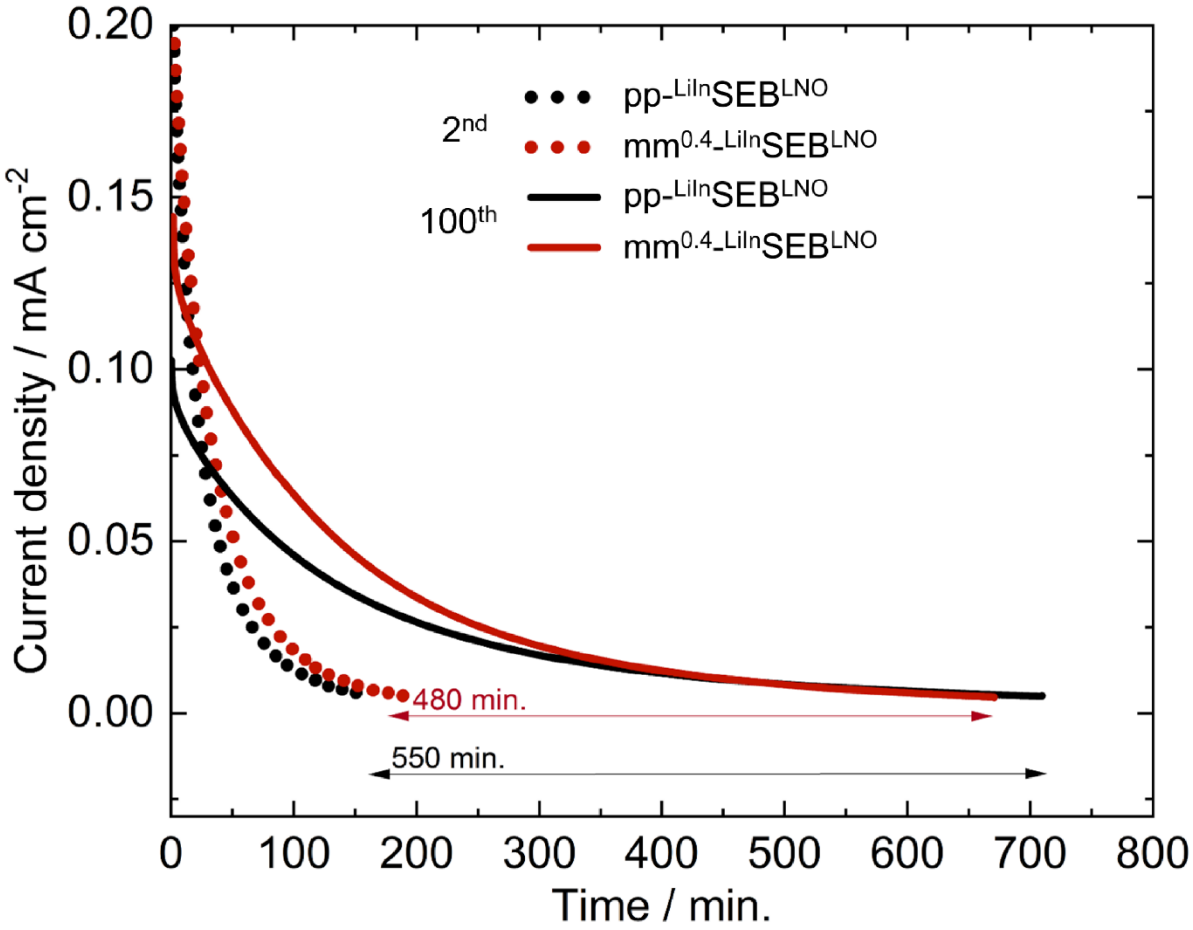

Figure S11. Chronoamperometry maintains the voltage at 3.15 V vs. In/LiIn while measuring the current response, as well as the time required for the current to decrease to less than 2% of its initial value. In the second cycle, the charge times for mm$^{0.4}$-^{LiIn}SEB^{LNO} and pp-^{LiIn}SEB^{LNO} are approximately 191 and 161 minutes, respectively. After 100 cycles, the charge times for mm$^{0.4}$-^{LiIn}SEB^{LNO} and pp-^{LiIn}SEB^{LNO} are approximately 671 and 710 minutes, respectively. The time difference between the second and 100th cycles is 480 minutes for mm$^{0.4}$-^{LiIn}SEB^{LNO} and 550 minutes for pp-^{LiIn}SEB^{LNO}.

.

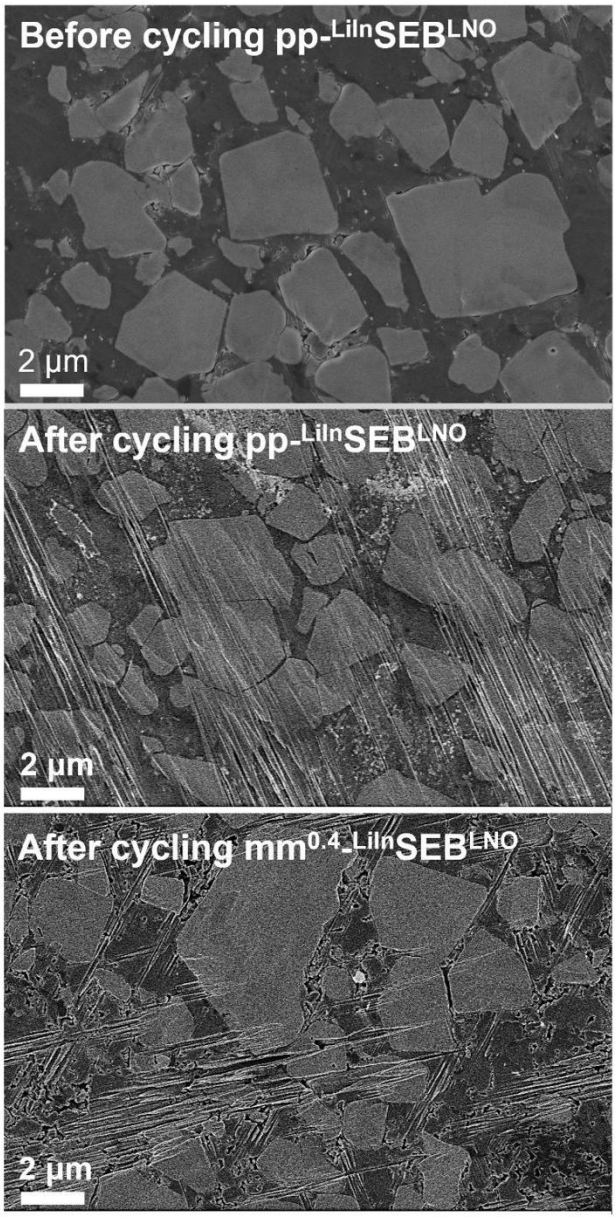

Figure S12. SEM images of composite cathodes cross-sectioned by ion beam milling. (a) Cathode composite of pp-^{LiIn}SEB^{LNO} before cycling, (b) cathode composite of mm$^{0.4}$-^{LiIn}SEB^{LNO} after 100 cycles at a rate of 0.1C, and (c) cathode composite of mm$^{0.4}$-^{LiIn}SEB^{LNO} after 100 cycles at a rate of 0.1C.

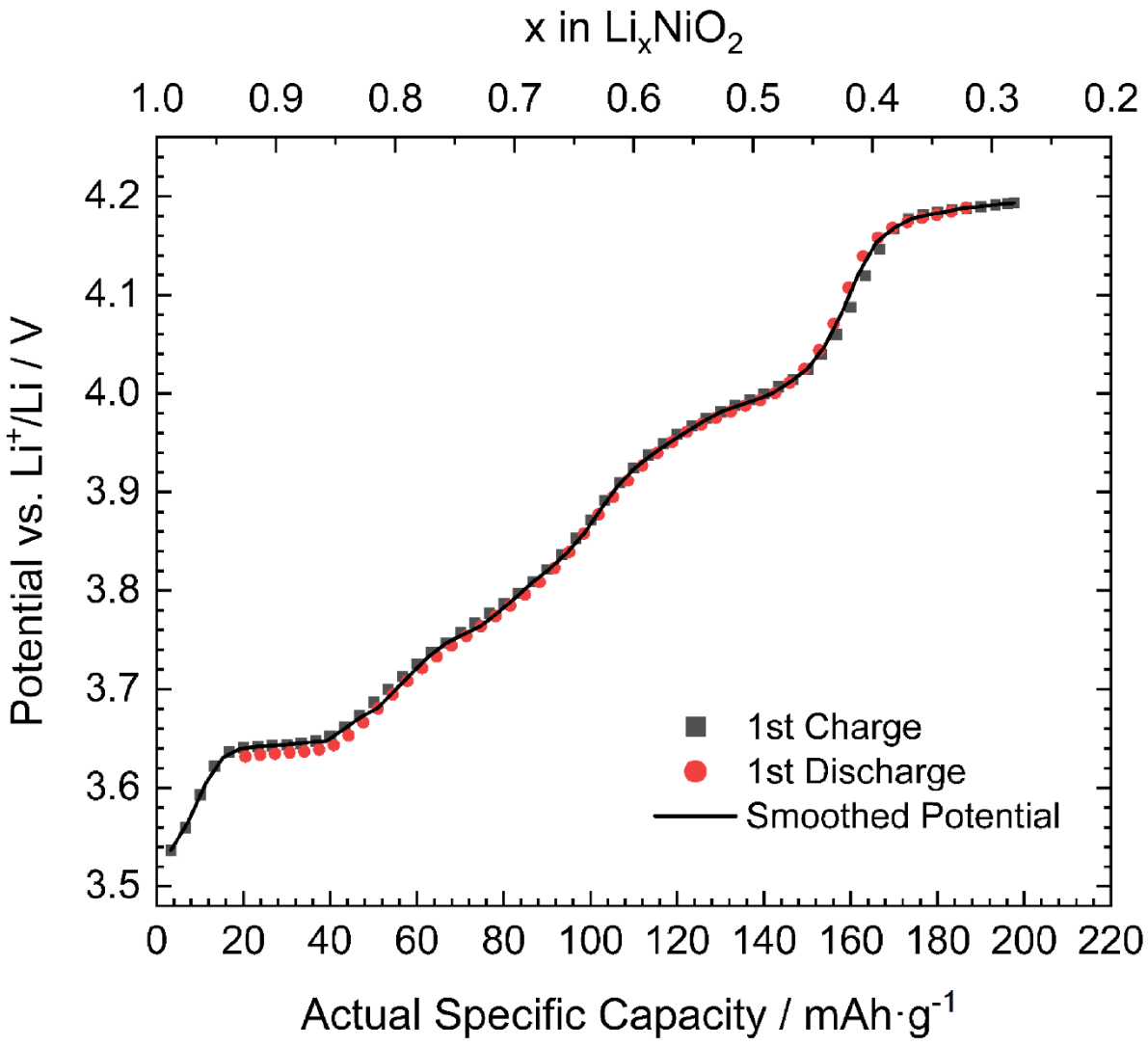

Figure S13. Relationship between OCV and the SOC, represented by the lithium content x in Li_xNiO_2. This is derived from the galvanostatic intermittent titration technique (GITT) of a $^{Li}LEB^{LNO}$ using 1 M $LiPF_6$ in EC:DEC (1:1 vol.%), a lithium metal anode and LNO cathode sheet at a 0.1C rate. Each 10-minute charge or discharge interval is followed by a two-hour relaxation period to measure the OCV. We calculate lithium content x in Li_xNiO_2 by using the known capacity for each GITT pulse step.

Table S2. Fitting results of EIS of mm$^{0.4}$-^{LiIn}SEB^{LNO} and pp-^{LiIn}SEB^{LNO} using transition line model (TLM) under the 0.1C cycling at 1st, 2nd, 50th, and 100th cycles.

	Sample	mm$^{0.4}$-^{LiIn}SEB^{LNO}				pp-^{LiIn}SEB^{LNO}			
	Cycle	1st	2nd	50th	100th	1st	2nd	50th	100th
Cathode	$R_{cathode}$ / Ω cm^2	22.4	51.5	233.4	579.0	17.7	40.6	427.0	939.3
	R_{ct} / Ω cm^2	7.0	13.3	235.8	527.8	11.5	16.8	456.3	1089.5
	R_{ele} / Ω cm^2	2.8	3.1	7.3	7.9	2.6	2.8	7.1	10.1
	R_{ion} / Ω cm^2	68.5	196.2	223.7	627.4	24.7	95.1	392.5	799.8
Anode	R_a / Ω cm^2	3.9	3.4	29.4	41.4	4.7	3.5	23.6	25.2
Separator	$R_Ω$ / Ω cm^2	43.9	41.7	55.6	57.0	30.0	28.3	34.7	37.4

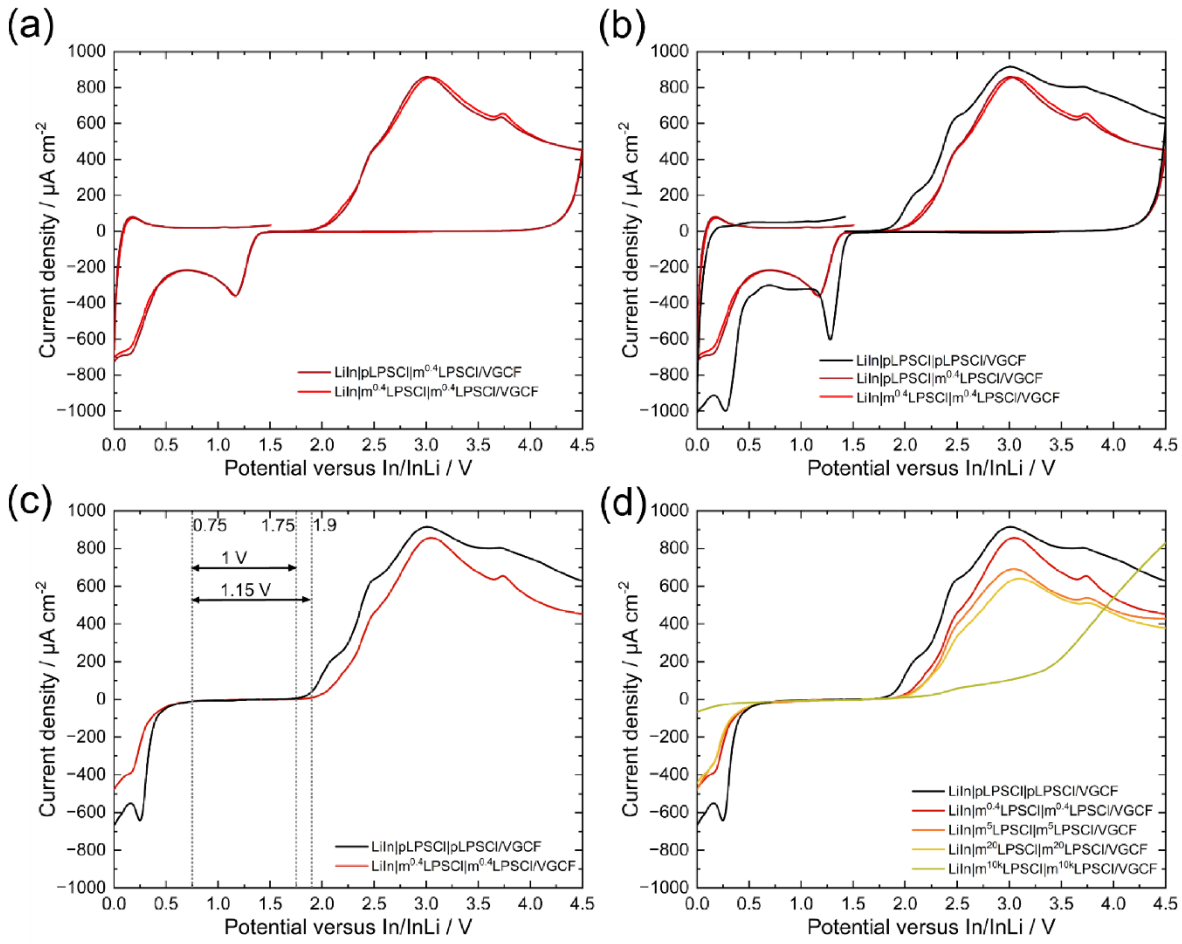

Figure S14. (a) The electrochemical differences between LiIn|pLPSCl and LiIn|$m^{0.4}$LPSCl interfaces are evaluated via CV at 25 °C using two cell configurations LiIn|pLPSCl|$m^{0.4}$LPSCl/VGCF and LiIn|$m^{0.4}$LPSCl|$m^{0.4}$LPSCl/VGCF. Voltage scans from OCV to 4 V vs. In/InLi at a scan rate of 1 mV·s^{-1}, reversing to 0 V, and then returning to the starting potential. (b) The electrochemical stability of pLPSCl/VGCF and $m^{0.4}$LPSCl/VGCF is compared using the cell configurations LiIn|pLPSCl|pLPSCl/VGCF, LiIn|pLPSCl|$m^{0.4}$LPSCl/VGCF, and LiIn|$m^{0.4}$LPSCl|$m^{0.4}$LPSCl/VGCF. The CV process is the same as in (a). (c) To analyze the oxidative and reductive processes separately, CV is conducted for LiIn|pLPSCl|pLPSCl/VGCF and LiIn|$m^{0.4}$LPSCl|$m^{0.4}$LPSCl/VGCF. The voltage is scanned from OCV to either 0 V or 4 V vs. In/InLi at a rate of 1 mV·s^{-1}. (d) CV is used to compare different types of m^{x}LPSCl (from $m^{0.4}$LPSCl to m^{10k}LPSCl), which act as both the separator and catholyte in LiIn|m^{x}LPSCl|m^{x}LPSCl/VGCF cells. These are also compared with pLPSCl, which serves the same role in LiIn|pLPSCl|pLPSCl/VGCF cells. The CV process is the same as in (c).

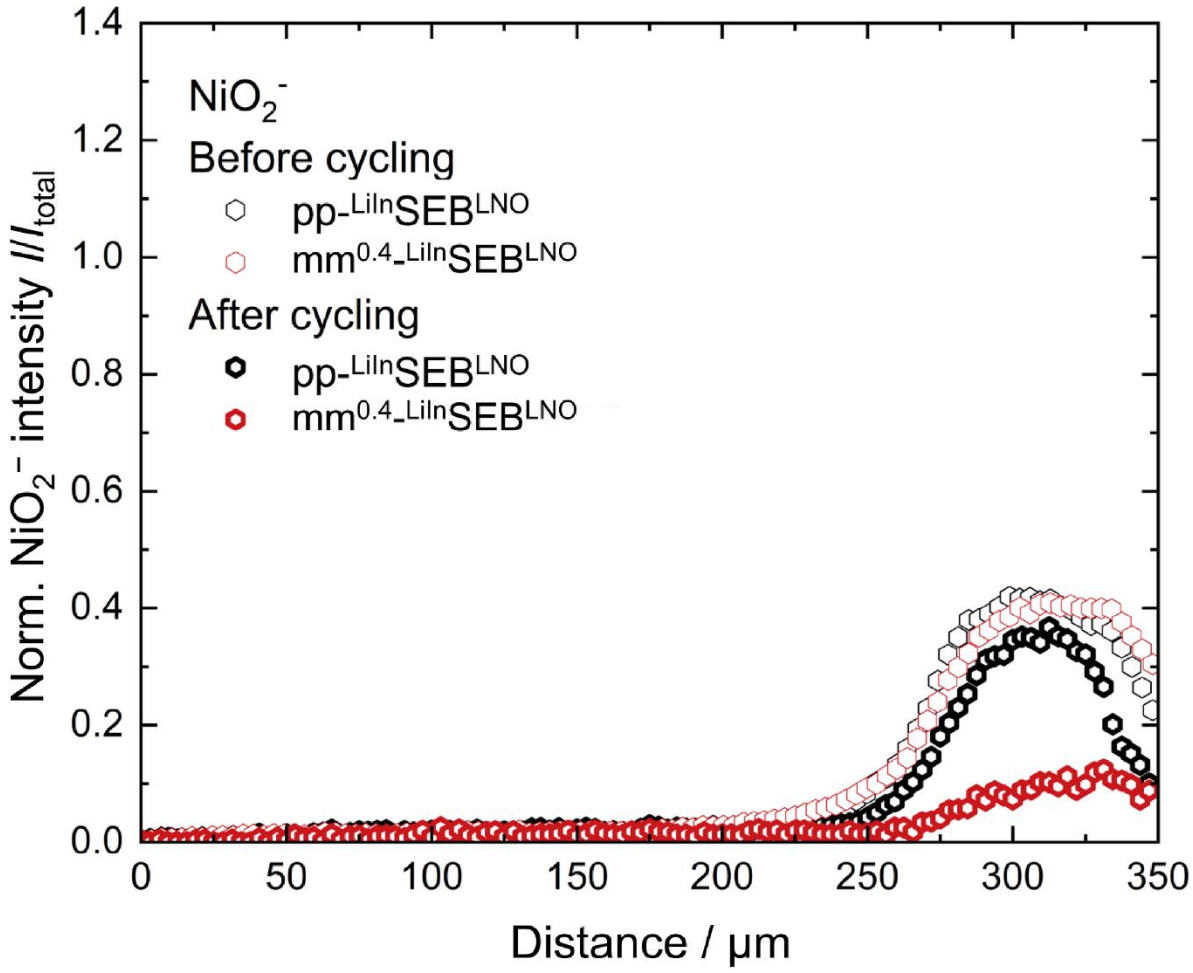

Figure S15. The NiO_2^- intensities (normalized by total intensity), in pp-^{LiIn}SEB^{LNO} and mm$^{0.4}$-^{LiIn}SEB^{LNO} (before and after cycling), are measured using ToF-SIMS surface spectra after creating wedge-shaped sputter craters.

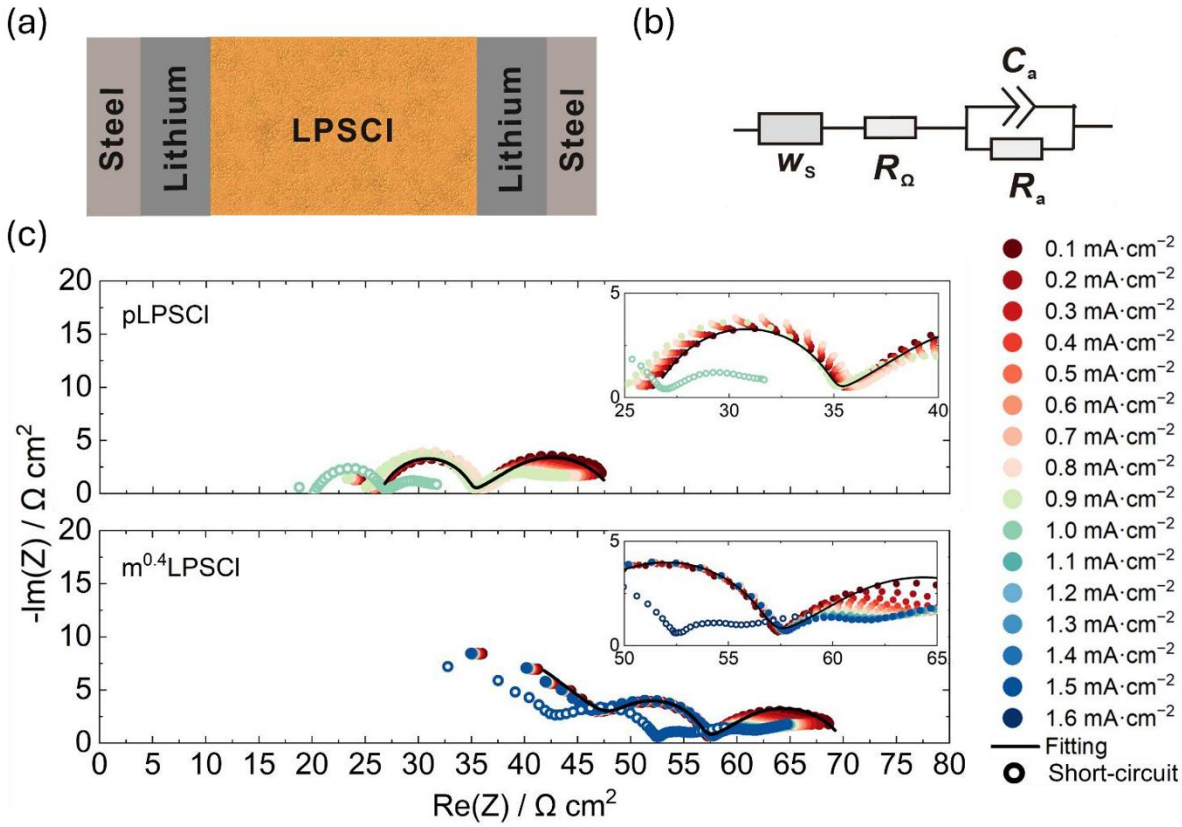

Figure S16. (a) The schematic illustrates that CCD tests are conducted in symmetric Li|LPSCl|Li cells. (b) Equivalent circuit for impedance fitting includes the electrolyte resistance (R_Ω), interfacial resistance between lithium metal and LPSCl (R_a), capacitance of interface between lithium metal and LPSCl (C_a), and Warburg short element (W_s) describing single ionic conductor diffusion process. (c) EIS measured after every cycle of CCD test shows that pLPSCl and m$^{0.4}$LPSCl experience short-circuiting at 1 mA·cm^{-2} and 1.6 mA·cm^{-2}, respectively. The EIS data for the current causing a short circuit is represented by hollow circles. Fitting is performed in the initial cycle, as depicted by the black line.

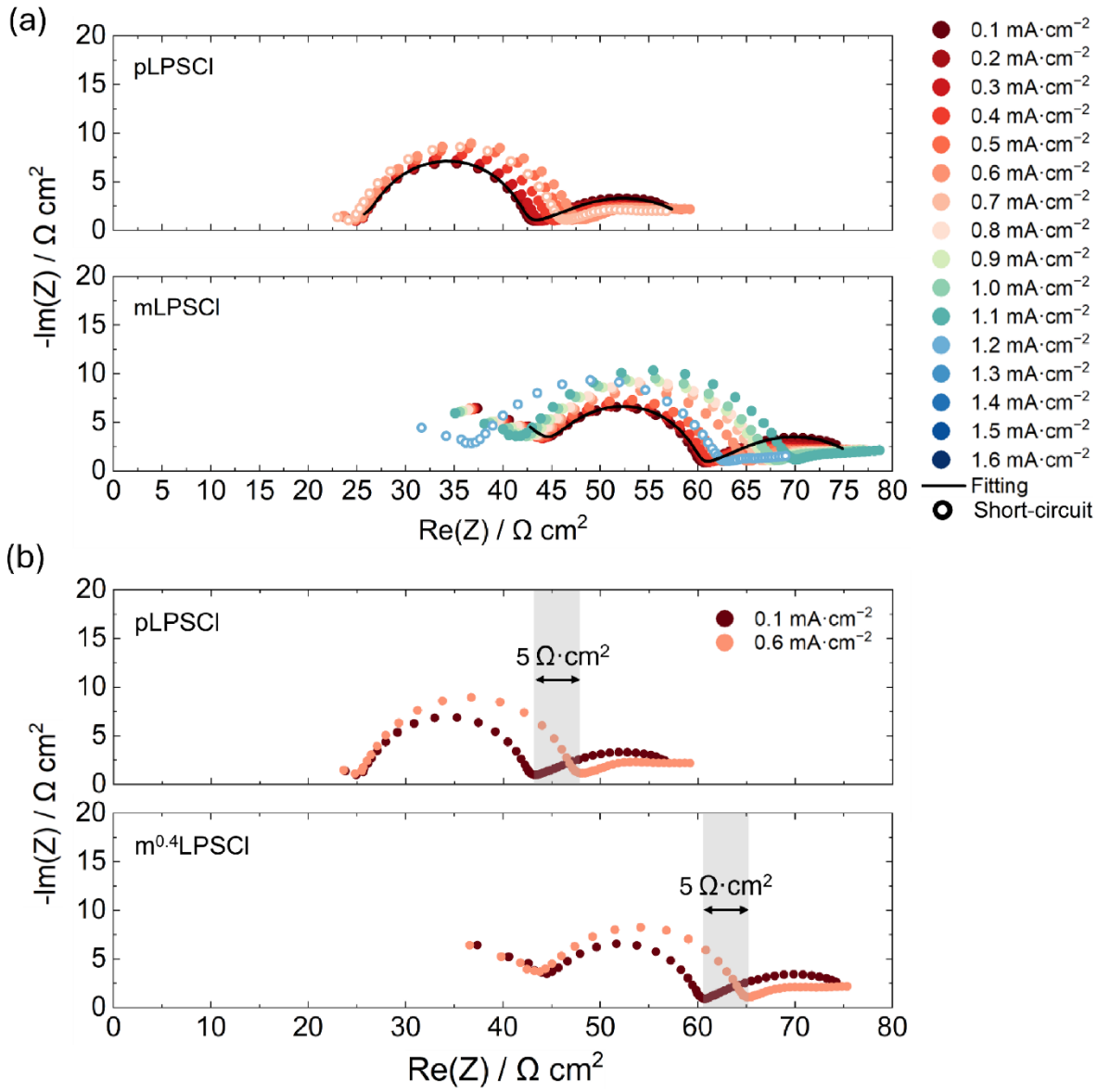

Figure S17. (a) EIS measured after every cycle of UCD test are conducted in symmetric Li|LPSCl|Li cells. The pLPSCl and $m^{0.4}$LPSCl experience short-circuiting at current densities of 0.7 mA·cm^{-2} and 1.2 mA·cm^{-2}, respectively. In addition, the short-circuiting currents are indicated with hollow circles. (b) The EIS spectra after UCD of 0.1 mA·cm^{-2} and 0.6 mA·cm^{-2} are presented for both pLPSCl and $m^{0.4}$LPSCl to compare the changes in impedance, which are around 5 Ω·cm^2.

.

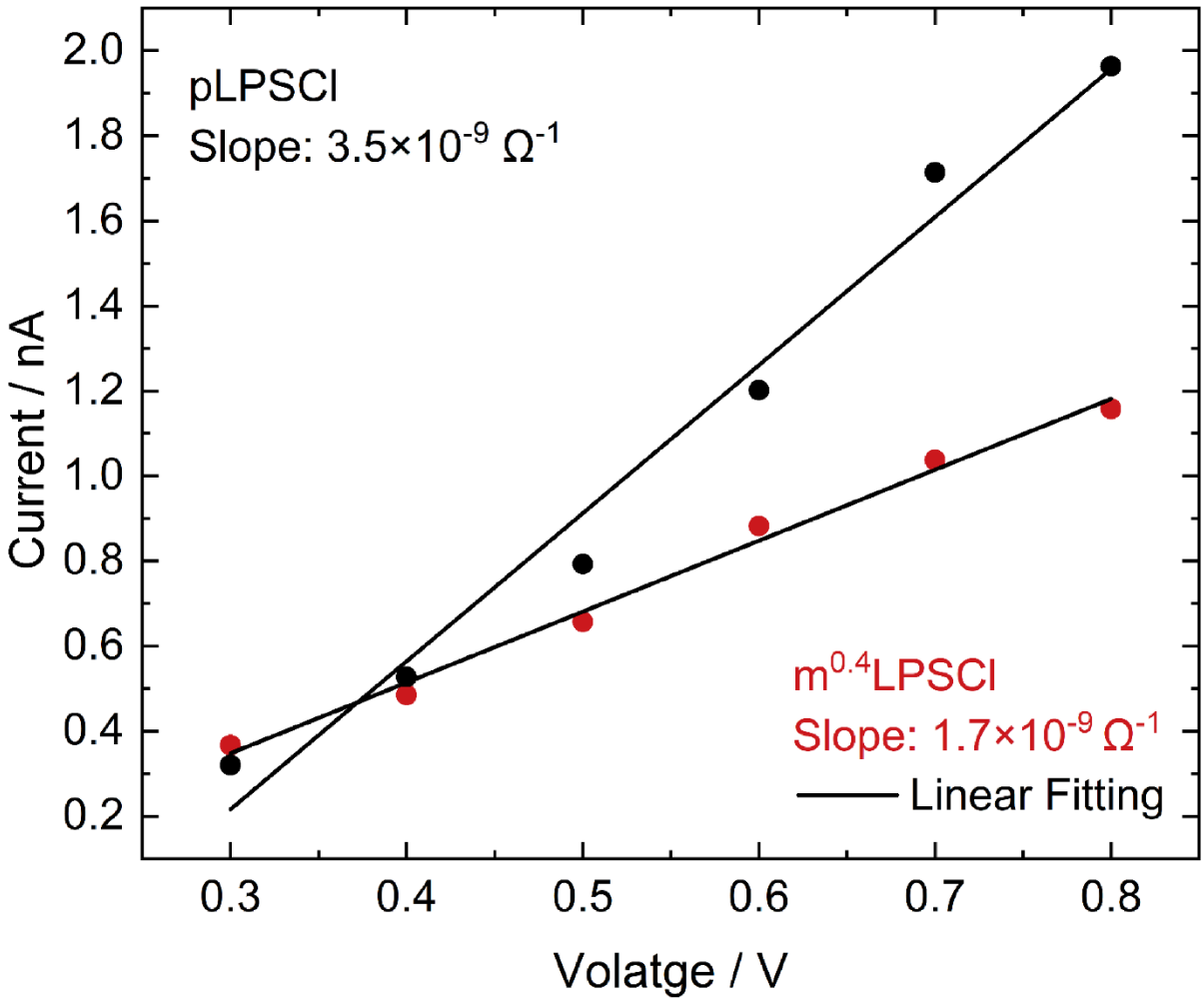

Figure S18. Current versus voltage plot is measured using DC polarization method at 25 °C. Electronic conductivity is determined from the slope obtained through linear fitting. The thickness of pLPSCl and $m^{0.4}$LPSCl pellets are 660 μm and 690 μm, respectively. The area of the pellets is 0.785 cm^2. The slope represents $R^{-1}$with the unit of Ω^{-1}, which is equivalent to Siemens (S).

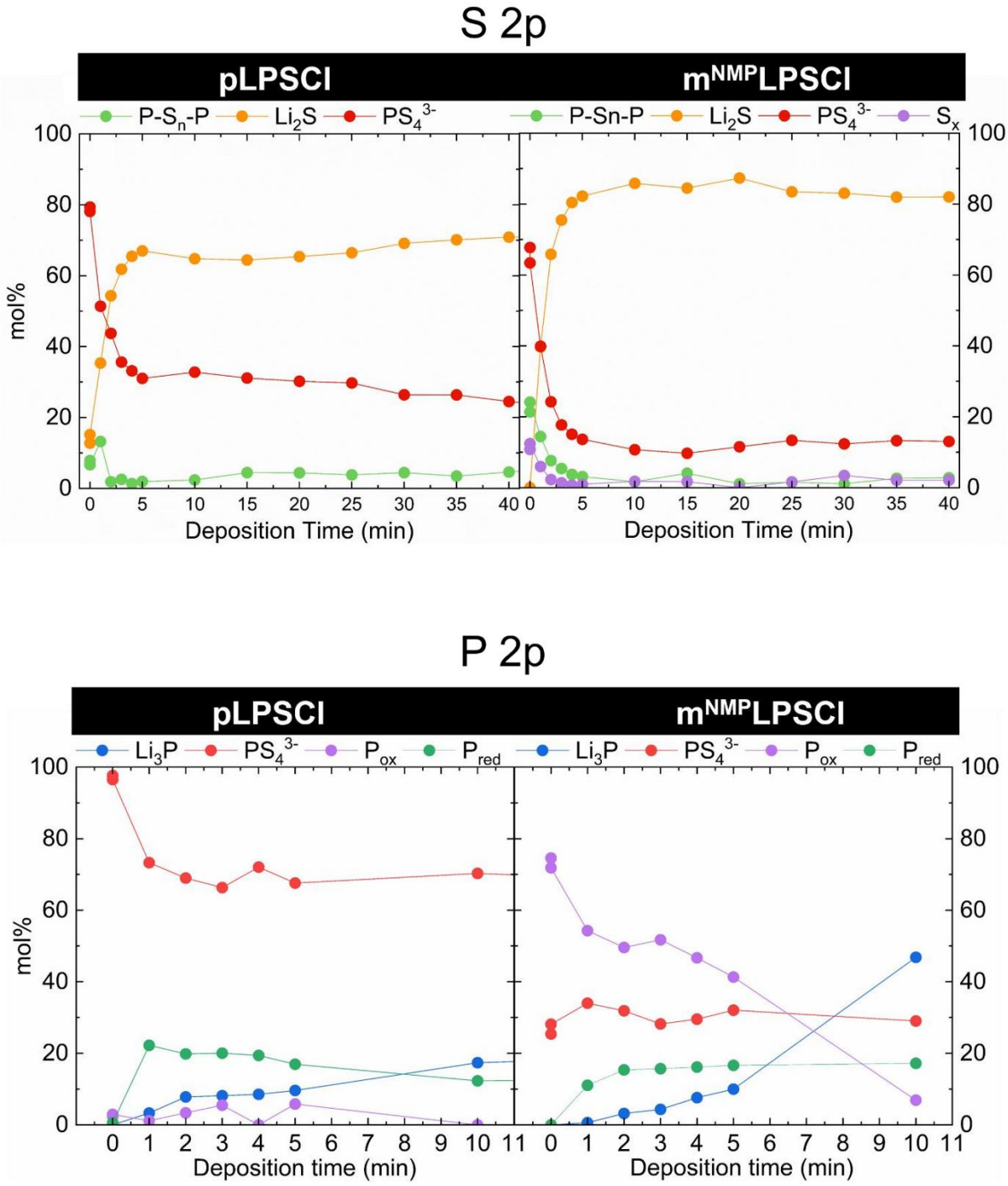

Figure S19. The evolution of decomposition products (in mol%) over lithium deposition time is analyzed for both S 2p and P 2p spectra. In the S 2p spectra, the products include P−$[S]_n$−P, Li_2S, PS_4^{3-}, and S_x. In the P 2p spectra, the decomposition products are Li_3P, PS_4^{3-}, P_{ox}, and P_{red}.

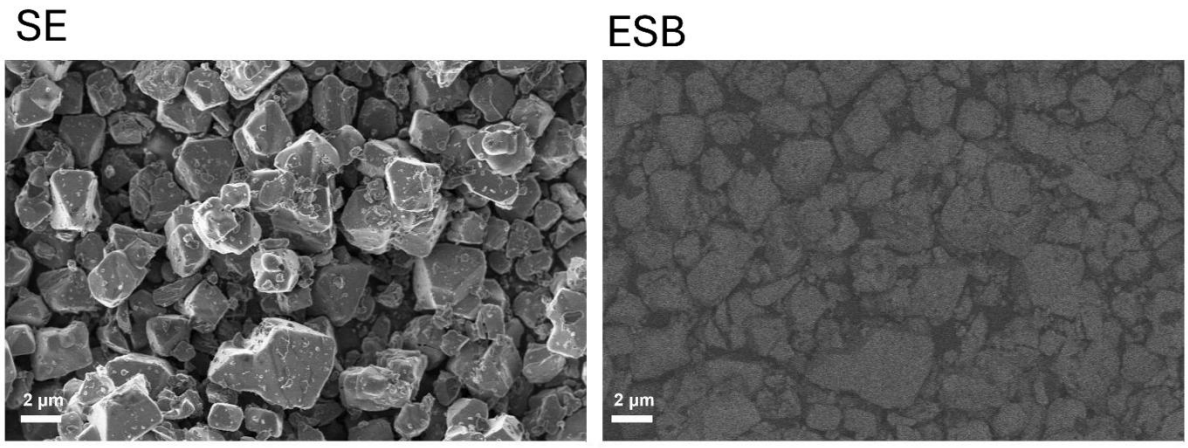

Figure S20. Secondary electron SEM images of LNO (left) reveals particle sizes ranging from 1 to 4 µm, while energy selective backscattered electron images (ESB) (right) show minimal impurities, visible as black spots due to different material densities.

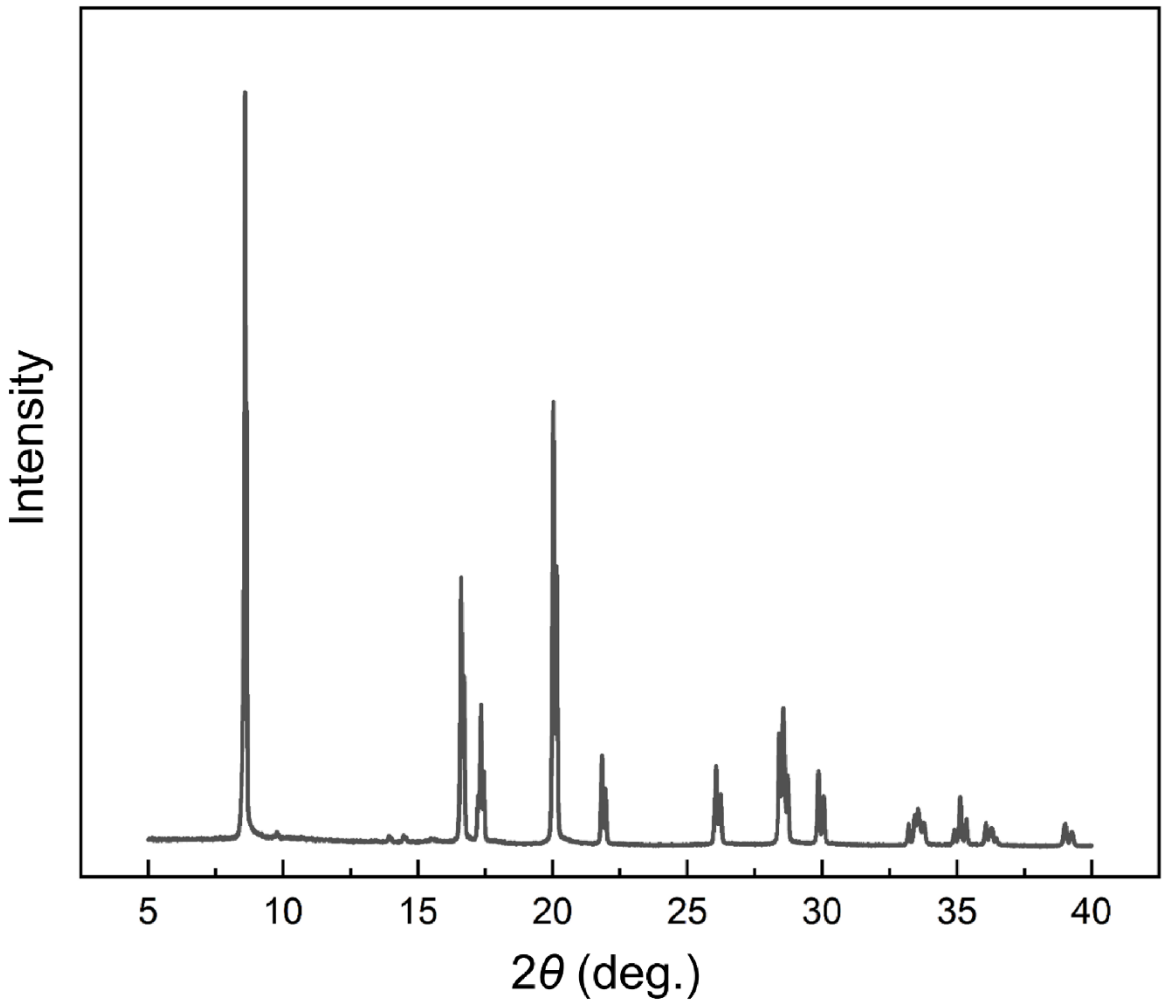

Figure S21. XRD is performed to check the crystalline structure of LNO.

3.4 Publication D

Publication D is under preparation for submission. Based on **Publication A**, which shows that cationic polymers are effective coating inducers, and **Publication B**, which highlights the role of anionic polymers in providing σ_{Li^+}; **Publication D** aims to utilize PEC to form a coating on LNO and Si by spray-drying, using a cationic polymer as a coating inducer and an anionic polymer to provide σ_{Li^+}.

However, the strong ionic interaction between the cationic and anionic polymers (see **Section 2.9.2**) prevents the PEC from dissolving in the solvent, which hinders the coating process. In this study, an anionic polymer with a flowing nature is modified by copolymerizing a neutral functional group to reduce its ionic interaction with the cationic polymer and to plasticize the anionic polymer. As a result, the resulting PEC exhibits a rubber-like mechanical property, which is beneficial as a coating. Additionally, the PEC is soluble in acetone, and the spray-drying method yields a uniform coating of about 2 nm on silicon and LNO particles.

The full cell using coated LNO and Si with Li_6PS_5Cl catholyte and anolyte demonstrates improved electrochemical performance compared to their pristine counterpart. To compare the performance of coated and pristine LNO cathodes or Si anodes in SEBs, half cells with LiIn as the counter electrode are used. Additionally, using self-synthesized LNO and applying an external pressure of 60 MPa ensures a clear focus on CEI degradation in the LNO half-cell. Overall, this study demonstrates that the PEC coating can efficiently mitigate CEI degradation between LNO and Li_6PS_5Cl, as well as SEI degradation between Si and Li_6PS_5Cl.

B.X.S. was responsible for the electrochemical analyses, and general characterization of materials. D.N. conducted the synthesis of anionic polymers and mechanical analysis of polyelectrolyte complex. T.W. performed the TOF-SIMS analysis, while T.D. performed the TEM experiments. S.L.B. conducted the XPS analysis. K.V. contributed to the LEB measurement. K.V., A.H., A.S., and F.H.R. contributed to the analysis and interpretation of the experimental data. The research concept was conceived by B.X.S. and F.H.R., who also prepared the manuscript. All authors contributed to the manuscript and the analysis of experimental results.

Polyelectrolyte Complexes as Coating on Nickel-Rich Cathode and Silicon Anode Particles to Stabilize Solid-State Batteries

Bing-Xuan Shi,[a] Daniil Nosov,[b] Timo Weintraut,[c] Thomas Demuth,[d] Felix Schnaubelt,[a] Sebastian Leonard Benz,[a] Kilian Vettori,[a] Jingui Yang,[e] Florian Strauss,[e] Kerstin Volz,[d] Anja Henss,[c] Alexander Shaplov,[b] Felix H. Richter*[a]

[a] Institute of Physical Chemistry & Center for Materials Research (LaMa), Justus-Liebig-University Giessen, Heinrich-Buff-Ring 17, 35392 Giessen, Germany

[b] Luxembourg Institute of Science and Technology, 5 Avenue des Hauts-Fourneaux, 4362 ESCH-SUR-ALZETTE, Luxembourg

[c] Institute of Experimental Physics 1 & Center for Materials Research (LaMa), Justus-Liebig-University Giessen, Heinrich-Buff-Ring 17, 35392 Giessen, Germany

[d] Department of Physics & Materials Sciences Center (WZMW), Philipps-University Marburg, Hans-Meerwein Straße 6, 35032 Marburg, Germany

[e] Institute of Nanotechnology (INT), Karlsruhe Institute of Technology (KIT), Kaiserstr. 12, 76131 Karlsruhe, Germany.

*Corresponding author, Felix.H.Richter@phys.chemie.uni-giessen.de

Key words: Solid-state batteries, solid electrolyte, polymer coating, polyelectrolyte complex, interface degradation.

Abstract

Sulfide-based solid electrolytes are key to advancing solid-state batteries but face interfacial instability with high-nickel cathode and silicon anode materials. Here, we develop a spray drying method to prepare a 1~3 nm thick polyelectrolyte complex (PEC) coating on high-nickel cathode and a silicon anode particles to improve cycling performance and rate capability of sulfide-based solid-state batteries. The prepared PEC dissolves in acetone without precipitation, unlike others that form insoluble aggregates, making it ideal for spray drying. Additionally, PEC has rubber-like mechanical properties that can accommodate the chemo-mechanical degradation of electrodes. A full cell with a PEC-coated $LiNiO_2$ (LNO) cathode and PEC-coated silicon anode shows improved performance. It retains around 56% of its capacity after 200 cycles, compared to 29% for its pristine counterpart. To study cathodic and anodic mechanisms individually, half cells are assembled using a LiIn alloy counter electrode paired separately with a LNO cathode, $LiNi_{0.9}Mn_{0.05}Co_{0.05}O_2$ (NCM90) cathode, and silicon anode. The PEC coating improves the cycling performance in both cathode and anode particles. Time-of-flight secondary ion mass spectrometry and X-ray photoelectron spectroscopy confirm that the PEC coating reduces interfacial side reactions in the half cells. Overall, this approach presents a novel coated material using a scalable coating method for cathode and anode materials, improving electrochemical performance.

Introduction

Solid electrolyte batteries (SEBs) are a specific sub-type of solid-state batteries that use inorganic solid electrolytes (SEs) as a catholyte and separator.[1] It potentially offers significant benefits over liquid electrolyte batteries (LEBs), including leak prevention, cost savings, and greater energy density.[2-4] Sulfide-based SEs, such as Li_6PS_5Cl (LPSCl), have sufficient ionic conductivity of ≈ 2 $mS \cdot cm^{-1}$ for realizing SEBs.[5, 6] However, severe interfacial degradation between electrode active materials (AMs) and the sulfide-based SEs[7, 8] compromises their electrochemical performance.[2, 9]

Nickel-rich cathode active materials (CAMs) are among the most widely used CAMs at present.[10, 11] The trend is shifting toward even higher Ni content in $LiNi_xMn_yCo_{1-x-y}O_2$ (NCM), such as $LiNi_{0.9}Mn_{0.05}Co_{0.05}O_2$ (NCM90), to increase the SEB energy density.[11] $LiNiO_2$ (LNO), with the highest Ni content, would be preferred to maximize the practical capacity and reduce the cost.[12] However, LNO undergoes more severe cathode-electrolyte interphase (CEI) degradation with LPSCl than NCMs.[13] Therefore, LNO serves as a valuable model for studying interfacial degradation in nickel-rich CAMs.

The oxidation of LPSCl above 2.2 V vs. Li^+/Li results in the formation of elemental sulfur and polysulfide species, such as $-[S]_n-$.[14, 15] These side products are insulating and reduce first-cycle Coulomb efficiency.[14, 16-18] Additionally, at a 0% state of charge (SOC), chemical reactions already take place at the CEI, causing a decrease in first-cycle capacity.[19] When the SOC increases to ≈ 4.2 V vs. Li^+/Li, oxygenated reactions cause the formation of a passivation layer and a rock-salt phase on nickel-rich CAMs, hindering charge transfer.[16, 20, 21] Moreover, nickel-rich CAMs undergo chemo-mechanical cracking due to oxygen loss and volumetric changes, especially above 4.2 V vs. Li^+/Li.[22, 23] To study CEI degradation, this research employs single-crystal LNO, which minimizes particle cracking [12, 22] but exhibits pronounced CEI passivation during cycling.[10, 12] The NCM90 provides additional evidence to support LNO results.

When in contact with the anode materials, LPSCl reduces below 1.7 V vs. Li^+/Li into LiCl, Li_2S, and Li_3P, forming a solid electrolyte interface (SEI).[15] silicon is a low-cost and air-stable anode material with a high theoretical capacity of 3579 $mAh \cdot g^{-1}$, approaching the theoretical capacity of lithium metal (3860 $mAh \cdot g^{-1}$).[24, 25] In addition, silicon conducts alloying process at ≈ 0.3 V vs. Li^+/Li and provides higher energy density than other alloy anode materials.[26] However, silicon undergoes substantial volume expansion during lithiation/delithiation (≈ 300%)[27], which degrades the SEI layer and increases LPSCl reduction, worsening electrochemical performance.[25, 28-31]

Surface coatings on nickel-rich CAMs[32, 33] and Si[34, 35] anode are applied to improve the interfacial stability at CEI and SEI, respectively. Coating materials should be electronically insulating and electrochemically stable.[36] To keep Li^+ transport resistance below 1 Ω cm^2 with a 1 nm thick coating, an ionic conductivity of only 0.1 $\mu S \cdot cm^{-1}$ is sufficient.[37] Consequently,

optimization of the coating thickness and coverage is necessary to avoid impeding Li^+ transport. However, inorganic coatings with high Young's modules (such as $LiNbO_3$, ≈ 195 GPa) can crack or detach during volume change.[37, 38] In contrast, the inherent flexibility of polymers (such as polyethylene oxide, ≈ 700 MPa)[39] minimizes coating fractures. On the other hand, polymer coatings require lower heat treatment temperatures and shorter processing times than inorganic materials, which can reduce manufacturing costs.[37, 38]

Our previous study found that polycations (PC) and amide polymers are effective coating inducers for nickel-rich CAMs due to electrostatic interactions, though their lack of Li^+ may cause capacity loss.[40, 41] In contrast, polyanions (PA) provide Li^+ but lack sufficient electrostatic attraction for effective coating.[40] As a result, it brings out the interest to explore polyelectrolyte complexes (PECs) that combine a PC as a coating inducer and a PA as the Li^+ source. However, several challenges need to be addressed. PECs often precipitate when mixed with anionic and cationic polymer solutions due to the electrostatic interactions between PC and PA,[42, 43] making them insoluble and unsuitable for wet-coating processes. Adding salts and water can screen the polymeric charges, forming a colloidal solution.[44] Nevertheless, a true solution is essential, as colloidal solutions with micrometer-sized polymer aggregates are unsuitable to form a uniform coating.[44, 45]

Additionally, PECs tend to become stiff in the dry state due to their high glass transition temperature (T_g) caused by strong electrostatic interactions,[46] potentially causing coating fractures during SEB fabrication and cycling.[37] Moreover, when the electrostatic interactions between PC and PA become strong—for example, with a charge density exceeding 15 mol%—the PEC mechanical properties deteriorate, leading to increased fragility and water adsorption.[43] Thermoplastic PECs can be copolymerized using plasticized monomers with increasing steric hindrance. Although thermoplastic PECs with hot pressing [43, 47, 48] or multilayering anionic and cationic polymers[49, 50] can form soft and self-standing films, these methods generally produce micrometer-thick films. Overall, PECs must be inherently flexible and solvent-soluble to form nanometer-scale coatings via wet coating.

In this study, we present a novel PEC coating (1~3 nm) on nickel-rich CAMs (LNO, NCM90) and silicon anode for LPSCl-based SEBs. PEC is formed using a PA, poly[(lithium 1-[3-(methacryloyloxy)propylsulfonyl]-1-(trifluoromethane sulfonyl)imide)-r-(poly(ethylene glycol) methyl ether methacrylate)], which reduces electrostatic interactions with the PC, poly(vinyl benzyl)trimethylammonium bis(trifluoromethane sulfonyl)imide. This designed PEC offers rubber-like properties without salts or plasticizers and can be spray-dried from an acetone solution.[40, 41] As a result, the designed PEC is an excellent candidate for coating applications. Using a PEC-coated LNO cathode with a PEC-coated silicon anode improves full-cell performance. To further assess individual electrode performance, half cell tests are conducted using LNO or silicon as the working electrode paired with a LiIn counter electrode. The PEC-coated NCM90 provides additional validation in half cell tests. Time-of-flight secondary ion mass spectrometry (ToF-SIMS) and X-ray photoelectron spectroscopy (XPS) confirm reduced degradation at the CEI and SEI for PEC-coated electrodes.

Results and discussion

2.1 Preparation and Characterization of polymer coated active materials

A transparent true polymer solution (solute particle size <1 nm) and low-boiling-point solvents are essential to achieve uniform coatings on AM particles via spray-drying.[40, 41] The coating procedure and chemical structures of the polymers are illustrated in **Figure 1**. We developed a novel PEC with reduced electrostatic interactions between the PC and PA to meet this criterion, enabling easy dissolution for uniform coating formation. Fourier-transform infrared spectroscopy (FTIR) confirms weak electrostatic attraction between PC and PA, as evidenced by slight $TFSI^-$ group shifts in the spectra (see **Figure S1**).

Using spray drying, we compare 1 wt% PC and PEC coatings (based on total AM weight) on AMs. Previous studies showed that 1 wt% polymer yields a ≈ 2 nm coating thickness.[40, 41] However, PA alone is excluded due to its flowing nature and inadequate electrostatic force for uniform NCM coating.[40] PC is a coating inducer in PEC,[41] while PA provides the Li^+ source.[40] Additionally, a PEC with PC:PA ratio of 3:2 by weight ensures a self-standing film and maximizes the anionic polymer content. We designate pristine LNO, PC-coated LNO, PEC-coated LNO, and PEC-coated NCM90 as P-LNO, PC-LNO, PEC-LNO, and PEC-NCM90, respectively. Similarly, pristine silicon, PC-coated silicon, and PEC-coated silicon are termed P-Si, PC-Si, and PEC-Si, respectively.

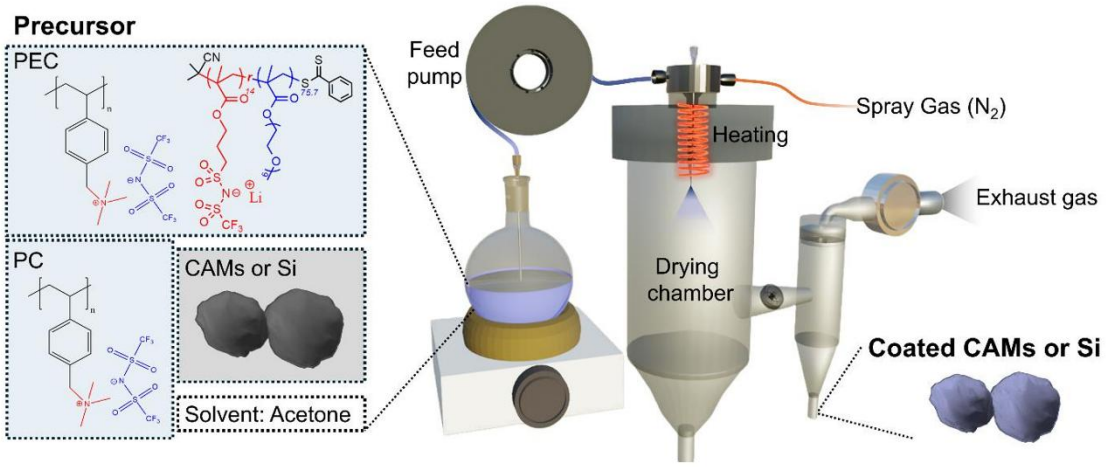

Figure 1. Schematic illustration of the process using spray drying to coat AM particles, including LNO, NCM90, and silicon. The coating materials include PEC or PC polymers, as shown in the left-hand side of the figure. The precursor (polymers and AMs dispersed in acetone) is atomized into droplets and dried in a chamber to form the coating immediately. The coated AM particles are collected, reaching ≈ 70 wt% of productivity.

(Scanning) transmission electron microscopy ((S)TEM) coupled with energy dispersive X-ray spectroscopy (EDX) is used to evaluate the coverage and thickness of PC and PEC coatings on LNO and silicon. **Figure 2** presents TEM bright field images, revealing that P-LNO and P-Si exhibit exposed crystalline lattice planes, whereas PC- and PEC-coated samples display a uniform 1~3 nm thin amorphous layer in front of the crystalline layers. These findings are consistent with our prior study on PC-coated NCM.[41] It is worth noting that the ionic conductivity of the PEC polymer is ≈ $3.5 \cdot 10^{-7}$ $S \cdot cm^{-1}$ at 25 °C (**Figure S2**), suggesting a 1~3 nm coating may add less than 1 $\Omega \cdot cm^2$ Li^+ transport resistance to the SEB.[37]

STEM-EDX analysis, shown in **Figure S3**, confirms a uniform coating on PEC-LNO, PC-LNO, PEC-Si, and PC-Si surfaces. Coated particles demonstrate significantly higher carbon signals originating from the polymer coating compared to uncoated particles, with the carbon intensity being most pronounced at the particle edges. Moreover, oxygen serves as an additional indicator to confirm the coating on PEC-Si and PC-Si surfaces. However, as oxygen is intrinsic to LNO, it cannot be used as an indicator in this case, as the oxygen content in LNO far exceeds the small amounts present in the coating.

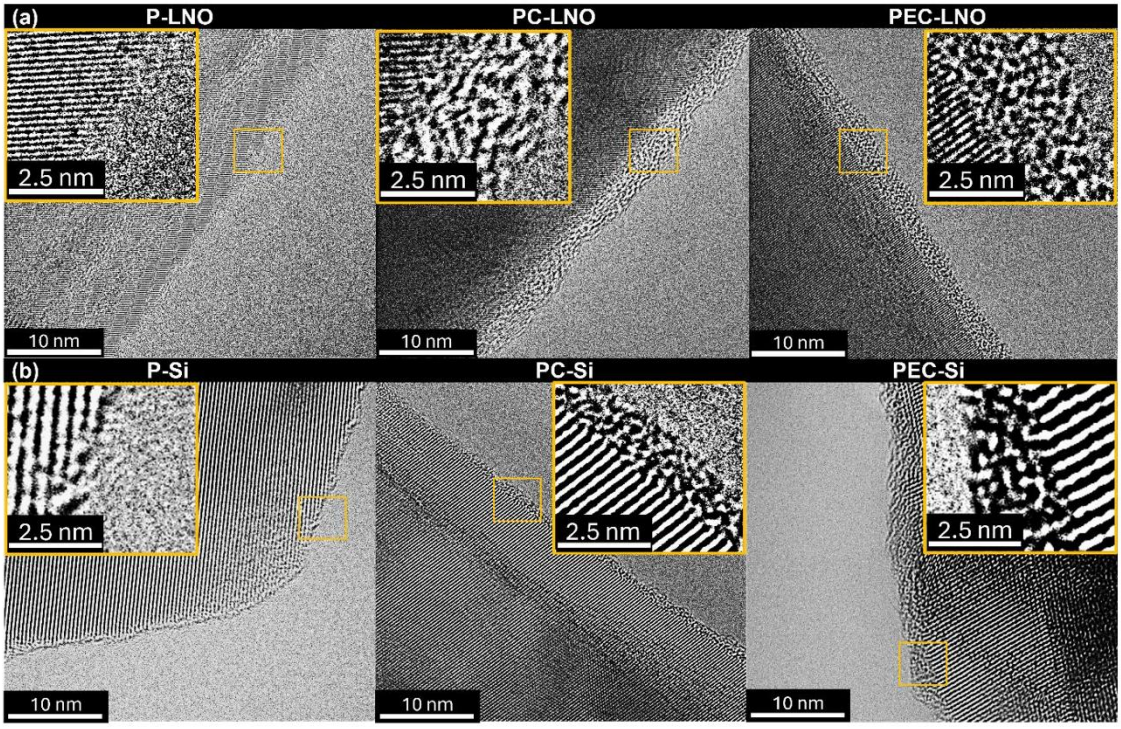

Figure 2. TEM images of (a) P-LNO, PC-LNO, and PEC-LNO, and (b) P-Si, PC-Si, and PEC-Si. The insets display magnified views of the coating layer on crystalline lattice planes, revealing a coating thickness of approximately 1~3 nm.

Scanning electron microscopy (SEM) with an energy-selective backscattered electron detector (ESB) (**Figure S4**) reveals no polymer aggregation on PEC-LNO and PC-LNO particles, supporting the TEM results of a uniform coating. In contrast, our previous study shows that with 1 wt% polymer, failed coatings exhibited detectable polymer aggregation particles.[40] On the other hand, the similar densities between silicon and carbon make detecting polymer aggregation on silicon challenging with ESB. Overall, SEM, TEM, and EDX analyses confirm a uniform PEC and PC coating on LNO and silicon particles, with a thickness of approximately 1~3 nm which can effectively prevent direct physical contact between the AM and LPSCl.

2.2 Electrochemical stability of the polymer coating

Cyclic voltammetry (CV) investigates the electrochemical stability window (ESW) between polymer and inactive materials, such as vapor-grown carbon fibers (VGCFs) and stainless steel, using pellet-type cells, with a scan range from 0 V to 4.5 V vs. In/LiIn. PEC-coated and PC-coated VGCFs prepared via spray drying are used as working electrodes to enhance contact area with LPSCl, with pristine VGCF as a comparison.[14] LiIn alloy is a counter electrode due to its thermodynamic and kinetic stability with LPSCl.[14, 51] The cell configuration is LiIn|LPSCl|LPSCl/VGCF.

Figure S5 shows that both PEC- and PC-coated VGCF exhibit a diminished current density and have no additional side reaction peaks compared to pristine VGCF, confirming the stability of PEC and PC against LPSCl. Moreover, the lower current density observed with PEC-coated VGCF compared to PC-coated VGCF suggests that rubber-like mechanical properties of PEC confer superior protection. This elasticity helps maintain continuous coverage on the VGCF, preventing the coating from detaching during cell preparation. Overall, both PEC- and PC-coated VGCF are electrochemically stable to LPSCl and has less side reaction at the VGCF|LPSCl interface.

2.3 Impact of coatings on the cycling stability of $^{Si}SEB^{LNO}$ full cell

Cycling stability of $^{SI}SEB^{LNO}$ (an area specific capacity of 3.3 mAh·cm^{-2} based on 200 mAh·g^{-1} of LNO, N/P ratio: 1.3) with a LPSCl/VGCF/Si|LPSCl|LPSCl/VGCF/LNO configuration is conducted under 60 MPa at different C-rates, 0.1C, 0.25C, 0.5C, 1C, followed by 0.1C for continuous cycling (**Figure 3a**). $^{SI}SEB^{LNO}$ using pristine and PEC-coated AMs is denoted as $^{P\text{-}Si}SEB^{P\text{-}LNO}$ and $^{PEC\text{-}Si}SEB^{PEC\text{-}LNO}$, respectively. The specific discharge capacity ($q_{discharge}$) and C-rates are calculated based on the amount of LNO.

$^{PEC\text{-}Si}SEB^{PEC\text{-}LNO}$ shows better performance than $^{P\text{-}Si}SEB^{P\text{-}LNO}$ across low and middle C-rates and in the cycling test (**Figure 3b**). However, the slight fluctuation detected in the galvanic plots ≈ 3.7 V at 1C (**Figure S6)** indicates that lithium is not alloying with Si but is instead temporarily plating as lithium metal on the surface of Si due to kinetic limitations.[52] In the first cycle of 0.05C, $^{PEC\text{-}Si}SEB^{PEC\text{-}LNO}$ shows improved $q_{discharge}$ ≈172 mAh·g^{-1}, which is 21 mAh·g^{-1} more

than $^{P\text{-}Si}SEB^{P\text{-}LNO}$ (151 mAh·g^{-1}). After 200 cycles, the retention (based on 6th and 200th cycles) of the $^{PEC\text{-}Si}SEB^{PEC\text{-}LNO}$ is 56%, about double that of the $^{P\text{-}Si}SEB^{P\text{-}LNO}$ (29%). To independently assess the impact of the PEC coating on cycling performance at the LNO cathode and silicon anode, $^{LiIn}SEB^{PEC\text{-}LNO}$ and $^{LiIn}SEB^{PEC\text{-}Si}$ half cells are investigated in the following sections.

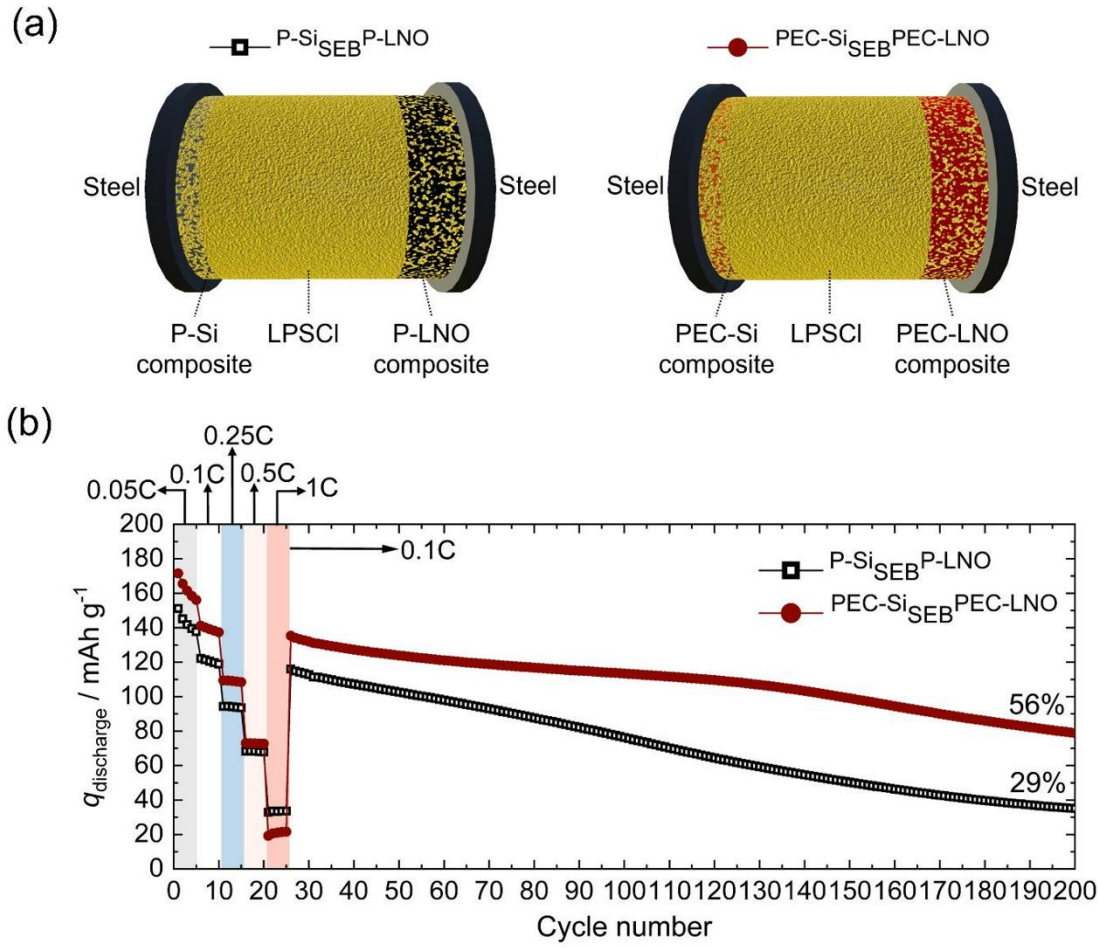

Figure 3. (a) Schematics of the full-cell configurations are provided, including $^{P\text{-}Si}SEB^{P\text{-}LNO}$ and $^{PEC\text{-}Si}SEB^{PEC\text{-}LNO}$ (area specific capacity: 3.3 mAh·cm^{-2}, LNO: 13.2 mg, Si: 1 mg, N/P ratio: 1.3) at 25 °C. (b) The $q_{discharge}$ is plotted over cycles, beginning with rates of 0.05C, 0.1C, 0.25C, 0.5C, and 1C for five cycles each. Following this, cycling continues at a consistent rate of 0.1C.

2.4 Rate Capability of $^{LiIn}SEB^{LNO}$ with PEC and PC coating on LNO

Pellet-type half cells with the configuration of LiIn|LPSCl|LPSCl/VGCF/LNO ($^{LiIn}SEB^{LNO}$, an area-specific capacity of 2.1 mAh·cm^{-2} based on 200 mAh·g^{-1} of LNO, an area-specific mass loading of 10.6 mg·cm^{-2} based on LNO) compare the rate capability of P-LNO, PC-LNO, and PEC-LNO coated cathode, denoted as $^{LiIn}SEB^{P\text{-}LNO}$, $^{LiIn}SEB^{PC\text{-}LNO}$, and $^{LiIn}SEB^{PEC\text{-}LNO}$, respectively. **Figure 4a** shows a schematic of the $^{LiIn}SEB^{LNO}$ configurations. To focus on the impact of CEI degradation, we prevent contact loss in $^{LiIn}SEB^{LNO}$ by applying 60 MPa during cycling and using single-crystal LNO to reduce particle cracking[12, 22].

Figure 4b shows that $^{LiIn}SEB^{PEC\text{-}LNO}$ significantly improves $q_{discharge}$ compared to $^{LiIn}SEB^{PC\text{-}LNO}$ and $^{LiIn}SEB^{P\text{-}LNO}$ across all C-rates. The galvanic plots of the first and final cycles are shown in **Figure S7**. In the first cycle at 0.1C, $^{LiIn}SEB^{P\text{-}LNO}$ delivers 138 mAh·g^{-1} with 67% Coulomb efficiency, $^{LiIn}SEB^{PC\text{-}LNO}$ gives 147 mAh·g^{-1} with 73%, and $^{LiIn}SEB^{PEC\text{-}LNO}$ achieves 157 mAh·g^{-1} with 76%. Two primary factors affecting the first-cycle Coulomb efficiency are the diffusion within the LNO bulk materials[53] and interfacial degradation at the CEI.[54-56] As the coating mainly alters surface rather than bulk properties, the improved first-cycle $q_{discharge}$ and Coulomb efficiency for $^{LiIn}SEB^{PEC\text{-}LNO}$ are due to reduced CEI degradation.

Figure 4c shows that $^{LiIn}SEB^{PEC\text{-}LNO}$ exhibits a similar differential capacity (dq/dE) of M/H2 (≈ 3.4 V vs. In/LiIn) as both $^{LiIn}SEB^{PC\text{-}LNO}$ and $^{LiIn}SEB^{P\text{-}LNO}$ in the first charge cycle. However, in the first discharge and 25th cycles, $^{LiIn}SEB^{PEC\text{-}LNO}$ demonstrates better dq/dE of M/H2 than $^{LiIn}SEB^{PC\text{-}LNO}$ and $^{LiIn}SEB^{P\text{-}LNO}$. The M/H2 is majorly affected by active mass (m_{act}) utilization,[22] which can decrease if LNO becomes isolated due to contact loss or an insulated CEI.[22] The improved dq/dE of M/H2 in the first discharge cycle indicates higher m_{act} utilization in $^{LiIn}SEB^{PEC\text{-}LNO}$ compared to $^{LiIn}SEB^{P\text{-}LNO}$ and $^{LiIn}SEB^{P\text{-}LNO}$. This improvement may result from the PEC coating reducing insulated CEI formation, such as elemental sulfur and -[S]$_n$-,[14, 15] improving first-cycle Coulomb efficiency. Notably, these insulated CEI products dominate in the first cycle but diminish thereafter.[54]

On the other hand, $^{LiIn}SEB^{PEC\text{-}LNO}$ has improved dq/dE at H1/M (≈ 3 V vs. In/LiIn)[57] compared to $^{LiIn}SEB^{P\text{-}LNO}$ in the first and 25th cycles, with $^{LiIn}SEB^{PC\text{-}LNO}$ exhibiting intermediate performance. H1/M transition is affected by both m_{act} utilization and kinetic limitations.[22] A partially conductive rather than fully insulated CEI can contribute to kinetic limitations.[22] As M/H2 related to m_{act} utilization is similar across all samples during the first charge, $^{LiIn}SEB^{PEC\text{-}LNO}$ appears to improve the interfacial kinetics of the CEI during the first charge. Subsequent cycle improvement of H1/M stems from a combined effect of enhanced m_{act} utilization and interfacial kinetics. Moreover, the improved H2/H3 (≈ 3.6 V vs. In/LiIn), affected by both m_{act} utilization and kinetics,[22] is observed for $^{LiIn}SEB^{PEC\text{-}LNO}$ in the first and 25th cycles. The improved H2/H3 suggests reduced oxygenated reactions at the CEI over cycling.[21, 22] In conclusion, $^{LiIn}SEB^{PEC\text{-}LNO}$ shows the best performance of all tested SEBs, mainly due to reduced CEI degradation.

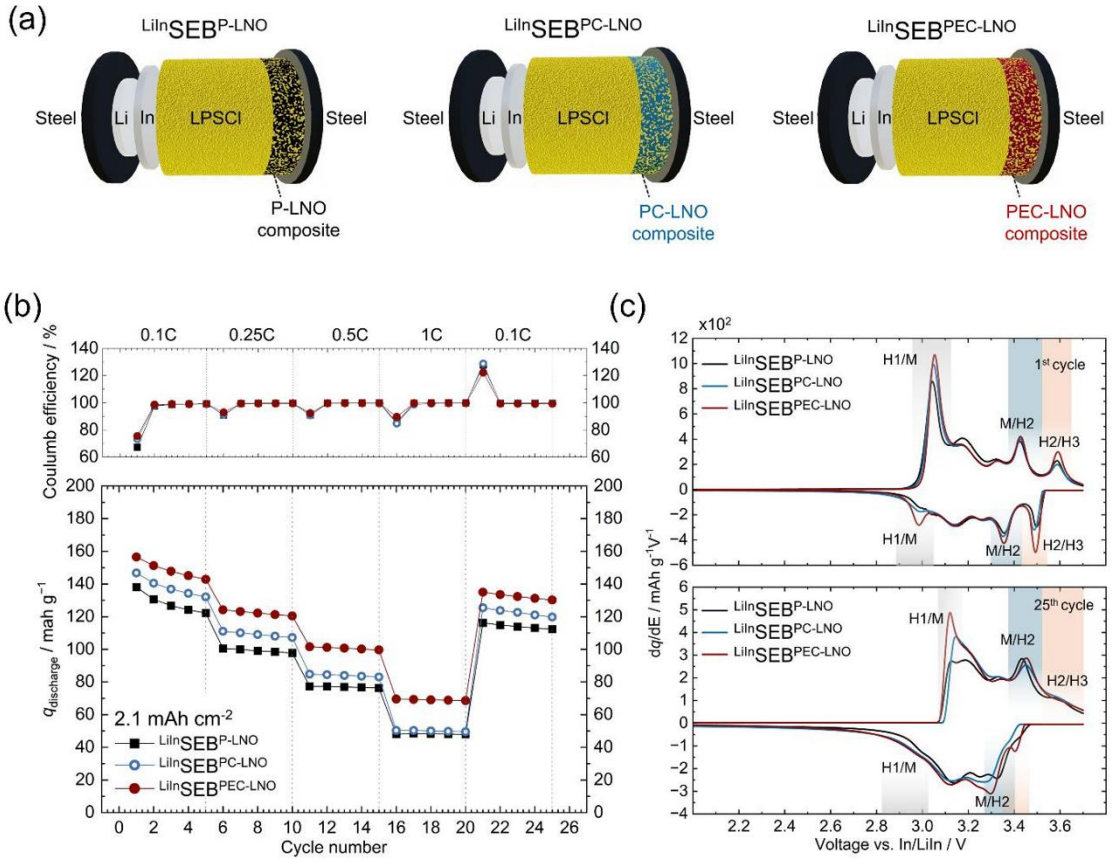

Figure 4. The rate capability of $^{LiIn}SEB^{LNO}$ (2.1 mAh·cm^{-2} and 10.6 mg·cm^{-2} of LNO) including $^{LiIn}SEB^{P\text{-}LNO}$, $^{LiIn}SEB^{PC\text{-}LNO}$, and $^{LiIn}SEB^{PEC\text{-}LNO}$ is analyzed using pellet-type cells at 25 °C. (a) Schematics of the respective cell configurations. (b) The left figure shows Coulomb efficiency (top) and $q_{discharge}$ (bottom) across different C-rates (0.1C, 0.25C, 0.5C, 1C, and back to 0.1C). (c) The right figure presents the dq/dE plots for the first (top) and 25th (bottom) cycles at 0.1C, highlighting the LNO phase transitions (H1↔M↔H2↔H3).

2.5 Cycling Stability of $^{LiIn}SEB^{LNO}$ with the PEC coating on LNO

$^{LiIn}SEB^{PEC\text{-}LNO}$ and $^{LiIn}SEB^{P\text{-}LNO}$ using the same device as in the rate capability test, evaluate LNO cathode cycling performance under 0.1C at 25 °C. Electrochemical impedance spectroscopy (EIS) measurements are taken at 3.15 V vs. In/LiIn during the first, second, 50th, and 100th cycles by following steps. First, cells are charged to 3.15 V vs. In/LiIn, followed by chronoamperometry (CA) at 3.15 V vs. In/LiIn until the current decreases to 2%. This step ensures a consistent SOC and offers insights into the Li^+ diffusion pathway length (L_{diff}).[41, 58] EIS is then performed from 1 MHz to 100 μHz to evaluate the cathode resistance ($R_{cathode}$). 3.15 V vs. In/LiIn ensures EIS is conducted at low charge transfer resistance (R_{ct}) while avoiding degradation at higher voltages.[59, 60] Subsequently, cell charging is continued to 3.7 V vs. In/LiIn,

relaxed for 2 hours, then discharged to 2.0 V vs. In/LiIn with another 2-hour relaxation to determine m_{act}.[22, 41] **Figure 5a** displays the first-cycle galvanic plots for both SEBs, with CA and EIS measurements marked.

Figure 5b shows that for the first and 100th cycles, ^{LiIn}SEB$^{PEC\text{-}LNO}$ has a higher $q_{discharge}$ and capacity retention (first: 160 mAh·g^{-1}, 100th: 109 mAh·g^{-1}, retention: 68%) than $^{P\text{-}LNO}$SEB^{LiIn} (first: 137 mAh·g^{-1}, 100th: 79 mAh·g^{-1}, retention: 58%). m_{act} loss and L_{diff} increase are key factors affecting cycling stability.[22, 41] L_{diff} reflects kinetic limitations arising from partially conductive CEI degradation.[22, 41] m_{act} loss results from contact loss and an insulated CEI that isolates LNO particles.[22, 41] After 100 cycles, there is no contact loss or LNO particle cracking in both SEBs, as investigated via ion beam milling and SEM (see **Figure S8**). As a result, CEI degradation primarily declines ^{LiIn}SEB^{LNO} cycling performance by degrading m_{act} and/or L_{diff}.

Figure S9 presents m_{act} results obtained via open circuit voltage (OCV) measurements. The detailed calculation is reported in our previous publication.[22, 41] Generally, the OCV-SOC relationship reveals the Li^+ content (i.e., the 'x' in Li_xNiO_2). To establish a reference for OCV vs. SOC, a LEB composed of LNO and a lithium anode is utilized (see **Figure S10**). The LE helps mitigate capacity loss by minimizing degradation at the CEI, contact loss, and cracking.[61] Based on the OCV-SOC reference, the specific discharge capacity at a given SOC (q_{SOC}) can be determined. According to equation [1], m_{act} is calculated by measured discharge capacity (Q_{meas}) and q_{SOC}.[22, 41]

$$m_{act}(\mathrm{g}) = \frac{Q_{meas}\,(\mathrm{mAh})}{q_{SOC}\left(\frac{\mathrm{mAh}}{\mathrm{g}}\right)} \qquad [1]$$

Ideally, the SEB should have a m_{act} of 8.3 mg. In the first cycle, ^{LiIn}SEB$^{PEC\text{-}LNO}$ shows a higher m_{act} of 8.1 mg, than ^{LiIn}SEB$^{P\text{-}LNO}$ (7.7 mg). The difference between the ideal and actual m_{act} arises from cathode distribution inefficiencies and SEB internal resistance. The improved first-cycle m_{act} of ^{LiIn}SEB$^{PEC\text{-}LNO}$ aligns with the better M/H2 results in the rate capability test (see **Figure 4**), confirming the PEC coating can reduce the formation of an insulating CEI in the first cycle, such as elemental sulfur and -[S]$_n$-.[14, 15] However, after 100 cycles, both ^{LiIn}SEB$^{PEC\text{-}LNO}$ and ^{LiIn}SEB$^{P\text{-}LNO}$ have similar m_{act} retention ≈ 74%, prompting a discussion on L_{diff} in the subsequent paragraphs.

Figure 5c presents the CA results of the second and 100th cycles, excluding the effect of first-cycle formation from LiIn alloy.[22, 41] The time it takes for the current to decrease below 2% is directly proportional to L_{diff}.[41, 58] Initially, ^{LiIn}SEB$^{PEC\text{-}LNO}$ and ^{LiIn}SEB$^{P\text{-}LNO}$ display current reduction times, around 111 and 161 seconds, respectively. The shorter time in ^{LiIn}SEB$^{PEC\text{-}LNO}$ is due to improved interfacial kinetics from the PEC coating in the initial cycle at 3.15 V vs. In/LiIn. This result aligns with the better H1/M transition in the rate capability test (see **Figure 4**).

Moreover, at the 100th cycle, ^{LiIn}SEB$^{P\text{-}LNO}$ takes approximately 710 minutes, whereas ^{LiIn}SEB$^{PEC\text{-}LNO}$ requires only about 485 minutes. This suggests that the PEC coating can help reduce the L_{diff} growth caused by CEI degradation. Furthermore, L_{diff} can be determined by fitting the Warburg impedance using a particle size distribution model (EIS-PSD), as described in our previous research[22, 41] and detailed in the supporting information (see **Figure S11**). The L_{diff} of ^{LiIn}SEB$^{PEC\text{-}LNO}$ increased from 1.2 µm to 4.2 µm, whereas ^{LiIn}SEB$^{P\text{-}LNO}$ increased from 1.5 µm to 6.2 µm. Oxygenated side reaction products such as Li_2SO_4 and Li_3PO_4 with ionic conductivities ≈ 10^{-4}~10^{-5} S·cm^{-1} [62, 63] do not directly isolate LNO particles, resulting in similar m_{act} retention in both cells. As a result, improved capacity retention in ^{LiIn}SEB$^{PEC\text{-}LNO}$ arises from mitigating L_{diff} growth at the CEI. Overall, both EIS-PSD analysis and CA results show that the L_{diff} growth at CEI of ^{LiIn}SEB$^{PEC\text{-}LNO}$ is mitigated.

The $R_{cathode}$ can be influenced by effective contact area (impacting m_{act})[22, 41] and CEI kinetics (impacting L_{diff})[64]. $R_{cathode}$ is analyzed by EIS after CA at 3.15 V vs. In/LiIn, with Nyquist plots shown in **Figure 5d** and transition line model (TLM)[65, 66] fitting results in **Figure S12**. The similar apex frequency in both SEBs indicates that impedance growth during cycling for both cells stems from the same CEI degradation process.[61, 67]

In the first cycle at 3.15 V vs. In/LiIn, the $R_{cathode}$ of ^{LiIn}SEB$^{PEC\text{-}LNO}$ is 11 Ω·cm^2, 7 Ω·cm^2 lower than that of ^{LiIn}SEB$^{P\text{-}LNO}$ (18 Ω·cm^2). This aligns with the better m_{act} utilization and shorter L_{diff} for ^{LiIn}SEB$^{PEC\text{-}LNO}$ than ^{LiIn}SEB$^{P\text{-}LNO}$ in the initial cycle. After 100 cycles, the $R_{cathode}$ for ^{LiIn}SEB$^{P\text{-}LNO}$ (939 Ω·cm^2) shows a more pronounced increase compared to ^{LiIn}SEB$^{PEC\text{-}LNO}$ (218 Ω·cm^2). As a result, PEC coating can mitigate the increase in $R_{cathode}$ after cycling. Since m_{act} retention is similar for both cells and ^{LiIn}SEB$^{PEC\text{-}LNO}$ has less L_{diff} growth than ^{LiIn}SEB$^{P\text{-}LNO}$, EIS results confirm that the PEC coating can improve CEI kinetics during cycling by reducing oxygenated reactions.

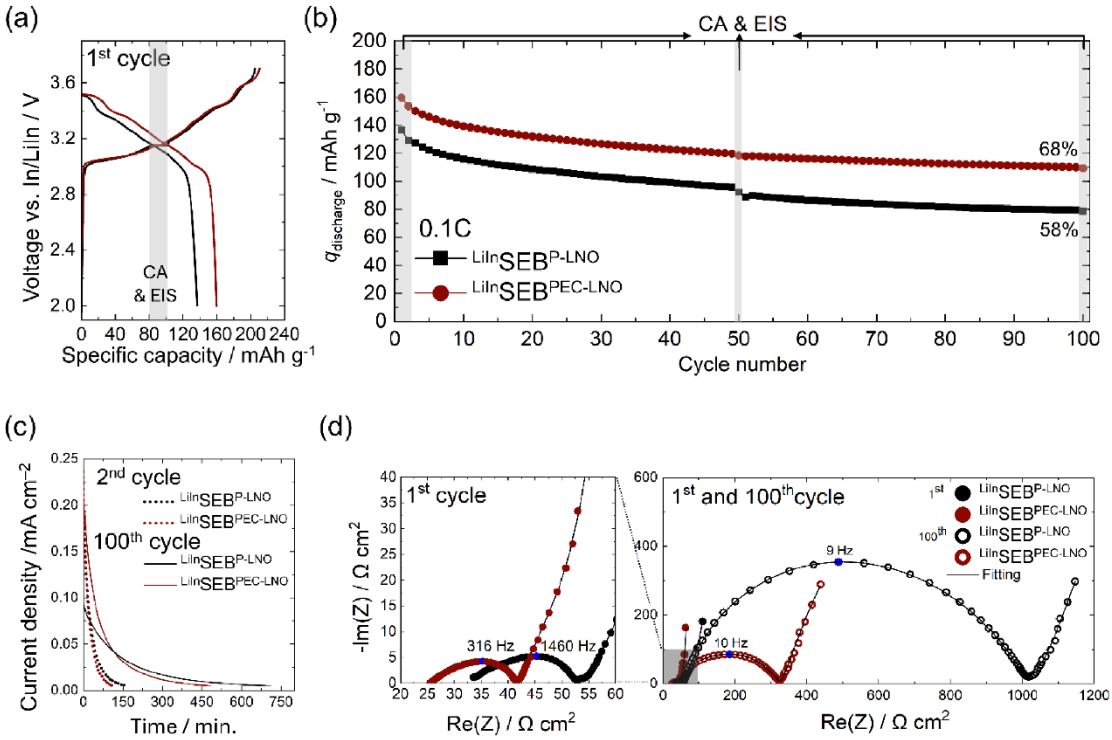

Figure 5. The cycling performance of $^{LiIn}SEB^{LNO}$ (2.1 mAh·cm^{-2} and 10.6 mg·cm^{-2} of LNO), including $^{LiIn}SEB^{P\text{-}LNO}$ and $^{LiIn}SEB^{PEC\text{-}LNO}$, is conducted under 0.1C at 25 °C. EIS and CA are taken at 3.15 V vs. In/LiIn during the first, second, 50th, and 100th cycles. (a) The galvanic plot shows the first cycle of cells are charged to 3.15 V vs. In/LiIn, followed by CA (dashed line) and EIS. Subsequently, cells are recharged to 3.7 V vs. In/LiIn and relaxed for 2 hours, then cells are discharged to 2.0 V vs. In/LiIn and relaxed again for 2 hours. (b) The cycling stability is presented by plotting the $q_{discharge}$ against the number of cycles. (c) CA at 3.15 V vs. In/LiIn reveals an increase in L_{diff} from second to 100th cycle. (d) Nyquist plots measured by EIS show the impedance increase from the first to 100th cycle. The apex frequency in both cells is marked in blue.

To further assess whether the PEC coating enhances the electrochemical performance of NCM90, we employ $Li_{5.5}PS_{4.5}Cl_{0.8}Br_{0.7}$ (LPSClBr, 9.1 mS·cm^{-1})[68] as the separator and LPSCl as the catholyte. Pellet-type half cells with the configuration of LiIn|LPSClBr|LPSCl/VGCF/NCM90 ($^{LiIn}SEB^{NCM90}$, an area-specific capacity of 3.5 mAh·cm^{-2} based on 200 mAh·g^{-1} of NCM90, an area-specific mass loading of 17.7 mg·cm^{-2} based on NCM90) compare the rate capability followed with cycling test of P-NCM90 and PEC-NCM90 coated cathode, denoted as $^{LiIn}SEB^{P\text{-}NCM90}$ and $^{LiIn}SEB^{PEC\text{-}NCM90}$, respectively. Similar to $^{LiIn}SEB^{LNO}$, 60 MPa during cycling is applied.

^{LiIn}SEB$^{PEC\text{-}NCM90}$ shows better rate performance and cycling stability than ^{LiIn}SEB$^{P\text{-}NCM90}$ (**Figure 6**). In the first cycle of 0.05C, ^{LiIn}SEB$^{PEC\text{-}NCM90}$ shows improved $q_{discharge}$ ≈ 199 mAh·g^{-1}, 11 mAh·g^{-1} more than $^{P\text{-}Si}$SEB$^{P\text{-}LNO}$ (188 mAh·g^{-1}). In the 8th cycle at 0.25C, ^{LiIn}SEB$^{PEC\text{-}NCM90}$ shows improved $q_{discharge}$ ≈ 156 mAh·g^{-1}, 13 mAh·g^{-1} more than ^{LiIn}SEB$^{P\text{-}NCM90}$ (143 mAh·g^{-1}). After 400 cycles, the retention (based on 8th and 400th cycles) of the ^{LiIn}SEB$^{PEC\text{-}NCM90}$ is 90% (140 mAh·g^{-1} at 400th cycle), 12% more than ^{LiIn}SEB$^{P\text{-}NCM90}$ (78 % and 112 mAh·g^{-1} at 400th cycle).

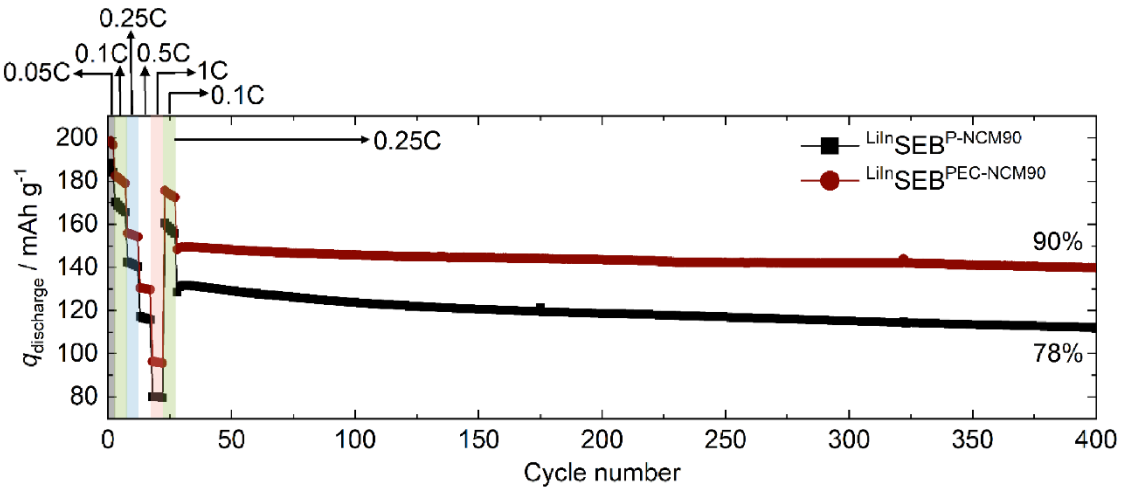

Figure 6. The cycling performance of ^{LiIn}SEB^{NCM90} (3.5 mAh·cm^{-2} and 17.7 mg·cm^{-2} of NCM90), including ^{LiIn}SEB$^{P\text{-}LNO}$ and ^{LiIn}SEB$^{PEC\text{-}LNO}$, is conducted. The $q_{discharge}$ is plotted over cycles, beginning with 0.05C for 2 cycles, then 0.1C, 0.25C, 0.5C, and 1C for 5 cycles each, and back to 0.1C for 5 cycles, followed by 0.25C for 373 cycles. The retention is calculated based on 8th and 400th cycles.

2.6 Analysis of Interfacial Degradation in ^{LiIn}SEB^{LNO} by TOF-SIMS

TOF-SIMS semi-quantitatively[69] detects CEI decomposition product fragments in the cathode composite of ^{LiIn}SEB^{LNO} (see **Figure 7**), including elemental sulfur and -[S]$_n$- (S_4^-), phosphoxides (PO_x^- including PO^-, PO_2^- and PO_3^-), and sulfoxides (SO_x^- including SO^-, SO_2^- and SO_3^-), before and after cycling.[70-73] To examine interfaces within the cathode composite (steel|LPSCl, VGCF|LPSCl, and LNO|LPSCl)[70], wedges are created by gradually increasing the sputter dose density from left (close to steel|LPSCl) to right across a sputtered rectangle. This approach allows visualization of the depth distribution of degradation products in the surface spectrum, as schematically shown in **Figure S13**. Following the formation of wedge-shaped craters, ToF-SIMS mappings of cathode composite before and after cycling are displayed as linear scans. Due to consistent overlap of LNO intensities (NiO_2^-) across samples (**Figure S14**), the average NiO_2^- intensity is used in each figure to mark where sputtering reaches the LNO particles.

Before cycling, PO_x^-, SO_x^-, and S_4^-, overlap nicely across sputtering regions. Notably, the contact between LNO (fully lithiated) and LPSCl during sample preparation can already lead to the formation of PO_x^- and SO_x^-.[71] As a result, before cycling, PO_x^- and SO_x^- show slightly higher intensity near the LNO particles in $^{LiIn}SEB^{P\text{-}LNO}$ than in $^{LiIn}SEB^{PEC\text{-}LNO}$.

After cycling, $^{LiIn}SEB^{P\text{-}LNO}$ has higher S_4^-, SO_x^-, and PO_x^- intensity than $^{LiIn}SEB^{PEC\text{-}LNO}$ across the wedge profile. This indicates that the PEC coating can mitigate CEI degradation between LNO and LPSCl during cycling. In addition, the PEC coating can inhibit the first-cycle side reaction that forms elemental sulfur and P-$[S]_n$-P, aligning with the ESW results measured by CV and supporting the first cycle m_{act} result in rate capability and cycling stability test. Interestingly, the SO_x^- intensity is low at the start of sputtering (near steel|LPSCl) and increases as sputtering reaches the LNO surface. In contrast, PO_x^- intensity is observed across the entire range. This result aligns with Walther et al., who observed similar outcomes near the steel|LPSCl interface.[70] Further investigation is warranted to deepen our understanding. Overall, ToF-SIMS confirms that PEC coating improves the CEI stability in comparison to uncoated LNO.

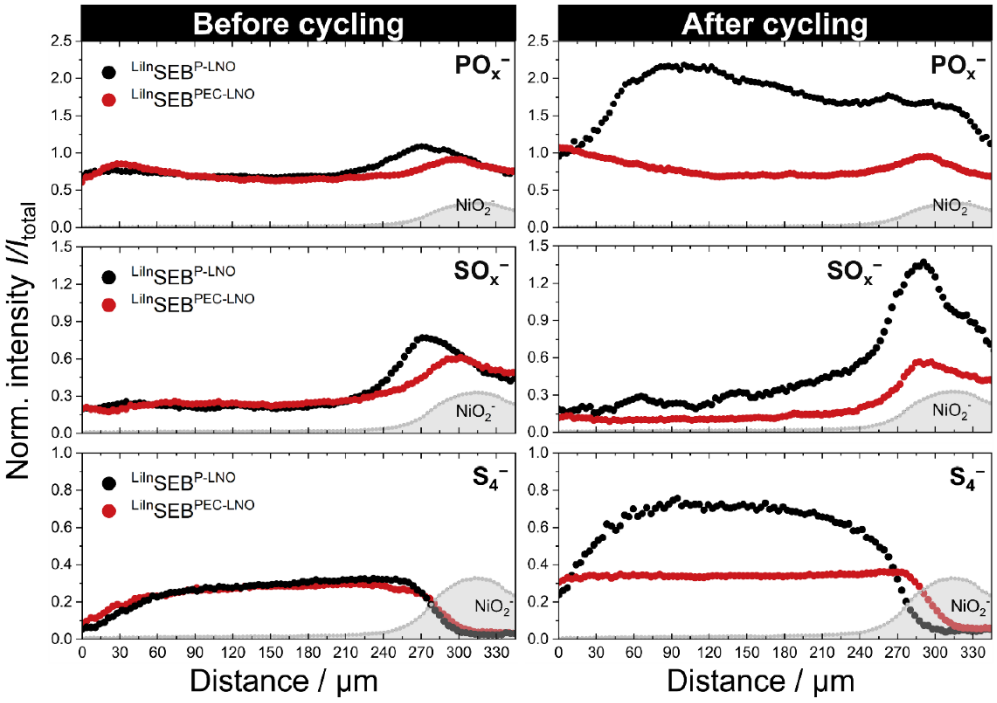

Figure 7. After creating wedge-shaped craters, ToF-SIMS detects chemical fragments in cathode composites before (left) and after (right) cycling. Phosphoxide fragments (PO_x^- including PO^-, PO_2^- and PO_3^-) are displayed at the top. Sulfoxide fragments (SO_x^- including SO^-, SO_2^- and SO_3^-) are in the middle. Elemental sulfur and -$[S]_n$- fragments (S_4^-) are shown at the bottom. The average NiO_2^- values are represented by the gray area in each graph. All fragment intensities are normalized to the total intensity.

2.7 Rate Capability of $^{LiIn}SEB^{Si}$ with the PEC coating on Si

To study the coating effect on the silicon anode, pellet-type half cells with the configuration of LiIn|LPSCl|LPSCl/VGCF/Si ($^{LiIn}SEB^{Si}$, an area-specific capacity of 4.5 mAh·cm^{-2} based on 3500 mAh·g^{-1} of Si, an area-specific mass loading of 1.3 mg·cm^{-2} based on Si) compare the rate capability of P-Si, PC-Si, and PEC-Si composite, denoted as $^{LiIn}SEB^{P\text{-}Si}$, $^{LiIn}SEB^{PC\text{-}Si}$, and $^{LiIn}SEB^{PEC\text{-}Si}$, respectively (see **Figure 8a**). The rate capability test is conducted under 60 MPa at different C-rates: 0.05C, 0.1C, 0.2C, 0.5C, 1C, and then returned to 0.1C. While this pressure may not entirely prevent contact loss from silicon's 300% volume expansion,[74] comparing the interfacial stability between coated and pristine silicon under the same conditions remains valuable.

Figure 8b shows that $^{LiIn}SEB^{PEC\text{-}Si}$ improves the specific charge capacity (q_{charge}) compared to $^{LiIn}SEB^{PC\text{-}Si}$ and $^{LiIn}SEB^{P\text{-}Si}$ across all C-rates. **Figure S15** shows the galvanic plots of the first, second, and 30th cycles. However, $^{LiIn}SEB^{PC\text{-}Si}$ and $^{LiIn}SEB^{P\text{-}Si}$ exhibit similar rate capabilities. In the first cycle at 0.05C, $^{LiIn}SEB^{P\text{-}Si}$ delivers q_{charge} of 2873 mAh·g^{-1}, $^{LiIn}SEB^{PC\text{-}Si}$ gives 2867 mAh·g^{-1}, and $^{LiIn}SEB^{PEC\text{-}Si}$ achieves 3048 mAh·g^{-1}. The first-cycle Coulomb efficiency for all $^{LiIn}SEB^{Si}$ remains consistent at around 95%, significantly higher than that of $^{LiIn}SEB^{LNO}$ (67~76%), which varies more widely between pristine and coated samples. This is because the main factor contributing to the first-cycle efficiency loss in $^{LiIn}SEB^{Si}$ appears to be contact loss[29] and/or lithium trapping in silicon bulk material[75]. However, a 1~3 nm coating is not expected to mitigate contact loss caused by volume changes.

Figure 8c compares the dq/dE of $^{LiIn}SEB^{Si}$ for the second and 30th cycles at 0.05C, while **Figure S16** presents it for the first cycle. dq/dE highlights the phase transitions from crystalline silicon (c-Si) to $Li_{3.5}Si$ during the first discharge cycle below –0.45 V vs. In/LiIn, and the subsequent phase transitions between $Li_{3.5}Si$↔$Li_{2.0}Si$↔amorphous silicon (a-Si).[76] During the first-cycle charge process and the second cycle, $^{LiIn}SEB^{PEC\text{-}Si}$ exhibits the more pronounced peak of delithiation from $Li_{3.5}Si$→$Li_{2.0}Si$, outperforming $^{LiIn}SEB^{PC\text{-}Si}$ and $^{LiIn}SEB^{P\text{-}Si}$, which can be attributed to the improved SEI kinetics and mitigated m_{act} loss.[77-79]

Furthermore, by the 30th cycle, $^{LiIn}SEB^{PEC\text{-}Si}$ demonstrates an more improved dq/dE and less peak shift across all phase transitions, $Li_{3.5}Si$↔$Li_{2.0}Si$↔a-Si, outperforming both $^{LiIn}SEB^{PC\text{-}Si}$ and $^{LiIn}SEB^{P\text{-}Si}$. It has been reported in the literature that the $Li_{2.0}Si$↔a-Si is influenced by m_{act} loss.[77-79] As a result, this suggests that the PEC coating helps mitigate m_{act} loss after 30 cycles. However, as the coating does not address contact loss from volume changes,[37] the PEC coating may improve m_{act} utilization by limiting SEI resistance growth, which otherwise isolates the silicon particle.

To further check if the rate capability is influenced by the mass loading in the silicon composite, we increase the area capacity in both $^{LiIn}SEB^{PEC\text{-}Si}$ and $^{LiIn}SEB^{P\text{-}Si}$ from 4.5 mAh·cm^{-2} to 9 mAh·cm^{-2} by double the anode composite amount, as shown in **Figure S17**. $^{LiIn}SEB^{Si}$ with 9

mAh cm^{-2} shows decreased rate capability compared to ^{LiIn}SEB^{Si} with 4.5 mAh·cm^{-2}. However, ^{LiIn}SEB^{PEC-Si} still improves the q_{charge} compared to ^{LiIn}SEB^{P-Si} across all C-rates, which confirms the PEC coating can improve the rate capability even the loading of silicon increases.

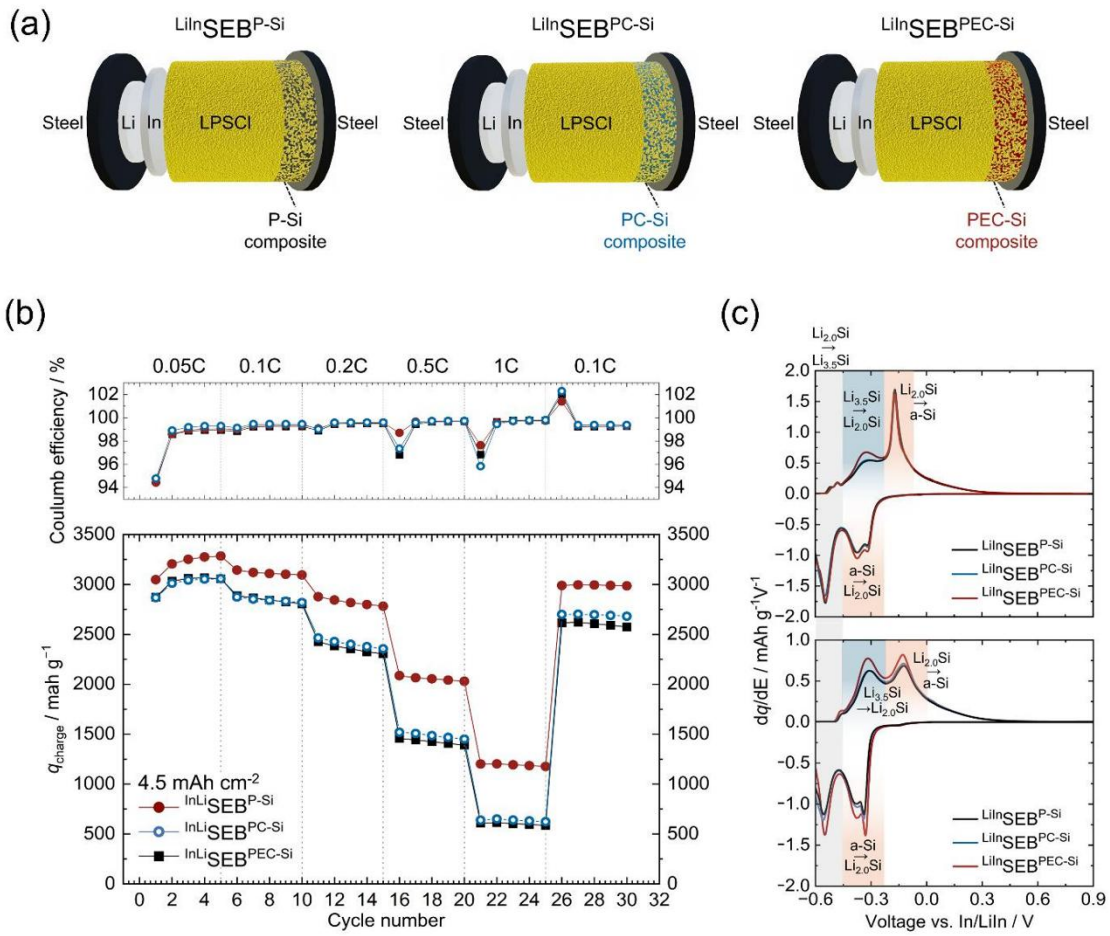

Figure 8. Rate capability of ^{LiIn}SEB^{Si} (LiIn|LPSCl|LPSCl/VGCF/Si, 4.5 mAh·cm^{-2} and 1.3 mg·cm^{-2} of Si) including ^{LiIn}SEB^{P-Si}, ^{LiIn}SEB^{PC-Si}, and ^{LiIn}SEB^{PEC-Si} is analyzed using pellet-type cells. (a) A schematic of SEBs configurations is provided in Figure (a). (b) Coulomb efficiency (top) and q_{charge} (bottom) are presented across different C-rates (0.05C, 0.1C, 0.2C, 0.5C, 1C, and back to 0.1C). (c) dq/dE plots for the second (top) at 0.05C and 30th (bottom) cycles at 0.1C, highlights the silicon phase transitions (a-Si→$Li_{3.5}Si$↔$Li_{2.0}Si$↔ a-Si).

2.8 Cycling Stability of $^{LiIn}SEB^{Si}$ with the PEC coating on Si

For the first, second, and 103rd cycles, $^{LiIn}SEB^{P\text{-}Si}$ and $^{LiIn}SEB^{PEC\text{-}Si}$ (4.5 mAh·cm^{-2}) are charged at 0.05C to 0 V (vs. In/LiIn), followed by CA at 0 V until the current drops to 2%. EIS is then used to evaluate silicon anode composite resistance (R_{anode}) from 1 MHz to 100 μHz at 0 V. CA coupled with EIS ensures stable measurements at a fixed SOC with sufficient ionic and electronic conductivity[29]. The galvanic plot of the first cycle, including the CA and EIS process, is shown in **Figure 9a**. From the third cycle to the 102nd cycles, $^{LiIn}SEB^{Si}$ are cycled at 0.1C. However, we cannot access the m_{act} via OCV due to the voltage hysteresis of Si[80]. This may need further study in the future.

Figure 9b shows that $^{LiIn}SEB^{PEC\text{-}Si}$ achieves a q_{charge} of 3086 mAh g^{-1} in the first cycle, surpassing $^{LiIn}SEB^{P\text{-}Si}$ (2834 mAh g^{-1}). After 103 cycles, $^{LiIn}SEB^{PEC\text{-}Si}$ retains 56% of its initial q_{charge} at 0.05C more than $^{LiIn}SEB^{P\text{-}Si}$ (41%), demonstrating that the PEC coating improves cycling stability. **Figure S18** presents the cross-section of the anode composites after cycling, examined using ion beam milling combined with SEM. Contact loss surrounding the micrometer-sized silicon particles is evident in $^{LiIn}SEB^{PEC\text{-}Si}$ and $^{LiIn}SEB^{P\text{-}Si}$. Notably, no cracking within silicon particles is observed after cycling. This may be attributed to the elastic softening effect caused by lithium incorporation into silicon, reducing the hardness (from 10.6 GPa of pure silicon to 1.5 GPa of $Li_{3.75}Si$) and Young's modulus (from 92 GPa of pure silicon to 12 GPa of $Li_{3.75}Si$).[81] Since the PEC coating neither prevents contact loss and particle cracking nor alters silicon intrinsic conductivity, its primary benefit lies in reducing side reactions at the SEI, thereby enhancing cycling stability.

Figure 9c shows the CA results for the second and 103th cycles, excluding first-cycle formation effects from LiIn alloying.[22, 41] The L_{diff} is similar for both $^{LiIn}SEB^{PEC\text{-}Si}$ and $^{LiIn}SEB^{P\text{-}Si}$, around 280 minutes in the second cycle and 500 minutes in the final cycle. This suggests that the PEC coating does not mitigate L_{diff} growth at SEI. The side reaction products such as Li_2S (ionic conductivity ≈ 10^{-8} S·cm^{-1})[82] can isolate silicon particles, resulting in a loss of m_{act} instead of L_{diff} growth. As a result, we can deduce that PEC coating enhances cycling stability by mitigating m_{act} loss, aligning with the $Li_{2.0}Si$↔a-Si transition results observed in the rate capability test.

The R_{anode} is evaluated by EIS at 0 V vs. In/LiIn (see **Figure 9d** and TLM fitting[65, 66] in **Figure S19**). The R_{anode} for $^{LiIn}SEB^{PEC\text{-}Si}$ is 12 Ω·cm^2 in the first cycle, lower than $^{LiIn}SEB^{P\text{-}Si}$ (19 Ω·cm^2), indicating improved SEI due to the PEC coating. After 103 cycles, R_{anode} for $^{LiIn}SEB^{P\text{-}Si}$ increases significantly to 68 Ω·cm², compared to 28 Ω·cm² for $^{LiIn}SEB^{PEC\text{-}Si}$. The R_{anode} is influenced by effective contact area (impacting m_{act})[22, 41] and SEI kinetics (impacting L_{diff})[64]. Due to similar L_{diff} results for $^{LiIn}SEB^{PEC\text{-}Si}$ and $^{LiIn}SEB^{P\text{-}Si}$, the PEC coating effectively mitigates the increase in R_{anode} for $^{LiIn}SEB^{PEC\text{-}Si}$ by less m_{act} loss.

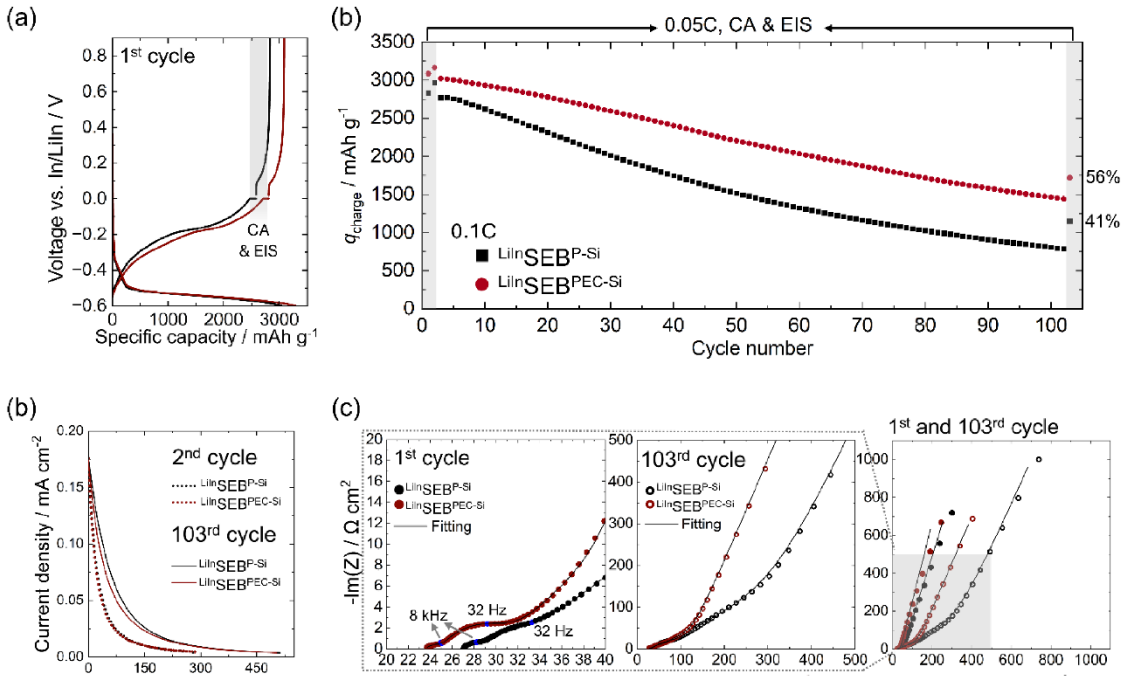

Figure 9. The cycling performance of $^{LiIn}SEB^{Si}$ (4.5 mAh·cm^{-2} and 1.3 mg·cm^{-2} of Si), including $^{LiIn}SEB^{P\text{-}Si}$ and $^{LiIn}SEB^{PEC\text{-}Si}$, is conducted under 0.1C at 25 °C from the third cycle to the 102nd cycle. EIS measurements are conducted under 0.05C at 0 V vs. In/LiIn in the first, second, and 103rd cycles. (a) The galvanic plot shows the first cycle of cells discharged to –0.6 V vs. In/LiIn. Subsequently, they are charged to 0 V, followed by CA (dashed line) and EIS, and then re-charged to 0.9 V vs. In/LiIn. (b) The cycling stability is presented by plotting the q_{charge} against the number of cycles. (c) CA reveals an increase in L_{diff} from the second to 103rd cycle. (d) Nyquist plots show the impedance increase from the first cycle to 103rd cycles at 0 V vs. In/LiIn. The apex frequency in both SEBs is marked in blue.

2.9 Analysis of Interfacial degradation in $^{LiIn}SEB^{Si}$ by XPS and TOF-SIMS

XPS is used to semi-quantitatively analyze the SEI of $^{LiIn}SEB^{P\text{-}Si}$ and $^{LiIn}SEB^{PEC\text{-}Si}$, focusing on the VGCF|LPSCl and Si|LPSCl interfaces after cycling. The steel|LPSCl interface is excluded because some silicon composite remains attached to the steel collector after disassembly, leaving only the VGCF|LPSCl and Si|LPSCl interfaces in the pellet for analysis.

Figure 10 shows the XPS spectra for S 2p and P 2p after cycling, indicating the chemical structure of the SEI. **Figure S20** shows that the XPS spectra for S 2p and P 2p before cycling are similar for $^{LiIn}SEB^{P\text{-}Si}$ and $^{LiIn}SEB^{PEC\text{-}Si}$. The Cl 2p spectrum is excluded because LiCl remains stable once formed[15], and additionally, there are minimal binding energy differences between Cl^- in LiCl and LPSCl, making it difficult to distinguish between them.[83] The S 2p spectra show Li_2S at 160.4 eV, PS_4^{3-} at 161.5 eV, S_x at 163.2 eV, and a shoulder at 162.1 eV indicates $-[S]_n-$.[15, 72] The P 2p spectra show signals at 131.9 eV (PS_4^{3-}), 132.9 eV (oxidized P species, e.g., P_{ox}), 160.4 eV (reduced P species,[15] e.g., elemental P), and 130.1 eV (Li_3P)[83].[72] Following the ideal reduction of the LPSCl shown in equation [2][14, 15], the ideal SEI side reaction products are Li_2S and Li_3P.

$$LPSCl + 8\ Li^+ + 8\ e^- \rightarrow LiCl + Li_3P + 5\ Li_2S \qquad [2]$$

After cycling, the S 2p spectrum shows that $^{LiIn}SEB^{P\text{-}Si}$ significantly increases Li_2S, rising from 6% to 47%, compared to 6% to 36% for $^{LiIn}SEB^{PEC\text{-}Si}$. This confirms that the PEC coating effectively mitigates side reactions at the SEI. The mechanism behind the formation of S_x species in both $^{LiIn}SEB^{P\text{-}Si}$ and $^{LiIn}SEB^{PEC\text{-}Si}$ after cycling remains unclear and needs further research. Despite this, S_x and $-[S]_n-$ components are similar for both cells before and after cycling. Interestingly, the P 2p spectrum shows a very low Li_3P ratio after cycling for both cells, warranting further investigation.

To support the XPS results, TOF-SIMS (see **Figure S21**) reveals more Li_2S (LiS^- fragment) for $^{LiIn}SEB^{P\text{-}Si}$ than for $^{LiIn}SEB^{PEC\text{-}Si}$ after cycling, consistent with the XPS S 2p spectrum. However, Li_3P is not detected in TOF-SIMS, aligning with the XPS P 2p spectrum. Overall, XPS and TOF-SIMS confirm that the PEC coating can effectively reduce side reaction products, specifically Li_2S, at the SEI.

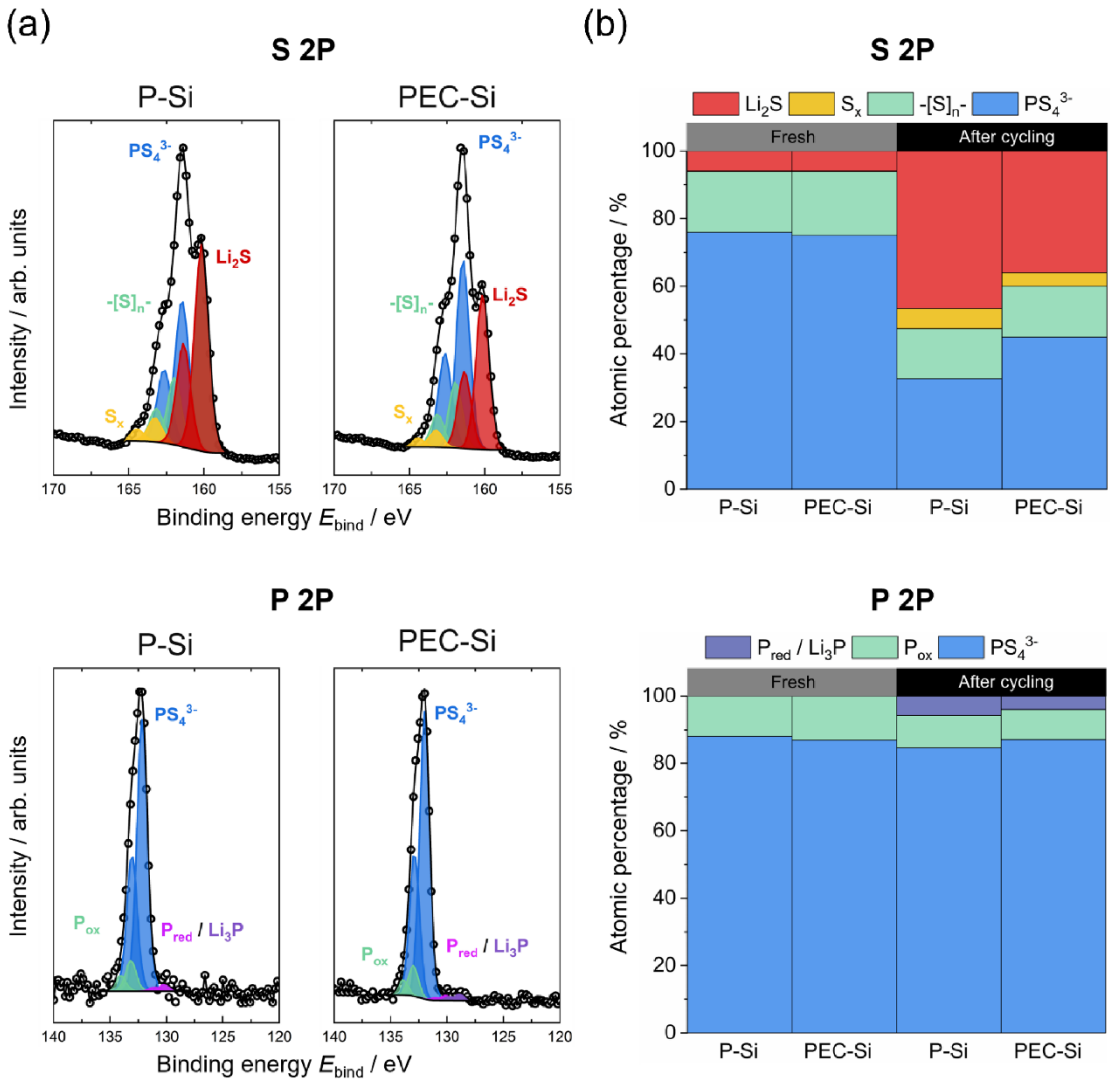

Figure 10. (a) S 2p, and P 2p XPS spectra compare the side reaction products of $^{LiIn}SEB^{P\text{-}Si}$ (P-Si) and $^{LiIn}SEB^{PEC\text{-}Si}$ (PEC-Si) after cycling. (b) The relative ratios of S 2p and P 2p for the various byproducts are determined from the fitting of XPS spectra.

3. Conclusion

To enhance CEI stability between the nickel-rich CAMs and LPSCl as well as SEI stability between the silicon anode and LPSCl in solid-state batteries, we introduce a novel PEC polymer coating applied to electrode particles via spray drying. The PEC coating combines PC as a coating inducer and PA for the lithium ion source, with reduced electrostatic forces allowing it to dissolve in solutions for wet coating applications. Additionally, the PEC exhibits rubber-like mechanical properties, effectively accommodating chemo-mechanical degradation. TEM images coupled with EDX analysis show a 1~3 nm PEC layer uniformly covered on LNO and silicon particles. In a full-cell test with a LNO cathode and silicon anode, the PEC coating enhances capacity retention by 27% after 200 cycles. To separate the PEC influence on the cathode and anode interfaces, cells with LiIn counter electrodes are paired separately with LNO and silicon. The PEC coating enhances capacity retention by 10% on the LNO cathode and 15% on the silicon anode after 100 cycles. The mitigation of side reactions by the PEC coating is confirmed through TOF-SIMS and XPS analyses. Overall, these findings highlight the potential of polymer coatings to enhance cycling performance, underscoring their importance in developing high-performance batteries.

4. Experimental Methods

Reagents and Materials

Poly(ethylene glycol)methyl ether methacrylate (PEGMEMA, M_n=500 g/mol, Aldrich), 2-cyano-2-propyl benzodithioate (CPDB, 97%, Aldrich), lithium bis(trifluoromethanesulfonyl)imide (LiTFSI, 99%, Acros), (vinylbenzyl)trimethylammonium chloride (VBTA-Cl, 99%, Aldrich), sodium persulfate ($Na_2S_2O_8$, 98%, Aldrich), ortho-xylene (o-xylene, anhydrous 97%, Aldrich), acetone (ACS reagent 99.5%, Aldrich and HPLC grade 99.9%, Acros), dimethylformamide (DMF, HPLC grade 99.5%, Acros), VGCF (Aldrich), silicon (particle size ≈ 1~5 μm, 99.9% metal basis purity, Alfa Aesar), $LiNi_{0.9}Mn_{0.05}Co_{0.05}O_2$ (NCM90, particle size ≈ 3~5 μm and a BET specific surface area of 0.5~0.9 $m^2 \cdot g^{-}$, MSE Supplies) are used as received after drying under vacuum (0.5 mbar) at 120 °C for 2 days..

LNO is synthesized through the procedure detailed in the subsequent section and our previous publication.[12] LPSCl is purchased from NEI Corporation. LPSClBr is synthesized following a previous publication.[68] When used as a separator, LPSCl and LPSClBr are utilized without wet-milling process. However, for its application as a catholyte, LPSCl is wet milled[84-86] to reduce its particle size, following the procedure detailed in the subsequent section.

2,2'-Azobisisobutyronitrile (AIBN, initiator, 98%, Aldrich) is recrystallized from methanol. Indium foil (100 μm, ChemPUR GmbH) is punched into circular electrodes with a diameter of 9 mm. Lithium foil (125 μm thick, Albemarle Rockwood Lithium GmbH) is punched into circular electrodes with a diameter of 6 mm.

Synthesis of single crystal LNO

To obtain single crystal LNO, 10 g of $LiOH \cdot H_2O$ is manually ground in an agate mortar for 30 minutes. Then, 16.18 g of NiO is added and again ground for 30 minutes. The mixture is loaded into alumina crucibles and annealed under an oxygen flow at 780 °C for 6 hours. After that, the samples are annealed at 680 °C for another 6 hours. Both heating and cooling ramps are set to 100 °C·hour^{-1}. The resulting black brick-like LNO precursor is manually ground in an agate mortar for 20 minutes. To ensure sufficient lithiation, 6.39 g Li_2CO_3 is added to LNO precursor, and the mixture is manually ground in an agate mortar for 20 minutes again. The mixture is loaded into alumina crucibles and annealed under an oxygen flow at 750 °C for 40 hours and after that at 680 °C for another 20 hours. Both heating and cooling ramps are set to 100 °C·hour^{-1}. To eliminate excess Li_2CO_3, the LNO precursor is washed by ice-cooled deionized water (1 g LNO precursor, per 30 mL water), vigorously agitated for 1 min. The mixture is immediately centrifuged at 4000 rpm for 2 minutes, and the supernatant is discarded. The washing process is repeated three times, with a total water contact time of less than 12 minutes for the LNO precursor. To remove water, a final washing step with ethanol is performed. The resulting LNO precursor is dried in a vacuum oven at 60 °C overnight. Afterward, LNO

precursor is loaded into alumina crucibles and annealed at 680 °C for 3 h under oxygen flow (100 $cm^3 \cdot min^{-1}$). Finally, the obtained LNO is manually ground for 20 minutes in an agate mortar and sieved (45 µm mesh size) inside an argon-filled glovebox (LabMaster, MBraun, Garching, Germany), with O_2 and H_2O levels maintained below 0.1 ppm. The LNO powder is then sieved again with 20 µm mesh size. 13.34 g LNO is obtained. The synthesized LNO is analyzed with SEM (see **Figure S4**) and XRD (see **Figure S22**).[12]

Wet-milling process for LPSCl

15 g of LPSCl is mixed with 50 mL of o-xylene and 80 g of 1 mm ZrO_2 balls in an 80 mL ZrO_2 pot. Subsequently, the mixture is wet-milled by a Fritsch premium line Pulverisette 7 at 500 rpm for 10 minutes, followed by a resting period of 10 minutes. This cycle is repeated six times. After the ball milling is finished, the mixture is sieved (mesh size 100 µm) to remove the ZrO_2 balls and centrifuged to get the LPSCl powder. The ZrO_2 balls are washed three times with o-xylene using a Hielscher UP100H Ultrasonic Processor to remove any residues of LPSCl adhering to the ZrO_2 balls. The collected LPSCl is dried by Buchi B-585 at 120 °C with $2 \cdot 10^{-2}$ mbar for 2 days. Finally, the LPSCl is manually ground in an agate mortar for 10 minutes to break up aggregates, then sieved (mesh size 20 µm). The milling instrument is located outside the glovebox, but sample transfers are protected from air exposure. The rest of the procedure is conducted entirely inside an argon-filled glovebox (LabMaster, MBraun, Garching, Germany), with O_2 and H_2O levels maintained below 0.1 ppm.

Synthesis of poly(vinylbenzyl)trimethylammonium bis(trifluoromethanesulfonyl)imide (PC)

PC is synthesized by first performing free radical polymerization of VBTA-Cl, followed by an ion exchange with LiTFSI. A solution of VBTA-Cl (5.00 g, 23.58 mmol) and $Na_2S_2O_8$ (1.68 g, 7.07 mmol) in 20 ml of deionized H_2O is prepared in a round-bottom flask equipped with a magnetic stirring bar. The solution is purged with nitrogen and heated to 75 °C. Polymerization is further carried out at 75 °C for 48 h. After completion, the reaction mixture is transferred into a dialysis bag and dialyzed extensively against deionized water. The resulting polymer solution is then concentrated to 50 mL using a rotary evaporator.

For ion exchange, the concentrated polymer solution is added dropwise to a solution of LiTFSI (7.50 g, 26.13 mmol) in 20 ml of deionized H_2O. A white precipitate formed immediately upon mixing. The solution is stirred at room temperature for an additional 2 h. The product is isolated by centrifugation, washed three times with deionized water to remove impurities, and then dried under vacuum at 80 °C and 0.1 mbar for 72 h. Yield: 6.88 g (64 %). T_g = 83 °C (by DSC); T_g = 97 °C (by TMA); T_{onset} = 290 °C (by TGA in air); 1H Nuclear Magnetic Resonance (NMR) (see **Figure S23**) (400.0 MHz, acetone-d_6) δ(ppm): 7.32 (s, 2H), 6.68 (s, 2H), 4.58 (s, 2H), 3.12 (s, 9H), 1.68 (s, 3H).

Poly[(lithium 1-[3-(methacryloyloxy)propylsulfonyl]-1-(trifluoromethanesulfonyl)imide)-r-(poly(ethyleneglycol) methyl ether methacrylate)] synthesis (PA)

First, lithium 1-[3-(methacryloyloxy)propylsulfonyl]-1-(trifluoromethanesulfonyl)imide is synthesized in full accordance with the procedure published previously.[87]

PA is prepared via RAFT random copolymerization of ILM and poly(ethylene glycol)methyl ether methacrylate (PEGM). A solution of ILM (0.50 g, 1.40 mmol), PEGM (3.26 g, 6.50 mmol), CPDB (18.5 mg, 0.083 mmol) and AIBN (2.74 mg, 0.017 mmol, [AIBN]:[CPDB] = 1:5 by mol) in anhydrous DMF (12.0 mL, 11.3 g, [DMF]:[ILM+PEGM] = 3:1 by weight) is transferred to a Schlenk flask equipped with magnetic stirring bar. The solution is degassed via three freeze-pump-thaw cycles and flashed with argon, whereupon the flask is placed into a bath preheated at 60 °C. Polymerization is further carried out at 60 °C for 48 h. The resultant viscous pink polymer solution is diluted with DMF and precipitated into the excess of diethyl ether, PA is collected by decantation of the solvents, then redissolved in acetone and precipitated in the excess of diethyl ether for the second time. Isolated copolymer represented pink sticky mass that is dried at 60 °C and 0.1 mbar for 24 h in B-585 oven (Buchi Glass Drying Oven, Switzerland) filled with P_2O_5. Yield: 2.40 g (64%). M_n = 41000 g mol^{-1}, M_w/M_n = 1.50 (by GPC); T_g = -53 °C (by DSC); T_g = -50 °C (by TMA); T_{onset} = 150 °C (by TGA in air).

Synthesis of PEC

PECs are synthesized by mixing two oppositely charged polyelectrolytes, specifically a PC and PA, as detailed below. The poly(ionic liquid) mixing ratios are optimized to achieve the maximum anionic polymer content capable of forming a self-standing film.

A solution of PC (0.6 g, 1.32 mmol of cationic ion pairs, 60 wt% based on weight of PEC) in 10 mL of acetone is added dropwise to a solution of PA (0.4 g, 0.14 mmol of anionic ion pairs, 40 wt% based on weight of PEC) in 10 mL of acetone under continuous stirring. The mixture is stirred for 1 hour at 25 °C. Following mixing, the solution is dried on a hot plate at 60 °C overnight. Further drying is performed in a vacuum oven (0.1 mbar) at 60 °C for 1 week to ensure the complete removal of residual acetone. The polymer is then stored inside an argon-filled glovebox (LabMaster, MBraun, Garching, Germany), with O_2 and H_2O levels maintained below 0.1 ppm, to prevent the moisture or humidity influence.

Polymer-coated AMs

A BUCHI Mini-Spray Dryer B-290 is used to coat various polymers and PECs onto AMs (NCM90, LNO and silicon). The general procedure is provided here.

For spray drying, 2 g of AMs are poured into the solution of 20 mg of polymer (1 wt% relative to AMs) in 30 mL of acetone to prepare the precursor suspension. The suspension is stirred vigorously for 1 h at room temperature. The inlet temperature for spray drying is set to 120 °C,

the vacuum pumping rate is adjusted to 37 $m^3 \cdot h^{-1}$ and the nitrogen flow is maintained at 40 L/min. The spray drying is then performed with a precursor suspension feed rate of 8 mL/min. The spray drying parameters are optimized to achieve approximately 70 wt% of productivity. After spray drying, the coated AMs are dried at 50 °C and 0.1 mbar for 1 week.

Polymer-coated VGCF

For the PEC and PC-coated VGCF, a precursor is prepared by dissolving 10 mg of PC or PEC polymers in 20 mL of acetone. To create a VGCF solution precursor for spray drying, 100 mg of VGCF is sonicated in 20 mL of acetone and then added dropwise to the polymer solution. This mixture is ultrasonicated for 30 minutes to achieve a homogeneous solution. Subsequently, the coated VGCF is formed using a spray-drying process under the same conditions as those used for the coated electrodes. After spray drying, the coated AMs are dried at 50 °C under 0.1 mbar for one week and then stored in the glove box.

Nuclear Magnetic Resonance (NMR)

To analyze PA, NMR spectra are recorded on AMX-600 (Bruker, Germany) or AMX-400 (Bruker, Germany) spectrometer at 25 °C in the indicated deuterated solvent and are listed in ppm. The signals corresponding to the residual protons and carbons of the deuterated solvent are used as an internal standard for ^{1}H and ^{13}C NMR, respectively. The C_6F_6 is utilized as an external standard for ^{19}F NMR.

To analyze PC, Bruker Avance II recorded the ^{1}H NMR spectra of PVBTA-TFSI at 400 MHz in deuterated acetone. The chemical shifts are recorded by parts per million (ppm). The signals corresponding to the residual protons of the deuterated solvent are used as an internal standard for ^{1}H NMR.

Fourier-Transform Infrared Spectroscopy (FTIR)

FTIR spectra are recorded using a Thermo Fisher Scientific iD5 ATR spectrometer over a wavenumber range of 550–4000 cm^{-1} with a total of 96 scans. All measurements are conducted inside an argon-filled glovebox (LabMaster, MBraun, Garching, Germany), with O_2 and H_2O levels maintained below 0.1 ppm, to prevent moisture interference.

X-ray diffraction (XRD)

XRD is used to check the LNO crystalline structure. LNO powders are filled into glass capillaries with 0.5 mm inner diameter. The samples are mounted in an Empyrean 3 diffractometer (Malvern PANalytical) with Mo-Kα source and measured in Debye–Scherrer geometry. The angular 2Θ range is 5°–40° with a step size of 0.007° and a scan speed of 1° min^{-1}.

Scanning electron microscopy (SEM)

SEM (GeminiSEM 560) at an acceleration voltage of 2 kV with aperture size of 20 µm is adopted to characterize the morphology of LNO particles, LNO cathode composite, and silicon anode composite after cycling. Backscattered electron images and secondary electron images are recorded. The LNO particle samples are measured in powder form, sticking tightly on the conductive copper tape. The examination of particle cracking in the LNO cathode and silicon anode composite after cycling is checked by SEM after ion beam milling with a Leica EM TIC 3X. The ion beam milling process is conducted at 6 kV and 2.2 mA for a duration of 6 hours, at a temperature of −100 °C.

Transmission Electron Microscopy (TEM)

Powders of the various particles are dispersed onto lacey carbon copper mesh grids and subsequently pumped in a vacuum stand to remove excess material before being inserted into the (S)TEM. Measurements are conducted using a double Cs-corrected JEOL JEM 2200FS microscope operated at an acceleration voltage of 200 kV with a convergence angle of 15.07 mrad. TEM bright field images are captured using a TVIPS TemCam XF416FS camera, while the STEM-EDX data is acquired with a Bruker Nano XFlash Detector 5060. STEM overview images are obtained using an annular detector with the angular range of 70-280 mrad.

Time-of-flight secondary ion mass spectrometry (ToF-SIMS)

All ToF-SIMS measurements are conducted on an M6 Plus instrument (IONTOF GmbH, Münster, Germany) in negative ion mode. All surface spectra are acquired using the Nanoprobe 50 LMIG in bunched mode with 30 keV Bi_3^+ clusters as primary ion species. Surface spectra on the silicon samples are acquired in an area of 200x200 µm^2 with 128x128 pixels and a dose density of $1 \cdot 10^{12}$ ions·cm^{-2}. 5 surface spectra are measured per sample. For wedge preparation of the LNO samples the DSC/S sputter gun with 2 kV Cs^+ is used in a 300x100 µm^2 area with 200 ms maximum dwell time. Subsequent surface spectra of the wedges are acquired at 400x400 µm^2 and 256x256 pixels or 450x450 µm^2 with 512x512 pixels with a dose density of $5 \cdot 10^{11}$ ions·cm^{-2}. For data evaluation, the ion images are binned to 128x128 pixels, and a region with the same x-scale (350 µm) and 20 lines in x-direction is chosen. 20 line scans of the wedges in x-direction are then summed up using the SurfaceLab 7.4 Software and normalized on total ion intensity for comparison. (IONTOF GmbH, Münster, Germany).

X-ray photoelectron spectroscopy (XPS)

X-ray photoelectron spectroscopy (XPS) is conducted using a PHI5000 Versa Probe IV from Physical Electronics GmbH equipped with an aluminum anode (Al Kα = 1486.6 eV). The settings include a beam power of 50 W, voltage of 15 kV, and a beam diameter of 200 µm. The analyzer pass energy is set to 224 eV for survey scans and 55 eV for detailed spectra. Samples are transported in an argon-filled transfer module. Data evaluation utilizes CasaXPS software. The XPS spectra of the samples are initially calibrated using the adventitious carbon signal at

284.8 eV to identify the main S 2p component (PS_4^{3-}). The XPS spectra can then be calibrated based on PS_4^{3-} signal at 161.6 eV.[70]

Ionic conductivity

Symmetrical steel|PEC polymer|steel is used to test the ionic conductivity. The steel is 10 mm in diameter. The PEC has a thickness of approximately 400 µm and a diameter of 0.6 mm. To avoid any influence of moisture or humidity on the ionic conductivity test, cell assembly is conducted inside an argon-filled glovebox (LabMaster, MBraun, Garching, Germany), with O_2 and H_2O levels maintained below 0.1 ppm. The ionic conductivity of PEC is measured by EIS using VMP-300 Biologic potentiostat with the climate chamber (Weiss Technik) controlling the temperature from -10 °C to 50 °C. EIS sinusoidal amplitude is set at 10 mV in the frequency range from 1 MHz to 100mHz.

Cyclic voltammetry (CV)

CV is used to test the electrochemical stability in the cell configuration LiIn|LPSCl|LPSCl/VGCF. To prepare a 99 mg LPSCl/VGCF composite, 9 mg of VGCF is mixed with 90 mg of LPSCl by using ball milling with 30 Hz and 1 hour (mini-mill PULVERISETTE 23). Subsequently, 80 mg of LPSCl is compressed into a 10 mm diameter pellet that functions as a separator within a PEEK insulator. An additional 30 mg of the LPSCl/VGCF composite is then pressed onto one side of this separator. Indium metal (100 µm thick and 9 mm in diameter) and lithium metal (125 µm thick and 6 mm in diameter) foils are positioned on the opposite side as the counter electrode, with indium metal in direct contact with LPSCl. The entire cell stack is compressed under a force of 30 kN for 3 minutes using Atlas Autotouch automatic press. The cell is encased in an external aluminum frame that exerts approximately 50 MPa of pressure.

Open-circuit voltage (OCV) vs. capacity reference

To create an open-circuit voltage (OCV) vs. capacity reference curve, a liquid cell with LNO as the CAM and lithium metal as the anode is prepared. The cathode consists of a 94/3/3 ratio of LNO, Super P Carbon and PVDF binder, respectively. This cathode is prepared in a tape casting procedure from a slurry with NMP as solvent with a solid content of 56% and a doctor blade thickness of 60 µm. For the cell assembly, a cathode with 12 mm diameter is punched from the dried sheet (120 °C for 12 h in vacuum) and pressed at 2000 atm. The electrolyte is 1 M $LiPF_6$ in EC:DEC (1:1 vol.%) with a glass fiber separator and a Celgard separator (in contact with the cathode side). 14 mm diameter lithium metal anode is used as the anode. CR2032 coin cell casings with aluminum coating on the cathode are used to avoid parasitic currents that appear especially in the first cycles. First, two formation cycles to 4.17 V vs. Li^+/Li are applied at 3 V for 36 hours to ensure stable SEI formation. Then, the cell is charged to upper cutoff voltage of 4.3 V vs. Li^+/Li. Next, 0.1C pulses for 10 minutes with 2 h subsequent relaxation each are applied 80 times with an upper cutoff voltage of 4.3 V vs. Li^+/Li. This is repeated

for the discharge. After this pulse-relaxation procedure (similar to GITT experiments), a final checkup cycle similar to the second formation cycle is applied to ensure no drastic changes occurred during the experiment.

Cathode and anode composite preparation

The cathode and anode composite preparation is conducted inside an argon-filled glovebox (LabMaster, MBraun, Garching, Germany), with O_2 and H_2O levels maintained below 0.1 ppm. The cathode composite is formed by mixing the weight ratio of 69.3% NCM90 or LNO (either pristine or coated), 29.7% LPSCl, and 1% VGCF. The anode composite is formed by mixing the weight ratio of 20% silicon (either pristine or coated), 70% LPSCl, and 10% VGCF. The mixing of the cathode and anode composite is conducted by ball milling method using mini-mill PULVERISETTE 23 with 30 Hz and 1 hour. The cathode and anode composite are used for $^{Si}SEB^{LNO}$, $^{Liln}SEB^{LNO}$, $^{Liln}SEB^{NCM90}$, and $^{Liln}SEB^{Si}$.

$^{Si}SEB^{LNO}$ full cell assembly and cycling stability test

The $^{Si}SEB^{LNO}$ configuration is LPSCl/VGCF/Si|LPSCl|LPSCl/VGCF/LNO, where LNO composite serves as the cathode, silicon composite as the anode, and LPSCl is used as anolyte, catholyte, and separator. When using the PEC-LNO cathode composite coupled with the PEC-Si anode composite, the SEB is denoted as $^{PEC\text{-}Si}SEB^{PEC\text{-}LNO}$. When using the P-LNO cathode composite coupled with a P-Si anode composite, the SEB is denoted as $^{P\text{-}Si}SEB^{P\text{-}LNO}$.

Cell assembly is conducted using pellet-type asymmetric cells inside an argon-filled glovebox (LabMaster, MBraun, Garching, Germany), with O_2 and H_2O levels maintained below 0.1 ppm. For the separator, 100 mg of LPSCl is hand-pressed into a 10 mm diameter pellet inside a cylindrical PEEK insulator. Subsequently, 5 mg silicon anode composite (1 mg Si, 3.5 mg LPSCl, 0.5 mg VGCF) is hand-pressed onto one side of the separator, while 19 mg of LNO cathode composite (13.2 mg LNO, 5.6 mg LPSCl, 0.2 mg VGCF) is hand-pressed onto the opposite side. Based on the practical capacity of LNO (≈ 200 mAh·g), and the theoretical capacity of silicon (≈ 3500 mAh·g), the cathode specific surface capacity is calculated to be 3.3 mAh cm^{-2}, with an N/P ratio of 1.3.

Post-assembly, $^{Si}SEB^{LNO}$ is pressed under 30 kN for 3 minutes using automatic Atlas Autotouch automatic press, yielding a 800 µm separator alongside a 65 µm composite cathode and 15 µm composite anode. During the cycling stability test, the assembled cell is placed in an external stainless-steel frame that applies a stack pressure of approximately 60 MPa.

The cycling stability test of $^{Si}SEB^{LNO}$ is conducted at a constant temperature of 25 °C in MACCOR electrochemical workstation. $^{Si}SEB^{LNO}$ is first charged and discharged under C-rates of 0.1C, 0.25C, 0.5C, and 1C, within a voltage ranging from 2.0 V to 3.7 V. The charge process is carried out to 4.3 V, followed by a subsequent discharge process to 2.0 V. Each C-rate has

five cycles. Following this, cycling continued at a consistent rate of 0.1C to evaluate long-term cycling performance.

$^{LiIn}SEB^{LNO}$ and $^{LiIn}SEB^{NCM90}$ half cell assembly and electrochemical test

For the half cell testing of the LNO and NCM90 cathode, a LiIn alloy is used as the anodic counter electrode. LPSCl serves as both the catholyte and separator paired with the LNO cathode composite, while LPSClBr fulfills the same role with the NCM90 cathode composite. Hence, the $^{LiIn}SEB^{LNO}$ configuration is LiInLPSCl|LPSCl/VGCF/LNO. When using P-LNO, PC-LNO, and PEC-LNO as cathode active materias, the SEB is denoted as $^{LiIn}SEB^{P\text{-}LNO}$, $^{LiIn}SEB^{PC\text{-}LNO}$, and $^{LiIn}SEB^{PEC\text{-}LNO}$, respectively. Similariy, the cell configuration of $^{LiIn}SEB^{NCM90}$ is LiIn|LPSClBr|LPSCl/VGCF/NCM90. When using P-NCM90 and PEC-NCM90 as cathode active materias, the SEB is denoted as $^{LiIn}SEB^{P\text{-}NCM90}$ and $^{LiIn}SEB^{PEC\text{-}NCM90}$, respectively.

Cell assembly is conducted using pellet-type asymmetric cells inside an argon-filled glovebox (LabMaster, MBraun, Garching, Germany), with O_2 and H_2O levels maintained below 0.1 ppm.

For $^{LiIn}SEB^{LNO}$, 80 mg of LPSCl is hand-pressed into a 10 mm diameter pellet inside a cylindrical PEEK insulator to form the separator. 12 mg of LNO cathode composite (8.3 mg LNO, 3.6 mg LPSCl, and 0.1 mg VGCF) is hand-pressed onto one side of the separator. For $^{LiIn}SEB^{NCM90}$, 80 mg of LPSClBr is hand-pressed into a 10 mm diameter pellet inside a cylindrical PEEK insulator to form the separator. 20 mg of NCM90 cathode composite (13.8 mg NCM90, 3.6 mg LPSCl, and 0.1 mg VGCF) is hand-pressed onto one side of the separator.

The counter electrode, indium (100 µm thick and 9 mm in diameter, attached to the side of separator) and lithium metal foils (125 µm thick and 6 mm in diameter, attached to the side of current collector) are positioned onto the other side of the separator.

Post-assembly, $^{LiIn}SEB^{LNO}$ and $^{LiIn}SEB^{NCM90}$ are pressed under 30 kN for 3 minutes using automatic Atlas Autotouch automatic press, yielding a 650 µm separator alongside a 40 µm composite LNO and a 70 µm composite NCM90. During the electrochmeical test, the assembled cell is placed in an external stainless-steel frame that applies a stack pressure of approximately 60 MPa.

$^{LiIn}SEB^{LNO}$ and $^{LiIn}SEB^{NCM90}$ are tested for rate capability and cycling stability at a constant temperature of 25 °C using a MACCOR electrochemical workstation. The testing voltage range is set from 2.0 V to 3.7 V vs. In/LiIn, with the charge process to reach 3.7 V followed up with discharge process to reach 2.0 V. The C-rates are calculated based on the practical capacity of LNO and NCM90, which is around 200 mAh g^{-1}. After each charge and discharge process, a two-hour relaxation period is applied to the SEBs to get the OCV information. For the rate capability test:

- $^{LiIn}SEB^{LNO}$ (2.1 mAh cm^{-2}) is charged and discharged at C-rates of 0.1C, 0.25C, 0.5C, 1C, and then returned to 0.1C. Each C-rate has five cycles.

- $^{LiIn}SEB^{NCM90}$ (3.5 mAh cm^{-2}) is charged and discharged at C-rates of 0.05C, 0.1C, 0.25C, 0.5C, and 1C. Each C-rate has five cycles.

For the cycling stability test:

- $^{LiIn}SEB^{LNO}$ (2.1 mAh cm^{-2}) is cycled under 0.1C coupled with CA and EIS measured at 3.15 V vs. In/LiIn during the first, second, 50^{th}, and 100^{th} cycles, using a fresh cell.

- $^{LiIn}SEB^{NCM90}$ (3.5 mAh cm^{-2}) is cycled under 0.25C right after rate capability test mentioned above.

For the EIS measured during the cycling stability test, $^{LiIn}SEB^{LNO}$ are tested under 0.1C within a voltage window ranging from 2.0 V to 3.7 V vs. In/LiIn at a constant temperature of 25 °C in a VMP-300 (BioLogic) electrochemical workstation. Before EIS, $^{LiIn}SEB^{LNO}$ is charged under 0.1C to a voltage of 3.15 V vs. In/LiIn. CA is then performed continuously at this voltage until the observed current diminishes below 2% of the charging current. EIS measurements between 1 MHz and 100 μHz are carried out immediately after the CA. EIS sinusoidal amplitudes are set at 10 mV (from 1 MHz to 10 mHz), 5 mV (from 10 mHz to 1 mHz), and finally, 3 mV (from 1 mHz to 100 μHz). Amplitudes are adjusted per frequency to approximate a linear current response and reduce errors. Smaller AC amplitudes enhance linearity. After EIS, $^{LiIn}SEB^{LNO}$ is recharged to 3.7 V vs. In/LiIn, relaxed for 2 hours, then discharged to 2.0 V vs. In/LiIn with another 2-hour relaxation

$^{LiIn}SEB^{Si}$ half cell assembly and electrochemical test

For the half cell testing of silicon anode, a LiIn alloy is used as the anodic counter electrode. LPSCl serves as both the anolyte and separator paired with the silicon anode composite, Hence, the $^{LiIn}SEB^{Si}$ configuration is LiInLPSCl|LPSCl/VGCF/Si. When using P-Si, PC-Si, and PEC-Si as anode active materials, the SEB is denoted as $^{LiIn}SEB^{P\text{-}Si}$, $^{LiIn}SEB^{PC\text{-}Si}$, and $^{LiIn}SEB^{PEC\text{-}Si}$, respectively.

Cell assembly is conducted using pellet-type asymmetric cells inside an argon-filled glovebox (LabMaster, MBraun, Garching, Germany), with O_2 and H_2O levels maintained below 0.1 ppm. For the separator, 80 mg of LPSCl is hand-pressed into a 10 mm diameter pellet inside a cylindrical PEEK insulator. Subsequently, 5 mg anode composite (1 mg Si, 3.5 mg LPSCl, 0.5 mg VGCF) or 10 mg anode composite (2 mg Si, 7 mg LPSCl, 1 mg VGCF) is hand-pressed onto one side of the separator. The counter electrode, indium (100 μm thick and 9 mm in diameter, attached to the side of separator) and lithium metal foils (125 μm thick and 6 mm in diameter, attached to the side of current collector) are positioned onto the other side of the

separator. Notably, for a 10 mg anode composite, the indium and lithium metal counter electrode require two pieces each, doubling the amount compared to a 5 mg composite.

Post-assembly, $^{LiIn}SEB^{Si}$ is pressed under 30 kN for 3 minutes using automatic Atlas Autotouch automatic press, yielding a 650 µm separator alongside a 15 µm or 30 µm of thickness for 5 mg or 10 mg composite silicon. During the electrochemical test, the assembled cell is placed in an external stainless-steel frame that applies a stack pressure of approximately 60 MPa.

$^{LiIn}SEB^{Si}$ is tested for rate capability and cycling stability at a constant temperature of 25 °C using a MACCOR electrochemical workstation. The testing voltage range is set from 0.9 V to -0.6 V vs. In/LiIn, with the discharge process to reach -0.6 V followed up with charge process to reach 0.9 V. The C-rates are calculated based on the theoretical capacity of silicon, which is around 3500 $mAh \cdot g^{-1}$. After each charge and discharge process, a two-hour relaxation period is applied to the SEBs. For the rate capability test, both $^{LiIn}SEB^{Si}$ with 1 mg silicon (4.5 $mAh\ cm^{-2}$) and 2 mg silicon (9.0 $mAh\ cm^{-2}$) are charged and discharged at C-rates of 0.05C, 0.1C, 0.25C, 0.5C, 1C and then returned to 0.1C. Each C-rate has five cycles. For the cycling stability test, $^{LiIn}SEB^{Si}$ (4.5 $mAh\ cm^{-2}$) is cycled under 0.1C from 3rd to 102nd cycle, with CA and EIS conducted at 0.05C and 0 V vs. In/LiIn during the first, second, and 103rd cycles.

For the EIS measured during the cycling stability test, $^{LiIn}SEB^{Si}$ are tested under 0.05C within a voltage window ranging from 0.9 V to -0.6 V vs. In/LiIn at a constant temperature of 25 °C in a VMP-300 (BioLogic) electrochemical workstation. Before EIS, $^{LiIn}SEB^{Si}$ is charged under 0.05C to a voltage of 0 V vs. In/LiIn. CA is then performed continuously at this voltage until the observed current diminishes below 2% of the charging current.

EIS measurements between 1 MHz and 100 µHz are carried out immediately after the CA. EIS sinusoidal amplitudes are set at 10 mV (from 1 MHz to 10 mHz), 5 mV (from 10 mHz to 1 mHz), and finally, 3 mV (from 1 mHz to 100 µHz). Amplitudes are adjusted per frequency to approximate a linear current response and reduce errors. Smaller AC amplitudes enhance linearity. After EIS, $^{LiIn}SEB^{Si}$ is recharged to 0.9 V vs. In/LiIn, relaxed for 2 hours, then discharged to -0.6 V vs. In/LiIn with another 2-hour relaxation

Acknowledgements

B.X.S. and F.H.R. acknowledge German Federal Ministry of Education and Research (BMBF) for their financial support through the project FLiPS (03XP0261). Similarly, T.W., S.L.B., T.D., K.V., and A.H. appreciate the funding received from the BMBF as part of the FestBatt competence cluster (03XP0433C, 03XP0433D). Additionally, A.H. extends special thanks for the support provided under the BMBF Professorinnenprogramm III.

Author Contributions

B.X.S. was responsible for the electrochemical analyses, and general characterization of materials. D.N. conducted the synthesis of anionic polymers and mechanical analysis of polyelectrolyte complex. T.W. and B.X.S. performed the TOF-SIMS analysis, while T.D. performed the TEM experiments. S.L.B. conducted the XPS analysis. K.V. contributed to the LEB measurement. K.V., A.H., A.S., and F.H.R. contributed to the analysis and interpretation of the experimental data. The research concept was conceived by B.X.S. and F.H.R., who also prepared the manuscript. All authors contributed to the manuscript and the analysis of experimental results.

Reference

1. S. Sen and F. H. Richter, *Advanced Science*, 2023, **10**, 2303985.
2. J. Schnell, T. Günther, T. Knoche, C. Vieider, L. Köhler, A. Just, M. Keller, S. Passerini and G. Reinhart, *Journal of Power Sources*, 2018, **382**, 160-175.
3. D. H. S. Tan, Y. S. Meng and J. Jang, *Joule*, 2022, **6**, 1755-1769.
4. X. Yu, R. Chen, L. Gan, H. Li and L. Chen, *Engineering*, 2023, **21**, 9-14.
5. S. Sen, E. Trevisanello, E. Niemöller, B.-X. Shi, F. J. Simon and F. H. Richter, *Journal of Materials Chemistry A*, 2021, **9**, 18701-18732.
6. Q. Zhang, D. Cao, Y. Ma, A. Natan, P. Aurora and H. Zhu, *Advanced Materials*, 2019, **31**, 1901131.
7. A. Banerjee, X. Wang, C. Fang, E. A. Wu and Y. S. Meng, *Chemical Reviews*, 2020, **120**, 6878-6933.
8. Y. Yusim, E. Trevisanello, R. Ruess, F. H. Richter, A. Mayer, D. Bresser, S. Passerini, J. Janek and A. Henss, *Angewandte Chemie International Edition*, 2023, **62**, e202218316.
9. R. Chen, Q. Li, X. Yu, L. Chen and H. Li, *Chemical Reviews*, 2020, **120**, 6820-6877.
10. A. Chakraborty, S. Kunnikuruvan, S. Kumar, B. Markovsky, D. Aurbach, M. Dixit and D. T. Major, *Chemistry of Materials*, 2020, **32**, 915-952.
11. C. M. Julien and A. Mauger, *Energies*, 2020, **13**, 6363.
12. R. Rueß, D. Gomboso, M. Ulherr, E. Trevisanello, Y. Ma, A. Kondrakov, T. Brezesinski and J. Janek, *Journal of The Electrochemical Society*, 2023, **170**, 020533.
13. H. Komatsu, S. Banerjee, M. L. Holekevi Chandrappa, J. Qi, B. Radhakrishnan, S. Kuwata, K. Sakamoto and S. P. Ong, *The Journal of Physical Chemistry C*, 2022, **126**, 17482-17489.
14. D. H. S. Tan, E. A. Wu, H. Nguyen, Z. Chen, M. A. T. Marple, J.-M. Doux, X. Wang, H. Yang, A. Banerjee and Y. S. Meng, *ACS Energy Letters*, 2019, **4**, 2418-2427.
15. S. Wang, M. Tang, Q. Zhang, B. Li, S. Ohno, F. Walther, R. Pan, X. Xu, C. Xin, W. Zhang, L. Li, Y. Shen, F. H. Richter, J. Janek and C.-W. Nan, *Advanced Energy Materials*, 2021, **11**, 2101370.
16. J. Auvergniot, A. Cassel, J.-B. Ledeuil, V. Viallet, V. Seznec and R. Dedryvère, *Chemistry of Materials*, 2017, **29**, 3883-3890.
17. G. F. Dewald, S. Ohno, M. A. Kraft, R. Koerver, P. Till, N. M. Vargas-Barbosa, J. Janek and W. G. Zeier, *Chemistry of Materials*, 2019, **31**, 8328-8337.
18. S. Randau, F. Walther, A. Neumann, Y. Schneider, R. S. Negi, B. Mogwitz, J. Sann, K. Becker-Steinberger, T. Danner, S. Hein, A. Latz, F. H. Richter and J. Janek, *Chemistry of Materials*, 2021, **33**, 1380-1393.
19. S.-K. Jung, H. Gwon, S.-S. Lee, H. Kim, J. C. Lee, J. G. Chung, S. Y. Park, Y. Aihara and D. Im, *Journal of Materials Chemistry A*, 2019, **7**, 22967-22976.
20. T. Bartsch, F. Strauss, T. Hatsukade, A. Schiele, A. Y. Kim, P. Hartmann, J. Janek and T. Brezesinski, *ACS Energy Letters*, 2018, **3**, 2539-2543.
21. T.-T. Zuo, R. Rueß, R. Pan, F. Walther, M. Rohnke, S. Hori, R. Kanno, D. Schröder and J. Janek, *Nature Communications*, 2021, **12**, 6669.

22. G. Conforto, R. Ruess, D. Schröder, E. Trevisanello, R. Fantin, F. H. Richter and J. Janek, *Journal of The Electrochemical Society*, 2021, **168**, 070546.
23. C. S. Yoon, D.-W. Jun, S.-T. Myung and Y.-K. Sun, *ACS Energy Letters*, 2017, **2**, 1150-1155.
24. M. Kim, H. Ahn, J. Choi and W. B. Kim, *Energy Technology*, 2023, **11**, 2201321.
25. A. Franco Gonzalez, N.-H. Yang and R.-S. Liu, *The Journal of Physical Chemistry C*, 2017, **121**, 27775-27787.
26. M. J. Loveridge, M. J. Lain, I. D. Johnson, A. Roberts, S. D. Beattie, R. Dashwood, J. A. Darr and R. Bhagat, *Scientific Reports*, 2016, **6**, 37787.
27. G. G. Eshetu, H. Zhang, X. Judez, H. Adenusi, M. Armand, S. Passerini and E. Figgemeier, *Nature Communications*, 2021, **12**, 5459.
28. Z. Xiao, C. Wang, L. Song, Y. Zheng and T. Long, *Journal of Solid State Electrochemistry*, 2022, **26**, 1125-1136.
29. H. Huo, M. Jiang, Y. Bai, S. Ahmed, K. Volz, H. Hartmann, A. Henss, C. V. Singh, D. Raabe and J. Janek, *Nature Materials*, 2024, **23**, 543-551.
30. D. Cao, X. Sun, Y. Li, A. Anderson, W. Lu and H. Zhu, *Advanced Materials*, 2022, **34**, 2200401.
31. S. Jayasubramaniyan, S. Kim, M. Ko and J. Sung, *ChemElectroChem*, 2024, **11**, e202400219.
32. J. Yan, H. Huang, J. Tong, W. Li, X. Liu, H. Zhang, H. Huang and W. Zhou, *Interdisciplinary Materials*, 2022, **1**, 330-353.
33. Y. Duan, S.-P. Chen, L. Zhang, L. Guo and F.-N. Shi, *Energy & Fuels*, 2024, **38**, 5607-5631.
34. X. Zhan, M. Li, S. Li, X. Pang, F. Mao, H. Wang, Z. Sun, X. Han, B. Jiang, Y.-B. He, M. Li, Q. Zhang and L. Zhang, *Energy Storage Materials*, 2023, **61**, 102875.
35. W. Song and O. B. Chae, *Batteries*, 2024, **10**, 327.
36. T. Nakamura, K. Amezawa, J. Kulisch, W. G. Zeier and J. Janek, *ACS Applied Materials & Interfaces*, 2019, **11**, 19968-19976.
37. S. P. Culver, R. Koerver, W. G. Zeier and J. Janek, *Advanced Energy Materials*, 2019, **9**, 1900626.
38. R. Amin, U. Nisar, M. M. Rahman, M. Dixit, A. Abouimrane and I. Belharouak, *Journal of Materials Chemistry A*, 2024, **12**, 14186-14205.
39. M. K. Wilson, C. Augustin, A. Abhilash, B. Jinisha, A. Antony, M. K. Jayaraj and S. Jayalekshmi, *Polymer Bulletin*, 2024, **81**, 6003-6024.
40. B.-X. Shi, F. Weber, Y. Yusim, T. Demuth, K. Vettori, A. Münchinger, G. Titvinidze, K. Volz, A. Henss, R. Berger and F. H. Richter, *Journal of Materials Chemistry A*, 2024, DOI: 10.1039/D4TA07265K.
41. B.-X. Shi, Y. Yusim, S. Sen, T. Demuth, R. Ruess, K. Volz, A. Henss and F. H. Richter, *Advanced Energy Materials*, 2023, **13**, 2300310.
42. V. S. Meka, M. K. G. Sing, M. R. Pichika, S. R. Nali, V. R. M. Kolapalli and P. Kesharwani, *Drug Discovery Today*, 2017, **22**, 1697-1706.
43. S. G. M. van Lange, D. W. te Brake, G. Portale, A. Palanisamy, J. Sprakel and J. van der Gucht, *Science Advances*, 2024, **10**, eadi3606.
44. S. Meng, Y. Liu, J. Yeo, J. M. Ting and M. V. Tirrell, *Colloid and Polymer Science*, 2020, **298**, 887-894.

45. B. Jirgensons, M. E. Straumanis and A. W. Hutchison, *Journal of The Electrochemical Society*, 1955, **102**, 234Ca.
46. S. Manoj Lalwani, C. I. Eneh and J. L. Lutkenhaus, *Physical Chemistry Chemical Physics*, 2020, **22**, 24157-24177.
47. Y. N. Solier, P. Mocchiutti, M. C. Inalbon and M. Á. Zanuttini, *Macromolecular Materials and Engineering*, 2022, **307**, 2200108.
48. J. Engelhardt, H. Zuilhof, J. van der Gucht, L. C. P. M. de Smet and E. Maaskant, *ACS Applied Polymer Materials*, 2024, **6**, 4409-4418.
49. G. Decher, J. D. Hong and J. Schmitt, *Thin Solid Films*, 1992, **210-211**, 831-835.
50. M. Gai, J. Frueh, V. L. Kudryavtseva, R. Mao, M. V. Kiryukhin and G. B. Sukhorukov, *Scientific Reports*, 2016, **6**, 37000.
51. S. Luo, Z. Wang, X. Li, X. Liu, H. Wang, W. Ma, L. Zhang, L. Zhu and X. Zhang, *Nature Communications*, 2021, **12**, 6968.
52. L. A. Selis and Jorge M. Seminario, *RSC Advances*, 2018, **8**, 5255-5267.
53. C. Hong, Q. Leng, J. Zhu, S. Zheng, H. He, Y. Li, R. Liu, J. Wan and Y. Yang, *Journal of Materials Chemistry A*, 2020, **8**, 8540-8547.
54. R. Koerver, I. Aygün, T. Leichtweiß, C. Dietrich, W. Zhang, J. O. Binder, P. Hartmann, W. G. Zeier and J. Janek, *Chemistry of Materials*, 2017, **29**, 5574-5582.
55. A.-K. Hatz, R. Calaminus, J. Feijoo, F. Treber, J. Blahusch, T. Lenz, M. Reichel, K. Karaghiosoff, N. M. Vargas-Barbosa and B. V. Lotsch, *ACS Applied Energy Materials*, 2021, **4**, 9932-9943.
56. J. Ruhl, L. M. Riegger, M. Ghidiu and W. G. Zeier, *Advanced Energy and Sustainability Research*, 2021, **2**, 2000077.
57. M. Mock, M. Bianchini, F. Fauth, K. Albe and S. Sicolo, *Journal of Materials Chemistry A*, 2021, **9**, 14928-14940.
58. M. D. Levi and D. Aurbach, in *Characterization of Materials*, DOI: https://doi.org/10.1002/0471266965.com125, pp. 1-21.
59. E. Trevisanello, R. Ruess, G. Conforto, F. H. Richter and J. Janek, *Advanced Energy Materials*, 2021, **11**, 2003400.
60. W. Waag, S. Käbitz and D. U. Sauer, *Applied Energy*, 2013, **102**, 885-897.
61. R. Ruess, S. Schweidler, H. Hemmelmann, G. Conforto, A. Bielefeld, D. A. Weber, J. Sann, M. T. Elm and J. Janek, *Journal of The Electrochemical Society*, 2020, **167**, 100532.
62. M. Touboul, N. Sephar and M. Quarton, *Solid State Ionics*, 1990, **38**, 225-229.
63. K. Homma, Y. Liu, M. Sumita, R. Tamura, N. Fushimi, J. Iwata, K. Tsuda and C. Kaneta, *The Journal of Physical Chemistry C*, 2020, **124**, 12865-12870.
64. M. Weiss, F. J. Simon, M. R. Busche, T. Nakamura, D. Schröder, F. H. Richter and J. Janek, *Electrochemical Energy Reviews*, 2020, **3**, 221-238.
65. J. Moškon and M. Gaberšček, *Journal of Power Sources Advances*, 2021, **7**, 100047.
66. T.-T. Zuo, F. Walther, J. H. Teo, R. Rueß, Y. Wang, M. Rohnke, D. Schröder, L. F. Nazar and J. Janek, *Angewandte Chemie International Edition*, 2023, **62**, e202213228.

67. L. Zhang, Y. Dai, C. Li, Y. Dang, R. Zheng, Z. Wang, Y. Wang, Y. Cui, H. Arandiyan, Z. Shao, H. Sun, Q. Zhuang and Y. Liu, *Energy Storage Materials*, 2024, **69**, 103378.
68. S. Li, J. Lin, M. Schaller, S. Indris, X. Zhang, T. Brezesinski, C.-W. Nan, S. Wang and F. Strauss, *Angewandte Chemie International Edition*, 2023, **62**, e202314155.
69. J. C. Vickerman, *Molecular Surface Mass Spectrometry by SIMS*, Wiley, 2009.
70. F. Walther, F. Strauss, X. Wu, B. Mogwitz, J. Hertle, J. Sann, M. Rohnke, T. Brezesinski and J. Janek, *Chemistry of Materials*, 2021, **33**, 2110-2125.
71. F. Walther, S. Randau, Y. Schneider, J. Sann, M. Rohnke, F. H. Richter, W. G. Zeier and J. Janek, *Chemistry of Materials*, 2020, **32**, 6123-6136.
72. F. Walther, R. Koerver, T. Fuchs, S. Ohno, J. Sann, M. Rohnke, W. G. Zeier and J. Janek, *Chemistry of Materials*, 2019, **31**, 3745-3755.
73. T. Lombardo, F. Walther, C. Kern, Y. Moryson, T. Weintraut, A. Henss and M. Rohnke, *Journal of Vacuum Science & Technology A*, 2023, **41**.
74. D. He, M. Yuan, B. Hu, C. Zou, X. Zhao, C. Zhao, J. Wang and H. Ding, *Journal of Physics: Conference Series*, 2024, **2679**, 012005.
75. D. Rehnlund, F. Lindgren, S. Böhme, T. Nordh, Y. Zou, J. Pettersson, U. Bexell, M. Boman, K. Edström and L. Nyholm, *Energy & Environmental Science*, 2017, **10**, 1350-1357.
76. M. Graf, C. Berg, R. Bernhard, S. Haufe, J. Pfeiffer and H. A. Gasteiger, *Journal of The Electrochemical Society*, 2022, **169**, 020536.
77. S. Casino, T. Beuse, V. Küpers, M. Börner, T. Gallasch, M. Winter and P. Niehoff, *Journal of Energy Storage*, 2021, **41**, 102812.
78. A. Ulvestad, H. F. Andersen, I. J. T. Jensen, T. T. Mongstad, J. P. Mæhlen, Ø. Prytz and M. Kirkengen, *Scientific Reports*, 2018, **8**, 8634.
79. A. Ulvestad, H. F. Andersen, J. P. Mæhlen, Ø. Prytz and M. Kirkengen, *Scientific Reports*, 2017, **7**, 13315.
80. L. Köbbing, A. Latz and B. Horstmann, *Advanced Functional Materials*, 2024, **34**, 2308818.
81. B. Hertzberg, J. Benson and G. Yushin, *Electrochemistry Communications*, 2011, **13**, 818-821.
82. C. D. Alt, N. U. C. B. Müller, L. M. Riegger, B. Aktekin, P. Minnmann, K. Peppler and J. Janek, *Joule*, DOI: 10.1016/j.joule.2024.07.006.
83. S. Wenzel, S. J. Sedlmaier, C. Dietrich, W. G. Zeier and J. Janek, *Solid State Ionics*, 2018, **318**, 102-112.
84. P. Minnmann, L. Quillman, S. Burkhardt, F. H. Richter and J. Janek, *Journal of The Electrochemical Society*, 2021, **168**, 040537.
85. J. M. Lee, Y. S. Park, J.-W. Moon and H. Hwang, *Frontiers in Chemistry*, 2021, **9**.
86. L. Karger, B. N. Nunes, Y. Yusim, A. Mazilkin, R. Zhang, W. Zhao, A. Henss, A. Kondrakov, J. Janek and T. Brezesinski, *Advanced Materials Interfaces*, 2024, **11**, 2301067.
87. A. S. Shaplov, P. S. Vlasov, M. Armand, E. I. Lozinskaya, D. O. Ponkratov, I. A. Malyshkina, F. Vidal, O. V. Okatova, G. M. Pavlov, C. Wandrey, I. A. Godovikov and Y. S. Vygodskii, *Polymer Chemistry*, 2011, **2**, 2609-2618.

Supporting Information

Polyelectrolyte Complexes as Coating on Nickel-Rich Cathode and Silicon Anode Particles to Stabilize Solid-State Batteries

Bing-Xuan Shi,[a] Daniil Nosov,[b] Timo Weintraut,[c] Thomas Demuth,[d] Felix Schnaubelt,[a] Sebastian Leonard Benz,[a] Kilian Vettori,[a] Jingui Yang,[e] Florian Strauss,[e] Kerstin Volz,[d] Anja Henss,[c] Alexander Shaplov,[b] Felix H. Richter*[a]

[a] Institute of Physical Chemistry & Center for Materials Research (LaMa), Justus-Liebig-University Giessen, Heinrich-Buff-Ring 17, 35392 Giessen, Germany

[b] Luxembourg Institute of Science and Technology, 5 Avenue des Hauts-Fourneaux, 4362 ESCH-SUR-ALZETTE, Luxembourg

[c] Institute of Experimental Physics 1 & Center for Materials Research (LaMa), Justus-Liebig-University Giessen, Heinrich-Buff-Ring 17, 35392 Giessen, Germany

[d] Department of Physics & Materials Sciences Center (WZMW), Philipps-University Marburg, Hans-Meerwein Straße 6, 35032 Marburg, Germany

[e] Institute of Nanotechnology (INT), Karlsruhe Institute of Technology (KIT), Kaiserstr. 12, 76131 Karlsruhe, Germany.

*Corresponding author, Felix.H.Richter@phys.chemie.uni-giessen.de

Key words: Solid-state batteries, solid electrolyte, polymer coating, polyelectrolyte complex, interface degradation.

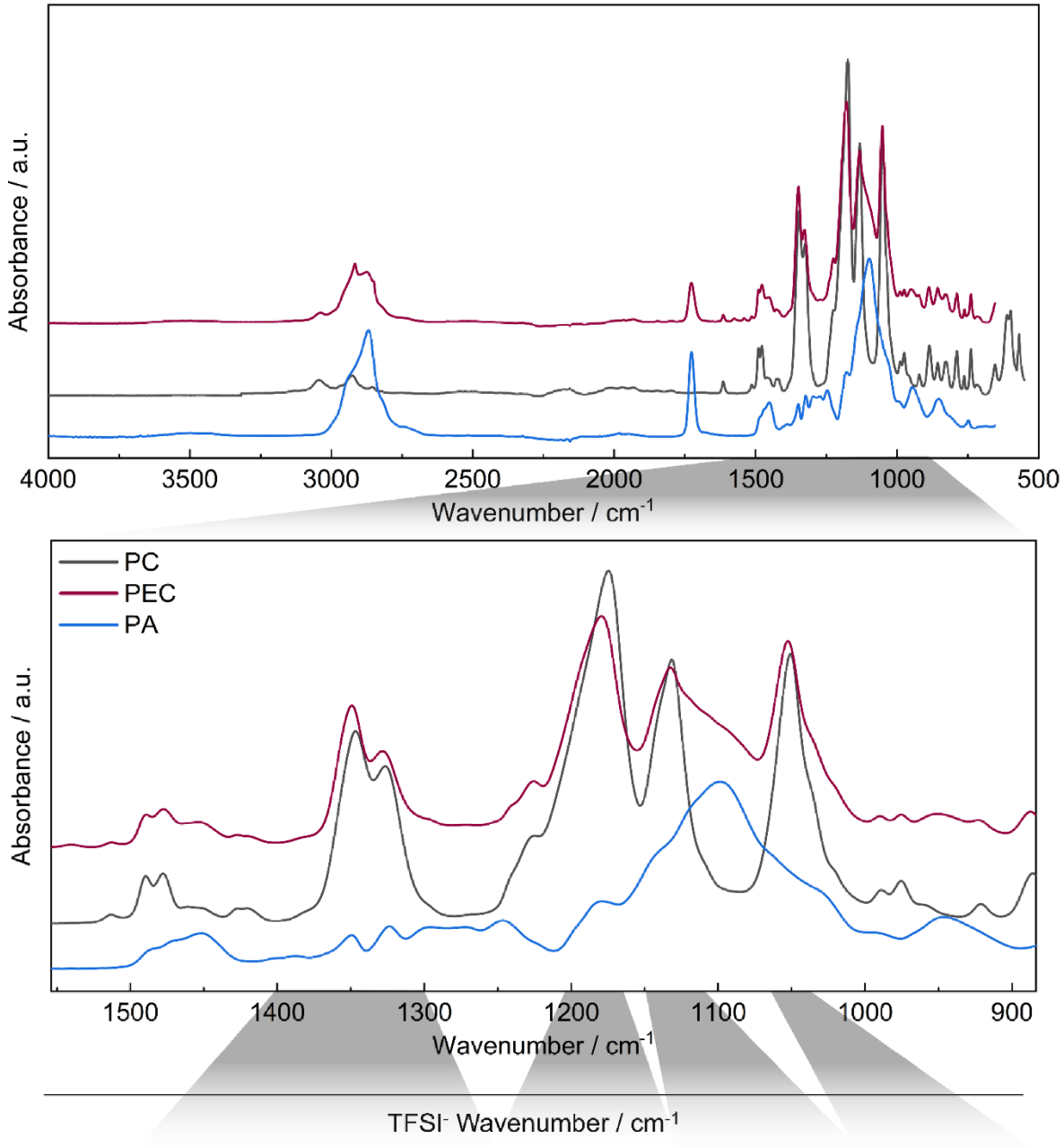

TFSI⁻ Wavenumber / cm^{-1}

PC	1349	1328	1179	1133	1052
PEC	1346	1327	1174	1132	1050
PA	1349	1324	1179		

Figure S1. FTIR reveals slight wavelength shifts in the TFSI⁻ group. The top figure displays the full spectrum from 4000 to 500 cm^{-1}, while the middle figure highlights the IR range specific to the TFSI⁻ group (1550 to 880 cm^{-1}). The bottom table summarizes the shift values for the TFSI⁻ group.

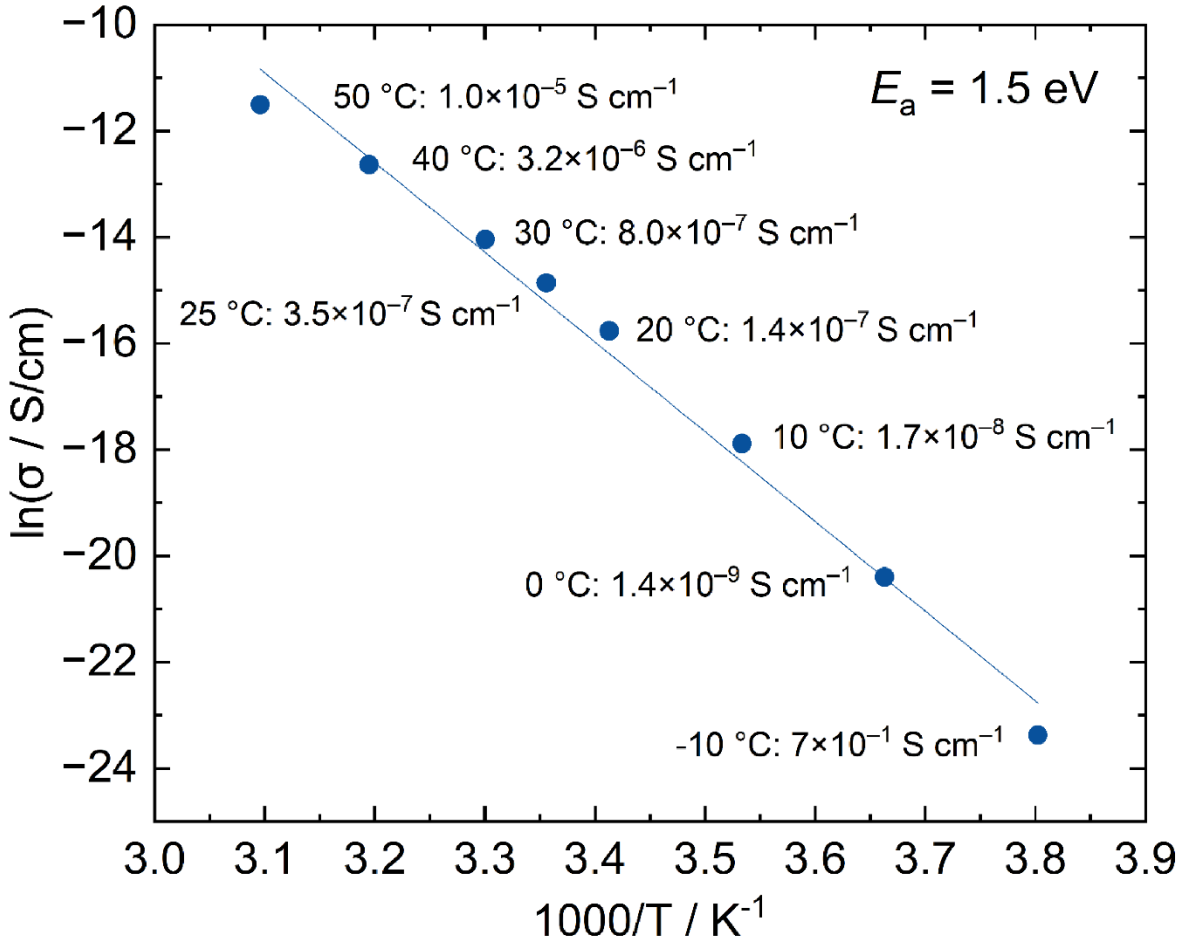

Figure S2. The conductivity of the PEC polymer film obtained by the cell with the configuration, steel|PEC|steel. The temperature range is measured from -10 to 50 °C. The activation energy, E_a = 1.5 eV, is calculated by the slope of the log(σ / S/cm) vs 1000/T / K^{-1}, following the Arrhenius equation: $\sigma = \sigma_0 \cdot e^{-E_a/kT}$. σ is the conductivity measured by EIS. σ_0 is the pre-exponential factor. E_a is the activation energy. k is the Boltzmann constant $8.617 \cdot 10^{-5}$ eV/K. T is the temperature in Kelvin.

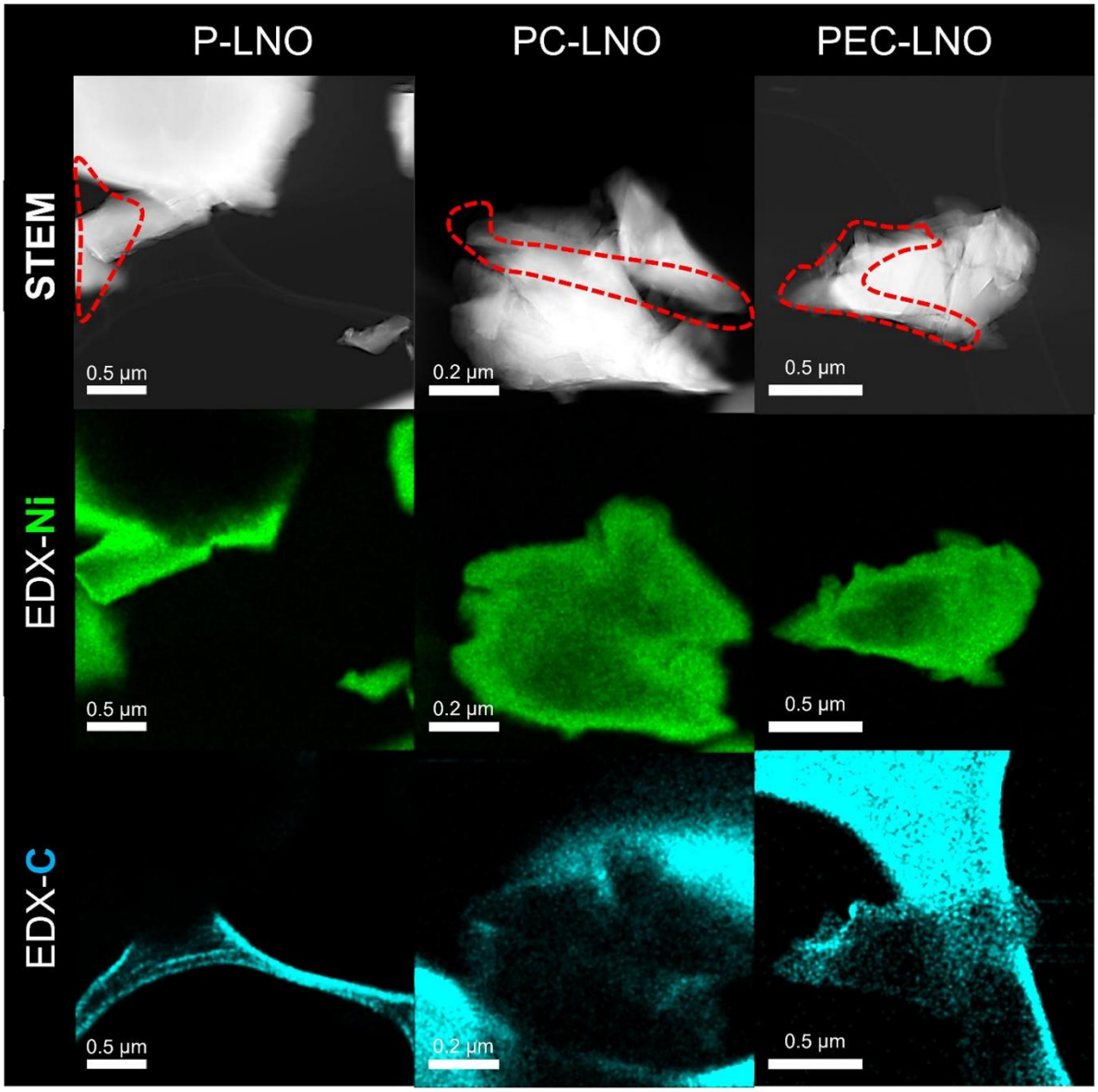

Figure S3a. The first row shows the STEM images, with the red region corresponding to the quantification analysis in **Figure S3c**. EDX elemental maps of P-LNO, PC-LNO, and PEC-LNO particles highlight Ni and C intensity, characteristic of the LNO and polymer, respectively.

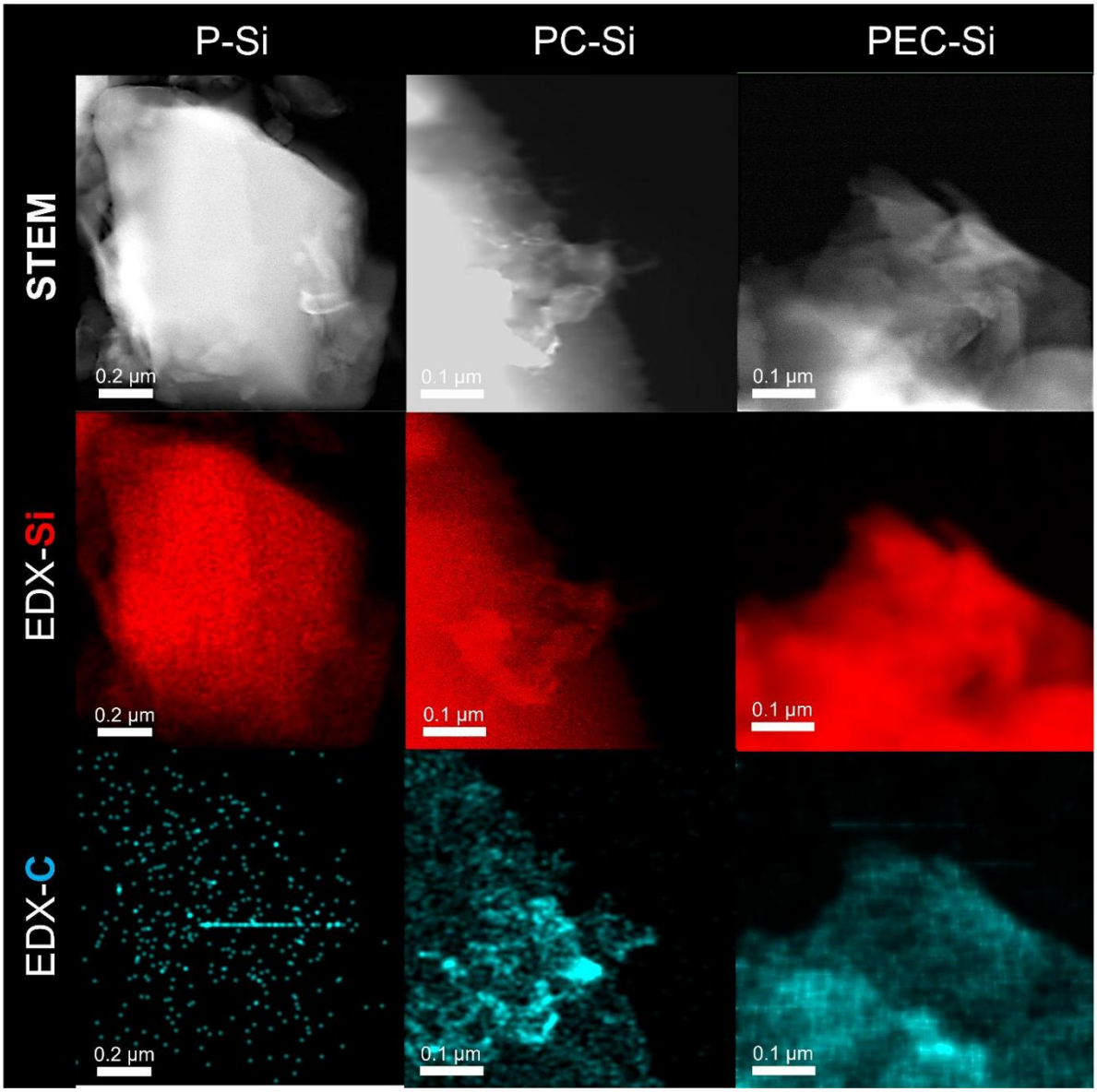

Figure S3b. The first row shows the STEM image with the quantification analysis in **Figure S3c**. EDX elemental maps of P-Si, PC-Si, and PEC-Si particles highlight Si and C intensity, characteristic of the silicon and polymer, respectively.

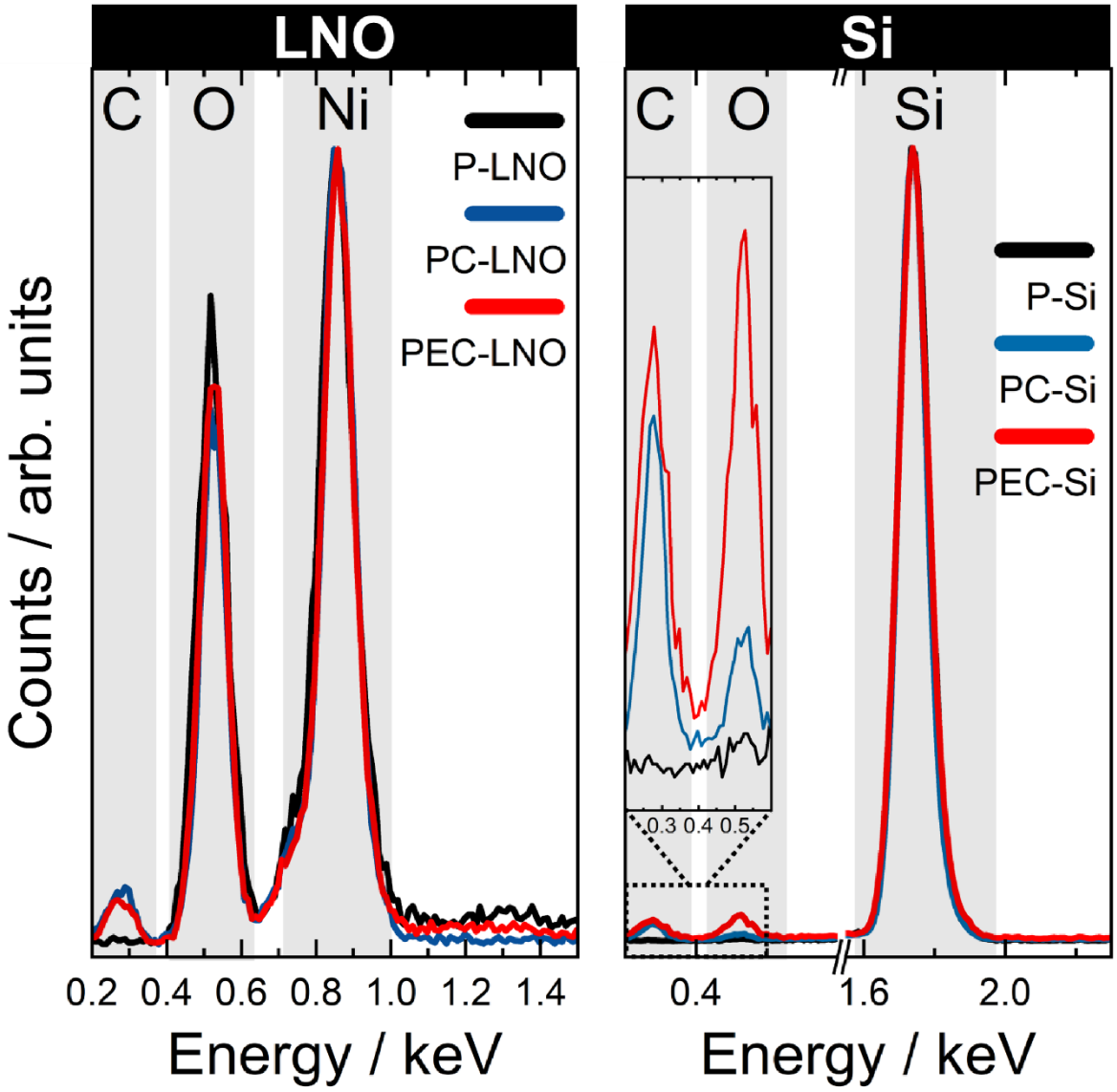

Figure S3c. EDX spectra of the selected region (the edge of the particles) from the mapping are used to assess polymer intensity. For LNO, Ni represents the electrode material, while C indicates the polymer. Similarly, the ratios of Si, C, and O are analyzed, with C and O representing the polymer characteristic intensity.

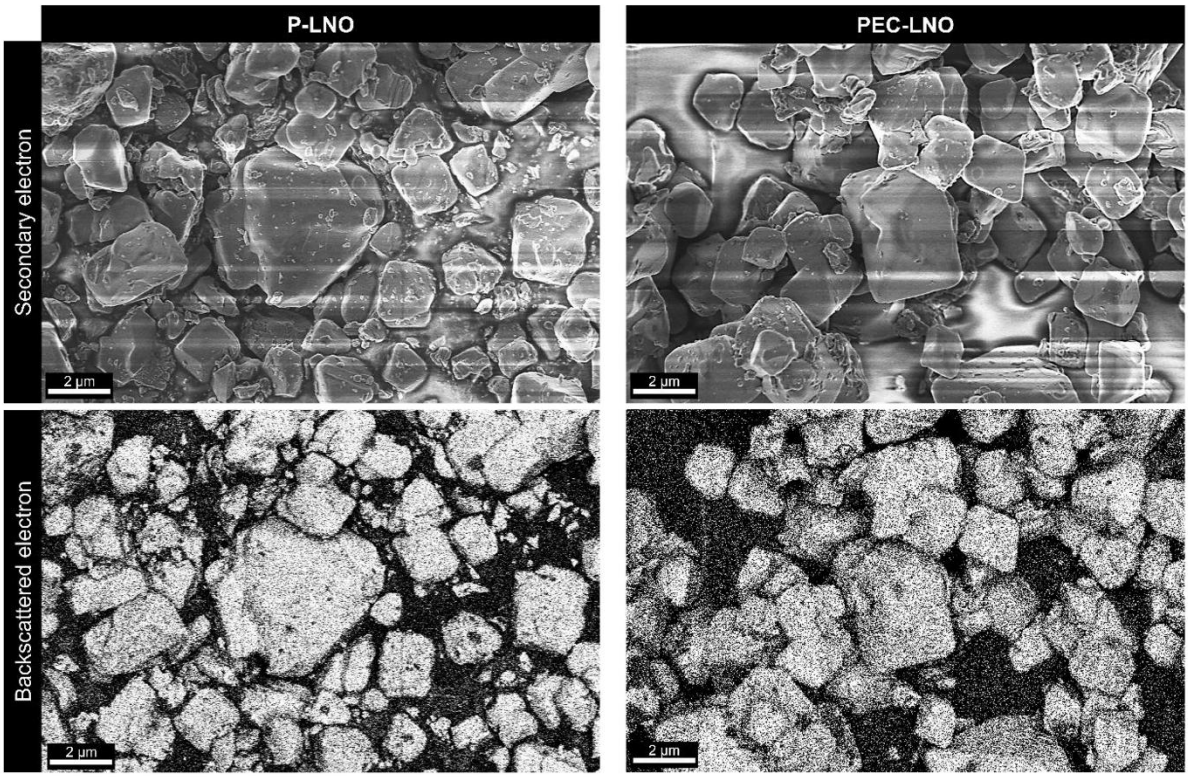

Figure S4. SEM analysis of P-LNO (left) and PEC-LNO (right) is presented, with secondary electron images at the top and energy-selective backscattered electron images at the bottom.

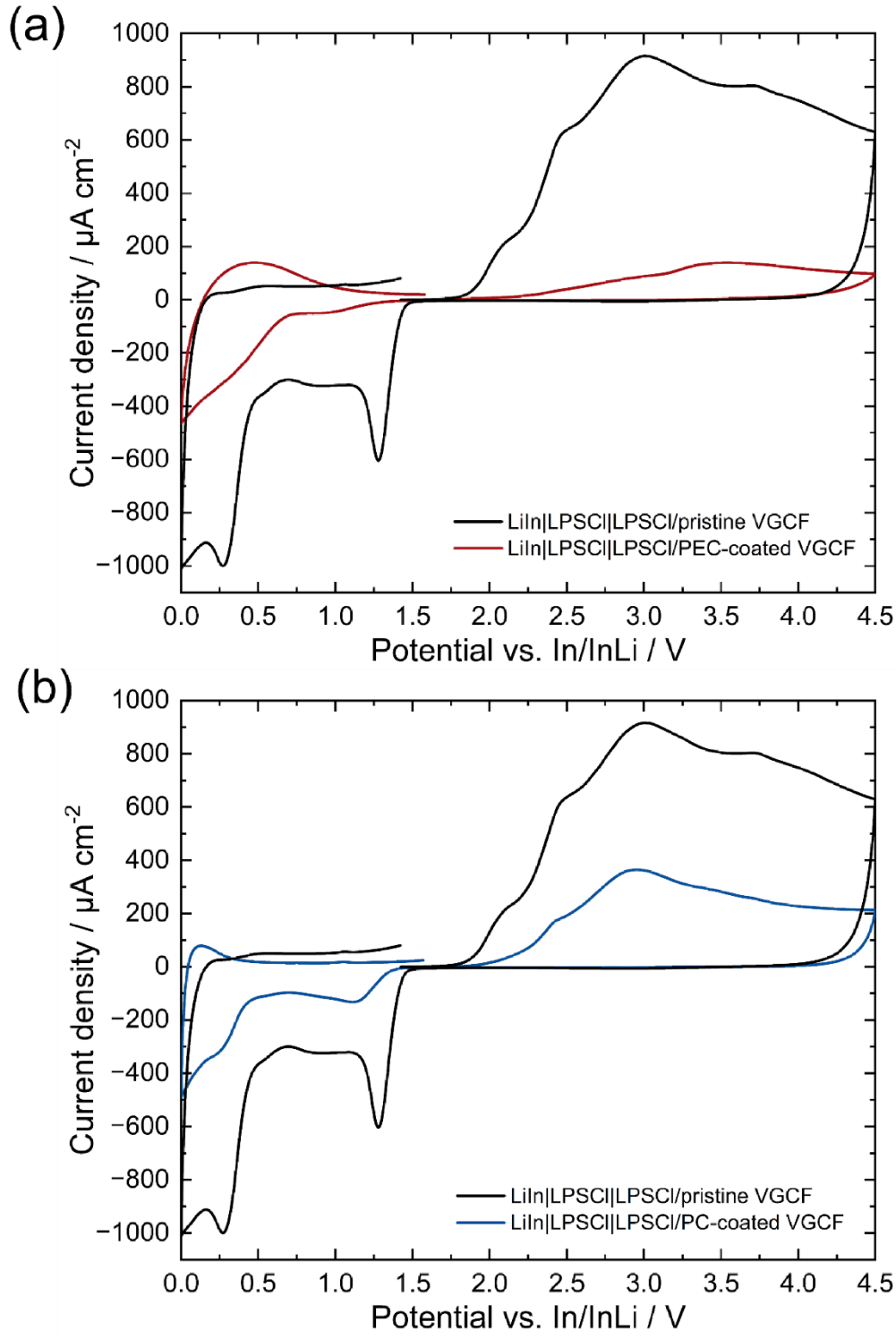

Figure S5. The electrochemical stability window is measured by CV for the range from 0 V to 4.5 V (vs. In/LiIn) with a scan rate of 1 mV s^{-1}, initiating from the OCV. VGCF is used as the working electrode, LPSCl is used as the separator, and InLi alloy is used as the counter electrode. (a) PEC-coated VGCF and (b) PC-coated VGCF composite are compared with pristine VGCF.

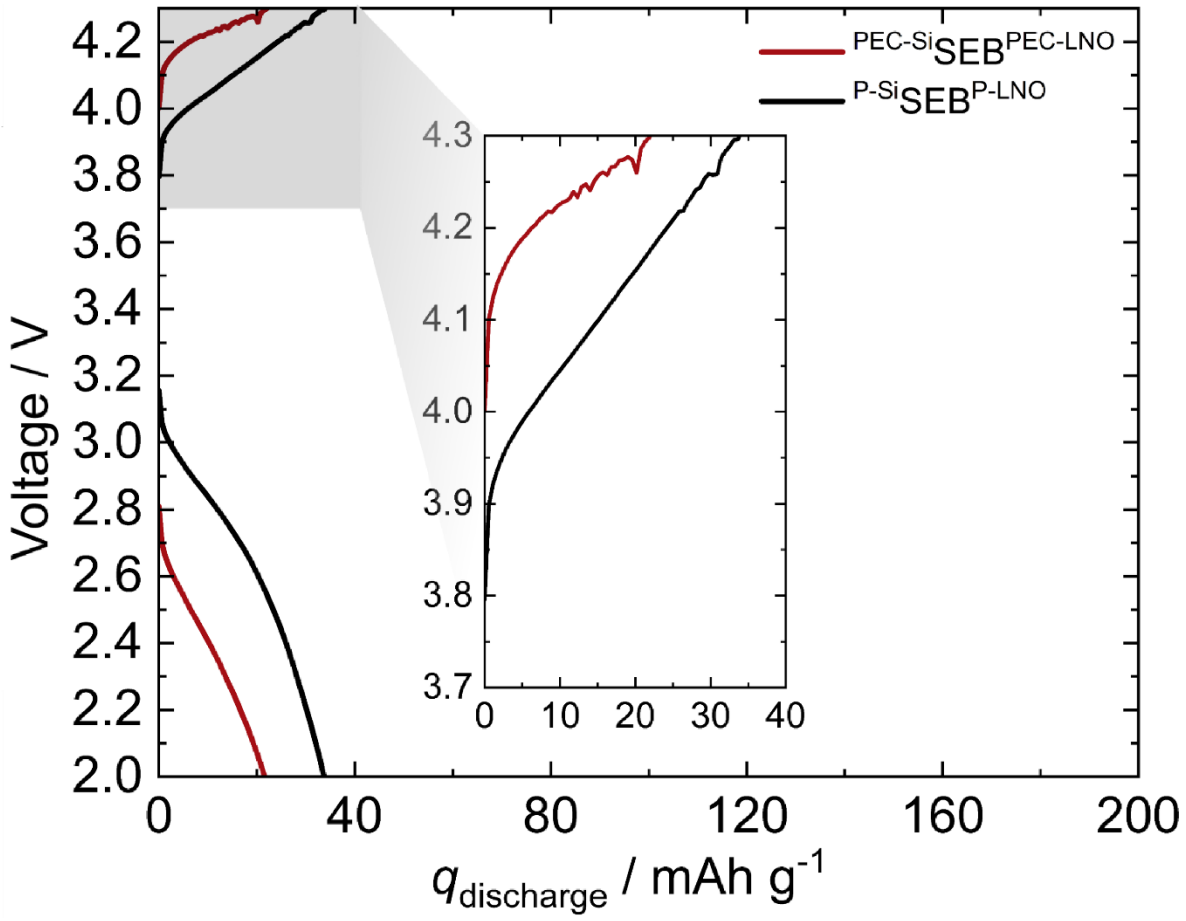

Figure S6. The galvanic plot of $^{P\text{-}Si}SEB^{P\text{-}LNO}$ and $^{PEC\text{-}Si}SEB^{PEC\text{-}LNO}$ for the 25th cycle at 1C is presented. The inset shows the zoom-in of the capacity range from 0 to 40 mAh g^{-1} and voltage range from 3.7 to 4.3 V to confirm the fluctuation during this range due to dendrite formation.

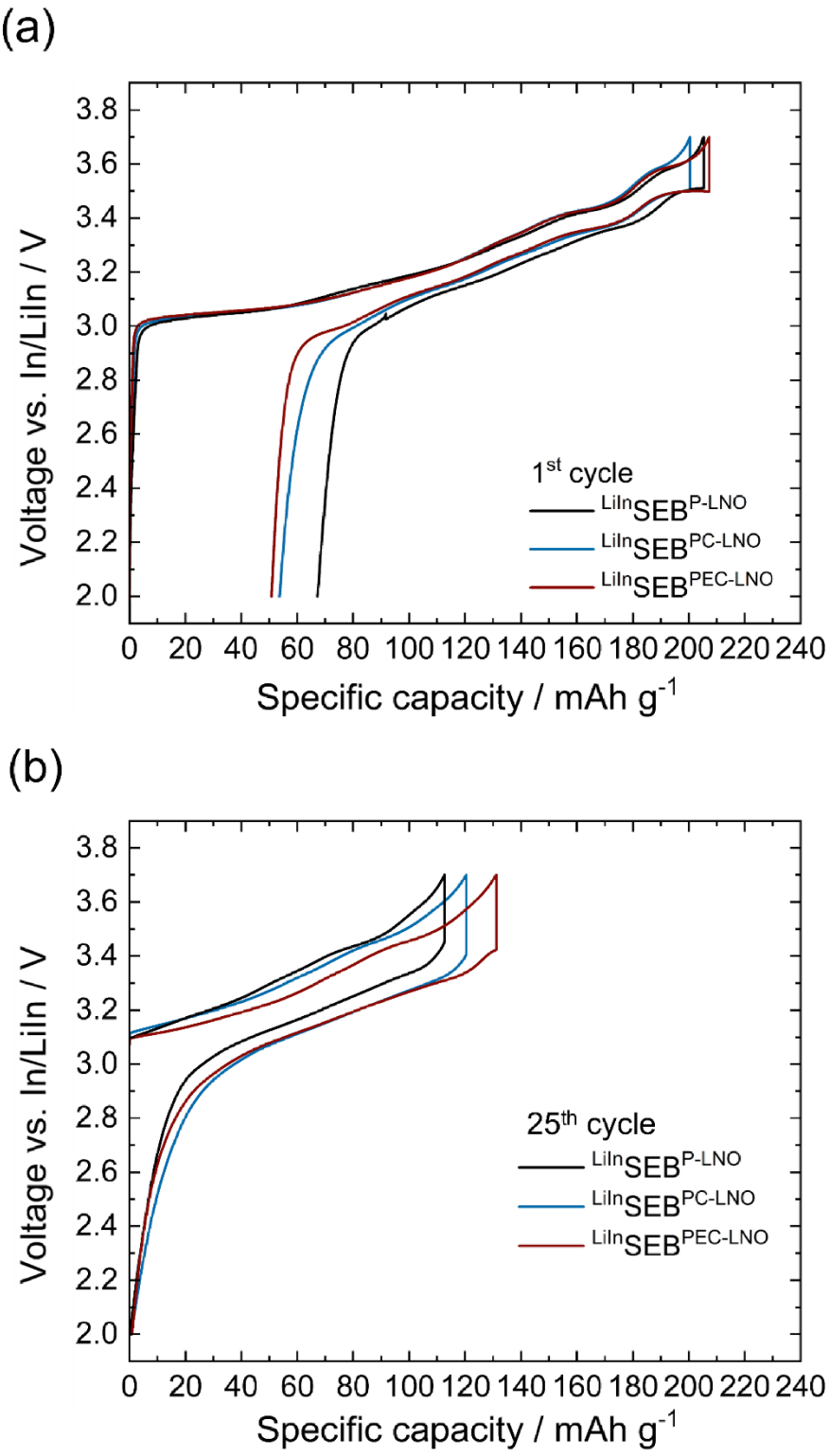

Figure S7. The galvanic plots at 0.1C of $^{LiIn}SEB^{P\text{-}LNO}$, $^{LiIn}SEB^{PC\text{-}LNO}$, and $^{LiIn}SEB^{PEC\text{-}LNO}$ for (a) the 1st cycle and (b) the 25th cycle are presented.

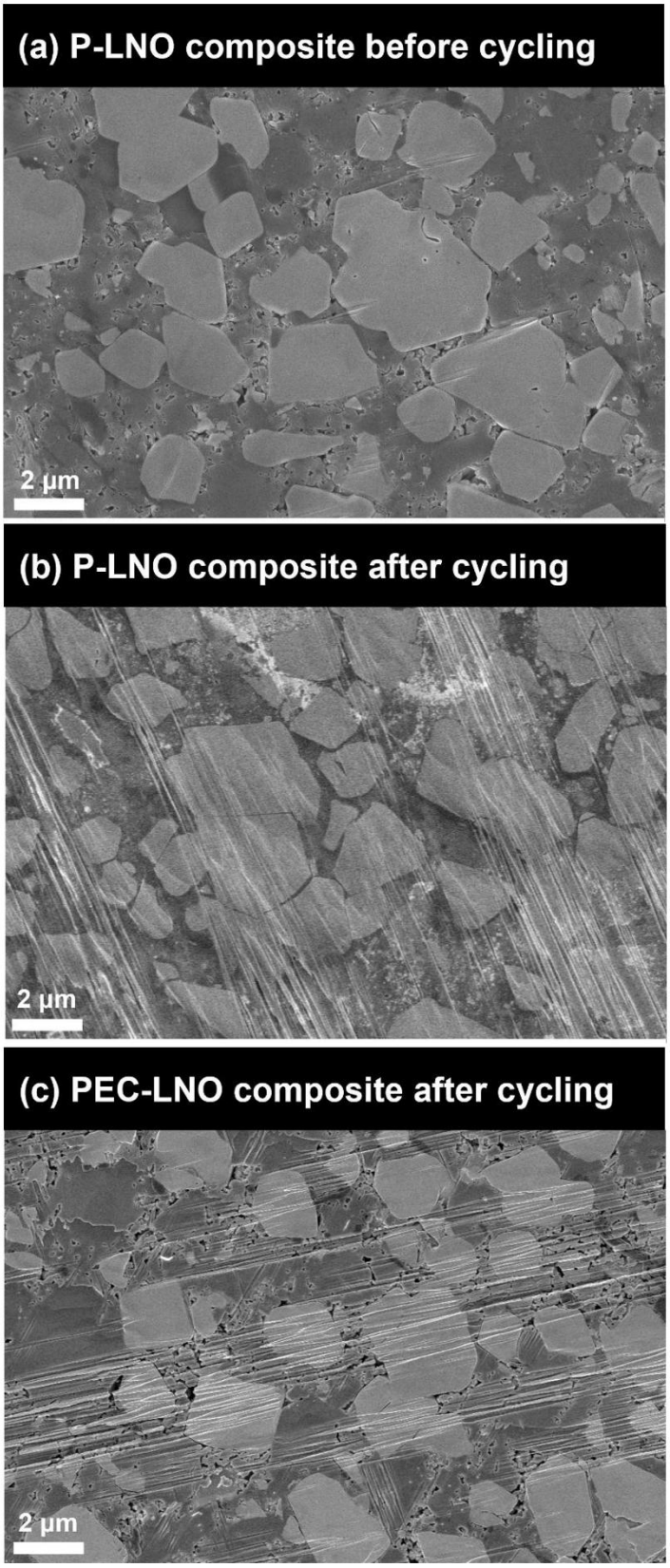

Figure S8. SEM images of cross-sectioned composite cathodes prepared by ion beam milling are shown, including (a) P-LNO cathode composite before cycling, (b) P-LNO cathode composite after 100 cycles at a 0.1C rate, and (c) PEC-LNO cathode composite after 100 cycles at a 0.1C rate.

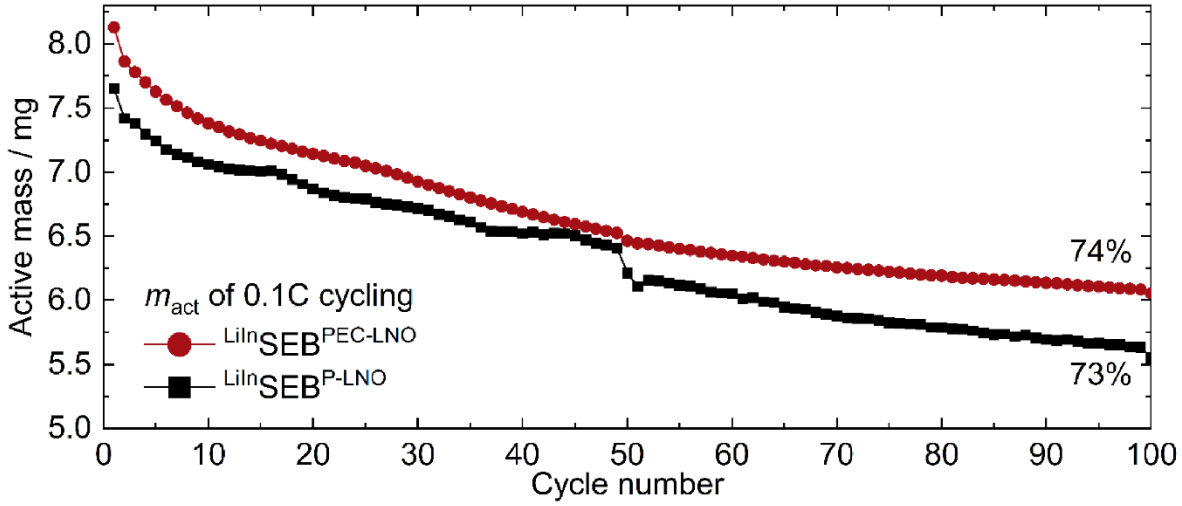

Figure S9. The m_{act} values for LiInSEB^{P-LNO} and LiInSEB$^{PEC-LNO}$ after 100 cycles at 0.1C and 25 °C are calculated from their cycling performance.

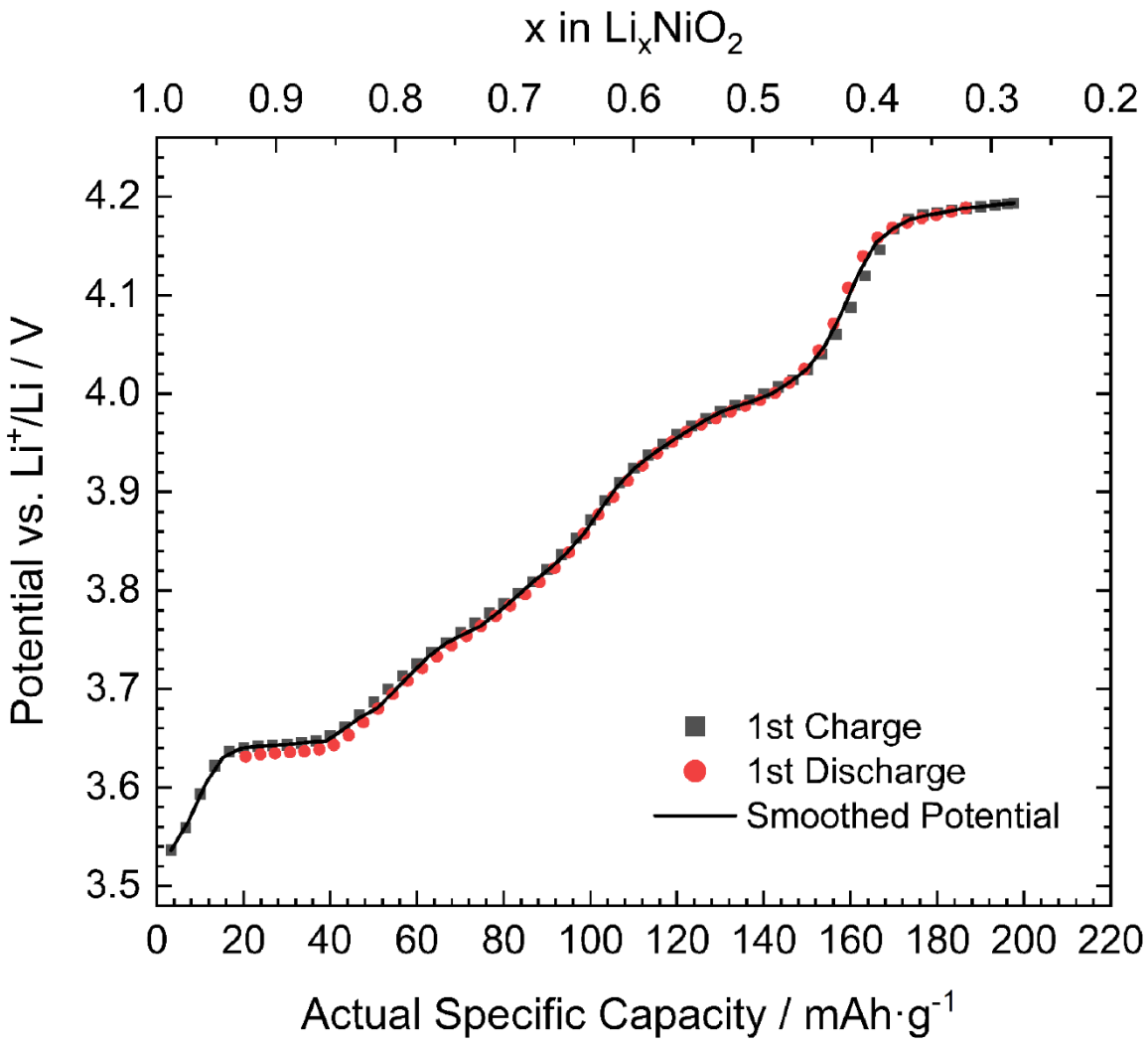

Figure S10. Relationship between OCV and the SOC, represented by the lithium content x in Li_xNiO_2. This is derived from the galvanostatic intermittent titration technique (GITT) of a $^{Li}LEB^{LNO}$ using 1 M $LiPF_6$ in EC: DEC (1:1 vol.%) LE, a lithium metal anode and LNO cathode sheet at a 0.1C rate. Each 10-minute charge or discharge interval is followed by a two-hour relaxation period to measure the OCV. We calculate lithium content x in Li_xNiO_2 by using the known capacity for each GITT pulse step.

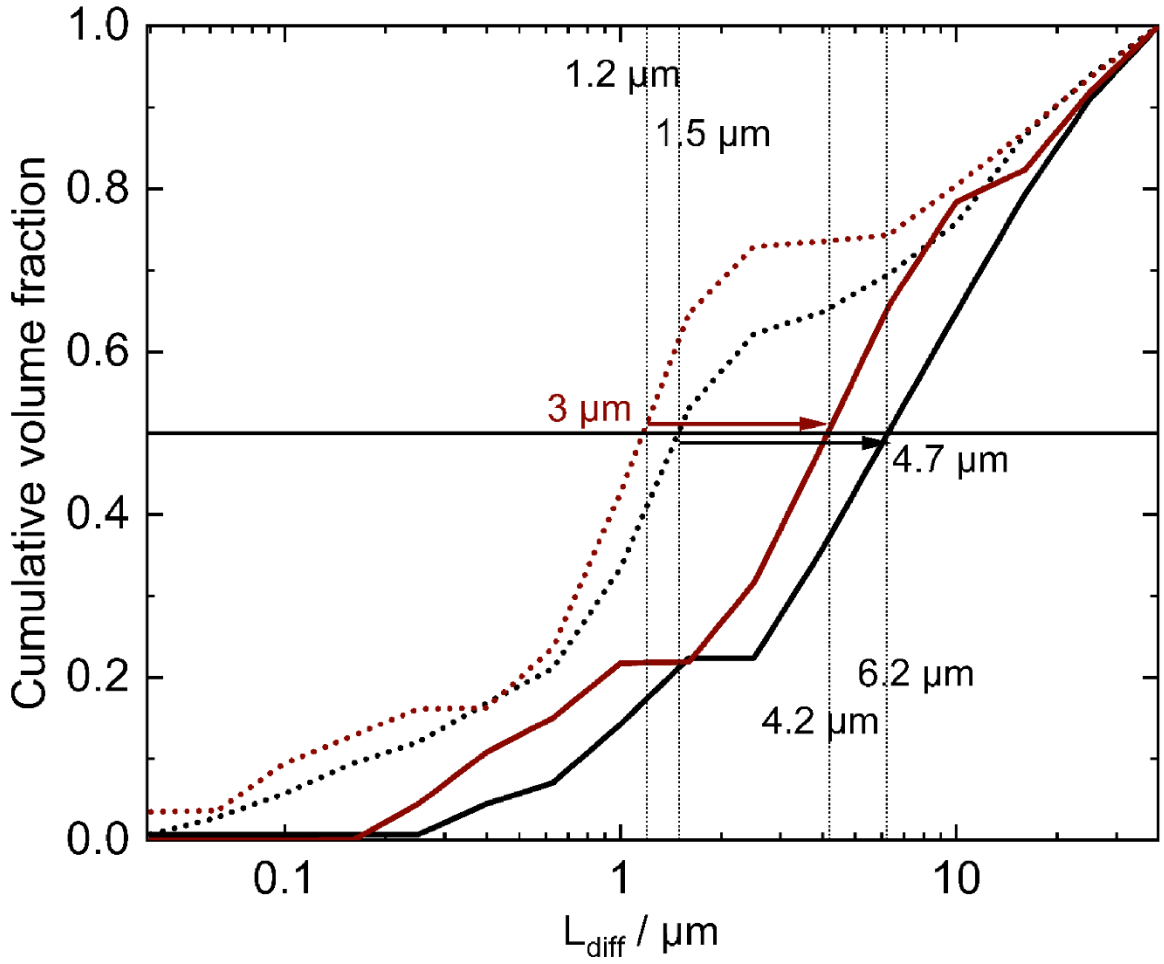

Figure S11. The L_{diff} within the cathode composite is determined by fitting the Warburg impedance, as described in our previous research.[1, 2] This fitting is derived from the EIS data (**Figure 6C**) using the finite-space Warburg element for cylindrical particles (Z_{fs}), in combination with a particle size distribution model (EIS-PSD) (**Figure S12**). The Z_{fs} is used to model the diffusion process throughout the entire sample volume, accounting for the ion-blocking boundary at the current collector and the inner core of the LNO particles. Hence, The Z_{fs} captures the complex geometry of Li^+ diffusion within the LNO particles. At sufficiently low frequencies, when the ion-blocking boundary is reached, a continuous transition is observed in the Nyquist plot, with the phase angle shifting from 45° and gradually approaching 90°.[3, 4] To determine the finite-space Warburg impedance through EIS, the lower frequency limit is set at 100 µHz. The diffusion length (L_{diff}) is derived from the thickness of the cylindrical particles, obtained by fitting the EIS finite-space diffusion tail using equations [1] and [2] based on the transition line model.

$\tau_i = L_{\mathrm{diff}}^2/\widetilde{D}_{Li}$ **[1]**, and $Z_{\mathrm{fs}}^{\mathrm{cylindrical}} = \frac{1}{C_{\mathrm{diff}}}\left(\sum_i \frac{\Delta\phi_i}{\tau_i}\frac{\sqrt{i\omega\tau_i}}{\coth\sqrt{i\omega\tau_i}}\right)$ **[2]**

In equation [1], τ_i is the characteristic time constant of Li^+ diffusion. The diffusion coefficient of Li^+ in LNO ($\widetilde{D}_{Li}$) is assumed to be around 10^{-11} $cm^2\,s^{-1}$ at 25 °C.[1, 2] In equation [2], the volume fraction of the particle contribution is denoted as $\Delta\phi_i$, indicating the amount of the LNO particle which has L_{diff} of τ_i to reach the finite condition. $C_{diff} = dq/dE$ equating to 355 mAh V^{-1} g^{-1} is the total differential capacity at 3.15 V (vs. In/LiIn) calculated from cycling results of a $^{Li}LEB^{LNO}$ (see **Figure S10**). ω is the radial frequency. Fitting the impedance data leads to L_{diff} and $\Delta\phi_i$, presented cumulatively in **Figure S11**.

(a)

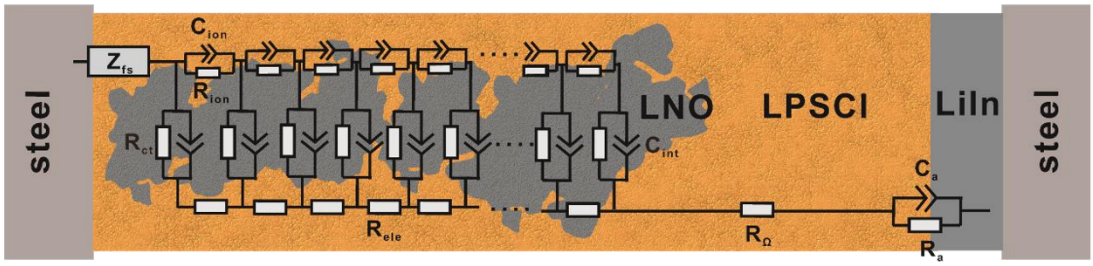

(b)

		LiIn**SEB**$^{PEC\text{-}LNO}$				LiIn**SEB**$^{P\text{-}LNO}$			
	Cycle	1st	2nd	50th	100th	1st	2nd	50th	100th
Cathode composite	$R_{cathode}$ / Ω cm²	11.3	31.3	248.4	218.1	17.7	40.6	427.0	939.3
	R_{ct} / Ω cm²	7.4	8.0	150.8	167.4	11.5	16.8	456.3	1089.5
	R_{ele} / Ω cm²	2.2	3.1	18.2	36.2	2.6	2.8	7.1	10.1
	R_{ion} / Ω cm²	15.0	120.0	390.9	248.1	24.7	95.1	392.5	799.8
Anode	R_a / Ω cm²	3.4	5.1	15.7	31.4	4.7	3.5	23.6	25.2
Separator	R_Ω / Ω cm²	25.4	24.4	27.7	31.4	30.0	28.3	34.7	37.4

Figure S12. (a) Schematic illustration of the TLM for impedance fitting in the cathode composite includes charge transfer resistance (R_{ct}), electronic transport (R_{ele}), and ionic transport (R_{ion}), complemented by interfacial capacitances (C_{int}) and ionic transport capacitances (C_{ion}). Contact resistance ($R_{contact}$) between electrode materials includes electronic transport (R_{ele}) and ionic transport (R_{ion}).[5, 6] The similar apex frequency in both SEBs (**Figure 6c**), marked in blue on the Nyquist plots, aligns with the R_{ct} frequency range. The finite-space Warburg element (Z_{fs}) represents the influence of current constriction.[1] The complete SEB model incorporates electrolyte resistance (R_Ω), LiIn anode resistance (R_a), and LiIn anode capacitance (C_a). R_{ct} is used to assess CEI degradation over cycling. However, the Gerischer-type impedance makes it difficult to accurately separate R_{ct} from R_{ele} and R_{ion} in the cathode composite.[6] Therefore, the cathode resistance ($R_{cathode}$) is calculated via equation [3][6]:

$$R_{\text{cathode}} = \sqrt{R_{\text{ct}} \cdot (R_{\text{ele}} + R_{\text{ion}})} \qquad [3]$$

(b) Fitting results of EIS using TLM under the 0.1C cycling at 1st, 2nd, 50th, and 100th cycles.

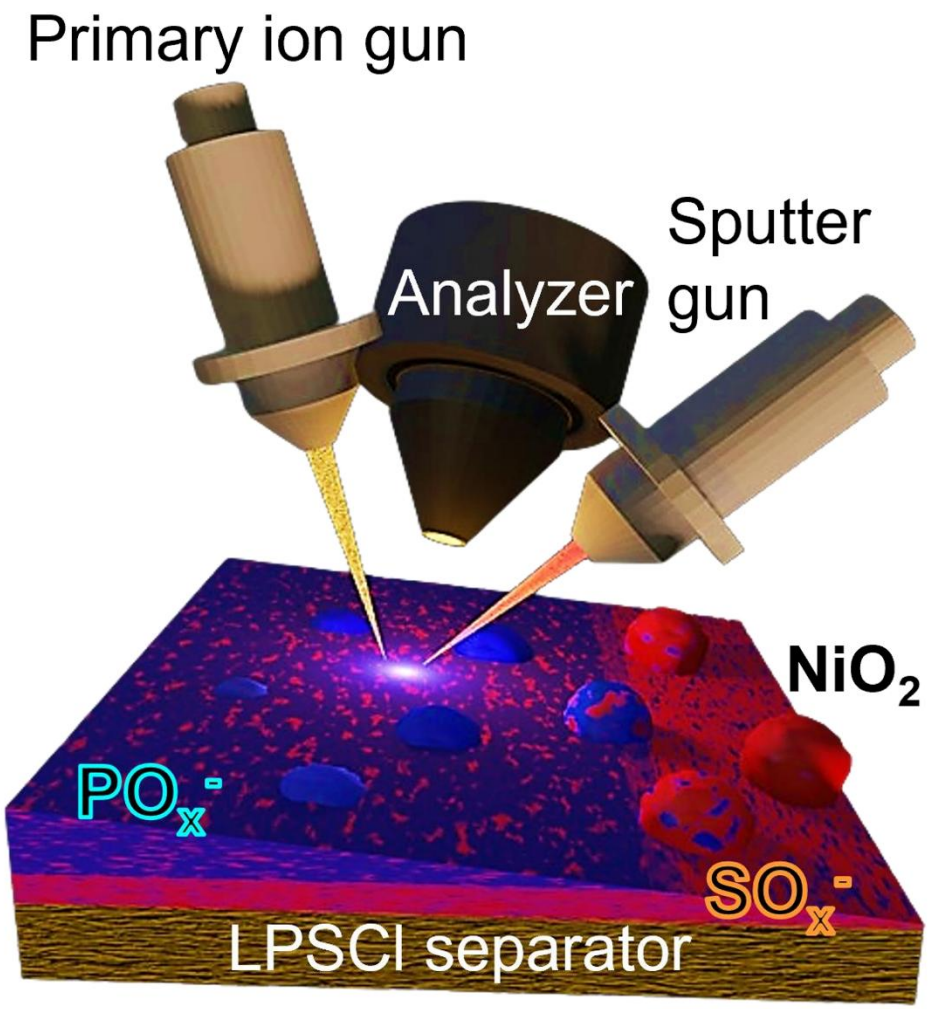

Figure S13. A schematic illustrates wedge-shaped crater formation by increasing sputter dose density from left to right. Subsequently, ToF-SIMS is used to detect the side reaction products. ToF-SIMS detects PO_x^- (PO_2^- and PO_3^-) and SO_x^- (SO_2^- and SO_3^-) decomposition products in the cathode composite of $^{LiIn}SEB^{P\text{-}LNO}$ and $^{LiIn}SEB^{PEC\text{-}LNO}$ before and after cycling.

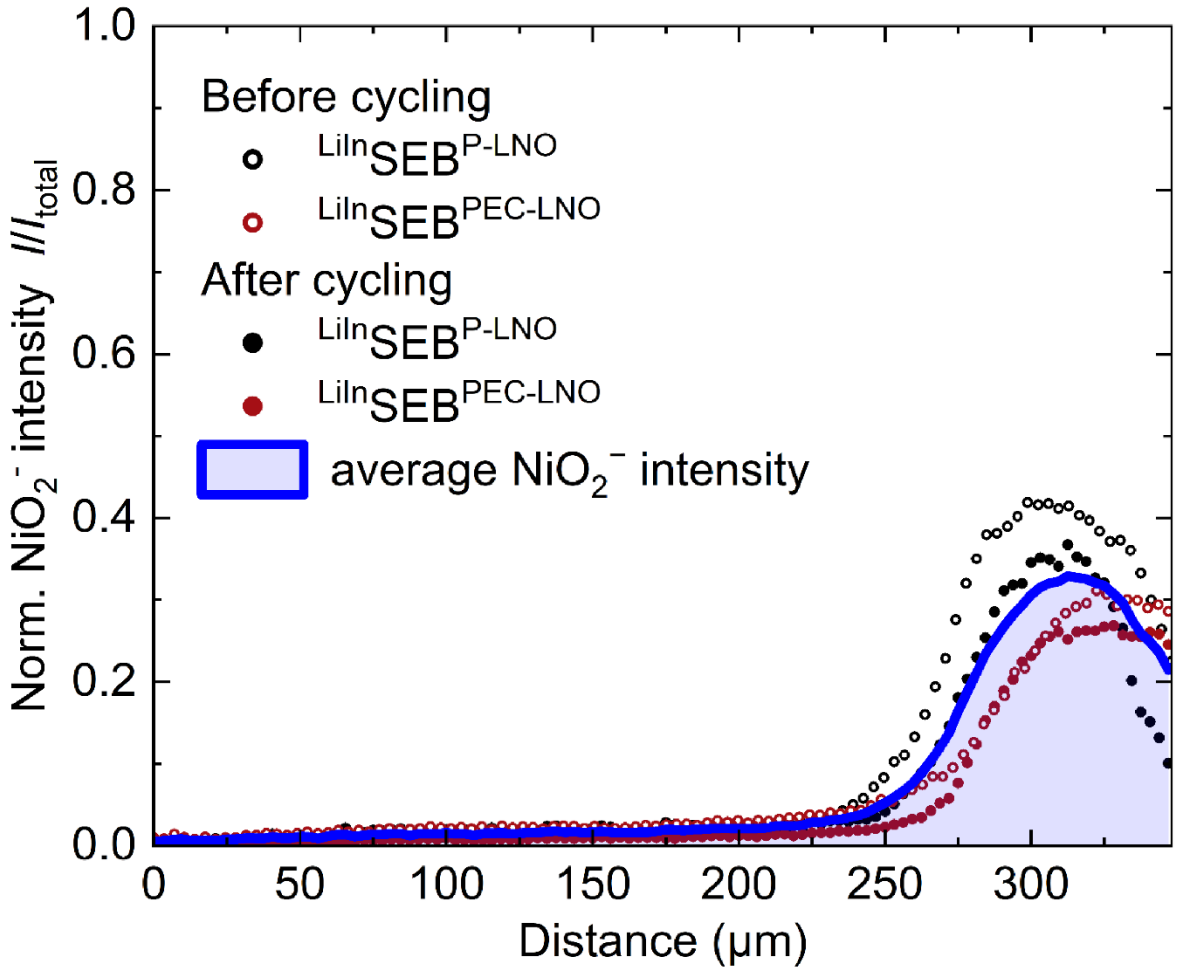

Figure S14. The NiO_2^- intensities (normalized by total intensity), in $^{LiIn}SEB^{P\text{-}LNO}$ and $^{LiIn}SEB^{PEC\text{-}LNO}$ (before and after cycling), are measured using ToF-SIMS surface spectra after creating wedge-shaped sputter craters.

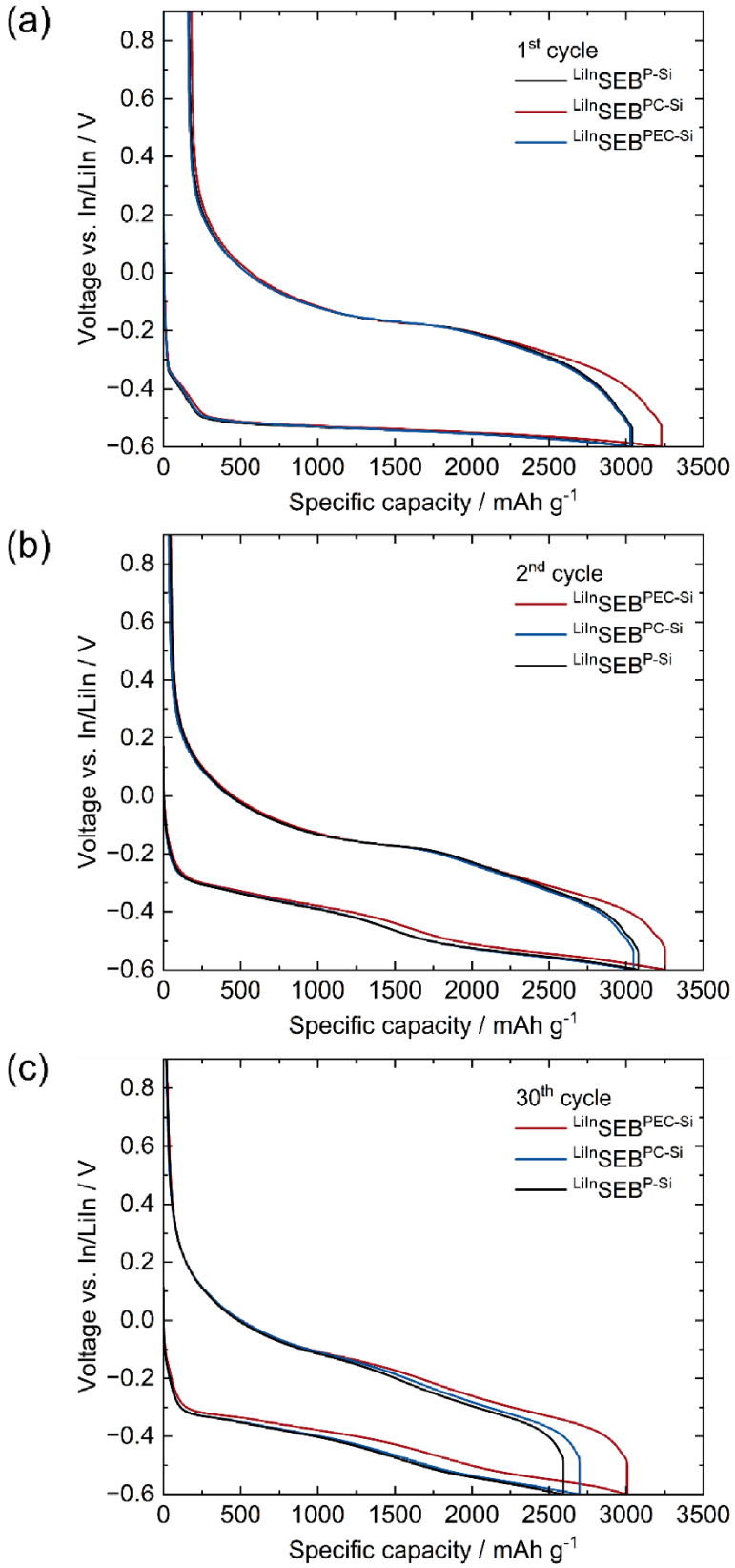

Figure S15. The galvanic plots of $^{LiIn}SEB^{P\text{-}Si}$, $^{LiIn}SEB^{PC\text{-}Si}$, and $^{LiIn}SEB^{PEC\text{-}Si}$ for (a) the 1st cycle at 0.05C, (b) the 2nd cycle at 0.05C, and (c) the 30th cycle at 0.1C are presented.

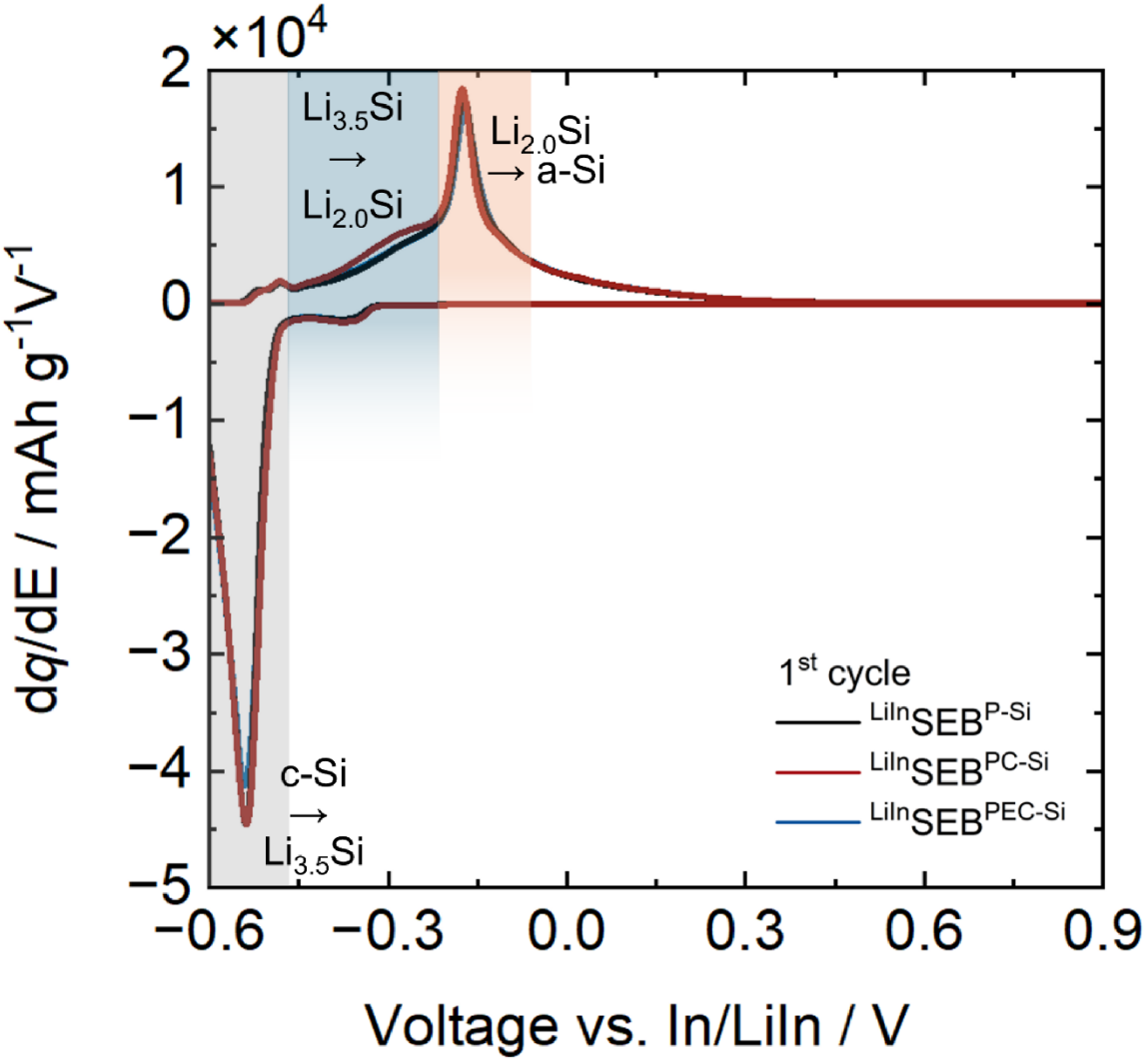

Figure S16. d*q*/dE plots for the first cycles at 0.1C, highlighting the silicon phase transitions (c-Si→$Li_{3.5}Si$↔$Li_{2.0}Si$↔ a-Si).

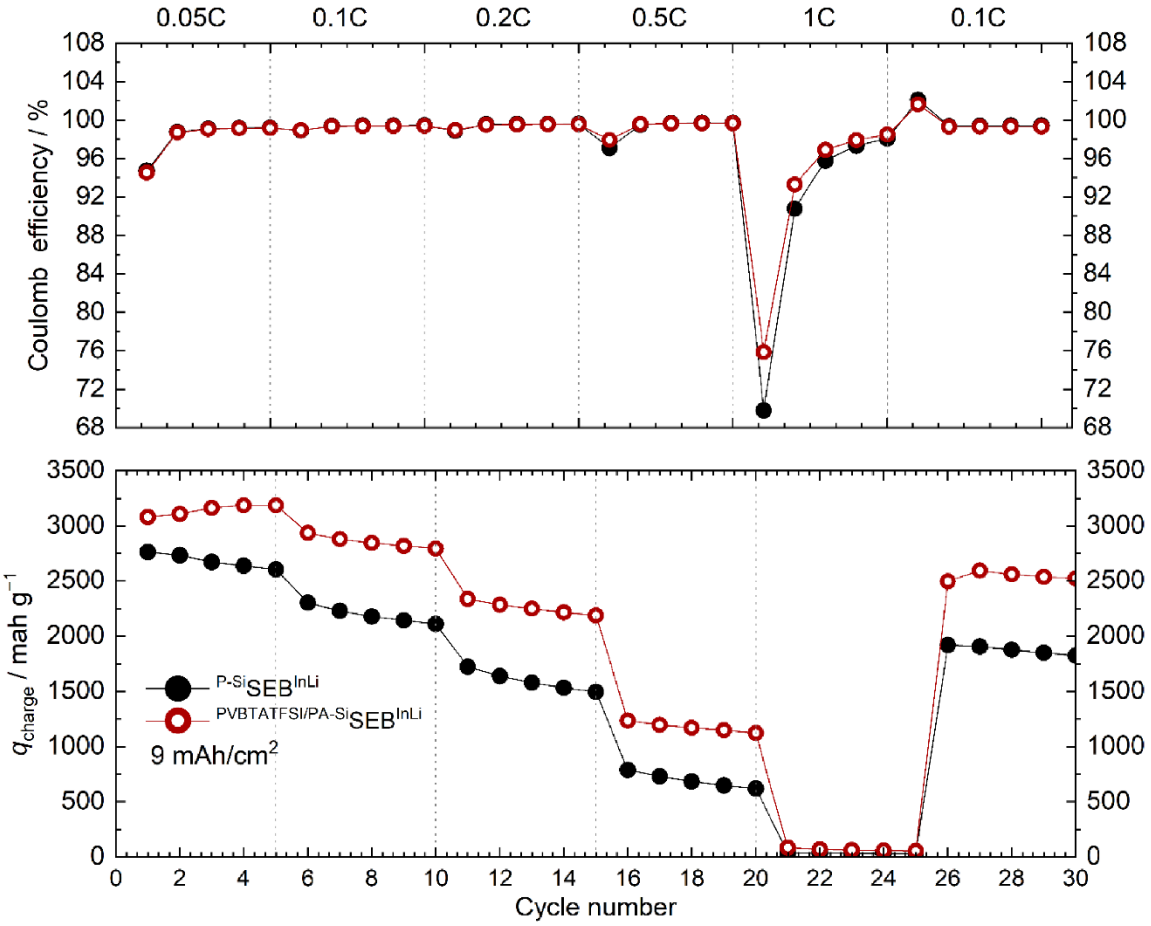

Figure S17. Rate capability of $^{LiIn}SEB^{Si}$ (LiIn|LPSCl|LPSCl/VGCF/Si, 9 mAh cm^{-2}, Si: 2.6 mg cm^{-2}), including $^{LiIn}SEB^{P\text{-}Si}$ and $^{LiIn}SEB^{PEC\text{-}Si}$, is analyzed using pellet-type cells. Coulomb efficiency (top) and q_{charge} (bottom) are presented across different C-rates (0.05C, 0.1C, 0.2C, 0.5C, 1C, and back to 0.1C).

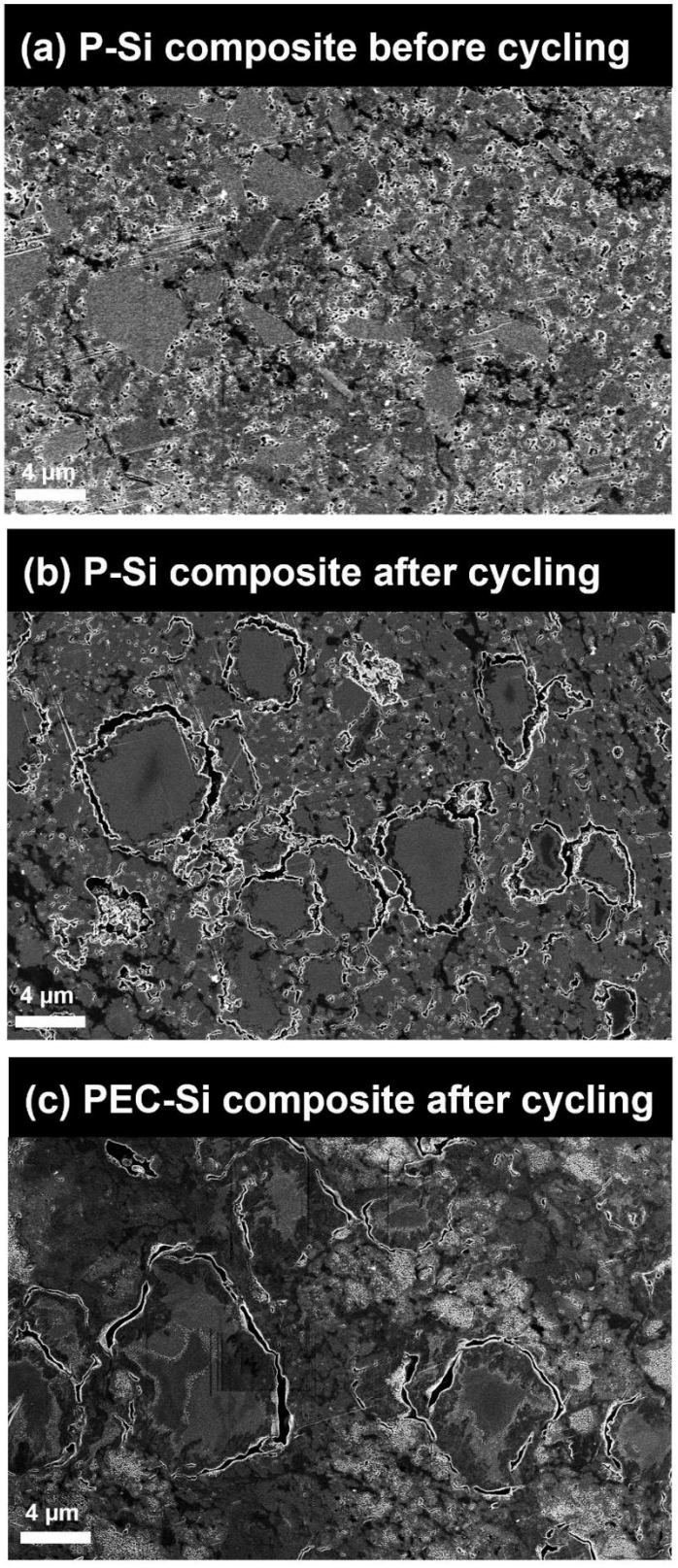

Figure S18. SEM images of cross-sectioned composite cathodes prepared by ion beam milling. (a) P-Si anode composite before cycling, (b) P-Si anode composite after 103 cycles, and (c) PEC-Si anode composite after 103 cycles.

(a)

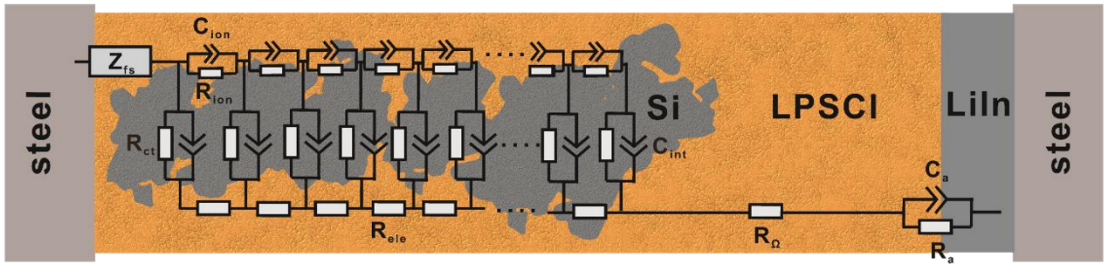

(b)

		$^{Liln}SEB^{PEC\text{-}Si}$			$^{Liln}SEB^{P\text{-}Si}$		
	Cycle	1st	2nd	100th	1st	2nd	100th
Anode composite	R_{anode} / Ω cm²	11.9	12.7	28.0	19.0	19.1	67.6
	R_{ct} / Ω cm²	5.7	6.2	30.3	20.3	19.7	212.8
	R_{ele} / Ω cm²	9.0	10.3	10.3	2.2	2.7	5.8
	R_{ion} / Ω cm²	15.7	15.7	15.7	15.7	15.7	15.7
Liln counter electrode	R_a / Ω cm²	1.6	1.6	52.7	1.6	1.6	59.8
Separator	R_{Ω} / Ω cm²	23.6	23.6	26.7	26.9	26.3	28.8

Figure S19. (a) Schematic illustration of the TLM for impedance fitting includes resistances for R_{ct}, R_{ele}, and R_{ion} in the anode composite, complemented by C_{int} and C_{ion}. $R_{contact}$ in the anode composite includes R_{ele} and R_{ion}. The apex frequency in the first cycle at 8 kHz and 32Hz indicates $R_{contact}$ and R_{ct} for both SEBs, respectively (see **Figure 9c**).[5, 7, 8] The Z_{fs} represents the influence of current constriction.[1] The complete SEB model incorporates R_{Ω}, R_a, and C_a. R_{ct} is used to assess SEI degradation over cycling. However, the Gerischer-type impedance makes it difficult to accurately separate R_{ct} from R_{ele} and R_{ion} in the anode composite.[6] As a result, silicon anode composite resistance (R_{anode}) is calculated via equation [4][6]:

$$R_{\text{anode}} = \sqrt{R_{\text{ct}} \cdot (R_{\text{ele}} + R_{\text{ion}})} \qquad [4]$$

(b) Fitting results of EIS using TLM under the 0.05 C cycling at 1st, 2nd, and 100th cycles.

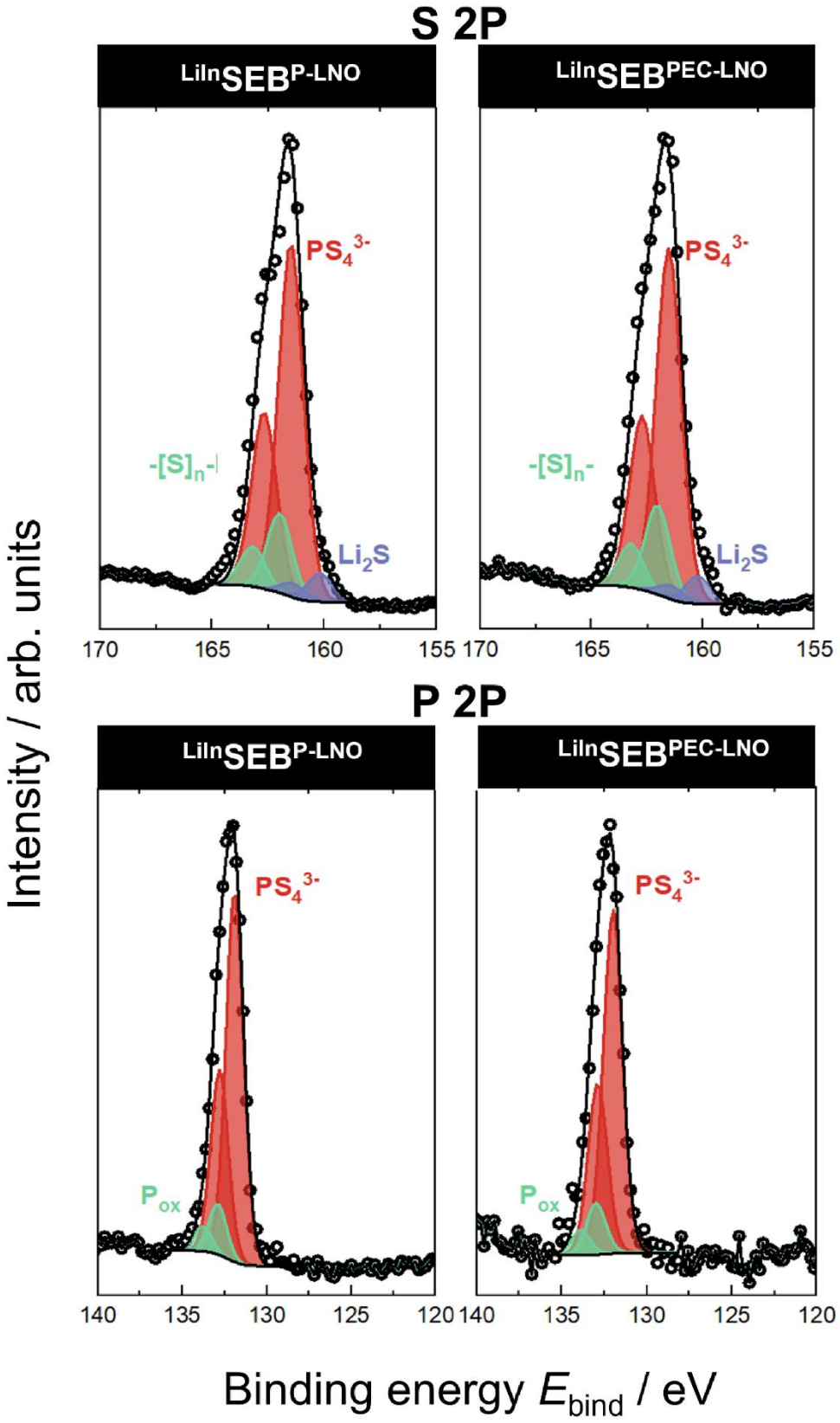

Figure S20. S 2p, and P 2p XPS spectra compare the side reaction products of $^{LiIn}SEB^{P\text{-}Si}$ and $^{LiIn}SEB^{PEC\text{-}Si}$ after cycling.

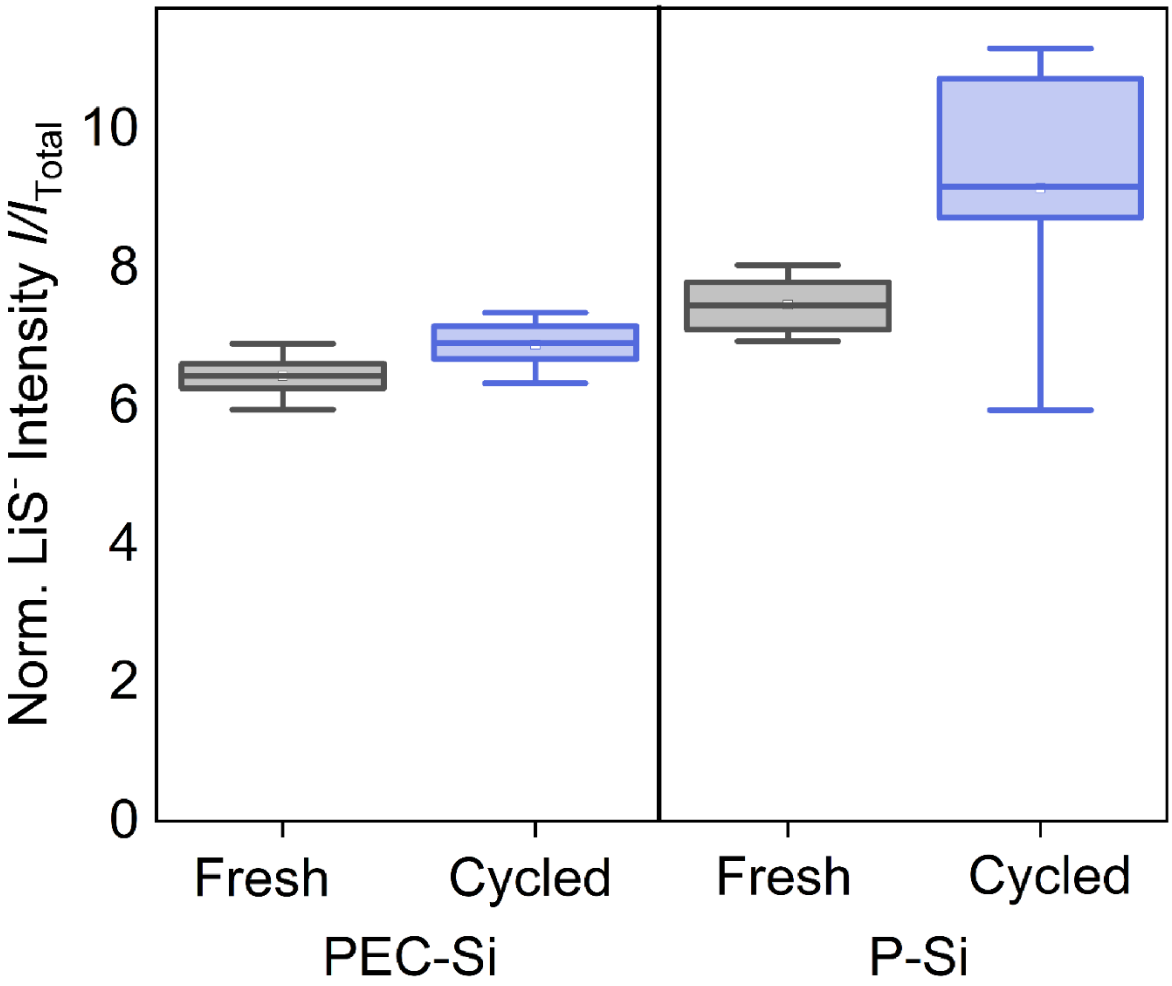

Figure S21. ToF-SIMS detects the LiS^- fragment which represenrts Li_2S decomposition products at the SEI in $^{LiIn}SEB^{P\text{-}Si}$ and $^{LiIn}SEB^{PEC\text{-}Si}$. The LiS^- fragment intensity is presented as boxplots with normalized intensities based on six data points.

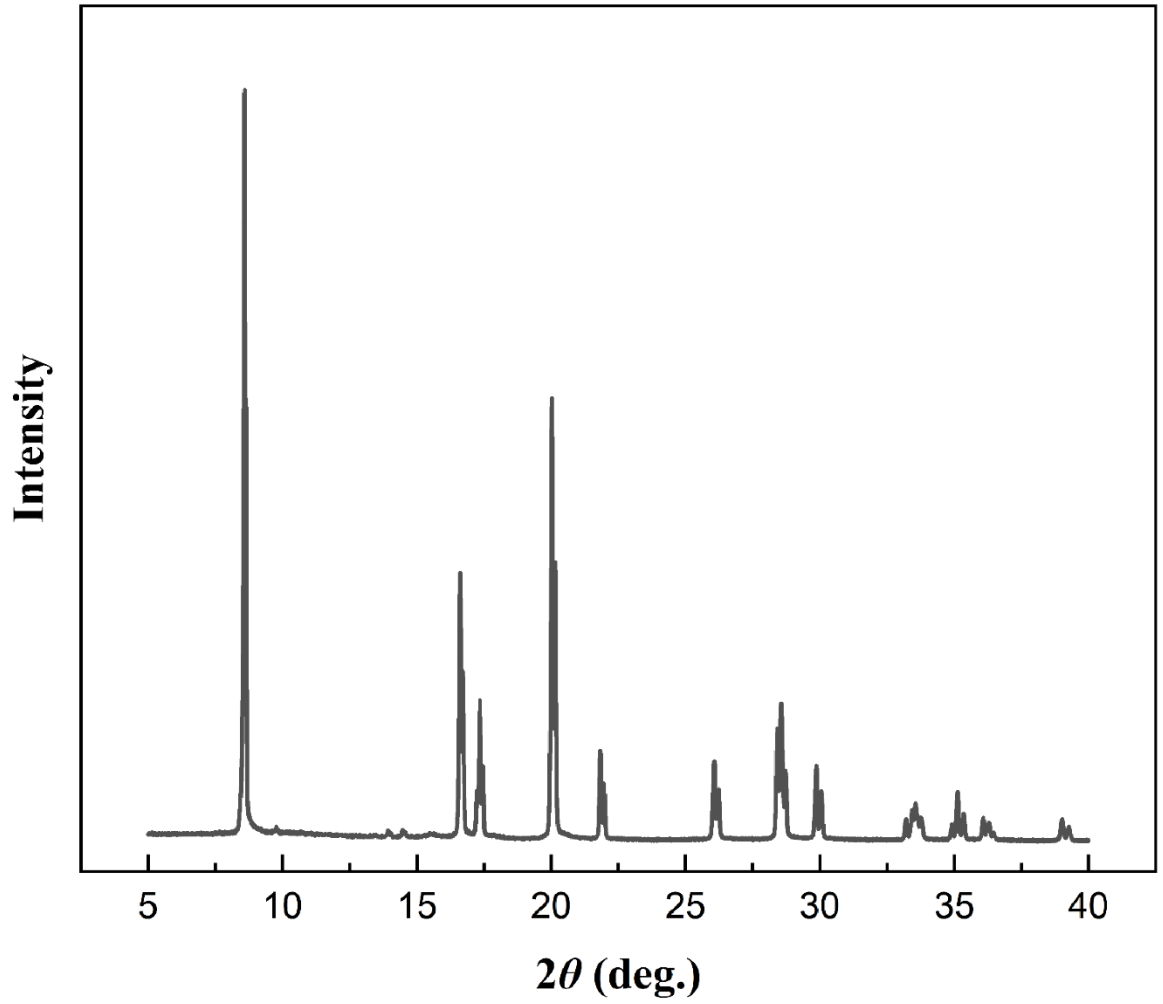

Figure S22. XRD is performed to check the crystalline structure of LNO.

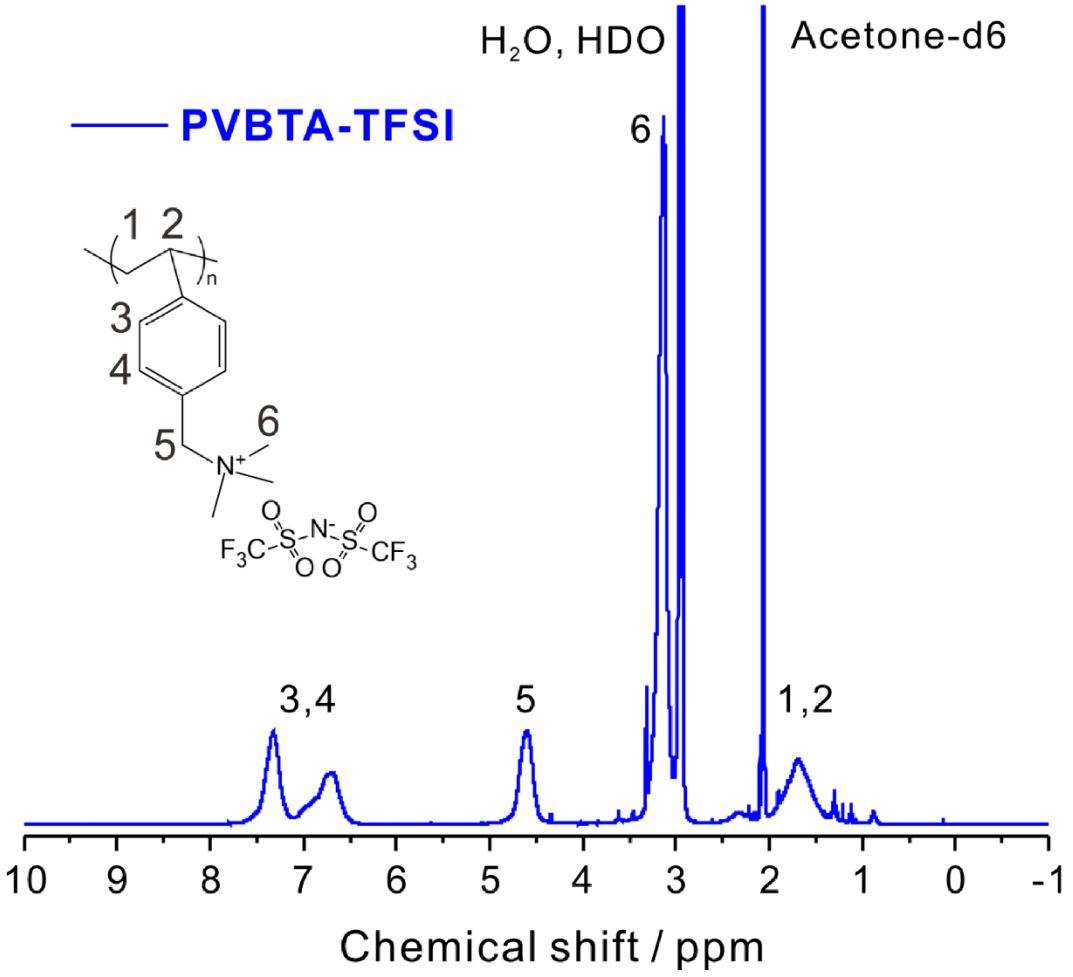

Figure S23. ^{1}H NMR spectra (400 MHz) of PVBTA-TFSI in deuterated acetone. δ(ppm): 7.32 (s, 2H), 6.68 (s, 2H), 4.58 (s, 2H), 3.12 (s, 9H), 1.68 (s, 3H)

References

1. G. Conforto, R. Ruess, D. Schröder, E. Trevisanello, R. Fantin, F. H. Richter and J. Janek, *Journal of The Electrochemical Society*, 2021, **168**, 070546.
2. B.-X. Shi, Y. Yusim, S. Sen, T. Demuth, R. Ruess, K. Volz, A. Henss and F. H. Richter, *Advanced Energy Materials*, 2023, **13**, 2300310.
3. J. Song and M. Z. Bazant, *Journal of The Electrochemical Society*, 2013, **160**, A15.
4. J. Song and M. Z. Bazant, *Electrochimica Acta*, 2014, **131**, 214-227.
5. R. Ruess, S. Schweidler, H. Hemmelmann, G. Conforto, A. Bielefeld, D. A. Weber, J. Sann, M. T. Elm and J. Janek, *Journal of The Electrochemical Society*, 2020, **167**, 100532.
6. T.-T. Zuo, F. Walther, J. H. Teo, R. Rueß, Y. Wang, M. Rohnke, D. Schröder, L. F. Nazar and J. Janek, *Angewandte Chemie International Edition*, 2023, **62**, e202213228.
7. L. Zhang, Y. Dai, C. Li, Y. Dang, R. Zheng, Z. Wang, Y. Wang, Y. Cui, H. Arandiyan, Z. Shao, H. Sun, Q. Zhuang and Y. Liu, *Energy Storage Materials*, 2024, **69**, 103378.
8. E. Trevisanello, R. Ruess, G. Conforto, F. H. Richter and J. Janek, *Advanced Energy Materials*, 2021, **11**, 2003400.

4. Summary and Outlook

Figure 17 illustrates the improvements of the CEI and SEI contributed by the polymer coating and modified Li_6PS_5Cl. **Publications A** and **B** focus on polymer-coated NCM, while **Publication D** investigates polymer-coated LNO and Si. The key advantages of polymer coatings are their relatively low Young's modulus, binding ability, and easier processing than inorganic coatings. On the other hand, **Publication C** explores a solvent-based modification for the sulfide-based SE, highlighting its potential for industrial scalability.

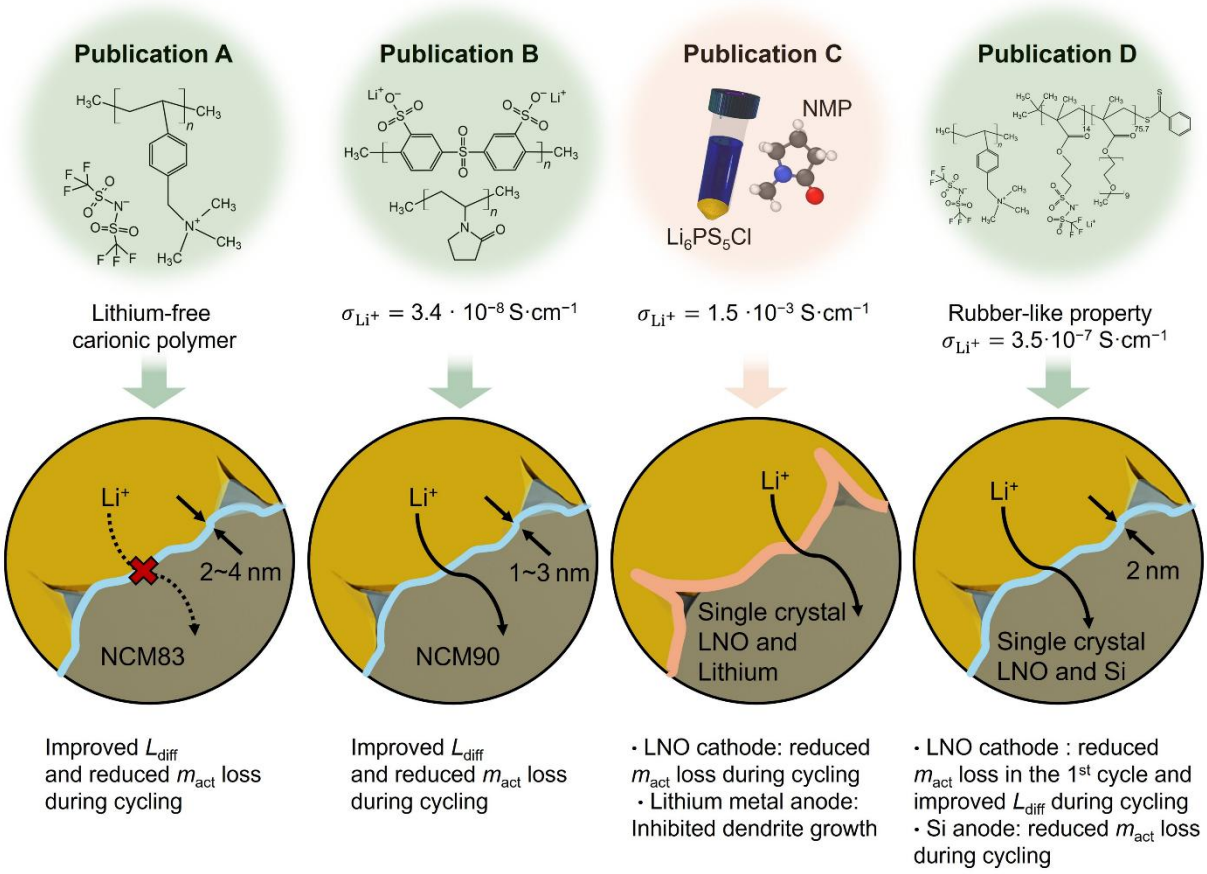

Figure 17. Overview of the four publications, highlighting the key materials innovations and ionic conductivities in the top row of four circles and the corresponding interface-degradation mechanisms in the bottom row of four circles. All the improvements achieved by polymer coatings and the modified Li_6PS_5Cl are explained by mitigating the loss of m_{act} and growth of L_{diff}. The thickness of each polymer coating is indicated within the bottom circles.

The spray-drying method offers a scalable coating process that creates coatings with less than 4 nanometers thickness. Notably, the spray-drying method requires the solvent to be stable against the materials. Additionally, the boiling point should be as low as possible. For instance, the boiling point of NMP is over 200 °C, which cannot be dried successfully during the spray-drying process. Although the custom-designed spray-drying instrument can maybe operate at temperatures well above 200 °C, it remains unclear whether the high temperatures might affect the stability of the polymer coating.

Achieving complete coverage of polymer coatings on high-nickel CAMs requires sufficient electrostatic interactions between the CAM surface and the polymer. Therefore, the polymer must contain functional groups that enhance electrostatic interactions, such as amide functional group and cationic ionic species. However, while the polycation coating improves cycling stability, as demonstrated in **Publication A**, its lack of lithium source leads to capacity loss. Moreover, PVP degrades performance due to its ionic insulation. Although the polyanion can provide σ_{Li^+}, a polyanion alone does not generate enough electrostatic force for high-nickel CAMs and thus needs a coating inducer. As a result, **Publications B** and **D** utilize PVP and PVBTA-TFSI as coating inducers coupled with polyanions, respectively. Additionally, copolymerizing the amide functional group with a polyanion can achieve similar effects, although further research is needed.

Moreover, the rubber-like coating improves protection by accommodating electrode volume changes during cycling. It is also less prone to defects during fabrication and at the contact points between electrode particles. However, **Publication D** brings out the necessity to investigate an optimization of the Young's modulus range of the polymer coating layer in future work. Especially for the Si anode, which experiences about a 300% volume change, the Young's modulus plays a critical role in the effectiveness of the coating protection during cycling.

Achieving a σ_{Li^+} greater than 0.1 μS·cm^{-1} in a polymer coating about 1 nm thick is critical for first-cycle capacity and rate capability. A polycation coating without a lithium-ion source may give additional interfacial resistance, leading to capacity loss. Therefore, incorporating a polyanion that provides σ_{Li^+} is essential. Charge transfer at the coating/Li_6PS_5Cl and coating/CAM interfaces should also be considered. While the studies in this dissertation do not show a pronounced contribution from this factor, it warrants further study.

In the EIS measurements, the charge-transfer resistance at the CEI overlaps with the transport resistance arising from poor contact between CAM or Si particles. Although the transport resistance can be measured before cycling by assembling a symmetrical cell with electronically and ionically blocking electrodes,[200] separating these resistances at a specific SOC becomes challenging during cycling. This is because the SOC changes charge-transfer resistance and the diffusion coefficient of the electrode bulk material during cycling. As a result, it is worthy to design an experimental device that separates charge-transfer resistance from transport resistance. This approach may also help elucidate the charge transfer processes at the coating/Li_6PS_5Cl and coating/CAM interfaces.

The results of this dissertation show that polymer coatings reduce side reactions at CAM/Li_6PS_5Cl and

prevents chemo-mechanical cracking in CAMs. For high-nickel NCMs, coatings mitigate m_{act} loss by reducing degradation and CEI formation. Additionally, coatings slow the L_{diff} growth through decreased cracking and CEI degradation. However, CEI degradation, cracking, and contact loss can somewhat cross-affect m_{act} loss and L_{diff} growth. **Publication D** uses single-crystal LNO as a reference material and controls the pressure at 60 MPa, which helps focus on CEI degradation as the primary contributor to m_{act} loss and L_{diff} growth. As a result, the polymer coating reduces m_{act} loss, which only occurs in the first cycle, by mitigating elemental sulfur and polysulfide side reactions. In addition, the polymer coating layer reduces L_{diff} growth during cycling by mitigating formation of oxygenated products, such as sulfates and phosphates.

Nevertheless, the Si anode does not exhibit particle cracking but suffers severe contact loss due to dramatic volume changes. This capacity loss is primarily attributed to contact loss and SEI degradation, which produces insulating side reaction products. Consequently, the polymer coating can mitigate m_{act} loss due to SEI degradation of the silicon anode. Further investigation is warranted to optimize the mechanical properties of polymer coatings and to explore binder strategies that mitigate contact loss during cycling of Si anode particles.

The modified Li_6PS_5Cl in **Publication C** is tested with the same LNO reference and measurement conditions in **Publication D**, enabling a direct comparison of the protective effects of Li_6PS_5Cl modification and polymer coatings. Interestingly, the modification layer mitigates the m_{act} loss during cycling but does not improve m_{act} in the first cycle. Furthermore, L_{diff} growth is the same for both modified and pristine Li_6PS_5Cl. This indicates that the CEI formation process between modified Li_6PS_5Cl/LNO and Li_6PS_5Cl/polymer-coated LNO may be different. Moreover, it demonstrates the possibility of combining modified Li_6PS_5Cl as a catholyte with polymer-coated LNO can maybe have more improvement of the SEB performance.

On the other hand, the modified Li_6PS_5Cl helps mitigate dendrite formation from the lithium metal anode by promoting the formation of Li_3N as a component of the SEI. This observation suggests that alternative solvents with different properties could be used to design the artificial SEI. However, polysulfide formation is unfavorable because it increases interfacial resistance due to its ionic insulation and may even induce current inhomogeneity, leading to dendrite formation. Consequently, reducing polysulfide formation is a key milestone for future work.

5. Appendix

5.1 References

1. A. P. Hauel, *Transactions of The Electrochemical Society*, 1939, **76**, 435.
2. S. Arya and S. Verma, in *Rechargeable Batteries*, 2020, DOI: https://doi.org/10.1002/9781119714774.ch8, pp. 131-175.
3. S. Sen and F. H. Richter, *Advanced Science*, 2023, **10**, 2303985.
4. Z. Lu, D. D. MacNeil and J. R. Dahn, *Electrochemical and Solid-State Letters*, 2001, **4**, A200.
5. Q. Li, X. Yu and H. Li, *eTransportation*, 2022, **14**, 100201.
6. J. Janek and W. G. Zeier, *Nature Energy*, 2016, **1**, 16141.
7. J. Janek and W. G. Zeier, *Nature Energy*, 2023, **8**, 230-240.
8. P. Albertus, V. Anandan, C. Ban, N. Balsara, I. Belharouak, J. Buettner-Garrett, Z. Chen, C. Daniel, M. Doeff, N. J. Dudney, B. Dunn, S. J. Harris, S. Herle, E. Herbert, S. Kalnaus, J. A. Libera, D. Lu, S. Martin, B. D. McCloskey, M. T. McDowell, Y. S. Meng, J. Nanda, J. Sakamoto, E. C. Self, S. Tepavcevic, E. Wachsman, C. Wang, A. S. Westover, J. Xiao and T. Yersak, *ACS Energy Letters*, 2021, **6**, 1399-1404.
9. M. Shoji, E. J. Cheng, T. Kimura and K. Kanamura, *Journal of Physics D: Applied Physics*, 2019, **52**, 103001.
10. Y.-G. Lee, S. Fujiki, C. Jung, N. Suzuki, N. Yashiro, R. Omoda, D.-S. Ko, T. Shiratsuchi, T. Sugimoto, S. Ryu, J. H. Ku, T. Watanabe, Y. Park, Y. Aihara, D. Im and I. T. Han, *Nature Energy*, 2020, **5**, 299-308.
11. S. Sen, E. Trevisanello, E. Niemöller, B.-X. Shi, F. J. Simon and F. H. Richter, *Journal of Materials Chemistry A*, 2021, **9**, 18701-18732.
12. A. Manthiram, X. Yu and S. Wang, *Nature Reviews Materials*, 2017, **2**, 16103.
13. J. Schnell, H. Knörzer, A. J. Imbsweiler and G. Reinhart, *Energy Technology*, 2020, **8**, 1901237.
14. R. Wei, S. Chen, T. Gao and W. Liu, *Nano Select*, 2021, **2**, 2256-2274.
15. Y. Ren, K. Chen, R. Chen, T. Liu, Y. Zhang and C.-W. Nan, *Journal of the American Ceramic Society*, 2015, **98**, 3603-3623.
16. J. S. Kim, S. Jung, H. Kwak, Y. Han, S. Kim, J. Lim, Y. M. Lee and Y. S. Jung, *Energy Storage Materials*, 2023, **55**, 193-204.

17. X. Li, J. Liang, X. Yang, K. R. Adair, C. Wang, F. Zhao and X. Sun, *Energy & Environmental Science*, 2020, **13**, 1429-1461.

18. S. Narayanan, U. Ulissi, J. S. Gibson, Y. A. Chart, R. S. Weatherup and M. Pasta, *Nature Communications*, 2022, **13**, 7237.

19. Y. Li, S. Song, H. Kim, K. Nomoto, H. Kim, X. Sun, S. Hori, K. Suzuki, N. Matsui, M. Hirayama, T. Mizoguchi, T. Saito, T. Kamiyama and R. Kanno, *Science*, 2023, **381**, 50-53.

20. Q. Zhang, D. Cao, Y. Ma, A. Natan, P. Aurora and H. Zhu, *Advanced Materials*, 2019, **31**, 1901131.

21. A. Bielefeld, D. A. Weber and J. Janek, *ACS Applied Materials & Interfaces*, 2020, **12**, 12821-12833.

22. H. Cho, J. Kim, M. Kim, H. An, K. Min and K. Park, *Journal of Power Sources*, 2024, **597**, 234132.

23. H. Rostami, J. Valio, P. Tynjälä, U. Lassi and P. Suominen, *ChemPhysChem*, 2024, **25**, e202400459.

24. W. Cao, J. Zhang and H. Li, *Energy Storage Materials*, 2020, **26**, 46-55.

25. R. Robert, C. Villevieille and P. Novák, *Journal of Materials Chemistry A*, 2014, **2**, 8589-8598.

26. K. Mizushima, P. C. Jones, P. J. Wiseman and J. B. Goodenough, *Materials Research Bulletin*, 1980, **15**, 783-789.

27. Y. Lyu, X. Wu, K. Wang, Z. Feng, T. Cheng, Y. Liu, M. Wang, R. Chen, L. Xu, J. Zhou, Y. Lu and B. Guo, *Advanced Energy Materials*, 2021, **11**, 2000982.

28. J. Ma, T. Liu, J. Ma, C. Zhang and J. Yang, *Advanced Science*, 2024, **11**, 2304938.

29. J. Kasnatscheew, S. Röser, M. Börner and M. Winter, *ACS Applied Energy Materials*, 2019, **2**, 7733-7737.

30. M. Bianchini, M. Roca-Ayats, P. Hartmann, T. Brezesinski and J. Janek, *Angewandte Chemie International Edition*, 2019, **58**, 10434-10458.

31. K. H. Choi, X. Liu, X. Ding and Q. Li, *Ionics*, 2020, **26**, 1063-1080.

32. C. S. Yoon, K.-J. Park, U.-H. Kim, K. H. Kang, H.-H. Ryu and Y.-K. Sun, *Chemistry of Materials*, 2017, **29**, 10436-10445.

33. C. M. Julien and A. Mauger, *Energies*, 2020, **13**, 6363.

34. F. I. Saaid, M. F. Kasim, T. Winie, K. A. Elong, A. Azahidi, N. D. Basri, M. K.

Yaakob, M. S. Mastuli, S. N. Amira Shaffee, M. Z. Zolkiffly and M. R. Mahmood, *Heliyon*, 2024, **10**, e23968.

35. P. Kurzhals, F. Riewald, M. Bianchini, H. Sommer, H. A. Gasteiger and J. Janek, *Journal of The Electrochemical Society*, 2021, **168**, 110518.

36. R. Rueß, D. Gomboso, M. Ulherr, E. Trevisanello, Y. Ma, A. Kondrakov, T. Brezesinski and J. Janek, *Journal of The Electrochemical Society*, 2023, **170**, 020533.

37. C. A. Heck, M.-W. von Horstig, F. Huttner, J. K. Mayer, W. Haselrieder and A. Kwade, *Journal of The Electrochemical Society*, 2020, **167**, 160521.

38. B. Aktekin, A. E. Sedykh, K. Müller-Buschbaum, A. Henss and J. Janek, *Advanced Functional Materials*, 2024, **34**, 2313252.

39. D. Pritzl, T. Teufl, A. T. S. Freiberg, B. Strehle, J. Sicklinger, H. Sommer, P. Hartmann and H. A. Gasteiger, *Journal of The Electrochemical Society*, 2019, **166**, A4056.

40. Y. Bi, Q. Li, R. Yi and J. Xiao, *Journal of The Electrochemical Society*, 2022, **169**, 020521.

41. I. Hamam, N. Zhang, A. Liu, M. B. Johnson and J. R. Dahn, *Journal of The Electrochemical Society*, 2020, **167**, 130521.

42. S. E. Renfrew and B. D. McCloskey, *Journal of the American Chemical Society*, 2017, **139**, 17853-17860.

43. L. A. Kaufman and B. D. McCloskey, *Chemistry of Materials*, 2021, **33**, 4170-4176.

44. H. Visbal, S. Fujiki, Y. Aihara, T. Watanabe, Y. Park and S. Doo, *Journal of Power Sources*, 2014, **269**, 396-402.

45. T. Bartsch, F. Strauss, T. Hatsukade, A. Schiele, A. Y. Kim, P. Hartmann, J. Janek and T. Brezesinski, *ACS Energy Letters*, 2018, **3**, 2539-2543.

46. A. A. Delluva, J. Kulberg-Savercool and A. Holewinski, *Advanced Functional Materials*, 2021, **31**, 2103716.

47. M. Mock, M. Bianchini, F. Fauth, K. Albe and S. Sicolo, *Journal of Materials Chemistry A*, 2021, **9**, 14928-14940.

48. H. Li, W. Hua, X. Liu-Théato, Q. Fu, M. Desmau, A. Missyul, M. Knapp, H. Ehrenberg and S. Indris, *Chemistry of Materials*, 2021, **33**, 9546-9559.

49. S. S. Zhang, *Energy Storage Materials*, 2020, **24**, 247-254.

50. H. Zhang, H. Liu, L. F. J. Piper, M. S. Whittingham and G. Zhou, *Chemical Reviews*, 2022, **122**, 5641-5681.

51. G. Conforto, R. Ruess, D. Schröder, E. Trevisanello, R. Fantin, F. H. Richter and J. Janek, *Journal of The Electrochemical Society*, 2021, **168**, 070546.

52. S. Sicolo, M. Sadowski, K. Vettori, M. Bianchini, J. Janek and K. Albe, *Chemistry of Materials*, 2024, **36**, 492-500.

53. C. Hong, Q. Leng, J. Zhu, S. Zheng, H. He, Y. Li, R. Liu, J. Wan and Y. Yang, *Journal of Materials Chemistry A*, 2020, **8**, 8540-8547.

54. A. Van der Ven, J. C. Thomas, Q. Xu, B. Swoboda and D. Morgan, *Physical Review B*, 2008, **78**, 104306.

55. J. P. Peres, C. Delmas, A. Rougier, M. Broussely, F. Perton, P. Biensan and P. Willmann, *Journal of Physics and Chemistry of Solids*, 1996, **57**, 1057-1060.

56. Q. Xie, Z. Cui and A. Manthiram, *Advanced Materials*, 2021, **33**, 2100804.

57. H. Li, A. Liu, N. Zhang, Y. Wang, S. Yin, H. Wu and J. R. Dahn, *Chemistry of Materials*, 2019, **31**, 7574-7583.

58. W. Lee, S. Muhammad, T. Kim, H. Kim, E. Lee, M. Jeong, S. Son, J.-H. Ryou and W.-S. Yoon, *Advanced Energy Materials*, 2018, **8**, 1701788.

59. L. de Biasi, A. Schiele, M. Roca-Ayats, G. Garcia, T. Brezesinski, P. Hartmann and J. Janek, *ChemSusChem*, 2019, **12**, 2240-2250.

60. H.-H. Ryu, K.-J. Park, C. S. Yoon and Y.-K. Sun, *Chemistry of Materials*, 2018, **30**, 1155-1163.

61. S. P. Culver, R. Koerver, W. G. Zeier and J. Janek, *Advanced Energy Materials*, 2019, **9**, 1900626.

62. T.-T. Zuo, R. Rueß, R. Pan, F. Walther, M. Rohnke, S. Hori, R. Kanno, D. Schröder and J. Janek, *Nature Communications*, 2021, **12**, 6669.

63. L. Wang, T. Maxisch and G. Ceder, *Chemistry of Materials*, 2007, **19**, 543-552.

64. I. Takahashi, H. Kiuchi, A. Ohma, T. Fukunaga and E. Matsubara, *The Journal of Physical Chemistry C*, 2020, **124**, 9243-9248.

65. Z. Han, D. Zhang, H. Wang, G. Zheng, M. Liu and Y. He, *Acta Physico-Chimica Sinica*, 2024, **40**, 2307034.

66. W. Liu, P. Oh, X. Liu, M.-J. Lee, W. Cho, S. Chae, Y. Kim and J. Cho, *Angewandte Chemie International Edition*, 2015, **54**, 4440-4457.

67. M. Uitz, V. Epp, P. Bottke and M. Wilkening, *Journal of Electroceramics*, 2017,

38, 142-156.

68. I. P. Parkin, *Applied Organometallic Chemistry*, 2000, **14**, 227-228.
69. R. Kanno and M. Murayama, *Journal of The Electrochemical Society*, 2001, **148**, A742.
70. D. Ravaine, *Journal of Non-Crystalline Solids*, 1980, **38-39**, 353-358.
71. H. Guo, Q. Wang, A. Urban and N. Artrith, *Chemistry of Materials*, 2022, **34**, 6702-6712.
72. F. Mizuno, A. Hayashi, K. Tadanaga and M. Tatsumisago, *Advanced Materials*, 2005, **17**, 918-921.
73. F. Mizuno, A. Hayashi, K. Tadanaga and M. Tatsumisago, *Solid State Ionics*, 2006, **177**, 2721-2725.
74. C. Dietrich, D. A. Weber, S. Culver, A. Senyshyn, S. J. Sedlmaier, S. Indris, J. Janek and W. G. Zeier, *Inorganic Chemistry*, 2017, **56**, 6681-6687.
75. R. Mercier, J. P. Malugani, B. Fahys, J. Douglande and G. Robert, *Journal of Solid State Chemistry*, 1982, **43**, 151-162.
76. C. Dietrich, M. Sadowski, S. Sicolo, D. A. Weber, S. J. Sedlmaier, K. S. Weldert, S. Indris, K. Albe, J. Janek and W. G. Zeier, *Chemistry of Materials*, 2016, **28**, 8764-8773.
77. S. Neuberger, S. P. Culver, H. Eckert, W. G. Zeier and J. Schmedt auf der Günne, *Dalton Transactions*, 2018, **47**, 11691-11695.
78. K. Minami, A. Hayashi and M. Tatsumisago, *Journal of the American Ceramic Society*, 2011, **94**, 1779-1783.
79. Y. Seino, T. Ota, K. Takada, A. Hayashi and M. Tatsumisago, *Energy & Environmental Science*, 2014, **7**, 627-631.
80. I.-H. Chu, H. Nguyen, S. Hy, Y.-C. Lin, Z. Wang, Z. Xu, Z. Deng, Y. S. Meng and S. P. Ong, *ACS Applied Materials & Interfaces*, 2016, **8**, 7843-7853.
81. M. R. Busche, D. A. Weber, Y. Schneider, C. Dietrich, S. Wenzel, T. Leichtweiss, D. Schröder, W. Zhang, H. Weigand, D. Walter, S. J. Sedlmaier, D. Houtarde, L. F. Nazar and J. Janek, *Chemistry of Materials*, 2016, **28**, 6152-6165.
82. S. Wenzel, D. A. Weber, T. Leichtweiss, M. R. Busche, J. Sann and J. Janek, *Solid State Ionics*, 2016, **286**, 24-33.
83. C. Dietrich, D. A. Weber, S. J. Sedlmaier, S. Indris, S. P. Culver, D. Walter, J. Janek and W. G. Zeier, *Journal of Materials Chemistry A*, 2017, **5**, 18111-18119.

84. H. Gamo, A. Nagai and A. Matsuda, *Scientific Reports*, 2021, **11**, 21097.

85. M. Tachez, J.-P. Malugani, R. Mercier and G. Robert, *Solid State Ionics*, 1984, **14**, 181-185.

86. K. Homma, M. Yonemura, T. Kobayashi, M. Nagao, M. Hirayama and R. Kanno, *Solid State Ionics*, 2011, **182**, 53-58.

87. Z. Liu, W. Fu, E. A. Payzant, X. Yu, Z. Wu, N. J. Dudney, J. Kiggans, K. Hong, A. J. Rondinone and C. Liang, *Journal of the American Chemical Society*, 2013, **135**, 975-978.

88. E. C. Self, Z. D. Hood, T. Brahmbhatt, F. M. Delnick, H. M. Meyer, III, G. Yang, J. L. M. Rupp and J. Nanda, *Chemistry of Materials*, 2020, **32**, 8789-8797.

89. S. T. Kong, Ö. Gün, B. Koch, H. J. Deiseroth, H. Eckert and C. Reiner, *Chemistry – A European Journal*, 2010, **16**, 5138-5147.

90. Z. Liu, T. Zinkevich, S. Indris, X. He, J. Liu, W. Xu, J. Bai, S. Xiong, Y. Mo and H. Chen, *Inorganic Chemistry*, 2020, **59**, 226-234.

91. D. Liu, W. Zhu, Z. Feng, A. Guerfi, A. Vijh and K. Zaghib, *Materials Science and Engineering: B*, 2016, **213**, 169-176.

92. H.-J. Deiseroth, S.-T. Kong, H. Eckert, J. Vannahme, C. Reiner, T. Zaiß and M. Schlosser, *Angewandte Chemie International Edition*, 2008, **47**, 755-758.

93. H. M. Chen, C. Maohua and S. Adams, *Physical Chemistry Chemical Physics*, 2015, **17**, 16494-16506.

94. B. Aktekin, L. M. Riegger, S.-K. Otto, T. Fuchs, A. Henss and J. Janek, *Nature Communications*, 2023, **14**, 6946.

95. Q. Zheng, Y. Song, W. Huang, J. Yang, T. Li and Y. Xu, *Energy Storage Materials*, 2023, **63**, 103038.

96. D. H. S. Tan, E. A. Wu, H. Nguyen, Z. Chen, M. A. T. Marple, J.-M. Doux, X. Wang, H. Yang, A. Banerjee and Y. S. Meng, *ACS Energy Letters*, 2019, **4**, 2418-2427.

97. S. Wang, M. Tang, Q. Zhang, B. Li, S. Ohno, F. Walther, R. Pan, X. Xu, C. Xin, W. Zhang, L. Li, Y. Shen, F. H. Richter, J. Janek and C.-W. Nan, *Advanced Energy Materials*, 2021, **11**, 2101370.

98. G. F. Dewald, S. Ohno, M. A. Kraft, R. Koerver, P. Till, N. M. Vargas-Barbosa, J. Janek and W. G. Zeier, *Chemistry of Materials*, 2019, **31**, 8328-8337.

99. Y. Zhu, X. He and Y. Mo, *ACS Applied Materials & Interfaces*, 2015, **7**, 23685-23693.

100. J. Hu, S. Yang, Y. Pei, X. Wang, Y. Liao, S. Li, A. Yue, J.-Q. Huang and H. Yuan, *Particuology*, 2024, **86**, 55-66.

101. T. K. Schwietert, V. A. Arszelewska, C. Wang, C. Yu, A. Vasileiadis, N. J. J. de Klerk, J. Hageman, T. Hupfer, I. Kerkamm, Y. Xu, E. van der Maas, E. M. Kelder, S. Ganapathy and M. Wagemaker, *Nature Materials*, 2020, **19**, 428-435.

102. R. Koerver, F. Walther, I. Aygün, J. Sann, C. Dietrich, W. G. Zeier and J. Janek, *Journal of Materials Chemistry A*, 2017, **5**, 22750-22760.

103. J. Auvergniot, A. Cassel, D. Foix, V. Viallet, V. Seznec and R. Dedryvère, *Solid State Ionics*, 2017, **300**, 78-85.

104. F. Walther, R. Koerver, T. Fuchs, S. Ohno, J. Sann, M. Rohnke, W. G. Zeier and J. Janek, *Chemistry of Materials*, 2019, **31**, 3745-3755.

105. J. Auvergniot, A. Cassel, J.-B. Ledeuil, V. Viallet, V. Seznec and R. Dedryvère, *Chemistry of Materials*, 2017, **29**, 3883-3890.

106. A. Han, R. Tian, L. Fang, F. Wan, X. Hu, Z. Zhao, F. Tu, D. Song, X. Zhang and Y. Yang, *ACS Applied Materials & Interfaces*, 2022, **14**, 30824-30838.

107. K. Wissel, L. M. Riegger, C. Schneider, A. I. Waidha, T. Famprikis, Y. Ikeda, B. Grabowski, R. E. Dinnebier, B. V. Lotsch, J. Janek, W. Ensinger and O. Clemens, *ACS Applied Energy Materials*, 2023, **6**, 7790-7802.

108. R. F. Indrawan, H. Gamo, A. Nagai and A. Matsuda, *Chemistry of Materials*, 2023, **35**, 2549-2558.

109. H. Wang, Z. D. Hood, Y. Xia and C. Liang, *Journal of Materials Chemistry A*, 2016, **4**, 8091-8096.

110. H.-D. Lim, H.-K. Lim, X. Xing, B.-S. Lee, H. Liu, C. Coaty, H. Kim and P. Liu, *Advanced Materials Interfaces*, 2018, **5**, 1701328.

111. N. H. H. Phuc, K. Morikawa, M. Totani, H. Muto and A. Matsuda, *Solid State Ionics*, 2016, **285**, 2-5.

112. S. J. Sedlmaier, S. Indris, C. Dietrich, M. Yavuz, C. Dräger, F. von Seggern, H. Sommer and J. Janek, *Chemistry of Materials*, 2017, **29**, 1830-1835.

113. N. H. H. Phuc, M. Totani, K. Morikawa, H. Muto and A. Matsuda, *Solid State Ionics*, 2016, **288**, 240-243.

114. A. Ito, T. Kimura, A. Sakuda, M. Tatsumisago and A. Hayashi, *Journal of Sol-Gel Science and Technology*, 2022, **101**, 2-7.

115. S. Teragawa, K. Aso, K. Tadanaga, A. Hayashi and M. Tatsumisago, *Journal of Materials Chemistry A*, 2014, **2**, 5095-5099.

116. S. Teragawa, K. Aso, K. Tadanaga, A. Hayashi and M. Tatsumisago, *Chemistry Letters*, 2013, **42**, 1435-1437.

117. S. Teragawa, K. Aso, K. Tadanaga, A. Hayashi and M. Tatsumisago, *Journal of Power Sources*, 2014, **248**, 939-942.

118. Y. Subramanian, R. Rajagopal and K.-S. Ryu, *Scripta Materialia*, 2021, **204**, 114129.

119. R. Maniwa, M. Calpa, N. C. Rosero-Navarro, A. Miura and K. Tadanaga, *Journal of Materials Chemistry A*, 2021, **9**, 400-405.

120. D. Y. Oh, Y. J. Nam, K. H. Park, S. H. Jung, K. T. Kim, A. R. Ha and Y. S. Jung, *Advanced Energy Materials*, 2019, **9**, 1802927.

121. X. Wang, L. Ye, C.-W. Nan and X. Li, *ACS Applied Materials & Interfaces*, 2022, **14**, 46627-46634.

122. A.-K. Hatz, R. Calaminus, J. Feijoo, F. Treber, J. Blahusch, T. Lenz, M. Reichel, K. Karaghiosoff, N. M. Vargas-Barbosa and B. V. Lotsch, *ACS Applied Energy Materials*, 2021, **4**, 9932-9943.

123. J. Ruhl, L. M. Riegger, M. Ghidiu and W. G. Zeier, *Advanced Energy and Sustainability Research*, 2021, **2**, 2000077.

124. T.-T. Zuo, F. Walther, S. Ahmed, R. Rueß, J. Hertle, B. Mogwitz, K. Volz and J. Janek, *ACS Energy Letters*, 2023, **8**, 1322-1329.

125. S. W. Boettcher, S. Z. Oener, M. C. Lonergan, Y. Surendranath, S. Ardo, C. Brozek and P. A. Kempler, *ACS Energy Letters*, 2021, **6**, 261-266.

126. D. d. Olmo, M. Pavelka and J. Kosek, *Journal of Non-Equilibrium Thermodynamics*, 2021, **46**, 91-108.

127. Y. Qi, M. W. Swift, E. J. Fuller and A. A. Talin, *MRS Bulletin*, 2023, **48**, 1239-1246.

128. T. Nakamura, K. Amezawa, J. Kulisch, W. G. Zeier and J. Janek, *ACS Applied Materials & Interfaces*, 2019, **11**, 19968-19976.

129. P. Peljo and H. H. Girault, *Energy & Environmental Science*, 2018, **11**, 2306-2309.

130. T. Krauskopf, F. H. Richter, W. G. Zeier and J. Janek, *Chemical Reviews*, 2020, **120**, 7745-7794.

131. Q. Huang and Q. Wang, *Chinese Physics B*, 2016, **25**, 018213.

132. C. D. Alt, N. U. C. B. Müller, L. M. Riegger, B. Aktekin, P. Minnmann, K. Peppler

and J. Janek, *Joule*, 2024, **8**, 2755-2776.

133. L. M. Riegger, S. Mittelsdorf, T. Fuchs, R. Rueß, F. H. Richter and J. Janek, *Chemistry of Materials*, 2023, **35**, 5091-5099.

134. S. Wenzel, S. J. Sedlmaier, C. Dietrich, W. G. Zeier and J. Janek, *Solid State Ionics*, 2018, **318**, 102-112.

135. in *Chemical Kinetics of Solids*, 1995, DOI: https://doi.org/10.1002/9783527615537.ch01, pp. 1-18.

136. D. K. Singh, A. Henss, B. Mogwitz, A. Gautam, J. Horn, T. Krauskopf, S. Burkhardt, J. Sann, F. H. Richter and J. Janek, *Cell Reports Physical Science*, 2022, **3**, 101043.

137. Y. S. Byeon, D. Kim, S. A. Han, J. H. Kim and M.-S. Park, *Advanced Energy and Sustainability Research*, 2024, **5**, 2400135.

138. Y. Jiang, A. Lai, J. Ma, K. Yu, H. Zeng, G. Zhang, W. Huang, C. Wang, S.-S. Chi, J. Wang and Y. Deng, *ChemSusChem*, 2023, **16**, e202202156.

139. R. Ruess, S. Schweidler, H. Hemmelmann, G. Conforto, A. Bielefeld, D. A. Weber, J. Sann, M. T. Elm and J. Janek, *Journal of The Electrochemical Society*, 2020, **167**, 100532.

140. E. Trevisanello, R. Ruess, G. Conforto, F. H. Richter and J. Janek, *Advanced Energy Materials*, 2021, **11**, 2003400.

141. F. Zhang, Y. Guo, L. Zhang, P. Jia, X. Liu, P. Qiu, H. Zhang and J. Huang, *eTransportation*, 2023, **15**, 100220.

142. L. Guan, Y. Shi, C. Gao, T. Wang, J. Zhou and R. Cai, *Electrochimica Acta*, 2023, **440**, 141669.

143. H. Liu, Y. Liang, C. Wang, D. Li, X. Yan, C.-W. Nan and L.-Z. Fan, *Advanced Materials*, 2023, **35**, 2206013.

144. J. C. Stallard, L. Wheatcroft, S. G. Booth, R. Boston, S. A. Corr, M. F. L. De Volder, B. J. Inkson and N. A. Fleck, *Joule*, 2022, **6**, 984-1007.

145. F. P. McGrogan, T. Swamy, S. R. Bishop, E. Eggleton, L. Porz, X. Chen, Y.-M. Chiang and K. J. Van Vliet, *Advanced Energy Materials*, 2017, **7**, 1602011.

146. S. F. Pugh, *The London, Edinburgh, and Dublin Philosophical Magazine and Journal of Science*, 1954, **45**, 823-843.

147. L. Wang, R. Xie, B. Chen, X. Yu, J. Ma, C. Li, Z. Hu, X. Sun, C. Xu, S. Dong, T.-S. Chan, J. Luo, G. Cui and L. Chen, *Nature Communications*, 2020, **11**, 5889.

148. K. Takada, *Langmuir*, 2013, **29**, 7538-7541.

149. J. Haruyama, K. Sodeyama, L. Han, K. Takada and Y. Tateyama, *Chemistry of Materials*, 2014, **26**, 4248-4255.

150. W.-P. Chen, H. Duan, J.-L. Shi, Y. Qian, J. Wan, X.-D. Zhang, H. Sheng, B. Guan, R. Wen, Y.-X. Yin, S. Xin, Y.-G. Guo and L.-J. Wan, *Journal of the American Chemical Society*, 2021, **143**, 5717-5726.

151. S.-K. Jung, H. Gwon, S.-S. Lee, H. Kim, J. C. Lee, J. G. Chung, S. Y. Park, Y. Aihara and D. Im, *Journal of Materials Chemistry A*, 2019, **7**, 22967-22976.

152. F. Walther, F. Strauss, X. Wu, B. Mogwitz, J. Hertle, J. Sann, M. Rohnke, T. Brezesinski and J. Janek, *Chemistry of Materials*, 2021, **33**, 2110-2125.

153. F. Walther, S. Randau, Y. Schneider, J. Sann, M. Rohnke, F. H. Richter, W. G. Zeier and J. Janek, *Chemistry of Materials*, 2020, **32**, 6123-6136.

154. F. Strauss, J. H. Teo, A. Schiele, T. Bartsch, T. Hatsukade, P. Hartmann, J. Janek and T. Brezesinski, *ACS Applied Materials & Interfaces*, 2020, **12**, 20462-20468.

155. K. Homma, Y. Liu, M. Sumita, R. Tamura, N. Fushimi, J. Iwata, K. Tsuda and C. Kaneta, *The Journal of Physical Chemistry C*, 2020, **124**, 12865-12870.

156. T.-T. Zuo, F. Walther, J. H. Teo, R. Rueß, Y. Wang, M. Rohnke, D. Schröder, L. F. Nazar and J. Janek, *Angewandte Chemie International Edition*, 2023, **62**, e202213228.

157. S. Wenzel, T. Leichtweiss, D. Krüger, J. Sann and J. Janek, *Solid State Ionics*, 2015, **278**, 98-105.

158. C. D. Alt, N. U. C. B. Müller, L. M. Riegger, B. Aktekin, P. Minnmann, K. Peppler and J. Janek, *Joule*, 2024, DOI: https://doi.org/10.1016/j.joule.2024.07.006.

159. S.-K. Otto, L. M. Riegger, T. Fuchs, S. Kayser, P. Schweitzer, S. Burkhardt, A. Henss and J. Janek, *Advanced Materials Interfaces*, 2022, **9**, 2102387.

160. J. M. Lee, Y. S. Park, J.-W. Moon and H. Hwang, *Frontiers in Chemistry*, 2021, **9**.

161. D. K. Singh, T. Fuchs, C. Krempaszky, B. Mogwitz and J. Janek, *Advanced Science*, 2023, **10**, 2302521.

162. J. L. Barton, J. O. Bockris, apos, m. and A. R. J. P. Ubbelohde, *Proceedings of the Royal Society of London. Series A. Mathematical and Physical Sciences*, 1962, **268**, 485-505.

163. C. Monroe and J. Newman, *Journal of The Electrochemical Society*, 2003, **150**, A1377.

164. Y. Lu, C.-Z. Zhao, H. Yuan, X.-B. Cheng, J.-Q. Huang and Q. Zhang, *Advanced Functional Materials*, 2021, **31**, 2009925.

165. H. Sun, A. Celadon, S. G. Cloutier, K. Al-Haddad, S. Sun and G. Zhang, *Battery Energy*, 2024, **3**, 20230062.

166. K. Park and J. B. Goodenough, *Advanced Energy Materials*, 2017, **7**, 1700732.

167. M. Rosso, C. Brissot, A. Teyssot, M. Dollé, L. Sannier, J.-M. Tarascon, R. Bouchet and S. Lascaud, *Electrochimica Acta*, 2006, **51**, 5334-5340.

168. C. Monroe and J. Newman, *Journal of The Electrochemical Society*, 2005, **152**, A396.

169. G. Pustorino, H. Jagad, W. Li, M. Feng, M. Poma, J. Ko, P. Johari and Y. Qi, *Chemistry of Materials*, 2025, **37**, 313-321.

170. D. Cao, X. Sun, Q. Li, A. Natan, P. Xiang and H. Zhu, *Matter*, 2020, **3**, 57-94.

171. H. Liu, X.-B. Cheng, J.-Q. Huang, H. Yuan, Y. Lu, C. Yan, G.-L. Zhu, R. Xu, C.-Z. Zhao, L.-P. Hou, C. He, S. Kaskel and Q. Zhang, *ACS Energy Letters*, 2020, **5**, 833-843.

172. M. Solazzo, F. J. O'Brien, V. Nicolosi and M. G. Monaghan, *APL Bioengineering*, 2019, **3**.

173. P. Gorai, T. Famprikis, B. Singh, V. Stevanović and P. Canepa, *Chemistry of Materials*, 2021, **33**, 7484-7498.

174. Y. Hong, S. Yoo, J. Han, J. Kim, Y. Lee, Y. Jho, Y. S. Kim and D. S. Hwang, *Communications Chemistry*, 2024, **7**, 182.

175. Y. Li, X. Zhang, G. He and F. Zhang, *International Journal of Hydrogen Energy*, 2017, **42**, 2360-2369.

176. D. Brandell, J. Mindemark and G. Hernández, *Polymer-based Solid State Batteries*, Walter de Gruyter GmbH & Co KG, 2021.

177. E. Akiyama, Y. Nagase, N. Koide and K. Araki, *Liquid Crystals*, 1028, **July 1**, 1029-1037.

178. D. Mecerreyes, *Progress in Polymer Science*, 2011, **36**, 1629-1648.

179. Y. Tominaga and K. Yamazaki, *Chemical Communications*, 2014, **50**, 4448-4450.

180. A. S. Michaels, *Industrial & Engineering Chemistry*, 1965, **57**, 32-40.

181. R. Saikaew, W. Meesorn, J. O. Zoppe, C. Weder and S. T. Dubas, *Macromolecular Materials and Engineering*, 2019, **304**, 1900245.

182. J. K. Bediako, E. S. M. Mouele, Y. El Ouardi and E. Repo, *Chemical Engineering*

Journal, 2023, **462**, 142322.

183. V. S. Meka, M. K. G. Sing, M. R. Pichika, S. R. Nali, V. R. M. Kolapalli and P. Kesharwani, *Drug Discovery Today*, 2017, **22**, 1697-1706.

184. B. Philipp, H. Dautzenberg, K.-J. Linow, J. Kötz and W. Dawydoff, *Progress in Polymer Science*, 1989, **14**, 91-172.

185. A. D. Kulkarni, Y. H. Vanjari, K. H. Sancheti, H. M. Patel, V. S. Belgamwar, S. J. Surana and C. V. Pardeshi, *Artificial Cells, Nanomedicine, and Biotechnology*, 2016, **44**, 1615-1625.

186. M. Buriuli and D. Verma, in *Advances in Biomaterials for Biomedical Applications*, eds. A. Tripathi and J. S. Melo, Springer Singapore, Singapore, 2017, DOI: 10.1007/978-981-10-3328-5_2, pp. 45-93.

187. J. N. Putro, V. B. Lunardi, F. E. Soetaredjo, M. Yuliana, S. P. Santoso, I. G. Wenten and S. Ismadji, *Processes*, 2021, **9**, 1796.

188. V. A. Kabanov and A. B. Zezin, *Pure and Applied Chemistry*, 1984, **56**, 343-354.

189. E. Tsuchida, *Journal of Macromolecular Science, Part A*, 1994, **31**, 1-15.

190. A. E. Neitzel, Y. N. Fang, B. Yu, A. M. Rumyantsev, J. J. de Pablo and M. V. Tirrell, *Macromolecules*, 2021, **54**, 6878-6890.

191. S. G. M. van Lange, D. W. te Brake, G. Portale, A. Palanisamy, J. Sprakel and J. van der Gucht, *Science Advances*, 2024, **10**, eadi3606.

192. S. Meng, Y. Liu, J. Yeo, J. M. Ting and M. V. Tirrell, *Colloid and Polymer Science*, 2020, **298**, 887-894.

193. Q. Wang and J. B. Schlenoff, *Macromolecules*, 2014, **47**, 3108-3116.

194. M. Tirrell, *ACS Central Science*, 2018, **4**, 532-533.

195. H. M. Fares and J. B. Schlenoff, *Journal of the American Chemical Society*, 2017, **139**, 14656-14667.

196. J. Fu, H. M. Fares and J. B. Schlenoff, *Macromolecules*, 2017, **50**, 1066-1074.

197. B. Jirgensons, M. E. Straumanis and A. W. Hutchison, *Journal of The Electrochemical Society*, 1955, **102**, 234Ca.

198. Q. Gan, N. Qin, Y. Zhu, Z. Huang, F. Zhang, S. Gu, J. Xie, K. Zhang, L. Lu and Z. Lu, *ACS Applied Materials & Interfaces*, 2019, **11**, 12594-12604.

199. M. Li, L. Wang, B. Yang, T. Du and Y. Zhang, *Electrochimica Acta*, 2014, **123**, 296-302.

200. P. Minnmann, L. Quillman, S. Burkhardt, F. H. Richter and J. Janek, *Journal of*

The Electrochemical Society, 2021, **168**, 040537.

5.2 List of scientific publications

July, 2021	*The role of polymers in lithium solid-state batteries with inorganic solid electrolytes*; Sen, Sudeshna Trevisanello, Enrico Niemöller, Elard Shi, Bing-Xuan Simon, Fabian J. Richter, Felix H.; J. Mater. Chem. A, 2021,9, 18701-18732
May, 2023	*Mitigating Contact Loss in Li_6PS_5Cl-Based Solid-State Batteries Using a Thin Cationic Polymer Coating on NCM*; Bing-Xuan Shi, Yuriy Yusim, Sudeshna Sen, Thomas Demuth, Raffael Ruess, Kerstin Volz, Anja Henss, Felix H. Richter; Adv. Energy Mater., 13: 2300310.
November, 2024	*Lithiated polymer coating for interface stabilization in Li_6PS_5Cl-based solid-state batteries with high-nickel NCM*; Bing-Xuan Shi, Franjo Weber, Yuriy Yusim, Thomas Demuth, Kilian Vettori, Andreas Münchinger, Giorgi Titvinidze, Kerstin Volz, Anja Henss, Rüdiger Berger, and Felix H. Richter; J. Mater. Chem. A, 2025,13, 2600-2614

5.3 List of patent applications

October, 2023	Polymer-coated Electrode Active Material, Its Manufacturing and Usage, with application No. EP22199267.0 and PCT publication No. WO 2024/068975 A1.
September, 2024	Modified Sulfur-containing Solid Electrolyte and Method for Producing It, with application No. EP24199168.6.

5.4 List of conference contributions

October, 2022	17th International Symposium on Polymer Electrolytes (ISPE-17) Oral presentation
March, 2023	Polystorage Winter School 2023 in Sestriere, Italy Best Poster Award
September, 2023	European Symposium On Polymer Electrolytes For Battery Applications (ESPE 23) in Karlsruhe, Germany Best Poster Award
September,	International Meeting on Lithium Batteries in Hong Kong, China

2024	Poster presentation

6. Acknowledgements

First and foremost, I would like to express my deepest gratitude to my supervisors, **Felix H. Richter** and **Prof. Dr. Jürgen Janek**. In Mandarin, there is a word—師傅 (Shīfù)—which I feel best represents my highest respect and appreciation for them. **Felix** has been an invaluable mentor in my scientific research and paper writing. While I still see much room for improvement in myself, his encouragement has always motivated me. His patience and support have been a driving force, helping me move forward, especially during moments of self-doubt or frustration. The idea of using polycation as a coating material in my first publication originated from him. I still vividly remember my first experiment in B106, where we synthesized the polycation together—his enthusiasm and insightful discussions made it an inspiring experience. Over the past four years, he has consistently shown a supportive and encouraging attitude, always urging me to explore new ideas. I always look forward to sharing my new experimental ideas with him.

I am also deeply grateful to **Prof. Janek**, who has significantly shaped my understanding of electrochemistry. Every course he teaches is genuinely impactful, allowing me to understand scientific phenomena from new perspectives. Every course from him makes me feel like I am experiencing a whole new trip. His lectures have broadened my way of thinking and deepened my understanding of the field of solid-state diffusion and chemical potential, and I sincerely hope to have more opportunities to learn from him in the future.

Secondly, I would like to extend my heartfelt appreciation to my **parents**. Their unwavering support has been my foundation, always catching me when I felt sad or frustrated. Despite the 9,372 km between Taipei and Giessen, I always feel their care and warmth. They are my home and my most significant source of strength.

Thirdly, I want to thank my **colleagues**, who are also my **friends**. We shared incredible moments—traveling, hanging out, and enjoying different activities. These experiences are precious to me, and even now, thinking back on our funny moments brings a smile to my face. They know me well enough to tolerate my terrible jokes, and I believe I may have even "infected" some of them with my weird but amusing jokes. I am also grateful for their support in experiments and our many inspiring discussions.

Finally, I want to express my sincerest thanks to my girlfriend, **Yang Yu**. She introduced me to using Blender software, helping me create fancy schematics and guiding me in figure design. More than that, she has been a constant source of support, alleviating much of the pressure during my doctoral journey and bringing precious memories and joy to my everyday life.

Ultimately, I wish **all my supervisors, friends, parents, and girlfriend** the best of luck and happiness in the future. These are my deepest acknowledgments and warmest wishes.